325

CNS-REP-42

Fermilab Library
0 1160 0092335 3

ISSN 1343-2230
CNS – REP – 42
December, 2001

CNS Report

CNS/RIKEN Workshop

on

Physics with Low-Energy RI Beams

RIKEN Campus, Wako, Japan

August 23-25, 2000

Center for Nuclear Study(CNS)

Graduate School of Science, the University of Tokyo
Wako Branch at RIKEN, Hirosawa 2-1, Wako, Saitama, 351-0198 Japan
Correspondence: cnsoffice@cns.s.u-tokyo.ac.jp

FERMILAB
FEB 4 2002
LIBRARY

CNS/RIKEN Workshop

「Physics with Low-Energy RI Beams」

Ohkouchi Hall, RIKEN Wako Campus

August 23 (Wednesday) – 25 (Friday), 2000

Organizing Committee

S. Kubono, S. Shimoura, I. Tanihata, K. Asahi,
T. Kajino, T. Otsuka, H. Horiuchi, T. Shimoda,
Y. Gono, H. Miyatake, T. Shinozuka, K. Kato,
T. Teranishi, H. Ueno, Y. Mochizuki, N. Itagaki,
T. Kishida, Y. Kobayashi, Y. Mizoi, Y. Yanagisawa, H. Watanabe

Preface

The CNS/RIKEN workshop on Physics with Low-Energy RI Beams has been held during August 23-25, 2000 at Ohkouchi hall of RIKEN Wako campus.

The radioactive-isotope beam (RIB) is now applied not only to the studies of nuclear physics, but also to other scientific regions such as nuclear astrophysics, material science and so on. Especially for the energy region of below 10 MeV/nucleon, it should be noticed that the low-energy RIB with the high intensity is very useful to study nuclear spectroscopy, which can be also combined with the conventional methods.

Although we can use RIBs with the medium and high energies at RIKEN and other facilities in the world, facilities with low-energy RIBs regularly available are limited, and available beam intensity, energy and species are also limited. In Japan, however, E-group at KEK has been intensively studying and developing the facility of the very-low-energy RIB, and also, Center for Nuclear Study (CNS) has been now developing "CRIB" , which can produce the RIB with high intensities and the energy region of below 10 MeV/nucleon, in cooperated with RIKEN.

In this workshop, we reviewed and summarized the present status of the science with RIB in nuclear physics, nuclear astrophysics, material science and so on, and discussed the future plans of physical study using the high-intensity and low-energy RIB. Especially, we focused on the studies with CRIB and discussed them from both experimental and theoretical points of view.

This workshop was supported in part by Grant-in-Aid for Scientific Research of the Ministry of Education, Culture, Sports, Science and Technology of Japan, Grant number B-2 10440070 of S. Kubono, and Grant number B-2 11440081 of S. Shimoura.

Contents

【1】Nuclear Physics of Unstable Nuclei

Reaction Mechanisms for Synthesis of the Superheavy Elements – Present Status and Future Developments –	Y. Abe (YITP)	3
Synthesis of Superheavy Elements by using Neutron Rich Radio-Isotope Beams	M. Ohta (Konan Univ.)	11
Decay properties of superheavy nuclei predicted by nuclear mass formulas	H. Koura (Waseda Univ.)	22
Fusion Reaction of Neutron-Rich Nuclei	Y. X. Watanabe (RIKEN)	30
sd-pf 殻領域における有効相互作用と不安定核の構造	Y. Utsuno (JAERI)	38
Shell model study on Thomas-Ehrman shifts in *sd*-shell nuclei and its relevance to *rp*-process nucleosynthesis	H. Nakata (Chiba Univ.)	65
Single particle wave functions and density distribution for oxygen isotopes	R. Fujimoto (Univ. of Tokyo)	73
Analysis of the Coulomb breakup reaction of ^{6}He	T. Myo (Hokkaido Univ.)	78
Soft dipole resonance in ^{6}He	S. Nakayama (Univ. of Tokushima)	83
Molecular states in highly-excited ^{12}Be	M. Ito (Hokkaido Univ.)	89
Cluster structure in the Light Unstable Nuclei	Y. Kanada-En'yo (KEK)	96
Superdeformation in the newly discovered superheavy elements	Zhongzhou Ren (RCNP)	102
Study of the *s*-waves in ^{10}Li nuclei and the mirror, ^{10}N	H. Masui (Hokkaido Univ.)	109
Coherence and decoupling in E1 and E2 excitations in nuclei near drip lines	H. Sagawa (Univ. of Aizu)	118
Structure of ^{11}Be: Magnetic Moment and Coulomb Displacement Energy	T. Suzuki (Nihon Univ.)	128
理研における超重元素探索実験	K. Morita (RIKEN)	

【2】CRIB and its Applications

Mirror Nuclear Moments in the Light Mass Region	M. Fukuda (Osaka Univ.)	137
Electromagnetic moments of neutron-rich nuclei	H. Ogawa (TIT)	143
CRIB の概要と物理	S. Kubono (CNS)	149
Installation of Low-Energy RI Beam Separator CRIB	Y. Yanagisawa (RIKEN)	158
Technique of Low-Energy RI Beam Separation by CRIB and Experiment of Elastic Resonance Scattering on Unstable Nulcei	T. Teranishi (CNS)	160
Production of RI beams by fusion reactions	T. Kishida (RIKEN)	165
In-beam gamma-ray spectroscopy at CRIB	Y. Gono (Kyushu Univ.)	172
Coulomb excitation experiments with low-energy unstable nuclear beams at CRIB	T. Morikawa (Kyushu Univ.)	180
Cluster Transfer Reactions for Neutron-Rich Nuclei	S. Shimoura (CNS)	186
Systematic measurement of deep inelastic scatterings involved by unstable nuclei	Y. Mizoi (CNS)	189

【3】Nuclear Astrophysics

A Trial to Measure $^{12}C+^{4}He \rightarrow ^{16}O$ Reaction Rate of Astrophysical Interest in Kyusyu University	S. Morinobu (Kyushu Univ.)	195
Screening effects by bound electrons in nuclear reactions at extremely low energies	N. Takigawa (Tohoku Univ.)	202
Nuclear Astrophysics with Laser-induced Inverse Compton *gamma* Rays	H. Utsunomiya (Konan Univ.)	208
Supernova and r-process: challenges with unstable nuclei	K. Sumiyoshi (NCT)	218
Abundance Anomaly in Globular Cluster Red Giants	M. Aikawa (Hokkaido Univ.)	225
Determination of Ω_b; Constraints from Big Bang Nucleosynthesis and CMB Anisotropy Measurements	M. Orito (NAO)	227
Present Status of Nuclear Data Evaluation Work at JAERI Nuclear Data Center	T. Nakagawa (JAERI)	233
Discovery of *s*-process Element-rich Extremely Metal-deficient Star and the Impact on Stellar Models	N. Iwamoto (NAO)	241
A method to deduce a direct capture reaction rate from a corresponding transfer reaction	N. Imai (Univ. of Tokyo)	248
Experimental methods for nuclear astrophysics research	T. Motobayashi (Rikkyo Univ.)	254

【4】Techniques for Production and Experiment of RIB

KEK-JAERI RNB facility	H. Miyatake (KEK)	263
Production of low energy radioactive nuclear beam and measurement of the (α, n) reaction for astrophysical inetrest at JAERI tandem facility	T. Hashimoto (Science Univ. of Tokyo)	271
Design conception and ion-optical properties of DUMAS	T. Noro (RCNP)	279
The Fragment Separator at RCNP	T. Shimoda (Osaka Univ.)	287
理研RIビーム分離装置	T. Kubo (RIKEN)	

【5】Applications of RIB

Measurement of β-unstable ^{12}B mobilty in suprefluid helium	S. Shimizu (Osaka Univ.)	299
A research project on chemical properties of the heavy actinide and trans-actinide elemetnts	A. Yokoyama (Osaka Univ.)	303
Spectroscopy of Highly Charged Ions using Tokyo-EBIT	S. Otani (Univ. of Electro-Communications)	313
原子炉出力上昇の時定数が一割以上も食い違うI-137, Br-88 の P_n 値の精度を 2% にしたい	K. Shinmatsu (Aichi Shukutoku Univ.)	318
不安定核プローブによる結晶中不純物の超微細相互作用の研究	K. Sato (ISIR)	
RIプローブによる固体中の原子ジャンプ過程の研究	Y. Yoshida (Shizuoka Inst. of Sci. and Tech.)	
RIイオンガイド法による極低速RIビームの可能性	M. Wada (RIKEN)	

【1】 Nuclear Physics of Unstable Nuclei

Reaction Mechanisms for Synthesis of the Superheavy Elements – Present Status and Future Developments –

Yasuhisa Abe
Yukawa Institute for Theoretical Physics
Kyoto Univ. Kyoto 606-8502, Japan

October 2000

Abstract

Recent developments of the nuclear reaction theory for synthesis of the superheavy elements are briefly reviewed. Emphasis is made on dynamical spects of fusion process of massive systems. Remarks for further studies are also given at the end.

1 Introduction

The limit of nuclear stability in heavy mass region is macroscopically understood by the liquid drop model, i.e., by the fissility parameter x being to be equal or larger than 1. This is the reason why there is almost no abundance for heavier elements than U. But quantum effects of nucleonic motion are known to give rise to an additional stability or binding energy among known nucleides, which provides the basis of the nuclear shell model. The extension of the idea to unknown heavier systems leads to the existence of the superheavy elements which is already a long-standing prediction. It is sure that there exists a stable region in the very heavy unknown region of the nuclear chart, though there are still certain ambiguities concerning where is the center of the stability in the superheavy region. By the phenomenological single particle model, for example, it is predicted to be around Z= 114 and N=184, i.e., there the additional binding energy, so-called the shell correction energy is at maximum among the neighbouring nucleides of the region.[1] But it is rather peculiar that there has been no reaction theory proposed for how to synthesize them. Therefore, experiments have been made more or less empirically.[2]

2 Nuclear reaction processes

The most usual way is to use heavy-ion (HI) fusion reactions. But mechanisms of HI-fusion reactions in massive systems are not yet known well, while in lighter systems they are well understood. Once we have a reasonable theory which enables us to predict HI-fusion probability, i.e., formation probability of the compound nuclei, then, residues cross sections could be predicted by the use of the statistical theory of decay, based on the concept of the compound nucleus of N. Bohr.[3] The formula for residue cross sections is given as

$$\sigma_{res}(E_{c.m.}) = \frac{\pi}{k^2}\Sigma(2J+1)\cdot P^J_{fus}(E_{c.m.})\cdot P^J_{surv}(E_{ex}) \tag{1}$$

, where $P_{fus}(E_{c.m.})$ and $P_{surv}(E_{ex})$ denote the fusion probability as a function of incident energy and the survival probability as a function of excitation energy of the compound nucleus. That is, we have to take into account the whole reaction process from encounter of heavy ions to evaporation residues, as schematically shown in Fig. 1. As seen from Fig. 1,

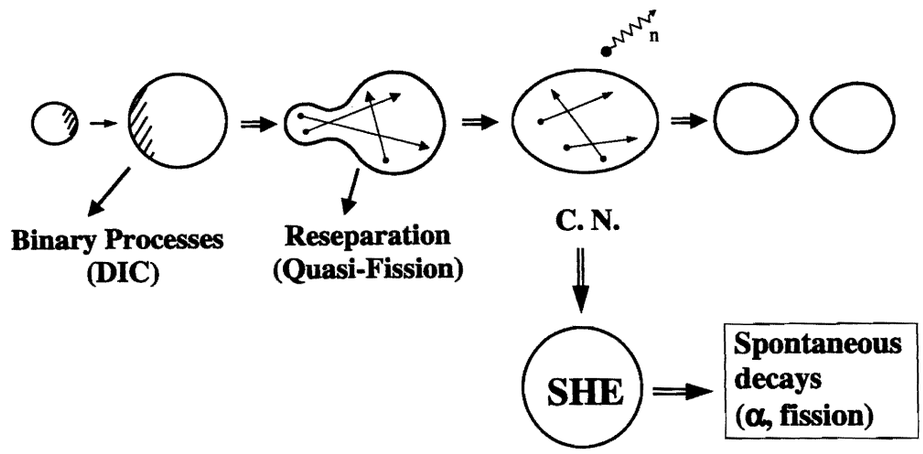

Figure 1: Reaction processes for SHE synthesis is schematically displayed from an encounter of incident heavy ions to SHE residue. It should be noted that fusion is achieved by two successively processes; approaching phase and dynamical evolution of composite system.

there are two processes for fusion, i.e., before reaching the spherical compound nuclei or around; approaching phase before two incident nuclei touch each other and evolution of the composite system toward the compound nuclei with large probability of reseparation. This means that the fusion probability P_{fus} is given as follows,

$$P_{fus} = P_{cont} \cdot P_{form} \tag{2}$$

, where P_{cont} and P_{form} denote contact probability of the incident ions and formation probability of the compound nuclei, respectively. In lighter systems, P_{form} is not necessary,i.e., is equal to 1, while in massive systems P_{form} is extremely important, because there are so-called quasi-fission and fast-fission processes competing with compound nucleus formation. Anyhow, the two factors in Eq. 1 have opposite energy-dependences, and will be discussed below more in detail. The statistical theory of decay of the compound nucleus is wellknown and well established, though there are still ambiguities in parameters. Since decay modes are dominantly neutron emission and fission, the survival probability is expressed as follows,

$$P^J_{surv}(E_{ex}) = \frac{\Gamma^J_n(E_{ex})}{\Gamma^J_n(E_{ex}) + \Gamma^J_f(E_{ex})} \tag{3}$$

, where Γ_n and Γ_f denotes probabilities of neutron emission and of fission decay, respectively. The former is given by Weisskopf formula [4] while the latter by Bohr-Wheeler one[5], or Kramers formula [6] including friction effects. For cases with excitation energy higher than 1n, 2n, ... emission thresholds, we have to repeat the factor given in Eq. 3 with corresponding excitation energies. In realistic calculations to be compared with experimental energy spectra, cascade type computer codes are used, taking into account kinetic energy distribution of neutron emitted at each step. If the compound nuclei formed is in rather high excitation,

the system immediately undergoes fission, because of the extremely low or almost no barrier against fission in the superheavy nucleides, as is naturally with the fissility parameter being close to 1. That is, the survival probability is a rapidly decreasing function of excitation energy. Therefore, the excitation energy of the compound nuclei initially formed should be as low as possible. For that purpose, one has to choose favourable combinations of projectile and target nuclei, taking into account reaction Q-value. Let us take examples of synthesizing the element Z=118 with neutron number N=176, and the element Z=120 with N=178. In Fig. 2, excitation energies of compound nuclei formed at Bass interaction barrier top [7] are shown over all the possible combinations of projectiles and targets. As is readily seen, there are two distinct minima in each system. In the former system, they are around Kr + Pb and Xe + Gd combinations, the former of which is just the system that Berkeley group [8] made experiments with. Then, they are surely favourable in the survival probability $P_{surv}(E_{ex})$. But there is the other factor $P_{fus}(E_{cm})$ in Eq. 1 which determines residue cross sections, combined with $P_{surv}(E_{ex})$. Naturally, it increases as incident energy increases, firstly for getting rid of Coulomb barrier as is in lighter systems (described by P_{cont}) and secondly for passing over the conditional saddle point, i.e., for overcoming so-called fusion hindrance (described by P_{form}). It automatically gives rise to an increase of excitation energy of the compound nuclei formed, which results in a decrease of the survival probability. Therefore, one has to compromise two conflicting factors, i.e., has to find an optimum incident energy to maximize the final residue cross sections.

2.1 dissipation-fluctuation dynamics toward the compound nuclei

As mentioned above, there is the fusion hindrance in massive systems, which is clearly exemplified by the extra-push or the extra-extra-push energy necessary for the system to fuse into compound nuclei,and which is known to be more pronounced in systems with larger values of Zp*Zt.[9] The situation is readily seen in the schematic Fig. 3. So, the combination corresponding to the first minimum (smaller Z_p) in Fig. 2 would be unfavourable and even more to the second one, though more favoured in excitation energy as stated above. In order to synthesize the superheavy elements, we have to find the optimum condition over all the possible combinations of projectiles and targets, taking into account not only P_{surv} but also P_{fus}. The dynamical evolutions toward the compound nuclei are usually solved by the use of multi-dimensional Langevin equation. Recently, an analytic expression [10] of probability for passing over an inverted parabolic barrier under dissipation has been obtained. In one dimensional case, it is reduced into a simple error function. Using that expression, extra-push energy necessary for fusion is estimated as

$$K_c = (\frac{\beta + \beta'}{2w})^2 \cdot B \tag{4}$$

, where β is the reduced friction γ/m and β' is equal to $\sqrt{\beta^2 + 4w^2}$ with w being the curvature of the barrier. B denotes the height of the barrier relative to the energy of the contact configuration. In the weak friction limit, $\beta \simeq 0$, $K_c \simeq B$ which is trivial, while in the overdamped limit, $\beta \gg 2 \cdot w$, $K_c \simeq (\beta/w)^2 \cdot B \simeq 10 \cdot B$ with One-body model.[11] The problem remains is an extension to the multi-dimensional cases for the purpose of applications to realistic cases, but a concise expression such as Eq. 4 is not easy to obtain. Realistic calculations of energy-dependence of fusion probabilities are being made by solving Langevin, Smoluchowski Eqs. numerically. The latter Eq. is only suitable for the cases of complete dissipation of incident energy, i.e., collective momenta are completely in equilibrium and then evolutions of coordinates, i.e. diffusions are treated. This is more or less consistent with the results obtained in the calculations of the approaching phase discussed below. But if the dissipation is not so strong, one has to employ the former one, i.e., Langevin Eq.[12]

Attempts are also being made to take into account effects of multi-dimensional evolutions in an analytical way.[13]

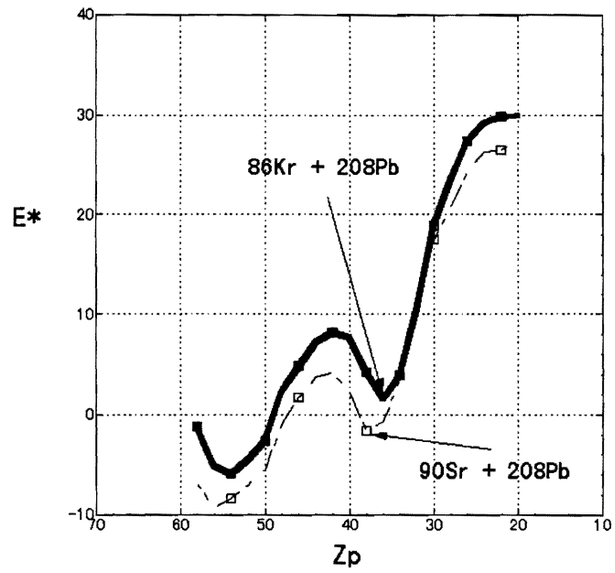

Figure 2: Excitation energies of compound nuclei formed at Bass barrier are given over possible projectiles. Neutron numbers of projectiles and targets are optimized, i.e., are chosen so as to give the lowest value for excitation energy. Two minima are essentially due to shell effects of the projectiles and targets. Hot fusion path corresponds to the smaller Z_p side, i.e., the righthand side.

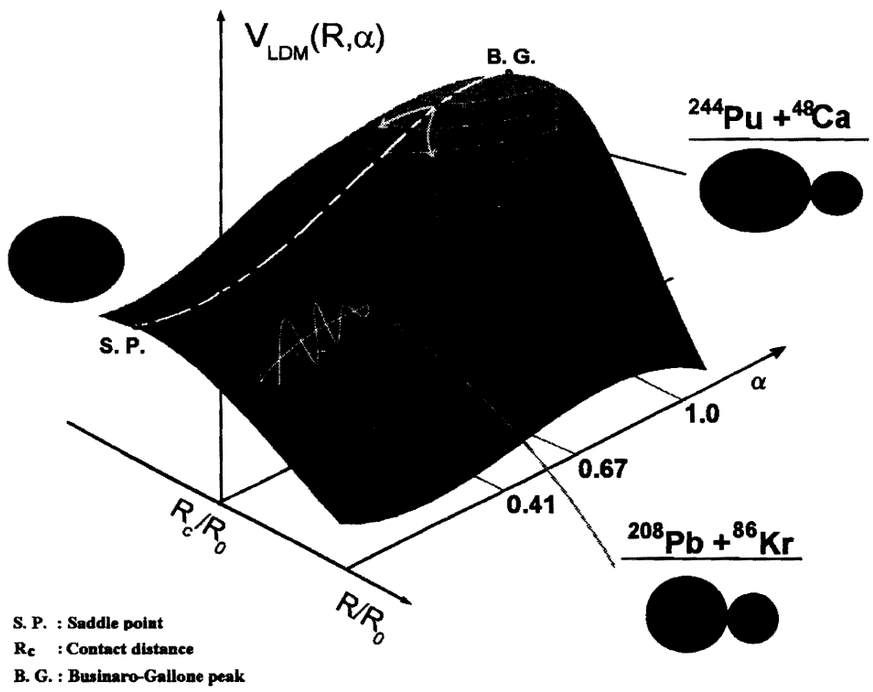

Figure 3: Characteristic feature of liquid drop energy surface is schematically shown. It is crucial that distance between contact point and conditional saddle varies as mass-asymmetry α changes. In larger α (like ^{244}Pu+^{48}Ca), they are very close, while in smaller α, i.e., near the mass-symmetry (like ^{208}Pb+^{86}Kr), they are far apart and in addition, height of conditional saddle relative to contact is larger. The system has to overcome it under strong energy dissipation in order to fuse into spherical compound nucleus or around.

2.2 dynamics of contact of two incident nuclei

Another recent development is about the approaching phase up to contact of incident heavy ions, i.e., contact of two nuclear surface, after which dynamical evolutions of shapes of the composite system are described by the multi-dimensional Langevin equation as discussed above. In other words, results of the analyses of the approaching phase provide precise initial conditions for subsequent dynamical evolutions of the whole system. In order to facilitate the analyses, we employ the surface friction model.[14] The classical equation of motion is given as follows,

$$\frac{dp_r}{dt} = -\frac{\partial U}{\partial r} - K_r \frac{p_r}{m} + R_r(t) \tag{5}$$

, where

$$K_r = k_r^0 \cdot \left(\frac{\partial U_N}{\partial r}\right)^2, K_r^0 = 3.5 \times 10^{-23} s/MeV \tag{6}$$

As the nuclear potential we employ that of Gross and Kalinowski [15] which is essentially a folding potential. A preliminary result is shown in Fig. 4[16], where you can see that the incident energy is fully damped at the contact. Now an extension is being made so as to include angular momentum dissipation.

3 Remarks

For quantitative predictions of residue cross sections of the superheavy elements, we need to know precisely physical parameters such as inertia masses, friction coefficients for collective degrees of freedom as functions of excitation or temperature. Especially it is the case for cold fusion path. So far, we have employed One-body model for friction which is quite strong and essentially temperature-independent, although friction should tend to zero in the low excitation limit. Microscopic theories such as Linear Response Theory [17] predict energy-, or temperature-dependences, which should be somehow incorporated into the phenomenological analyses of the reactions. The same applies to inertia mass tensor.

One more point about the limitation of the classical model. Since the probabilities obtained by the classical fluctuation-dissipation dynamics are very small in certain cases, the dissipative quantum tunneling probability[18], which is expected to be small, should also be investigated seriously in both fusion and fission processes.

The author appreciates long time collaborations with Konan group, which have given rise to many fruitful results and to new insights on the subject. He also likes to thank Drs. D. Boilley and B. Giraud concerning the collaboration on the analytic expressions for passing-over probability, and Dr. G. Kosenko concerning the analyses of the contact dynamics that are being done at RIKEN. Acknowledgments should be addressed also to Drs. S. Yamaji and P. Möller for their courtesies of providing their computer programs. At last but not at least he likes to thank the experimental groups at Dubna, GSI, GANIL and RIKEN for having provided opportunities for discussions and new experimental information promptly, which have stimulated the theoretical studies enormously.

References

[1] P. Möller, J.R. Nix, W.D. Myers and W.J. Swiatecki, *The Atom. and Nucl. Data Tables* **59** (1995) 185.

[2] see for example, a review article by S. Hofmann, *Rep. Prog. Phys.* **61**, (1998) 639.

[3] N. Bohr, *Nature* **137** (1936) 344.

[4] V. Weisskopf, *Phys. Rev.* **52** (1937) 295.

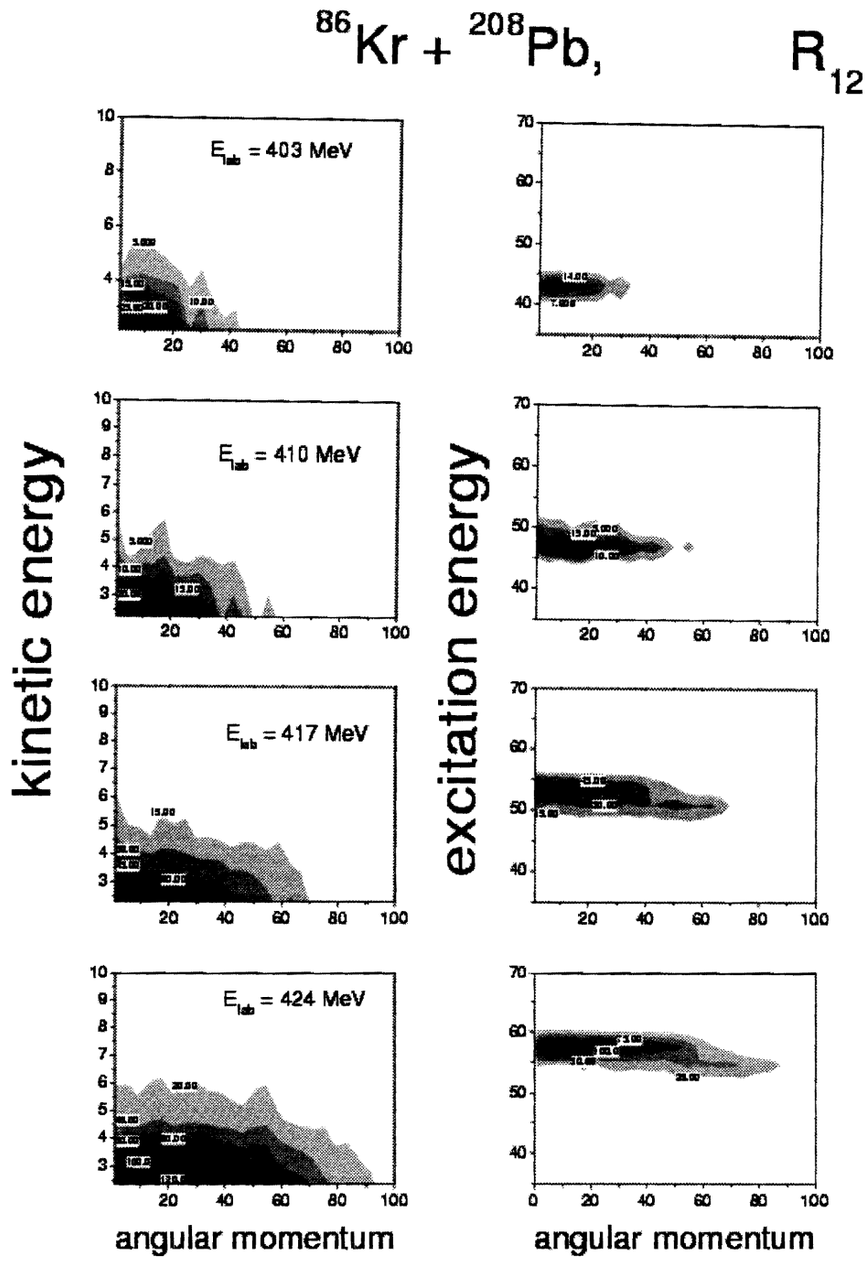

Figure 4: Energy properties of contact configuration are given for ^{86}Kr+^{208}Pb system. The right panels show the kinetic energy distributions for several incident energies above the barrier top. It is readily seen that the average kinetic energies are zero over all the angular momenta and the incident energies. Actually, momentum distributions are Gaussian, though not shown here. Therefore, the relative motion is completely damped and is in equilibrium with the nucleonic heat bath. The left panels show the corresponding excitation energies. It should be noticed here that these features are common in the superheavy element region, but are not in lighter systems.

[5] N. Bohr and J.A. Wheeler, *Phys. Rev.* **56** (1939) 426.

[6] H.A. Kramers, *Physica VII* **4** (1940) 284.

[7] R. Bass, *Nuclear Reactions with Heavy Ions* (Springer, 1980) Chapt. 7.

[8] V. Ninov et al., *Phys. Rev. Letters* **83** (1999) 1104.

[9] W.J. Swiatecki, *Phys. Scripta* **24** (1981) 113
S. Bjornholm and W.J. Swiatecki, *Nucl. Phys.* **A391** (1982) 471
K.-H. Schmidt and W. Morawek, *Rep. Prog. Phys.* **54** (1991) 949.

[10] Y. Abe, D. Boilley, B. Giraud and T. Wada, *Phys. Rev.* **E61** (1999) 1125.

[11] J. Blocki, Y. Boneh, J.R. Nix, J. Randrup, M. Robel, A. Sierk and W.J. Swiatecki, *Ann. Phys.* **113** (1978) 330.

[12] Y. Abe, S. Ayik, P.-G. Reinhard and E. Suraud, *Phys. Reports* **C275** (1996) 49.

[13] J.D. Bao, D. Boilley, T. Wada and Y. Abe, to be published.

[14] P. Fröbrich, B. Strack and M. Durand, *Nucl. Phys.* **A406** (1983) 557.
see also the next Ref. 22.

[15] D.H.E. Gross and H. Kalinowski, *Phys. Reports* **45** (1978) 175.

[16] G. Kosenko and Y. Abe, to be published.

[17] S. Yamaji, F.A. Ivanyuk and H. Hofmann, *Nucl. Phys.* **A612** (1997) 1
H. Hofmann and F.A. Ivanyuk, *Phys. Rev. Letters* **82** (1999) 4603
see also E. Suraud et al., *Nucl. Phys.* **A542** (1992) 141.

[18] H. Grabert, P. Schramm and G.-L. Ingold, *Phys. Reports* **168** (1988) 115.

Synthesis of Superheavy Elements by using Neutron Rich Radio-Isotope Beames

Masahisa OHTA [a 1]

[a] *Department of Physics, Konan University, Okamoto, Kobe 658-8501 Japan*

Abstract

The systematics of the evaporation residue cross section to form nuclei whose Z number is extending from 104 to 118 has been presented. Even though the shell correction is not taken into account in the calculation of the fusion probability by using 3-dimensional Langevin equation, the functional form for the fusion probability extracted from the results of the theoretical calculation by the Langevin equation and the Smolchovsky equation makes us enable to grasp easily the systematics of the excitation function of the evaporation residue cross section in the superheavy mass region. The main purpose is to investigate which entrance channel and what bombarding energy are preferable for the symthesis of superheavy elements beyond Z$\sim$110. It is also our purpose to see how the situation on the yield of the cross section around Z$\sim$110 changes when we use neutron rich radioactive beams.

1 Introduction

The reliable theoretical information for the evaporation residue cross section in the super-heavy mass region together with the life time of α decay is inevitable for the planning of the experiment to synthesize the unknown new elements by

[1] This work was done under the collaboration with Y.Aritomo(JINR, Dubna), T.Wada(Konan University), T.Ichikawa(Konan University), K.Hashizume(Konan University), Y.Abe(YITP, Kyoto University), S.Yamaji(RIKEN) and E.Cherepanov(JINR, Dubna). After this meeting, some revision have been made on the functional form of the formation probability from the view point of the more reliable physical back ground. The results presented here will be modified slightly for the prediction of the cross section to synthesize the compound nucleus with Z=104, 106, 108, 110, 112 and 114, but for the case of Z=116 and 118 one or two orders modification will be expected for several fusion reactions system. However, these modifications do not affect the main part of the discussion extended here. The recent results are ready for publication.

fusion reaction. Because, concerning with the cross section the yield is comparable or less than the limit of the highest technical measurement available right now and in addition the domain of the incident energy of the fusion reaction where we can get the substantial cross section may be sharply restricted around the fusion barrier energy, i.e., (HI, 1n$\sim$ 4n) reaction[1].

The evaporation residue cross section is approximately composed of two factors; the fusion or formation probability and the survival probability in the competition of the fission and the neutron evaporation process. One of the powerful way to calculate the formation probability is given by solving the diffusion equation or the Langevin equation in the nuclear deformation space[2–6]. But this model contains still a large ambiguity because the description of the deformation potential near the contact configuration contains a lot of ambiguity, and how the incident kinetic energy is converted into the internal degree of freedom of the colliding system is an open problem. As for the survival probability, in order to apply extendedly the traditional theoretical formula[7] for the decay width of the fission and the neutron evaporation to the super-heavy mass region, the experimental data of the decay width for the compound nucleus with large Z number is necessary to fix the parameters involved in the formula. Therefore, we have to be ready for the one or two order's uncertainties in the estimation of the evaporation residue cross section in the present stage.

However, before we make an effort to get an precise and perfect prediction for the evaporation residue cross section, it will useful for a planning of the synthesis of new elements to understand the gross feature of the fusion reaction and the survival probability in the super-heavy mass region. The aim of the present talk is to show the systematics of the evaporation residue cross section for the experimentally available neutron rich target-projectile reaction system which produce the compound nucleus with Z number from 104 to 118. The present theoretical calculation contains the dynamics of the fusion process and the competition of the fission and the evaporation of neutron in the decay process. We have analyzed the 82 actual reaction channels which form the neutron rich compound nucleus as possible as we can.

The derivation of the functional form of the formation probability and the prescription of the estimation of the survival probability are explained briefly in the following sections. It is found in the present model calculation that the so called "fusion hindrance" which is appreciate in the small incident mass asymmetry makes a substantial influence on the final cross section, and there exists a case that the lighter projectiles Ca and Ti are favourable nevertheless facing with the hot fusion.

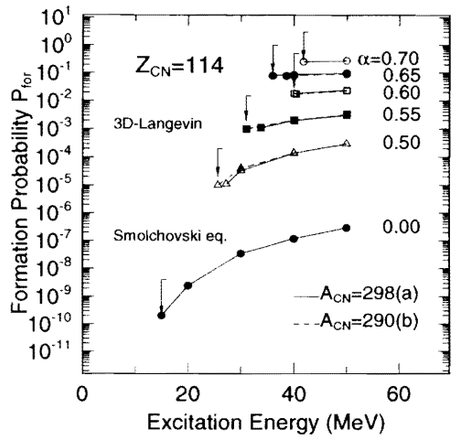

Fig. 1. Formation probability to produce the compound nucleus with $Z = 114$ and $N = 298, 290$. The probability for the symmetric entrance channel $\alpha = 0$ is calculated by using the Smolchowski equation by Aritomo [3,4]. For the case of various entrance channel $0.5 \leq \alpha \leq 0.7$, three dimensional Langevien equation is solved by Okazaki [5]. The position of the Bass potential barriers are indicated by the arrows.

2 Formation probability

The functional form of the formation probability $P_{for}(Z, \alpha, E^*)$ to form a compound nucleus with any Z, from any incident channel with mass asymmetry α and at any excitation energy E^* has been extracted from the theoretical results calculated by the Smolchovski equation[3,4] and the three-dimensional Langevin equation[5,6]. The theoretical calculation of the formation of the compound nucleus with Z=114 is drawn in Fig1. Here, the incident angular momentum is fixed as $l = 10\hbar$.

From Fig.1, we can see a beautiful trend of the formation probability. This trend encourages us to parametrize these data to get a simple functional form for the formation probability. When the mass asymmetry of the incident channel α decreases in forming the same compound nucleus, the formation probability decreases also from unity to 10^{-10}. The position of the Bass potential energy indicated by arrows is changing gradually as α varies. This decreasing feature with α can be roughly parametrized at each excitation energy by

$$10^{-10/(1+\exp\frac{\alpha-0.5}{\Delta})}, \quad (\Delta = 0.08).$$

The excitation energy dependence of the probability above the Bass energy can be parameterize in modifying the above exponent by multiplying a factor $(a/E^* + b)$.[2]

Next step is how to treat the formation probability for the nucleus with different Z. From Ref.[4], we can see that for the mass asymmetric reaction channel, the difference ΔV between the liquid droplet potential[8] at the contact configuration and the saddle shape is proportional almost exactly to

$$\Delta V = Z - 100, \quad \text{for } (102 < Z < 116)$$

(see Fig.11 of Ref.[4]). If we assume drastically that the kinetic energy of the colliding nucleus is dissipated into the internal energy at the contact point and then we start to calculate the probability to form a spherical shape by using the diffusion equation[4], the formation probability (the probability to reach a spherical shape) is proportional to

$$e^{-(z-100)/T}$$

where T means the temperature of the composite nucleus.

Taking account of the above factors, we get the following expression for the formation probability $P_{for}(Z, \alpha, E^*)$:

$$\log_{10} P_{for}(Z, \alpha, E^*) = \frac{-2.6 - (\frac{4.6}{E^*} + 0.195)(Z - 100)}{1 + \exp[\frac{\alpha - 0.5}{\Delta}]}$$

For the excitation energy corresponding to the incident energy of the Bass barrier height E^*_{Bass}, we can get P_{for} for Z=102, 108, 114 and 120 as shown in Fig.2, where the open circles show the case of mass symmetric channel and the solid diamond shows the case to form the compound nucleus with Z=102. They are well reproduced by the function $P_{for}(Z, \alpha, E^*)$.

3 Survival probability

The survival probability of the compound nucleus has been estimated by using the information of $\Gamma_n/(\Gamma_n+\Gamma_f)$ as a function of Z, N and E^*. Here we assumed that the decay process of the compound nucleus is limited to the fission and the neutron evaporation. The excitation function of $\Gamma_n/(\Gamma_n + \Gamma_f)$ is derived

[2] This parametrization has been improved by replacing with the functional form of $(a/\sqrt{E^*} + b)$.

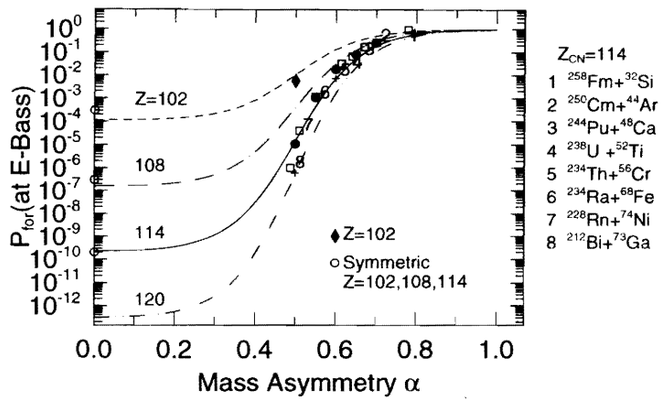

Fig. 2. The values of the empirical formula for the formation probability at the Bass barrier height $P_{for}(Z, \alpha, E^* = E^*_{Bass})$ are drown by the curves. The Z-number is labeled with the line. The calculated points are indicated by the various kind of marks.

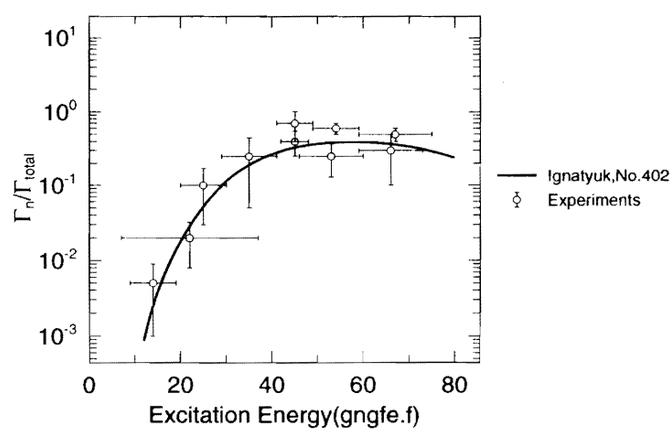

Fig. 3. The theoretical prediction for the excitation energy dependence of $\Gamma_n/(\Gamma_n + \Gamma_f) = \Gamma_n/\Gamma_{tot}$ is compaired with the experimented data.

by Γ_n/Γ_f which is expressed as[9]

$$\frac{\Gamma_n}{\Gamma_f} = \frac{k_{coll}(gr.st.)}{k_{coll}(saddle)k_{Kramars}} A_o \exp[2\sqrt{a_n E_n^*} - 2\sqrt{a_f E_f^*}]$$

where $E_n^* = E_{int}^* - B_n$, $E_f^* = E_{int}^* - B_f$, $A_o = 4A^{2/3}a_f E_n^*/K_o a_n[2\sqrt{a_f E_f^*} - 1]$, $K_o = \hbar^2/2mr_o^2$. k_{coll} means the rotational enhancement factor, and the Kramars factor[10] is expressed as $K_{Kramars} = \hbar\omega_1(\sqrt{1+x^2} - x)/\sqrt{E_{int}^*}$, $x = \gamma/2\omega_o$. The level density parameter in the ground state deformation is assumed as [9]

$$a_n = \frac{A}{10}\{1 + \frac{\delta_{shell}(T=0)}{E_n^*}[1 - \exp(-\frac{E_n^*}{E_D})]\}$$

Here E_D is the shell dumping factor (we take 20MeV here).

Since we have a lack of the information on the level density parameter a_f at the saddle point deformation, we assume a certain relation between a_n and a_f so as to reproduce the experimental data [11–14] of $\Gamma_n/(\Gamma_n+\Gamma_f)$. If we take the relation between a_n and a_f, we can not only reproduce the experimental data $\Gamma_n/(\Gamma_n+\Gamma_f)$ by using the above formula but also use it extendedly for another case with large Z-number. The result is shown in Fig.3. We confirm that this parameter set works well for producing the experimented data around the nucleus with Z=102. The isotope and Z-dependence of Γ_n/Γ_f are compared with the experimental data [15] in Fig.4.

The survival probability is then calculated according to the definition shown in the following which is expressed in terms of $\Gamma_n/(\Gamma_n+\Gamma_f)$ at each evaporation step:

$$P_{sur}^{(l)} = \prod_{i=1}^{N} \frac{\Gamma_n^{(i)}}{\Gamma_n^{(i)} + \Gamma_f^{(i)}}$$

where i means the each step of the neutron emission and the angular momentum dependence is coming from the l-dependent fission barrier. The actual calculation is done by using random numbers and assuming the kinetic energy of emitted neutron as $\epsilon_n^{1/2}\,\mathrm{e}^{-\epsilon_n/T}$[16].

4 Systematics of Cross Section

In the calculation presented in the previous section, we have confirmed that the weighted survival probability $(2l+1)P_{sur}^{(l)}$ is limited around $l \sim 30\hbar$ for the compound nucleus with $Z = 102 \sim 118$ [16], one of which is shown in Fig.5. Therefore, in the calculation of the evaporation residue cross section, we use the sharp cut off in the angular momentum space at $20\hbar$.[3]

$$\sigma_{ER}(Z,\alpha,E^*) = \frac{\pi}{k^2}\sum(2l+1)P_{for}(Z,\alpha,E^*)P_{sur}^{(l)}(Z,E^*).$$

[3] In the recent improvement, the summation is treated in the right way. It is found that the difference is only by factors.

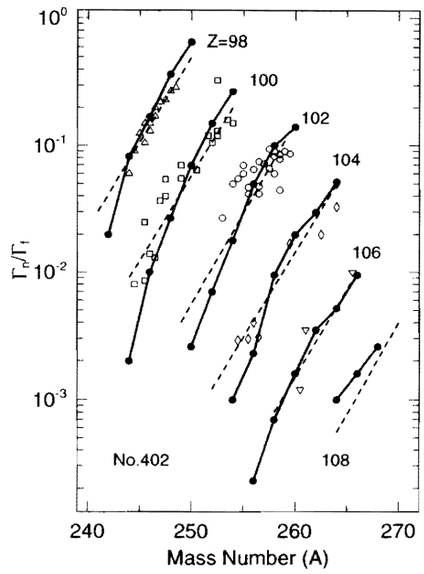

Fig. 4. The experimental data [15] for the isotope dependence of Γ_n/Γ_f are compaired with the theoretical value.

We selected the following neutron rich projectiles:
^{48}Ca, ^{50}Ti, ^{54}Cr, ^{58}Fe, ^{64}Ni, ^{70}Zn, ^{76}Ge, ^{82}Se, ^{86}Kr, ^{88}Sr, ^{96}Zr, ^{100}Mo,
and also selected the following neutron rich targets:
^{154}Sm, ^{160}Gd, ^{164}Dy, ^{170}Er, ^{176}Yb, ^{180}Hf, ^{186}W, ^{194}Os, ^{198}Pt, ^{204}Hg, ^{208}Pb, ^{209}Po, ^{228}Ra, ^{232}Th, ^{224}Pu, ^{250}Cm, ^{252}Cf.

We have investigated 82 reaction channels forming the compound nucleus with $Z = 104 \sim 118$ by arranging the above lists of projectiles and targets. For the case of the incident energy below the Bass potential barrier, the penetrability of the inverse parabolic multiplied to the P_{for} so as to reproduce the experimental data especially for the ^{208}Pb target seriese [17].

The value of the maximum cross section for all 82 channels are plotted against the incident mass asymmetry α as shown in Fig.6. The cross section forming the compound nucleus with various Z number by the same projectile are connected by the various lines and labeled the name of element. In order to produce the higher Z element fixing a projectile, the mass of the target should be increased. As a results, the asymmetry parameter α become larger. For the projectile heavier than Zn and Ni, the lines indicate the descending nature as α increases.

On the contrary, for the lighter projectiles Ti and Ca, the situation is different. Due to the significant increase of the formation probability for the lighter

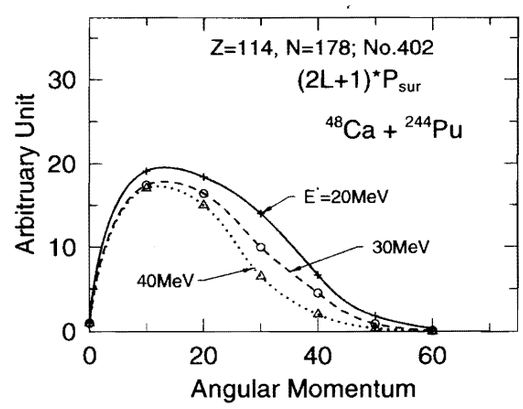

Fig. 5. Angular momentum dependence of the weighted survival probability is plotted for three different excitation energy of the compound nucleus.

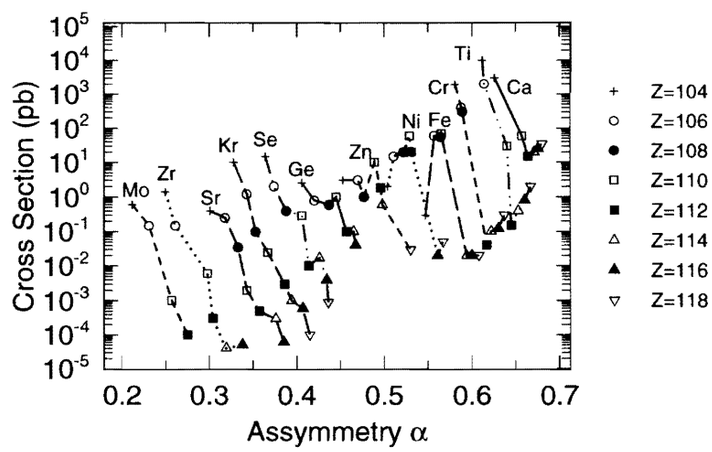

Fig. 6. The values of the maximum cross section for the fusion evaporation residue reaction. The data for the same projectile is connected by the line. The Z-number of the compound nucleus is identified by the different marks which are indicated in the right hand side of the figure. If you connect the open triangles (Z=114) for example, you can find that the cross section exceeds 1pb for $\alpha \sim 0.65$. The same is for $Z \geq 116$.

projectiles or the removal of the fusion hindrance for large α, the formation probability defeats the decrease of the survival probability arising from the large excitation energy in the situation of hot fusion. As a results, the increase

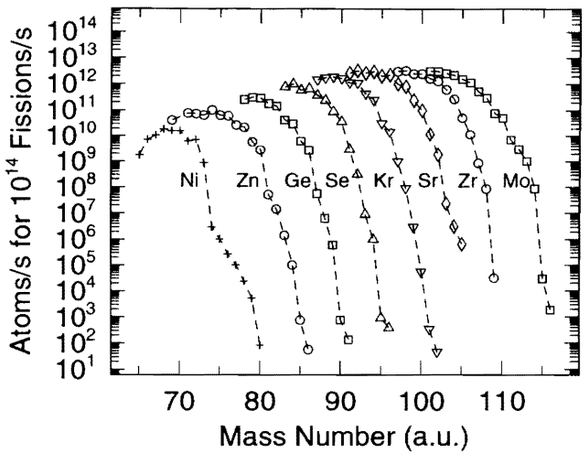

Fig. 7. Yield of the fission fragments presented by Ridikas *et al.*[18].

of the cross section for $Z \geq 114$ can be seen in the region of $\alpha > 0.6$.[4]

5 Utilization of neutron rich projectiles

Recently, Ridikas *et al.*[18] have presented the possibility of the use of neutron rich projectiles ranging from Mo to Ni isotopes by using the fission fragment.(Fig.7) According to our systematics mentioned above, lighter projectiles are rather preferable to form superheavy elements. As an example, we investigate the evaporation residue cross section using Se isotopes. The maximum cross section are plotted against the neutron number of the compound nucleus (Fig.8).

It is found that in general the cross section increases as the increase of the neutron number of the projectile due to the decrease of the mean neutron separation energy, *i.e.*, the faster neutron evaporation leading to the predominance of the evaporation process against the fission process.

The drop down for the case of Z=108 at ^{90}Se and for the case of Z=114 at ^{90}Se in Fig.8 are corresponding to the decrease of the shell correction energy

[4] It is noted that for the case of Z=116 and 118 the results presented in the meeting will be modified so much. The revised calculation shows that only Ca projectile can realize the measurement with over pico barns. Another large modification is that the reaction with the projectiles Sr, Kr, Se and Ge show the large cross section ($10^{-2} \sim 1$ pb) in the case of Z=116 and 118 comparing with the result presented in Fig.6. Please refer to the forthcoming paper.

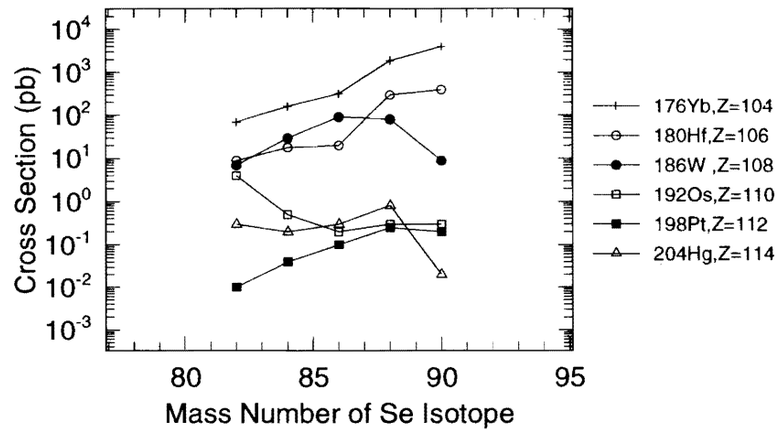

Fig. 8. Maximum cross section forming the compound nucleus with Z=104, 106, 108, 110, 112 and 114 by using Se isotope projectiles.

of the compound nucleus. The same is true for the case of Z=110 at 82, 84 and 86 Se.

6 Concluding remarks

The calculation from the present model show that the cross section of the synthesis of superheavy elements with $Z \geq 114$ changes its trend around $\alpha = 0.5$, i.e., the cross section for the elements with $Z \geq 114$ again increases with α and the pico barn measurement becomes possible in the incident channel mass asymmetry α greater than ~ 0.65 by using Ca and Ti projectile. This fact supports the hot fusion reaction. The present model also shows that the utilization of the neutron rich radio isotope projectile is very hopeful for the experiments to find new heavy elements with the nano barn measurement.

References

[1] S. Hofmann, Rep. Prog. Phys. **61** 639 (1998).

[2] Y. Abe, Y. Aritomo, T. Wada and M. Ohta, J. Phys. G: Nucl. Part. Phys. **23** 1275 (1997).

[3] Y.Aritomo, T.Wada, M.Ohta and Y.Abe, Phys. Rev. C**55**, R1011 (1997).

[4] Y.Aritomo, T.Wada, M.Ohta, and Y.Abe, Phys. Rev. C **59**, 796 (1999).

[5] M.Ohta, K.Okazaki, T.Wada, Y.Aritomo and Y.Abe, Acta Physica Hungarica - Heavy Ion Physics **10**, 253 (1999).

[6] T.Wada, T.Tokuda, K.Okazaki, M.Ohta, Y.Aritomo and Y.Abe, Proc. of 4th Int. Conf. on Dynamical Aspects of Nuclear Fission, Slovak 1998 (World Scientific, 2000) p.77.

[7] R.Vandenbosch and J.R.Huizenger, *Nuclear Fission* (Academic Press, New York, 1973), p233.

[8] P.Möller, J.R.Nix, W.D.Myers and W.J.Swiatecki, Atomic Mass Nucl. Data Table **59**, 185 (1995).

[9] A.V.Ignatyuk, K.K.Istekov and G.N.Smirenkin, Sov. J. Nucl. Phys. **30**, 626 (1979).

[10] H.A.Kramers, Physica VII4 284 (1940).

[11] T.Sikeland, J.Maly and D.F.Lebeck, Phys. Rev. **169**, 1000 (1968).

[12] T.Sikeland, A.Ghiorso and M.J.Nurmia, Phys. Rev. **172**, 1232 (1968).

[13] A.N.Andreyev *et al.*, Z. Phys. **A345**, 389 (1993).

[14] G.N.Flerov *et al.*, Nucl. Phys. **A160**, 181 (1970).

[15] G.H.Ter-Akopyan *et al.*, Nucl. Phys. **A255**, (1975) 509.

[16] M. Ohta, Proceeding of the Workshop "Fusion Dynamics at the Extreams", 25-27th May, 2000 in Dubna (World Scientific), to be published.

[17] S.Hofmann *et al.*, Z. Phys. A**350**, 277 (1995); **350**, 281 (1995).

[18] D.Ridikas *et al., to be published.*

Decay properties of superheavy nuclei predicted by nuclear mass formulas

H. Koura
Advanced Research Institute for Science and Engineering, Waseda University

Our group has recently constructed a nuclear mass formula [1, 2, 3] composed of a gross part and a shell part. For the shell part, we first calculate spherical proton and neutron shell energies by using single-proton and single-neutron potentials, which we have newly constructed [4, 5]. These potentials reproduce fairly well the experimental single-particle levels of 15 doubly-magic and magic-submagic nuclides in a wide nuclidic region ranging from ^{4}He, ^{8}He to ^{208}Pb. The most distinctive characteristic of this mass formula is that the shell energy of a deformed nucleus is expressed as an appropriate mixture of spherical shell energies added to an average deformation energy. This mass formula gives ground-state masses and shapes of nuclei ranging from light nuclei ($Z \geq 2$, $N \geq 2$) to superheavy nuclei. The standard deviation of the calculated masses from the experimental masses of the 1995 Mass Evaluation [6] is about 680 keV.

In response to the recent increase of interest in superheavy elements we give some results based on the new mass formula. We also compare our predicted quantities with those of two relatively new mass formulas, the Finite Range Droplet Model (FRDM) formula [7] and the Extended Thomas-Fermi plus Strutinsky Integral (ETFSI) formula [8].

We first show the spherical single-particle levels in two superheavy nuclides $^{310}126$ and $^{298}114$ (these single-particle levels were used as factors to construct the mass formula rather than deduced from the mass formula). The neutron gap at $N = 184$ is 2.49 MeV for $^{310}126$, and 2.50 MeV for $^{298}114$. The proton gap at $Z = 114$ is 1.88 MeV for $^{298}114$, and that at $Z = 126$ is 1.77 MeV for $^{310}126$. These values are considerably smaller than the magic gaps in the known doubly-magic nuclide ^{208}Pb, where the $N = 126$ neutron gap is 3.43 MeV and the $Z = 82$ proton gap is 4.21 MeV. This fact suggests that the magicities in SHE are less pronounced than in ^{208}Pb (and also in ^{132}Sn).

We next show the shell energies of our formula in the superheavy region. In this figure we see that the alleged magicity at $Z = 114$ is not so remarkable, while the nucleus $^{310}126$ is doubly-magic although its double-magicity is weaker than those of ^{132}Sn and ^{208}Pb as expected.

According to our mass formula, the β-stability line roughly goes straight from ^{257}Fm to $^{297}113$.

We show the deformation parameter α_2 of our calculation and β_2 of other two mass formulas. The figures of our and FRDM's formulas suggest that many nuclides around $N = 184$ have spherical shapes.

The α-decay Q-values are calculated, and the α-decay half-lives are estimated with use of a phenomenological formula [9, 10]. These results are compared with experimental data and other predictions. Our α-decay Q-values present a feature of magicity at $Z = 114$ and at $Z = 126$ as relatively wide gaps between isotope lines, while a similar figure with use of FRDM has a larger gap only at $Z = 114$, and that with use of ETFSI (not shown here) shows no gap. Our α-decay half-lives T_α depend on nuclides rather moderately, or regularly, compared with the other two predictions. We also compare Q_α and T_α with the recent experimental data in the vicinity of

the nuclide $^{288}114$ [11]. The differences between the experimental values and the theoretical ones [7, 8, 12] are within 700 keV, not unexpected from the general deviations of the calculated Q_α-values from the Q_α-values of known lighter nuclides.

Although the mass formula is concerned only with the equilibrium shapes of nuclei, we can use the same method to calculate the nuclear energies in other shapes. We show the energy surfaces against the nuclear deformation for some superheavy nuclei. For the nuclide $^{283}112$, the height of the fission barrier is only about 3 MeV and its width is relatively narrow, and the spontaneous fission half-life is expected to be rather short. On the contrary, for the nuclides $^{293}118$ and $^{289}110$, the fission barrier heights are about 7 MeV and about 5 MeV, respectively, and their widths are fairly wide. Therefore, the spontaneous fission of these nuclides is expected to have very long partial half-lives, much longer than the α-decay half-lives. By the way we have chosen $^{289}110$ as the nuclide expected to have the longest half-life among the β-stable superheavy nuclides reachable by $\beta^+\varepsilon$ decays. The α-decay half-life of $^{289}110$ is estimated to be about 1 year.

With the aid of our mass formula, we could form a picture of the decays of superheavy nuclei. Further theoretical as well as experimental investigations are necessary to make this picture more accurate.

References

[1] H. Koura, T. Tachibana, M. Uno and M. Yamada, *JAERI-Conf* **96-008**, 284 (1996).

[2] H. Koura, M. Uno, T. Tachibana and M. Yamada, *Exotic Nuclei and Atomic Masses (ENAM 98)*, ed. B.M. Sherill, D.J. Morrissey and C.N. Davids, (AIP Conference Proceedings 455, 1998), p. 114.

[3] H. Koura, M. Uno, T. Tachibana and M. Yamada, *Nucl. Phys.* **A674**, 44 (2000).

[4] H. Koura and M. Yamada, *Technical Report of Advanced Research Institute for Science and Engineering, Waseda University,* **No.99-14**, (1999).

[5] H. Koura and M. Yamada, *Nucl. Phys.* **A671**, 96 (2000).

[6] G. Audi and A.H. Wapstra, *Nucl. Phys.* **A595**, 409 (1995).

[7] P. Möller, J.R. Nix, W.D. Myers and W.J. Swiatecki, *Atomic Data and Nuclear Data Tables* **59**, 185 (1995).

[8] Y. Aboussir, J.M. Pearson, A.K. Dutta and F. Tondeur, *Atomic Data and Nuclear Data Tables* **61**, 127 (1995).

[9] V.E. Viola, Jr. and G.T. Seaborg, *J. Inorg. Nucl. Chem.* **28**, 741 (1966).

[10] Z. Patyk, J. Skalski, A. Sobiczewski and S. Ćwiok, *Nucl. Phys.* **A502**, 591c (1989).

[11] Yu.Ts. Oganessian, et al., *Phys. Rev. Lett.* **83**, 3154 (1999); *Nature* **400**, 242 (1999); *Phys. Rev.* **C62**, 041604(R) (2000); preprint.

[12] R. Smolańczuk, *Phys. Rev.* **C56**, 812 (1997).

1.(1) Shell energies

i) Single-particle potential (spherical)*)

• Central component (5 parameter potential)

$$V_{\mathrm{cen}}(r) = V_0 \frac{1}{\{1+\exp[(r-R_v)/a_v]\}^{a_v/\kappa}} \left\{ 1 + V_{\mathrm{dp}} \frac{1}{1+\exp[-(r-R_v)/a_v]} \right\}$$

Extension of Woods-Saxon potential

• Spin-orbit component (3 parameter)

$$V_{ls}(r) = V_{ls0} \frac{1}{2m} \frac{1}{r} \frac{d}{dr} \frac{1}{\{1+\exp[(r-R_{ls})/a_{ls}]\}}$$

(Coulomb energy is added to the proton potential)

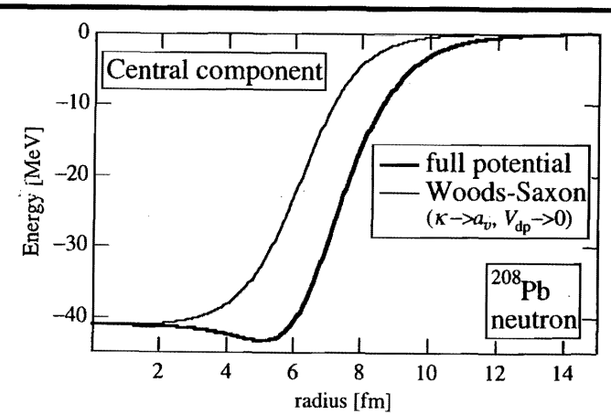

*)H. Koura and M. Yamada, Nucl. Phys. A671, pp96-118

ii) Shell energies

■ Caclulation of the crude shell energy

Energy of n neutrons (or n protons) put into the single-particle potential of the nucleus (Z, N)

↓

Subtraction from the above energy a smooth part which is a smooth function of n, Z, N. (a substitute of the Strutinsky method)

Neutron and proton crude shell energies

■ Modification of the shell energies

(a) BCS-type pairing

↓

(b) reduction
• Effect of configuration mixing?

Refined neutron and proton shell energies

Spherical

■ Deformation *(Explained in the next sheet)*

Shell energies

iii) Deformation effect of shell energies

- **Nuclear shapes**

$$R(\theta)=\frac{R_0}{\lambda}\left[1+\alpha_2 P_2(\cos\theta)+\alpha_4 P_4(\cos\theta)+\alpha_6 P_6(\cos\theta)+\cdots\right].$$

We take **axially and reflectionally symmetric shapes up to α_6 deformation**

- **Shell energies**

$$E_{sh}(Z, N)=\min_{\alpha_2,\alpha_4,\alpha_6}\left[E_{in}(Z, N;\alpha_i)+\overline{E_{def}(Z, N;\alpha_i)}\right]$$

- $E_{in}(Z, N; \alpha_i)$: intrinsic shell energy
- $\overline{E_{def}(Z, N; \alpha_i)}$:average deformation energy

The intrinsic shell energy of a deformed nucleus is expressed as **a weighted sum of spherical shell energies** of its neighboring nuclei.

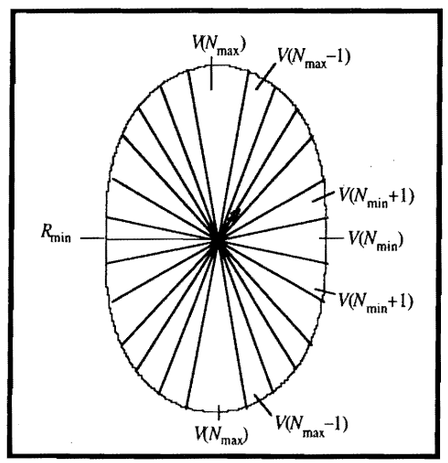

A schematic illustration of the decomposition of a deformed nucleus into spherical nuclei. $V(N)$ corresponds to the fraction of the spherical nucleus with the neutron number N.

Shell energies $E_{sh}(Z, N)$

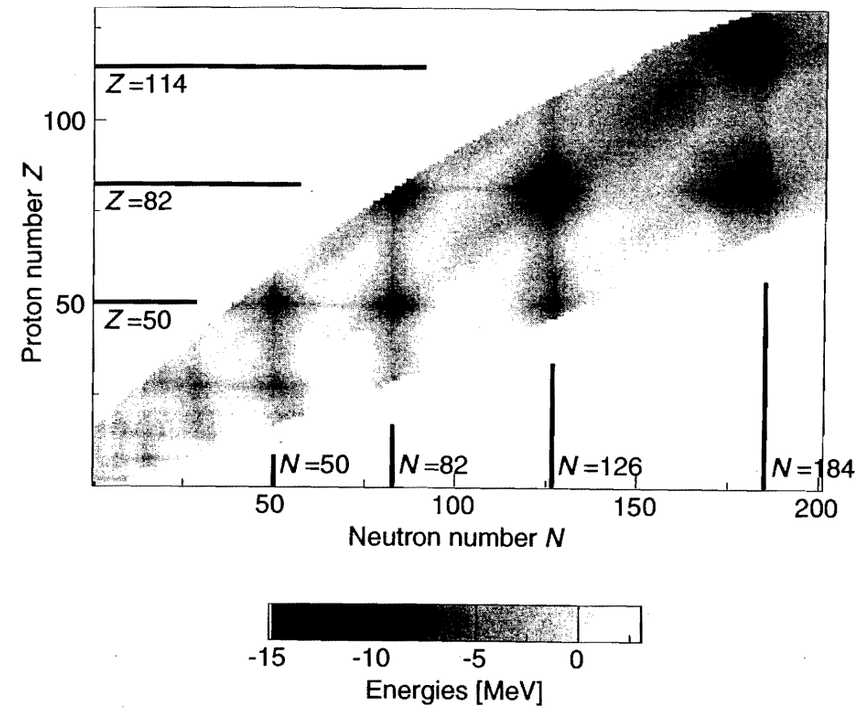

1.(2) Mass formula

$$M(Z, N)=M_{gross}(Z, N)+M_{eo}(Z, N)+M_{shell}(Z, N)$$

• $M_{shell}(Z, N)$:obtained as $E_{sh}(Z,N)$ in the last procedure

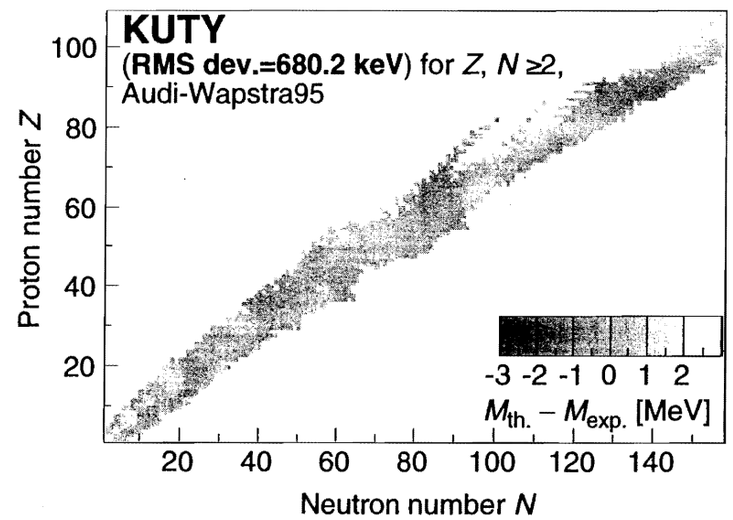

Other mass formulas (having similar applicability)

FRDM formula (P. Möller et al., 1995)
(Finite Range Droplet Model)
designed for $Z, N \geq 8$
RMS Dev. from Exp. : **678 keV** (KUTY formula: **642 keV**)

ETFSI formula (Y. Aboussir et al., 1995)
(Extended Thomas-Fermi + Strutinsky Integral)
designed for $A \geq 36$
RMS Dev. from Exp. : **732 keV** (KUTY formula: **630 keV**)

2. Application to superheavy elements (SHE)

2.(1) Single-particle levels in SHE (Our calculations)

Single-neutron levels

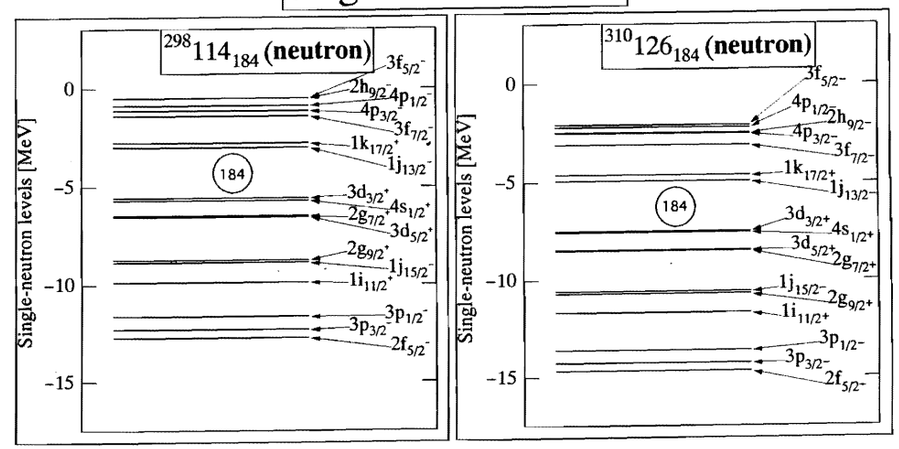

In ^{208}Pb, N=126 gap is 3.43 MeV

Single-proton levels

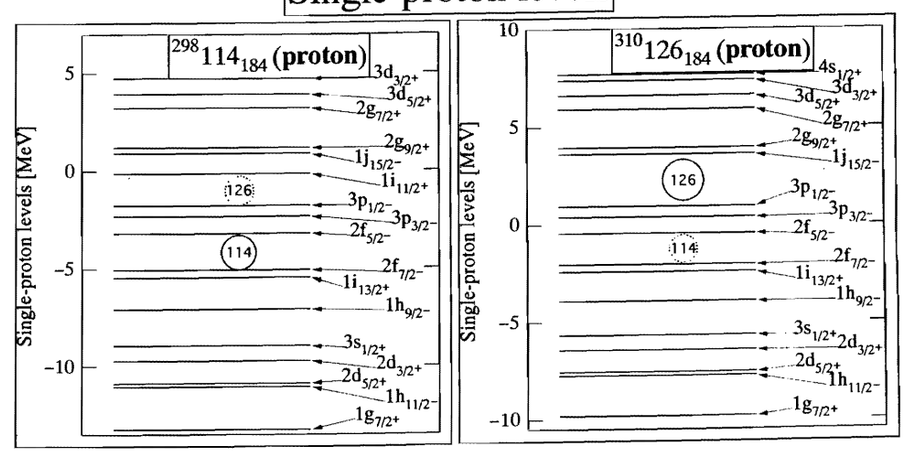

In ^{208}Pb, Z=82 gap is 4.21 MeV

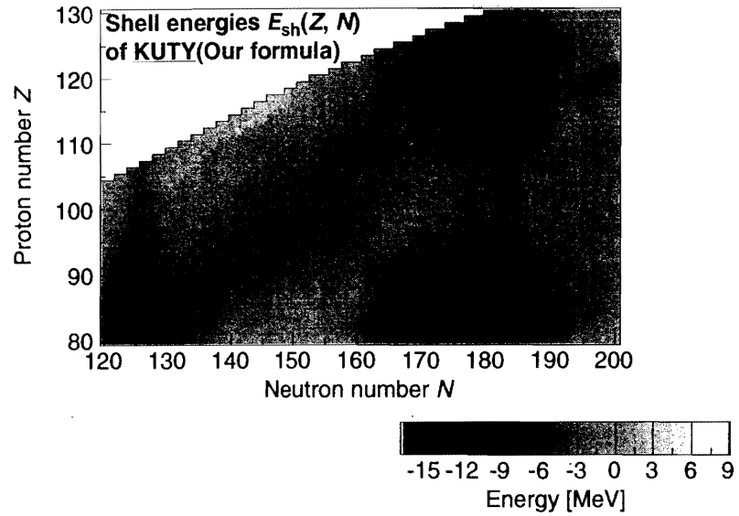

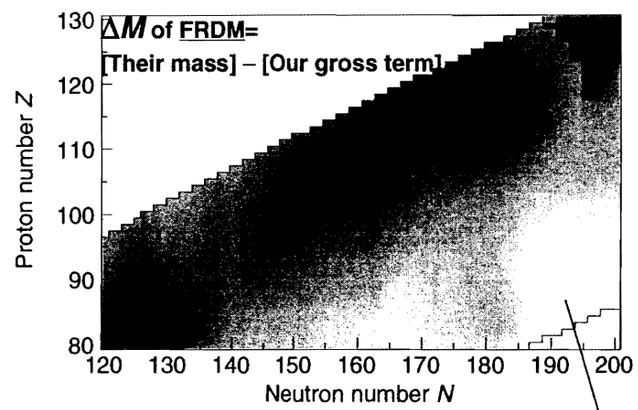

Far from the β-stability line, FRDM's masses are generally larger than KUTY's. (Not our present concern.)

Deformation parameter α_2 or β_2

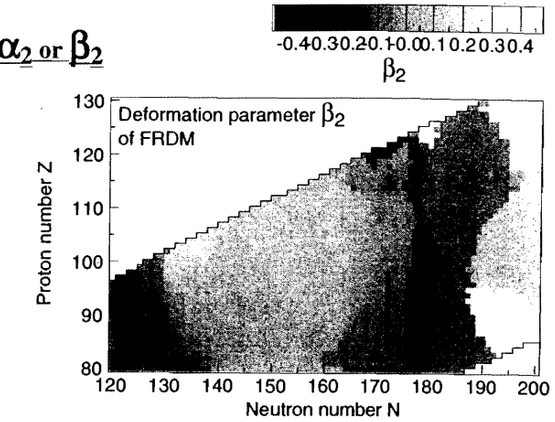

FRDM

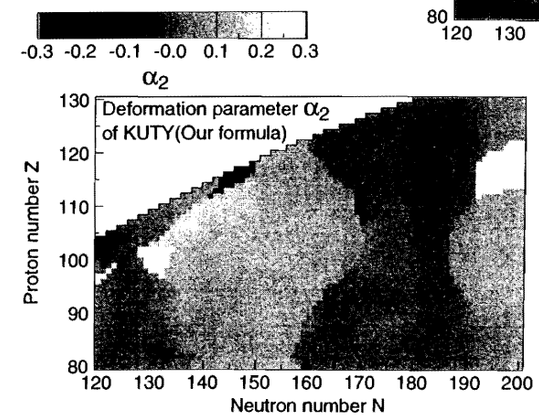

KUTY(Our formula)

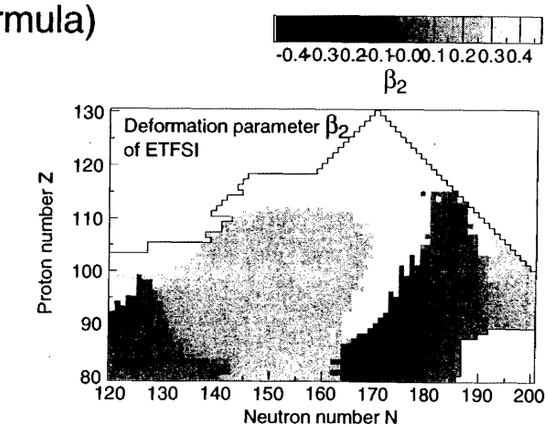

ETFSI

α-decay Q-values Q_α

KUTY (Our formula)

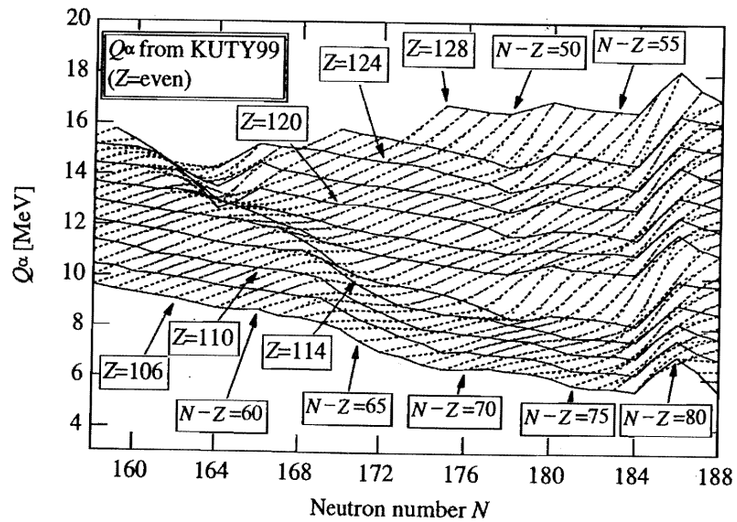

FRDM

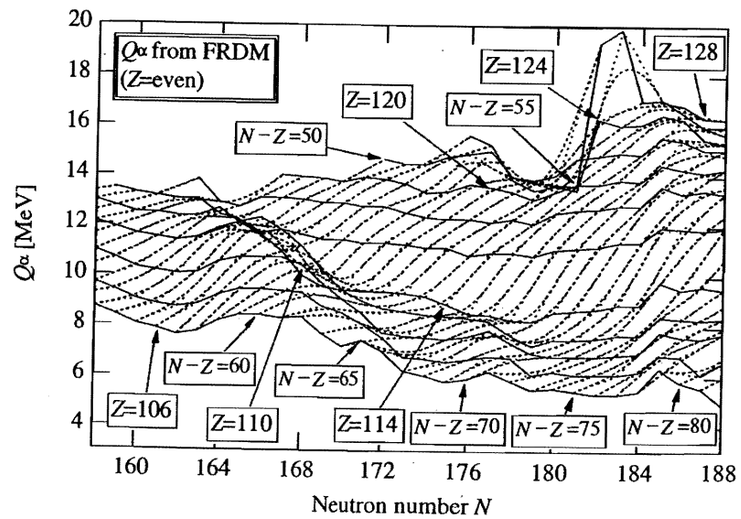

Recent experimental Q_α

$^{287}114$, $^{288}114$, $^{289}114$ and $^{292}116$ nuclei
(by Oganessian et al. (1999, 2000))

$Q_\alpha(^{284}112)$= 9.30 MeV,	$T(^{284}112)\approx$9.8 s
$Q_\alpha(^{287}114)$=10.44 MeV,	$T(^{287}114)\approx$ 5 s
$Q_\alpha(^{288}114)$= 9.98 MeV,	$T(^{288}114)\approx$1.9 s
$Q_\alpha(^{289}114)$= 9.85 MeV,	$T(^{289}114)\approx$ 20 s
$Q_\alpha(^{292}116)$=10.71 MeV,	$T(^{292}116)\approx$33 ms

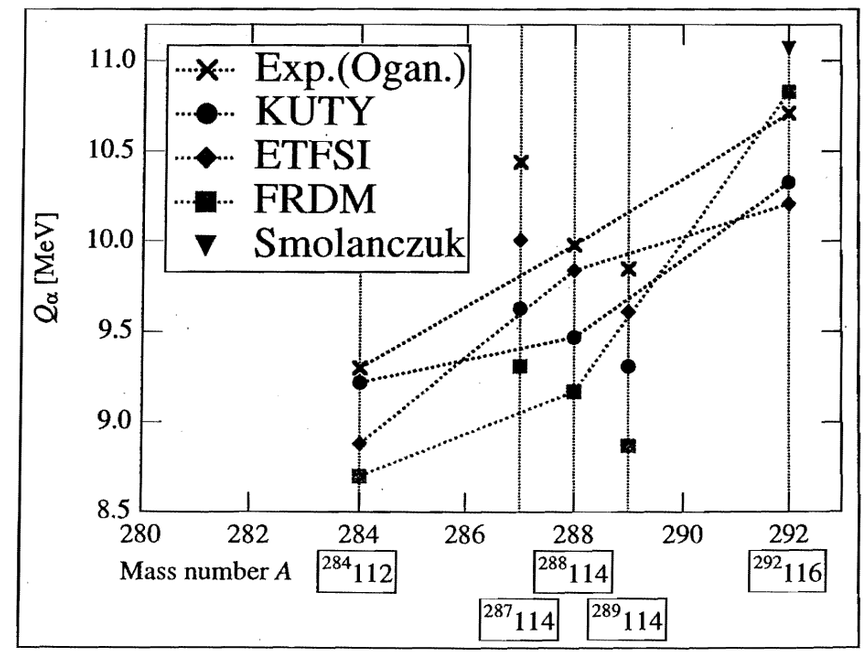

2.(4) **Spontaneous fission**

Heights of the first suddle points are roughly estimated

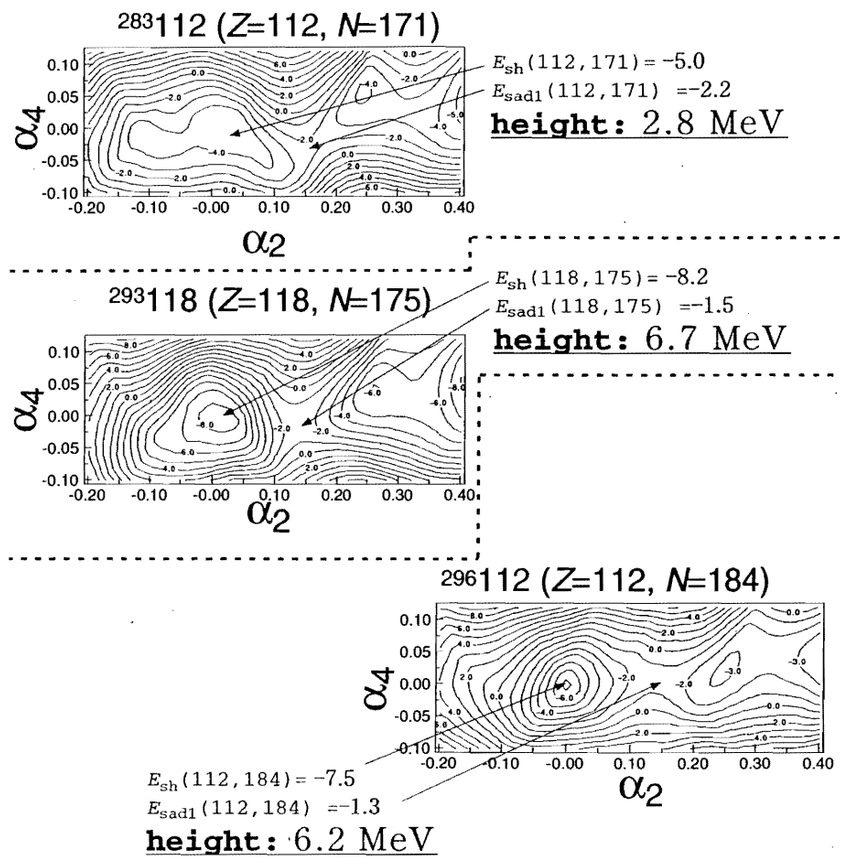

Energy surface on the deformation parameter plane (α_2, α_4).

$^{289}110_{179}$ (β-stable nucleus reachable by $\beta^+\varepsilon$-decay with the long T_α)

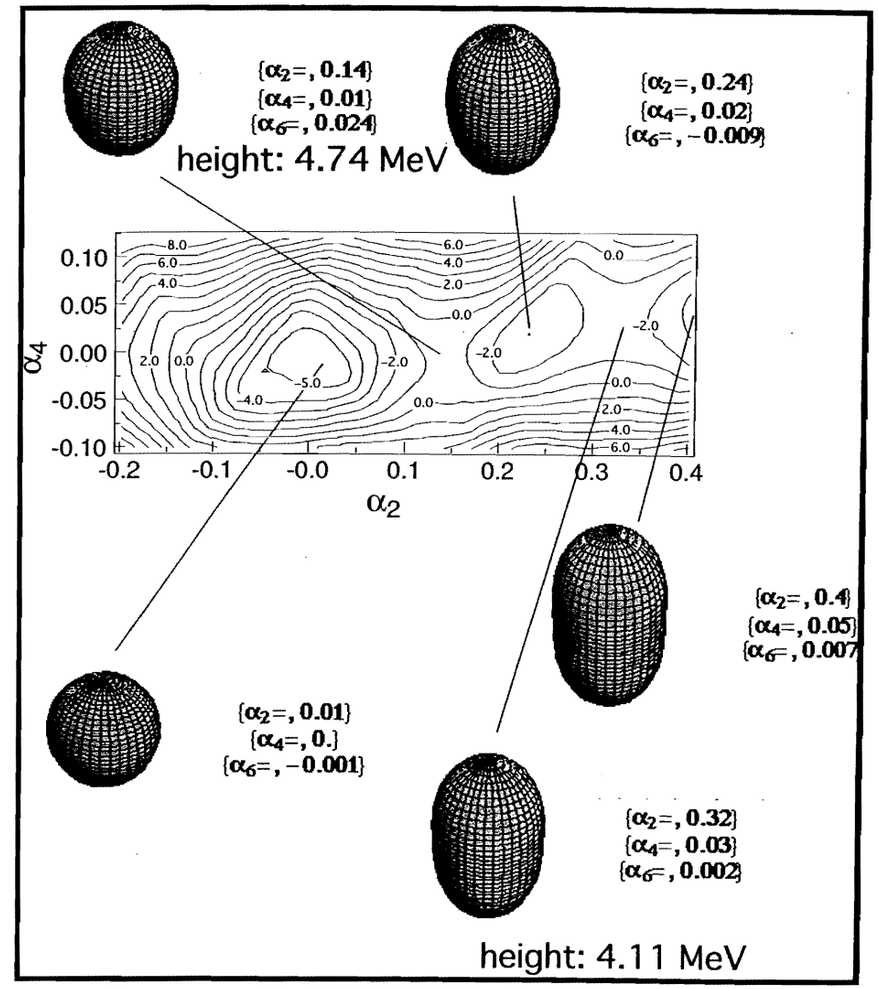

$T\alpha(110,179) \approx 1$year)

Fusion Reaction of Neutron-Rich Nuclei

Y. X. Watanabe (RIKEN)

It is known that the heavy ion fusion cross section is strongly enhanced in the energy region near and below the classical fusion barrier as compared to the expectation from the one-dimensional barrier penetration model [1]. Various mechanisms have been proposed to explain such enhancement of sub-barrier fusion cross sections: the zero-point motion of collective surface vibrations [2], coupling to inelastic excitation and nucleon transfer channels [3], and neck formation between the colliding nuclei [4]. These effects can also be treated in terms of distribution of fusion barriers [5, 6].

Because of the possibility of using neutron-rich radioactive projectiles to synthesize new heavy nuclei [7], there is great interest in the magnitudes of sub-barrier fusion cross sections with neutron-rich nuclei. Several theoretical predictions [8, 9, 10, 11, 12, 13] have suggested that there will be significant enhancements to the fusion cross sections for halo nucleus owing to the larger radius of the halo wave function, coupling to the soft $E1$ mode, and coupling to the projectile breakup channels.

Measurements of sub-barrier fusion with radioactive projectiles have been performed for ^{38}S + ^{181}Ta at NSCL(MSU) [14], ^{6}He + ^{209}Bi at Notre Dame [15], and ^{6}He + ^{238}U at Louvain-la-Neuve [16]. The authors of Ref. [15] suggest the possibility of neutron transfer channels. At RIKEN, we have studied ^{29,31}Al + ^{197}Au, ^{10,11}Be + ^{209}Bi [17], and ^{6,8}He + ^{40}Ar. In this talk, we report these experiments and results.

References

[1] M. Beckerman, *Physics Reports* **129**(1985), 145.

[2] H. Esbensen, *Nuclear Physics* **A352**(1981), 147.

[3] C. H. Dasso, S. Landowne and A. Winther, *Nuclear Physics* **A405**(1983), 381.

[4] C. E. Aguiar, V. C. Barbosa, L. F. Canto and R. Donangelo, *Nuclear Physics* **A472**(1987), 571.

[5] P. H. Stelson, *Physics Letters* **B205**(1988), 190.

[6] N. Rowley, *Nuclear Physics* **A538**(1992), 205c.

[7] J. P. Dufour and A. Fleury, *Physical Review* **C23**(1981), 801.

[8] N. Takigawa and H. Sagawa, *Physics Letters* **B265**(1991), 23.

[9] C. H. Dasso and R. Donangelo, *Physics Letters* **B276**(1992), 1.

[10] M. S. Hussein, M. P. Pato, L. F. Canto and R. Donangelo, *Physical Review* **C46**(1992), 377.

[11] N. Takigawa and M. Kuratani and H. Sagawa, *Physical Review* **C47**(1993), R2470.

[12] C. H. Dasso and A. Vitturi, *Physical Review* **C50**(1994), R12.

[13] K. Hagino, A. Vitturi, C. H. Dasso and S. M. Lenzi, *Physical Review* **C61**(2000), 037602-1.

[14] K. E. Zyromski, *et al.*, *Physical Review* **C55**(1997), R562.

[15] J. J. Kolata, *et al.*, *Physical Review Letters* **81**(1998), 4580.

[16] M. Trotta, *et al.*, *Physical Review Letters* **84**(2000), 2342.

[17] A. Yoshida, *et al.*, *Physics Letters* **B389**(1996), 457.

Ion	Target (mg/cm^2)	Energy (MeV)	ΔE	Intensity (cps)	Prod. Meth.	Exp. Meth.	Efficiency	Facility
^{29}Al	^{197}Au 10×0.4	161~216	<1.4MeV	1×10^5	fragmentation	fission,MWPC	~30%	RIKEN
^{31}Al	^{197}Au 10×0.4	119~200	<1.5MeV	3×10^4	fragmentation	fission,MWPC	~30%	RIKEN
^{38}S	^{181}Ta 0.5	150~260	<1MeV	2~7×10^3	fragmentation	fission,PPAC		MSU
^{32}S	^{181}Ta 0.5	150~300	0.2MeV			fission,SSD		MSU
^{11}Be	^{209}Bi 4×1.0	28~66	<1MeV	1×10^5	fragmentation	α-decay,SSD	33%	RIKEN
^{10}Be	^{209}Bi 4×1.0	32~60	<1MeV	2×10^5	fragmentation	α-decay,SSD	33%	RIKEN
^{6}He	^{109}Bi 1	19~28	1.5MeV	2×10^5	^{9}Be(^{7}Li,^{6}He)	α-decay,SSD	21%	Notre Dame
^{6}He	^{238}U 0.6	15~29		0.1~5×10^6		fission,SSD	<70%	Louvain-la-Neuve
^{4}He	^{238}U 0.6	18~23		1~4×10^8		fission,SSD	<70%	Louvain-la-Neuve
^{8}He	^{40}Ar 64×0.2	16~24	<0.5MeV	0.6~1×10^3	fragmentation	residue,MUSIC	-	RIKEN
^{6}He	^{40}Ar 64×0.2	14~20	<0.5MeV	~2×10^3	fragmentation	residue,MUSIC	-	RIKEN

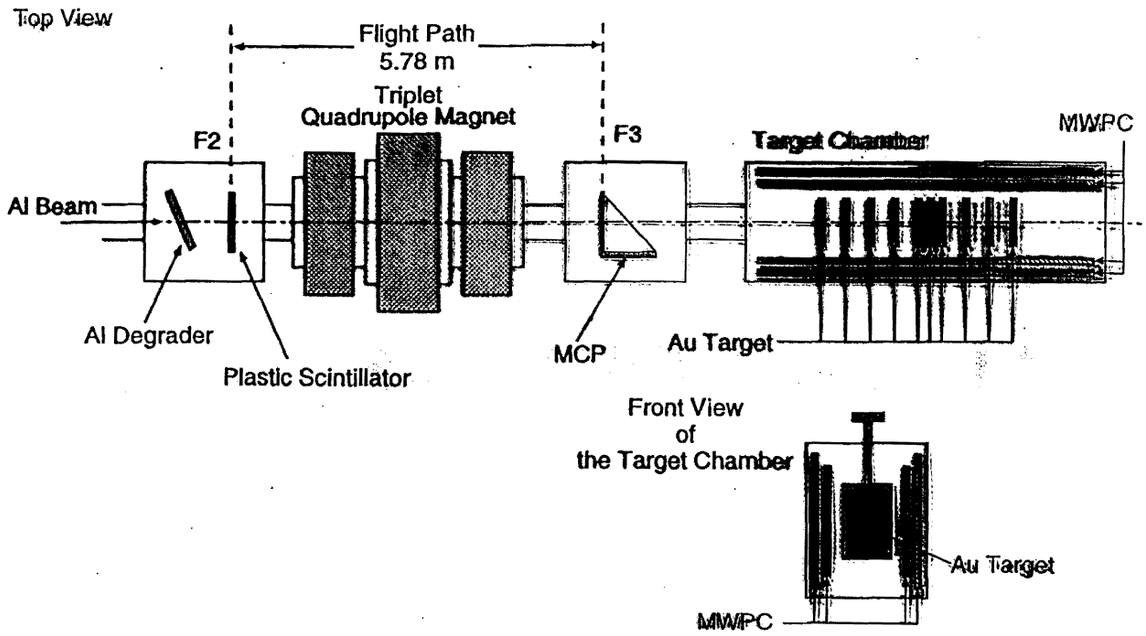
Top View
Flight Path
5.78 m
Triplet
Quadrupole Magnet
F2
F3
Target Chamber
MWPC
Al Beam
Al Degrader
Plastic Scintillator
MCP
Au Target
Front View
of
the Target Chamber
Au Target
MWPC

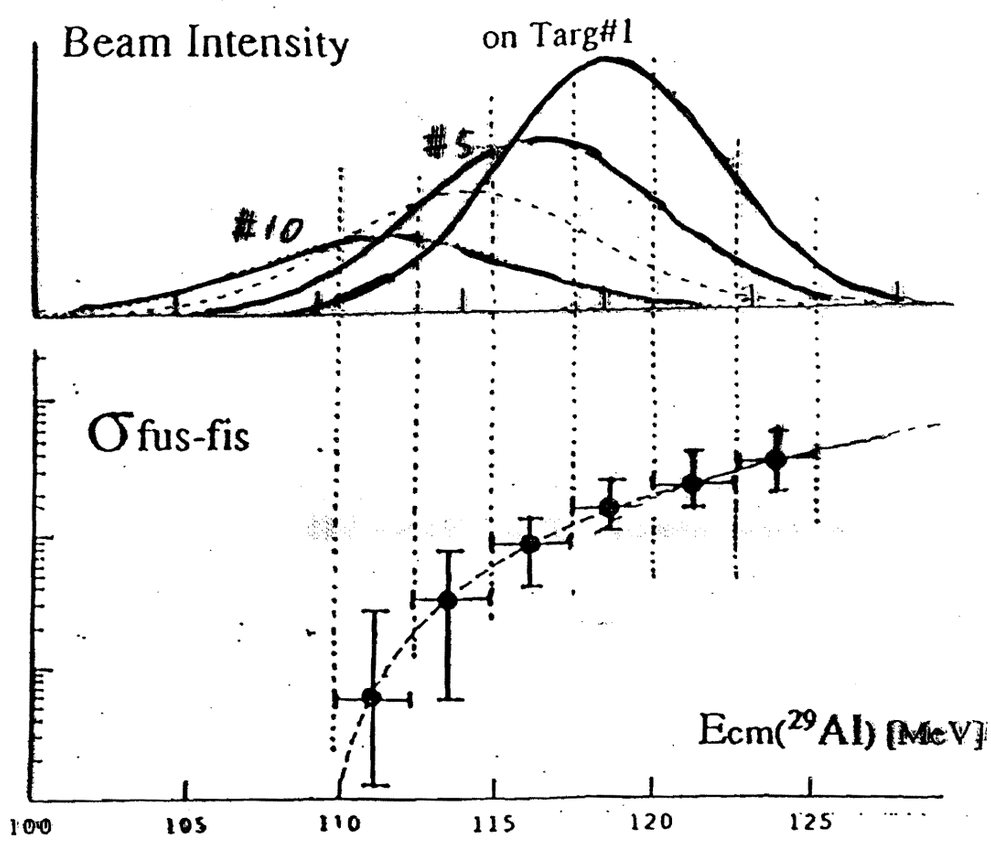
Beam Intensity
on Targ#1
#5
#10
σfus-fis
Ecm(29Al) [MeV]
100
105
110
115
120
125

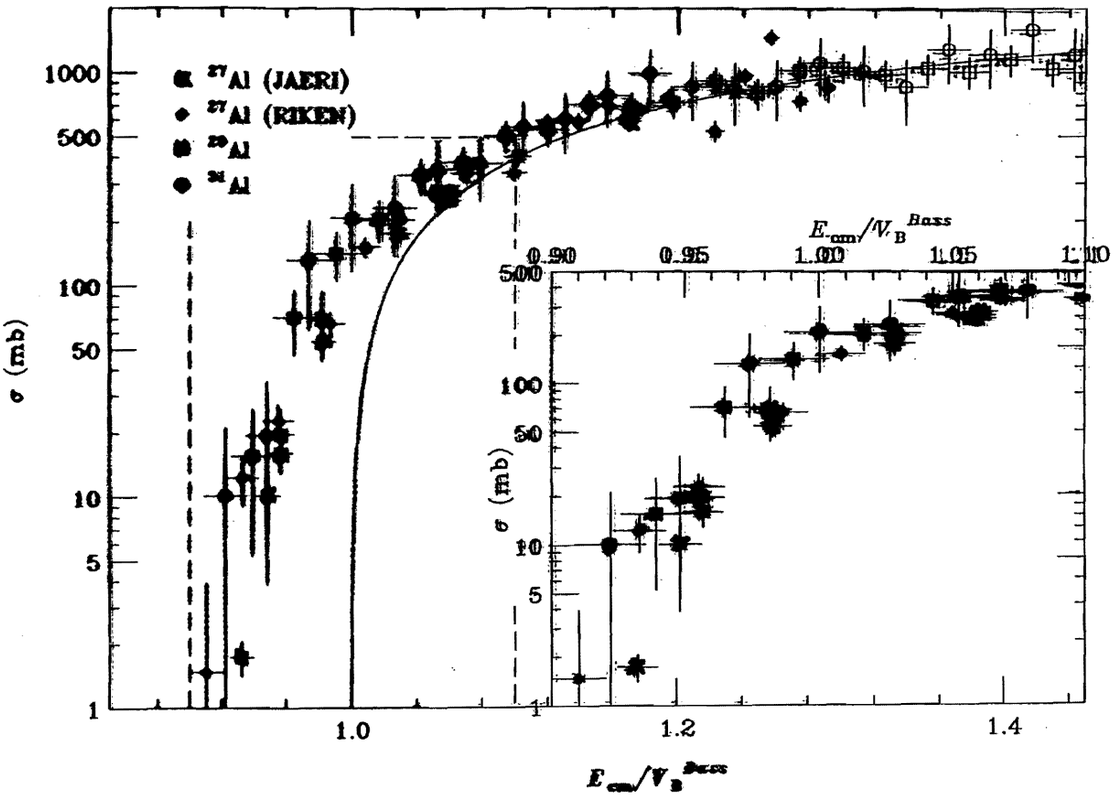
^{27}Al (JAERI)
^{27}Al (RIKEN)
^{29}Al
^{31}Al
σ (mb)
1000
500
100
50
10
5
1
1.0
1.2
1.4
E_{cm}/V_B^{Bass}
0.90
0.95
1.00
1.05
1.10

9, 10, 11 Be + 209 Bi

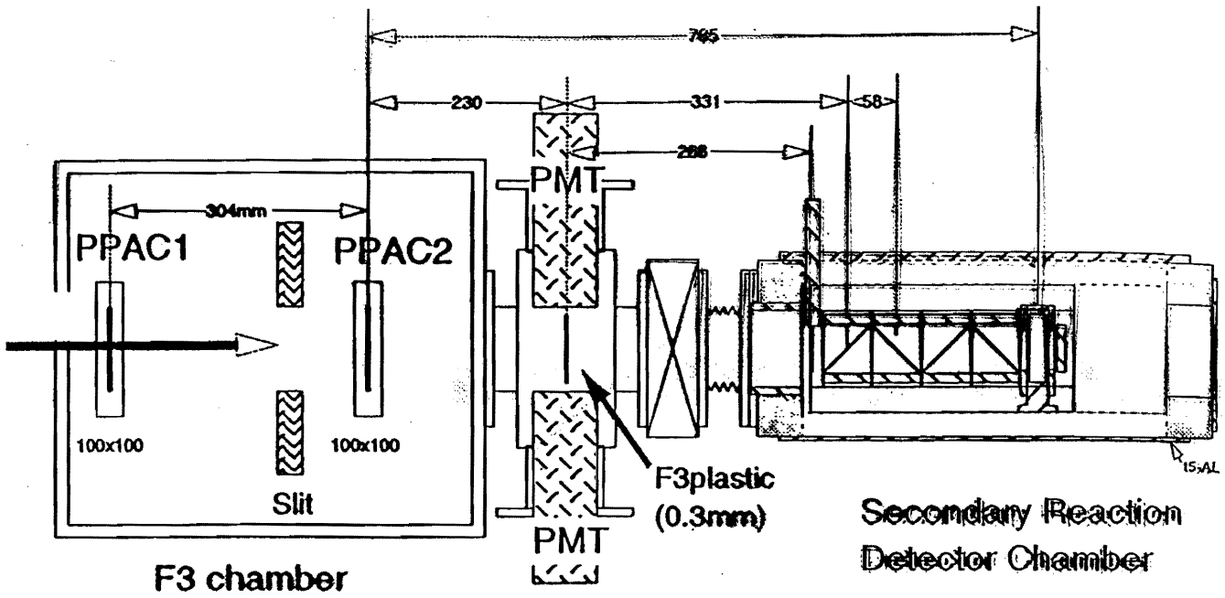

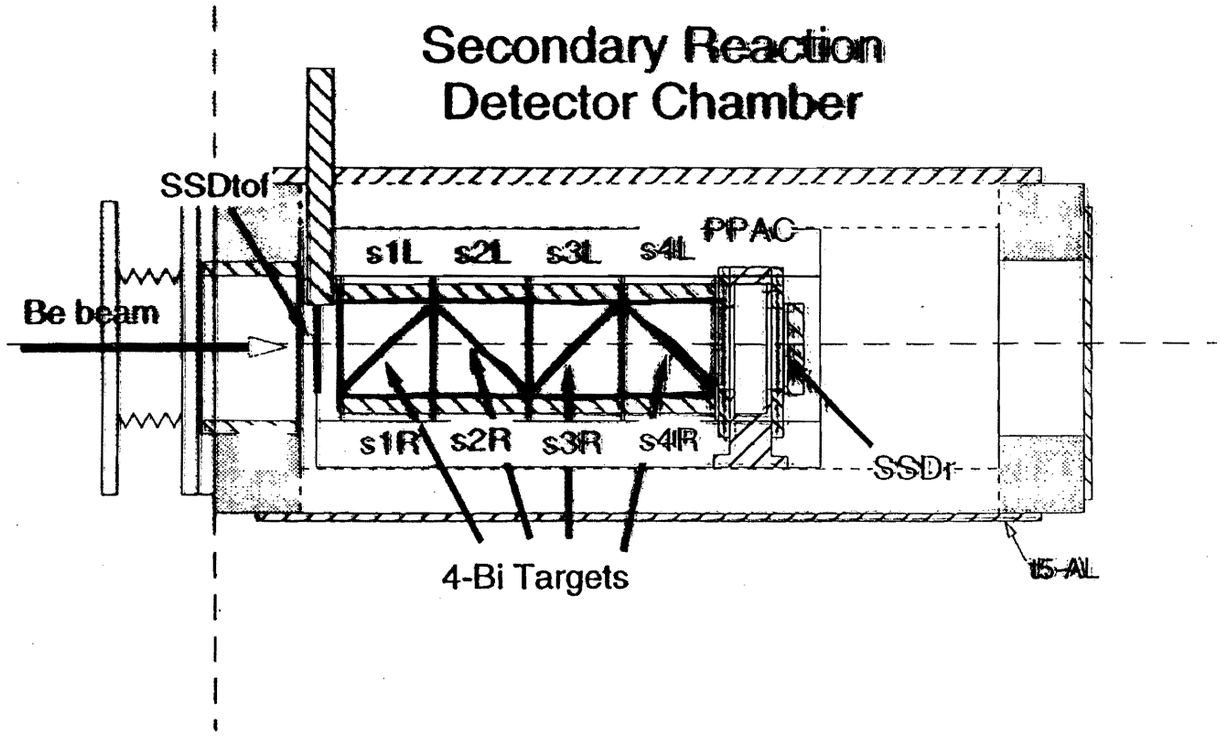

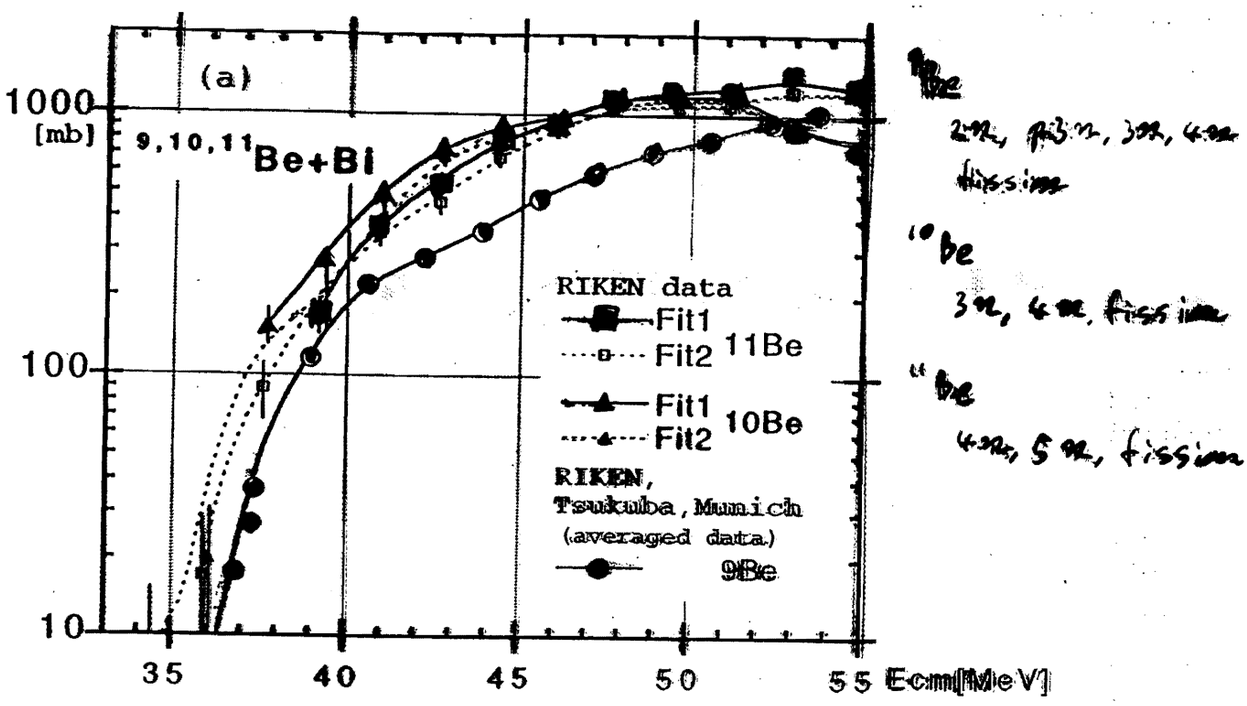
(a)
1000
[mb]
9,10,11Be+Bi
100
10
RIKEN data
Fit1
Fit2
11Be
Fit1
Fit2
10Be
RIKEN,
Tsukuba, Munich
(averaged data)
9Be
35
40
45
50
55
Ecm[MeV]

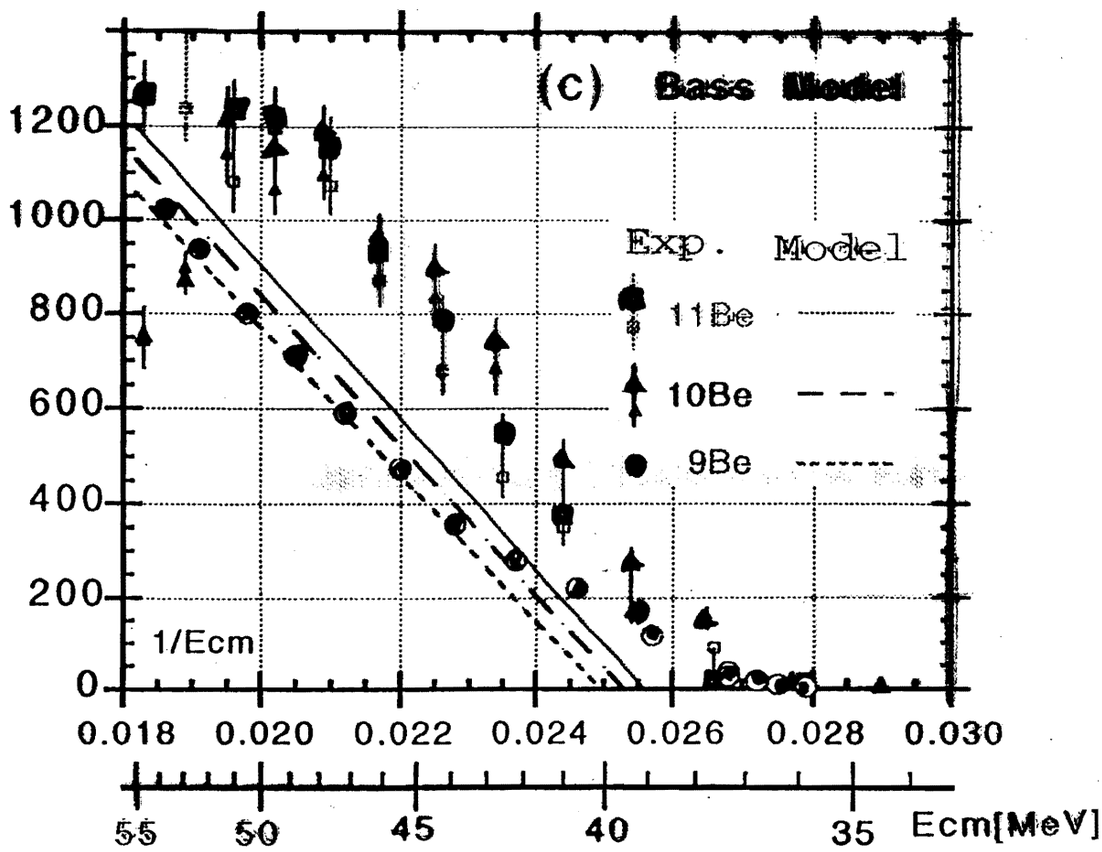
(c) Bass Model
1200
1000
800
600
400
200
0
Exp. Model
11Be
10Be
9Be
1/Ecm
0.018
0.020
0.022
0.024
0.026
0.028
0.030
55
50
45
40
35
Ecm[MeV]

4, 6, 8 He + 40 Ar

MUSIC Detector

MUlti-Sampling Ionization Chamber

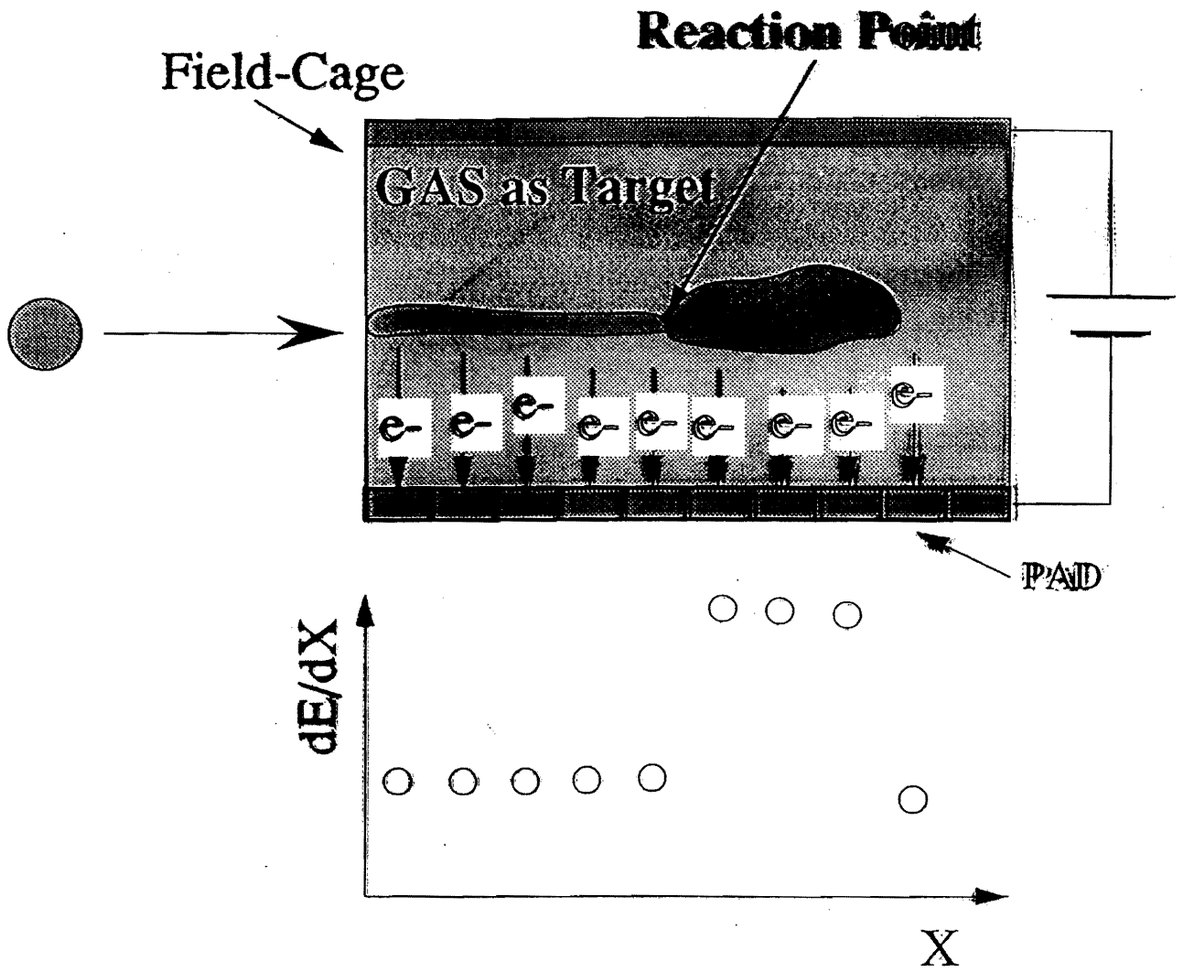

React in Detector

→ **High Efficiency**

dE/dX Multi-Sampling

→ **Excitation Function**

→ **Target Thickness**

New MUSIC

→ **3D-Tracking**
Event Selection

fusion

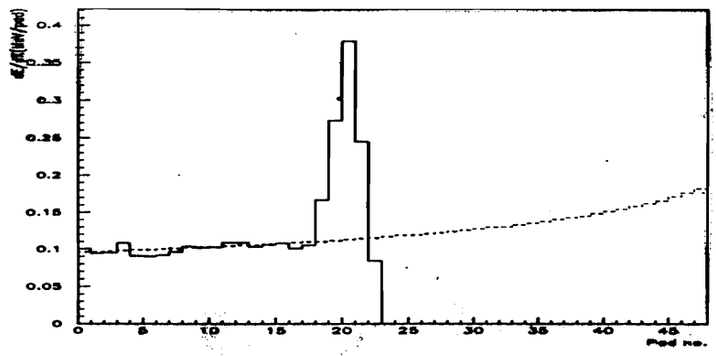

elastic scattering

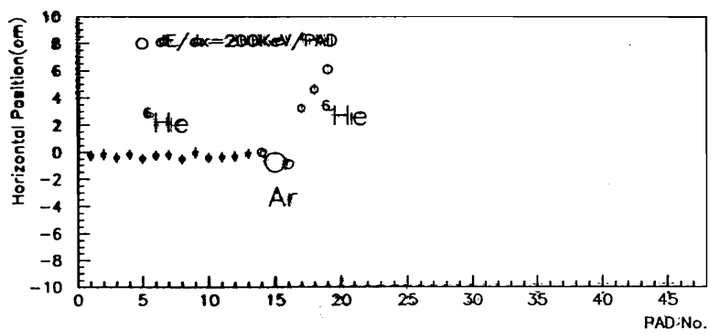

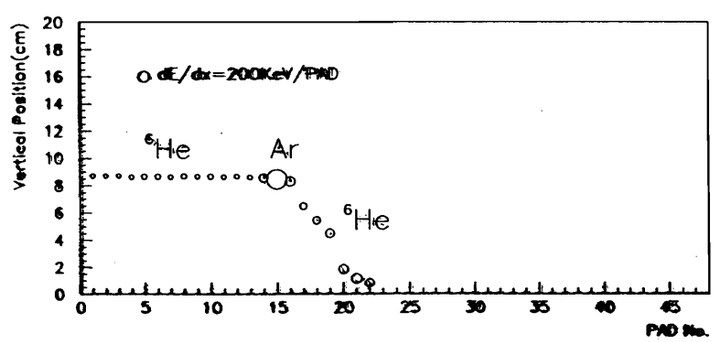

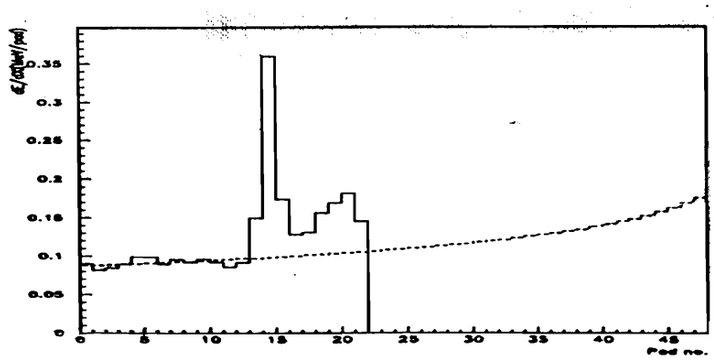

sd-pf 殻領域における
有効相互作用と不安定核の構造

原研　　宇都野 穣

―― 共同研究者 ――

東大理／理研　　大塚 孝治

専修大 法　　水崎 高浩

会津大数理セ　　本間 道雄

8/21－22　理研ワークショップ

「クラスター研究会　――テンソル力と核構造――」

内容

sd－pf 殻領域における殻構造の
遷移とその殻模型による理解.

- Introduction
  ～ sd－pf 殻領域における魔法数 ～
- 変化する殻構造.
  - pf 殻の例
  - monopole interaction の役割
  - sd－pf 殻領域の 1粒子エネルギー
  - 不安定核の構造との関連.

Introduction

○殻構造　　sd-pf 殻領域

安定核領域 …… N=20 の魔法数が安定

⇕

不安定核領域 … N=20 魔法数消滅 (Z≃12)

T. Motobayashi et al., Phys. Lett. B 346, 9 (1995)

N=16 魔法数の出現 (Z≃8)

A. Ozawa et al., Phys. Rev. Lett. 84, 5493 (2000)

"Island of inversion" (Warburton et al. による予想)

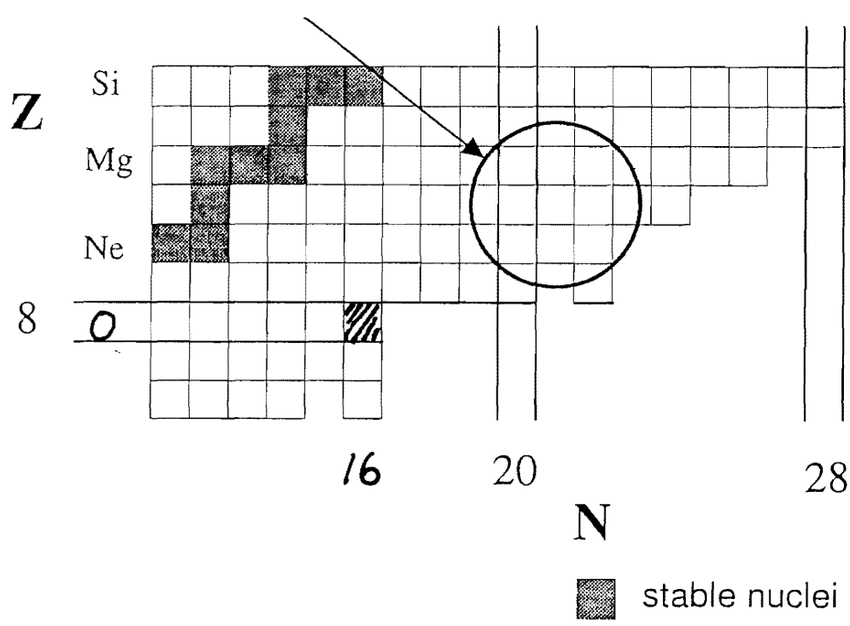

Energy levels and B(E2) values of Mg

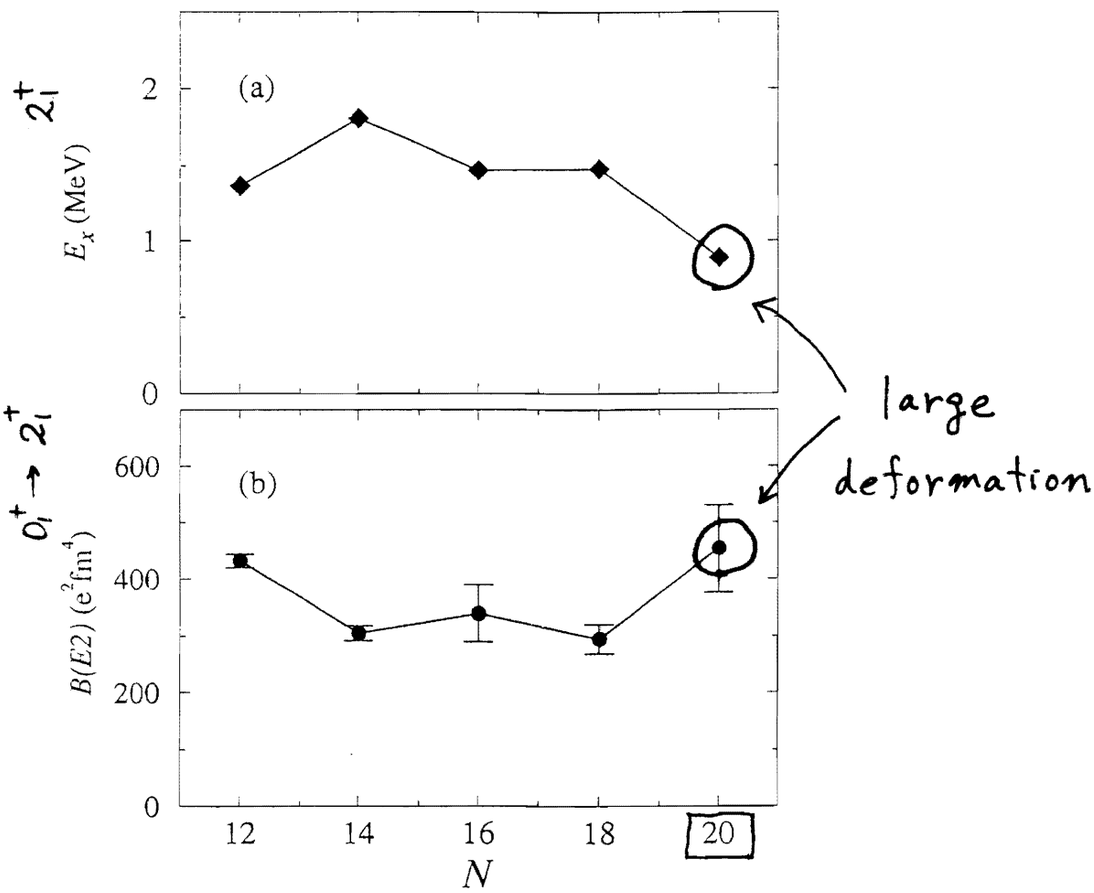

Exp. (^{32}Mg) : C. Détraz et al., PRC 19, 164 (1979);
D. Guillemaud-Mueller et al., NP A426, 37 (1984)
T. Motobayashi et al., PLB 346, 9 (1995)

New Magic Number, $N = 16$, near the Neutron Drip Line

A. Ozawa,[1] T. Kobayashi,[2] T. Suzuki,[3] K. Yoshida,[1] and I. Tanihata[1]

[1]*The Institute of Physical and Chemical Research (RIKEN), Hirosawa 2-1, Wako-shi, Saitama 351-0198, Japan*

[2]*Department of Physics, Tohoku University, Miyagi 980-8578, Japan*

[3]*Department of Physics, Niigata University, Niigata 950-2181, Japan*

(Received 15 February 2000)

We have surveyed the neutron separation energies (S_n) and the interaction cross sections (σ_I) for the neutron-rich p-sd and the sd shell region. Very recently, both measurements reached up to the neutron drip line, or close to the drip line, for nuclei of $Z \leq 8$. A neutron-number dependence of S_n shows clear breaks at $N = 16$ near the neutron drip line ($T_Z \geq 3$), which shows the creation of a new magic number. A neutron-number dependence of σ_I shows a large increase of σ_I for $N = 15$, which supports the new magic number. The origin of the new magic number is also discussed.

PACS numbers: 21.10.Dr, 21.10.Pc, 25.60.Dz, 27.30.+t

Recently, nuclear structure for neutron-rich nuclei has attracted much attention because of its exotic nature, such as a halo and a skip [1]. However, experimental observations have been limited to neutron-rich nuclei due to access difficulties. Recent improvements of secondary-beam techniques now allow us to measure the mass and the interaction cross sections (σ_I) for nuclei on the neutron drip line or close to the drip line. Direct mass measurements have reached or been near the drip line for $Z \leq 8$ [2]. On the other hand, measurements of σ_I have reached the drip line for $Z \leq 8$, except for ^{22}C [3]. Both improvements allow us to survey the systematics of neutron separation energies (S_n) and σ_I for the neutron-rich p-sd and the sd shell region. It is noted that recent progress involving a Glauber model analysis for σ_I allows us to distinguish the angular momentum of a valence neutron and provides some spectroscopic information [3]. The analysis is a good tool to investigate nuclear structure for neutron-rich nuclei, where spectroscopic information, even for spin parity, is not known at all.

The shell structure is one of the very important quantities concerning nuclear structure. Recently, magic numbers in the neutron-rich region were extensively studied, both experimentally and theoretically. For example, the disappearance of the $N = 20$ closed shell was shown in ^{32}Mg experimentally in terms of a low-lying 2^+ level [4] and a large $B(E2; 0_1^+ \rightarrow 2_1^+)$ value [5]. Also, mixing of $2s_{1/2}$ and $1p_{1/2}$ orbitals eliminates the $N = 8$ magic number in neutron-rich Li and Be isotopes [6,7]. Although the disappearance of magic numbers has been discussed, as shown above, no appearance of a magic number has thus far been shown experimentally.

In this Letter, we survey S_n and σ_I for the neutron-rich p-sd and the sd shell region to investigate a new magic number. $N = 16$ for nuclei near the neutron drip line shows a new magic number in the systematics of a neutron-number dependence of S_n and σ_I.

We show a neutron (N) number dependence of experimentally observed S_n [2] for nuclei with odd N and even Z (odd N and odd Z) in Figs. 1(a) and 1(b), respectively. In Fig. 1, a magic number appears as a decrease of S_n along with an increase of N [9]. The traditional magic numbers ($N = 8, 20$) are clearly seen close to the stable nuclei as breaks in the small T_z lines. However, the break at $N = 8$ ($N = 20$) disappears at $T_z = 3/2$ ($T_z = 4$), which is also known in connection with other experimental quantities, as discussed above. On the other hand, a break in the S_n line appears at $N = 16$ for $T_z \geq 3$, as clearly shown in

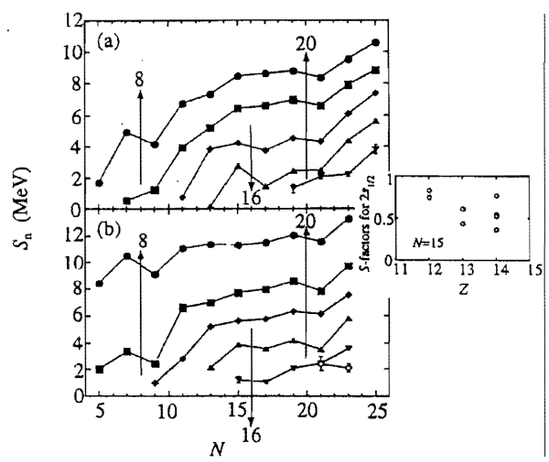

FIG. 1. (a) Neutron (N) number dependence for experimentally observed neutron separation energies (S_n) [2] for nuclei with odd N and even Z. The closed circles, closed squares, closed diamonds, closed triangles, and closed inverse triangles show different isospin numbers (T_z) from 1/2 to 9/2. (b) Neutron (N) number dependence for experimentally observed S_n [2] for nuclei with odd N and odd Z. The closed circles, closed squares, closed diamonds, closed triangles, closed inverse triangles, and open diamonds show different T_z from 0 to 5. In the figures, we do not show experimental errors below ± 10 keV. The solid lines are guides to the eye. The breaks correspond to magic numbers, as shown by arrows. The inset shows deduced spectroscopic factors (S factors) for nuclei with $N = 15$, which are data deduced from (d, p) reactions [8].

0031-9007/00/84(24)/5493(3)$15.00 © 2000 The American Physical Society

$$H = \frac{p^2}{2M} + \frac{1}{2}M\omega^2 r^2 + \alpha\, \ell \cdot s$$

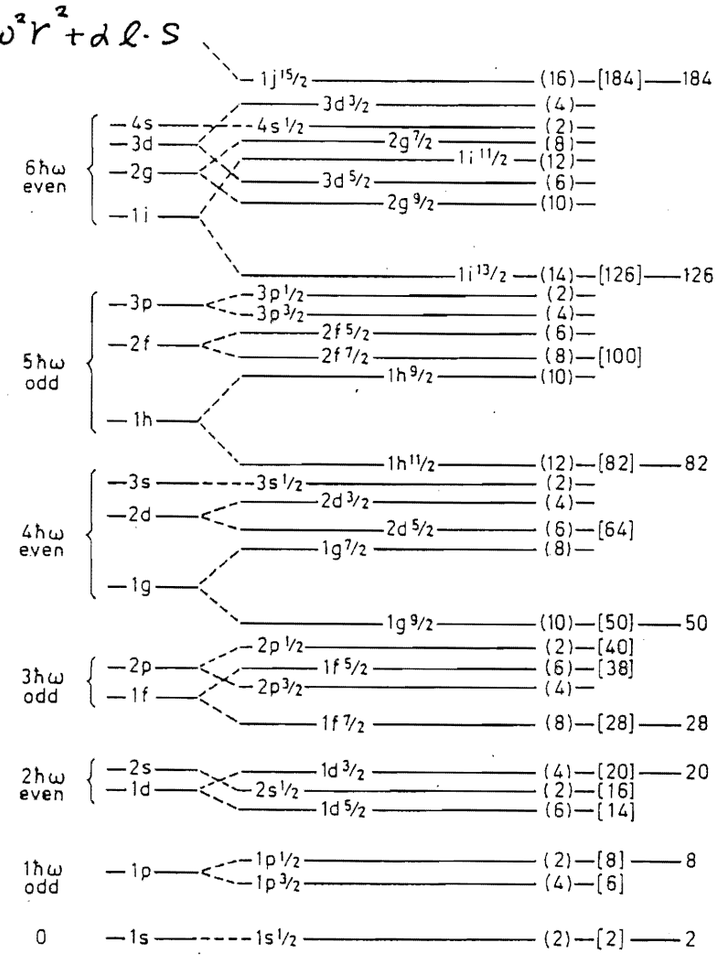

sd-shell

Figure 2-23 Sequence of one-particle orbits. The figure is taken from M. G. Mayer and J. H. D. Jensen, *Elementary Theory of Nuclear Shell Structure*, p. 58, Wiley, New York, 1955.

▼ *Spectra of odd-A nuclei compared with predictions of one-particle model (Fig. 2-24)*

The evidence on the spins and parities of the low-lying states of odd-A nuclei is summarized in Fig. 2-24 and is compared with the predictions of the simple one-particle model described in the text.

Since the one-particle model assumes that the core remains in the $I\pi = 0+$ configuration of the even-even ground state, we must expect to find states foreign to this model at excitation energies of the order of the energy, $E(2+)$, of the first excited $I\pi = 2+$ states of even-even nuclei (for the observed values of $E(2+)$, see Fig. 2-17). Thus, we have included in Fig. 2-24 only the states with excitation energies less than $\frac{1}{2}E(2+)$ in the case of states with the same parity as the ground
▲ state; for states of the opposite parity, the highest excitation energy included

Shell Model and Realistic Interactions

this transparency is from Dr. Nowacki

- Hilbert Space $\Longrightarrow$ Valence Space

- V_{nn} (nucleon - nucleon) $\Longrightarrow$ G Matrix

  Perturbation Theory

... BUT IT DOES NOT WORK !!!

		Expt.	KB	KLS	Bonn A	Bonn B	Bonn C
			2_1^+ excitation energy				
	^{44}Ca	1.16	1.45	1.43	1.31	1.25	1.26
	^{46}Ca	1.35	1.45	1.42	1.26	1.22	1.23
$N=28$	^{48}Ca	3.83	1.80	1.60	1.23	1.30	1.41
	^{50}Ca	1.03	1.41	1.35	1.27	1.10	1.17
	$\langle (f_{7/2})^8 \vert \Psi_{GS} \rangle$		0.468	0.381	0.214	0.345	0.437
			^{56}Ni Model space $(f_{7/2}p_{3/2})^{16}$				
$N=Z=28$	^{56}Ni	2.70	0.39	0.31	0.43	0.42	0.42
	$\langle (f_{7/2})^{16} \vert \Psi_{GS} \rangle$		0.04	0.015	0.018	0.011	0.019
	$\langle n_{3/2} \rangle$		4.5	5.2	5.7	5.2	5.0

Realistic Interactions do not reproduce

$N = Z = 28$ Shell Closure.

WHY ??

N=28 の shell gap について.

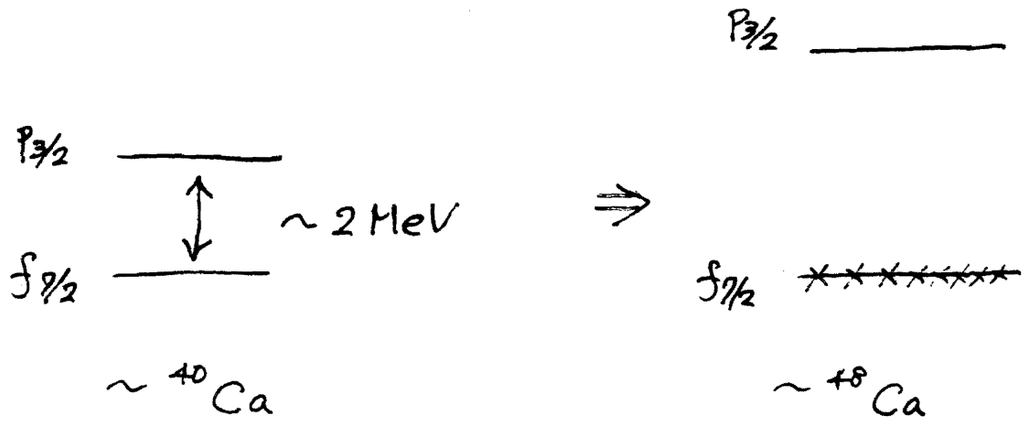

$f_{7/2}$ に核子が入ることにより.

$f_{7/2}$ が他の軌道よりもより安定になる.

⇓

$f_{7/2} - f_{7/2}$ の "平均" interaction は.

$f_{7/2} - r$ ($r = f_{5/2}, p_{3/2}, p_{1/2}$) のよりも

強い引力.

orbit 間の
"平均" interaction とは?

Monopole interaction

J dependenceを平均化したinteraction：

$$V_{ij}^{T} = \frac{\Sigma_J (2J+1) \langle ij | V | ij \rangle_{JT}}{\Sigma_J (2J+1)}, \qquad \text{for } T = 0, 1.$$

；diagonal matrix element のJに関 平均化

を用いて

$$H_{ij}^{(mT)} = \sum_{k=i,j} \left\{ \frac{a_{kk}}{2} \hat{n}_k (\hat{n}_k - 1) + \frac{b_{kk}}{2} \left(\hat{T}_k^{\,2} - \frac{3}{4} \hat{n}_k \right) \right\} \quad \text{orbit 内}$$

i, j: orbit

$$+ a_{ij} \hat{n}_i \hat{n}_j + \frac{b_{ij}}{2} \left\{ \left(\hat{T}_i + \hat{T}_j \right)^2 - \hat{T}_i^{\,2} - \hat{T}_j^{\,2} \right\}, \quad \text{orbit 間}$$

where

Bansal – French formula

$$a_{ij} = \frac{1}{4} \left(3V_{ij}^1 + V_{ij}^0 \right), \qquad b_{ij} = V_{ij}^1 - V_{ij}^0$$

- isospin dependence, two-body interaction

  isospin coupling を fix → i, j 間 monopole $\propto A_{ij} \hat{n}_i \hat{n}_j$

  A_{ij} : orbit i, j 間の average interaction の strength

  1) $T_i = T_j = T_i + T_j = 0$; $(N=Z)$ $\quad A_{ij} = \frac{1}{4} \left(3V_{ij}^1 + V_{ij}^0 \right)$

  2) i, j に proton (neutron) だけ; $\quad A_{ij} = V_{ij}^1$

  不安定核では この isospin dependence が特に重要

  - V_{ij}^0 : strongly attractive, $\quad V_{ij}^1$: weak

- total binding energy に大きく寄与

- orbit-number dependence

  → N, Z とともに変化する single-particle structure

  ⇓

  "effective single particle energy"

V (MeV)

monopole int. V_{ij}^{T} for pf shell.

1: $f_{7/2}$

2: $p_{3/2}$

3: $f_{5/2}$

4: $p_{1/2}$.

i	j	T	KB	KB3	FPD6
1	1	0	-1.15383	-1.50250	-1.46240
1	2	0	-0.96825	-1.26825	-1.20067
1	3	0	-1.63417	-1.93417	-1.84556
1	4	0	-1.06888	-1.36887	-1.24028
2	2	0	-1.47410	-1.47410	-1.45482
2	3	0	-0.93263	-0.93262	-1.22322
2	4	0	-2.04475	-2.04475	-1.84312
3	3	0	-0.95071	-0.95071	-1.34367
3	4	0	-0.75358	-0.75358	-1.17177
4	4	0	-1.07400	-1.07400	-1.19210
1	1	1	-0.12775	-0.24071	-0.20750
1	2	1	-0.10381	0.19619	0.17390
1	3	1	-0.22529	0.07471	-0.08238
1	4	1	-0.14144	0.15856	0.23946
2	2	1	-0.51767	-0.51767	0.01050
2	3	1	-0.01533	-0.01533	0.09292
2	4	1	-0.37300	-0.37300	0.14820
3	3	1	0.04880	0.04880	-0.08736
3	4	1	0.06333	0.06333	0.15152
4	4	1	-0.24900	-0.24900	-0.14060

KB3 : A. Poves and A.P. Zuker, Phys. Rep. 70, 235 (1981)

FPD6 : W. A. Richter et al., Nucl. Phys. A523, 325 (1991)

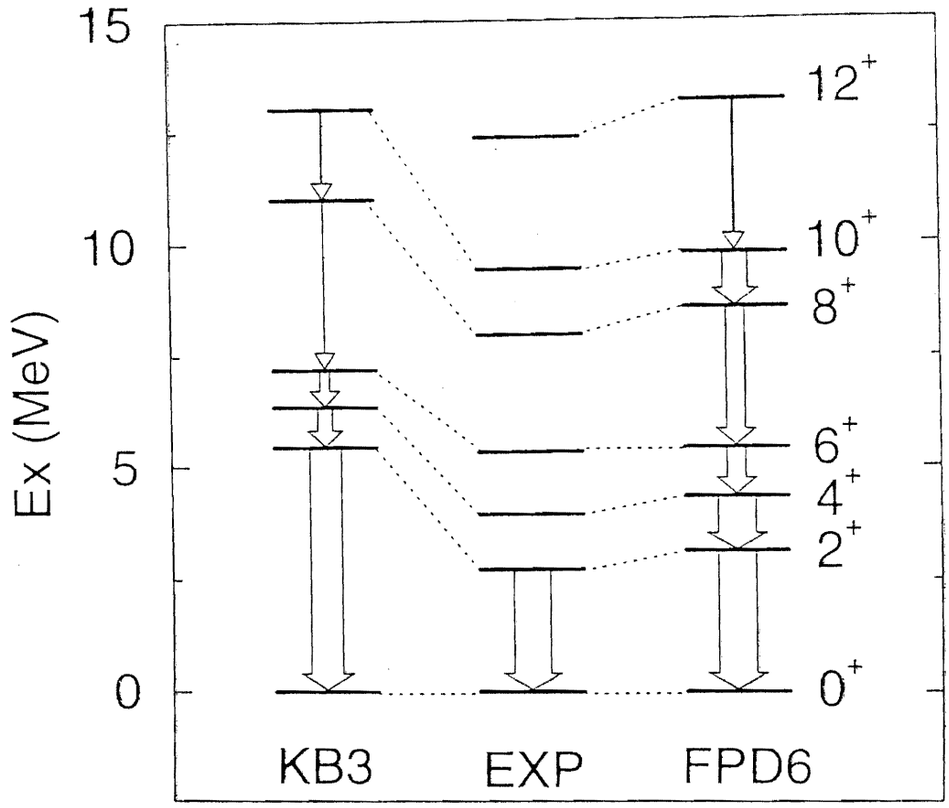

FIG. 1. Experimental (EXP) yrast levels of ^{56}Ni compared with QMCD results with FPD6 and KB3 Hamiltonians. The $B(E2;(L+2)_1^+ \rightarrow L_1^+)$ value is indicated by the width of the arrow, which is so that the experimental $B(E2;2_1^+ \rightarrow 0_1^+)$ value takes its mean value, i.e., 120 e^2 fm^4 [15].

1590

T. Otsuka et al., Phys. Rev. Lett. 81, 1588 (1998).

monopole interaction について
の一般的傾向.

- T=0 は強い引力
- T=1 は弱い引力 もしくは弱い斥力
  同じ orbit 間は引力がやや強い傾向.

G-matrix のような微視的理論では.
上の傾向は再現されるが. 定量的には
不十分なこともありうる.

O, F の S_{2n} values

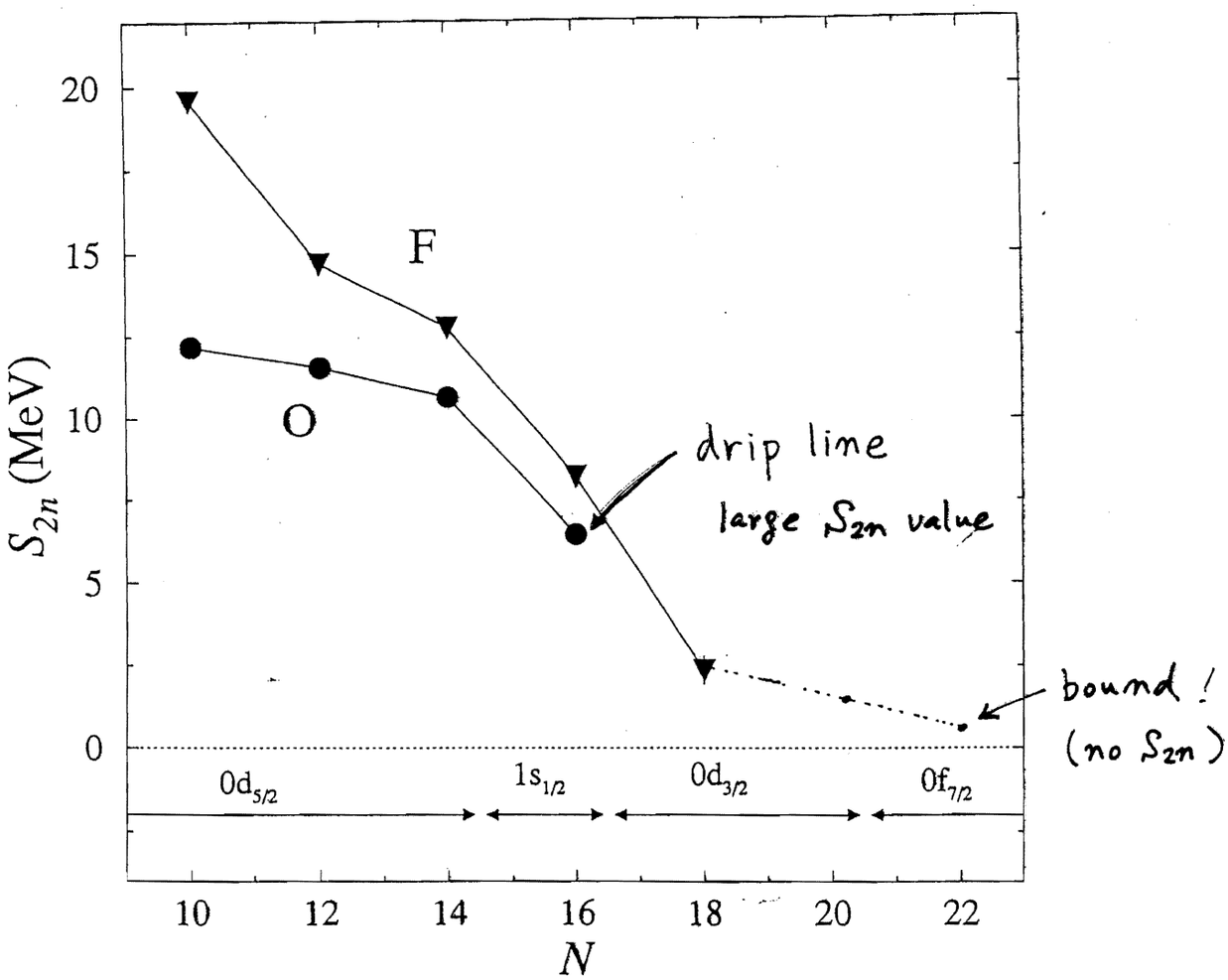

^{31}F : H. Sakurai et al., PLB 448, 180 (1999)

V_{ij}^{T} for sd-pf shell

i	j	T	SDPF	KOUSD
1	1	0	-2.44347	-1.95189
1	2	0	-4.15682	-3.61920
1	3	0	-2.74700	-2.23510
1	4	0	-3.10212	
1	5	0	-1.91045	
2	2	0	-2.94697	-2.35245
2	3	0	-2.85463	-2.41286
2	4	0	-2.90692	
2	5	0	-1.92199	
3	3	0	-3.26280	-3.18390
3	4	0	-2.00437	
3	5	0	-3.06849	
4	4	0	-1.46615	
4	5	0	-1.23033	
5	5	0	-1.87311	
1	1	1	-0.38617	-0.07043
1	2	1	-0.01022	-0.64238
1	3	1	-0.02652	-0.12292
1	4	1	0.08261	
1	5	1	0.06549	
2	2	1	-0.60044	-0.53793
2	3	1	0.10389	-0.43612
2	4	1	-0.08372	
2	5	1	-0.08974	
3	3	1	-2.02460	-1.94930
3	4	1	-0.17483	
3	5	1	-0.48163	
4	4	1	-0.16233	
4	5	1	-0.13191	
5	5	1	-0.65779	

1: $d_{3/2}$

2: $d_{5/2}$

3: $s_{1/2}$

4: $f_{7/2}$

5: $p_{3/2}$

O isotopes (exact diagonalization)

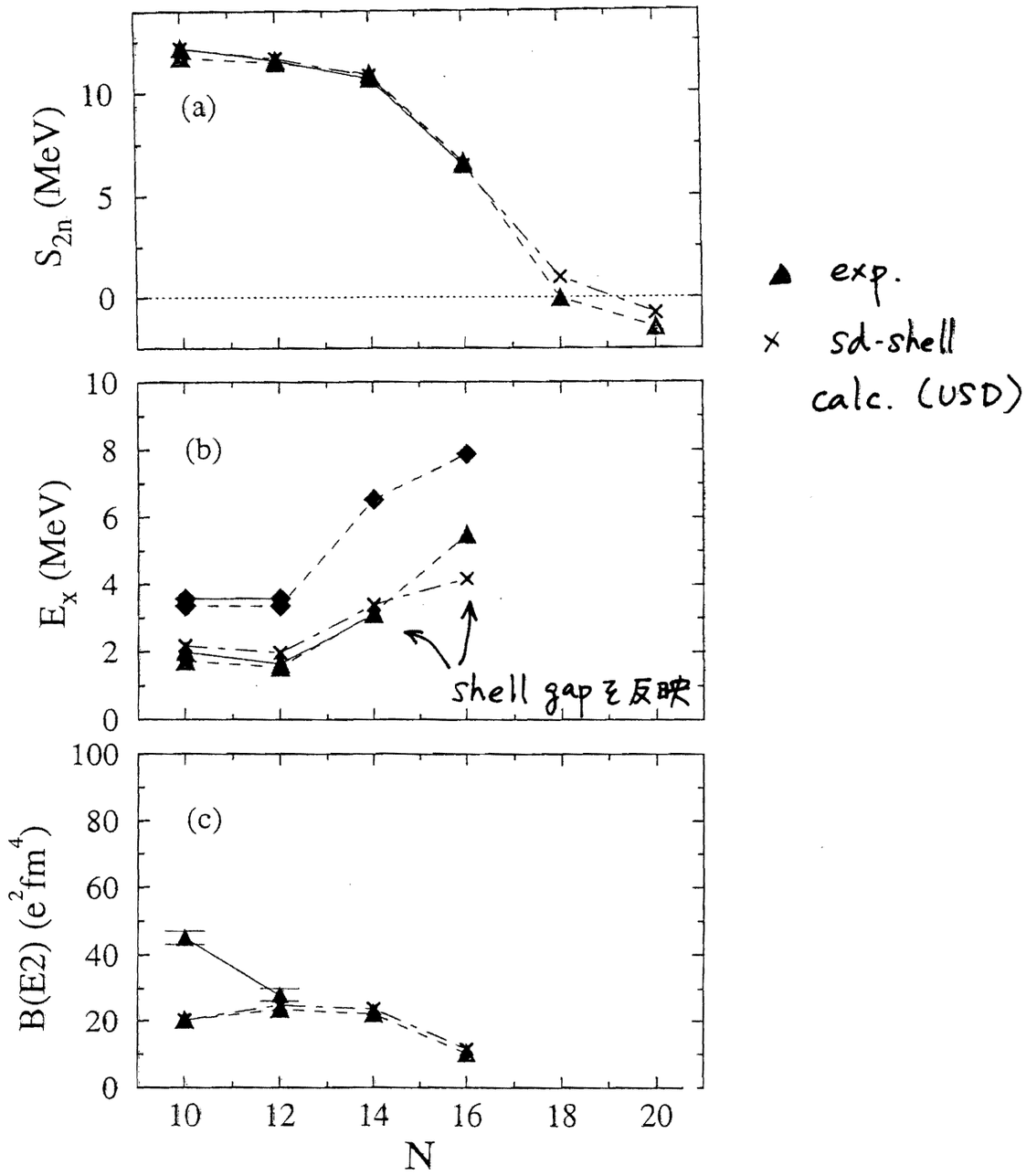

Effective single particle energy

= 2体力の効果を取り入れる (monopole interaction)

→ N, Z により変化する.

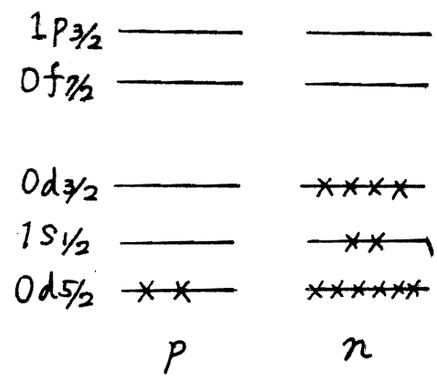

1. 与えられた N, Z に対し. 自然な配位を考える.

2. その配位のエネルギーを. bare な single particle energy と monopole interaction により見積もる.

(isospin の coupling は lowest であると仮定する)

3. occupied orbit に対しては separation energy, unoccupied orbit に対しては additional binding energy により. その orbit の effective single particle energy を定義する.

N = 14 の effective shell gap.

($d_{5/2}$ - $s_{1/2}$) for neutrons

unit : MeV

Z \ N	8	9	10	11	12	13	14	15	16	17	18	19	20
8	0.8	0.9	1.6	2.3	2.9	3.6	4.2	4.1	2.1	2.0	2.0	2.0	2.0
9	0.9	2.5	2.0	2.7	3.3	4.0	4.6	4.4	2.4	2.4	2.4	2.3	2.3
10	1.3	1.5	3.6	3.1	3.7	4.3	4.9	4.7	2.8	2.7	2.7	2.7	2.6
11	1.6	1.9	2.6	4.6	4.1	4.7	5.3	5.1	3.1	3.1	3.0	3.0	2.9
12	2.0	2.3	2.9	3.6	5.5	5.0	5.6	5.4	3.4	3.4	3.3	3.3	3.3
13	2.4	2.7	3.3	3.9	4.5	6.4	5.9	5.7	3.7	3.7	3.7	3.6	3.6
14	2.7	3.1	3.7	4.3	4.8	5.4	7.3	5.7	3.8	2.0	1.9	1.9	1.9
15	2.3	2.7	3.3	3.9	4.5	5.0	5.6	5.3	2.7	0.9	0.9	0.9	0.8
16	1.2	1.5	2.2	2.8	3.3	3.9	4.5	4.2	2.3	1.7	1.7	1.6	1.6
17	1.8	2.2	2.8	3.4	3.9	4.5	5.0	4.7	2.9	2.9	2.2	2.2	2.2
18	2.4	2.8	3.4	4.0	4.5	5.1	5.6	5.3	3.4	3.4	3.4	2.8	2.7
19	3.0	3.4	4.0	4.5	5.1	5.6	6.2	5.8	4.0	4.0	3.9	3.9	3.3
20	3.6	4.0	4.6	5.1	5.7	6.2	6.7	6.3	4.5	4.5	4.5	4.4	4.4

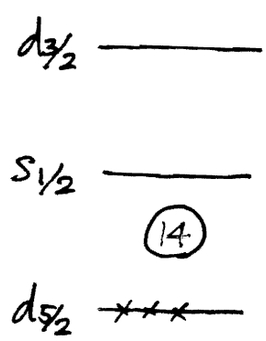

N = 16 の effective shell gap

($s_{1/2} - d_{3/2}$) for neutrons

unit : MeV

Z \ N	8	9	10	11	12	13	14	15	16	17	18	19	20
8	4.8	4.7	4.6	4.5	4.4	4.3	4.2	4.1	6.0	6.0	5.7	5.3	5.0
9	3.5	4.0	3.9	3.8	3.7	3.6	3.5	3.5	5.4	5.4	5.0	4.7	4.4
10	2.8	2.8	3.2	3.2	3.1	3.0	2.9	2.9	4.8	4.7	4.4	4.1	3.8
11	2.2	2.1	2.0	2.5	2.4	2.4	2.3	2.3	4.2	4.1	3.8	3.5	3.2
12	1.5	1.5	1.4	1.4	1.8	1.8	1.7	1.8	3.6	3.5	3.2	2.9	2.6
13	0.9	0.9	0.8	0.8	0.7	1.2	1.1	1.2	3.0	2.9	2.6	2.3	2.0
14	0.3	0.3	0.2	0.2	0.1	0.1	0.5	0.7	2.4	2.3	2.0	1.7	1.5
15	-0.5	-0.6	-0.6	-0.6	-0.7	-0.7	1.0	2.3	3.5	3.4	3.1	2.8	2.5
16	0.7	0.6	0.6	0.5	0.5	0.4	2.1	2.3	5.2	3.8	3.5	3.3	3.0
17	2.9	2.8	2.7	2.6	2.6	2.5	2.4	2.6	4.3	4.1	3.5	3.2	3.0
18	2.9	2.8	2.7	2.6	2.6	2.5	2.4	2.6	4.3	4.1	3.8	3.2	3.0
19	2.9	2.8	2.7	2.6	2.6	2.5	2.4	2.6	4.3	4.1	3.8	3.5	3.0
20	2.9	2.8	2.7	2.6	2.5	2.5	2.4	2.6	4.3	4.0	3.8	3.5	3.2

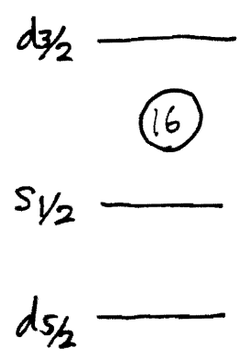

N = 20 n effective shell gap

($d_{3/2} - f_{7/2}$) for neutrons

unit : MeV

	8	9	10	11	12	13	14	15	16	17	18	19	20
8	1.5	1.4	1.3	1.2	1.2	1.1	1.0	0.9	0.8	0.9	1.3	1.7	2.1
9	2.7	2.0	1.9	1.8	1.7	1.7	1.6	1.5	1.3	1.4	1.8	2.2	2.6
10	3.3	3.2	2.4	2.4	2.3	2.2	2.1	2.0	1.8	2.0	2.4	2.8	3.2
11	3.8	3.7	3.6	2.9	2.8	2.7	2.6	2.5	2.4	2.5	2.9	3.3	3.7
12	4.3	4.2	4.1	4.0	3.3	3.2	3.1	3.0	2.9	3.0	3.4	3.8	4.2
13	4.8	4.7	4.6	4.5	4.4	3.7	3.6	3.5	3.3	3.5	3.9	4.3	4.6
14	5.3	5.2	5.1	5.0	4.9	4.8	4.1	4.0	3.8	4.0	4.4	4.8	5.1
15	6.0	5.9	5.7	5.6	5.5	5.4	4.7	4.2	4.1	4.3	4.6	5.0	5.3
16	6.2	6.1	6.0	5.8	5.7	5.6	5.0	4.8	4.3	4.5	4.9	5.2	5.6
17	2.5	2.4	2.3	2.2	2.2	2.1	3.2	3.1	3.7	5.3	4.8	5.1	5.5
18	2.4	2.3	2.2	2.2	2.1	2.0	3.1	3.0	3.6	3.9	5.5	5.0	5.4
19	2.3	2.2	2.1	2.1	2.0	1.9	3.0	2.9	3.5	3.8	4.1	5.8	5.3
20	2.2	2.1	2.1	2.0	1.9	1.9	2.9	2.8	3.4	3.7	4.1	4.4	6.0

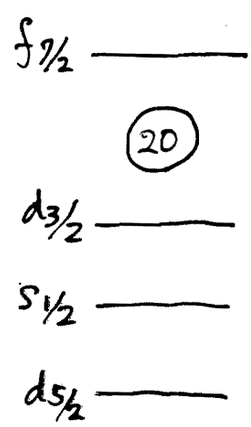

Neutron's effective single-particle energy for N=20 nuclei

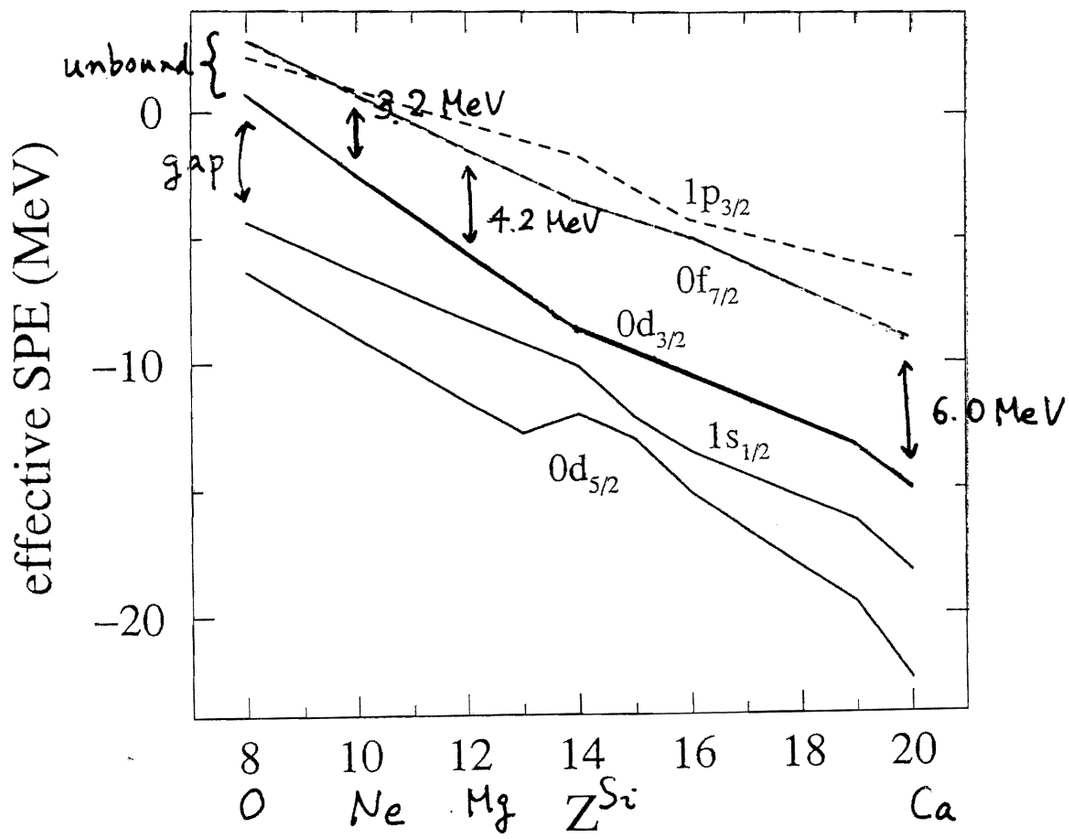

- Zの増加とともに effective SPE は下がる
  ← T=0 の monopole interaction : strongly attractive

- $0d_{3/2}$ と $0f_{7/2}$ の間の gap は Z とともに広がる.
  ← $V^{T=0}_{d_{5/2},d_{3/2}} = \underline{-4.16}$ MeV, $V^{T=0}_{f_{7/2},d_{5/2}} = \underline{-2.91}$ MeV

Effective SPE と ^{32}Mg の構造

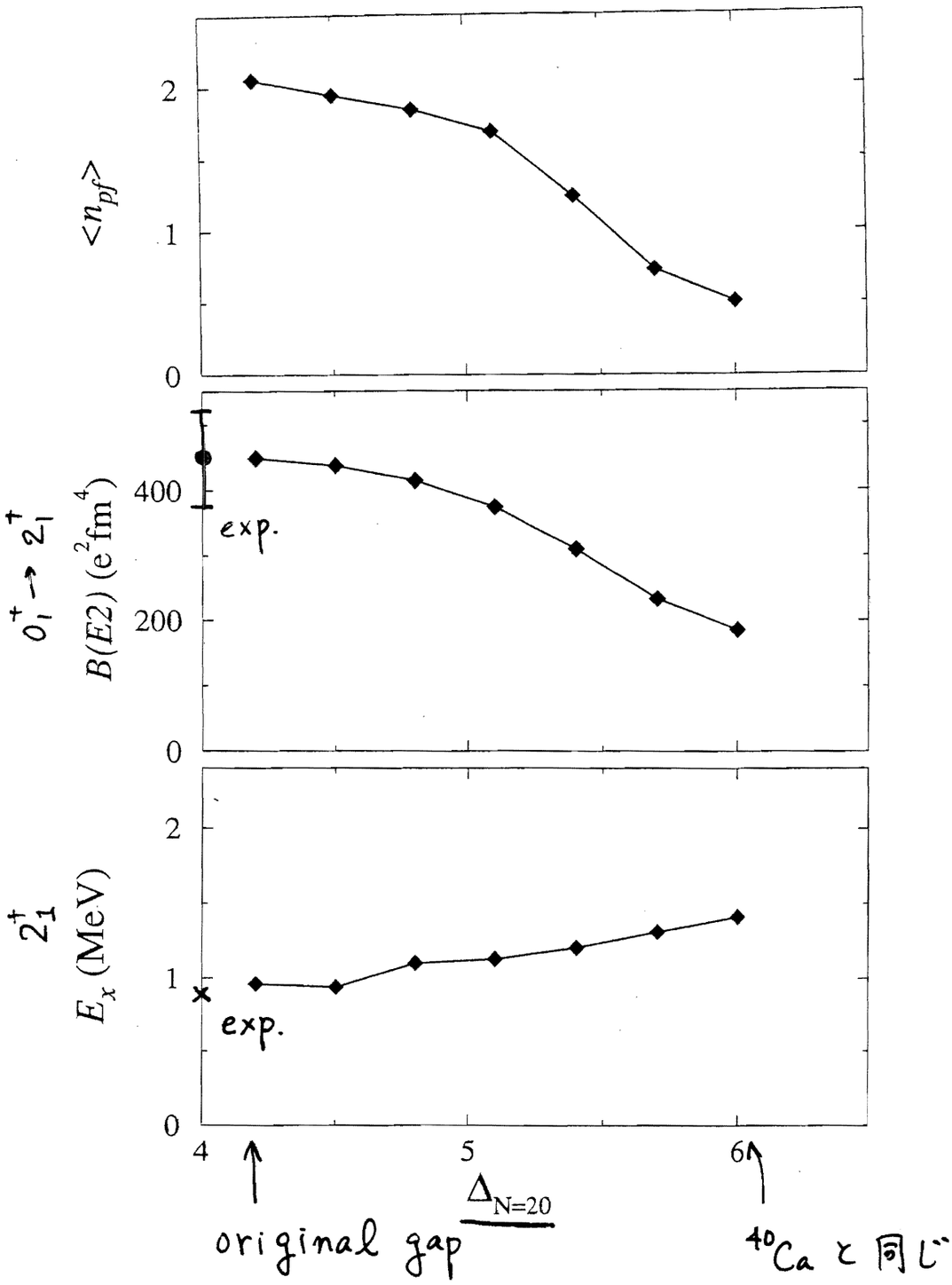

Exp. : T. Motabayashi et al., PLB 346, 9 (1995)

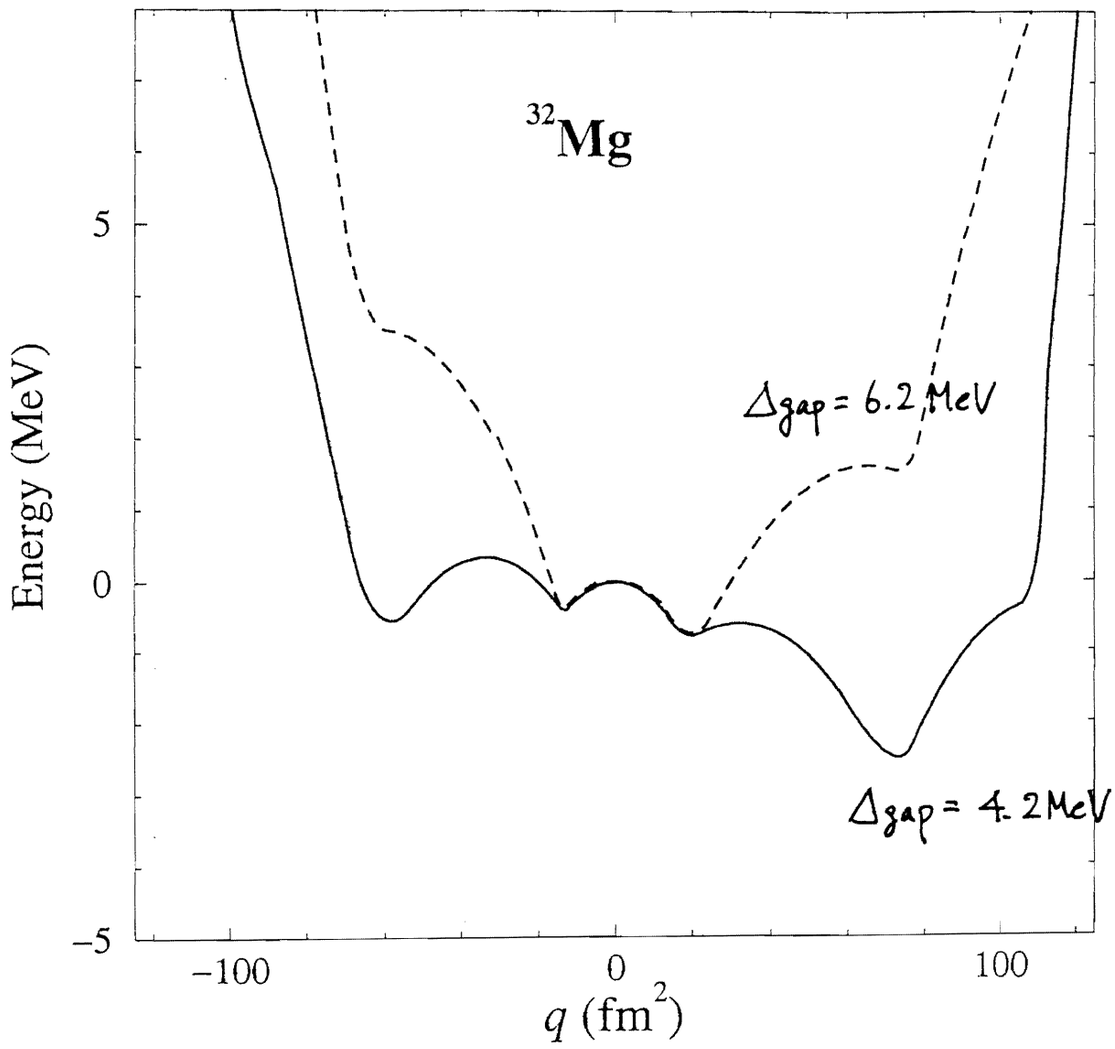
^{32}Mg
Energy (MeV)
5
0
−5
−100
0
100
q (fm^2)
Δ_{gap} = 6.2 MeV
Δ_{gap} = 4.2 MeV

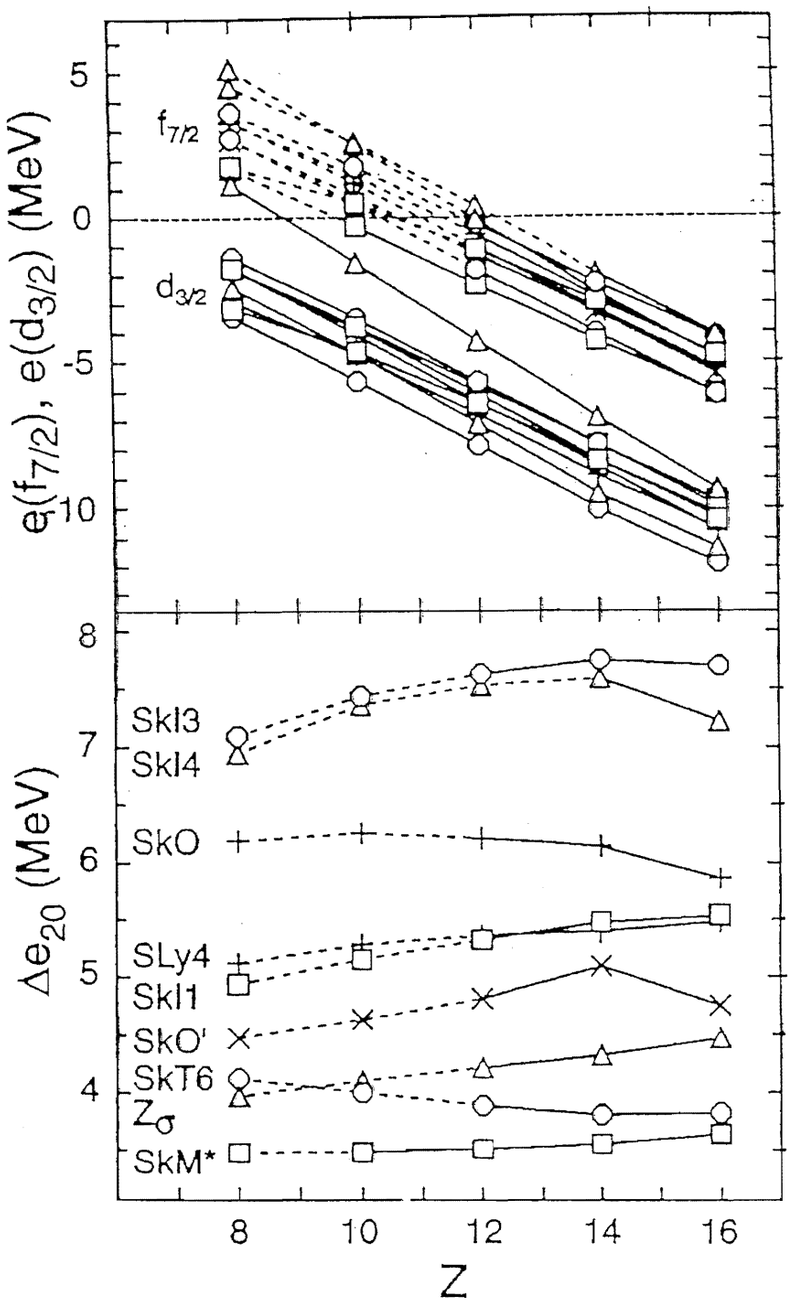

FIG. 6. Top: Single-neutron $d_{3/2}$ and $f_{7/2}$ energies as functions of Z predicted in several Skyrme-HF models. The positive-energy levels are marked by a dashed line. Bottom: the size of the corresponding single-particle $N=20$ gap, Δe_{20}.

Reinhard et al.

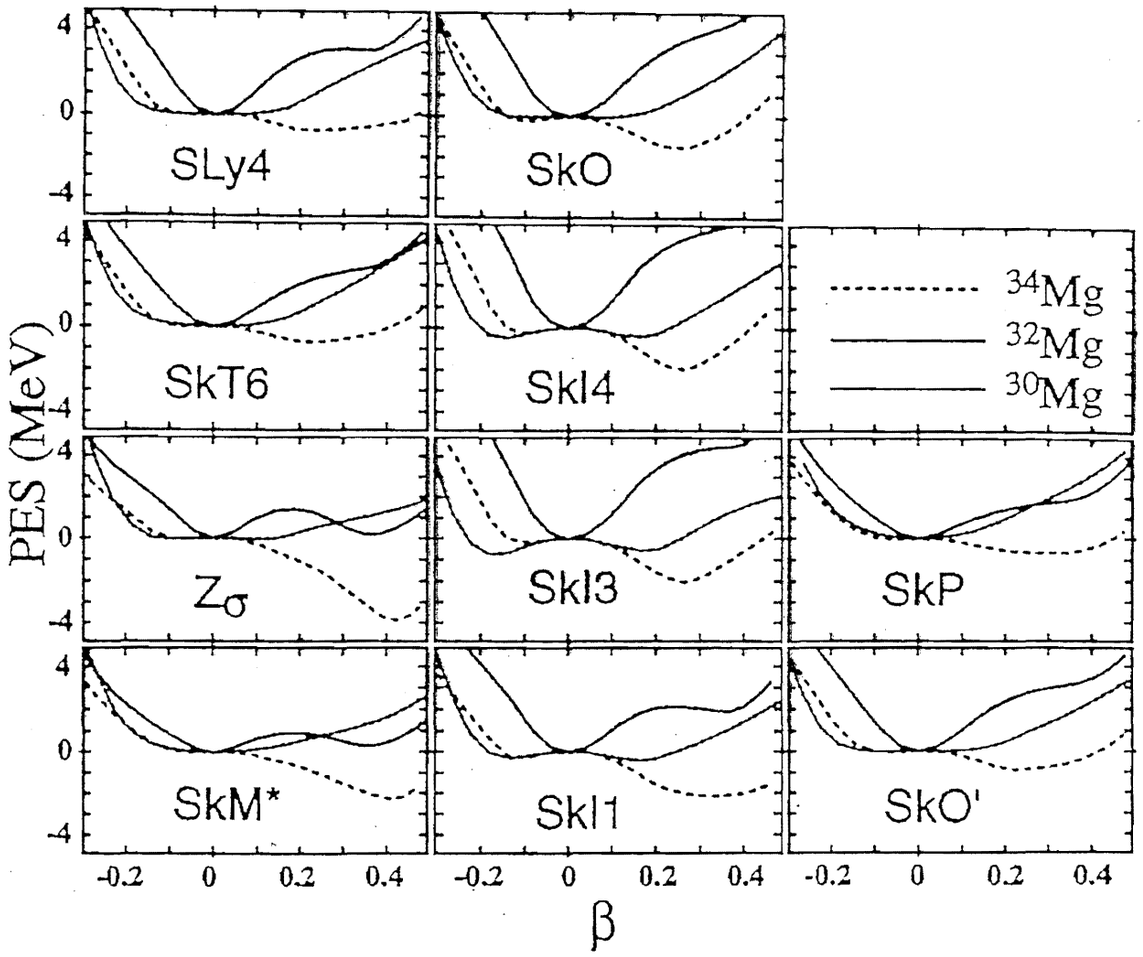

FIG. 2. Potential energy surfaces for ^{30,32,34}Mg as functions of quadrupole deformation β for the set of Skyrme parametrizations.

poses, we employ the Inglis cranking approximation which is obtained from the above expressions by letting $\hat{H} \rightarrow \hat{h}_0$, with $\hat{h}_0$ being the mean-field Hamiltonian. In the following, the results of calculations of the potential energy surfaces (PES) always pertain to the total energies corrected for the zero-point motion, as in Eq. (3.16).

Summary

- 殻模型に基づき殻構造の変遷を理解する上で、相互作用の monopole interaction が特に重要である。

- $N=16$ 魔法数の出現は、
  i) ^{16}O core に既に存在する $s_{1/2}-d_{3/2}$ gap
  ii) 弱い $T=1$ monopole interaction により $\sim^{16}O$ の shell gap が保たれること。
  iii) valence proton が不在なことによる変形の抑制
  が重要である。

- $N=20$ shell gap は、$Z\sim8$ では小さく、proton 数とともに広がる。
  変形による energy gain も、$N=20$ 魔法数消滅に対し、重要な役割を果たす。

Shell model study on Thomas-Ehrman shifts in *sd*-shell nuclei and its relevance to *rp*-process nucleosynthesis

H. Nakada

Department of Physics, Chiba University, Chiba 263-8522, Japan

1 Introduction

The structure of *sd*-shell nuclei along the β-stable line has well been described by the shell model, with the standard USD Hamiltonian [1]. While this Hamiltonian maintains isospin symmetry (except for the overall energy shifts due to the Coulomb force), the recent experiments on proton-rich nuclei have disclosed that the Thomas-Ehrman shifts (TES, the level shifts between mirror nuclei) sometimes amounts to several hundreds keV. The TES could significantly influence the scenario of the *rp*-process nucleosynthesis and related astrophysical phenomena (novae and X-ray bursts). In order to obtain reliable prediction concerning the *rp*-process, it is important to describe the TES correctly.

2 TES and residual interaction

Quite recently, we have shown [2], by analyzing the measured TES in $A \cong 16$ mirror nuclei, that the residual nuclear interaction (RNI) has smaller matrix elements as the single-particle orbit distributes over a broader range. This effect is significant for the $(1s_{1/2})_p$ orbit in proton-rich nuclei of this mass region.

The observed energy spectra of ^{16}N and ^{16}F show a remarkable difference, as illustrated in Fig. 1. Even the ground state spins do not match. If the $(0p_{1/2})^{-1} \otimes (0d_{5/2}1s_{1/2})^1$ model space is assumed, the lowest four states in ^{16}N and ^{16}F are classified into the $|0p_{1/2}^{-1}0d_{5/2}; J = 2^-, 3^-\rangle$ and $|0p_{1/2}^{-1}1s_{1/2}; J = 0^-, 1^-\rangle$ multiplets. Shell model Hamiltonian in this model space is determined phenomenologically, from the low-lying levels of ^{17}O and ^{17}F (for single-particle energies) as well as from those of ^{16}N and ^{16}F (for RNI). The RNI matrix elements thus obtained are shown in Table 1. While V_{np} is similar to V_{pn} for the $(0p_{1/2}^{-1}0d_{5/2})$ elements, the $(0p_{1/2}^{-1}1s_{1/2})$ elements show obvious discrepancy. The $V_{np}(0p_{1/2}^{-1}1s_{1/2}; J)$ element is smaller by a factor of about 0.7 than $V_{pn}(0p_{1/2}^{-1}1s_{1/2}; J)$, both

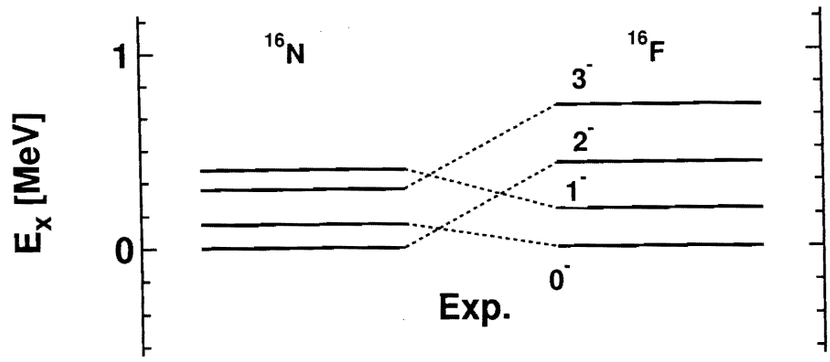

Figure 1: Experimental energy levels of ^{16}N and ^{16}F.

for $J = 0^-$ and 1^-.

The recent data on 0_2^+ of ^{16}Ne [3] also indicate the RNI reduction. By applying a reduction factor for the matrix elements regarding $(1s_{1/2})_p$ (denoted by ξ_s) to the USD interaction matrix elements, the low $E_x(0_2^+)$ of ^{16}Ne is reproduced. Figure 2 depicts the results of the shell model calculation in the small model space $(0p_{1/2})^{-2} \otimes (0d_{5/2}1s_{1/2})^2$, in comparison with the data. Though the agreement in the excitation energies between experiments and the calculation is not satisfactory, it is sufficient for qualitative argument. The TES in 0_2^+ between ^{16}N and ^{16}F cannot be accounted for by other mechanisms like, say, nucleus-dependence of the single-particle energies, which gives even higher $E_x(0_2^+)$ for ^{16}Ne than the $\xi_s = 1$ (*i.e.* no reduction for $(1s_{1/2})_p$) case. For detailed discussion, see Ref. [2].

We have also implemented a semi-microscopic calculation, in which the M3Y inter-

Table 1: Matrix elements of residual proton-neutron interaction $V_{pn}(j_1j_2;J)$ and $V_{np}(j_1j_2;J)$ deduced from ^{16}N and ^{16}F (MeV), and their ratio. Taken from Ref. [2].

j_1	j_2	J^π	$V_{pn}(j_1j_2;J)$	$V_{np}(j_1j_2;J)$	V_{np}/V_{pn}
$0p_{1/2}^{-1}$	$0d_{5/2}$	2^-	1.653	1.560	0.944
$0p_{1/2}^{-1}$	$0d_{5/2}$	3^-	1.951	1.857	0.952
$0p_{1/2}^{-1}$	$1s_{1/2}$	0^-	0.902	0.641	0.710
$0p_{1/2}^{-1}$	$1s_{1/2}$	1^-	1.179	0.834	0.707

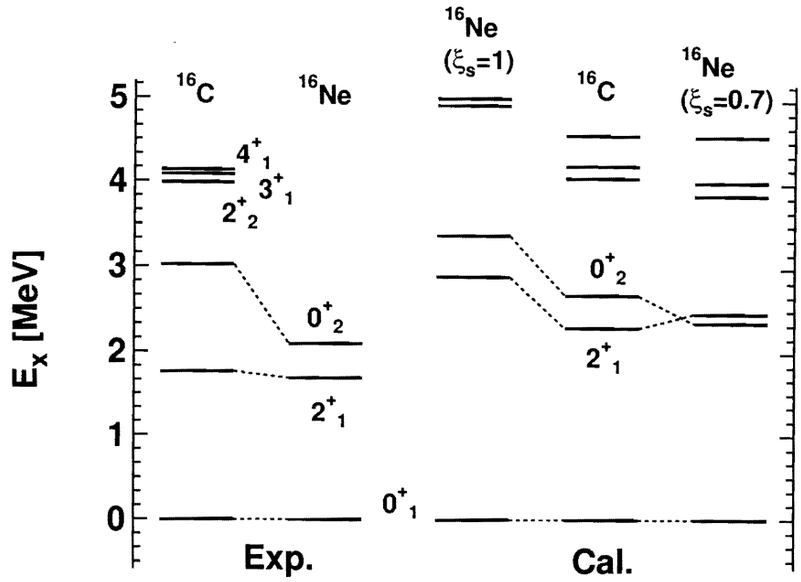

Figure 2: Energy levels of ^{16}C and ^{16}Ne. Taken from Ref. [2].

action matrix elements are evaluated with the Woods-Saxon (WS) single-particle wave functions. From the proton-neutron ratios of the matrix elements in the WS+M3Y model, which are shown in Fig. 3, it is confirmed that the RNI reduction originates in the broad radial distribution of the relevant single-particle orbit, and that the reduction is important in $(1s_{1/2})_p$.

3 Shell model calculation for light *sd*-shell nuclei with isospin breaking interaction

We extensively study structure of the light *sd*-shell nuclei, both stable and unstable ones, in the shell model framework. We restrict ourselves to the $A \approx 20$ region at present, but aim to describe even the TES, by reproducing the energy levels to a good precision. For this purpose, we develop a new Hamiltonian which has isospin-breaking effects. The single-particle energies are taken from the ^{17}O and ^{17}F data, by which the isospin-breaking effect in the single-particle energies is introduced. In order to take into account the above mechanism (reduction of the RNI for orbits having broad radial distribution), we modify the USD interaction as follows.

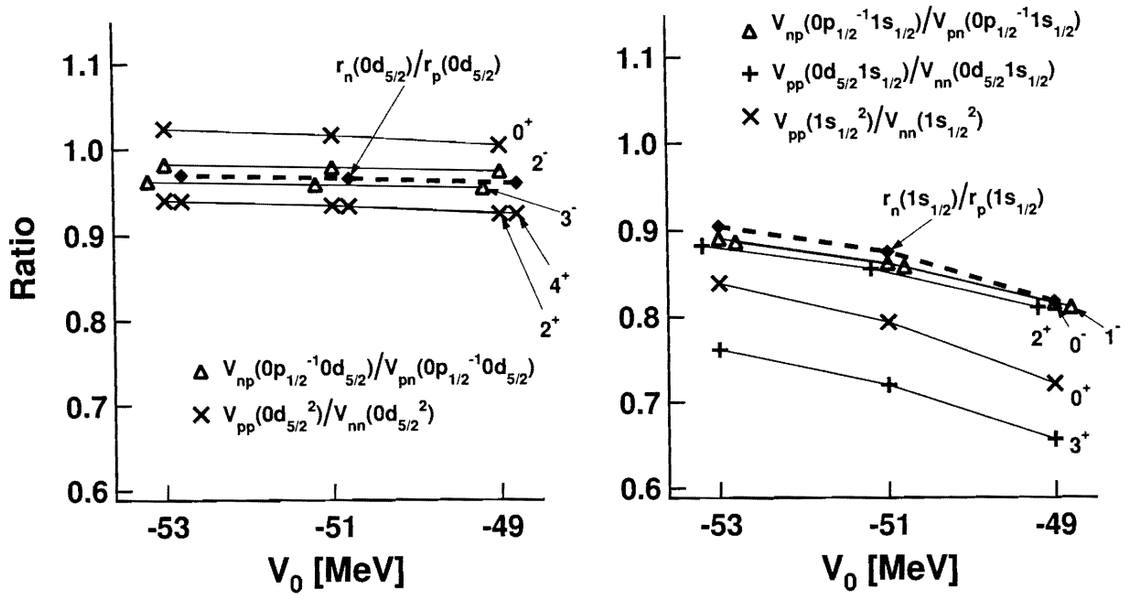

Figure 3: Proton-neutron ratio of the M3Y interaction matrix elements (& of rms radii of single-particle orbits), evaluated with the single-particle wave functions in the Woods-Saxon (WS) potential. The depth of the WS potential (central part) V_0 is slightly varied. Taken from Ref. [2].

1. Multiply $T = 1$ interaction matrix elements by ~ 0.9 (so as to reproduce the energy levels of ^{18}O).

2. Add the Coulomb matrix elements to V_{pp}, which contributes to the diagonal elements by 0.4 MeV.

3. Reduce V_{pp} (in addition to 1), by 20% for diagonal elements regarding $(1s_{1/2})_p$ and by 5% otherwise (so as to reproduce the levels of ^{18}Ne).

4. For V_{pn}, reduce $T = 0$ elements by $\sim 5\%$. Also apply additional factors for $(1s_{1/2})_p$ (so as to reproduce the levels of ^{18}F).

The level scheme of ^{18}F is compared in Fig. 4. The present Hamiltonian reproduces the experimental levels well, except for intruder states. It is no worse than the original USD Hamiltonian.

The energy levels of the ^{18}O–^{18}Ne mirror nuclei are presented in Fig. 5. The proton separation energy S_p of ^{18}Ne (short bar) and the Gamow window for ^{17}F(p,γ) at $T =$

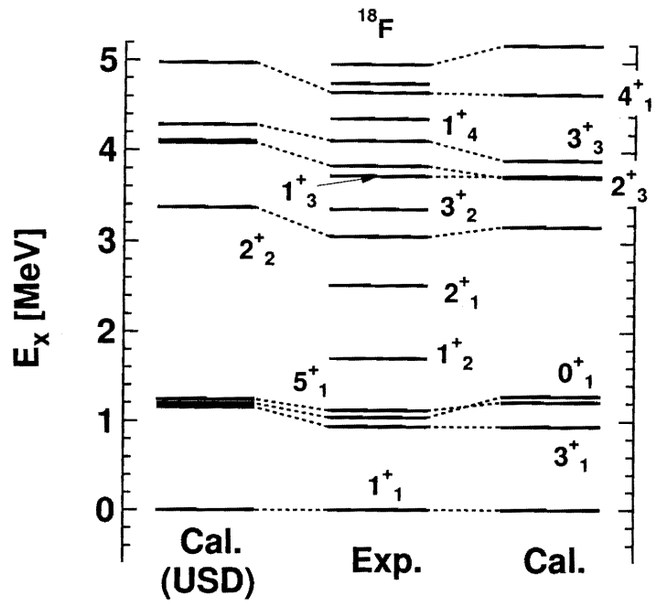

Figure 4: Energy levels of ^{18}F.

1.5×10^9 K (error bar) are indicated at the right most part of the figure. The 3_1^+ state of ^{18}Ne may play a significant role in the onset of the *rp*-process [4], because this state can be reached by an *s*-wave proton capture on the ^{17}F ground state. The energy of the 3_1^+ state is confirmed recently [5], showing large TES from its mirror partner and being inside the Gamow window for (p, γ) at $T = 1.5 \times 10^9$ K. This 3_1^+ state is well reproduced by the present calculation.

Large TES is suggested also for 1_2^+ of ^{20}Na by a recent experiment [6], which becomes around the bottom of the Gamow window for ^{19}Ne(p, γ) at $T = 1.5 \times 10^9$ K. It is noted that, dependent on the excitation energy, this 1^+ level may be important to the *rp*-process via the proton capture in the *s*-wave. On the other hand, the TES in the 3_3^+ level is small, though its energy is close to 1_2^+. Our shell model calculation reproduces this tendency. Thus the reduction of the RNI and its orbital-dependence well accounts for the TES of light *sd*-shell nuclei.

4 Summary and future perspective

From the recent data on proton-rich nuclei, we have clarified that the residual nuclear interaction has smaller matrix elements as the relevant single-particle orbits distributes over a broader range. This effect is significant in $(1s_{1/2})_p$, giving rise to large TES in the

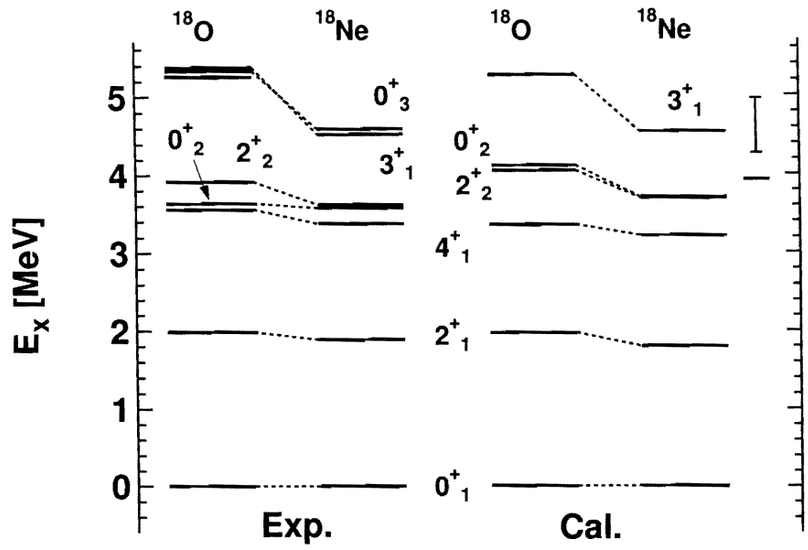

Figure 5: Energy levels of ^{18}O–^{18}Ne mirror nuclei.

$A \approx 20$ region.

In the conventional approaches to the TES, the identical configurations are assumed between mirror partners, and the Coulomb effects are evaluated for the single-particle wave functions. On the other hand, the present picture derives charge asymmetry in the shell-model many-body wave functions (*e.g.* asymmetry in the spectroscopic amplitudes), in addition to the asymmetry in the single-particle wave functions. The charge asymmetry in the wave functions may have influence on static moments and transition properties. In particular, the β-decay strengths could be a clear and sensitive probe. An anomaly has been reported in the Gamow-Teller decay strengths for the ^{20}O–^{20}Mg mirror nuclei [7]. The RNI reduction for $(1s_{1/2})_p$ accounts for a significant part of the anomaly, as will be discussed elsewhere.

The TES may influence the scenario of the *rp*-process. For instance, 3_1^+ of ^{18}Ne and 1_2^+ of ^{20}Na, both of which can be populated by the *s*-wave proton capture, are subject to large TES and come into the Gamow window. It is of interest to renew the *rp*-process simulations by including the recent progress in nuclear structure physics on the TES.

The TES occurs via the single-particle mechanism (as in the conventional approach) [8, 9] as well as via the many-body effects (*e.g.* RNI reduction). In practice the TES occurs for these two effects to be consistent. Although consistent treatment of the two

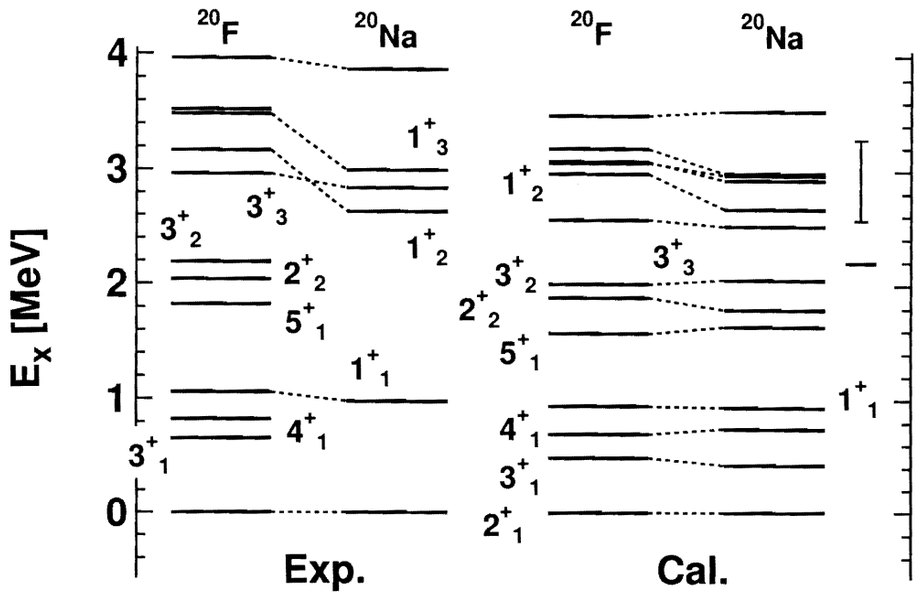

Figure 6: Energy levels of ^{20}F–^{20}Na mirror nuclei.

effects is difficult at the present stage, the success of the present approach encourages us to develop a phenomenological shell model describing the low-energy nuclear structure (including the TES) so precisely as desired in the astrophysics. For further confirmation and improvement of this approach, collaboration between experimentalists and theorists is essential.

References

[1] B. A. Brown and B. H. Wildenthal, Ann. Rev. Nucl. Part. Sci. **38** (1988) 29.

[2] K. Ogawa, H. Nakada, S. Hino and R. Motegi, Phys. Lett. B **464** (1999) 157.

[3] K. Föhl *et al.*, Phys. Rev. Lett. **79** (1997) 3849.

[4] M. Wiescher, J. Görres and F.-K. Thielemann, Astrophys. J. **326** (1988) 384.

[5] A. García *et al.*, Phys. Rev. C **43** (1991) 2012; D. W. Bardayan *et al.*, Phys. Rev. Lett. **83** (1999) 45.

[6] S. Kubono *et al.*, private communication.

[7] A. Piechaczek *et al.*, Nucl. Phys. A **584** (1995) 509.

[8] R. Sherr and G. Bertsch, Phys. Rev. C **32** (1985) 1809; R. Sherr and H. T. Fortune, Phys. Rev. C **58** (1998) 3292; H. T. Fortune and R. Sherr, Phys. Rev. C **61** (2000) 024313.

[9] S. Aoyama, N. Itagaki, K. Katō and K. Ikeda, Phys. Rev. C **57** (1998) 975; S. Aoyama, K. Katō and K. Ikeda, Prog. Theor. Phys. **99** (1998) 623.

Single particle wave functions and density distribution for oxygen isotopes

R.Fujimoto, T.Otsuka, B.A.Brown, Y.Utsuno, R.Kanungo, K.Ozawa, and I.Tanihata

Abstract

We investigate the interaction cross sections of oxygen isotopes using effective single particle energies and wave functions which are obtained from Woods-Saxon potential. A drastic increase of the interaction cross sections in ^{23}O and ^{24}O has been recently observed, and this behavior is partially explained within the present model.

1 Introduction

The nuclear structure for neutron-rich nuclei have many exotic properties and have been studied eagerly. In light region, the experimental measurement is in process of reaching up to the neutron drip line. For example, the neutron separation energies (S_n) and the interaction cross sections (σ_I) for *p-sd* and *sd* shell region have been measured and compiled in Ref. [1]. In the experimental data, the observed σ_I for oxygen isotopes shows sudden increase at the neutron number $N = 15$ (*i.e.* ^{23}O). However, the neutron separation energy (S_n) of ^{23}O is still about 3 MeV, [2] and it is unreasonable to consider that this drastic increase is due to a halo structure, like for example in ^{11}Li, which has an extremely large radius. Therefore, it is very interesting to study the scheme of this large cross sections.

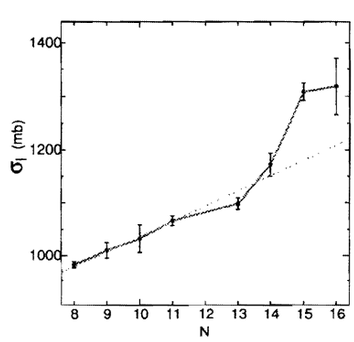

Figure 1: The experimental interaction cross sections [1]. The dotted line denotes a line proportional to $A^{1/3}$, which is fitted to the data from ^{16}O to ^{22}O.

2 Calculations

2.1 effective single particle energies

We investigate the radii of oxygen isotopes through a shell model procedure. To investigate the variation of shell configuration, it is useful to consider a monopole interaction. The monopole interaction between the orbitals i and j is defined as follows:

$$\begin{aligned} H_{ij}^{(mT)} &= \sum_{k=i,j} \left\{ \frac{a_{kk}}{2}\hat{n}_k(\hat{n}_k - 1) + \frac{b_{kk}}{2}\left(\hat{T}_k^2 - \frac{3}{4}\hat{n}_k\right)\right\} \\ &\quad + a_{ij}\hat{n}_i\hat{n}_j + \frac{b_{ij}}{2}\left\{(\hat{T}_i + \hat{T}_j)^2 - \hat{T}_i^2 - \hat{T}_j^2\right\}, \end{aligned} \tag{1}$$

$$l \begin{cases} a_{ij} = \frac{1}{4}(3V_{ij}^1 + V_{ij}^0), & b_{ij} = V_{ij}^1 - V_{ij}^0 \\ V_{ij}^T = \frac{\sum_J (2J+1)\langle ij|V|ij\rangle_{JT}}{\sum_J (2J+1)}, & \text{for} \quad T = 0, 1. \end{cases} \tag{2}$$

Here, n_k and T_k stand for the number and isospin operators of the designated orbit, respectively. We can recognize this monopole interaction as a two-body interaction where the angular dependence of the interaction is averaged out. Next, an effective single particle energy (s.p.e.) for the valence neutrons around ^{16}O can be calculated from this monopole interaction and bare single particle energies. This is single particle energy by taking into account the two-body interaction among valence neutrons, which is defined as follows:

- For an occupied orbit, the effective s.p.e. is defined by the one-neutron separation energy from this orbit.
- For an unoccupied state, the effective s.p.e. is given by the additional binding energy to this orbit.

We calculate the effective s.p.e. of sd-shell orbits ($1s1/2$, $0d3/2$, $0d5/2$) for oxygen isotopes. For matrix element of two-body interaction (*i.e.* $\langle ij|V|ij\rangle_{JT}$ in Eq.2), we adopt the interaction proposed in Ref. [3]. This interaction is based on USD [4], Kuo-Brown [5] and Millener-Kurath [6] interaction and is almost similar to the USD interaction in this region.

Fig. 2 shows the effective s.p.e. of each orbits for oxygen isotopes. There are some remarkable points about the variation of effective s.p.e. The level of $1s1/2$ goes up as neutrons fill $0d5/2$ orbit. This is caused by the repulsive monopole interaction between $1s1/2$ and $0d1/2$. But at $N = 16$, where two neutrons occupy the $1s1/2$ orbit, the effective s.p.e. decrease because of the pairing effect. On the contrary, the $0d5/2$ orbit does not show this behavior and it goes down as the mass number increases from 8 to 14. We can easily understand this is due to the pairing effect among nucleons in the $0d5/2$ state.

As a result, the shell gap between the $0s1/2$ and $1d5/2$ grows larger until the nucleon number N exceeds 15.

2.2 single particle wave functions

We determine the single particle wave functions from the effective s.p.e. obtained in the previous section. We set parameters of Woods-Saxon potential so that its eigen values reproduce the effective

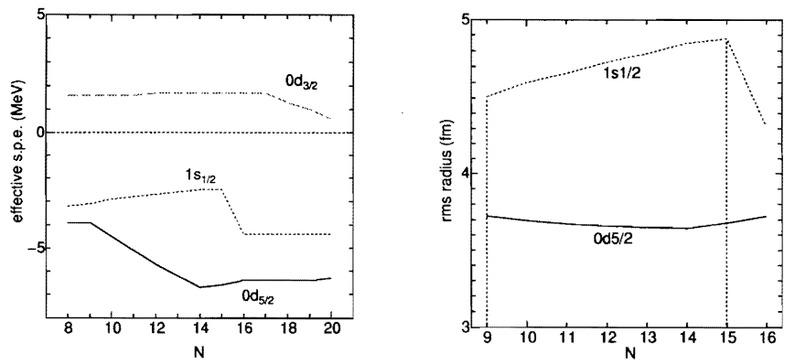

Figure 2: Left : The effective s.p.e. of sd-shell orbits. The calculation is done for oxygen isotopes ($Z = 8$). Right : The rms radii of wave functions of valence neutrons.

s.p.e. of $1s1/2$ and $0d5/2$ orbits. The parameters are R, a, V_{ls} and V_0 (Eq.4). R and V_{ls} are determined as $1.27A^{1/3}$ (A : mass number) and $V_{ls} = -0.44V_0$, respectively. The value of a are selected so as to give the most desirable results. In this case ($a = 0.75$), a is somewhat big compared with the normal cases. The result, however, is not so sensitive to the a and this value is common through the calculations of oxygen isotopes.

We solve the Schrödinger equation and adjust its eigen value by changing V_0. The eigen functions of these Schrödinger equations can be considered as the single particle wave functions of each valence nucleons.

$$f(r) = \frac{1}{1 + e^{(r-R)/a}} \tag{3}$$

$$U(r) = V_0 f(r) + V_{ls}(\boldsymbol{l} \cdot \boldsymbol{s})\frac{1}{r}\frac{d}{dr}f(r) \tag{4}$$

$$R = 1.27A^{1/3}\text{fm}, \quad a = 0.75, \quad V_{ls} = -0.44V_0$$

The the root mean square (rms) radii of these resultant wave functions are shown in Fig. 2. Note that the rms of $1s1/2$ is much larger than that of $0d5/2$ at $N = 15$.

2.3 radii and cross sections

Now we have the single particle wave functions of valence nucleons, then we can evaluate the rms radii and interaction cross sections for the oxygen isotopes.

To calculate rms radii, we need the radius of ^{16}O core. We adopt the radius which is obtained by Skyrm-Hartree-Fock calculations, using SIII interaction. [7] Then, the rms radii of oxygen isotopes are given from ^{16}O core radius and radii of valence nucleons. These calculations are done under the normal configuration assumption. To compare with experiment data, we also evaluate the interaction cross sections by Glauber model. These results are shown in Fig. 3.

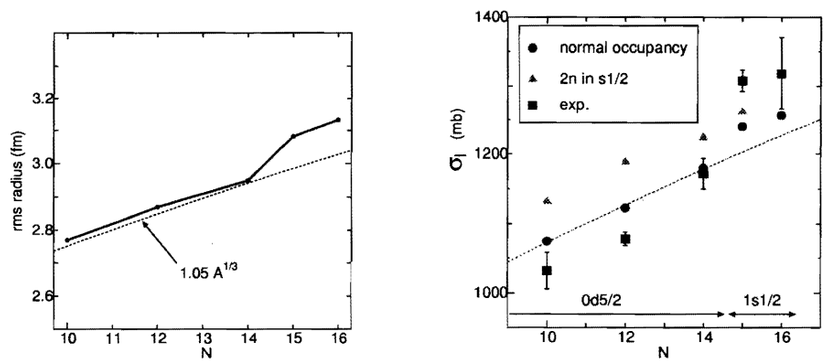

Figure 3: Left : The rms radii for oxygen isotopes. The dotted line denotes $1.05A^{1/3}$ line. Right : The interaction cross sections. The squares and circles mean experiment and calculation, respectively. The triangle denotes the calculation when two neutrons are in $1s1/2$.

3 Results and Discussion

The calculated radii and cross sections are shown in Fig. 3. We can see that the rms radii increases along the line proportional to $A^{1/3}$ up to $N = 14$, that is ^{22}O, but it shows sudden increase at $N = 15$. This tendency agrees with experimental data. At $N = 15$, neutrons start to occupy the $1s1/2$-orbit, and the rms radii for wave function of the $1s1/2$ is larger than that of $0d5/2$. As a result, rms radii of the oxygen isotopes suddenly increases when the $1s1/2$ orbit begin to be filled. In Fig. 3 interaction cross sections are also shown. The calculation shows similar behavior to the rms radii. It deviates from $A^{2/3}$ line at $N = 15$ and 16. But this deviation are not enough to describe the experimental data, which shows much drastic increase.

As a result, these calculations can partially explain the behavior of radii in oxygen isotopes when the neutron number change from 14 to 15. To reproduce the experimental cross sections, the $1s1/2$-orbit should have a much larger rms radius. Thus, it is significant to perform the more realistic calculations which includes the interaction between nucleons explicitly, focusing on the orbit $1s1/2$. In addition, it is also possible that the sized of the ^{16}O core changes to some extend.

To reveal this mechanism, further investigation is required from both the theoretical and experimental side.

References

[1] A.Ozawa, T.Kobayashi, T.Suzuki, K.Yoshida, and I.Tanihata, Phys.Rev.Lett. **84**, 5493, (2000)

[2] G.Audi and A.H. Wapstra, Nucl.Phys. **A 595**, 409, (1995).

[3] Y.Utsuno, T.Otsuka, T.Mizusaki and M.Homma, Phys.Rev. **C60** 054315 (1999).

[4] B.A.Brown and B.H.Wildenthal, Annu.Rev.Nucl.Part.Sci.

[5] T.T.S.Kuo and G.E.Brown, Nucl.Phys. **A114**, 241 (1968).

[6] D.J.Millener and D.Kurath, Nucl. Phys. **A255**, 315 (1975).

[7] M.Beiner, H.Flocard, N. Van Giai, and P.Quentin. Nucl. Phys. **A238**, 29 (1975).

Analysis of the Coulomb breakup reaction of ^{6}He

T. Myo, S. Aoyama[A], K. Katō, K. Ikeda[B]

Hokkaido Univ., [A]Kitami Institute of Technology, [B]RIKEN

October 30, 2000

Most of the states of unstable nuclei are unbound resonances and continuum states, which means that the studies of unstable nuclei are just related to the nuclear structure in the continuum energy region above the lowest threshold.

The Coulomb breakup reaction using typical neutron-rich nuclei like ^{6}He,^{11}Li and ^{11}Be, is one of the interesting phenomena to see the fundamental excitation mechanism of unstable nuclei. The important point in analyzing the Coulomb breakup reaction is to investigate the response properties of unbound states excited from the ground state having an exotic structure like a neutron halo or skin.

In seeing those responses, it is meaningful to extract the contributions from both resonances and continuum states in the transition strength simultaneously, which is also valuable to discuss the existence of a soft dipole resonance. For this purpose, we adopt complex scaling method (CSM) to express the many-body nunbound states, with extending the applicability of CSM to evaluate the transition strength to the resonant and continuum states, respectively [1, 2]. On the basis of the decomposition of unbound states, we can introduce the extended 3-body completeness relation (ECR)[5] in which each resonance and continuum term is expressed with CSM, and derive the decomposed components of the transition strength function.

In this report, we present our recent studies about the excitation mechanism of two neutron halo nuclei: ^{6}He through the 3-body breakup reaction into ^{4}He+n+n, with extracting the electric transition components to the 2- and 3-body unbound states. It is interesting to examine the role of 3-body unbound states including resonances and possibility of sequential breakup to analyze the experimental cross section[3].

Employing the 3-body model of ^{6}He as ^{4}He+n+n with CSM[4], we derive the contributions of not only the 3-body resonant states, but also those of the 2-body (^{5}He$^{(*)}$+n) or 3-body (^{4}He+n+n) continuum states in the electric multipole strengths. We evaluate the each component of them and analyse which states dominates the observed characteristic behavior of the strength distribution.

For $E1$ transition, our result shows that component of the sequential breakup process of ^{5}He$(3/2^-)$+n is dominant. It makes an enhancement at around 1 MeV from the 3-body threshold energy, which is just above the two body threshold of ^{5}He$(3/2^-)$+n, and its strength decreases slowly with the excitation energy. Similar structure also appear with applying the plane wave approximation for remaining one valence neutron in positive parity s- or d-wave orbits. This indicates that the low energy enhancement is interpreted as the 2-body threshold effect of ^{5}He$(3/2^-)$+$n(s_{1/2})$ in the 3-body breakup reaction. The component of ^{5}He$(3/2^-)$+$n(d_{5/2,3/2})$ makes a soft peak at around 2-3 MeV which can be seen as the slow decrease in the total strength.

The result of $E1$ transition is closely related to the structure of the ground state of ^{6}He in

which the dominant configuration is $(p_{3/2})^2$ for two valence neutrons. Large transition strength into ^{5}He$(3/2^-)+n$ indicates that one of the neutrons of $(p_{3/2})^2$ in the ground state of ^{6}He is excited to a continuum state of s- or d-wave orbit by the $E1$ transition operator. Furthermore, we see that the 3-body continuum states of ^{4}He$+n+n$ does not contribute strongly. This result is understood by considering that two $p_{3/2}$-neutrons in the ground state of ^{6}He, are hardly excited simultaneously in the breakup process. Another 2-body continuum component of ^{5}He$(1/2^-)+n$ hardly contributes to the strength because the probability of $(p_{1/2})^2$ is very small in the initial ground state, nearly a few percent. Furthermore, a large resonance width of ^{5}He$(1/2^-)$ also reduces and broaden the strength, and we cannot see a distinguishable structure of the 2-body component of ^{5}He$(1/2^-)+n$ in the transition strength.

The $E2$ transition are also important in the low energy strength distribution of the Coulomb breakup reaction. The significant difference between $E1$ and $E2$ transitions in ^{6}He is whether 3-body resonances exist in the final states of ^{4}He$+n+n$ or not. Within our model, we obtain two resonances of $2^+_{1,2}$.

For $E2$ transition, 2^+_1 resonance makes a resonant peak in the strength at around its resonance energy (0.81 MeV) due to the small decay width (0.13 MeV). On the other hand, the contribution from 2^+_2 (resonance energy is 2.35 MeV) is very small due to the large decay width (4.22 MeV). The component associated with 2-, or 3-body continuums are smaller than those of 2^+_1. However, in the continuum transitions, the 2-body continuum component of ^{5}He$(3/2^-)+n$ shows a peak at around 1 MeV, just above the 2-body threshold of this channel. This is interpreted as the threshold effect of ^{5}He+(p-orbital continuum neutron) component. This component mainly contributes to make a shoulder in the total strength at around 1.5 MeV from the ^{4}He$+n+n$ threshold energy. For another 2-body continuum component of ^{5}He$(1/2^-)+n$, its effect is very small, as well as in the case of the $E1$ transition. It is found that the 3-body continuum component of ^{4}He$+n+n$ relatively give a larger contribution than the case of $E1$ transition. This 3-body component also contributes to make a shoulder in the total transition strength.

It is found that the $E2$ transition distribution shows a distinguished resonance behavior of 2^+_1 state, but not of the 2^+_2 state. It may be very hard to observe experimentally the existence of the 2^+_2 state by using the Coulomb breakup reactions. On the other hand, the continuum strengths consisting of the ^{5}He$(3/2^-)+n$ and ^{4}He$+n+n$ channels make a shoulder-like structure. Through an observation of this structure, the continuum effect can be confirmed in the strength of the 3-body breakup process, in addition to that of resonances.

References

[1] T. Myo and K. Katō, Prog. Theor. Phys. **98**, 1275 (1997).

[2] T. Myo, A. Ohnishi and K. Katō, Prog. Theor. Phys. **99**, 801 (1998).

[3] T. Aumann *et.al*, Phys. Rev. **C59** 1252 (1999).

[4] S. Aoyama, S.Mukai, K.Katō and K.Ikeda, Prog. Theor. Phys. **93**, 99 (1995). Phys. Rev. Lett. **43** (1979) 111.

[5] T. Berggren, Nucl. Phys.**A109**, 265 (1968).

• Complex Scaling Method (CSM)

$$U(\theta) \,:\, \mathbf{r} \rightarrow \mathbf{r}_\theta = \mathbf{r} \cdot \exp(i\theta), \quad \mathbf{k} \rightarrow \mathbf{k}_\theta = \mathbf{k} \cdot \exp(-i\theta)$$

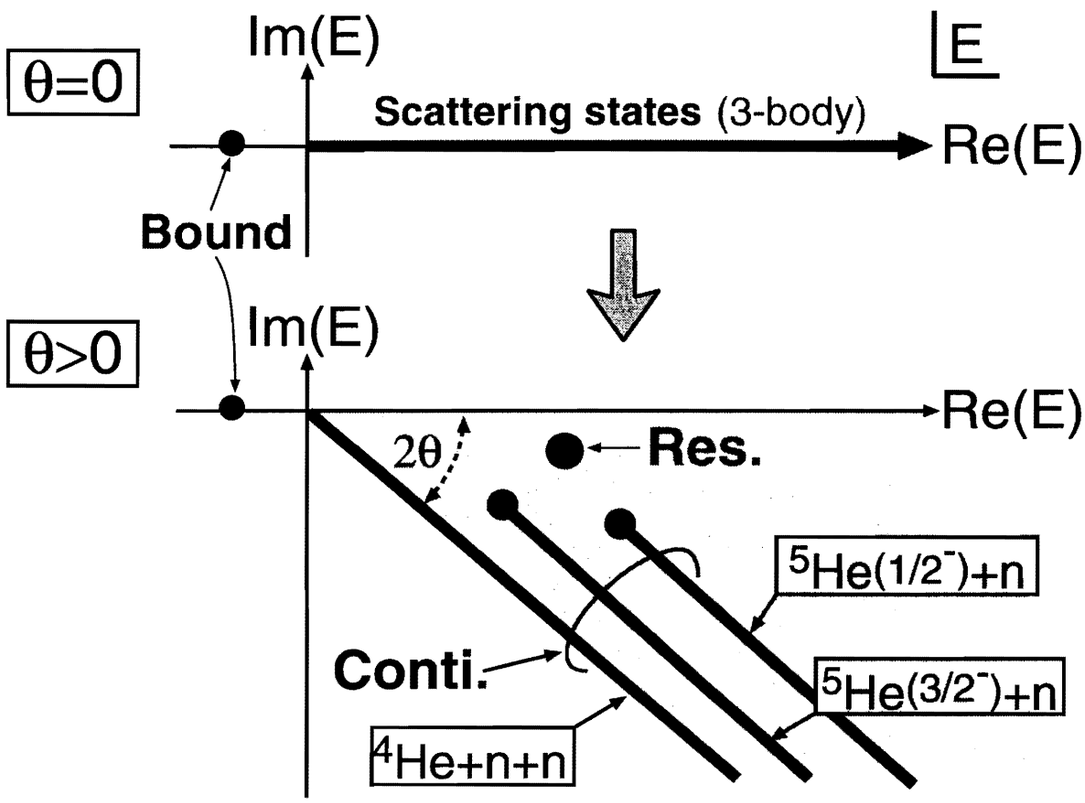

∘ Extended completeness relation

$$1 = \sum_B |\phi_B\rangle\langle\tilde{\phi}_B| + \sum_R |\phi_R\rangle\langle\tilde{\phi}_R| + \sum\!\!\!\!\!\!\int_C |\phi_C\rangle\langle\tilde{\phi}_C|$$

(^{5}He(*)+n, ^{4}He+n+n)

(this is our conjecture for the 3-body system)

[Ref]:J. Aguilar and J. M. Combes, Commun. Math. Phys.,22,1971,269.
E. Balslev and J. M. Combes, Commun. Math. Phys.,22,1971,280.

- Energy engenvalue with CSM

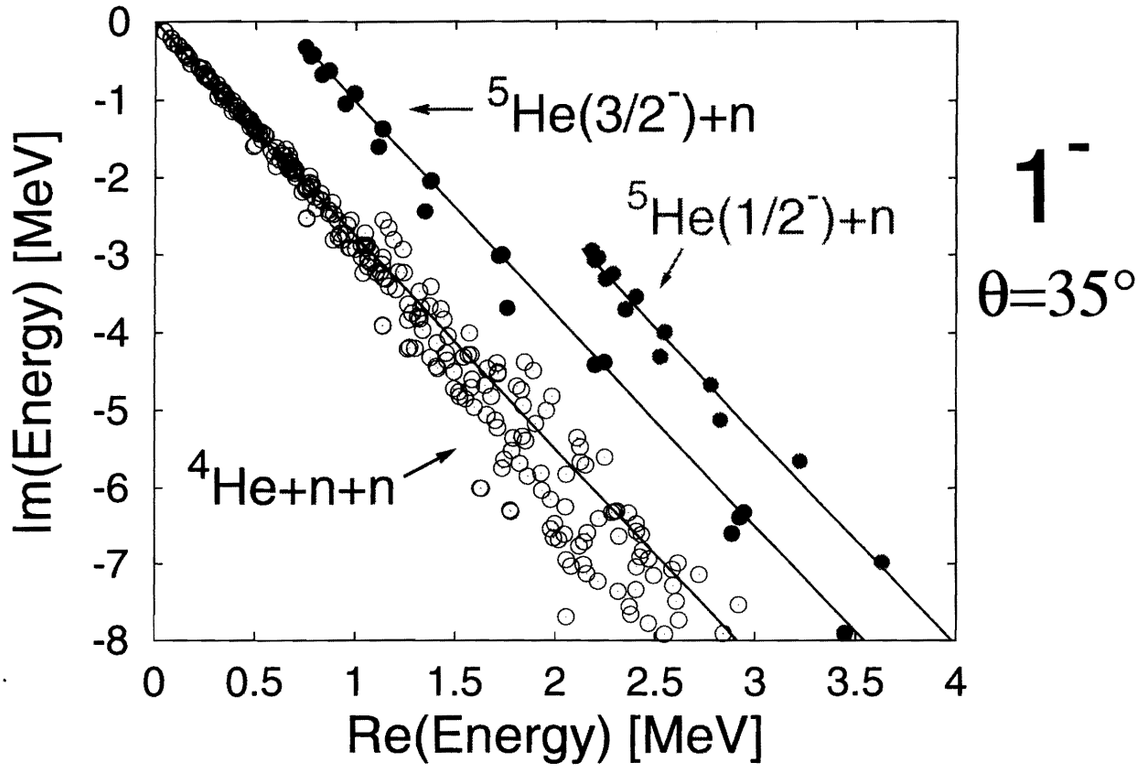

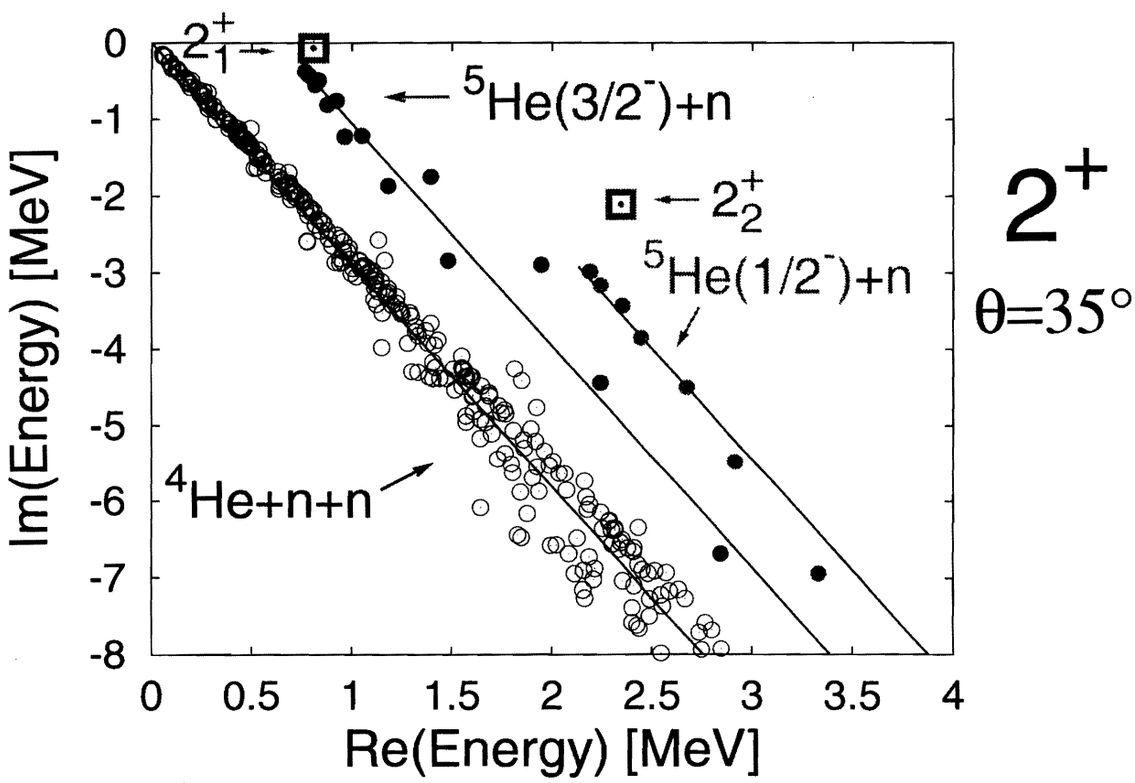

- E1 transition ($0^+ \rightarrow 1^-$)

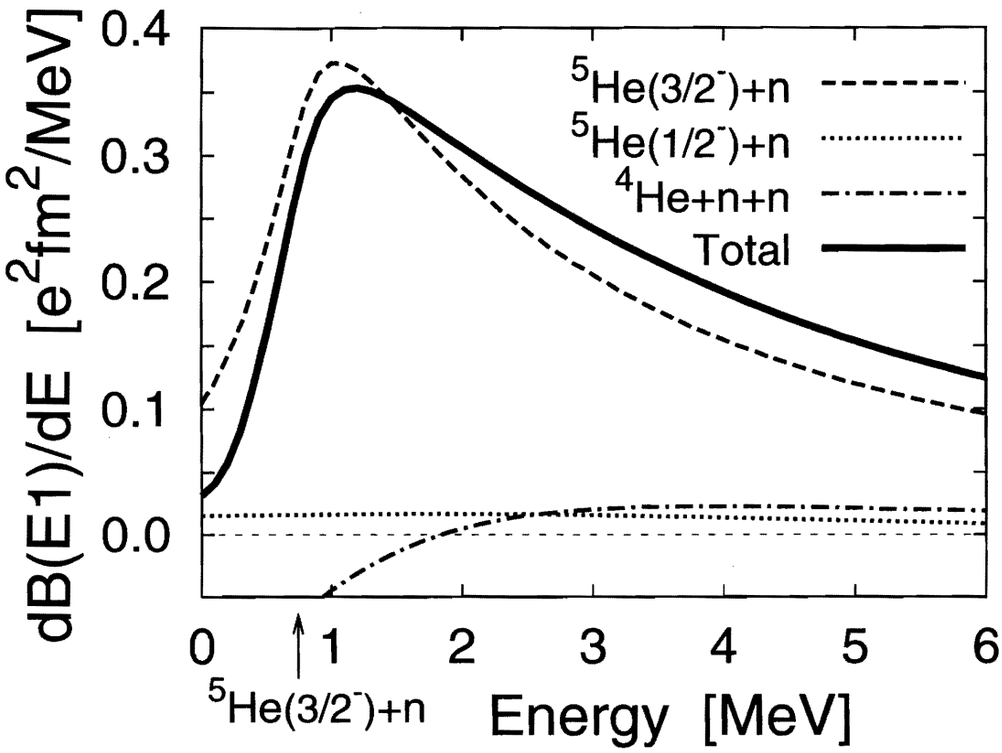

- E2 transition ($0^+ \rightarrow 2^+$)

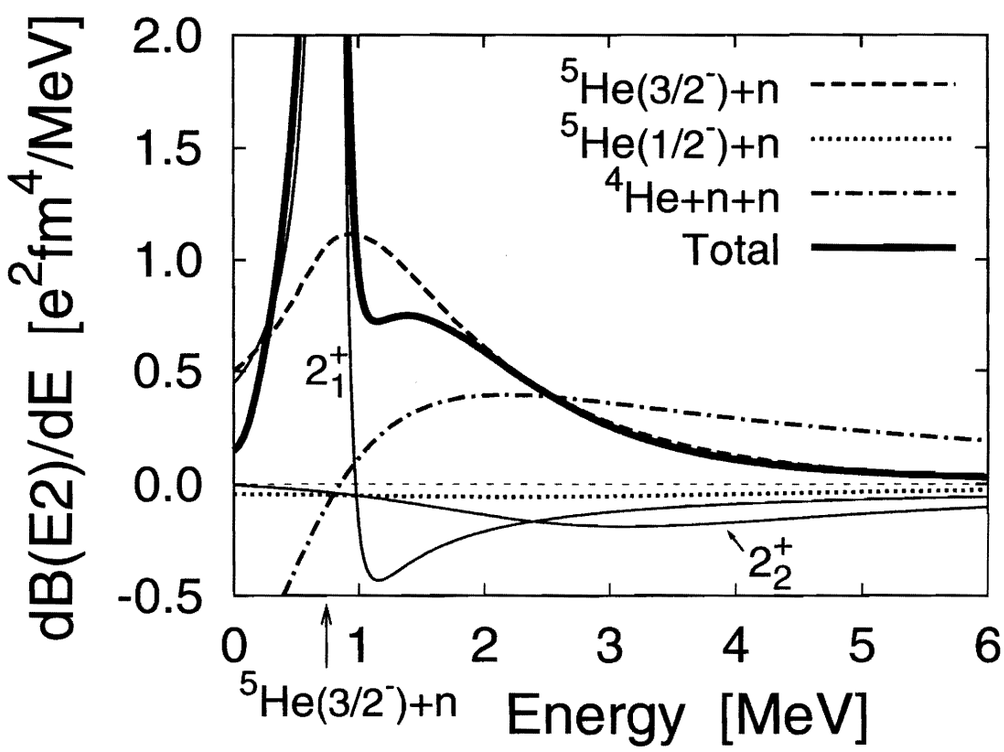

Soft dipole resonance in ^{6}He

S. Nakayama, Univ. of Tokushima

25/August/00

Abstract

An availability of selective probes for spin and isospin is a key to our knowledge of the nuclear response. The (^{7}Li,^{7}Be) reaction provide a new type of selective probes. Emitted ^{7}Be particles are in either the ground state ($3/2^-$; Be_0) and the first excited state ($1/2^-$; Be_1) via an ejectile excitation. The ejectile excitation was successfully separated with the ^{7}Be-γ coincidence method [1]. The ΔS=0 and ΔS=1 spectra were simultaneously deduced under the same kinematical condition by using Be_0 and Be_1 cross sections.

The soft dipole resonance (soft-DR) at excitation energies lower than the GDR or SDR in ^{6}He was investigated via the ^{6}Li(^{7}Li,^{7}Be) reaction at an incident energy of 65A MeV. The ground state of ^{6}Li has a cluster structure, d+α, with a large spectroscopic factor of 0.85. If the soft-DR in ^{6}He exists, it can be excited, remaining an α-cluster as a spectator, by transferring a deuteron-cluster (1^+) in ^{6}Li to a 2n-cluster (singlet S-state, 0^+), i.e., spin-flip transition. The soft-DR is expected to be identified by observing the spin-flip (ΔS=1) isovector excitations.

We observed ΔS=0 and ΔS=1 spectra. In the ΔS=0 spectrum, an analogue of the GDR (ΔS=0, ΔL=1) was observed around 9 MeV. Here, the GDR itself has been established by the ^{6}Li(γ,n) experiment. We found that the shape of the ΔS=0 spectrum agrees well with a spectrum obtained in the (γ,n) reaction. This fact shows that only the GDR is dominant in the present ΔS=0 spectrum. The difference between the ΔS=0 and ΔS=1 spectra was very remarkable in the low excitation energy region. A new ΔS=1 resonance, if exists, should be identified by subtracting a contribution of the SDR (ΔS=1, ΔL=1) from the ΔS=1 spectrum. Hoshino *et al.* performed a shell model calculation for dipole excitations via a charge exchange reaction from a ^{11}B target to a neutron rich nucleus ^{11}Be. They predicted that the spin-flip and spin-nonflip dipole excitations have very similar strength distributions each other. Actually, in the (^{7}Li,^{7}Be) reactions on ^{12}C, the SDR was observed in a similar way to the GDR regarding the excitation energy, width, and cross section. By assuming that the SDR is distributed with the same excitation energy and width as those of the GDR, the ΔS=1 spectrum was decomposed into two resonances. The resonant shape was fitted with a Lorentzian line shape. Thus a dipole excitation concentrated at low excitation energies (E_x=4±1 MeV and Γ=4±1 MeV) was observed via the ^{6}Li(^{7}Li,^{7}Be) reaction at 65A MeV. The values of the ΔS, ΔL, E_x, and σ presently deduced for the dipole excitation are consistent with those expected for the soft dipole resonance: a dipole oscillation mode between a core-cluster and a neutron-skin [2].

Reference

[1] S. Nakayama it et al., Nucl. Instrum. & Methods **A404**, 34 (1998).
[2] S. Nakayama it et al., Phys. Rev. Lett. **85**, 262 (2000).

Experimental Procedure

@ RCNP

Beam : 7Li 3+, 65 *A*MeV (a few nA)

Targets : 6Li, 12C, 28Si, 60Ni

7Be4+ : Grand RAIDEN at $\theta = 0.3^\circ$, 1°

γ - ray : NYMPHS (GSO-detector array)
GSO at $\theta = 55^\circ$ 90° 125° 150°
detection of Doppler effect

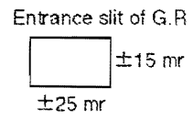

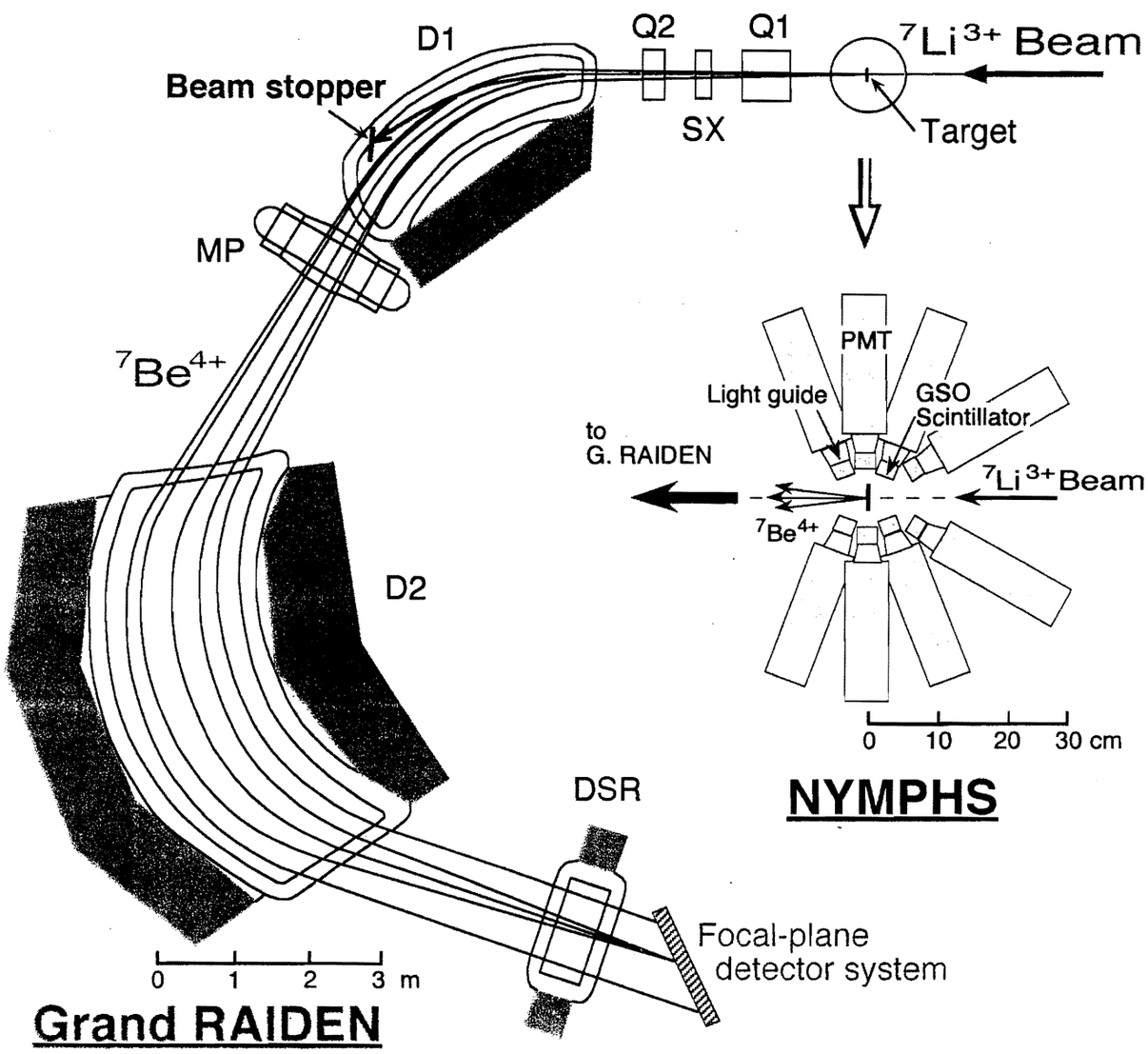

Charge exchange Spin-flip & Spin-nonflip Reaction

Nakayama, S. *et al.*
Nucl. Instrum. Methods A404 (1998) 34.
Phys. Rev. Lett. 83 (1999) 690.
Phys. Rev. C60 (1999) 047303.

$$^{7}Li + A \rightarrow {}^{7}Be + B$$

$T_z = +1/2$
$J^{\pi} = 3/2^-$

$T_z = -1/2$
$^{7}Be\ (J^{\pi} = 3/2^-)$ $\Delta T_z = +1$, $\Delta S=0$ / $\Delta S=1$

$^{7}Be^*\ (J^{\pi}=1/2^-)$ $\Delta T_z = +1$, $\Delta S=1$
$\rightarrow {}^{7}Be + \gamma$

$^{12}C(^{7}Li,^{7}Be)^{12}B$, E_L=65A MeV, θ_L<1.5°

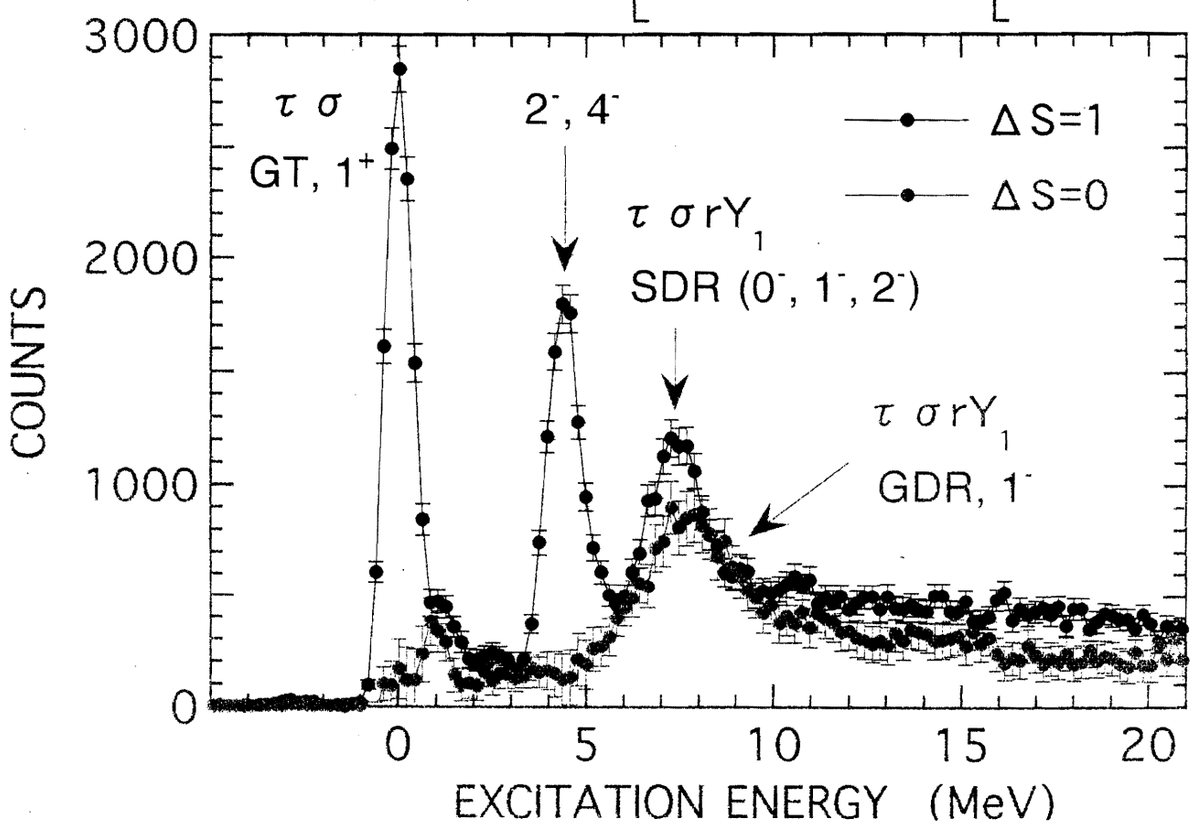

$^{6}Li(^{7}Li,^{7}Be)^{6}He$ @65A MeV

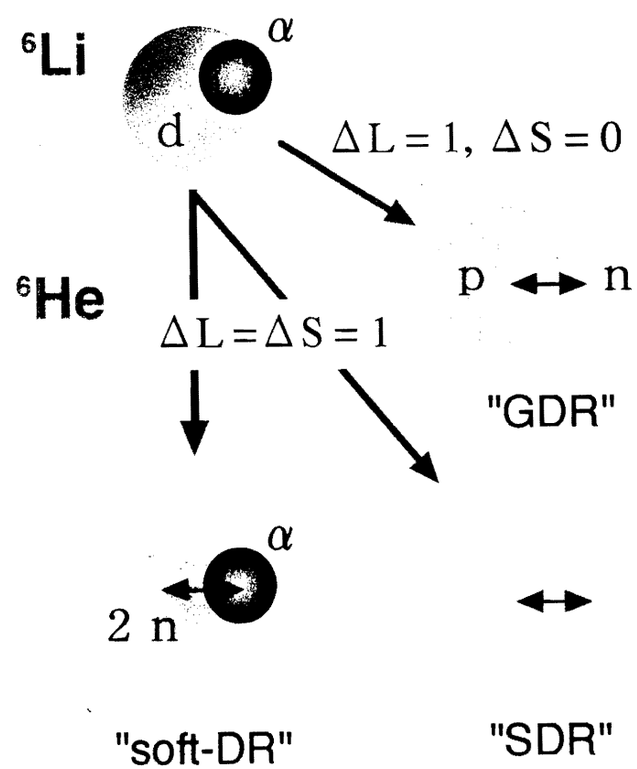

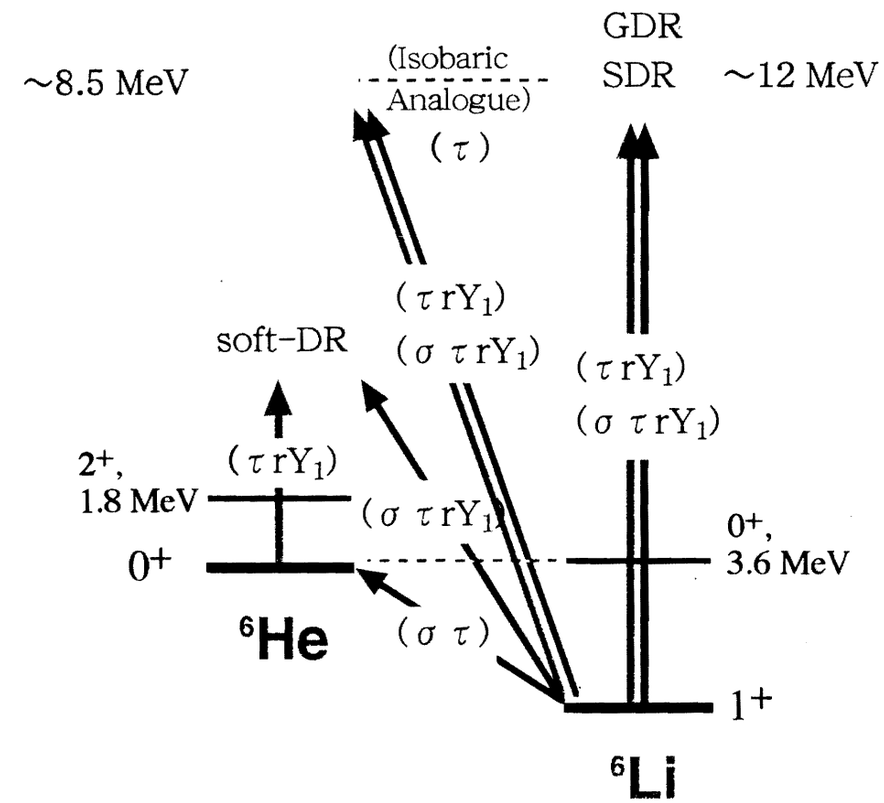

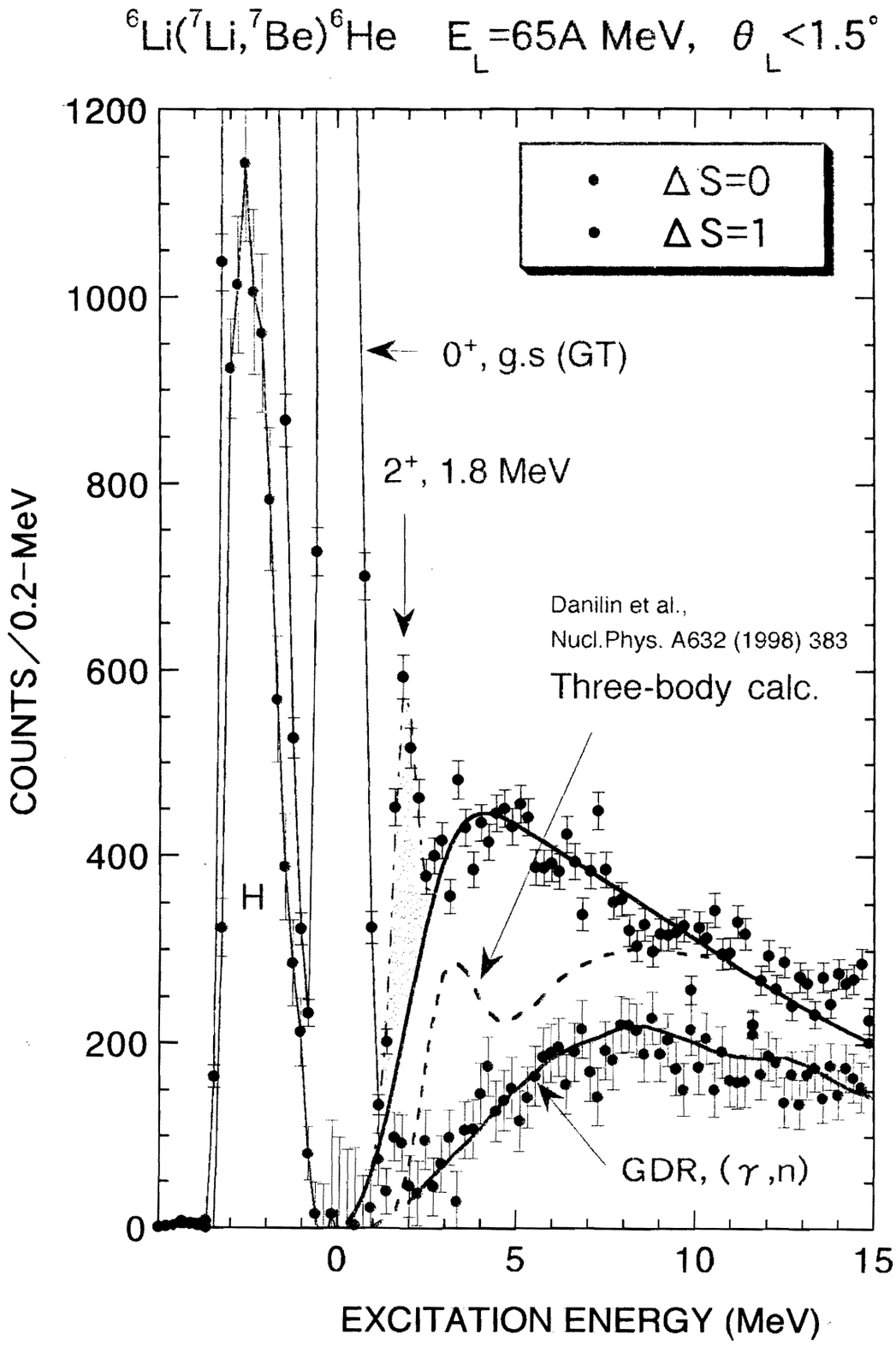
^{6}Li(^{7}Li,^{7}Be)^{6}He E$_L$=65A MeV, θ_L<1.5°
ΔS=0
ΔS=1
0$^+$, g.s (GT)
2$^+$, 1.8 MeV
Danilin et al.,
Nucl.Phys. A632 (1998) 383
Three-body calc.
H
GDR, (γ,n)
COUNTS/0.2-MeV
EXCITATION ENERGY (MeV)
1200
1000
800
600
400
200
0
0
5
10
15

Table 1: Isovector dipole resonances studied by the ^{6}Li(^{7}Li,^{7}Be)^{6}He reaction at 65 AMeV.

	GDR	SDR	RS
E_x (MeV)	12.1±1.5 [a)]	b)	4±1
Γ (MeV)	15±3	b)	4±1
$\sigma(0°)$ (mb/sr)	1.4±0.2	1.7±0.3	0.9±0.2

a) Excitation energy in ^{6}Li.

b) E_x and Γ for the SDR are assumed to be the same as those for the GDR.

Energy-weigted sum-rule (EWSR)

$$\mathrm{EWSR(GDR)} = C\,NZ/A$$

$$\mathrm{EWSR(soft\text{-}DR)} = C\,(N-Z)^2/A(A-4)$$

$$\text{where } C = \frac{9}{4\pi}\frac{\hbar^2 e^2}{2m}$$

[Y. Alhassid *et al.*, Phys. Rev. Lett. **49** (1982) 1482.]

$$\longrightarrow \frac{\mathrm{EWSR(GDR)}}{\mathrm{EWSR(soft\text{-}DR)}} = \frac{NZ(A-4)}{(N-Z)^2} = 4$$

Observed cross section x E_x (mb/sr x MeV)

$$\frac{\sigma\,(\mathrm{GDR})*E_x}{\sigma\,(\mathrm{RS})*E_x} = \frac{1.4*12.1}{0.9*4} = 4.7\pm1.5$$

Observable: $\Delta S=1$, $\Delta L=1$, E_x=4 MeV, $\sigma = 0.9$ mb/sr

➡ RS is a candidate for the soft-dipole resonance.

Molecular states in highly-excited ^{12}Be

M. Ito, K. Kato, Y. Sakuragi[1], E. Hiyama[2] and M. Kamimura[3]

Division of Physics, Graduate School of Science, Hokkaido University 060-0810 Sapporo, Japan

[1]*Department of Physics, Osaka City University 558-8585 Osaka, Japan*

[2]*Institute for Particle and Nuclear Studies, KEK 305-0801 Tsukuba, Japan*

[3]*Department of Physics, Kyushu University 812-8581 Fukuoka, Japan*

Abstract

Molecular resonances having the ^{6}He+^{6}He structure, which have recently observed in the highly excited states of ^{12}Be, are studied by the microscopic coupled-channels (CC) calculation based on the realistic nucleon-nucleon interaction, DDM3Y and the internal wave function of ^{6}He calculated by the microscopic α+n+n three-body model. The CC calculation predicts several molecular-rotational bands in the energy range of the observed resonances and the energies and the spins of the calculated resonance agree with the experimental data.

1 Introduction

A recent experiment of breakup reactions using neutron-rich ^{12}Be beams on proton and ^{12}C targets suggests an existence of exotic molecular states in ^{12}Be having ^{6}He+^{6}He and ^{8}He+^{4}He cluster structures [1]. The molecular states of ^{12}Be were observed as a final state interaction of these breakup fragments. The spins of these molecular states have also been evaluated by the angular-correlation measurements of the breakup fragments and the results indicate that the breakup occurs primarily through the ^{6}He+^{6}He molecular states in the 10 to 25 MeV excitation energy interval, with spins in the range of $4\hbar$ to $8\hbar$ [1].

Since the two neutron binding energy of ^{6}He is very small, it is well expected that the channel coupling effect of the individual ^{6}He nuclei will plays very important roles on the ^{6}He+^{6}He molecular-resonance formation. Moreover, the ^{6}He nucleus itself is known as exotic nuclei with a neutron halo or skin around the ^{4}He (α-particle) core nucleus [2] -[9]. The neutron halo/skin structure in these neutron-rich nuclei are often discussed in connection to the characteristic excitation modes, such as the so-called *soft modes*, associated with the relative motion of a core nucleus with respect to the center of mass (c.m.) of valence neutrons which form the neutron halo/skin [10, 11]. Therefore, it is very interesting to study the role of the neutron halo/skin structure and their dynamical modes in the formation of exotic molecular structure observed in the high-excitation energy region of the ^{12}Be nucleus.

In this report, we investigate the dynamical effects of the excitations of ^{6}He on the formation of exotic molecular states with ^{6}He+^{6}He structure in the highly-excited ^{12}Be, by performing the coupled-channel calculation of the ^{6}He+^{6}He elastic and inelastic scattering based on the realistic nucleon-nucleon interaction and microscopic internal wave functions of ^{6}He.

2 Framework

The diagonal and coupling potentials are calculated by the double-folding model with the DDM3Y interaction [12, 13]. More explicitly, the coupling potential between a channel α in which two ^{6}He nuclei are in the ith and kth states, respectively, and a channel β in which the two nuclei are in the jth and ℓth states is calculated with the corresponding transition densities, ρ_{ij} and $\rho_{k\ell}$, as

$$V_{\alpha,\beta}(\boldsymbol{R}) = \int \rho_{ij}(\boldsymbol{r_1})\, \rho_{k\ell}(\boldsymbol{r_2})\, v_{\rm NN}(\rho\,;\boldsymbol{s})\, {\rm d}\boldsymbol{r}_1 {\rm d}\boldsymbol{r}_2 \quad .$$

The Coulomb part of the diagonal and coupling potentials is calculated in a similar way to the nuclear part by the double folding of the nucleon-nucleon Coulomb interaction with the corresponding charge densities, although the Coulomb excitation plays little role in the present case.

For the ground state and the sharp-resonance 2_1^+ state, we employed the transition densities derived from the microscopic internal wave functions of ^{6}He calculated by Hiyama *et al.* [14]. Namely, the diagonal and transition density of the ^{6}He nucleus at a position $\boldsymbol{r}$ with respect to the c.m. of ^{6}He are calculated by the following equation:

$$\rho_{ij}(\boldsymbol{r}) = < \psi_i(\boldsymbol{\xi}) \mid \sum_{k=1}^{6} \delta(\boldsymbol{r} - \boldsymbol{r}_k) \mid \psi_j(\boldsymbol{\xi}) > \quad .$$

Here, $\psi_i(\boldsymbol{\xi})$ represents the internal wave function of ^{6}He calculated from the orthogonality-condition-model (OCM) calculation based on the α+n+n three-cluster model [2],

$$\psi_i(\boldsymbol{\xi}) = \mathcal{A}[\phi_n \phi_n \phi_\alpha u_i(\boldsymbol{r_1}, \boldsymbol{r_2})] \quad .$$

The calculated ground-state density shows a typical neutron-halo structure and its radial shape is quite consistent with those predicted by other theoretical models, such as the relativistic mean-field theory [9], as well as those extracted from the experimental data through the Glauber-model calculations [6]-[8]. The calculated r.m.s matter radius of ^{6}He is 2.43 fm [2], which is comparable to the experimental value of 2.48±0.03 fm [7]. The α+n+n OCM calculation also well reproduce the energy position of the sharp resonance 2_1^+ state (E_x=1.8 MeV). The calculated $B(E2 : 0^+ \rightarrow 2_1^+)$ value is about 2.8 e^{2}fm^4 which is comparable to the observed value, 3.2±0.6 e^{2}fm^4, by the Coulomb breakup reaction of ^{6}He [15].

A resonance-like structure at E_x=5.6±0.3 MeV in ^{6}He has been reported in the ^{6}Li(^{7}Li,^{7}Be)^{6}He reaction by Jänecke et al. [16]. A candidate of spin-parity for the resonance-like state is $J^\pi = 2^+$, although it is not fully determined due to the overlap of different multipolarities [16]. However, some theoretical calculations predict the existence of the 2_2^+ state around E_x=4~5 MeV [17, 18], which is consistent with the experimental result by Jänecke et al. [16]. Therefore, we take into account the excitation to the 2_2^+ state of ^{6}He in

the present calculaton. The transition density to this 2_2^+ around 5 MeV is calculated by the extended-collective model assuming the isoscalar-quadrupole deformation of ^{6}He [19]-[21]. In this model, the radial form factor for the transition density is given by

$$\begin{aligned} \rho_{2^+0^+}^{(\mathrm{SQM})}(r) &= -\alpha\{\frac{\mathrm{d}\rho_{2n}(r)}{\mathrm{d}r} + \frac{A_{\mathrm{core}}}{Z_{\mathrm{core}}}\frac{\mathrm{d}\rho_p^{\mathrm{core}}(r)}{\mathrm{d}r}\} \\ &\equiv g_{2n}^{(\mathrm{SQM})}(r) + g_{\mathrm{C}}^{(\mathrm{SQM})}(r) \quad . \end{aligned}$$

where A_{core}, Z_{core} are the mass number of the α-particle core (A_{core}=4), the atomic number of the α-particle core (Z_{core}=2), while $\rho_{2n}(r)$ and $\rho_p^{\mathrm{core}}(r)$ denote the halo-neutron and core-proton components of the nucleon density of ^{6}He, which are all given by the above-mentioned OCM calculation based on the α+n+n three-cluster model [2]. The second term, denoted by $g_{\mathrm{C}}^{(\mathrm{SQM})}(r)$, corresponds to the electric-quadrupole ($E2$) transition density. The strength α is determined so that the calculated $B(E2)$ value with the $E2$-transition density $g_{\mathrm{C}}^{(\mathrm{SQM})}(r)$ exhausts the energy-non-weighted sum rule value of soft-quadrupole mode (SQM) [22, 23] from which the theoretical $B(E2)$ value from the ground state to the 2_1^+ state, 2.8 e^{2}fm^4, is subtracted.

The monopole part of the diagonal density in the 2_2^+ states is assumed to be the same as that of the ground state. For the diagonal transition for the 2_2^+ state, we further introduce a quadrupole component of the diagonal density and assume the same radial form as that of the SQM transition density defined above. Its strength is determined from the Q moment calculated by assuming the relation between $B(E2)$ and Q moment of the standard collective-rotation model [24]. We take the excitation energy of 2_2^+ state to 5 MeV, which was suggested by the experimental results by Jänecke *et al.* [16].

In a recent experiment by Nakayama et al., a dipole 1^- excitation concentrated at low excitation energies of ^{6}He (E_{x}=4±1 and Γ=4±1) was observed via the ^{6}Li(^{7}Li,^{7}Be) reaction at 65A MeV [25]. However, the existence of soft-dipole resonance is still unclear and controversial theoretically [17, 18]. Since the width of the observed resonance-like state is broader ($\Gamma \sim 4$ MeV) than the that of the ^{6}He+^{6}He resonance states observed in the breakup experiment, of which value is less than 2 MeV [1], we do not take into account the excitation soft-dipole excitation in the present coupled-channel (CC) calculation.

In the present CC calculation, we include the $0^+\otimes 2_1^+$, $2_1^+\otimes 2_1^+$, $0^+\otimes 2_2^+$ inelastic-channels in addition to the elastic one ($0^+\otimes 0^+$). Then, we solve the CC equations numerically and calculate the S-matrix elements for the individual partial waves, J=0~10, in the energy range up to $E_{\mathrm{c.m.}}$=20 MeV. No imaginary potential is included in the calculation.

3 Results

The lowest panel of Fig. 1 shows the energy dependence of the partial-wave components of the total cross section divided by π/k^2, $(2J+1)(2-2\Re S_{\mathrm{el}}^{(J)})$, calculated from the elastic component of the S-matrix elements for J=4 partial wave. In this figure, the energy positon of the cross section is shifted to high energy side by about 0.3 MeV. The channel coupling to the excited states in ^{6}He gives rise to a number of sharp resonances in this partial wave.

Then, we have analyzed the channel component of the wave function for each resonance. Since the resonance wave functions are the scattering-state wave function, we solve the CC equation under the bound-state-like boundary condition in order to understand the details properties of the resonance wave functions. In this approximation, the radial wave functions in the individual channels are expanded in terms of L^2-integrable basis functions. We calculated the probability of finding the system in the individual channel components, which is represented by the squared modulus of the channel wave functions integrated over the whole radial range.

In upper four panels of Fig. 1, we show the probability of finding the system in some important channels for $J = 4$ partial wave obtained by the bound-state approximation, which is normalized to unity in each eigenstate. It is clearly seen that each resonance has a different channel structure. For example, the resonances around $E_{\mathrm{c.m.}} = 2.5$ MeV has a dominant component, the $L = J - 4$ component of the $[2_1^+ \otimes 2_1^+]_{I=4}$ mutual-excitation channel, while the broad resonance at $E_{\mathrm{c.m.}}$=3 MeV has two dominant channel components, the elastic and the $L = J - 2$ component of the $[0^- \otimes 2_1^+]_{I=2}$ single-excitation channel, etc, where I denotes the channel spin.

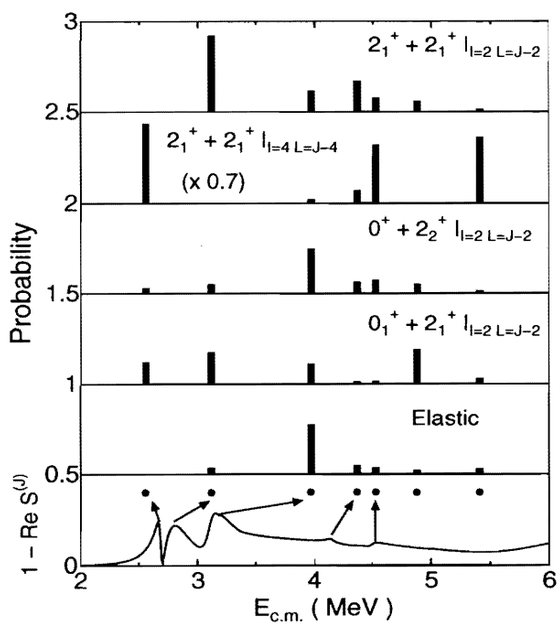

Figure1: Channel component of the wave function for each resonance in $J = 4$. The ordinate represents the probability of each channel component obtained by the bound-state approximation. The partial cross section for $J = 4$ is also shown in the lowest panel to identified the resonance positions. See text for details.

We have done the same kind of analysis of the resonance wave functions for other partial waves and classified the resonance states according to the channel structure. We found that in each J the individual states have a channel structure similar to one of the states in J=4. Each group of states show a clear rotational spectrum, as shown in Fig. 2, and the resonance

states in each rotational band have a common channel structure, namely have one or two dominant channel component as seen in Fig. 1 for J=4. We have identified four different rotational bands in this energy region.

In Fig. 2, the solid circles show the resonance positions observed in the breakup reaction [1]. We have also plotted two other resonances observed at E_x=14.9 MeV and 22.8 MeV, to which no spin assignment was made in the experiment [1] and, hence, plotted in parentheses at plausible spin positions. In this figure, the squares show the bands in which the dominant component is the $[0^+ \otimes 2_1^+]_{I=2,L=J-2}$ channels, respectively, while the bands shown by the inverse triangles, circles and diamonds has the dominant component of the $[0^+ \otimes 2_2^+]_{I=2,L=J-2}$, $[2_1^+ \otimes 2_1^+]_{I=2,L=J-2}$ and $[2_1^+ \otimes 2_1^+]_{I=4,L=J-4}$ channels, respectively.

It should be noted that the predicted resonances belong to different kind of bands, whereas they were assigned to be members of a single molecular band in Ref. [1]. It should also be noted that the dominant channel-components of the molecular bands shown in Fig. 2 are those of the non-elastic channels. Thus, the excitation of the ^{6}He nucleus plays an essential role in the resonance formation.

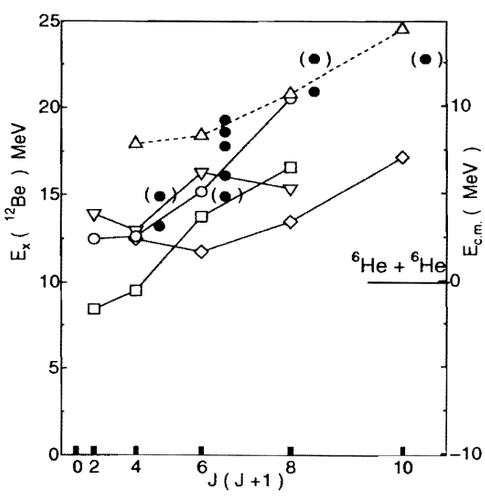

Figure 2: Molecular bands of the ^{6}He+^{6}He system obtained by the coupled-channel calculation. The solid circles represent the observed resonances [1]. See text for details.

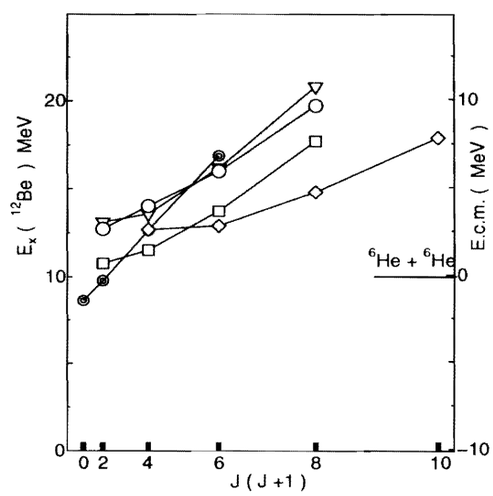

Figure 3: Molecular bands obtained by the potential scattering in the individual channels (single-channel calculation). See text for details.

The energy locations of obtained molecular bands are slightly low compared with the resonance positions observed by the breakup reaction. In Fig. 2, we also show the molecular band of $[2_2^+ \otimes 2_2^+]_{I=4}$ mutual-excitation channel with aligned $L = J - 4$ configuration, which is not taken into account in the present CC calculation, by dotted-line with triangles. The energy location of this band well agrees with that of the observed resonances states in the higher partial waves more than J=6. Therefore, it is well expected that the coupling to this channel will play very important roles for the ^{6}He+^{6}He resonance formation in such higher partial waves. The channel coupling effects are not so weak and the populations of the dominant channel component in each molecular band is less than about 50 % for the inelastic molecular bands. We could not clearly identified the molecular bands of the elastic

channels in the coupled-channel solution, because the channel-coupling effect is especially strong for the elastic (0^++0^+) channel, of which population in the individual CC resonance states is less than about 20 %.

In order to see the coupling effects quantitatively, we calculate the single-channel rotational bands in the elastic and excited channels, namely the sequence of the potential resonances generated by the diagonal potential in each channel. We show the obtained single-channel rotational bands in Fig. 3. The symbols of the individual molecular bands used in Fig. 3 represent the respective channels shown in Fig. 2. The departure of the coupled-channel bands (Fig. 2) from the corresponding single-channel ones (Fig. 3) will be a measure of the channel-coupling effect. The coupling gives rise to an energy gain by less than 1–4 MeV, indicating an attractive nature of the channel-coupling effect. The relatively strong coupling effect is consistent with a rather strong channel mixing in the individual resonance states generated by the coupled-channel calculations, as already discussed.

4 Summary and conclusion

In summary, we have performed the coupled-channel calculation of the ^{6}He+^{6}He scattering at low energies by taking into account the excitation to the 2_1^+ and 2_2^+ states of the colliding ^{6}He nuclei. The inter-nucleus interactions, both the diagonal and coupling ones, are calculated by the double-folding model with the use of the density-dependent M3Y NN interaction, DDM3Y, and ^{6}He densities calculated from the α+n+n three-body wave functions. The diagonal and transition densities for the ground and 2_1^+ states are calculated from the microscopic α+n+n three body models [14]. The transition densities to the 2_2^+ excitations are calculated by the extended-collective model assuming the quadrupole deformation of 2_2^+ state of ^{6}He [19]-[21]. The coupled-channel calculation predicts many resonance states in the energy range where the resonances were observed in the ^{12}Be $\rightarrow$ ^{6}He+^{6}He breakup experiment [1] and that the energies and spins of the calculated resonances agree with the experimental observations. The calculated resonances are found to be the members of different kinds of molecular rotational bands which are generated by the coupling among the molecular bands in the elastic and inelastic channels. Therefore, The excitations of ^{6}He plays an important role in the resonance formation in the collision of the ^{6}He+^{6}He system.

In conclusion, we propose the molecular resonances generated by the coupling to the 2_1^+ and 2_2^+ states in ^{6}He as a good candidate of the molecular-like states observed in the recent ^{12}Be breakup experiment. The results of the present CC calculation also suggest that the coupling to the mutual-2_2^+ excitation channels will play very important roles on the ^{6}He+^{6}He molecular-resonance formation. However, the spectroscopic information on the 2_2^+ state, such as the excitation energy and the decay width, is remained unclear experimentally. In addition, as we have just mentioned in the previous section, the most recent experiment by Nakayama *et al.* strongly suggests the existence of the soft-dipole resonance states, although the existence of soft-dipole resonance is still unclear and controversial theoretically [17, 18].

Therefore, more detailed information about the nuclear structure of excited ^{6}He itself up to 6 MeV, such as their spins and the strength of the electro-magnetic transition both theoretically and experimentally, is strongly desired in order to discuss the molecular resonance formations of the ^{6}He+^{6}He system. At the same time, one should make a more realistic calculation of the ^{6}He+^{6}He collision by taking into account the resonance character of the

2_2^+ state (and soft-dipole state if its existence will be well established both theoretically and experimentally) using more microscopic wave functions of ^{6}He, such as those based on the $\alpha+n+n$ three-body model.

References

[1] M. Freer et al., Phys. Rev. Lett. **82** (1999), 1383.

[2] S. Funada, H. Kameyama, Y. Sakuragi, Nucl. Phys. **A575** (1994), 93.

[3] Y. Suzuki, Nucl. Phys. **A528** (1991), 395; Y. Suzuki et al., Nucl. Phys. **A567** (1994), 957.

[4] B. V. Danilin et al., Phys. Rev. **C43** (1991), 2835

[5] M. V. Zhukov et al., Phys. Reports **231** (1993), 151.

[6] G. D. Alkhazov et al., Phys. Rev. Lett. **78** (1997), 2313.

[7] I. Tanihata et al., Phys. Rev. Lett. **55** (1985), 2676; I. Tanihata et al., Phys. Lett. **B160** (1985), 380.

[8] I. Tanihata et al., Phys. Lett. **B206** (1988), 592.

[9] I. Tanihata et al., Phys. Lett. **B289** (1992), 261.

[10] P. G. Hansen and Jonson, Europhys. Lett. **4** (1987), 409.

[11] K. Ikeda, INS Report JHP-7 (1988), in Japanese.

[12] G. R. Satchler and W. G. Love, Phys. Rep. **55** (1979), 183; G. R. Satchler, *Direct Nuclear Reactions* (Clarendon, Oxford 1983), p. 463

[13] M. El-Azab Farid and G. R. Satchler, Nucl. Phys. **A438** (1985), 525.

[14] E. Hiyama and M. Kamimura, private communication.

[15] T. Aumann et al., Phy. Rev. **C59** (1999), 1252

[16] J. Jänecke et al., Phy. Rev. **C54** (1996), 1070

[17] S. Aoyama, S. Mukai, K. Kato and K. Ikeda, Prog. Theor. Phys. **93** (1995) 99; **94** (1995) 343.

[18] B. V. Danilin et al., Nucl. Phys. **A632** (1998) 383.

[19] Y. Sakuragi, S. Funada and Y. Hirabayashi, Nucl. Phys. **A588** (1995), 65c;
S. Funada, Prog. Theor. Phys. **93** (1987), p.p. 373.

[20] G. R. Satchler, Nucl. Phys. **A472** (1987), 215; G. R. Satchler, *Direct Nuclear Reactions* (Clarendon, Oxford 1983), p. 597

[21] M. Ito and Y. Sakuragi, Phy. Rev. **C**, in press

[22] Y. Suzuki, Nucl. Phys. **A528** (1991), 395.

[23] H. Sagawa, N. Takigawa and Nguyen van Giai, Nucl. Phys. **A543** (1992), 575.

[24] A. Bohr and B. R. Mottelson *Nuclear Structure Volume II* (W. A. Benjamin, Inc. 1975), p. 44.

[25] S. Nakayama et al., Phy. Rev. Lett. **85** (2000), 262

Cluster structure in the Light Unstable Nuclei

Y. Kanada-En'yo[A] and H. Horiuchi[B]

[A] *Institute of Particle and Nuclear Studies, High Energy Accelerator Research Organization, Oho 1-1, Tsukuba-shi, 305-0801, Japan*
[B] *Dept. of Physics, Kyoto University, Kyoto 606-01, Japan*

Recently, the new excited states of the light unstable nuclei are observed experimentally, and varieties of structures are suggested. One of the hot subject is the molecule-like structure with the exotic shape in the neutron-rich nuclei. For example, the second $K^\pi = 0_2^+$ band in ^{10}Be can be described theoretically by the well developed clustering structure [1, 2, 3]. There are some experimental data which suggest the molecule-like structures in the excited states of ^{12}Be and ^{11}Be. People are interested in whether or not the clustering structures may develop in other neutron-rich nuclei.

Our aim in this paper is to study the features of the clustering structures in the light unstable nuclei. We adopt a theoretical approach of antisymmetrized molecular dynamics (AMD). The method of AMD has been already proved to be a powerful approach to describe various structures and clustering features of the excited states of light unstable nuclei as well as stable nuclei [4, 1]. We study the structures of the excited states of Be isotopes and ^{15}C, and show the possibility of the molecule-like structures based on the calculated results with AMD.

In the case of ^{12}Be, it is found that even the ground state has the developed clustering structure instead of the closed neutron p-shell state. The main component of the ground state is the $2\hbar\omega$ state in terms of the simple shell model configuration, which is the reason for the small GT strength of β decay to ^{12}B. That is to say the neutron magic number 8 disappears in ^{12}Be. It is interesting that the rotational band starting from the ground state reaches to the $J^\pi = 8^+$ state at about 20 MeV where the many excited states have been experimentally observed in the break up channels into ^{6}He+^{6}He and ^{4}He+^{8}He [5]. Other rotational bands with the molecule-like structures are seen in the results.Also in the results of ^{11}Be, some rotational bands with the 2α clustering states are found.

In the results of ^{15}C, we calculate the excited states near the ylast line. It is interesting that the linear cluster structures may appear on the ylast line for the negative parity when the total spin is larger than 13/2. On the other hands, according to AMD calculations the linear 3α structure is not necessarily stable in the ^{12}C. We think that the valence neutrons in ^{15}C play an important role for the stability of the linear clustering structure.

References

[1] Y. Kanada-En'yo, H. Horiuchi and A. Doté, Phys. Rev. C **60**, 064304 (1998)

[2] A. Doté, H. Horiuchi, and Y. Kanada-En'yo, Phys. Rev. C **56**, 1844 (1997).

[3] N. Itagaki and S. Okabe, preprint RIKEN-AF-NP-314 (1999).

[4] Y. Kanada-En'yo, Phys. Rev. Lett. **81**, 5291 (1998).

[5] M. Freer, et.al., Phys. Rev. Lett. **82**, 1383 (1999).

[6] N. Aoi, et al., Nucl. Phys. A**616** 181c (1997).

軽い不安定原子核のクラスター構造

KEK 素核研, 京大理[A]
延与佳子、堀内昶[A]

§ 1 はじめに

背景

不安定核の基底状態でのクラスター構造
⟸理論的示唆

励起状態における分子的構造の可能性
⟸実験
^{12}**Be** の励起状態：^{12}**Be*** ⇒ ^{6}**He+**^{6}**He**, ^{8}**He+**^{4}**He**
^{11}**Be** の励起状態：^{9}**Be(**^{13}**C,** ^{11}**C)**^{11}**Be**
H.G.Bohlen et.al, IL Nuovo Cimento Vol 111A, 841(1998)

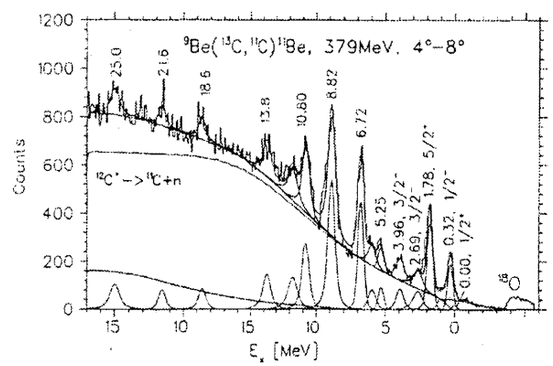

興味

不安定核のクラスター構造の性質の統一的に理解

§ 2. 手法

○ **波動関数** スレータ行列式

$$\Phi = c\Phi_{AMD} + c'\Phi'_{AMD} + c''\Phi''_{AMD} + \cdots$$

$$\varphi_i = \begin{cases} \text{空間: } \phi_{\mathbf{Z}_i}(\mathbf{r}_j) \propto \exp\left[-\nu(\mathbf{r} - \frac{\mathbf{Z}_i}{\sqrt{\nu}})^2\right] & \text{ガウス波束} \\ \text{アイソスピン } \chi_i = \begin{pmatrix} \frac{1}{2} + Z_{4i} \\ \frac{1}{2} - Z_{4i} \end{pmatrix} \otimes (p, n) \end{cases}$$

○ **励起状態**

全角運動量 J固有状態への射影

$$\Phi^{J\pm}_{MK} = P^J_{MK} P^{\pm} \Phi_{AMD} = \int d\Omega D^{J*}_{MK}(\Omega) R(\Omega)(1 \pm P)\Phi_{AMD}$$

についてエネルギー変分 **(VAP)** ⟹ $J^{\pm}_{1}$の状態

第一・第二励起状態: **Lower level** に直交

イラスト線上の構造変化: $J_z = M$の固有状態へ射影後に変分

○ **摩擦冷却法による変分** 射影後の変分 **(VAP)**

$$\frac{d\mathbf{Z}}{dt} = (\lambda + i\mu)\frac{1}{i\hbar}\frac{\partial}{\partial \mathbf{Z}^*}\frac{\langle\Phi(\mathbf{Z})|H|\Phi(\mathbf{Z})\rangle}{\langle\Phi(\mathbf{Z})|\Phi(\mathbf{Z})\rangle}, \qquad \text{C.C.}$$

○ **ハミルトニアン行列の対角化**

内部状態 $\{\Phi_{AMD}\}$ を対角化による重ね合わせ **(GCM** 的**)** ↔実験的諸量

○ **束縛状態近似** ガウス波束という制限による人工的な壁.

§ 3 結果

中心力: **MV1 = Volkov No.1 (2 体力)+ 3 体斥力**

LS 力: **G3RS**

Coulomb 力: ガウス関数の和で近似

Be アイソトープ

励起状態・基底状態でのクラスター構造の可能性

$\Longrightarrow$ 回転帯を形成：**20MeV** 程度までの高スピン状態

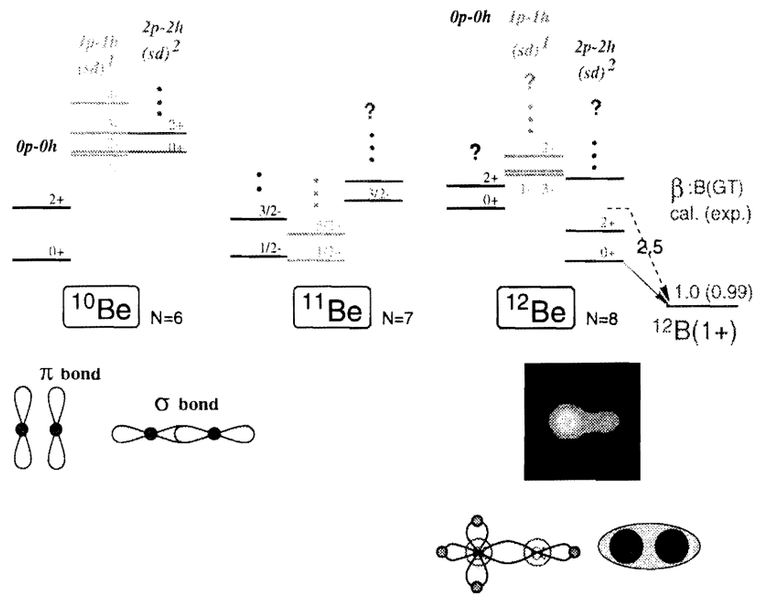

^{12}Be

MV1: $W = 1 - M, B = 0.0, H = 0.0, M = 0.65$

LS 力: $u_I = u_{II} = 3700$**MeV** $\Longleftarrow$ ^{11}**Be** の基底パリティを再現

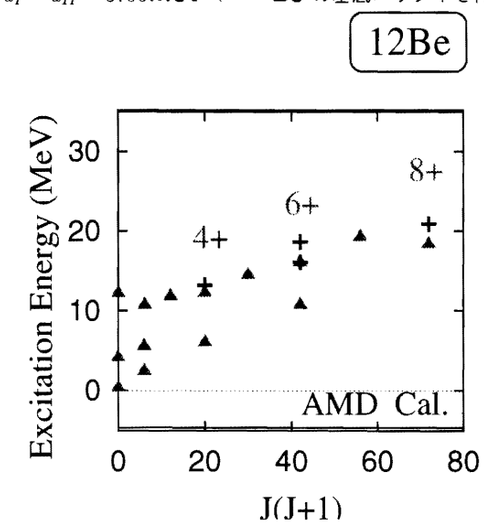

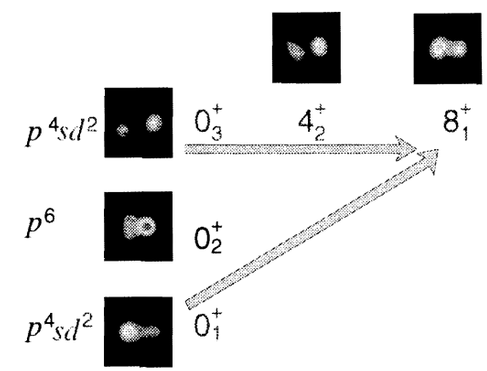

^{15}C のリニアクラスター構造

M 射影後変分の **AMD** 計算によるイラスト線上の構造変化

リニアなクラスター構造の可能性：

$$s_\pi^2 s_\nu^2 p_\pi^2 p_\nu^5 (sd)_\pi^2 (sd)_\nu^2 \Longrightarrow J^\pi > 15/2^-$$

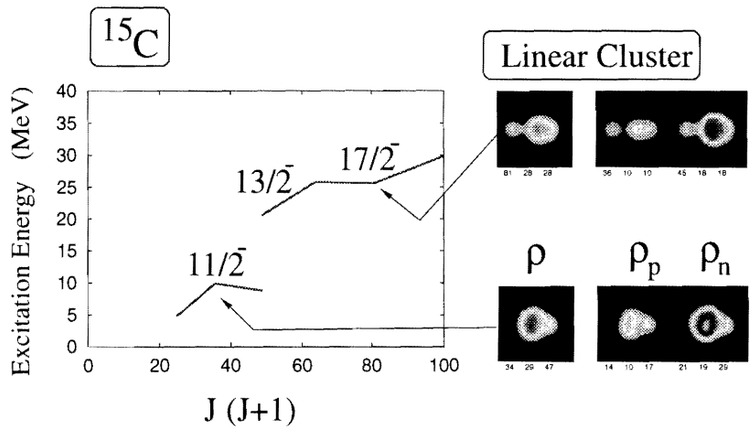

Linear cluster 回転帯の実験的観測の可能性は？

He transfer 反応 ^{9}**Be**(^{10}**Be**, ^{4}**He**)^{15}**C** ?

^{15}**C** 励起 **breakup** 反応 ^{15}**C**$^* \Rightarrow$ ^{6}**He**+^{9}**Be**, ^{4}**He**+^{11}**Be** ?

^{6}**He**+^{9}**Be**···**19 MeV**

^{4}**He**+^{11}**Be**···**13 MeV**

C でのリニアクラスター構造の安定性

なぜ、^{15}**C** でクラスターのリニアチェーン構造が現れるのか？

⇕

^{12}**C** での $K^\pi = 0_3^+$ バンドの 3α構造

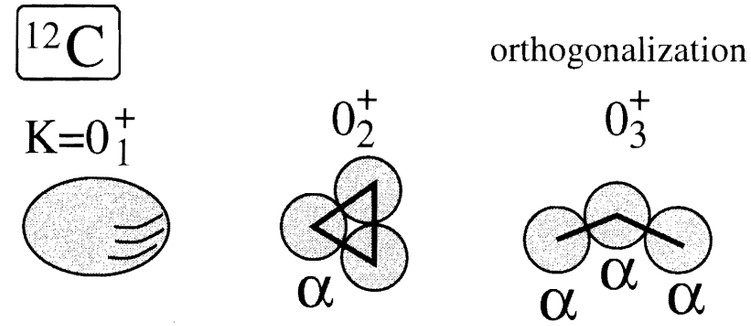

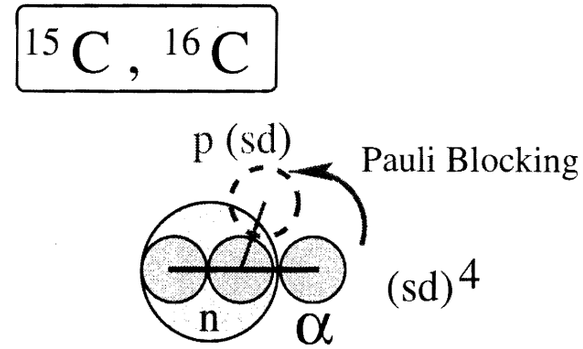

§ 5. まとめ

反対称化分子動力学を用いて
^{12}Be の励起状態の分子的構造を研究

- スピンパリティ射影後の変分計算による励起状態の記述.
- 分子的構造による回転帯構造 (8^+まで，2つの回転帯の交差)
- He 粒子崩壊についての考察.
- スピン Jの増加とともに構造変化.
  変形度が減少. 中性子スピン align. He クラスターの 2^+励起.

^{15}C の励起状態での分子的構造の可能性.

- イラスト線上の構造変化：
  高スピン状態で、3αリニアチェーン構造の可能性.
  ^{11}Be*+^{4}He への崩壊チャネル

§ 今後

- 崩壊幅：6He,8He の基底状態の精密な記述
- 中性子放出の安定性：11Be 励起状態の記述
- 有効相互作用の決定.　LS 力，密度依存力など 進行中
- 重い原子核への適用　進行中 $N=20$ 領域など
- イラスト線から離れた励起状態

Superdeformation in the newly discovered superheavy elements

Zhongzhou Ren[1,2] and Hiroshi Toki[1]
[1] Research Center for Nuclear Physics (RCNP), Osaka University, Osaka 567-0047, Japan
[2] Department of Physics, Nanjing University, Nanjing 210008, P. R. China

Abstract

The structures of newly discovered superheavy elements with the proton number Z=110-112,114,116,118 and of their α-decay chain nuclei are investigated using the self-consistent relativistic mean-field (RMF) theory. Extensive calculations show that the experimental data on the α-decay energies are well reproduced by the RMF theory. We find sometimes shape coexistence in superheavy nuclei and a superdeformed prolate configuration becomes the ground state of the new superheavy elements. The superdeformation could lead to a slightly deeper binding and give a longer lifetime for superheavy nuclei than expected. This may be a new mechanism for the appearance of the superheavy island. A systematic comparison with other models for the calculated binding energies and deformations is carried out, and predictions on the properties of unknown neighbouring superheavy nuclei are made for further comparison with future experiments.

1 Introduction

The nuclear synthesis of new superheavy elements in laboratory is currently a hot subject in nuclear physics. During the period from 1995 to 1996 Hofmann et al. [1-4] at GSI in Germany successfully produced the elements Z=110, 111, and 112 successively by using low-energy heavy-ion collisions. Experimental studies on superheavy elements have received another major breakthrough with the most recent discoveries at Dubna and Berkley [5-7]. In January 1999, it was reported that the new element Z=114 was produced at Dubna [5-6]. This was followed by the production of another isotope of the Z=114 element in April 1999 again at Dubna in collaboration with the physicists from Europe and Japan [5-6]. The physicists at Berkley successfully created other two new elements with Z=116 and 118 [7].

In this paper we will calculate the properties of superheavy nuclei by the relativistic mean-field (RMF) model [8-10]. The TMA force [9] is used in our calculation and its values are listed in Table 1. The TMA force was proposed by Sugahara and Toki [9] and the surface effects of finite nuclei were included by introducing A dependent coefficients in the coupling constants. We apply the TMA force to the experimental data of Z=110,111,112 found at GSI. This is also the second test on the validity of the effective force for superheavy nuclei.

2 Numerical results and discussions

The RMF results on binding energies, deformations, and radii of Z=110-112 nuclei found at GSI are listed in Table 1. Because the size of a nucleus is an important quantity, we list the radii of nuclei although they are not directly related to alpha decay data. The merit that we list the results in Tables is that other groups can easily test the correctness of our result and the future experiments will be compared with the numerical results directly. In Table 1, B denotes the calculated binding energy, whereas R_p and R_n are the root-mean-square radii for the proton- and neutron-density distributions, respectively. The symbols β_n and β_p in Table 1 denote the quadrupole deformations, respectively of neutrons and protons. Further, the symbols Q_α and T_α are used for the calculated alpha-decay energies and the corresponding lifetimes. The lifetimes are obtained following the Viola-Seaborg formula on alpha-decays [11,12]

$$\log(T_\alpha) \;=\; (aZ+b)(Q_\alpha)^{-1/2} \;+\; (cZ+d) \;+\; h_{\log} \qquad (1)$$

where T_α is given in second and Q_α in MeV, and Z is the proton number of the parent nucleus. This is a well-known formula and it is often used to estimate the lifetime of alpha-decays by the decay energies. The constants in this expression have been determined as $a = 1.66175$, $b = -8.5166$, $c = -0.20228$, $d = -33.9069$, and $h_{log} = 1.066$ for odd-N nuclei. These values are obtained by fitting the experimental data of middle and heavy nuclei [11,12]. For the purpose of comparisons we list the experimental alpha-decay energies and lifetimes in the last two columns of the table. For some nuclei, there are two or three chains of alpha decays. This is why there are two experimental values in last two columns for some nuclei.

We see in Table 1 that the calculated alpha decay energies agree well with the experimental data, especially for the elements Z=110-112 produced at GSI. We calculate the corresponding lifetimes of these nuclei by using the Viola-Seaborg formula. In most cases the ratio of theoretical lifetime to experimental one is between 10^{-3} and 10^{3}. Usually the ratio between the experimental lifetime and the theoretical one is around 10^{4} or even larger. Therefore we can say that the RMF prediction on lifetime is very good. The RMF model shows that there are

prolate deformations in these nuclei and the quadrupole deformation parameters are around 0.21. This agrees with other models [8].

When we perfom the RMF calculations of superheavy nuclei with $110 \leq Z$ and $170 \leq N$, we find an unexpected phenomenon. We find that there are usually several energy minima for almost every superheavy nucleus with neutron number $171 \leq N$. This finding suggests that there is shape coexistence in superheavy nuclei because the energy differences of different solutions are even less than 1 MeV in some cases. Three solutions play an important role for the ground state and they compete each other strongly. They are a moderate prolate solution, an oblate solution, and a superdeformed prolate solution with deformation parameter $\beta_2 \geq 0.4$. At the beginning we thought that the superdeformed solution may be an unphysical solution. But finally we were convinced that it is a physical solution because it appears gradually with the neutron number and becomes the ground state of some superheavy nuclei. We list the lowest two solutions in Table 2 for new superheavy nuclei produced at Dubna.

In the lower part of Table 2, we list the theoretical results for another experiment of Dubna. One sees again that there is shape coexistence in nuclei $^{283}112$ and $^{287}114$. The theoretical alpha decay energies agree with experimental data. The calculated lifetime is also reasonable.

After we have compared the RMF results with the Dubna data, we compare now our results with Berkeley data in Table 3. We see again the shape coexistence above $^{285}114$. As for the alpha decay energies, our results agree with the Berkeley data except for $^{293}118$ and $^{289}116$. For these two nuclei we slightly underestimate the experimental decay energies.

3 Conclusions

We have investigated the structure of newly discovered superheavy nuclei at GSI, at Dubna and at Berkeley in terms of the RMF theory. nuclei because previous studies only include some of newly discovered superheavy nuclei. We have found that the RMF results are in good agreement with the experimental data on the alpha decay energies and the lifetimes of the superheavy nuclei. Some new results for the quadrupole deformation of superheavy nuclei have been obtained. It is found that the shape coexistence could appear for superheavy nuclei and it will lead to a slightly deeper binding. In some cases a superdeformation becomes the ground state of superheavy nuclei. It will give a longer lifetime than expected. This could be a new mechanism for the appearance of superheavy islands. The results of the RMF theory for superheavy nuclei suggest that the existence of many more superheavy nuclei having lifetime of the order of a second or longer like $^{289}114$ and $^{287}114$. These nuclei are expected to form the island of superheavy elements.

Z. REN gratefully acknowledges the support provided to him under the COE Professorship Program of Monbusho of Osaka University. He is also supported by the National Natural Science Foundation of China.

References

1. S. Hofmann et al., Z. Phys. A **350** (1995) 277.
2. S. Hofmann et al., Z. Phys. A **350** (1995) 281.
3. S. Hofmann et al., Z. Phys. A **354** (1996) 229.
4. S. Hofmann et al., Rep. Prog. Phys. **61** (1998) 639.
5. Y. T. Oganessian et al, Nature (London) **400** (1999) 242.
6. Y. T. Oganessian et al, Phys. Rev. Lett. **83** (1999) 3154.
7. V. Ninov et al, Phys. Rev. Lett. **83** (1999) 1104.
8. M. Bender, Phys. Rev. **C61** , (2000) 031302.
9. Y. Sugahara, Ph. D. thesis, Tokyo Metropolitan University, 1994.
10. K. Rutz, M. Bender, T. Buervenich, T. Schilling, P. G. Reinhard, J. A. Maruhn, and W. Greiner, Phys. Rev. C **56** (1997) 238.
11. P. Moeller, J. R. Nix and K. L. Kratz, Atomic Data and Nuclear Data Table **66** (1997) 131.
12. V. E. Viola Jr. and G. T. Seaborg, J. Inorg. Nucl. Chem. **28** (1966) 741.

Table 1 The binding energies, deformations, nuclear radii, alpha-decay energies, and the lifetimes of superheavy nuclei. The last two columns the are experimental decay energies and lifetimes. The input pairing gaps: $\Delta_p = \Delta_n = 11.2\ MeV/\sqrt{A}$. The TMA force is used.

Nuclei	B (MeV)	β_n	β_p	R_n	R_p	Q_α	T_α	$Q_\alpha(exp.)$	$T_\alpha(exp.)$
$^{269}110$	1954.39	0.22	0.23	6.26	6.11	11.56	146μs	11.13 ± 0.02	$270^{+1300}_{-120}\mu$s
$^{265}108$	1937.65	0.24	0.25	6.24	6.08	9.92	389ms	10.57(10.52)	1.2ms
$^{261}106$	1919.27	0.25	0.26	6.21	6.05	9.17	11.84s	9.58(9.47)	0.15s
$^{257}104$	1900.14	0.26	0.26	6.19	6.02	8.61	131.0s	8.71(8.62)	13.6s
$^{253}102$	1880.45	0.26	0.27	6.16	5.98	8.25	374.3s	8.14 (8.02)	133s
$^{272}111$	1970.09	0.21	0.21	6.28	6.12	11.57	0.301 ms	10.82 ± 0.02	$1.5^{+2.0}_{-0.5}$ms
$^{268}109$	1953.36	0.22	0.23	6.26	6.10	10.49	28.4 ms	10.10(10.24)	10^{+100}_{-30}ms
$^{264}107$	1935.55	0.25	0.25	6.24	6.07	9.56	2.07 s	9.48(9.62)	$0.44^{+0.60}_{-0.16}$s
$^{260}105$	1916.81	0.26	0.27	6.21	6.04	8.93	32.1 s	9.20(9.15)	1.2s
$^{256}103$	1897.44	0.26	0.27	6.19	6.01	8.21	1366 s	8.46	66.3s
$^{277}112$	2000.38	0.19	0.19	6.31	6.15	10.84	27.9ms	11.45(11.65)	$0.24^{0.43}_{0.09}$ms
$^{273}110$	1982.92	0.21	0.21	6.30	6.12	10.84	6.93ms	11.08(9.73)	0.11(170)ms
$^{269}108$	1965.46	0.22	0.22	6.27	6.10	9.01	184s	9.17(9.23)	19.7s(7.1s)
$^{265}106$	1946.17	0.22	0.22	6.25	6.06	8.83	134.6s	8.77	7.4s(24.1s)
$^{261}104$	1926.70	0.22	0.22	6.22	6.03	8.79	34.7s	8.52	4.7s(32.7s)
$^{257}102$	1907.19	0.26	0.27	6.21	6.01	7.71	3.2×10^4s	8.34	15.0s

Table 2 Same as table 2 but for comparison with experimental data from Dubna. We also list some superderformed solutions which are denoted by the symbol $*$.

Nuclei	B (MeV)	β_n	β_p	R_n	R_p	Q_α	T_α	$Q_\alpha(exp.)$	$T_\alpha(exp.)$
$^{301}120$	2121.45	-0.25	-0.27	6.54	6.38				
$^{301}120^*$	2123.07	0.54	0.57	6.73	6.58	10.52	55.0 s		
$^{297}118$	2105.02	-0.23	-0.24	6.50	6.33				
$^{297}118^*$	2105.29	0.52	0.54	6.69	6.53	11.08	0.44 s		
$^{293}116$	2088.07	-0.21	-0.21	6.47	6.28	10.36	8.65 s		
$^{293}116^*$	2087.45	0.50	0.51	6.64	6.47				
$^{289}114$	2069.19	-0.19	-0.19	6.43	6.24				
$^{289}114^*$	2070.13	0.48	0.49	6.60	6.42	9.32	$2.30 * 10^3$ s	9.71 ± 0.02	30.4 s
$^{285}112$	2049.98	0.14	0.15	6.39	6.18				
$^{285}112^*$	2051.15	0.46	0.47	6.56	6.36	8.99	90.8 min	8.67	15.4 min
$^{281}110$	2031.78	0.16	0.17	6.37	6.15				
$^{281}110^*$	2031.84	0.42	0.42	6.51	6.29	9.77	4.61 s	8.83	1.6min
$^{277}108$	2013.31	0.18	0.19	6.35	6.13				
$^{287}114$	2056.04	-0.18	-0.18	6.40	6.22				
$^{287}114^*$	2056.99	0.48	0.49	6.58	6.40	9.63	251 s	10.29 ± 0.02	5.5 s
$^{283}112$	2038.32	0.16	0.17	6.38	6.18	10.61			
$^{283}112^*$	2037.79	0.45	0.46	6.53	6.34				

Table 3 Same as table 3 but for the data from Berkeley.
The symbols $*$ and $**$ denotes different configurations in a nucleus.

Nuclei	B (MeV)	β_n	β_p	R_n	R_p	Q_α	T_α	$Q_\alpha(exp.)$	$T_\alpha(exp.)$
$^{293}118$	2077.30	-0.18	-0.19	6.43	6.27				
$^{293}118^*$	2078.18	0.50	0.53	6.63	6.48	11.14	0.315 s	12.39 ± 0.04	0.236 ms
$^{293}118^{**}$	2075.29	0.25	0.27	6.48	6.23	(12.23**)			
$^{289}116$	2060.68	-0.18	-0.18	6.41	6.24				
$^{289}116^*$	2061.02	0.48	0.50	6.58	6.43	10.18	27.6 s	11.63	1.243 ms
$^{289}116^{**}$	2059.26	0.26	0.27	6.45	6.28	(11.92**)			
$^{285}114$	2042.88	0.16	0.17	6.38	6.20				
$^{285}114^*$	2042.90	0.47	0.49	6.55	6.39	11.97	0.25 ms	11.35 ± 0.04	0.9 ms
$^{281}112$	2026.57	0.17	0.18	6.36	6.17	10.81	33.2 ms	10.68 ± 0.02	1.4ms
$^{277}110$	2009.08	0.19	0.19	6.33	6.14	10.26	207. ms	10.18 ± 0.02	5.7 ms
$^{273}108$	1991.04	0.20	0.21	6.31	6.11	8.76	$1.18 * 10^3$ s	9.63 ± 0.20	1.65 s
$^{269}106$	1971.50	0.21	0.21	6.26	6.05	7.82	$4.59 * 10^5$ s	8.74 ± 0.20	43.10 s

Study of the s-waves in ^{10}Li nucleus and the mirror, ^{10}N

H. Masui, Meme Media Laboratory, Hokkaido University

25/Aug/00

Collaborators:

S. Aoyama[a], T. Myo[b], K. Kato[b], K. Ikeda[c]

[a] Information Processing Center, Kitami Institute of Technology
[b] Graduated School of Science, Hokkaido University
[a] The Institute of Physical and Chemical Research (RIKEN)

Abstract

We study the property of unstable nuclei using the Jost function method (JFM). The JFM is a very useful method to investigate the bound, resonant, and scattering states in a unified approach. We show that the JFM can be applied to calculate the partial decay widths in coupled-channel problems, and also, to investigate the virtual states in unstable nuclei. In an unstable nucleus ^{10}Li, it is suggested that the low-lying s-state or virtual state exists. We investigate the s-state of ^{10}Li by using the core-n potential model which is made by taking into account the pairing-blocking effect to the p-wave in the core. We obtain the result that the s-wave cross-section is strongly enhanced near the threshold, and it corresponds to the observation of the energy distribution of the projectile fragmentation

1 Introduction

Study for unstable nuclei has great importance to understand the nuclear excitation and the structure from a new point of view [1]. It has been known that the unstable nuclei have some different features from stable nuclei. For example, large root-mean-squared radii which are understood as a "halo" structure, have been observed for neutron-rich nuclei near the drip-line [2, 1]. Among these nuclei, ^{6}He and ^{11}Li are considered as the typical halo nuclei. Theoretical approaches for these nuclei have been done by using the core+n+n model. Binding energies and halo structures have been studied in detail by using this model. It is known well that, for ^{6}He, the core (^{4}He)+n+n model can successfully reproduce the essential nature of this halo nucleus. However, for ^{11}Li, to reproduce the binding energy, it might necessary to introduce some "special" mechanisms in the ^{9}Li+n subsystem, e.g. a strong state dependence for even- and odd-parity states, since the lack of the binding energy is too large. Thompson and Zhukov proposed a relatively strong attraction for the s-wave in the ^{9}Li-n potential, so that ^{10}Li has an s-wave "virtual" state [3]. Using such potentials, they discussed that the experimental binding energy of ^{11}Li ($\sim$ 0.31 MeV) is reproduced. Despite of the success, the mechanism of such a strong state dependence was not clearly explained yet. Recently, Katō, Yamada and Ikeda proposed a potential with a new mechanism that the s-orbit comes down to the same energy region of the p-orbits due to the pairing-blocking effect upon the pairing correlation of p-orbital neutrons in the core [4]. Using such a state dependent potential, we showed that the s-wave virtual state is obtained in the ^{9}Li+n system (the scattering length: $a_0 = -9.97$fm) and the position of the pole is $k = -i0.077\text{fm}^{-1}$ ($E_v = -0.135$MeV) in our calculation [5].

In this report, we firstly explain Jost function method, which we apply to calculate S-matrices, in Sec. 2. In Sec. 3, we discuss how to obtain the partial decay widths in coupled-channel systems, and show the actual calculations for ^{9}Li+n system, the s-wave virtual pole and the total cross-section, in each subsection. In Sec. 4, we summarize this report and give a discussion.

2 Jost Function Method

In this subsection we briefly review the Jost function method (JFM) in coupled-channel systems. For details, see Refs. [6, 7] and our papers, Refs. [8, 5].

We consider an N coupled-channel Schrödinger equation for radial parts,

$$\left[\frac{d^2}{dr^2} + k_n^2 - \frac{2\eta_n k_n}{r} - \frac{l_n(l_n+1)}{r^2}\right] u_n(r) = \frac{2\mu_n}{\hbar^2} \sum_{n'=1}^{N} V_{nn'} u_{n'}(r) \ . \tag{1}$$

Here, for channel n, k_n is a momentum measured form the threshold energy E_n, and η_n is a Coulomb factor. We define a matrix ϕ_{nm} to describe the regular solutions φ_n for u_n as

$$\varphi_n = \sum_{m=1}^{N} c_m \phi_{nm} \ , \tag{2}$$

where the c_m are coefficients for a linear combination of their regular bases. To solve Eq. (1), we express the matrix element ϕ_{nm} in the following form using unknown functions $\mathcal{F}_{nm}^{(\pm)}(k_n, r)$:

$$\phi_{nm}(r) \equiv \frac{1}{2}\left[H_n^{(+)}(k_n r)\mathcal{F}_{nm}^{(+)}(k_n, r) + H_n^{(-)}(k_n r)\mathcal{F}_{nm}^{(-)}(k_n, r)\right] . \tag{3}$$

Here, the $H_n^{(\pm)}(k_n r)$ are homogeneous solutions of Eq. (1) corresponding to incoming $(-)$ and outgoing $(+)$ waves and are given by Coulomb wave functions for $\eta_n \neq 0$ and Ricatti-Hankel functions for $\eta_n = 0$. As is standard in the variable-constant method for solving an inhomogeneous second-order differential equation, we introduce the additional constraint

$$H_n^{(+)}\left[\partial_r \mathcal{F}_{nm}^{(+)}\right] + H_n^{(-)}\left[\partial_r \mathcal{F}_{nm}^{(-)}\right] = 0 \ . \tag{4}$$

Using Eqs. (3) and (4), we obtain a first-order differential equation for $\mathcal{F}_{nm}^{(\pm)}(k_n, r)$ from Eq. (1),

$$\frac{\partial \mathcal{F}_{nm}^{(\pm)}}{\partial r} = \pm \frac{\mu_n}{i k_n \hbar^2} H_n^{(\mp)} \sum_{n'=1}^{N} V_{nn'} \left\{ H_{n'}^{(+)} \mathcal{F}_{n'm}^{(+)} + H_{n'}^{(-)} \mathcal{F}_{n'm}^{(-)} \right\} \ . \tag{5}$$

The boundary condition at the origin is taken from the definition that the wave function is regular at the origin:

$$\mathcal{F}_{nm}^{(\pm)}(k_n, 0) = \delta_{nm} \tag{6}$$

In the asymptotic region, the potential will vanish and the unknown functions become constants

$$\lim_{r\to\infty} \mathcal{F}_{nm}^{(\pm)}(k_n, r) = \mathcal{F}_{nm}^{(\pm)}(k_n) \tag{7}$$

which are equivalent to the "Jost functions" of Eq. (1).

By using the Jost functions $\mathcal{F}_{nm}^{(\pm)}(k_n)$, the S-matrix at the complex momenta k is given as

$$S_{nn'}(k) = \left(||\mathcal{F}^{(+)}(k)|| \cdot ||\mathcal{F}^{(-)}(k)||^{-1} \right)_{nn'} \ . \tag{8}$$

Therefore, the condition for the bound and resonant states, where only out-going waves survive in the asymptotic region, is equal to the condition for poles of the S-matrix:

$$\det||\mathcal{F}^{(-)}(k)|| = 0 \ . \tag{9}$$

In JFM, we use the complex rotation as $r \to re^{i\theta}$, and the angle θ is taken so as to cancel the imaginary part of the complex momentum, which makes divergence of resonant wave functions. For calculations of "virtual" states, we can take the rotation angle as $\theta = 0$ (this is the same case of bound states), if the right-hand side of Eq. (5) converges into zero at $r \to \infty$. Therefore, in principle, this method has no difficulty in the calculation even for "virtual" states.

3 Results

Unstable nuclei such as ^{10}Li has a different feature of other stable nuclei. To study such the system, we use JFM which is very useful and powerful tool to investigate the resonance state as well as bound and scattering state. First, we discuss how to obtain the partial decay widths in coupled-channel systems. Next, we study ^{10}Li which is the subsystem of a typical halo nucleus ^{11}Li in core+n model by using the pairing-blocking effect potential. We show the s-wave virtual state exists and it is reasonable with comparing to an energy distribution of .^{9}Li+n in the projectile fragmentation ^{11}Li+C$\to$^{9}Li+n+X [9].

3.1 Partial decay widths in S-matrix scheme

For a well-isolated resonant state, an S-matrix $S_{nn'}(E)$ is expressed in the Breit-Wigner form with a resonance energy E_r, a total width Γ, and partial decay widths to channels n and n' (Γ_n and $\Gamma_{n'}$, respectively) as

$$S_{nn'}(E) \equiv S_n^{\rm bg}(E)\,\delta_{nn'} - i\frac{\sqrt{\Gamma_n \cdot \Gamma_{n'}}}{E - E_r + i\Gamma/2} \ , \tag{10}$$

where $S_n^{\rm bg}$ is a direct scattering and a background term.

From Eq. (10), the partial decay width Γ_n is obtained as a residue of the S-matrix:

$$\begin{aligned} \Gamma_n &= |\,{\rm Res}\,(S_{nn}(E_{\rm res}))\,| \\ &= |\lim_{E\to E_{\rm res}} (E - E_{\rm res}) \cdot S_{nn}(E)\,| \ . \end{aligned} \tag{11}$$

Here $E_{\rm res}$ is the complex resonance energy $E_r - i\Gamma/2$ (corresponding complex momenta are $k_{\rm res}$). However, a direct numerical method for the calculation of Eq. (11)may cause a large numerical error. Since, as $E \to E_{\rm res}$, the difference $(E - E_{\rm res})$ becomes a very small value, while the S-matrix has a singularity at $E_{\rm res}$. To avoid the singularity of the S-matrix at the resonance energy $E_{\rm res}$, we use the ratio of the S-matrices with the assumption that the sum of the partial decay width is the total width,

$$\Gamma = \sum_n \Gamma_n \ . \tag{12}$$

Once the total width Γ is known, we can obtain the partial decay widths from the ratios $\Gamma_n/\Gamma_{n'}$. From Eq. (10), since the direct scattering term $S_n^{\rm bg}$ can be neglected as $E \to E_{\rm res}$, the ratio of partial decay widths becomes the ratio of the S-matrices.

By using the Jost functions, the S-matrix can be represented as Eq. (8), and we have the definition of the inverse matrix of $||\mathcal{F}^{(-)}(k)||$,

$$\left(||\mathcal{F}^{(-)}(k)||^{-1}\right)_{mn} = \frac{1}{\det||\mathcal{F}^{(-)}(k)||}\,\mathcal{G}_{mn}(k) \ , \tag{13}$$

where $\|\mathcal{G}(k)\|$ is an adjoint matrix of $\|\mathcal{F}^{(-)}(k)\|$. The origin of the pole in the S-matrix comes from the root of $\det\|\mathcal{F}^{(-)}(k_{\rm res})\| = 0$. However, this singularity can be avoided. Since $\det\|\mathcal{F}^{(-)}(k)\|$ is independent of the channel, it can be dropped, and we obtain the ratio of the partial decay widths as

$$\frac{\Gamma_n}{\Gamma_{n'}} = \left|\frac{S_{nn}(E_{\rm res})}{S_{n'n'}(E_{\rm res})}\right| = \left|\frac{\sum_m \mathcal{F}^{(+)}_{nm}(k_{\rm res},\infty)\cdot\mathcal{G}_{mn}(k_{\rm res})}{\sum_m \mathcal{F}^{(+)}_{n'm}(k_{\rm res},\infty)\cdot\mathcal{G}_{mn'}(k_{\rm res})}\right| . \tag{14}$$

This expression does not include any explicit singularities in either the denominator or the numerator. Therefore, the numerical errors from the singularities are avoided and the calculation of the ratio has good accuracy. This is the present S-matrix scheme, and we calculate partial decay widths according to Eq. (14).

method	Γ_1 (a.u.)	Γ_2 (a.u.)
Eq. (14) (Present: S-matrix)	5.1116×10^{-5}	1.369076×10^{-3}
Noro-Taylor[10] (Original: T-matrix)	5.9×10^{-5}	1.361×10^{-3}
Eq. (12) in Ref. [11] (T-matrix)	5.1×10^{-5}	1.368×10^{-3}
Eq. (24) in Ref. [11] (Current density)	5×10^{-5}	1.45×10^{-3}

Table 1: Comparison of results for the calculation with various methods.

3.2 Virtual states in ^{10}Li

Next, we proceed to study the unstable nuclei using JFM. We study the 1s-state in the ^{9}Li+n system (^{10}Li). In a theoretical approach, the 1s-state in ^{9}Li+n is discussed as a "virtual" state by Thompson and Zhukov [3]. Also, recently, an s-wave ^{9}Li-n folding potential based on a nucleon-nucleon interaction and the wave function of ^{9}Li with the pairing correlation is given by our group [4] (hereafter, we call our ^{9}Li-n folding potential as FP1). However, the explicit position of the virtual pole is not shown in both cases, Ref. [3]. and Refs. [4, 12].

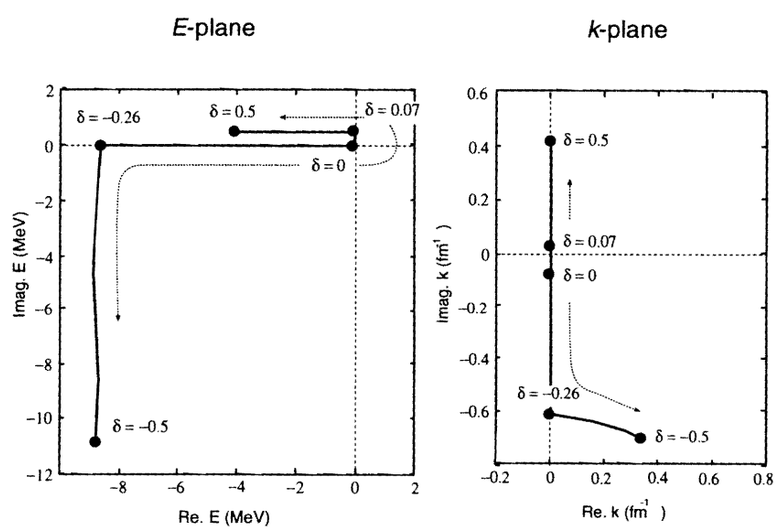

Figure 1: Poles of ^{9}Li-n potential

Therefore, we investigate the behavior of the 1s-state pole in the ^{9}Li+n system with changing the potential strength of FP1. Similarly to the case of the ^{4}He+n system, we use

a parameter $(1+\delta)$ for the attractive part of the ^{9}Li-n central potential. The trajectories of the pole of the $1s$-state are shown in Fig. 3 ((a) the momentum-plane and (b) the energy-plane). We vary the potential strength δ from -0.5 to 0.5. For $\delta = 0$, where we expected the $1s$-state to be a virtual state, the pole of the state is on the negative-imaginary axis in the complex momentum-plane, as shown in Fig. 3(a). Hence, it is clearly shown that the $1s$-state of the ^{9}Li+n system is a virtual state using our potential, FP1. For FP1, the virtual state is realized in the range of the strength δ as $-0.26 < \delta < 0.07$. In order to have a non-zero real part of the momentum, δ should be taken as less than -0.26. Even if we use such the weak attractive potential, however, as shown in Fig. 3(b), the pole is still in the third-quadrant of the complex energy-plane. This means that an experimental observation of the $1s$-state as a physical "resonant" state would be impossible.

Potentials	Scattering length a_0 (fm)	$1s$-pole: Energy (MeV)	Momentum (fm^{-1})
P0 [3]	0.7	-3.3	$-0.38i$
P1	-11	-0.11	$-0.071i$
P2	-18	-0.051	$-0.047i$
P3	-27	-0.025	$-0.033i$
P4	-44	-0.010	$-0.021i$
FP1 [4, 12]	-9.97	-0.135	$-0.077i$

Table 2: Poles of S-matrices and scattering lengths in the ^{9}Li-n system

We calculate the scattering length of the ^{9}Li+n system using FP1, and the position of the $1s$-pole using the potential of Thompson and Zhukov. The results are shown in Table 2. The calculated results of FP1, the energy $E = -0.135$ MeV and the scattering length $a_0 = -9.97$ fm, are very close to $E = -0.11$ MeV and $a_0 = -11$ fm, obtained with P1, Also, the experimental result obtained by Shimoura *et al.* [13] shows that the scattering length is determined as $a_0 = -16^{+4}_{-7}$ fm using the R-matrix analysis. Hence, our result is comparable to another theoretical calculation and is consistent with the experiment.

3.3 Effect to the cross-section

For the ^{9}Li+n scattering, we use FP1, applied in the virtual state calculation. To see the contribution of each partial wave clearly, we perform a single-channel calculation using a parameterization of Ref.[4] for p-waves, and investigate the difference by changing the parameter for s- and d-waves.

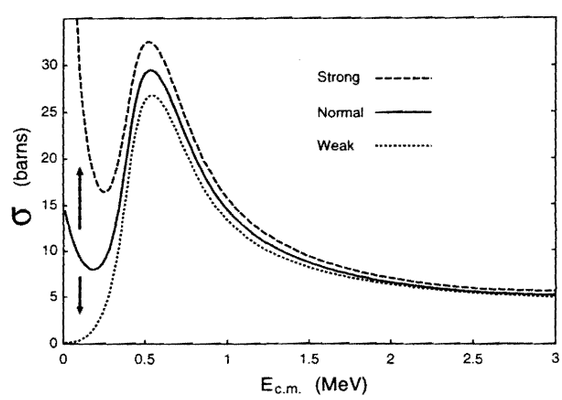

Figure 2: Total cross-section of ^{9}Li-n elastic scattering by varying the potential strength.

The potential is made by taking into account the dynamics of a pairing-blocking effect of p-wave neutrons for the core nucleus and a pairing correlation mechanism, then the potential depth for p-waves is pushed up and the attraction of the s- and the d-wave (even-parity states) potential becomes relatively stronger than the p-wave. In this model, the strength for the s- and d-waves still has some freedom to fix parameters. Hence, we slightly vary the strength for the even-parity state and investigate the relation between the position of the s-wave poles and the total cross-sections. In our previous calculation, which is one of the candidates, the s-wave pole is at $k = -i0.077$ fm^{-1} on the complex momentum plane (virtual state). Then, we have done the calculation with two different strengths, one is more attractive, which is determined so as to have the pole at almost origin; virtual state at $k = -i0.023$ fm^{-1} ($E = -0.012$ MeV) and another one is less attractive, which is the same order of the strength for the p-wave interaction; virtual state at $k = -i0.36$ fm^{-1} ($E = -2.89$ MeV).

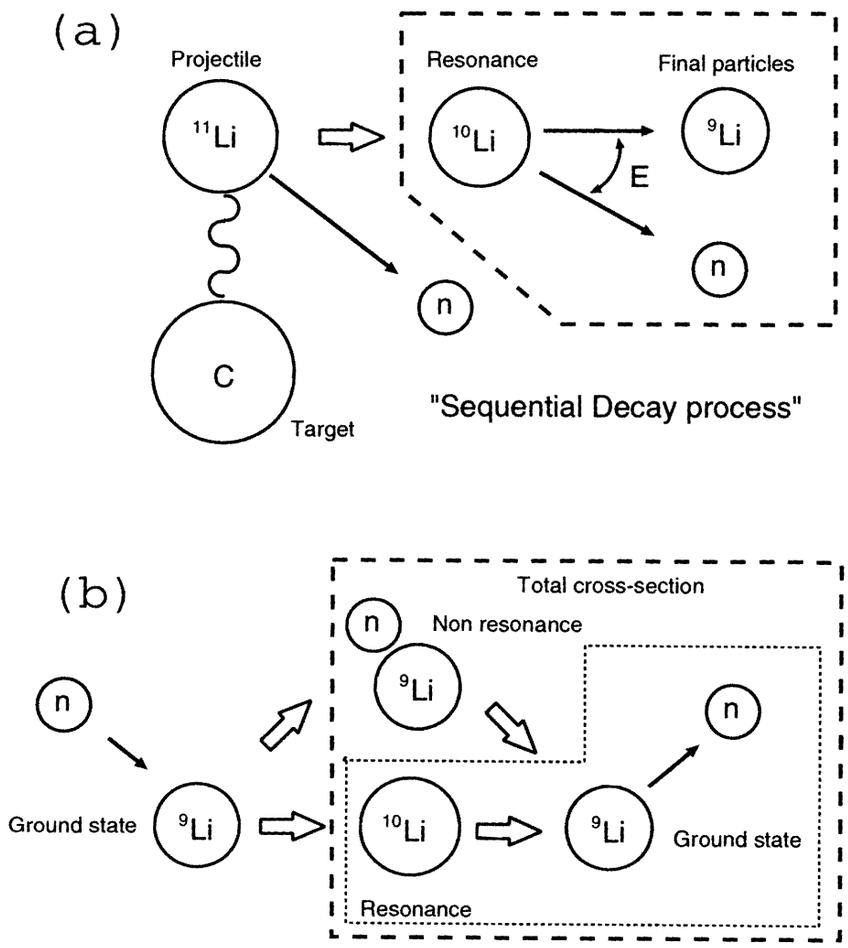

Figure 3: PF-TCS

Each calculated total cross-section shows a different behavior at the threshold energy, (see Fig. 2). For the weak strength, there is no enhancement, since the s-wave pole is very far from the threshold energy, $E = -2.89$MeV ($k = -i0.36$ fm^{-1}). Hence, the contribution of the s-waves to the total cross-section using this strength becomes very small. Also, for the normal case, the enhancement is not so large, due to the small contribution of the s-waves cross-sections as shown in Fig. 2. On the other hand, for the strong case, the enhancement

becomes very large, since the position of the s-wave pole is in close proximity to the threshold energy, $E = -0.012$ MeV ($k = -i0.023\,\mathrm{fm}^{-1}$), and the contribution to the total cross-section also becomes large at the threshold. We compare this result with the energy distribution of the projectile fragmentation obtained in Ref.[9].

When the sequential decay picture is the dominant process in the reaction, we can consider that an energy distribution gives information of the intermediate resonant nucleus (^{5}He or ^{10}Li). Here, we consider the ^{10}Li case, see Fig. 3. In the projectile fragmentation, the intermediate "resonant" nucleus ^{10}Li, decays apart into a neutron and a core nucleus ^{9}Li [9]. Then, at the resonant energy, the energy distribution of the projectile fragments has a resonant peak due to the contribution of the intermediate resonant particle ^{10}Li. Also, it is enhanced at the threshold energy when the "virtual" state exist in the intermediate state. On the other hand, it is well known that the elastic cross-section has a peak at the resonant energy, and is enhanced at the threshold energy when a virtual state exists. Therefore, the energy distribution of the fragmentation for the low-energy is considered to be similar to ones of the elastic scattering, since the elastic cross-section also has the peak for the resonant state and the enhancement for the virtual state.

In the upper part of Figs. 4(a) and 4(b), we show our calculated results for the total cross-sections. To compare the calculated total cross-sections with the energy distribution of the experiment [9], we smear the cross-sections using the resolution of the detector, Γ. And in the lower part, we show energy distributions of ^{4}He+n (^{5}He) and ^{9}Li+n (^{9}Li) in the experiment of projectile fragments obtained in Ref.[9].

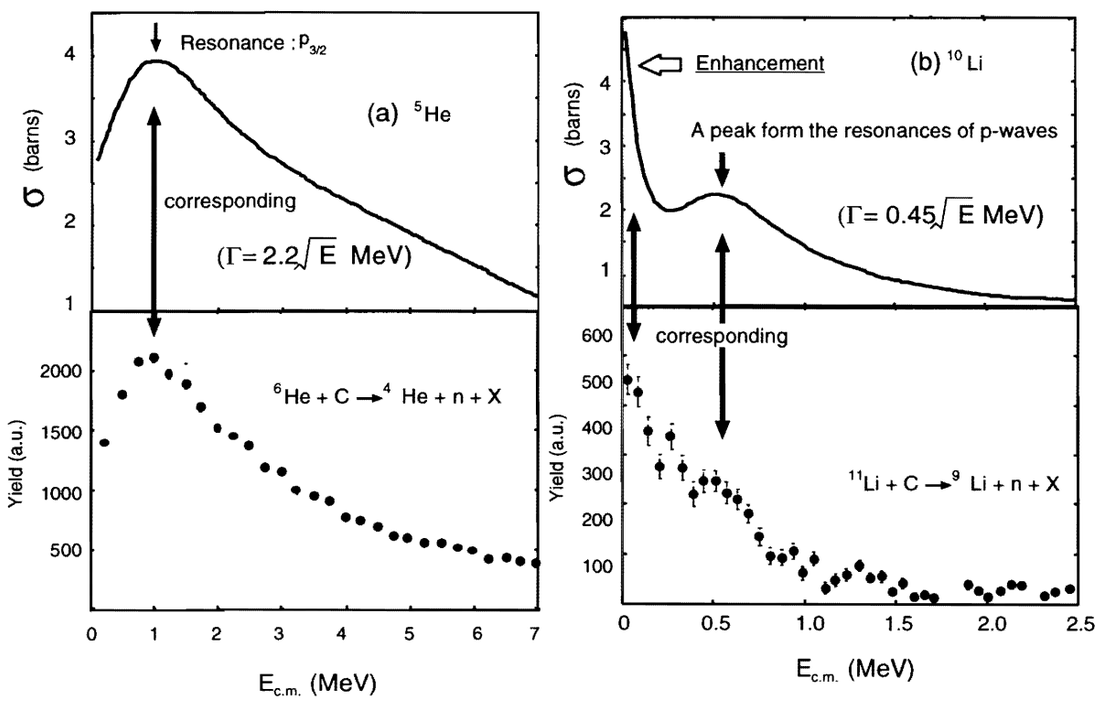

Figure 4: Poles of KKNN potential

In the ^{5}He case, the correspondence between the calculated total cross-section and the energy distribution is good by taking into the resolution of the detector as $\Gamma = 2.2\sqrt{E}$ MeV [9], (see Fig. 4(a)). Based on the good correspondence with the ^{5}He case, we investigate the ^{10}Li case as shown in Fig. 4(b). Our calculation of the total cross-section shows that the enhancement at the threshold energy comes from the s-wave virtual state. We obtain a good correspondence by using $\Gamma = 0.45\sqrt{E}$ MeV [9]. Therefore, we can make sure that the

enhancement at the threshold energy comes from the effect of the s-wave virtual state. The closer the position of the pole comes to the threshold energy, the higher the enhancement goes. Suppose that the ^{10}Li has no sharp s-wave resonance at low energy (< 1 MeV), such as our case, the enhancement only comes from the s-wave virtual state. Our potential model, which is made by microscopically with taking into account a pairing-blocking mechanism, has no sharp s-wave resonance at low energy (< 1 MeV) with varying the strength of the attraction as shown in the previous subsection. Hence, at this stage, the enhancement of the energy distribution at the threshold energy can be considered as an effect of the s-wave virtual state.

4 Summary and Discussion

In this report, we show a brief explanation for the Jost function method (JFM). As indicated by the results of actual calculations, this method is very useful to study the unstable nuclei. Using JFM, the partial decay widths are easily obtained with high accuracy.

We study the positions of s-poles of the S-matrix in the ^{10}Li system using JFM. Our aim is to obtain the information of the ^{9}Li-n interaction for the s-wave neutron, which is considered to play an important role in the formation of the halo structure in ^{11}Li, in comparison with the ^{4}He-n interaction, which is known well with less-ambiguity both in theoretical and experimental studies. In ^{10}Li, we obtained the virtual state solution using the FP1 potential. The results are comparable to those obtained by using potential P1 of Thompson and Zhukov [3]. Our results for the scattering length is also reasonable in comparison with the experimental one obtained by Shimoura *et al.*[13]. These results indicate that the validity of the microscopically constructed ^{9}Li-n potential (FP1) is strongly supported by the phenomenological potential (P1) and the experimental evidence (of the scattering length). We also investigated the s-pole behavior of the ^{9}Li-n potentials by varying the strength of the potential. In the ^{9}Li+n system, the virtual s-state appears over a wide range of the ^{9}Li-n potentials, including P0-P4 of Thompson and Zhukov and our FP1 with $-0.26 < \delta < 0.07$.

Next, we calculate the total cross-sections of the ^{9}Li+n elastic scattering using FP1. The effect of the s-wave virtual pole appears as the enhancement at the threshold energy. we obtained a good correspondence between the calculated total cross-section and the observed energy distribution [9]. From the comparison of the process of them, we can consider that these two quantities are related to each other. Hence, the character of the resonance peak and the enhancement at the threshold energy corresponds between the cross-section and the energy distribution. Therefore, we can conclude, at this stage, that using our potential model, there is no low-lying s-wave resonant state but is a "virtual" state, and then the enhancement of the energy distribution shows the existence of the s-wave virtual state with large possibility.

In the future work, we should perform coupled-channel calculations of the cross-sections to investigate the property of ^{9}Li-n reaction precisely, and must proceed to study the reaction mechanism of ^{11}Li+C$\rightarrow$^{9}Li+n+X process.

References

[1] I. Tanihata, J. Phys. **G22**(1996), 157.

[2] I. Tanihata, H. Hamagaki, O. Hashimoto, S. Nagamiya, Y. Shida, N. Yoshikawa, O. Yamakawa, K. Sugimoto, T. Kobayashi, D. E. Greiner, N. Takahashi and Y. Nojiri, Phys. Lett. **B160**(1985), 380.
I. Tanihata, H. Hamagaki, O. Hashimoto, N. Yoshikawa, K. Sugimoto, O. Yamakawa and T. Kobayashi, Phys. Rev. Lett. **55**(1985), 2676.

[3] I. J. Thompson and M. V. Zhukov, Phys. Rev. **C49**(1994), 1904.

[4] K. Katō, T. Yamada and K. Ikeda, Prog. Theor. Phys. **101**(1999), 119.

[5] H. Masui, S.Aoyama, T. Myo, K. Katō and K. Ikeda, Nucl. Phys. **A673**(2000), 207.

[6] S. A. Sofianos and S. A. Rakityansky, J. of Phys. **A30**(1997),3725.; **A31**(1998),5149.

[7] S. A. Rakityansky and S. A. Sofianos, Proceedings of "XVI European Conference of Few-Body Problems in Physics", Autrans, June 1998.

[8] H. Masui, S. Aoyama, T. Myo and K. Katō, Prog. Theor. Phys. **102**(1999), 1119.

[9] T. Kobayashi, RIKEN-AF-NP158 (pre-print), 1993.

[10] T. Noro and H. S. Taylor, J. Phys. **B13**(1980), L377.

[11] N. Moiseyev and U. Peskin, Phys. Rev. **A42**(1990), 255.

[12] S. Aoyama, K. Katō and K. Ikeda, Phys. Lett. **B414**(1997), 13.

[13] S. Shimoura, T. Teranishi, Y. Ando, M. Hirai, N. Iwasa, T. Kikuchi, S. Moriya, T. Motobayashi, T. Murakami, T. Nakamura, T. Nishio, H. Sakurai, T. Uchibori, Y. Watanabe, Y. Yanagisawa and M. Ishihara, Nucl. Phys. **A616**(1997), 208c.

Coherence and decoupling in E1 and E2 excitations in nuclei near drip lines

H. Sagawa

Center for Mathematical Sciences, the University of Aizu,
Aizu-Wakamatsu, Fukushima 965-8580, Japan

Email:sagawa@u-aizu.ac.jp

We have studied electric dipole (E1) strength distribution in neutron and proton drip line nuclei ${}^{12}_{4}Be_8$, ${}^{14}_{4}Be_{10}$ and ${}^{13}_{8}O_5$ by large scale shell model calculations with the effect of loosely-bound single particle wave functions. Large E1 strength are found in the low excitation energy region below E_x=3MeV in both ${}^{12}_{4}Be_8$ and ${}^{13}_{8}O_5$, while strong E1 strength are found only in high excitation energy region above E_x=7MeV in ${}^{14}_{4}Be_{10}$. The decoupling effect of extended wave functions and the coherence in the transition amplitudes enhance significantly the E1 strength in the low energy region. A manifestation of melting of the shell magicity at N=8 and Z=8 is pointed out in the systematics of E1 transitions in Be- and O-isotopes[1] in comparison with recent experimental data.

N/Z dependence of core polarization charges for electric quadrupole transitions are studied in C-isotopes by using a microscopic particle-vibration model in which Hartree-Fock and random phase approximations are used to calculate the single-particle wave functions and giant quadrupole resonances. A large quenching of the polarization charges are found in large N/Z nuclei because of the decoupling effect of the extended single particle wave functions. Recent experimental data of quadrupole moments of ${}^{15}B$ and ${}^{17}B$ are reproduced well by using the calculated polarization charges for shell model wave functions[2].

References

[1] H. Sagawa, Toshio Suzuki , H. Iwasaki and M. Ishihara, preprint (RIKEN-AF-NP-364, 2000) and Phys. Rev. C(2001) in press.

[2] H. Sagawa and K. Asahi, to be published.

Decoupling Phenomena between valence particles and core

stable nuclei

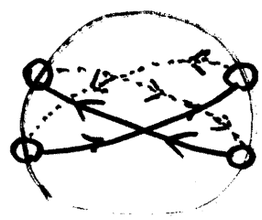

$$\frac{r_{valence}}{r_{core}} \sim (1 \sim 1.2)$$

skin/halo nuclei

$$\frac{r_{valence}}{r_{core}} \sim (1.5 \sim 2.0)$$

- low energy E1 strength below 3MeV in ^{12}Be and ^{13}O
  H. Sagawa et al, to be published
- soft dipole excitation in ^{11}Li and ^{11}Be
  T. Suzuki, HS., P.F. Bortignon, Nucl. Phys. A662 (2000) p.282
- Pigmy resonances in Oxygen isotopes
  H. Sagawa and T. Suzuki, Phys. Rev. C59(99) 3116
- quenching of effective charges

Competing Physical Mechanism near Drip Lines

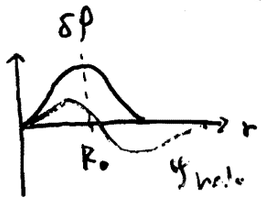

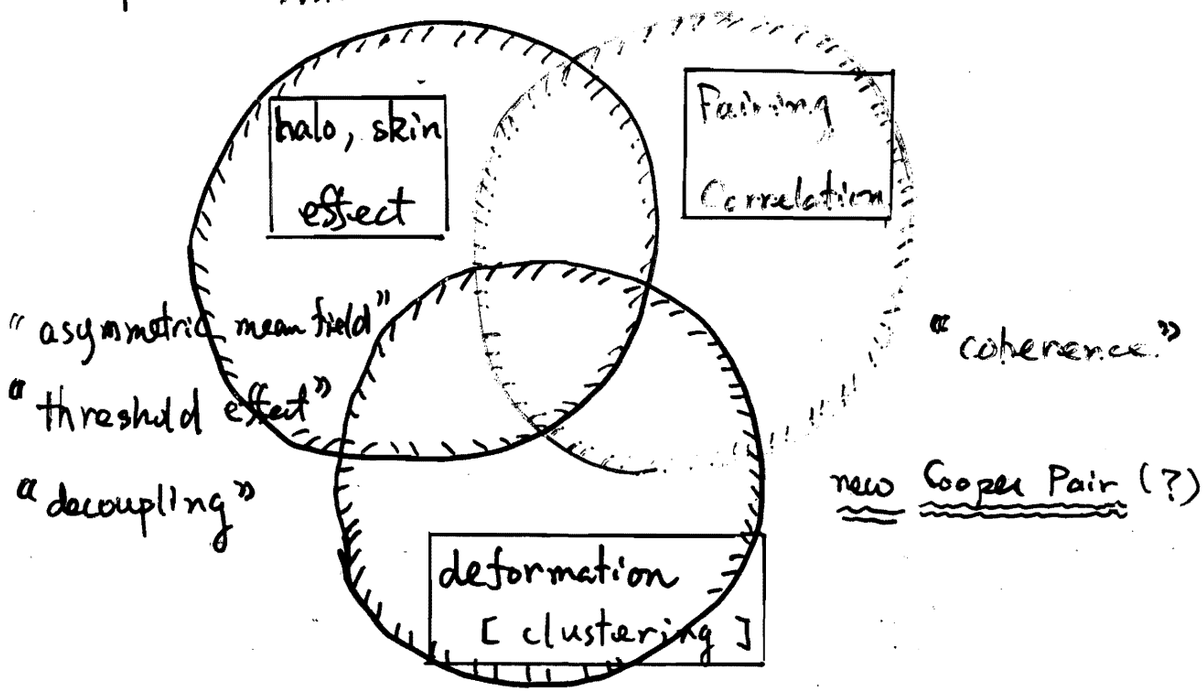

- ● E1 moment
- ● E2 moment
- o magnetic moment

Strong E1 strength below GDR

- halo nuclei and soft dipole (^{11}Be, ^{11}Li)

  quantum mechanical threshold

  ⇕

  classical vibration

- N = 8, Z = 8 magicities and low energy E1 transitions (^{12}Be, ^{14}Be, ^{13}O)

- decoupling of E1 strength in Oxygen-isotopes (^{16}O, ^{17}O, ^{18}O, ^{20}O, ^{22}O, ^{24}O)

- Pigmy and Nucleosynthesis

^{12}Be : a coherent "Cooper" pair

$$|^{12}\mathrm{Be}\rangle = \alpha\,|(1p_{1/2})^2\rangle + \beta\,|(2s_{1/2})^2\rangle + \gamma\,|(1d_{5/2})^2\rangle$$

$$\alpha \sim \beta \sim \gamma \sim \frac{1}{\sqrt{3}}$$

Navin et al., MSU experiment

<u>extended wave functions</u> for

$1p_{1/2}$ - and $2s_{1/2}$ - orbits $\Rightarrow$ decoupling to GDR

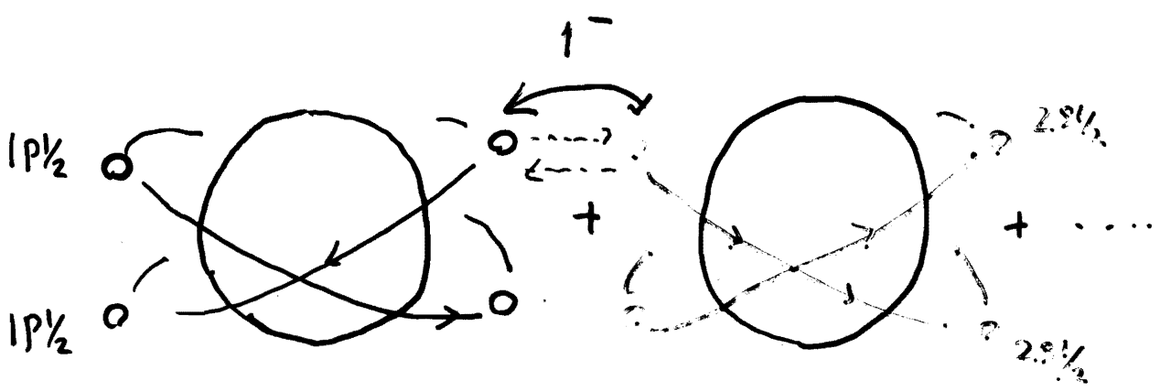

no energy loss except pairing blocking.

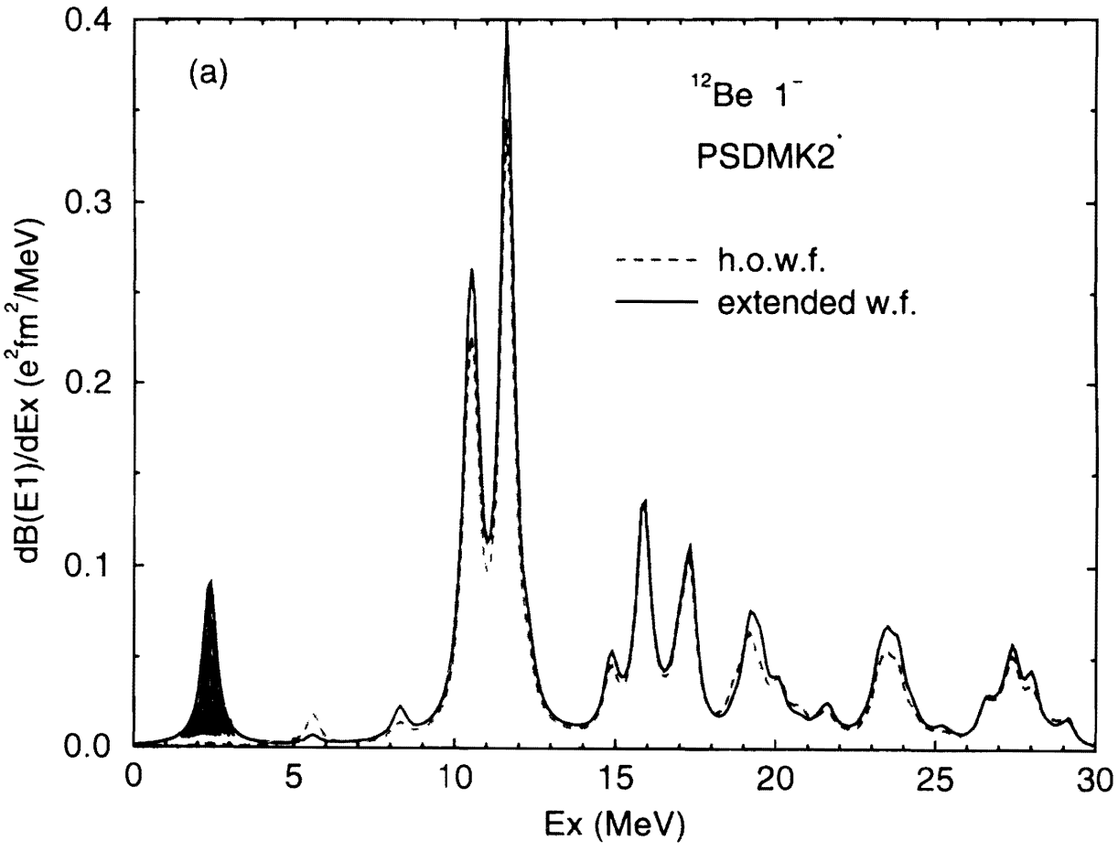
(a)
^{12}Be 1$^-$
PSDMK2'
h.o.w.f.
extended w.f.
dB(E1)/dEx (e^{2}fm^2/MeV)
Ex (MeV)
0.0
0.1
0.2
0.3
0.4
0
5
10
15
20
25
30

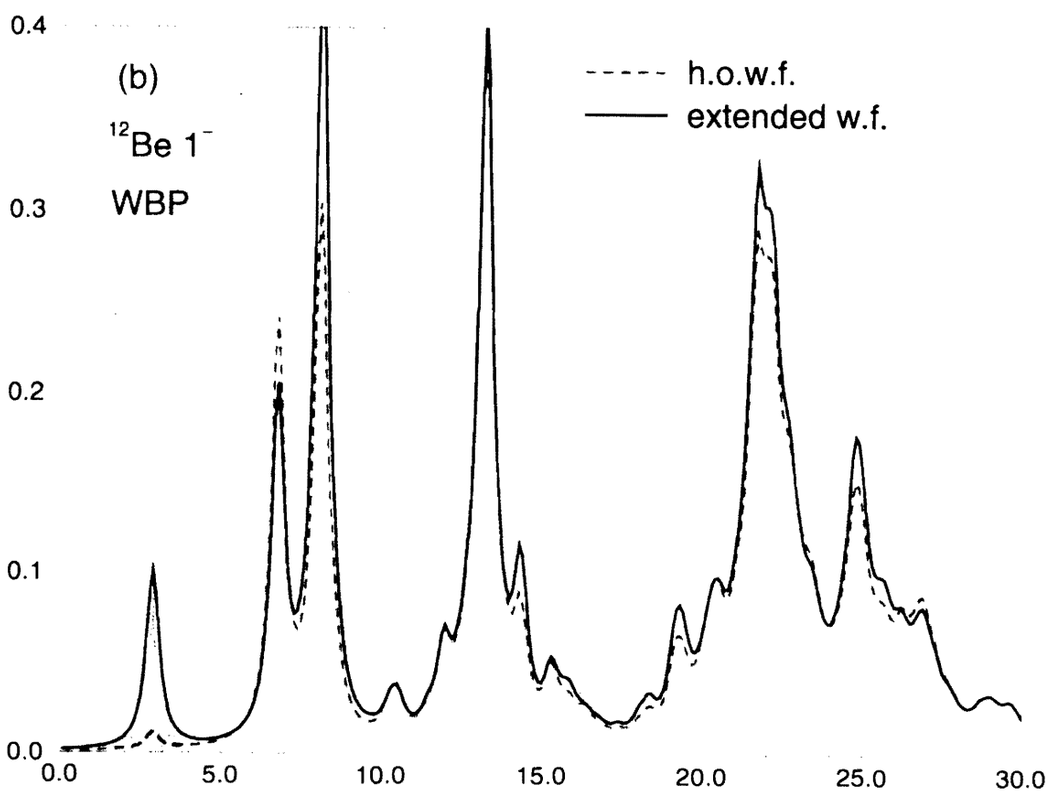
(b)
^{12}Be 1$^-$
WBP
h.o.w.f.
extended w.f.
0.0
0.1
0.2
0.3
0.4
0.0
5.0
10.0
15.0
20.0
25.0
30.0

Intermediate-energy Coulomb Excitation of ^{12}Be

low-lying 1^- state

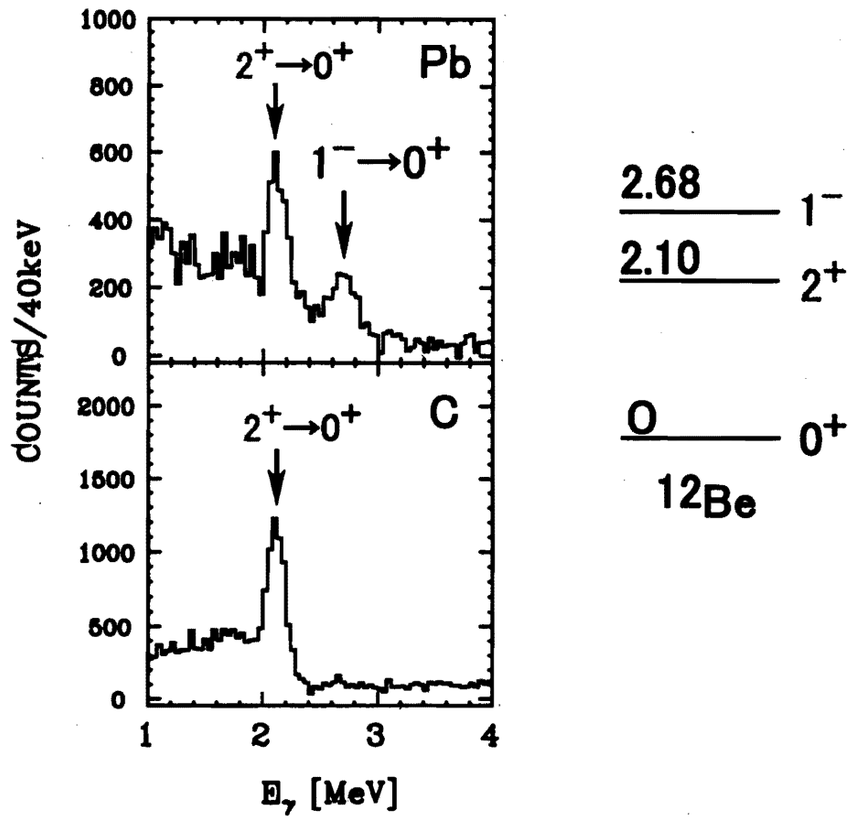

E1 strength

Angle-integrated cross sections

J^π	E_x [MeV]	Pb ($\theta_{cm} \leq 7.3°$) [mb]	C ($\theta_{cm} \leq 13.9°$) [mb]
1^-	2.68(3)	46.5 (11.5)	< 4.9
2^+	2.11(2)	81.8 (12.8)	54.9 (7.1)

Iwasaki et al. $B(E1;0^+ \rightarrow 1^-) = 0.051(13)\ e^2fm^2$
Phys. Lett. B (2000)

Theoretical calculation $0.063\ e^2fm^2$
H.Sagawa et.al. to appear in PRC
at $E_x = 2.36$ MeV

Particle-Vibration Coupling

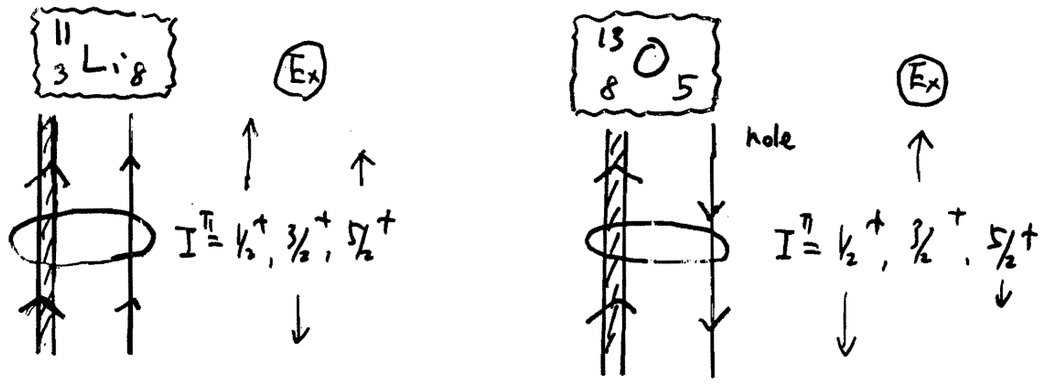

$|1^-_{\nu} \otimes |p_{3/2}\,_{\pi}\rangle$ $\qquad$ $|1^-_{\pi} \otimes |p_{3/2}^{-1}\,_{\nu}\rangle$

$$\langle (1^- \times p_{1/2})\, I \,|\, V_{\Theta\Theta} \,|\, (1^- \times p_{3/2})\, I \rangle = \begin{cases} +5 & I = 1/2^+ \\ -4 & 3/2^+ \\ +1 & 5/2^+ \end{cases}$$

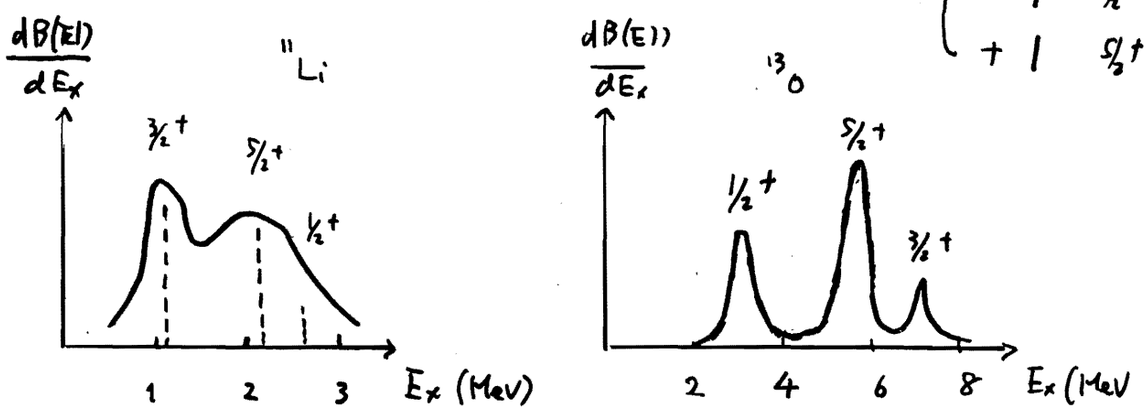

- GSI data

- Toshio Suzuki, H. Sagawa, P. F. Bortignon, N.P. A662 (2000) 282.
- H. Sagawa, Toshio Suzuki, H. Iwasaki, M. Ishihara, PRC (2000) in press.

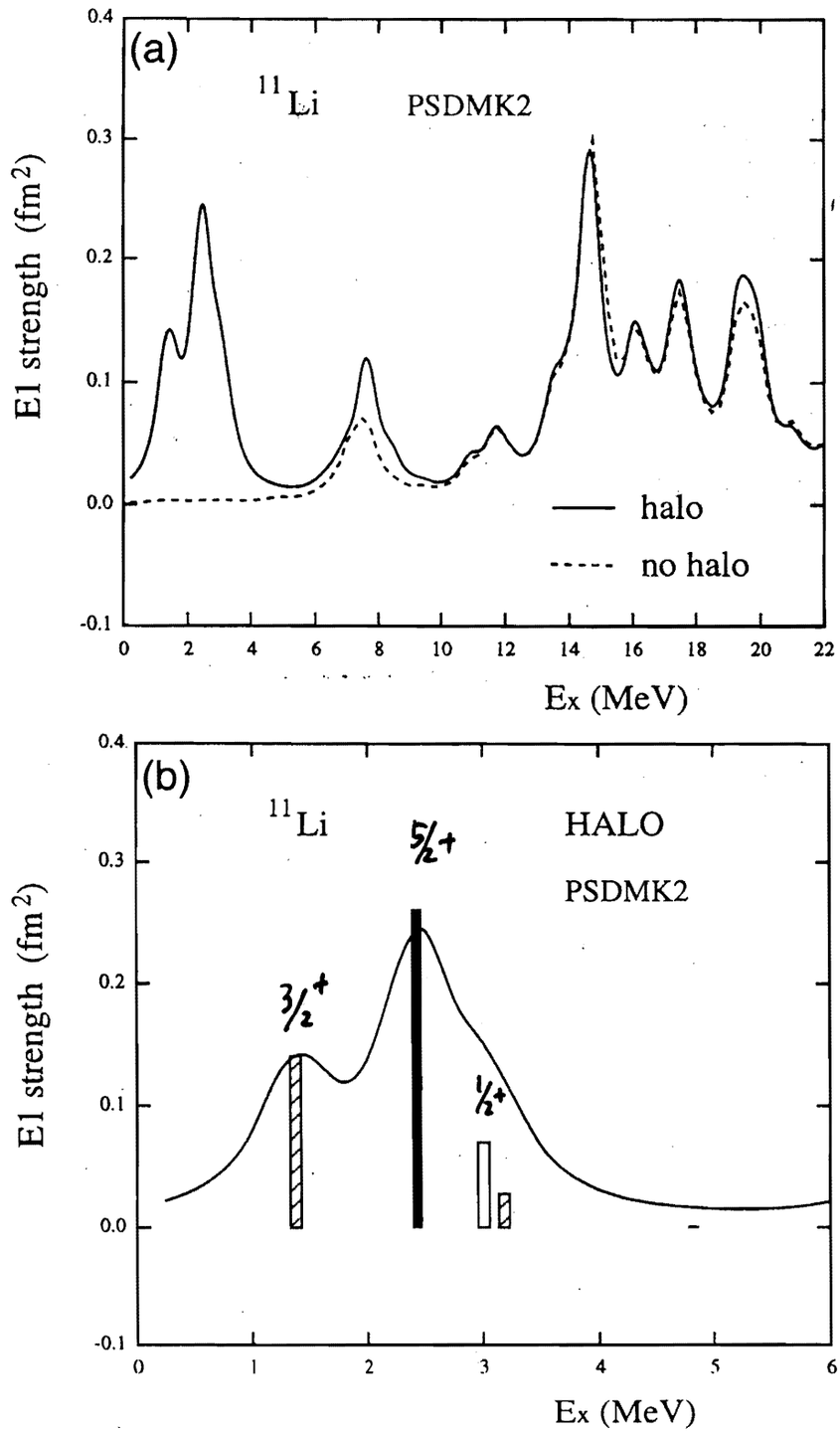

lectric dipole transition strengths in ^{11}Li; (a) $E_x \leq 22$ MeV and (b) $E_x \leq 6$ MeV. Soli
ı (a) show results with and without the halo effects, respectively. Here, 'no-halo' means
r wave functions, $0p_{1/2}$ and $1s_{1/2}$, are used for the corresponding Woods–Saxon
r the neutrons. In (b), white, dashed and solid bars represent contributions of the transit

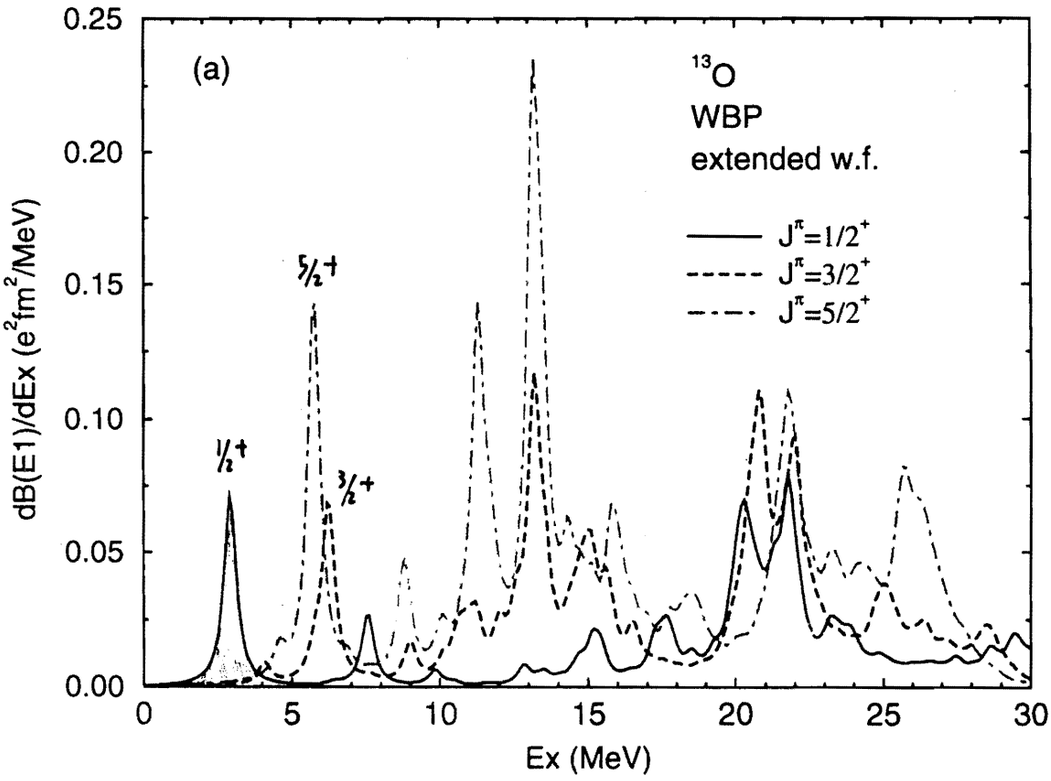
(a)
^{13}O
WBP
extended w.f.
$J^{\pi}=1/2^{+}$
$J^{\pi}=3/2^{+}$
$J^{\pi}=5/2^{+}$
1/2+
5/2+
3/2+
dB(E1)/dEx (e^2fm^2/MeV)
Ex (MeV)
0.25
0.20
0.15
0.10
0.05
0.00
0
5
10
15
20
25
30

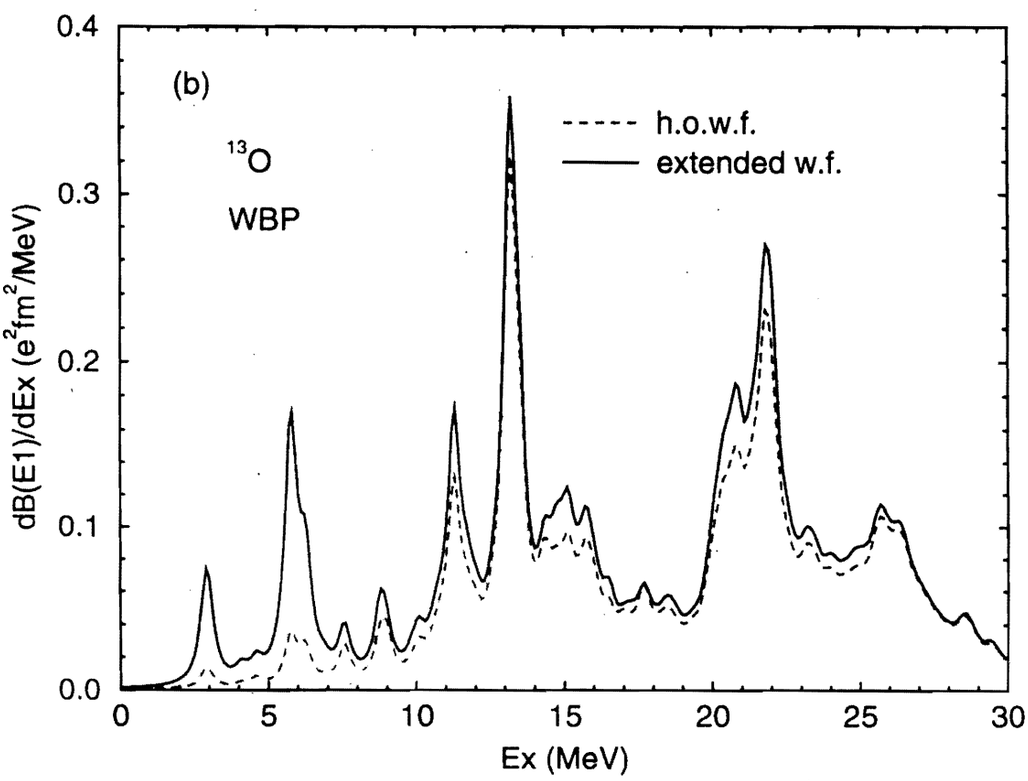
(b)
^{13}O
WBP
h.o.w.f.
extended w.f.
dB(E1)/dEx (e^2fm^2/MeV)
Ex (MeV)
0.4
0.3
0.2
0.1
0.0
0
5
10
15
20
25
30

STRUCTURE OF ^{11}Be: MAGNETIC MOMENT AND COULOMB DISPLACEMENT ENERGY

Toshio Suzuki

Department of Physics, College of Humanities and Sciences, Nihon University, Sakurajosui 3-25-40, Setagaya-ku, Tokyo 156-8550, Japan

Email: suzuki@chs.nihon-u.ac.jp

Magnetic moment of ^{11}Be is analyzed[1] and compared with a recent experiment[2]. Probability of the $|^{10}\,\mathrm{Be}(0^+) \times 1s_{1/2}\rangle$ component in the wave function of ^{11}Be is found to be $\alpha^2 \approx 60\pm5\%$, when a value of g_s^{eff} is taken to be 0.85$\sim$0.95 g_s^{free} for normal orbits and 1.0 g_s^{free} for the halo orbit.

Coulomb displacement energy of the isobaric analog state (IAS) of ^{11}Be is investigated based on the method as used in the analysis of the IAS of ^{11}Li[3]. The effects of the halo and the configuration of the halo wave function are studied including the contributions from charge-symmetry breaking and charge-independence breaking interactions. A value of $\alpha^2 \approx 0.6$ for the probability consistent with the analysis of the magnetic moment is obtained.

References

[1] T. Suzuki, T. Otsuka and A. Muta, Phys. Lett. **B364** (1995) 69.
[2] W. Geithner et al., Phys. Rev. Lett. **83** (1999) 3792.
[3] T. Suzuki and T. Otsuka, Nucl. Phys. **A635** (1998) 86.

^{11}Be の構造

1. Magnetic Moment

2. Coulomb Displacement Energy

$$|^{11}Be(1/2^+)\rangle = \alpha\,|^{10}Be(0^+) \times 1s_{1/2}\,;\,\tfrac{1}{2}^+\rangle$$

$$+\,\beta\,|^{10}Be(2^+) \times 0d_{5/2}\,;\,\tfrac{1}{2}^+\rangle$$

$P = \alpha^2$?

$\alpha^2 \sim 0.55$	VSM	
$\alpha^2 \sim 0.77$ 0.73	Stripping reaction on ^{10}Be	(1970's)
$\alpha^2 \sim 0.8$	$p(^{11}Be, {}^{10}Be)d$	Fortier et al. (1999)

$g_s^{eff} = 0.90 \sim 0.95 \; g_s^{free}$ $\quad (0.85 \; g_s^{free})$

$\alpha^2 = 0.56 \sim 0.60$ $\quad (0.65)$

$\mu_{exp} = -1.6816 \; \mu_N$ $\quad$ Geithner et al. PRL 83 ('99) 3792

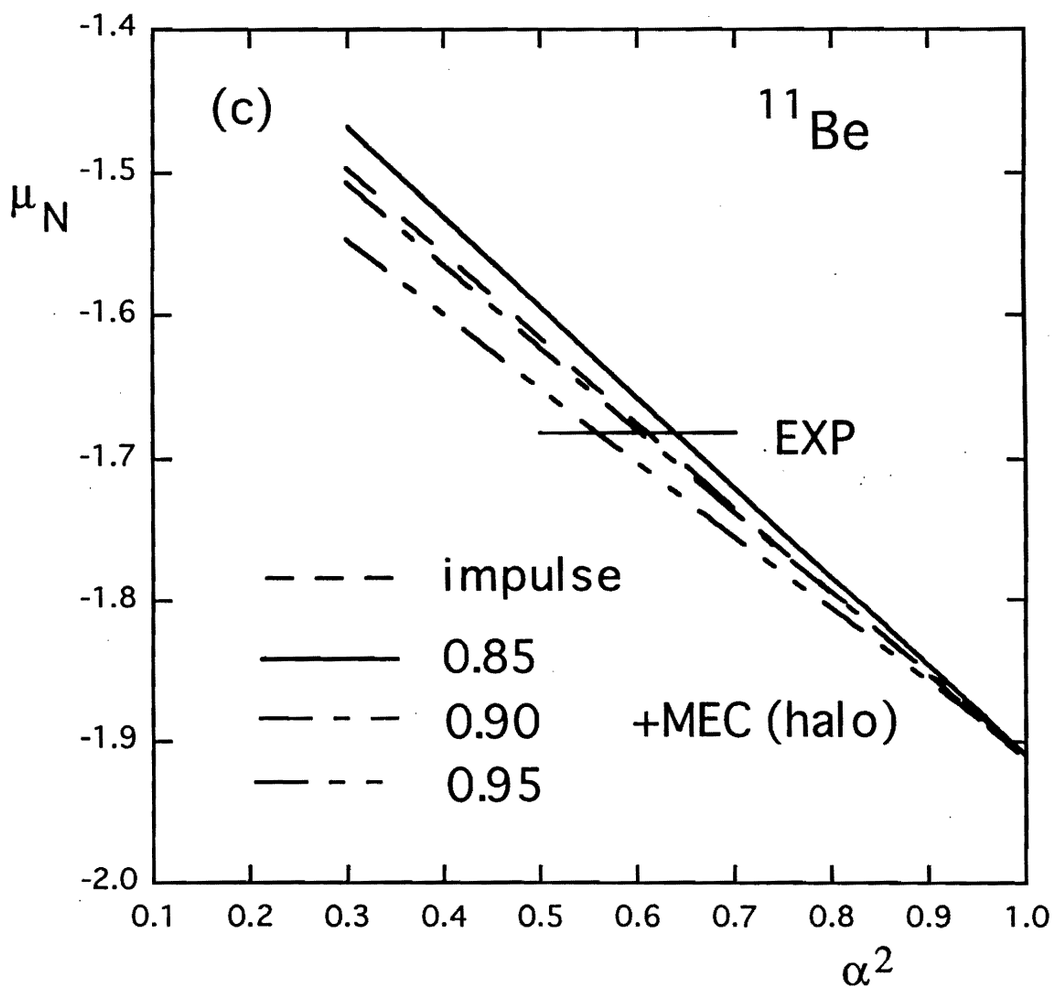

● ■ exp.

○ □ cal.

$$\Delta = a \frac{Z}{A^{1/3}} \qquad a = 1.06$$

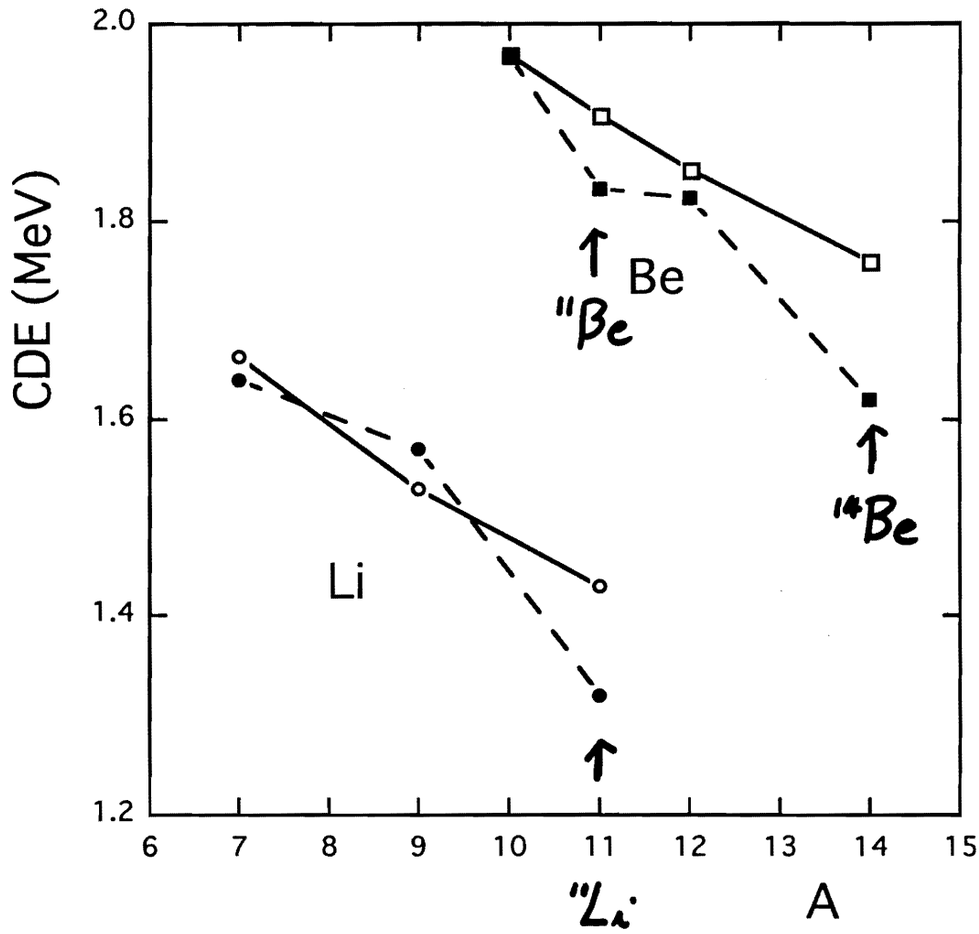

^{11}Li : Teranishi et al., PL B407 (1997) 110.

^{14}Be : Takeuchi et al. RIKEN Prog. Rep. (1999)

Coulomb displacement energy (CDE) of IAS of ^{11}Be

$^{11}Be - ^{11}B$ CDE

$$\Delta E_c^{exp} = 1.833 \text{ MeV}$$

$$\Gamma = 210 \pm 20 \text{ keV}$$

$$\Delta E_c = \frac{2}{3} \Delta E_c^{core}(A=10) + \frac{1}{3} \Delta E_c^{val}$$

$$|^{11}Be(1/2^+)\rangle = \alpha |^{10}Be(0^+) \times 1s_{1/2}\rangle + \beta |^{10}Be(2^+) \times 0d_{5/2}\rangle$$

$$\begin{cases} \Delta E_c^{core}(A=10, 0^+) = 1.967 \text{ MeV} \\ \Delta E_c^{core}(A=10, 2^+) = 2.022 \text{ MeV} \end{cases}$$

$$\rightarrow \Delta E_{c,exp}^{val} = 1.509 \pm 0.056 \text{ MeV}$$

H.O. $\Delta E_c^{\nu} \geq 1714$ keV $> \Delta E_{c,\,exp.}^{val}$

Need halo!

Halo (deformed WS)

V_c ; $\alpha^2 = 0.40 \pm 0.12$

V_c + CSB + CIB + others ; $\underline{\alpha^2 = 0.59 \pm 0.14}$

cf. $\mu \rightarrow \alpha^2 \sim 0.6 \pm 0.05$

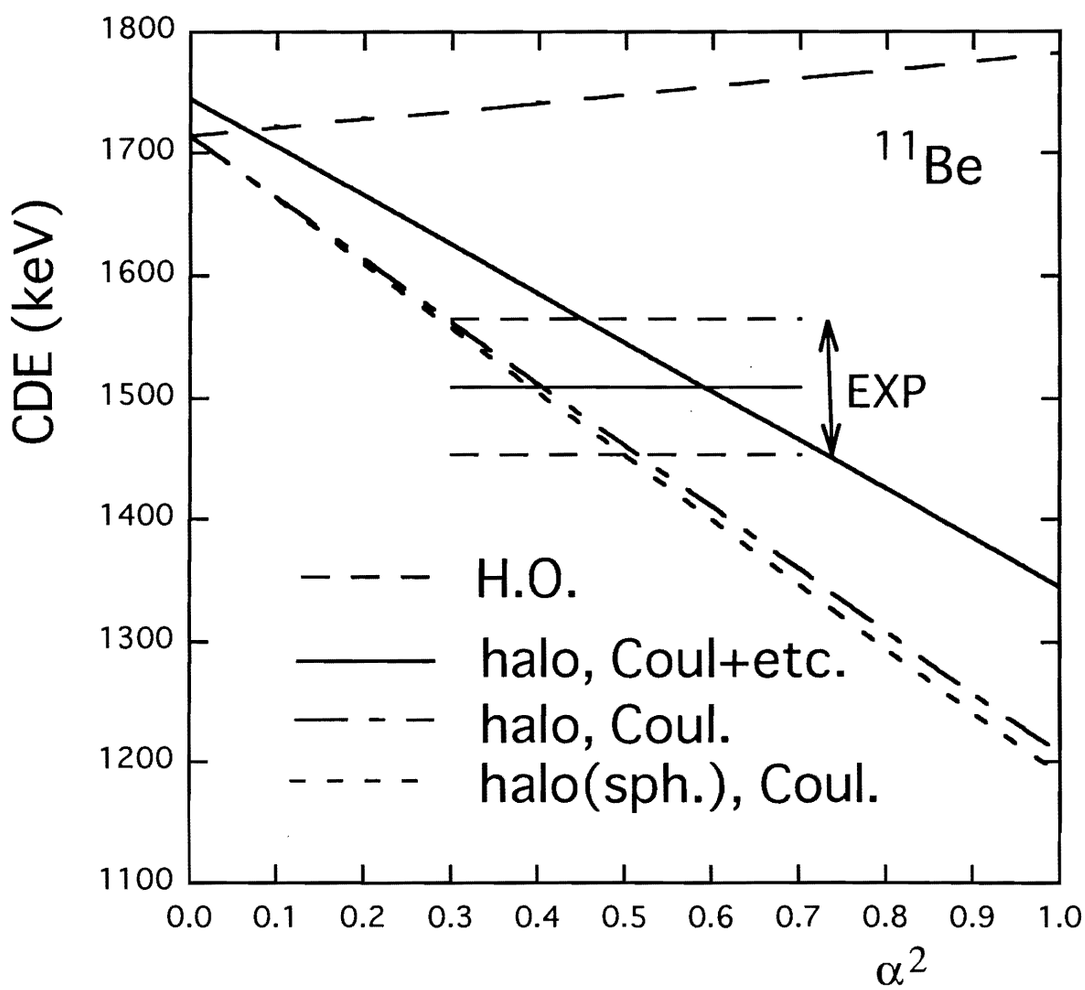

【2】 CRIB and its Applications

Mirror Nuclear Moments in the Light Mass Region

M. Fukuda and K. Matsuta, Osaka University

23/Aug/00

Abstract

Magnetic moments of ^{9}C, ^{13}O, and electric quadrupole moments of ^{13}O, ^{23}Mg, ^{27}Si have been newly measured with the β-NMR and β-NQR techniques. The magnetic moment of ^{9}C shows an anomaly that haven't been seen in the region nearer to the stability line. The quadrupole moments of ^{13}O and ^{27}Si are not able to be explained by simple models, which implies an excentricity in the effective charges or some other effects for these nuclei.

Magnetic moments (μ) of ^{9}C, ^{13}O have been measured with the β-NMR technique at RIKEN Ring Cyclotron using the RIPS. The details of the experiments are given in Ref. [1-3]. The result for ^{13}O magnetic moment is well accounted for by the shell model calculation, and is consistent with the systematics of mirror magnetic moments. On the other hand, for ^{9}C, the spin expectation value deduced from the mirror magnetic moments $\mu(^{9}\mathrm{C})$-$\mu(^{9}\mathrm{Li})$ indicates an anomalously large value of σ = 1.44 (σ = S / 2). This anomalous value can not be understood by any configuration mixings among the p shell. The result suggests possible irregular values of nucleon g-factors, some irregular breaking of pairing, or larger breaking of mirror symmetry, in the nuclei. This problem, therefore, is still open to challenging theoretical works. At the same time, further systematic, elaborate, experimental studies are encouraged.

Electric quadrupole moments (Q) of ^{13}O, ^{23}Mg, and ^{27}Si have been also measured with β-NQR technique at RIKEN and HIMAC [4-5]. The result for ^{23}Mg is in good agreement with shell model calculations. For ^{13}O, the shell model calculation that takes into account an effect of the loosely bound protons can not reproduce the experimental value. This implies a need for higher excitation components in the calculation. The result for ^{27}Si can not also be reproduced by the shell model calculation (OXBASH) with the standard effective charges for a proton and a neutron in the *sd* shell. For the mirror Q moments $Q(^{27}\mathrm{Si})$-$Q(^{27}\mathrm{Al})$, the quadrupole moment of odd-nucleon group (Q_{o}) and that of even-nucleon group (Q_{e}) can be deduced with the standard effective charges. In cases of loosely bound systems, such formulation can not be justified because the quadrupole moment depends strongly on the binding energy of loosely bound nucleons. However, The deduced Q_{o} is in good agreement with the OXBASH calculation, but the Q_{e} is $\sim$ 0 against the calculation. The different

deformations of the core between odd- and even-nucleon groups can be one of the possible explanation of this disagreement. This may come from the fact that the deformation changes largely from prolate to oblate in this mass region.

References

[1] K. Matsuta, M. Fukuda, M. Tanigaki, T. Minamisono, Y. Nojiri, M. Mihara, T. Onishi, T. Yamaguchi, A.Harada, M. Sasaki, T. Miyake, S. Fukuda, K. Yoshida, A. Ozawa, T.Kobayashi, I. Tanihata, J.R.Alonso, G.F. Krebs, and T.J.M. Symons, Nucl. Phys. A588 (1995) 153c.

[2] K. Matsuta, T. Minamisono, M. Tanigaki, M. Fukuda, Y. Nojiri, M. Mihara, T. Onishi, T. Yamaguchi, A.Harada, M. Sasaki, T. Miyake, K. Minamisono, T. Fukao, K. Sato, Y. Matsumoto, T. Ohtsubo, S.Fukuda, S. Momota, K. Yoshida, A. Ozawa, T. Kobayashi, I. Tanihata, J.R. Alonso, G.F. Krebs, and T.J.M. Symons, Hyperfine Interactions 97/98 (1996) 519.

[3] K. Matsuta, T. Minamisono, Y. Nojiri, M. Fukuda, M. Tanigaki, M. Mihara, T. Yamaguchi, T. Onishi, M. Sasaki, T. Miyake, S. Fukuda, S. Momota, K. Yoshida, A. Ozawa, T. Kobayashi, I. Tanihata, J.R. Alonso, G.F. Krebs and T.J.M. Symons, Proc. Int. Symp. on Non-Nucleonic Degrees of Freedom Detected in the Nucleus, p.57, (1997).

[4] K. Matsuta, K. Sato, M. Fukuda, M. Mihara, T. Yamaguchi, M. Saaski, T.Miyake, K. Minamisono, T.Minamisono, M. Tanigaki, T. Ohtsubo, T.Onishi, Y. Nojiri, S. Momota, S. Fukuda, K. Yoshida, A.Ozawa, K.Kobayshi, I.Tanihata, J.R. Alonso, G.F. Krebs, T.J.M. Symons, H.Kitagawa, and H.Sagawa, Phys. Lett. B 459 (1999) 81.

[5] K. Matsuta, T. Onishi, M. Fukuda, T. Minamisono, H. Akai, M. Sasaki, T. Yamaguchi, T. Miyake, K. Sato, K. Minamisono, F. Ohsumi, Y. Muramoto, S. Oui, C. Ha, K. Tanaka, K. Kidera, A. Morishita, A. Kitagawa, M. Torikoshi, M. Kanazawa, T. Nishio, S. Koda, T. Ohtsubo, S. Fukuda, Y. Nojiri, S. Momota, A. Ozawa, K. Yoshida, T. Suzuki, T. Kobayashi, I. Tanihata, S.S. Hanna, J.R. Alonso, G.F. Krebs and T.J.M. Symons, Hyperfine Interactions 120/121 (1999) 673.

軽核領域の
鏡映核電磁気モーメント

阪大理・福田光順

- 現在状況
- 磁気モーメント
  - $^{9}C - ^{9}Li$
  - $^{13}O - ^{13}B$
- 電気四重極モーメント
  - $^{13}O - ^{13}B$
  - $^{23}Mg - ^{23}Na$
  - $^{27}Si - ^{27}Al$
- その他（非鏡映核）

磁気モーメントの測定状況

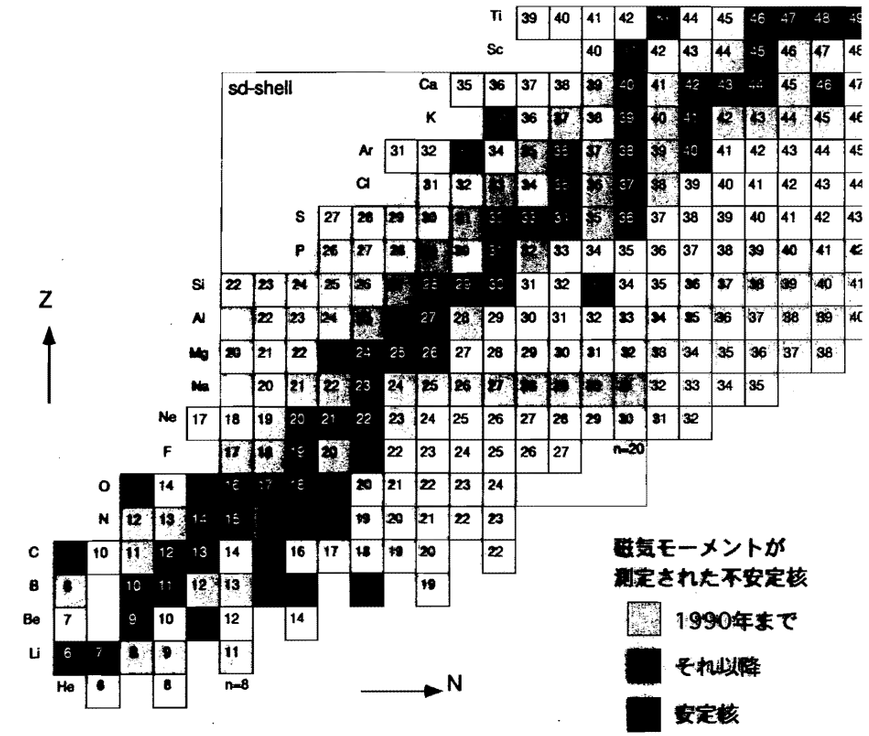

1990以降 18 ⇒ $\frac{14}{18}$：日本 ｛理研 10，阪大バンデ 4

☆ 鏡映核

$$\begin{cases} \mu(p) = g_s(p)\, S_0 + g_s(n)\, S_e + g_\ell(p)\, L_0 + g_\ell(n)\, L_e \\ \mu(n) = g_s(n)\, S_0 + g_s(p)\, S_e + g_\ell(n)\, L_0 + g_\ell(p)\, L_e \end{cases}$$

$$\begin{cases} Q(p) = \tilde{e}_p\, Q_0 + \tilde{e}_n\, Q_e \\ Q(n) = \tilde{e}_n\, Q_0 + \tilde{e}_p\, Q_e \end{cases}$$

電気四重極モーメントの測定状況

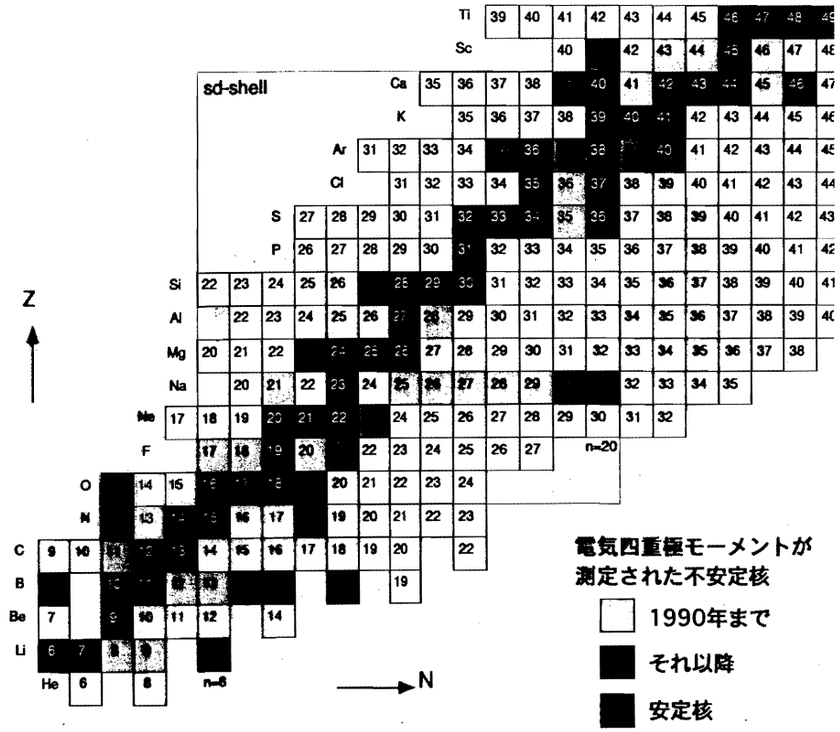

1990以降 18 → $\frac{12}{18}$ 日本

- 理研 7
- 阪大バンデ 3
- 放医研 2

$\mu(p) + \mu(n) = J + 0.880\langle\sigma_z\rangle$

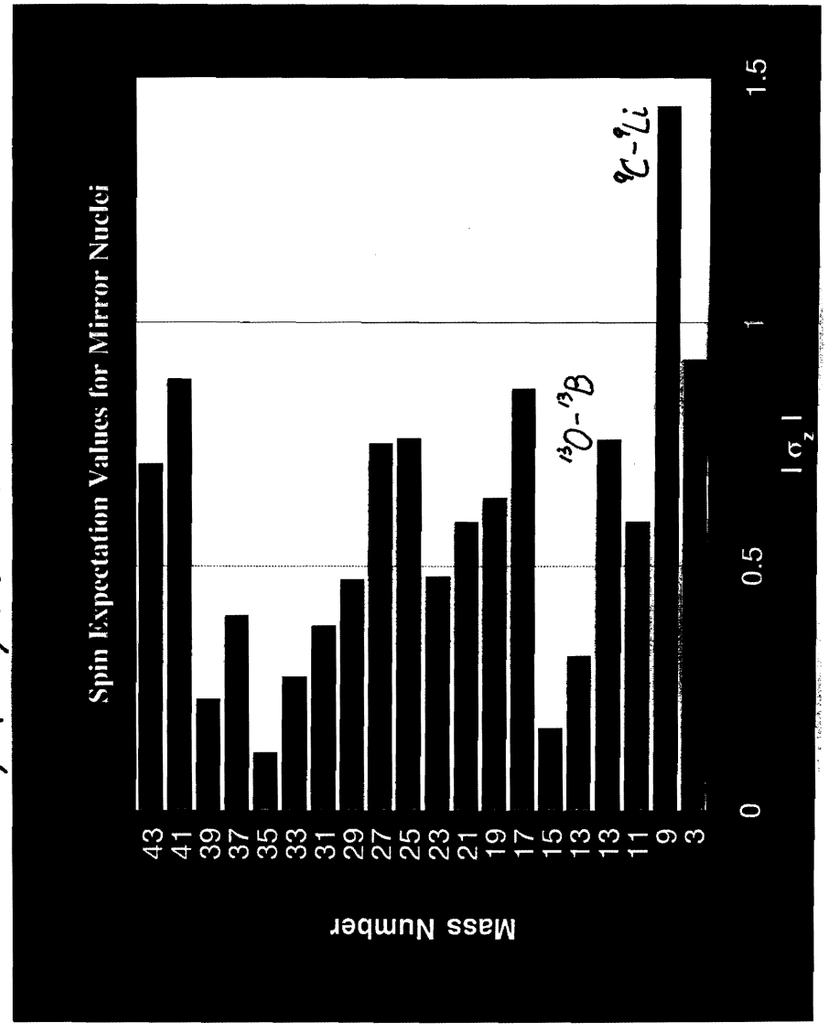

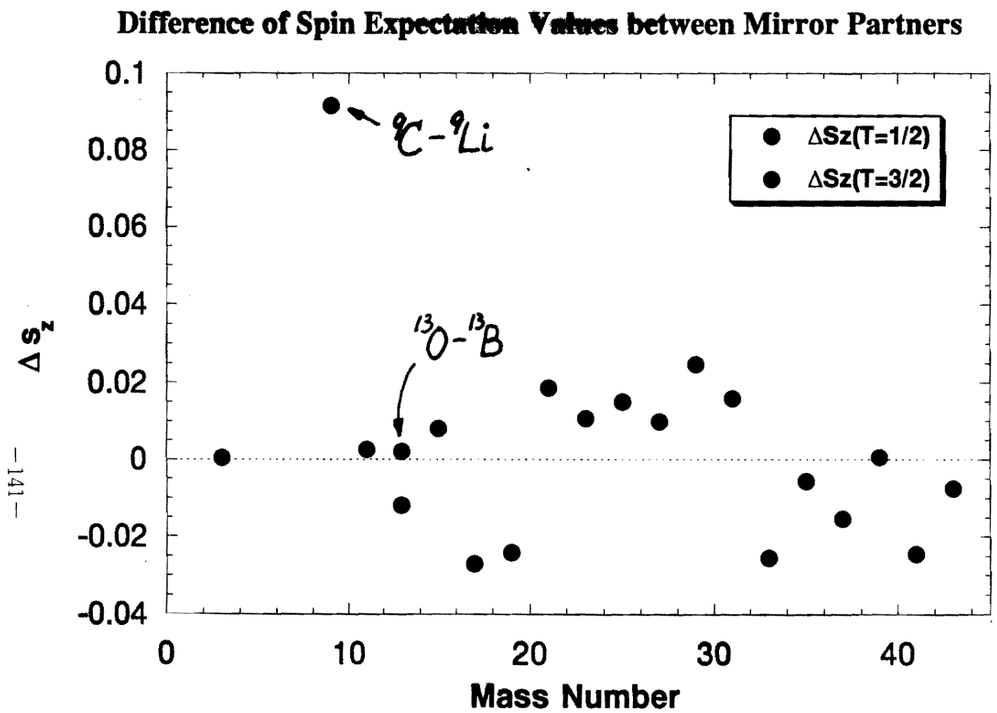

☆ Effective g-factors

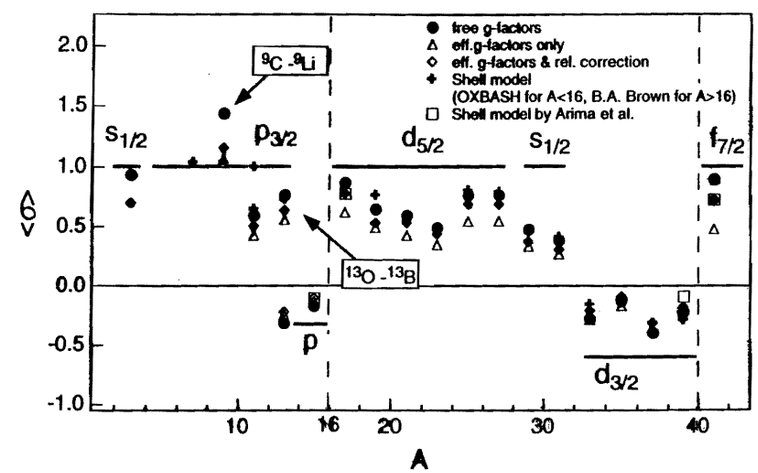

Fig. 6-1. Spin Expectation values extracted from the magnetic moments of mirror pairs up to $A = 41$. Open triangles denote the value extracted from experiment with effective g-factors (see appendix B or [46]). Open diamonds denote the value with effective g-factors and relativistic corrections [21]. Solid lines are Schmidt values. Spin expectation values for LS doubly closed shell ±1 nucleon nuclei (A = 15, 17, 39, 41) are results of Arima et al. In their calculation, the second order configration mixing with higher excitation energies was taken into account.

$Q(^{27}Si) - Q(^{27}Al)$

Shell Model (OXBASH) 計算値との比較

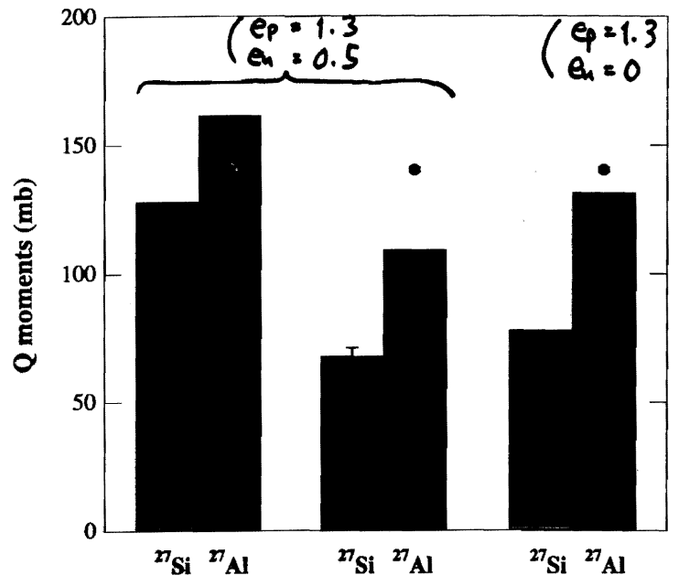

OXBASH ($Q_o = 101$, $Q_e = 60$)

$d_{5/2}$への励起なし ($Q_o = 75$, $Q_e = 22$)

e_p, e_n 変化

◎ e_p, e_n 固定

($Q_o = 105(7)$, $Q_e = 8(12)$)

◎ Q_o, Q_e 固定

($e_p = 1.6(1)$, $e_n = -0.3(2)$)

⇒ Odd-group と Even-group で core が別々に変形?

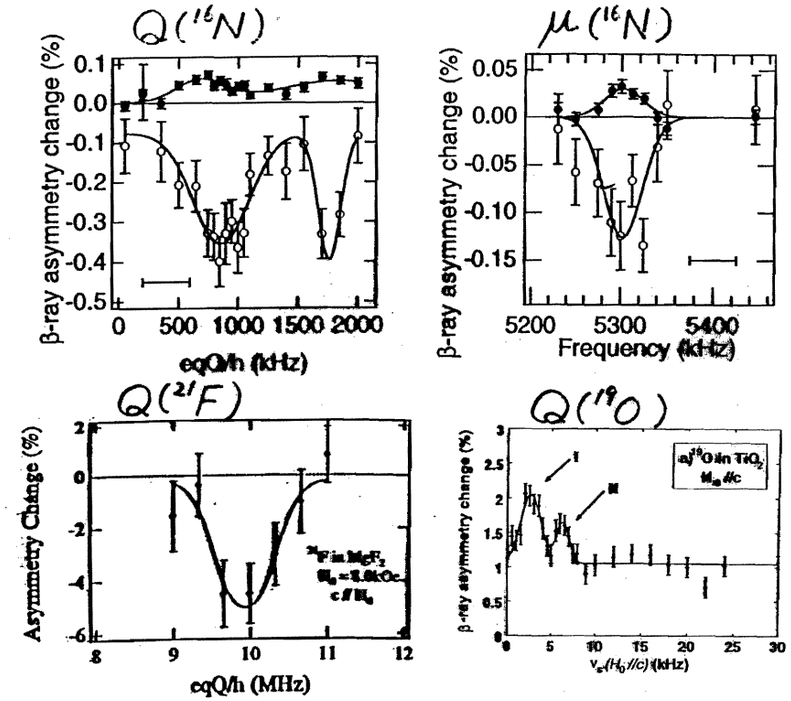

◎ neutron eff. charge e_n → 小さい

^{16}N : $e_n \sim 0.2$

^{19}O : $e_n \sim 0.3$

Electromagnetic moments of neutron-rich nuclei

H. Ogawa (Tokyo Institute of Technology)

13/Aug/00

Nuclear moments of neutron-rich nuclei have been measured using RIPS at RIKEN by means of spin-polarized beams from the fragmentation reaction [1,2] combined with the β-NMR method. Some intriguing findings in light mass neutron-rich nuclei have been emerged from the nuclear moment measurements.

For the magnetic moments μ of $^{17}\mathrm{B}_{\mathrm{g.s.}}$ and $^{17}\mathrm{N}_{\mathrm{g.s.}}$ [3], the differences between experimental and theoretical values are accounted for by assuming that the paring energy for the *sd* neutrons to form $J^{\pi} = 0^{+}$ is considerably reduced. The phenomenon of the reduction in the *sd*-neutron paring energy may be considered as manifestation of the weakening of the coupling between excess neutrons and a core, in nuclei far from stability.

The experimental electric quadrupole moment Q for $^{15}\mathrm{B}_{\mathrm{g.s.}}$ [4] was found very close to that for ^{13}B which is the neutron shell closed nucleus. On the other hand, Q moments for ^{15}B of shell model calculations with neutron effective charge $e_{\mathrm{n}} \approx 0.5$ [5], which is commonly employed values in *sd* shell, are much larger than the experimental Q. The theoretical Q could be accommodated to the observation by taking $e_{\mathrm{n}} \leq 0.1$. This suggested that the neutron effective charge e_{n} may become diminished in the region of neutron-rich nuclei. Therefore it would be interesting to clarify how the Q moment behaves when the neutron number further increases from ^{15}B to ^{17}B. For this purpose, recently the Q moment of ^{17}B was measured. The observed Q moment for ^{17}B is also close to that for the neutron shell-closed isotope ^{13}B. The smaller experimental $Q(^{17}\mathrm{B})$ suggests that the E2 polarization effect is hindered in this nucleus and reveals a tendency that the effective charge for neutrons becomes more and more quenched as the degree of neutron excess develops.

The $I^{\pi} = 1/2^{+}$ ground state of ^{15}C in a shell model is to a large extent described by the $^{14}\mathrm{C}(0^{+}) \otimes \nu(2s_{1/2})$ configuration, and its magnetic moment may provide a good information of the neutron g_s factor appropriate in a neutron-rich nucleus. The g_s value which is derived from the presently obtained magnetic moment for ^{15}C is in good agreement with effective g_s values normally used in shell model calculations in the region of stability.

Nuclear moment measurements have been performed in such a way, while we are attempting to develop atomic beam method which is applied to producing spin-polarized RI beam in order to overcome some intrinsic difficulties in the β-NMR experiment. Our simulation shows that highly polarized RI beam can be obtained by this system, enabling to extend the moment measurements of nuclei far from stability.

References

[1] K. Asahi et al., Phys. Lett. B251, 488 (1990).
[2] H. Okuno et al., Phys. Lett. B335, 29 (1994).
[3] H. Ueno et al., Phys. Rev. C53, 2142 (1996).
[4] H. Izumi et al., Phys. Lett. B366, 51 (1996).
[5] B.A. Brown and B.H. Wildenthal, Ann. Rev. Nucl. Part. Sci. 38, 29 (1988).

中性子過剰核の電磁気モーメント

東工大 理工学研究科　小川博嗣

- μ, Q モーメントの測定結果
  - sd 中性子対相互作用エネルギーの減少
  - E2有効電荷の減少
- 最近の測定結果　^{17}B , ^{15}C
- 新たな測定法　Atomic Beam法

sd殻 中性子の対相互作用エネルギーの減少

Ueno et al.

陽子 p 殻が空孔 ー 中性子 sd殻が粒子の中性子過剰核

^{17}N , ^{17}B , ^{15}B の磁気モーメントの実験値 の解析結果は

殻模型計算と比較して sd殻 2 中性子の合成スピン 2^+ の配位が多い

→ 安定核に比べ 対相互作用 $|V_{J=2^+,T=1} - V_{J=0^+,T=1}|$ が減少

sd殻 中性子の対相互作用エネルギー

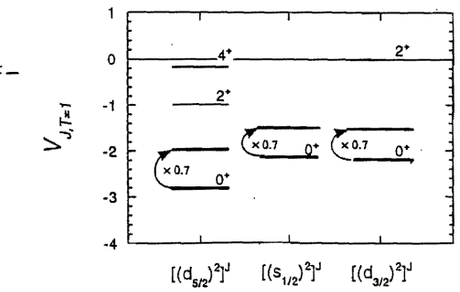

B アイソトープの磁気モーメント

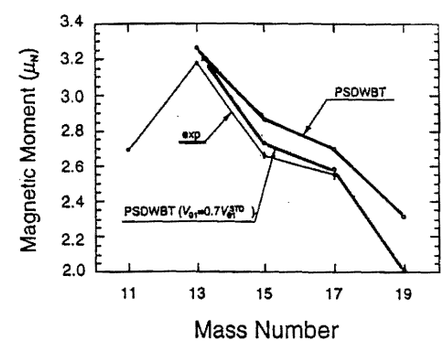

^{17}N のエネルギー準位、磁気モーメント

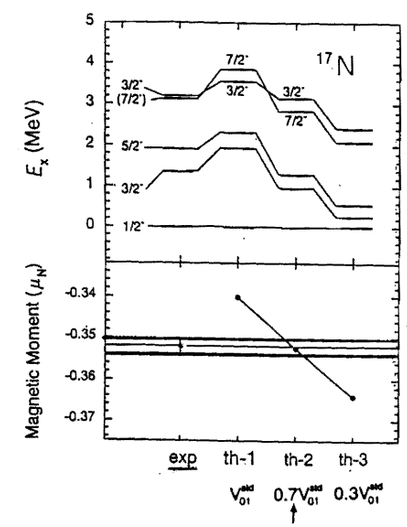

対相互作用エネルギー
$V_{J=0^+,T=1}$ を30%減少させると
実験値を良く再現する

中性子 E2 有効電荷の減少

Izumi et al.

Bアイソトープの電気四重極モーメント

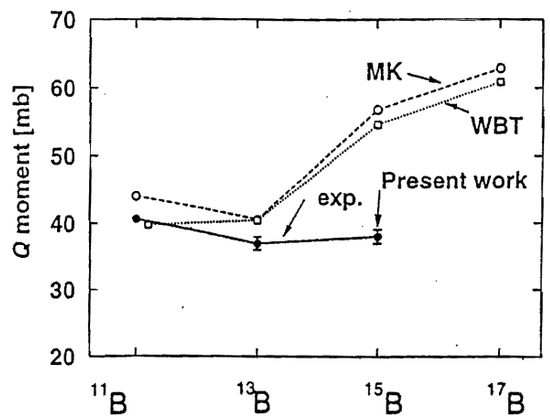

殻模型計算は
$e_p = 1.3$, $e_n = 0.5$
を使用した

^{11,13}B は実験と理論の一致が良いが
^{15}B の殻模型計算値は実験値に比べ大きくずれている

Qモーメントの有効電荷依存性

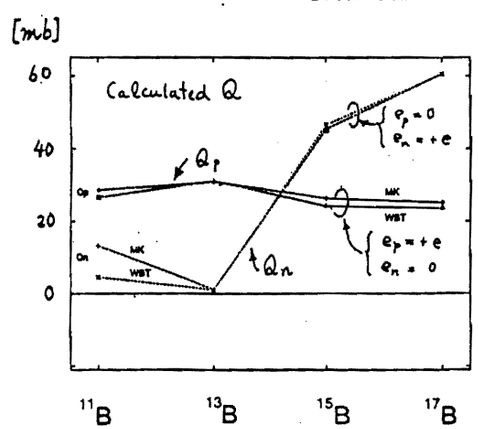

$$eQ = e_p Q_p + e_n Q_n$$

- アイソトープに依らず陽子 Q_p は ほぼ一定
- 中性子 Q_n は ^{11,13}B では小さいが ^{15,17}B では 非常に大きい

⇩

中性子の有効電荷 e_n は
Q(^{15}B) に sensitive !

実験値を再現させるためには

$e_n \lesssim 0.1$ ← very small
(cf 安定核近傍 e_n~0.5)

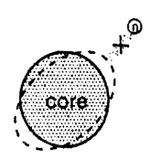

コアと価中性子の結合が弱くなっている？

Q moments for odd-mass B isotopes

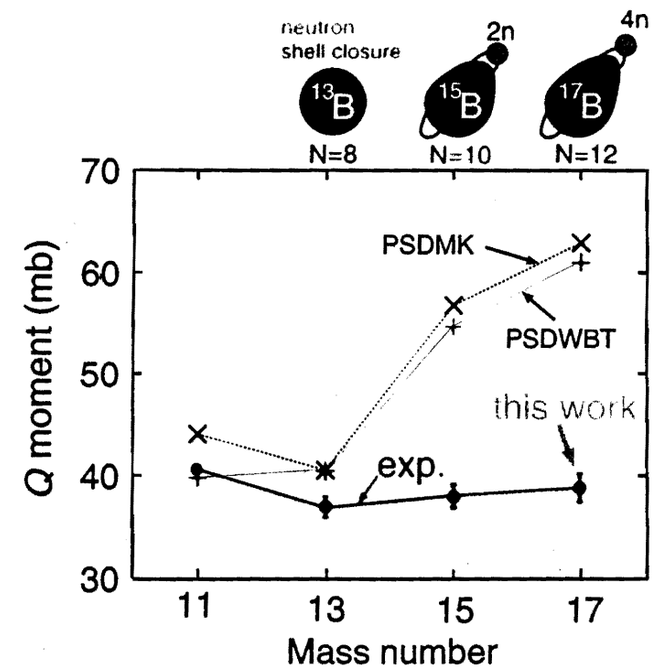

$$Q\,(^{17}\mathrm{B})_{exp} \approx Q\,(^{13}\mathrm{B})_{exp}$$

Q_{exp} ~ constant against mass.

^{15}C μ-moment spectrum

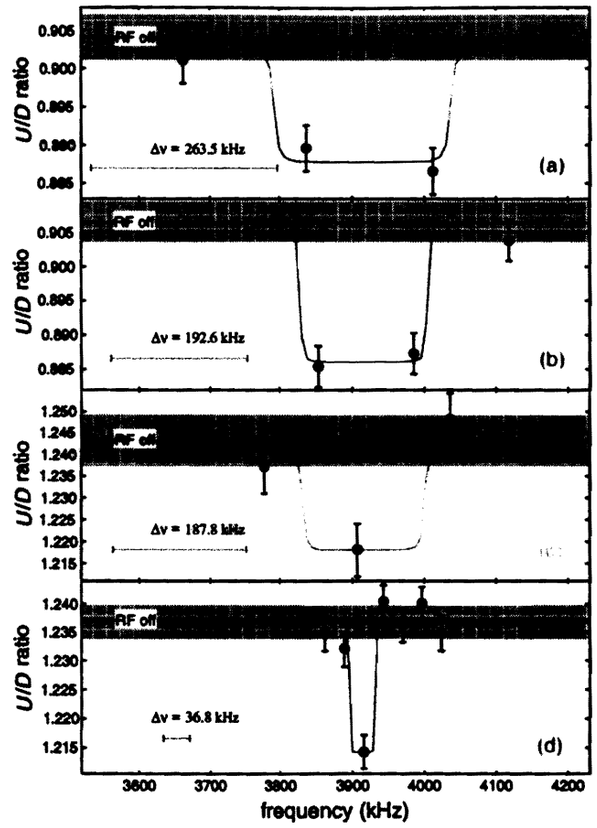

$\psi(^{15}\mathrm{C})$ configuration

		PSDMK	PSDWBT
$\lvert^{15}\mathrm{C}_{g.s.}(1/2^+)\rangle$	$= \alpha_1 \mid [\pi(p_{1/2})_{-2}]^{j=0^+} \otimes \nu(s_{1/2})\rangle$	81.64 %	89.22 %
	$+ \alpha_2 \mid [\pi(p_{3/2})_{-2}]^{j=0^+} \otimes \nu(s_{1/2})\rangle$	15.71 %	9.11 %
	$+ \alpha_3 \mid [\pi(p_{3/2})_{-1}(p_{1/2})_1]^{j=2^+} \otimes \nu(d_{5/2})\rangle$	2.15 %	1.32 %
	$+ \cdots$		

g_{free} g_{eff}

$$\begin{cases} \langle 1|\hat{\mu}_z|1\rangle = -1.913\ (-1.746) \Rightarrow \frac{1}{2} g_s \\ \langle 2|\hat{\mu}_z|2\rangle = -1.913\ (-1.746) \end{cases}$$

$$\langle 3|\hat{\mu}_z|3\rangle = -2.069\ (-2.062)$$

他の項の $\mu(^{15}\mathrm{C})$ への寄与は 3% 以下

$$(cf.\ \underline{|\mu(^{15}\mathrm{C})_{\mathrm{exp}}| = 1.720(9)\mu_N}) \approx \frac{1}{2} g_s$$

	PSDMK	PSDWBT
$g_{s(eff)}$	−3.63	−3.45

● 現在までの測定方法

入射核破砕反応による偏極生成
+
β-NMR 法によるモーメント測定

○ 核種によらず適用可能
○ 非常に速い方法　~100ns
× 偏極度　1~5%
× 試料で偏極度を保持する必要　$T1 \sim Z^{-2}$
× β asymmetry に頼った方法

● 新たな測定法

Atomic Beam法

飛行中にモーメント測定

⇒ μ, Q モーメントの測定
スピン決定

Atomic Beam法

$I = \frac{1}{2}$, $J = \frac{3}{2}$ の例

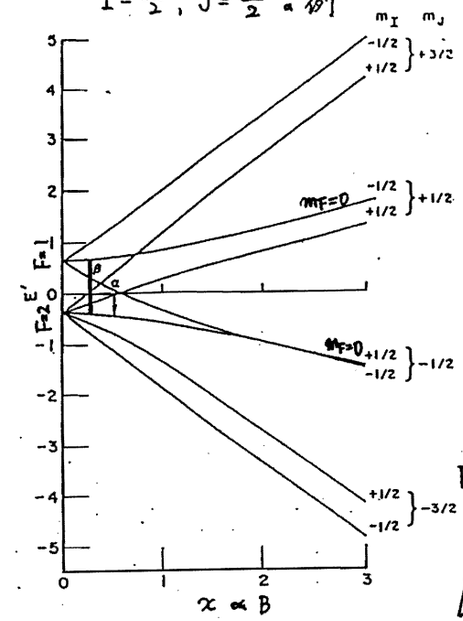

$$W(F, m_F) = \frac{h\Delta\nu}{2(2I+1)} + g_I' \mu_B B m_F \pm \frac{h\Delta\nu}{2}\sqrt{1 + \frac{4m_F}{2I+1}x + x^2}$$

$$x = (g_J - g_I)\mu_B B/(h\Delta\nu)$$

$$\Delta\nu = 2a = \nu_\beta$$

同位体間の比

$$\frac{a_{I_2}}{a_{I_1}} = \frac{g_{I_2}}{g_{I_1}}$$

← 不安定核
← 安定核

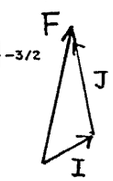

^{13}N spectrum

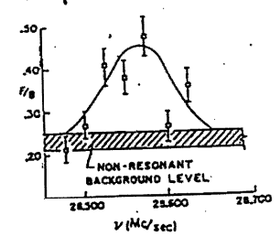

必要な統計量

S/N = 1 の場合でも

360 counts/1周波数 (5σ)

Atomic beam法の
利点
- スピン偏極緩和時間
- β線非対称度

} 関係ない

広範囲な Z 領域に適用可能

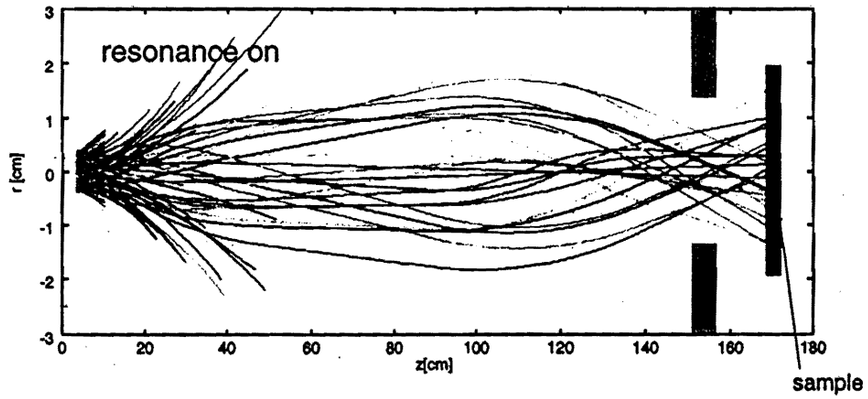

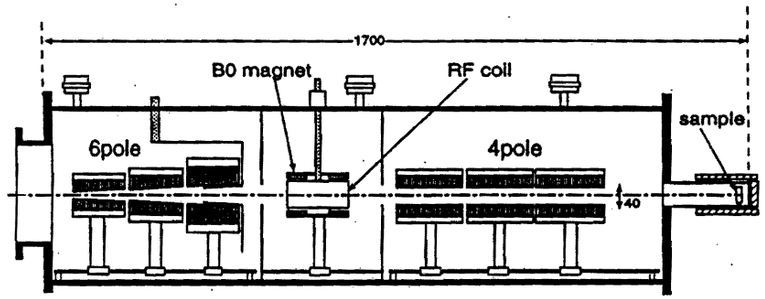

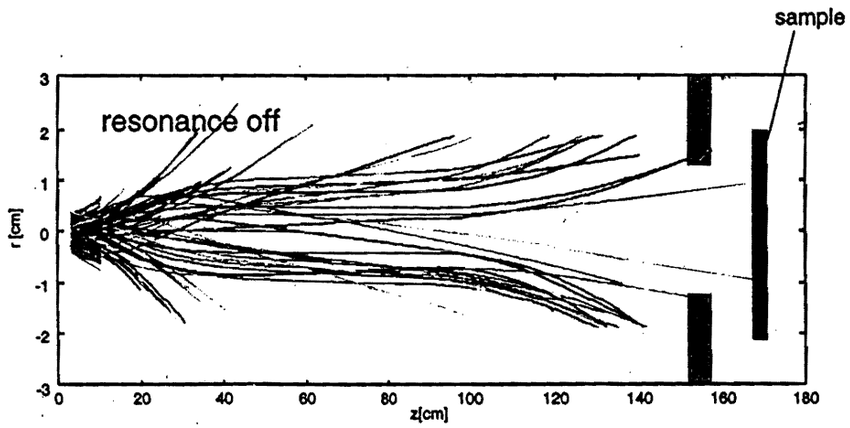

Summary

- μ, Q モーメントの測定結果より

  sd 中性子対相互作用エネルギーの減少

  E2有効電荷の減少

- μ(^{15}C) より g_s

- 新たな測定法　Atomic Beam法

Collaborator list

K. Asahi[1,2], H. Ueno[2], K. Sakai[1], T. Suzuki[1], H. Miyoshi[1], M. Nagakura[1], K. Yogo[1], A. Goto[1], T. Suga[1], T. Honda[1], N. Imai[3], Y.X.Watanabe[2], K. Yoneda[2], A. Yoshimi[2], N. Fukuda[3], N. Aoi[3], Y. Kobayashi[2], W.-D. Schmidt-Ott[4], G. Neyens[5], S. Teughels[5], A. Yoshida[2], T. Kubo[2], and M. Ishihara[6]

[1] *Dept. of Physics, Tokyo Institue of Technology*
[2] *Inst. of Physical and Chemical Researh (RIKEN)*
[3] *Dept. of Physics, Univ. of Tokyo*
[4] *II. Physikalisches Inst., Univ. Göttingen*
[5] *Inst. voor Kern- en stralingsfysica, Univ. of Leuven*
[6] *RIKEN-BNL Research Center*

ＣＲＩＢの概要と物理

東京大学原子核科学研究センター　久保野　茂

ラジオアイソトープビーム（ＲＩＢ）は、現在原子核物理にとどまらず、宇宙核物理や物性物理などの広い分野において新しい研究領域を拓きつつある。しかし、中・高エネルギーのＲＩＢ生成装置は、理研を初め多く利用されているが、本格的な低エネルギーＲＩＢ装置は、世界に数個所あるのみで、しかも利用可能なビームの強度や種類が限られているのが現状である。日本では、非常に低いエネルギー領域の開発的研究がＫＥＫのＥ－グループで昨年までなされてきたのみである。

核子あたり１０ＭｅＶ程度以下の低エネルギー大強度ＲＩＢは、これまでよく使われてきたインビーム核分光や直接反応などの研究手法の利用が可能であり、核構造や核反応研究に非常に有効である。しかし、理研のＲＩＰＳのように、中高エネルギーの重インビームによる入射核様核破砕反応から得る低エネルギーＲＩＢは、質、強度ともに落ちる。一方、ＩＳＯＬ型のＲＩＢ施設は、ＲＩＢ加速のための後段加速器や不安定核のイオン源が必要である。特に、イオン源は、絶対効率が要求されるので、元素毎にイオン源の開発が必要であり、小規模の研究グループには大きな負担となる。

今回、東京大学原子核科学研究センター（ＣＮＳ）では、理化学研究所と共同で、低エネルギー飛行分離型ＲＩＢ分離器 ＣＲＩＢ の建設を進めている。本装置は、理研ＡＶＦサイクロトロンからの大強度重イオンビームによる核反応によって生成した二次粒子を、ダブルアクロマティックスペクログラフ＋ウィーンフィルターを用いて、分離収集するものである。したがって、生成収集は、物理過程のみであるので、一端システムが完成すると、元素にとらわれずに安定なＲＩＢの供給が可能となるものと期待される。今後、ガス標的とハイパワーファラディカップを装着する。ガス標的が薄いという弱点は、一次ビーム強度を上げることによりカバーする。この方法によって、核子あたり１０ＭｅＶ領域で、安定線から１、２核子離れた領域のＲＩＢに対し、1 pμA、1 mg/cm^2 の時、収集効率を１０％と仮定すると毎秒１０$^{7-9}$個の生成が期待される。ＣＲＩＢの建設は今夏でガス標的、ウィーンフィルターを除く全ての部分が完成する。この部分は、来年３月完成を目標としている。今秋からビームを使ったＣＲＩＢのオプティクスの調整が始まる。なお、ＡＶＦサイクロトロンとイオン源の大強度化も、ＣＮＳとＲＩＫＥＮの共同研究として、同時進行している。

ＣＲＩＢを使った研究は、理研のＲＩＢＦプロジェクトが本格的に始まると、かなり豊富なマシンタイムが、可能となる予定である。研究課題は、不安定核の核物理や爆発過程の宇宙核物理、物性利用など多岐に渡るものと予想される。

参考のために、ＣＲＩＢの概要とその利用のパンフレットを次に添付する。

ＣＲＩＢ（ＣＮＳ低エネルギーＲＩＢ分離器）利用案内

２００１．１．２９

目次：

１．ＣＲＩＢ概要
２．ＣＲＩＢの主要パラメータ
３．ＣＲＩＢの光学的特徴
４．ＡＶＦビーム強度
５．２次ビームＲＩＢ（予想）
６．ガス標的
７．簡易２次ビーム装置の利用
８．実験研究の例

１．ＣＲＩＢ概要

ＣＲＩＢは、低エネルギー飛行分離型ＲＩビーム（ＲＩＢ）分離器である。この種の装置としては、ガス標的やウイーンフィルター（ＷＦ）を備えた世界で最初の本格的な低エネルギーの装置である。全体系が図１にある
図にあるように、（Ｆ０）ＱＭＤＱ（Ｆ１）ＤＭＱ（Ｆ２）ＱＱＷＦＱＱ（Ｆ３）の構成をもつ。Ｆ１は、運動量分散の焦点をもち、Ｆ２はアクロマティック収束点である。Ｆ３は、ＷＦにより速度分離された純度の高いＲＩＢが得られる。

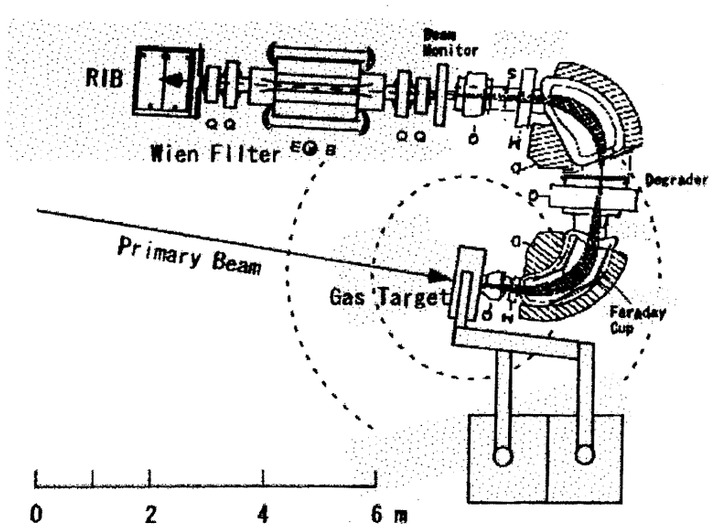

図１　ＣＲＩＢの平面図。

一次標的：　ＲＩビーム生成のための一次標的は、２つ用意されている。

（１）丸形メンブレーン散乱槽　――　散乱角度を変えることができる。
可動範囲；Θ(Lab.)= -5 ~ +57 度。
Ｆ１で、運動量分散を持ったスペクトル観測が可能。

（２）差動排気型ガス標的系　――　ガス循環型の運転が可能。
入り口、出口の口径は、変更可。
口径６ ｍｍの設定で、炭酸ガスで約５０Ｔｏｒｒ。
運転は、０度で行う。

実験用焦点面：　実験可能な焦点面は、３ヶ所ある。

（１）Ｆ１；　運動量分散をもつ。

（２）Ｆ２；　アクロマティック焦点。Ｆ１にデグレーダを入れることにより、ビームの純化が図られる。

（３）Ｆ３；　速度分離焦点。ビームの純度の高いＲＩＢが得られる。

実験用散乱槽は、約１(ビーム方向)x 1.2 x 0.6(高さ) m^3の直方体で、左右駆動機構が２本、上下駆動テーブルが２面ある。

また、直前に設置された、モニター槽には、左右上下のスリットと上下駆動の機構が１つある。

２．ＣＲＩＢの主要パラメータ

表１　ＣＲＩＢ主要パラメータ

軌道半径	84 -98 cm
最高エネルギー	110 Z^2/A MeV
分析エネルギー範囲	30 %
立体角	5.6 msr
運動量分解能（Ｆ１）	1/850
運動量分散（Ｆ２）	0
縦倍率	0.5
横倍率	1.2

３．ＣＲＩＢの光学的特徴

双極磁石などは、複雑なポール面を有するが、基本的なオプティクスは、図２の通り。（一次の光学計算）

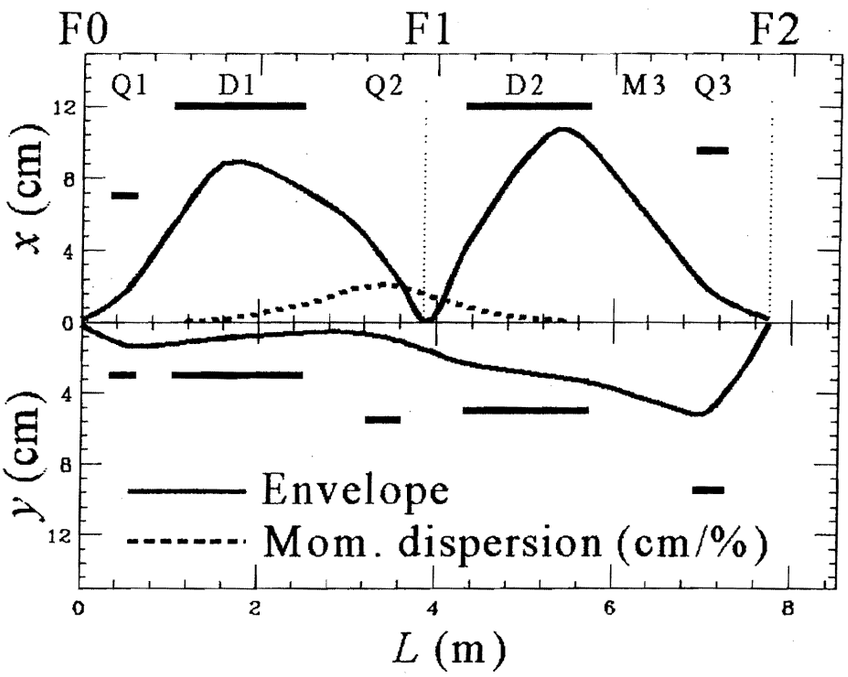

図２　ＣＲＩＢのビーム光学。直線は、ビームパイプあるいは、ポール面の位置。

４．ＡＶＦビーム強度

RIB 生成は、一次ビームの強度に比例する。最近の実績を表２に示す。ＡＶＦサイクロトロンの出口から、ＣＲＩＢ一次標的までの輸送効率は、昨年１１月のビームタイムでは、９０％強が得られている。今後、この強度は、ＡＶＦサイクロトロンの大強度化（フラットトップ化、中心領域改良）やイオン源開発により、上がるものと期待される。

Primary Beam Intensities from AVF Cyclotron (Current in eμA)

このデータは基本的にRIKEN Accl. Prog. Rep. 22 219 (1988)に基づいて算出している

電荷		1	2	3	4	5	6	7	8	9	10	11	12	13	14	15	16	17	18	19	20	21
^{11}B	eμA																					
	MeV/u	0.58	2.31	5.21	9.26	14.46																
^{12}C	eμA		12.75		3.4	1.2																
	MeV/u	0.49	1.94	4.38	7.00	7.80	17.50															
^{13}C	eμA																					
	MeV/u	0.41	1.66	3.73	6.63	10.36	14.91															
^{14}N	eμA		45	34.5	23.25	4	3.6															
	MeV/u	0.38	1.43	3.21	5.71	7.00	12.88	17.50														
^{16}O	eμA		23	33.75		18	18.75	3														
	MeV/u	0.27	1.09	2.46	4.38	6.84	9.84	13.40	17.50													
^{18}O	eμA							7														
	MeV/u	0.22	0.86	1.94	3.46	5.40	7.78	10.59	13.83													
^{19}F	eμA			6.75	6.9	4.95		2.7		0.0075												
	MeV/u	0.19	0.78	1.75	3.10	4.85	6.98	9.50	12.41	15.71												
^{20}Ne	eμA			16.5	17.25		14.25	7.5	5.25	0.165												
	MeV/u	0.18	0.70	1.58	2.80	4.38	6.30	8.58	11.20	14.18	17.50											
^{22}Ne	eμA								5													
	MeV/u	0.14	0.58	1.30	2.31	3.62	5.21	7.09	9.26	11.71	14.46											
^{24}Mg	eμA					1.5		0.375														
	MeV/u	0.12	0.49	1.09	1.94	3.04	4.38	5.95	7.78	9.84	12.15	14.70	17.50									
^{27}Al	eμA									0.7		0.16										
	MeV/u	0.10	0.38	0.86	1.54	2.40	3.46	4.71	6.15	7.78	9.60	11.62	13.83	16.23								
^{32}S	eμA					1.65		3.6		2.4		0.36		0.0038								
	MeV/u	0.07	0.27	0.62	1.09	1.71	2.46	3.35	4.38	5.54	6.84	8.27	9.84	11.55	13.40	15.38	17.50					
^{40}Ar	eμA						7.8	10.8	14.25	13.05		2	1.5	0.33	0.075							
	MeV/u	0.04	0.18	0.39	0.70	1.09	1.58	2.14	2.80	3.54	4.38	4.10	6.30	7.39	8.58	9.84	11.20	12.64	14.18			
^{84}Kr	eμA											3	3.45		4.05	3.75	2.25	0.795	0.375		0.24	0.015
	MeV/u	0.01	0.04	0.09	0.16	0.25	0.36	0.49	0.63	0.80	0.99	1.20	1.43	1.68	1.94	2.23	2.54	2.87	3.21	3.58	3.97	4.38

表２　最近のＡＶＦサイクロトロンからの引き出しビームの強度。

5．2次ビームＲＩＢ（予想）

RIB 生成に、一次ビームとして、１ pμA、標的に 1 mg/cm^2 を用いた時に得られるビーム強度の予想を図３に示す。ＣＲＩＢでの収集効率を１０％と仮定している。
ここでは、実験から得られた(p,n), (p,pn)反応の断面積を用いている。

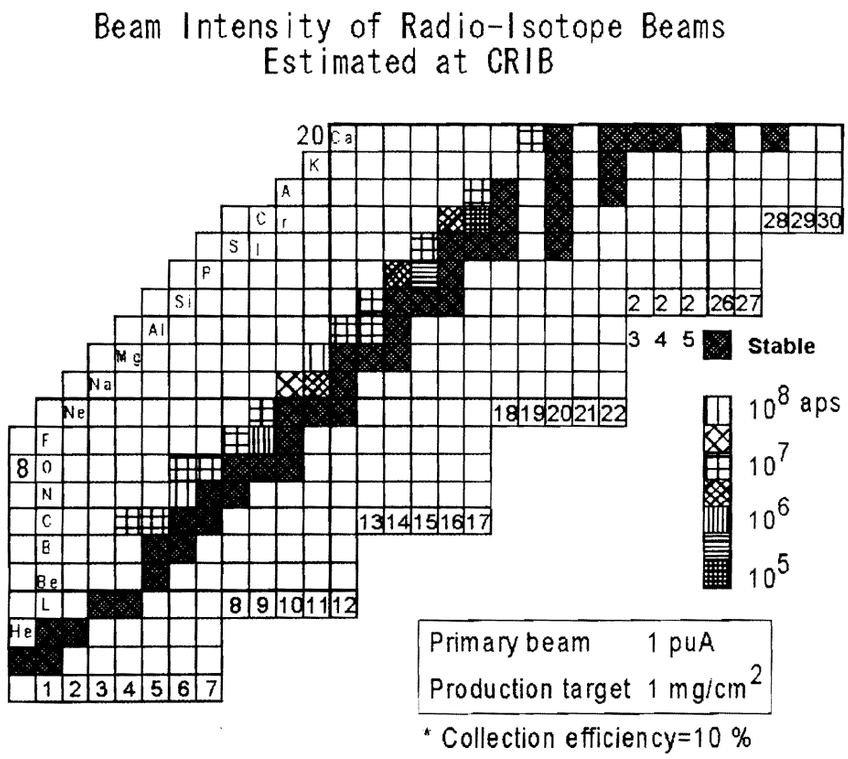

図３　ＣＲＩＢで生成されるＲＩＢ強度の予想。

<u>エネルギー分解能</u>；　運動量分散を持つ第１焦点面に置かれたスリットのサイズにより、選ぶことができる。生成方法が、（ｐ，ｎ）反応などの２体反応で、閾値の近くの入射エネルギーを使うと、エネルギーで１％程度の広がりで、ほぼ全断面積の生成が可能である。
<u>ビームサイズと広がり</u>；　前回のビームテストから、ＲＩＢ生成標的上では、2 x 2 mm^2 以下である事が分かったので、倍率から、1 x 2.4 mm^2 程度が期待される。角度の広がりは、縦、横それぞれ、±1.1, 2.6 度程度と期待される。

6．ガス標的

RIB生成には、純度の高いガスが有効な事が多い。例えば、（p，n）反応の逆運道学から作る方法は、非常に有効であると考えられる。また、大強度のビーム対応は、ガスが最適である。基本的に、九大の相良氏による方法を取り入れた、うち向き流入法をとる。模式的な概要図を図3に示す。

得られるガス圧の例。	窒素ガス	50 Torr = 0.82 mg
（6mm口径の場合）	水素ガス	20 Torr = 0.024 mg

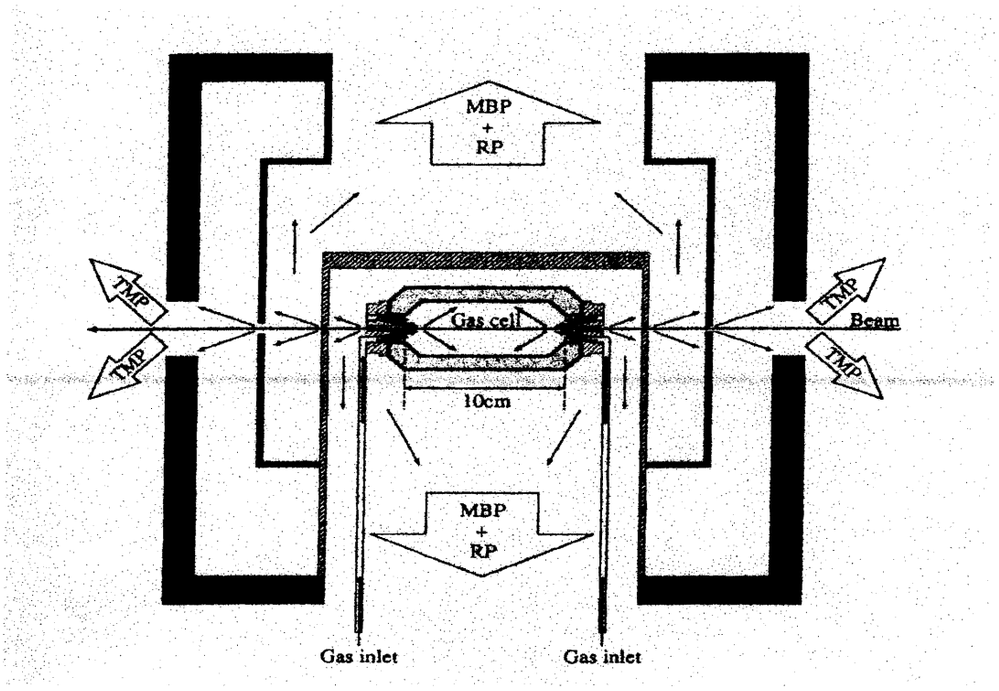

図4　窓フォイル無しのガス標的槽の概念図。

7．実験研究の例

ＣＲＩＢは、ＲＣＮＰのＤＵＭＡＳをもとに作られている。当時、開発として行われた研究例を図5，6に示す。

研究例： $^{12}C(^{7}Be, ^{7}Be)$ 弾性散乱の測定　@ E(Lab) = 140 MeV。

^{7}Be 生成反応； $^{1}H(^{7}Li, ^{7}Be)$ @ 147 MeV　Y=2 x 10^{4} aps。

エネルギー分解能＝ 1.6 MeV/140 Me V = 1.1 %

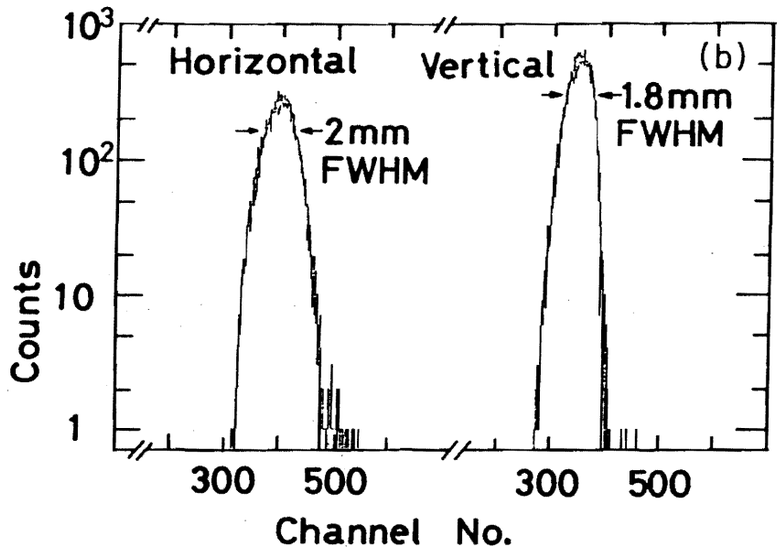

図 5　147 MeV の ^{7}Li ビームによる $^{1}H(^{7}Li, ^{7}Be)$反応から得られた ^{7}Be ビームの像。

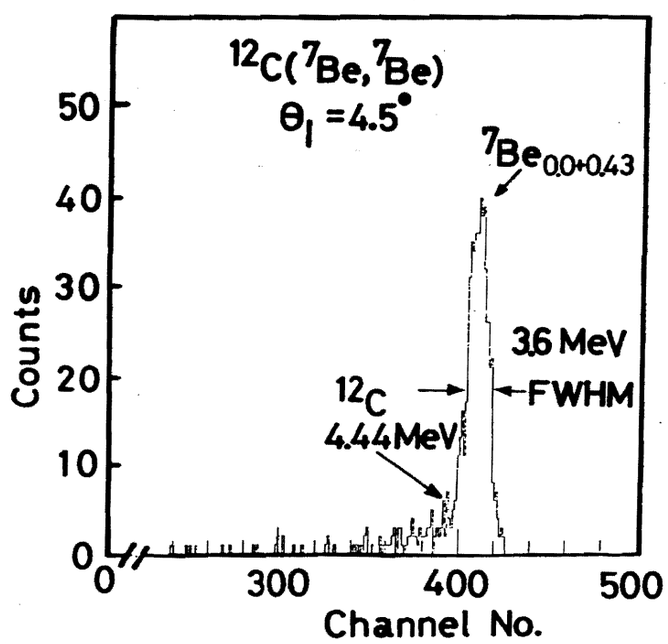

図 6　140 MeV $^{7}Be + ^{12}C$ の散乱のスペクトル。

８．簡易２次ビーム装置の利用

ＣＮＳのリニアック大照射室にあるビーム反応実験コースは、簡易２次ビームコースとして、利用可能である。ＣＲＩＢの実験散乱槽と全く同じものが設置されている。理研のＲＩＢＦ計画が本格的に稼働するまで、リニアックのビーム利用は比較的容易であると予想される。

Installation of Low-Energy RI Beam Separator CRIB

Y. Yanagisawa, T. Teranishi[a], S. Michimasa[a], M. Notani[a], Y. Ohshiro[a], S. Shimoura[a], K. Ue[a], S. Watanabe[a], N. Yamazaki[a], S. Kato[b], Y. Mizoi, M. Kase and S. Kubono[a]

The Institute of Physical and Chemical Research (RIKEN)
[a]Center for Nuclear Study, Graduate School of Science, University of Tokyo
[b]Department of Physics, Yamagata University

The radioactive isotope (RI) beams at around 10 MeV/nucleon established methods of nuclear spectroscopy, such as particle transfer reactions, can be applied to deduce spectroscopic information. Nuclear structure studies with in-beam gamma ray spectroscopy in the present energy region are also useful, because nuclear fusion reactions have large cross sections. We have installed a low-energy RI beam separator, called CRIB, which is an in-flight separator, at the RIKEN Accelerator Research Facility (RARF) [1]. This separator is installed as a part of the CNS-RIKEN collaboration. The in-flight method was not considered so seriously before because the effective target thickness usable for RI beam production is too thin. However, recent development of ion source technology for heavy ions enables one to produce RI beams of reasonably high intensity.

The AVF cyclotron (K = 70) at the RARF provides a variety of heavy-ion beams with energies up to about 10 MeV/nucleon and with intensities as high as 100 pnA. Figure 1 shows schematic layout of the RARF. The CRIB is located E7 room. CRIB consists of the magnetic spectrometer DUMAS [2] and a velocity filter (Wien filter). The facility enables one to obtain RI beam of energies below 10 MeV/nucleon.

The DUMAS was designed to be a doubly achromatic spectrometer with an intermediate dispersive focus between the two dipoles. The basic specifications of this magnetic system of the DUMAS part are listed in Table 1. Figure 2 shows a schematic view of the CRIB. Particles produced by nuclear reactions at the production target, for example, (p,n) and (^{3}He,n) reactions, are collected and separated through the spectrometer, and focused downstream where a secondary target is placed for a RI beam experiment. The production target is optionally used to the windowless gas target system [3,4]. The principle of isotope separation is based on the magnetic rigidity analysis and the energy loss of particles. [5,6]

The spectrometer consists of ten main magnets (Q1-D1-Q2-D2-Q3-Q4-Q5-E1-Q6-Q7) and two small correction magnets (M1 and M2), as shown in Fig. 2. The system can be divided into three independent sections.

Particles produced at the target are analyzed the magnetic rigidity with respect to their momenta in

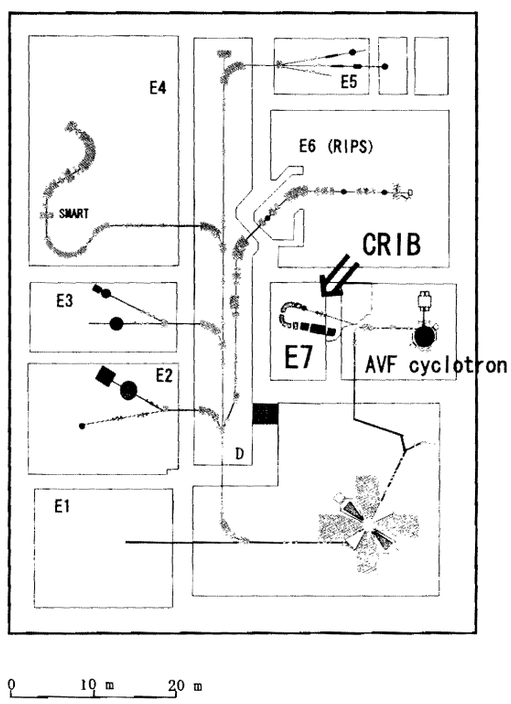

Figure 1: Layout of the RIKEN Accelerator Research Facility. The CRIB is installed the E7 room

Maximum energy	E_{max} = 110 Z^2/A MeV
Orbit radius	ρ = 84 - 98 cm
Spectrum range	± 7.7% in momentum
	(±15% in energy)
Maximum solid angle	$\Delta\Omega_{max}$ = 5.6 msr
	(75 mr (H) × 75 mr (V))
Deflection angle	185 deg
Length of central orbit	L = 7.80 m (ρ=90cm)
1st focal plane	
Size	40 cm (H) × 8 cm (V)
Energy dispersion	Δ x · E/ΔE
	= 700 mm (ρ = 98 cm)
	= 1015 mm (ρ = 84 cm)
Tilted angle	0 deg
Energy resolution	ΔE/E = 1/350
2nd focal plane	
Energy dispersion	0
Magnification	M_x = 1.5, M_y = 0.2

Table 1: Specifications of CRIB

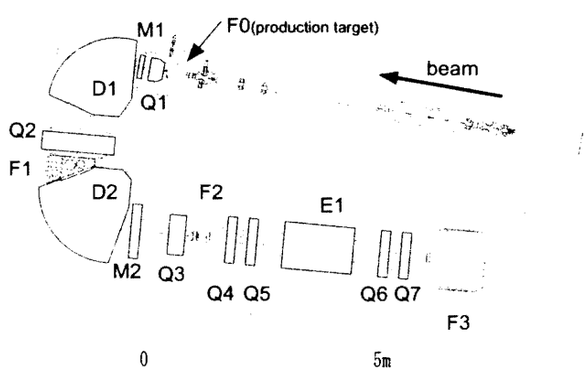

Figure 2: Schematic view of CRIB

the first section with the configuration of Q-M-D-Q and are focused dispersively on the first focal plane F1. The primary beam will be stopped on the wall of a water-cooled aluminum faraday cup inside the first dipole magnet. The second section with a configuration of D-M-Q compensates the dispersion of the first section and gives a doubly achromatic focus at F2. A degrader with a flat shape can be mounted on a holder at F1. The focus position at F2 is can be adjusted about 1m depending on requirements of experiments. These magnets are mounted on a platform which can rotate from -5 deg. to 60 deg. around the center of the F0 scattering chamber. Purpose of third section to include velocity filter is to increase purity of RI beam, especially proton-rich nuclei. The velocity filter is described in ref. [7]

The low-energy RI beam separator CRIB has been developed since end of 2000. Recently, first RI beam at CRIB, ^{10}C with 10 kcps, was measured by p(^{10}B,^{10}C)n reaction at F2. In the near future, various RI beams were produced by using CRIB at around 10 MeV/nucleon.

References

[1] Y. Yano, Proc. 12th Int. Conf. on Cyclotrons and their Applications, Berlin, eds. B. Martin and Z. Ziegler (World Scientific, 1989) p.13.

[2] T. Noro *et al.*, RCNP Annual Report 1983 173.

[3] T. Kishida *et al.*, Nucl. Instr. and Meth. **A438**, (1999) 70.

[4] T. Kishida *et al.*, in this proceedings.

[5] J.P. Dufour *et al.*, Nucl. Insr. and Meth. **A248**, (1986) 267.

[6] R. Anne *et al.*, Nucl. Instr. and Meth. **A257**, (1987) 215.

[7] T. Teranishi *et al.*, in this proceedings.

Technique of Low-Energy RI Beam Separation by CRIB and Experiment of Elastic Resonance Scattering on Unstable Nuclei

T. Teranishi[1*], S. Kubono[1], Y. Yanagisawa[2], S. Shimoura[1], Y. Mizoi[2], M. Notani[1], S. Michimasa[1], K. Ue[1], S. Watanabe[1], N. Yamazaki[1], M. Oshiro[1], T. Kishida[2] and S. Kato[3]

[1]*Center for Nuclear Study (CNS), University of Tokyo, RIKEN campus, Hirosawa 2-1, Wako, Saitama, 351-0198 Japan*

[2]*RIKEN (The Institute of Physical and Chemical Research), Hirosawa 2-1, Wako, Saitama, 351-0198 Japan*

[3]*Physics Department, Yamagata University, Yamagata, 990-8560 Japan*

**e-mail: teranisi@cns.s.u-tokyo.ac.jp*

Abstract

This paper discusses the technique of radio-isotope (RI) beam separation used for the low-energy RI beam separator CRIB, which is now under construction at Center for Nuclear Study (CNS), University of Tokyo. An experimental project of elastic resonance scattering by using CRIB is also briefly described.

1 RI Beam Separation by CRIB

The in-flight RI beam separator CRIB uses low-energy primary beams of $< \sim 10$ MeV/nucleon from an AVF cyclotron ($K = 70$) at RIKEN Accelerator Research Facility. High intensity primary beams of nearly 1 pμA for ions of $A < \sim 20$ are available at the production target position. In terms of production yield, such a high intensity can overcome the limitation in target thickness for the low-energy in-flight method. For example, a secondary beam of 10^7 aps can be achieved by using a 1-pμA primary beam and a 1-mg/cm^2 target when the production cross section is 10 mb. Production reactions to be used are mainly two-body reactions like (p,n) reactions in inverse kinematics, which produce forward focused RI beams with relatively small energy spread. Such secondary particles can be effectively collected by CRIB which has a large solid angle (about 5.6 msr) and momentum acceptance (about 15 %).

The separator consists of two dipole magnets (D1 and D2) and four quadrupole magnets (Q1, Q2, M3 and Q3) in a sequence of F0-Q1-D1-Q2-F1-D2-M3-Q3-F2, where F0, F1 and F2 represent the target point, the first and second focal planes, respectively (see Fig. 1). Figure 2 shows a result of first-order optics calculation for CRIB by using the code TRANSPORT [1]. The envelopes in horizontal (x) and vertical (y) directions are shown in the figure for the initial secondary-beam emittance of $\Delta x = \Delta y = \pm 1.5$ mm, $\Delta\theta_x = \Delta\theta_y = \pm 30$ mrad and $\Delta p/p = 0$. Only the horizontal focusing is achieved at F1, while F2 is doubly focussed. The magnification from F0 to F1 is 0.3 for x and those from F0 to F2 are 1.2 for x and 0.5 for y. At F2, the beam spot size can be in the order of 1 cm diameter which is small enough to perform experiments. The momentum dispersion in the horizontal direction is also shown by a dashed line and the dispersion at F1 is 1.6 m.

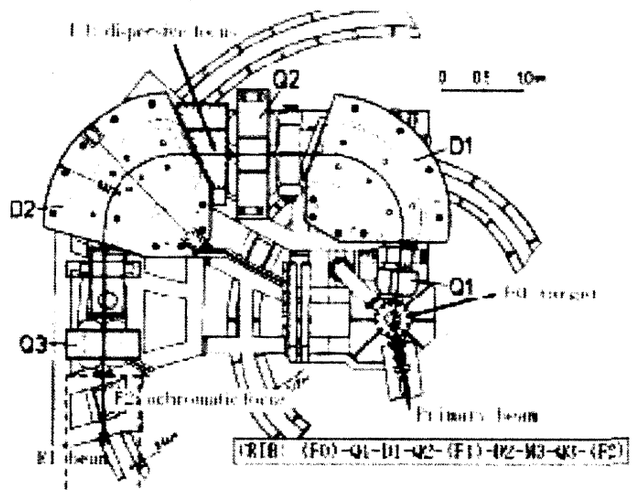

Fig. 1: Layout of CRIB.

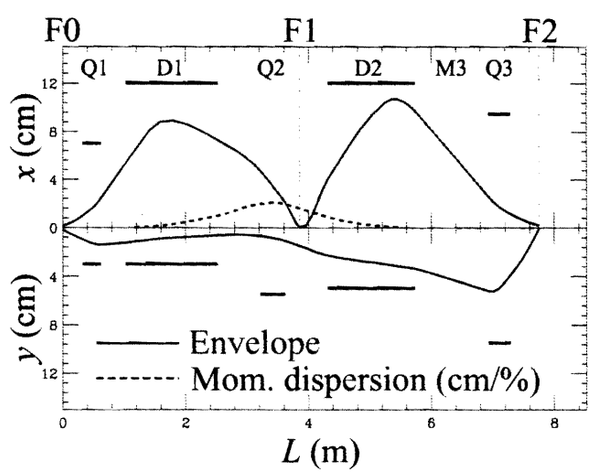

Fig. 2: Result of TRANSPORT calculation for CRIB. Solid lines are envelopes in x and y. Dashed line indicates the horizontal momentum dispersion.

As described below, CRIB has three types of particle-separation power (#1–3). The first half of CRIB F0-Q1-D1-Q2-F1 generates the momentum dispersion. A horizontal slit at F1 is used to select a region of magnetic rigidity for secondary particles of interest (#1 particle separation by $B\rho$). The momentum resolving power at F1 is about 800. The primary beam is usually stopped at a beam stopper (Faraday cup) inside the D1 magnet.

Only with the particle separation by magnetic rigidity (F1 slit), there can be many background nuclides which have the same magnetic rigidity as the secondary beam. Light particles like p, d, α and so on are often produced by nuclear reactions and usually have large momentum distributions. Therefore, these light particles pass through the F1 slit and reach to F2. Scattering of the primary beam at the wall of beam pipe, the edge of target holder and the inner walls of D1 magnet also produces background particles of the same nuclide as the primary beam.

To reduce background particles which pass through the F1 slit, one can install an energy degrader at the F1 plane, as often used for fragment separators [2, 3]. The magnetic rigidity before the F1 degrader ($B\rho_1$) is constant and defined by the F1 slit, while the magnetic rigidity after the degrader ($B\rho_2$) depends on Z and velocity (thus A) because of energy loss. Thus, the second half of CRIB F1-D2-M3-Q3-F2 with a horizontal slit at F2 serves as the second particle analyzer by $B\rho_2$. Among the group of nuclides which have the same $B\rho_1$, only nuclides with $A^{2.5}/Z^{1.5} \sim const.$ can go through the F2 slit (#2 particle separation by energy-loss method).

Without the degrader, the second half of CRIB compensates the momentum dispersion at F1 (D_1) and makes the F2 focal plane achromatic. The relation of dispersion compensation can be expressed as $D_1 + D_2/M_{x2} = 0$, where D_2 and M_{x2} are the dispersion and horizontal magnification, respectively, from F1 to F2. Inserting a flat plate degrader at F1 breaks the achromaticity from F0 to F2 because the energy dependence of energy loss changes the dispersion at F1. The dispersion at F1 with the flat degrader D_1' can be approximated by $D_1' \sim (1 - d/R)D_1$, where d is the degrader thickness and R is the range of particle in the degrader material. A degrader of wedge shape [2] may be used to keep the dispersion constant before and after the degrader ($D_1' = D_1$). Thickness of degrader is typically $d < 0.3R$. For low energy RI beams at $E/A < 10$ MeV, the degrader thickness is small (order of several mg/cm^2). It may be difficult to fabricate such a thin wedge degrader. Instead, one may use a curved-film degrader which has the same position dependence of effective thickness as the wedge shape.

It is also possible that one uses a simple flat degrader and modifies the dispersion at F1 instead, to keep the achromaticity at F2 [4]. For CRIB, we can adjust the dispersion before the F1 degrader by changing the strength of Q2 magnet. In this case, the dispersion should be set to $D_1 = -D_2/M_{x2}/(1 - d/R)$, so that the dispersion after the degrader becomes $D_1' = -D_2/M_{x2}$ and satisfies with the dispersion compensation relation.

We are now developing an Wien filter as an additional section of CRIB. (#3 particle-separation by velocity). The Wien filter system will be installed at downstream side of F2 and consist of quadrupole magnets and a velocity separator section of $\vec{E} \times \vec{B}$ type. This separation method may be useful when the energy-degrader method is not effective enough, for example, in separating a proton-rich nuclide from the neighboring isotones.

2 Study of Elastic Resonance Scattering

One of applications of the low-energy RI beams to nuclear physics is the study of resonant states in unstable nuclei, which are of interest with respect to exotic nuclear structure or nuclear astrophysics. The first experiment to be done at CRIB will be a search for resonant states in unstable nuclei via elastic scattering. Cross section of resonance elastic scattering near the threshold is very large if the partial width for the elastic channel is much larger than those of other reaction channels. Therefore, the experiment can be performed easily with low-intensity RI beams. We are planning to measure ^{10}C+p (^{11}N), ^{12}N+p (^{13}O) and some other RI+p resonances in proton-rich nuclei. Data of those resonances is important to

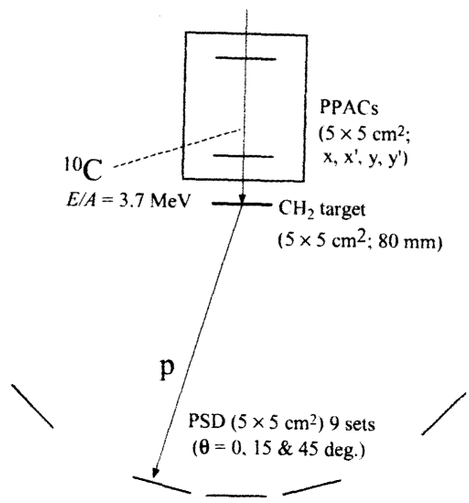

Fig. 3: Schematic view of experimental setup for elastic resonance scattering ^{10}C+p.

understand the proton-induced nuclear-reaction processes in stars. Resonant states beyond the proton-drip line (unbound nuclei) are interesting in conjunction with their mirror nuclei near the neutron-drip line.

An elastic scattering experiment can be performed in inverse kinematics with an RI beam and a proton target. In this situation, the center-of-mass energy and angle can be determined by measuring energy and angle of recoil proton in better resolution than by measuring those of the heavy ejectile. It is useful to apply the thick-target method [5], where the target thickness is chosen to be larger than the range of incident beam so that the beam is completely stopped in the target. The recoil proton goes out from the target with very small energy-loss in the target and gives information on scattering energy and angles. The proton is detected at forward angles in the laboratory frame. At a fixed angle, the proton energy spectrum has roughly the same shape as the excitation function $d\sigma/d\Omega(E)$ of elastic scattering. In the excitation function, a resonance can be identified as an interference pattern of potential scattering and resonance scattering. The center-of-mass scattering angle for the forward-emitted recoil proton is nearly 180°, where the scattering amplitude for the Coulomb potential goes to minimum and the effect of resonance amplitude becomes more prominent.

Figure 3 shows a schematic view of the experimental setup, which will be built at CRIB F2. The RI beam is tagged by two PPACs and stopped in a thick CH_2 target. The recoil proton comes out from the target and is detected by several sets of silicon detectors. Each set of silicon detectors is capable of measuring ΔE-E, timing and position in order to identify proton and to determine its energy and scattering angle.

Table 1 shows an estimate of production parameters for the ^{10}C beam, which will be used for the elastic scattering experiment. The production reaction is ^{10}B(p,n)^{10}C in inverse kinematics. The intensity of primary beam is expected to be 200 pnA at the energy of 6.3 MeV/nucleon. A hydrogen gas cell with thin window foils can be used as a production target. The secondary beam ^{10}C has an energy of 5.1 MeV/nucleon and its intensity is estimated to be about 10^5 aps by taking into account the production yield and acceptance of CRIB. Using the 10^5-aps beam, enough number of elastic scattering events can be accumulated in a day.

Table 1: Beam production parameters for ^{10}C

Primary beam	^{10}B
	$E = 6.3$ MeV/nucleon
	Intensity of 200 pnA
Production reaction	$^{10}B(p,n)^{10}C$ in inverse kinematics ($Q = -4.4$ MeV)
	Cross section of ~ 2 mb
Production target	H_2 130 $\mu g/cm^2$
CRIB acceptance	$\sim 50\%$ for produced ^{10}C
Degrader at F1	Al foil of 2 mg/cm^2
Secondary beam	^{10}C
	$E = 5.1$ MeV/nucleon
	$\Delta p/p = 5\%$
	Intensity of 10^5 aps

3 Summary

The technique of low-energy RI beam production and separation by CRIB has been discussed in terms of production yield and transport optics. The RI beams produced by CRIB can be easily applied to the experiments of elastic resonance scattering. Calculation of realistic beam-production parameters and the design of experimental setup are now in progress. The first experiment will be performed in the year 2001.

References

[1] D.C. Carey et al., Fermilab-Pub-98-310.

[2] J.P. Dufour et al., Nucl. Instr. and Meth. A248 (1986) 267.

[3] T. Kubo et al., Nucl. Instr. and Meth. B70 (1992) 309.

[4] S. Mitsuoka et al., Nucl. Instr. and Meth. A372 (1996) 489.

[5] K.P. Artemov et al., Sov. J. Nucl. Phys. 52 (1990) 408.

Production of RI beams by fusion reactions

Takashi. Kishida
The Institute of Physical and Chemical Research (RIKEN)

23/August/00

Abstract

The new beam line, CRIB, is appropriate as a secondary beam line by using fusion-evaporation reactions and inverse kinematics. One of the advantages to use fusion evaporation reactions is that it can produce proton-rich nuclei far from the stability line. On the other hand, a demerit is that it is difficult to purify the secondary beam. Such characteristics are illustrated in this article.

1 Introduction

The appropriate methods for the production of secondary beams are dependent on the energies of the primary beams. In the case of the secondary beam line, CRIB, the energy of the primary beam is less than 15 MeV/u, fusion-evaporation reactions can, therefore, be used for the production of RI beams based on inverse kinematics. The reaction products emitted in forward directions are transported and selected with the CRIB. The selected RI beams are used for secondary reactions, because they have enough energies. When we assume that the intensity of the primary beam is 1 pμA, the thickness of the production target is 1 mg/cm^2, and the transport efficiency is 10 %, then the intensity of the secondary beam becomes more than 10^6 pps for the reaction product with the production cross section of 100 mb.

One of the advantages to use fusion evaporation reactions for the production of RI beams is that it can produce proton-rich nuclei far from the stability line, while (p,n) reactions can only produce proton-rich nuclei next to stable isotopes. Another advantage is that fusion reactions can easily produce excited states, in particular, high spin states. If we can efficiently produce excited states whose half lives are larger than 100 ns, the CRIB can be used as an isomeric beam line.

On the other hand, a demerit to use fusion evaporation reactions is that it is difficult to control the secondary beam energies. This is because the fusion cross sections are strongly dependent on the energy of reactions. Therefore, if we select a reaction mode and a compound nucleus, the energies of the primary and secondary beam are necessarily fixed. Another demerit is that it is difficult to purify the secondary beam. In general, there are lots of the final states of fusion reactions, and many of the reaction products have similar masses, atomic numbers and production cross sections. Thus, it becomes difficult to select one final state from this mixture.

2 Requirements for secondary beam line

The requirements for a secondary beam line to transport fusion products are listed below. For high transmission efficiency, large geometrical and momentum acceptances are necessary. The beam line must be able to transport ions which have the magnetic rigidity of 0.5 – 1.3 Tm. The intermediate dispersive focus is necessary in order to separate the reaction products from the primary beam, and the double stage spectrometer system with the two

dipoles is necessary in order to reduce serious background due to the primary beam scattered by the beam pipe. The doubly achromatic optics is also essential for the secondary beam line to produce a small beam spot at the experimental focal point. The distance between the production target and the secondary target should be as short as possible in order to transport metastable excited states which have short half-lives.

OHP 1 shows the characteristics of three beam lines used at RIKEN: RIPS, E1C and CRIB. The E1C is unsuitable as a secondary beam line compared with the other two, because its geometrical and momentum acceptances are small, the dispersion at the first focal plane is not large, and it has only single spectrometer magnet. The RIPS was designed as a secondary beam line which transported radioactive isotopes produced with the projectile fragmentation method. Therefore, it satisfies the requirements for a secondary beam line. Its only shortcoming is that the distance between the production and secondary targets is large. The CRIB is the most suitable as a secondary beam line to transport fusion products as shown in OHP 1. On the other hand, it is unsuitable as a beam line to transport neutron-rich nuclei with high energies, because the maximum magnetic rigidity of the CRIB is small.

3 Production cross sections by fusion reactions

The energy range of ions accelerated by the AVF Cyclotron is determined by the dynamic range of RF frequency and the maximum magnetic rigidity of the AVF Cyclotron. By the dynamic range of RF frequency, the range of the beam energy from the AVF Cyclotron is determined as 3.8 – 14.5 MeV/u. But the upper limit of beam energy is almost always determined by the maximum magnetic rigidity of the AVF Cyclotron. OHP 2 shows this situation. Therefore, it can be concluded that the ion source ability to produce high charge state efficiently determined the range of beam energy and the mass range of ions to be accelerated. OHP 2 indicates that we can utilize heavy ions up to Kr as primary beams from the AVF Cyclotron.

Then the production cross sections of fusion products can be calculated by using the CASCADE code with the determined mass and energy regions of the primary beams from the AVF Cyclotron. As previously discussed, the upper limit of the mass region for the primary beam is assumed to be Kr-region. In order to use intense primary beam, a gas target will be used for the production target. We can, thus, assume that the possible gas materials are H, He, C, N, O, F, Ne and Ar.

Because it is impossible to describe here the whole results of the calculations, very rough description of tendencies of them is made below. When the energy of the primary beam is relatively low, the number of evaporation nucleons from the compound nucleus is relatively small, and only a few number of the final states are obtained. It means that the purity of the secondary beam becomes relatively high in this case. On the other hand, lots of the final states are obtained when the energy of the primary beam is high. Even when stable nuclei of the neutron-rich end are used for the primary beams, the obtained secondary beams are proton-rich unstable ones, because the compound nuclei emit many evaporation neutrons. When stable nuclei of the proton-rich end are used for the primary beam, the compound nuclei emit a few protons and alpha's as well as neutrons, and the Z/N-ratios of the obtained secondary beams are almost the same as that of the compound nuclei. Finally, the production cross sections of about 100 mb are obtained for fusion products which are one-neutron deficient from the stability line in the mass region up to Ti, 3 – 4 neutrons deficient from V to Kr, and 4 – 7 neutrons deficient from Rb to Xe.

4 Transport and purification

The produced proton-rich beams are transported and selected with the CRIB. For an example, we will discuss about the production of ^{67}Ge by using ^{20}Ne (^{54}Fe, α2pn) ^{67}Ge reaction. The energy of the primary beam, ^{54}Fe, is 5 MeV/u. The CRIB can transport 90 % of the

produced ^{67}Ge, in spite that the angular distribution of the reaction product has a large width due to the relatively small energy of the primary beam. But it is difficult to purify the secondary beam. OHP 3 shows the table of cross sections of the final states. The production cross sections of ^{66,67}Ga are almost the same as that of ^{67}Ge. OHP 4 shows the magnetic rigidity distributions of these products and the primary beam. The figure indicates that the primary beam will be easily removed at the dispersive focal plane, but, on the other hand, ^{66,67}Ga cannot be separated from ^{67}Ge by means of magnetic apparatus. In the present, we do not have an appropriate method for the purification of the secondary beams. It might be better to find good experiments with the secondary beam whose purity is not very good.

２次ビームライン比較表

	RIPS	E1C	CRIB
Geometrical Acceptance	±40mr (circle) 《5msr》	± 7mr(v) ±15mr(h) 《0.42msr》	±38mr (square) 《5.6msr》
Momentum Acceptance	±3%(full) (±4.5%)	±<2%(full) (±<3.4%)	±7.7%(full)
Max Bρ	5.76Tm	~1.8Tm	1.35Tm
Focus	《F1》 dispersive 2.4cm/% 《F2》 double achromatic 《F3》 double achromatic	《F1》 dispersive 0.45cm/% 《F2》 small dispersion	《F1》 dispersive 1.02cm/% 《F2》 zero dispersion
Flight Path	F1: 10.4m F2: 21.3m F3: 27.5m	F1: 3.65m F2: 7.63m	F1: 3.84m F2: 7.78m

ＡＶＦで加速可能なエネルギー

K-value	70
extraction radius	0.714 m
RF range	12 - 24 MHz
maximum B	1.7 Tesla
A / Q	< 4.2

➡ 3.8 - 14.5 MeV/u

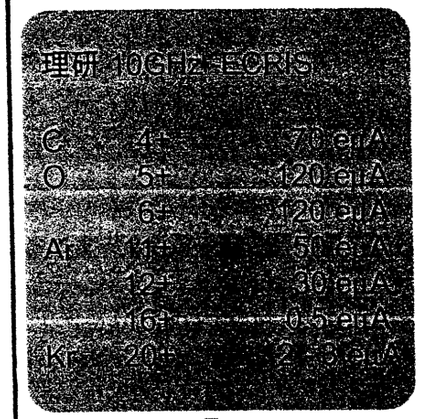

⬇

ＣＮＳ－イオン源
超伝導ＥＣＲＩＳ

World Records

O	5+	1000 eμA
	6+	1000 eμA
Ar	8+	1000 eμA
	11+	300 eμA
	12+	150 eμA
	14+	80 eμA
	16+	20 eμA
Kr	22+	66 eμA
	25+	35 eμA
	27+	7 eμA
Xe	30+	35 eμA
	31+	20 eμA
	33+	9 eμA
	36+	2 eμA

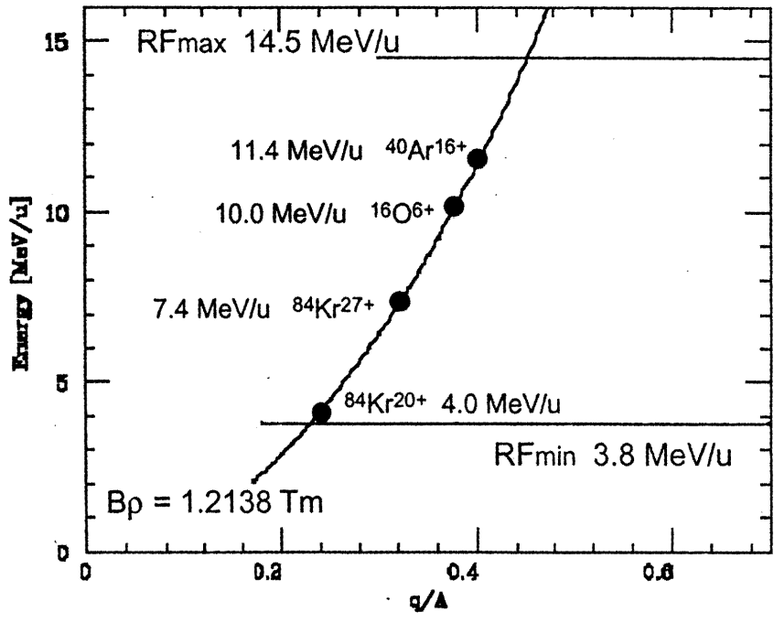

イオン源の能力が
最高エネルギーを決める

$^{54}Fe + ^{20}Ne$ (5 MeV/u)

^{64}Se	^{65}Se	^{66}Se	^{67}Se	^{68}Se	^{69}Se	^{70}Se 17.7	^{71}Se	^{72}Se	^{73}Se	^{74}Se	^{75}Se
^{63}As	^{64}As	^{65}As	^{66}As	^{67}As	^{68}As	^{69}As 65.2	^{70}As 80.5	^{71}As	^{72}As	^{73}As	^{74}As
^{62}Ge	^{63}Ge	^{64}Ge	^{65}Ge	^{66}Ge 35.2		^{68}Ge 41.3	^{69}Ge 78.6		^{71}Ge		
^{61}Ga	^{62}Ga	^{63}Ga	^{64}Ga 65.7	^{65}Ga 32.0			^{68}Ga		^{70}Ga		^{72}Ga
^{60}Zn	^{61}Zn	^{62}Zn	^{63}Zn 58.6		^{65}Zn				^{69}Zn		^{71}Zn
^{59}Cu	^{60}Cu	^{61}Cu 65.3	^{62}Cu		^{64}Cu		^{66}Cu	^{67}Cu	^{68}Cu	^{69}Cu	^{70}Cu

CNS / RIKEN　融合反応を使ったＲＩＢの生成

電荷（Bρ）分布

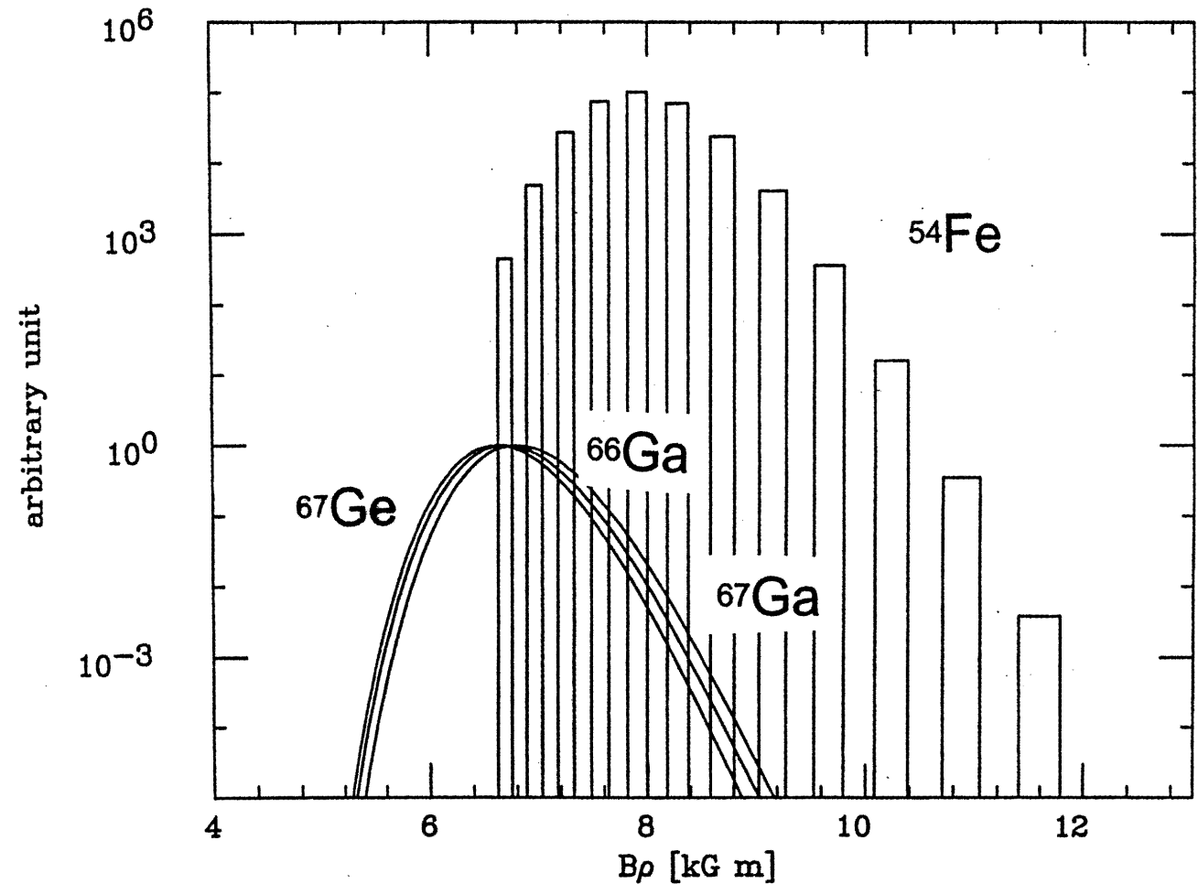
10^6
10^3
10^0
10^{-3}
arbitrary unit
^{54}Fe
^{66}Ga
^{67}Ge
^{67}Ga
4
6
8
10
12
Bρ [kG m]

In-beam gamma-ray spectroscopy at CRIB

Y. Gono, Kyushu University

23/Aug./00

Abstract

The in-beam γ-ray spectroscopy made by using unstable nuclear beams is expected to give us a chance to see new phenomena in nuclei so far not accessed by stable nuclear beams. Some examples of such reactions induced by unstable nuclear beams which may be effective for such a purpose are discussed.

Recent nuclear structure studies performed on N=Z nuclei revealed new features such as a possible pn-pairing effect [1]. The low spin collective states of N=Z nuclei were reported up to a nucleus N=Z=42, ^{84}Mo [2]. Those were studied using 2n emission channels which has a very small cross section, 0.007(3) mb in case to produce ^{84}Mo by a reaction ^{58}Ni + ^{28} Si. In this example the other reaction channels to emit pn and 2p have significantly larger cross sections, 1.3(3) mb for pn channel and 35(3) mb for 2p channel. Since a ^{30}S beam is expected to be produced by a reaction p(^{31}P, ^{30}S)2n at CRIB with a fairly large cross section, a larger cross section to produce ^{84}Mo by using a ^{58}Ni(^{30}S, 2p2n)^{84}Mo reaction can be expected. This will give us a chance to see higher spin states in these nuclei which are expected to show new phenomena such as pn-pairing as discussed in ref.[1].

A neutron rich beam such as ^{16}C and ^{18}O will also give unique chances to study high spin states of nuclei at a neutron rich side. A beam of ^{16}C can be produced by a 2p stripping reaction of a beam of ^{18}O. This beam can be used to study high spin states in ^{222}Ra, whose 1^- excited state is the lowest in an excitation energy among all the known isotopes, using a reaction ^{208}Pb(^{16}C, 2n)^{222}Ra. This gives us a chance to study high spin states of the most collective nucleus in an octupole mode. An ^{18}O beam may be produced in the same way as that of ^{16}C from a ^{22}Ne beam. This beam can be used to study an ^{168}Er nucleus using a reaction ^{150}Nd(^{20}O, 4n)^{168}Er. Low spin states of ^{168}Er have been well studied and many collective bands are known. However the

high spin states of these bands in this nucleus could not be studied by stable nuclear beams. Therefore it may be interesting to see the behavior of these bands at high spin..

References

[1] G. de Angelis et al., Phys. Lett. B415(1997)217, and references therein.
[2] D. Bucurescu et al., Phys. Rev. C56(1997)2497 and references therein.

C.Chandler et al., P.R. C56(1997)R2924

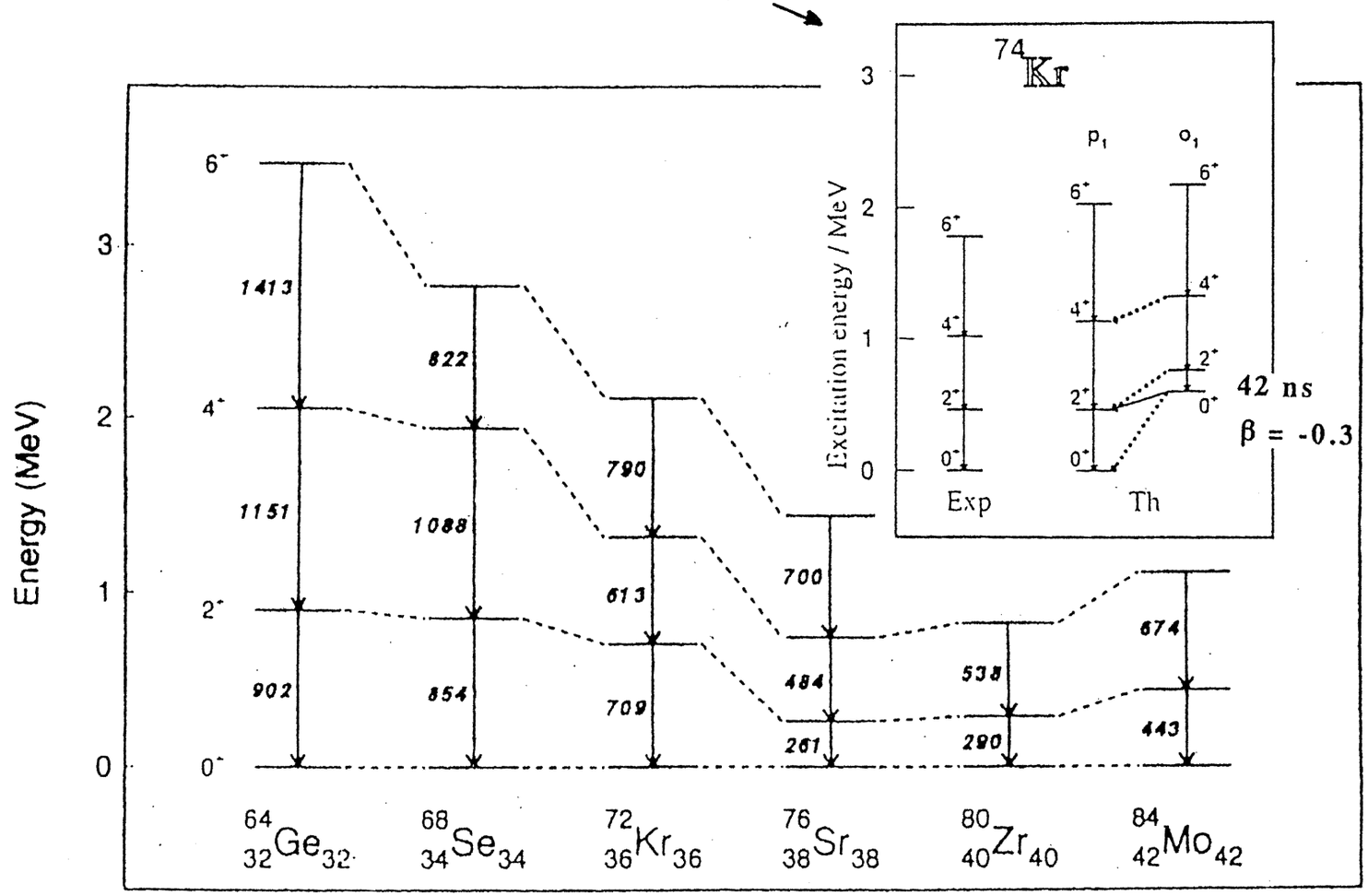

FIG. 3. The evolution of the yrast levels in $N=Z$ even-even nuclei.

D.Bucurescu et al., P.R. C56(1997)2497

Reaction and Cross Section for Production of N=Z Nuclei

Isotope	Reaction	E (MeV)	σ (μb)
^{64}Ge	$^{12}C(^{54}Fe, 2n)^{64}Ge$	165	500 ± 300
	$^{13}O(^{54}Fe, 2pn)^{64}Ge$	[p (^{14}N, ^{13}O) 2n]	
^{68}Se	$^{12}C(^{58}Ni, 2n)^{68}Se$	175	38 ± 16
	$^{13}O(^{58}Ni, 2pn)^{68}Se$		
^{72}Kr	$^{16}O(^{58}Ni, 2n)^{72}Kr$	170	60 ± 25
	$^{17}F(^{58}Ni, p2n)^{72}Kr$	[p (^{18}O, ^{17}F) 2n]	
^{76}Sr	$^{24}Mg(^{54}Fe, 2n)^{76}Sr$	175	10 ± 5
	$^{26}Si(^{54}Fe, 2p2n)^{76}Sr$	[p (^{27}Al, ^{26}Si) 2n]	
^{80}Zr	$^{24}Mg(^{58}Ni, 2n)^{80}Zr$	190	10 ± 5
	$^{26}Si(^{54}Fe, 2p2n)^{80}Zr$		
^{84}Mo	$^{28}Si(^{58}Ni, 2n)^{84}Mo$	195	7 ± 3
	$^{30}S(^{54}Fe, 2p2n)^{84}Mo$	[p (^{31}P, ^{30}S) 2n]	

Ge - Zr : C. J. Lister et al., Phys. Rev. C42(1990)R1191
Mo: W. Gelletly et al., Phys. Lett. B253(1991)287

Larger Cross Section with Unstable Nuclear Beam

$$^{16}O + {}^{58}Ni \rightarrow {}^{74}Kr^* \rightarrow \begin{cases} {}^{72}Kr + \underline{2n} & \underline{0.06\ mb\ (0.27)} \\ {}^{72}Br + \underline{pn} & \underline{28\ mb\ (127)} \\ {}^{72}Se + \underline{2p} & \underline{220\ mb\ (1000)} \end{cases}$$

B. J. Varley et al., Phys. Lett. B194(1987)463

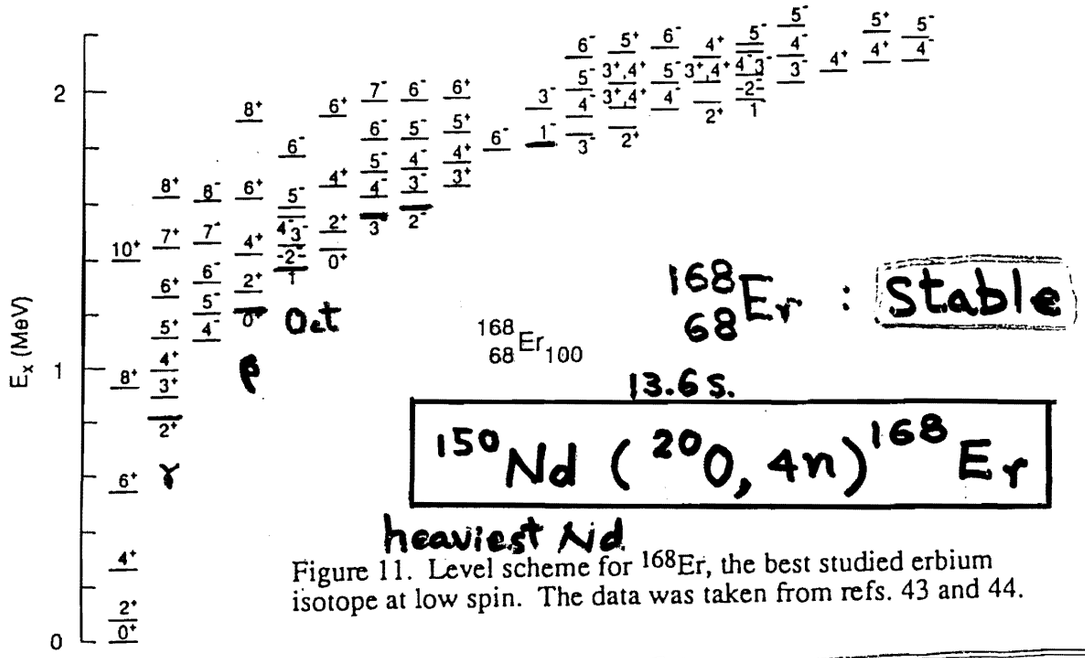

Figure 11. Level scheme for ^{168}Er, the best studied erbium isotope at low spin. The data was taken from refs. 43 and 44.

^{160}Er : neutron deficient

$^{124}Sn(^{40}Ar, 4n)$

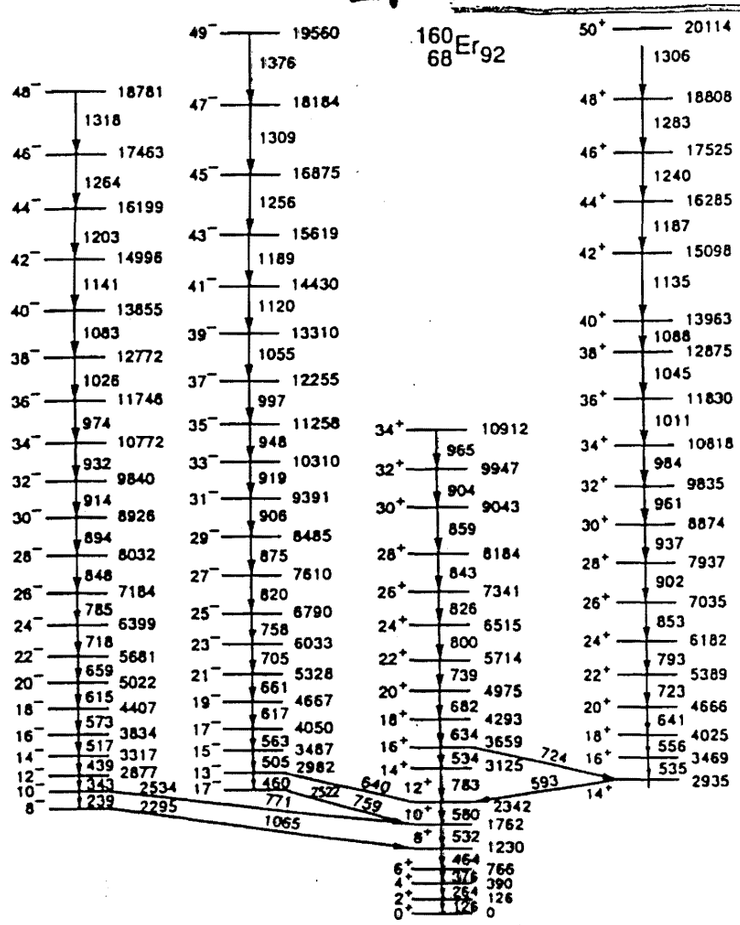

Figure 12.
Level scheme for ^{162}Er, the best studied erbium isotope at high spin. The data was taken from refs. 45 and 46.

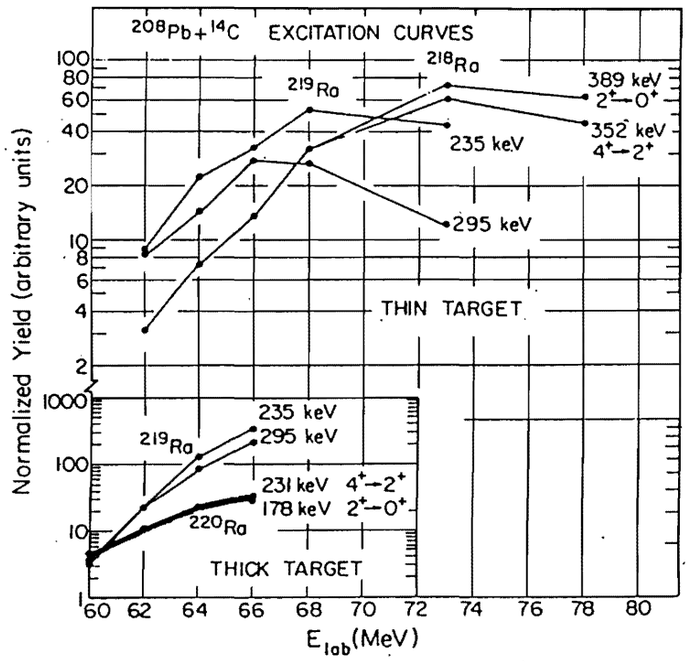

$^{208}Pb(^{14}C, 2n)^{220}Ra$

$T_{1/2} = 5730$ y

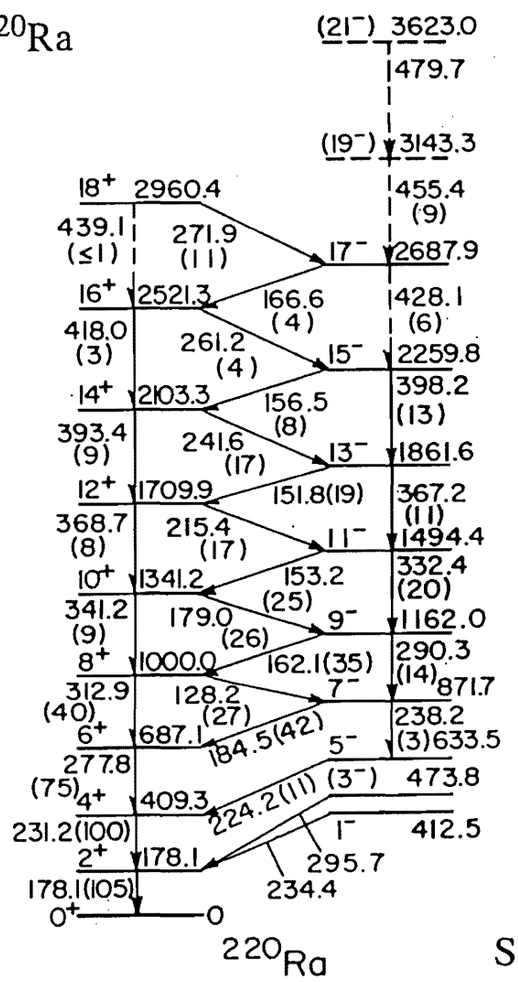

Shriner et al.(Yale)

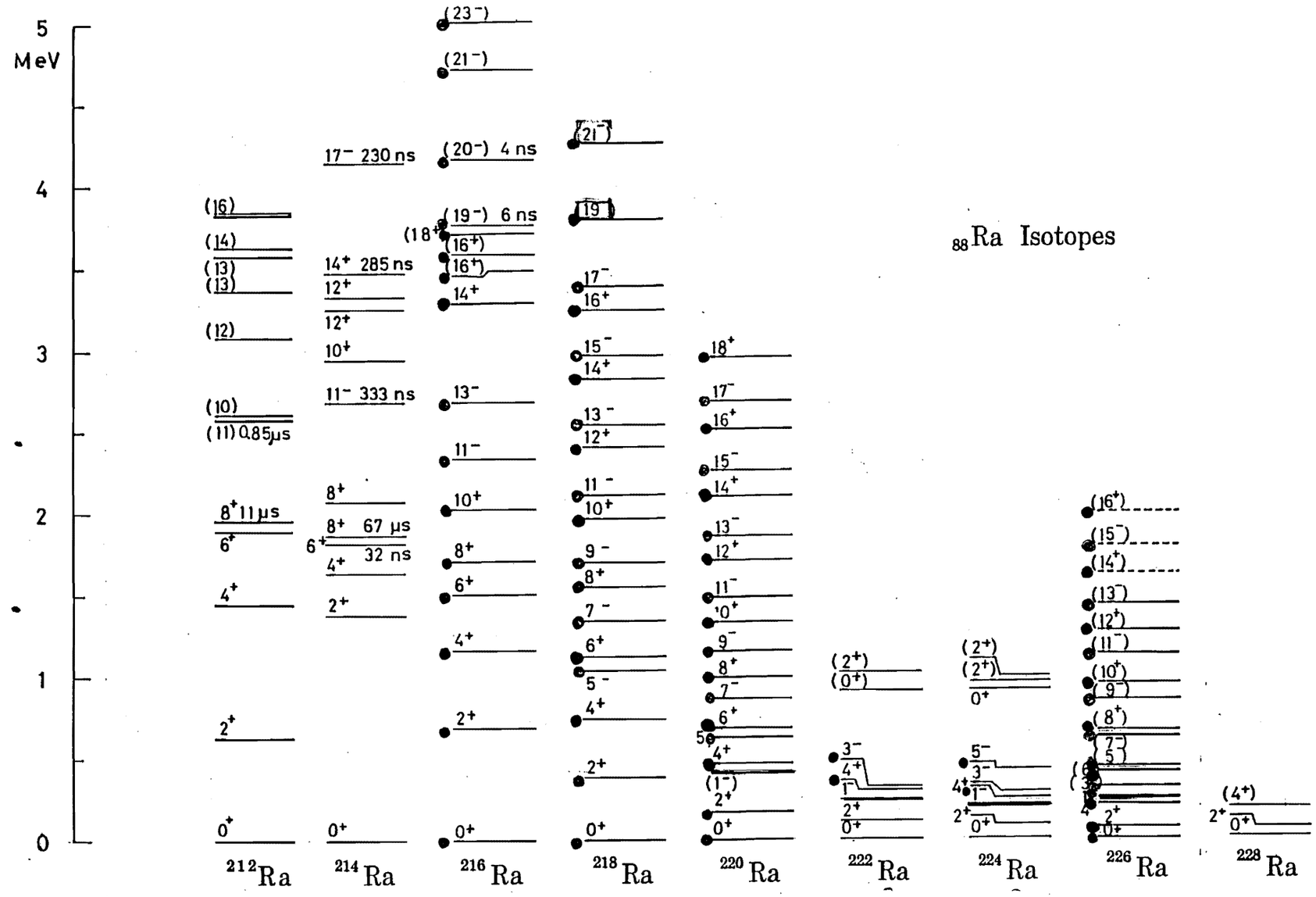
88Ra Isotopes
5
MeV
4
3
2
1
0
212Ra
214Ra
216Ra
218Ra
220Ra
222Ra
224Ra
226Ra
228Ra
(16)
(14)
(13)
(13)
(12)
(10)
(11) 0.85μs
8+ 11μs
6+
4+
2+
0+
17− 230 ns
14+ 285 ns
12+
12+
10+
11− 333 ns
8+
8+ 67 μs
6+
32 ns
4+
2+
0+
(23−)
(21−)
(20−) 4 ns
(19−) 6 ns
(18+)
(16+)
(16+)
14+
13−
11−
10+
8+
6+
4+
2+
0+
(21−)
(19−)
17−
16+
15−
14+
13−
12+
11−
10+
9−
8+
7−
6+
5−
4+
2+
0+
18+
17−
16+
15−
14+
13−
12+
11−
10+
9−
8+
7−
6+
5−
4+
(1−)
2+
0+
(2+)
(0+)
3−
4+
1−
2+
0+
(2+)
(2+)
0+
5−
3−
4+
1−
2+
0+
(16+)
(15−)
(14+)
(13−)
(12+)
(11−)
(10+)
(9−)
(8+)
(7−)
(5−)
2+
0+
(4+)
2+
0+

まとめ

1、N=Z 核の Shape Coexistence (Exotic shape search)
- Proton rich beam -

^{13}O, ^{17}F, ^{26}Si, ^{30}S

2、Interaction between collective bands at high spin
- Neutron rich beam -

^{20}O

3、Study of octupole collectivity in Ra region
- Neutron rich beam -

^{16}C

Coulomb excitation experiments with low-energy unstable nuclear beams at CRIB

T. Morikawa, Kyushu Univ.

23/Aug/2000

Abstract

We plan the Coulomb excitation experiments at CRIB for the study of collective nature of unstable nuclei. Use of the secondary isomeric beams is of our particular interest for the study of collective states built on the sizably deformed high-spin isomer. For the particle-γ coincidence measurement, a new charged particle detector system is being developed.

Use of unstable nuclear beams provides us the opportunity for the study of exotic nuclear states which cannot be reached by ordinary stable beams. By using low-energy secondary beams, a traditional Coulomb excitation technique can be applied for the study unstable nuclei. The advantage of this technique is that one can determine, in a model independent way, not only the collectivity of the nuclear states but the diagonal $E2$ matrix elements (Q-moments) by measuring the reorientation effect. Thus, one expects the possibility to study in detail the collective nature of nuclear states over quite a huge region of unstable nuclei.

At the CRIB facility, secondary beams are produced with high intensity primary beam from the RIKEN AVF cyclotron. The unstable nuclei are produced in the inverse kinematics, i.e. the combination of a heavy projectile and a light target. By using a primary beam of $A = 40 \sim 50$, one can produce a low energy secondary beam up to $A \sim 60$. Thus a number of unstable nuclei may be available. We are planning traditional Coulomb excitation experiments at the CRIB for the study of nuclear collective nature.

High-spin isomers are known in the $N \approx Z$ nuclei in the $f_{7/2}$ shell. They are formed by three or four stretch-coupled nucleons. Since these high-spin isomers are, or expected to be, sizably quadrupole deformed, one can expect a collective rotation built on the isomer. If such a collective state exists, it may be populated through the Coulomb excitation. It is thus interesting to do the Coulomb excitation experiments by using the secondary beams of *a)* $J^\pi = 12^+$ isomer in ^{52}Fe and *b)* $J^\pi = 19/2^-$ isomers in ^{43}Sc, ^{43}Ti, ^{53}Fe and ^{53}Co. Since the latter four nuclei are each other in the relation of mirror pairs and conjugate pairs. the Coulomb excitation with these isomeric beams may provide an unique testing ground on such a nuclear symmetry.

In the Coulomb excitation experiment of projectile excitation, the deexciting γ-rays are emitted from the projectile moving at a velocity of $\beta \sim 0.1$. Therefore, one needs the Doppler correction of the γ-ray energy by precisely detecting the scattering direction of the projectile. For this purpose, we are now developing a new charged particle detector system, which consists of parallel plates of thin plastic scintillator coupled to position sensitive photomultiplier tubes. The solid angle covered by this detector is about 70 % of 4π. The position resolution of ~ 1 mm was achieved in the test experiment.

This project is supported in part by a Grant-in-Aid for Scientific Research from the Japan Ministry of Education (Grant-in-Aid No. 12640282), and The Kurata Research Grant from The Kurata Foundation.

Isomeric States in A=40～50 Nuclei near N = Z Region

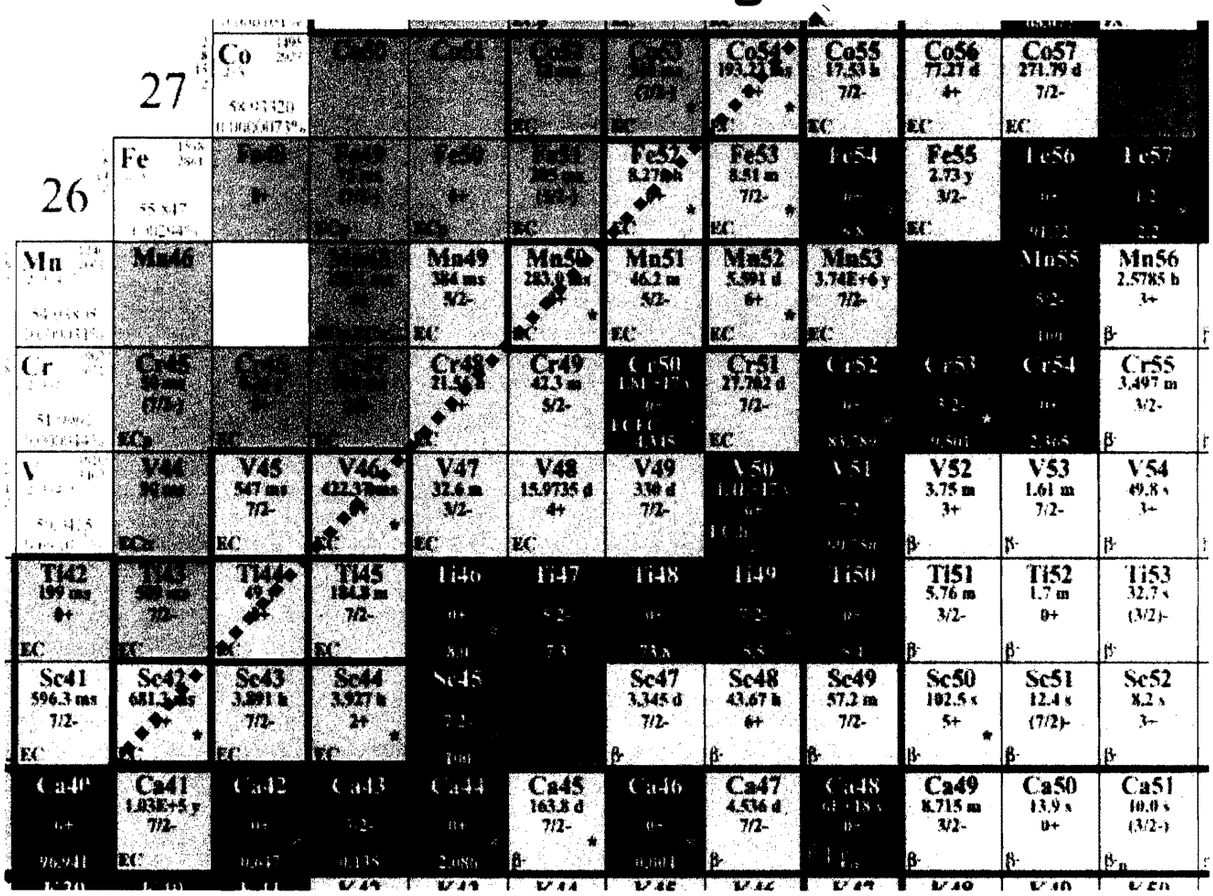

Sc-42: J=7+, 61s
Sc-43: J=19/2-, 468ns, |Q|=0.199
Ti-43: J=19/2-, 560ns, |Q|=0.3
Sc-44: J=6+, 58h, Q=-0.19
Mn-50: J=5+, 1.75m
Fe-52: J=12+, 45.9s
Fe-53: J=19/2-, 2.58m
Co-53: J=19/2-, 247ms
Co-54: J=(7+), 1.58m

Isomeric Beam and/or Ground State Beam Produced by (HI,xpyn) Reaction of Inverse-Kinematics

[redacted]

High-Spin Yrast Traps in N=Z Region
Collectivity, Deformation, Symmetry

Odd-Odd Low-Lying Isomers
Ground State of Unstable Isotopes
Collectivity, Deformation

Very Proton Rich Nuclei
Exotic Shape, Collectivity

Secondary Beam of High-Spin Isomer in Fe-52

350～400 MeV Ti-46 beam + C-12 Target
Fe-52 : 2p4n-Channel $\sigma \sim$ 10 mb
Fe-53 : 2p3n-Channel $\sigma \sim$ 100 mb

Recoil Energy ～ 250 MeV

Projectile Coulomb Excitation
Fe-52 Beam + Pb-208 Target
Safe Energy ～ 246 MeV

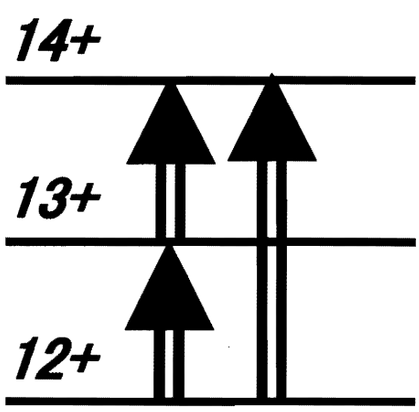

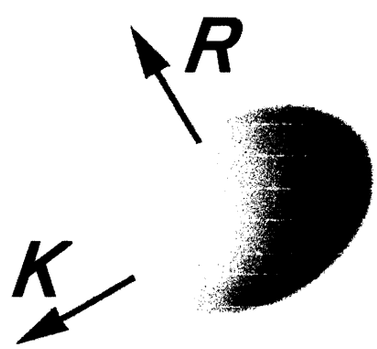

B(E2:12+ →13+) = 5.2 w.u.?
B(E2:0+ →2+) = 8.3 w.u.?

High-Spin Isomeric States in Conjugate/Cross-Conjugate Nuclei

Sc-43, Ti-43, Fe-53, Co-53

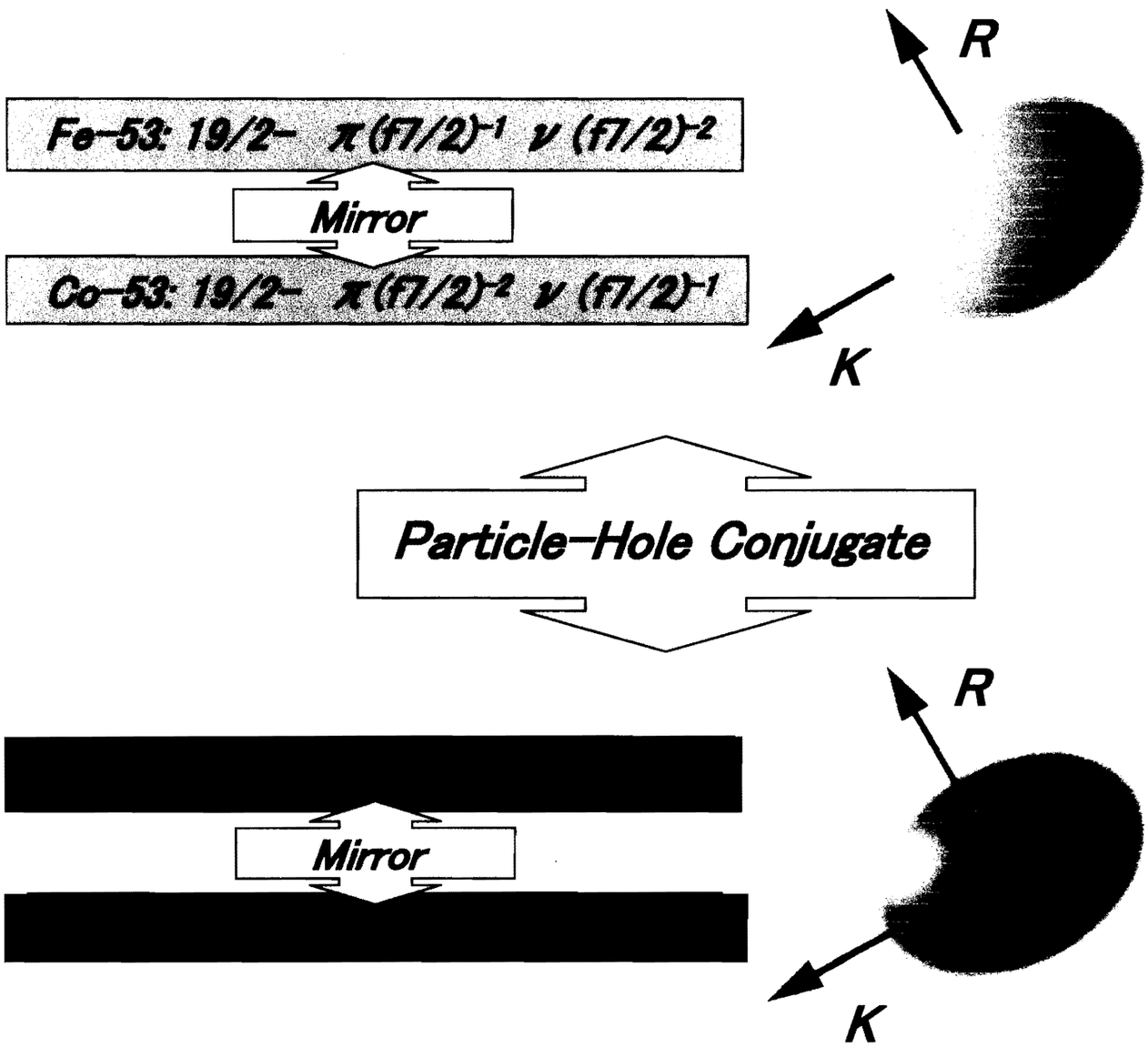

Schematic Drawing of Experimental Setup

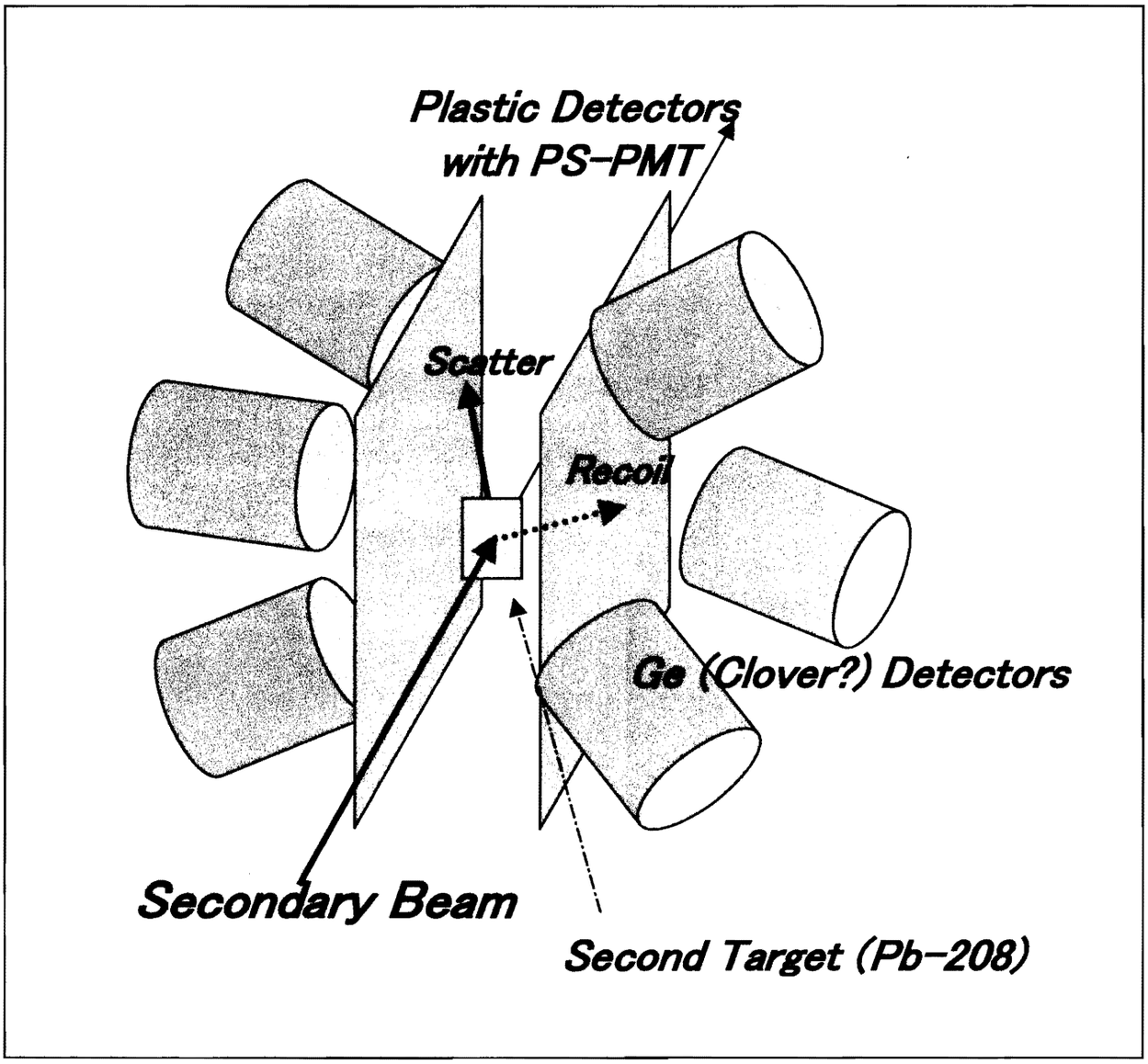

Cluster Transfer Reactions for Neutron-Rich Nuclei

S. Shimoura
CNS, University of Tokyo

Abstract
Possibility of ^{6}He transfer reactions to populate neutron-rich cluster states is discussed. A rough plan of experiments using CRIB is also presented.

It has been established that many states in light $4N$ nuclei (^{8}Be, ^{12}C, ^{16}O, ^{20}Ne etc.) have α cluster structures. It is interested how the cluster structures change when adding neutrons to such nuclei. There are several theoretical investigations in this point of view[1, 2, 3]. Experimentally, measurements of inelastic ^{10,12}Be excitations following to decay channels with ^{6}He suggests possibile cluster structures in the ^{12}Be nucleus[4, 5].

I propose here othor approaches to such cluster states by using exotic cluster transfer reactions. It is well known that states having α-cluster structures are populated selectively by α transfer reactions around 10 A MeV region such as (^{6}Li,d), (^{7}Li,t), (^{12}C,^{8}Be), etc, projectiles of which has well-developed α-cluster structure. When we extend this idea to non-alpha cluster transfer reactions, it is noticed that the ^{7}Li nucleus has a large spectroscopic factor for the ^{6}He$_{g.s.}$+p configuration[6]. This enables us to study ^{6}He transfer through the (^{7}Li,p) reaction. Moreover, inverse kinematics by using unstable nuclear beams, such as ^{6}He, on the ^{7}Li target may excite cluster structures consisting of unstable nuclei, such as ^{6}He+^{6}He (Fig. 1).

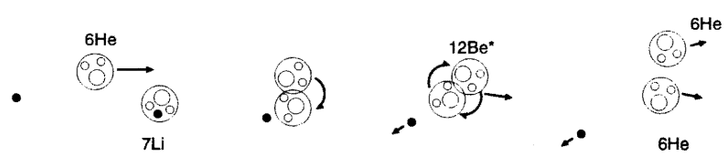

Figure 1: Schematic view of the ^{7}Li(^{6}He,^{12}Be*)^{1}H reaction followed by the ^{6}He+^{6}He decay.

The excitation energies are determined by measuring at least two of the recoil proton and the decaying particles. Particle-particle correlation measurements enables us to determine the angular momenta of the excited states

as well as the excitation energies (Fig. 2). As shown in the figure, the orbital angular momentum of 4 may be determined by the angular correlation patterns which has 4 maxima (minima).

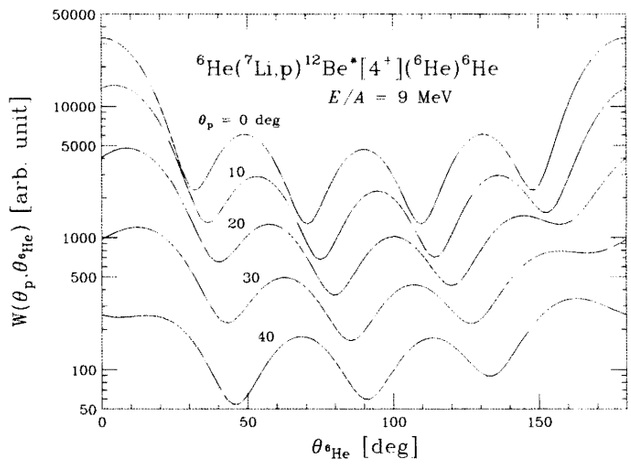

Figure 2: Calculated angular correlation function for the ^{6}He(^{7}Li,p)^{12}Be*[4$^+$](^{6}He)^{6}He reaction. All the angles are measured in the total center-of-mass system.

A rough calculation predicts that the cross sections for the 4^+ and 0^+ states at an incident energy of 9 A MeV are about 1 mb/sr and 10 μb/sr, respectively (Fig. 3). For the formar case, an yield of more than 100 events/hour is expected when we use 10^6-pps secondary ^{6}He beam and 7-mg/cm^2 ^{7}Li target.

As a position sensitive detector system with large solid angle, detector telescopes consisting of Si strip detectors and CsI(Tl) scintillators are now developing to gain efficiency and resolution of the excitation energies. Combination with position sensitive PPAC's is also under consideration.

References

[1] Y. Kanada-Enyo, H. Horiuchi, A. Dote, J. Phys. **G24** (1998) 1499.

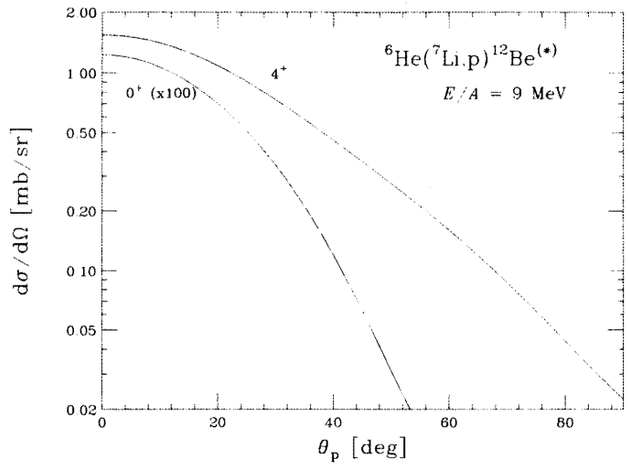

Figure 3: Estimation of differential cross sections for (^{7}Li,p) reactions.

[2] H. Furutani, et al., Prog. Theor. Phys. Suppl. **68** (1980) 193.

[3] M. Ito and Y. Sakuragi, Phys. Rev. C62 (2000) 064310.

[4] A.A. Korsheninnikov et al., Phys. Lett. B343 (1995) 53.

[5] M. Freer et al., Phys. Rev. Lett. 82 (1999) 1383; M. Freer et al., Phys. Rev. C63 (2001) 034301.

[6] S. Cohen and D. Kurath, Nucl. Phys. A101 (1967) 1.

Systematic measurement of deep inelastic scatterings involved by unstable nuclei

Y. Mizoi, CNS the University of Tokyo

31/Oct/00

Considering what kind of reaction involved by the low-energy unstable-nuclear beams which will be produced by CRIB is attractive, a deep inelastic scattering is one of very interesting candidates. Since early times when the study of heavy-ion nuclear reactions started with the innovation of heavy-ion acceleration techniques, deep inelastic scatterings involved by stable-nuclear beams are being hardly studied, and enormous beneficial and instructive informations concerning the heavy-ion reaction mechanisms and nuclear structures are being obtained by the results of them. In these days, the low-energy unstable-nuclear beams which will have efficiently high intensities and moderate energies about ten MeV/nucleon will be produced by CRIB and the study of deep inelastic scattering will be able to performed by using them.

Here, we describe phenomenological predictions which will be observed by the measurement of deep inelastic scattering involved by the unstable nuclei.

- In case of reactions involved by halo nuclei, if the halo nucleon plays as glue, a so-called negative angle scattering may be enhanced comparing to a reaction involved by stable nuclei. In order to observe this, the ejectile energies and angles should be measured and 2-dimensional histogram of them which was proposed by Wilczynski, should be plotted, and then we may see Fig. 1.

- Excess neutrons or protons may be easily transfered to a target, or break up, or pick up nucleon from a target nuclei, in order to balance the ratio of proton and neutron of the colliding system, phenomena of charge equilibrium or isospin neutralization may be observed.

- In addition if the halo neutron breaks up during reaction interacting between a projectile and a target, the ejectile neutron may have the information concerning the time dependence of reaction development, because the ejectile-neutron energy and momentum may depend on the breakup point. Figure 2 shows the schematic spectrum of neutron energy.

Figure 3 shows the schematic view of the experimental setup for the measurement of deep inelastic scatterings. Unstable-nuclear beams produced by CRIB will be irradiated to a target. Around the target a detector set which will be consisted of an ion chamber which will work as both a dE counter and a 3-dimensional tracking counter, and Si detectors which will work E counters. A species of ejectile will be identified by $dE - E$ particle-identification method. The ejectile energy will be determined by Si detectors and the ejectile angle will be determined by the ion chamber.

By measuring these phenomena, we will obtain the information concerning the reaction mechanisms involved by unstable nuclei and structures of unstable nuclei.

中性子過剰核（ハロー、スキン）の場合

過剰中性子が糊になるなら
負角散乱優勢に？

Example; (^{11}Be,Li) v.s. (^{10}Be,Li)

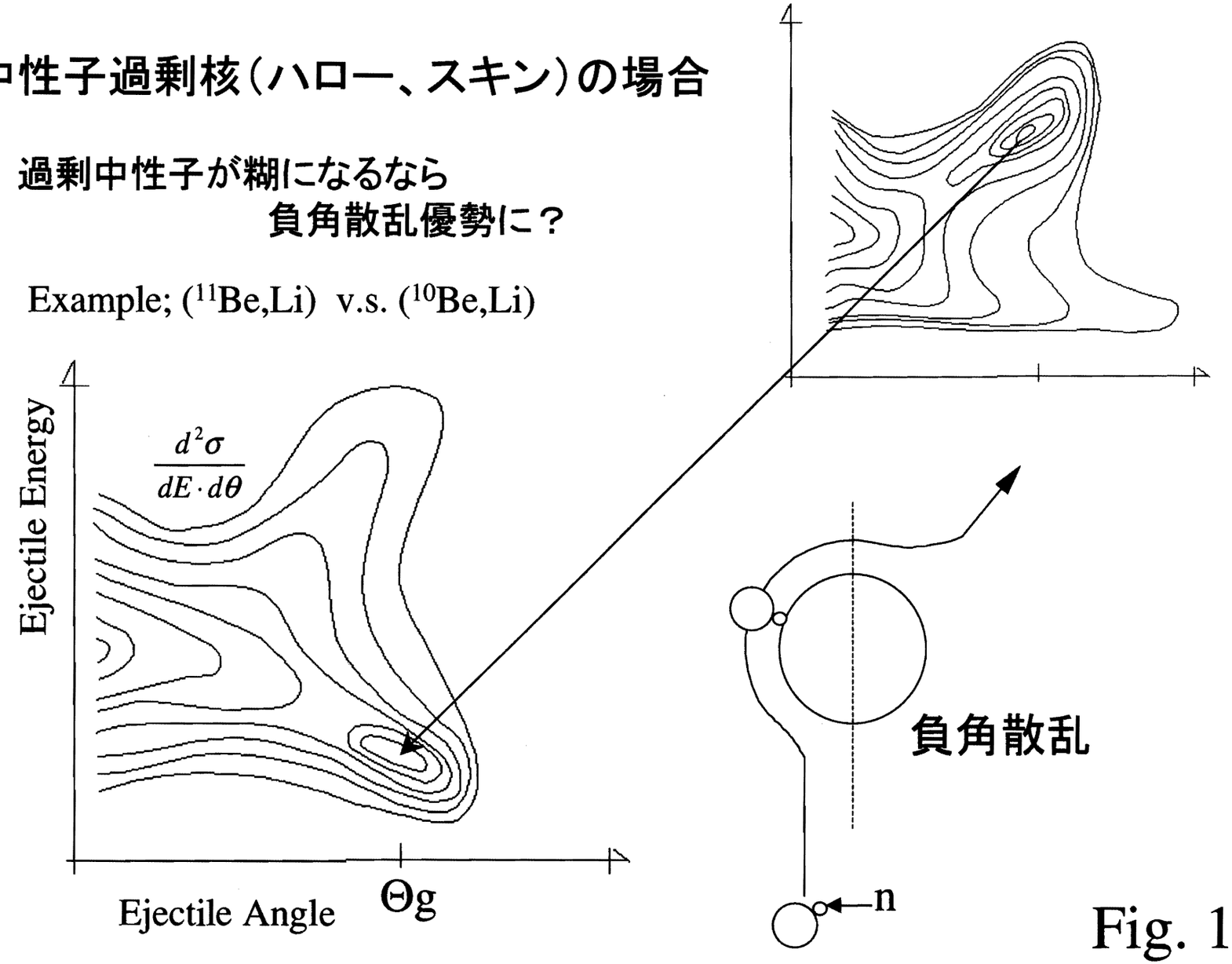

Fig. 1

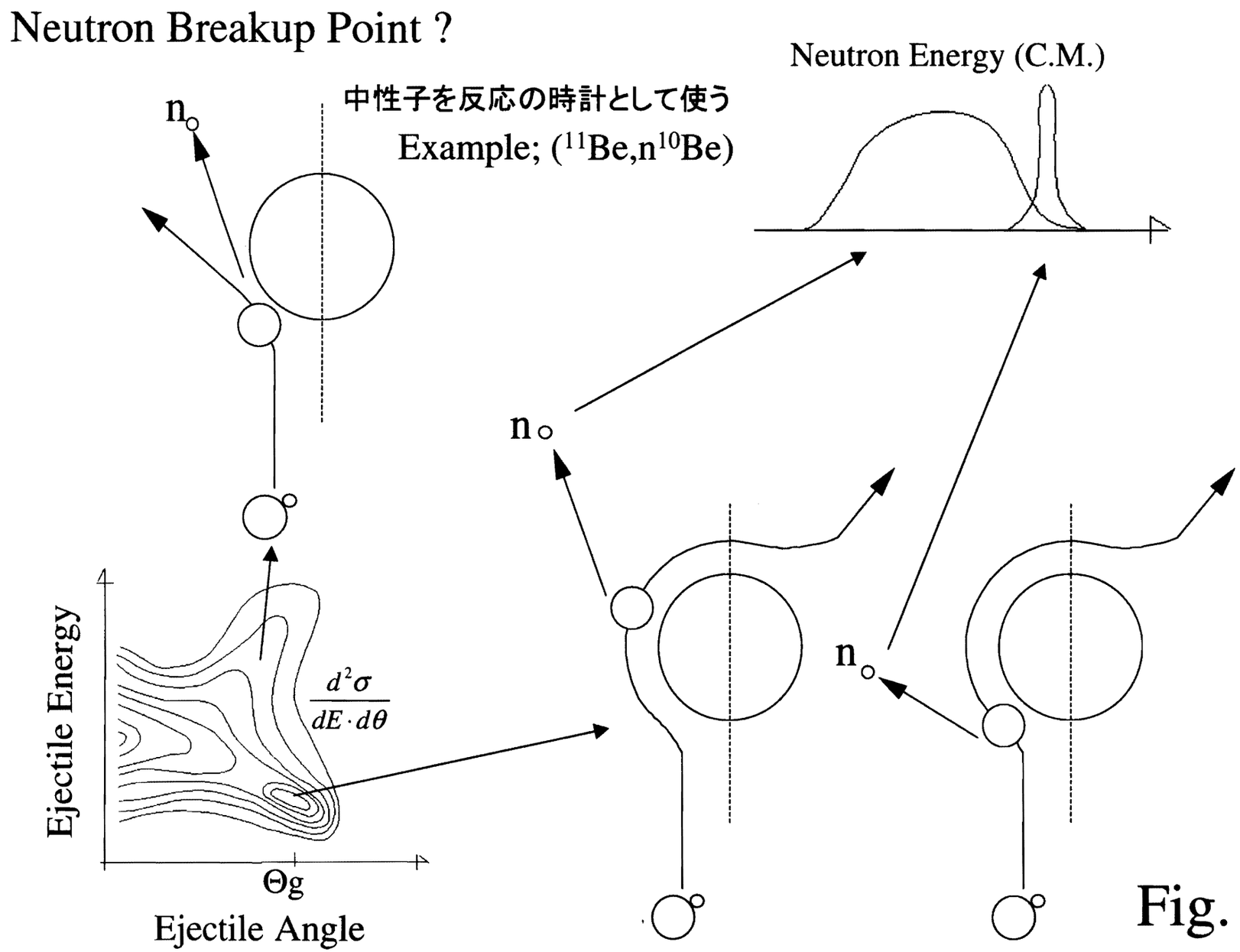
Neutron Breakup Point ?
中性子を反応の時計として使う
Example; (^{11}Be,n^{10}Be)
Neutron Energy (C.M.)
n
n
n
Ejectile Energy
$\frac{d^2\sigma}{dE \cdot d\theta}$
Θg
Ejectile Angle

Fig. 2

測定方法 (Setup Design)

$^{11}Be+^{209}Bi$ Vc ~ 40MeV
^{11}Be E_{Lab} ~ 60MeV
Θg ~ 60°

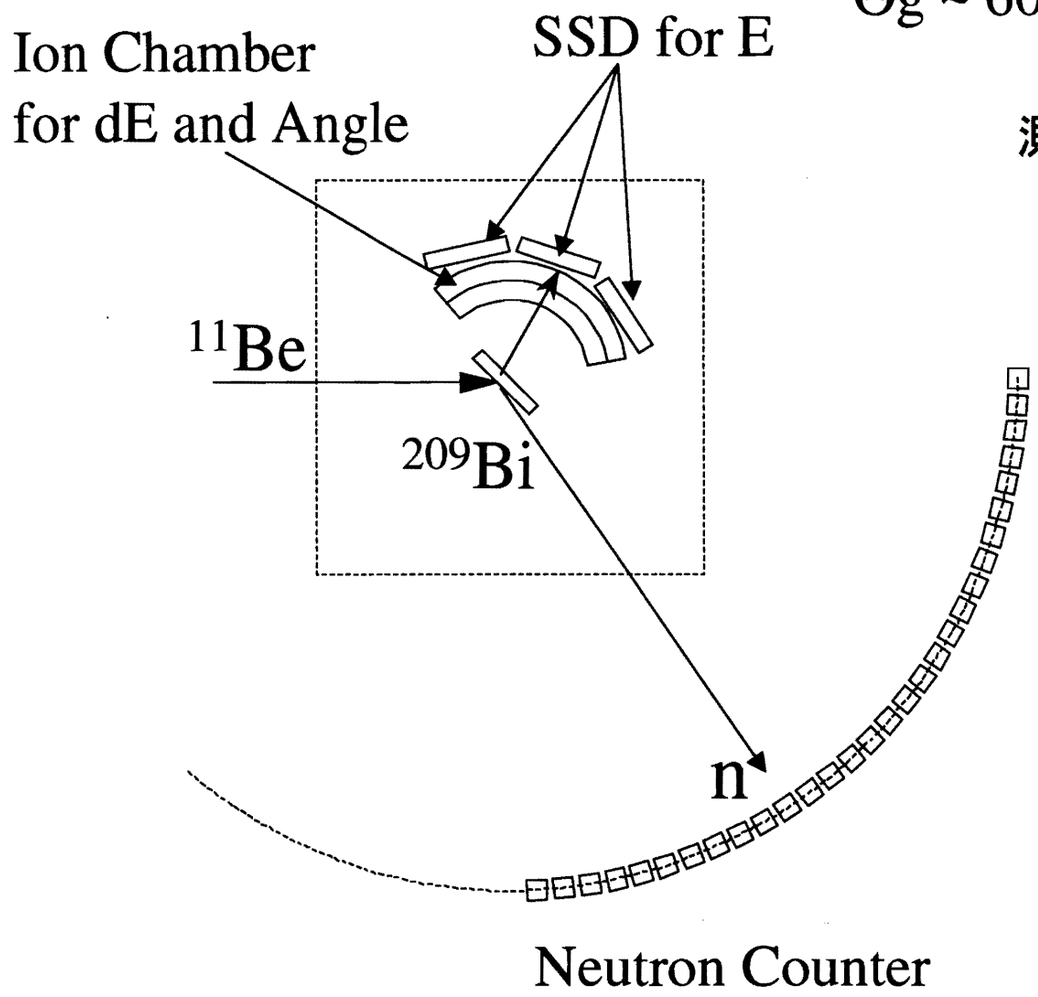

測定する反応

- Transfer Reaction
  - Neutron Transfer
  - Proton Transfer
  - A Few Nucleons Transfer
  - Massive Transfer
  - Incomplete Fusion
  - Complete Fusion (?)
- Breakup Reaction
  - Neutron Breakup

Extra; Polarization (^{11}Be,$^{12}B\uparrow$)

Fig. 3

【3】 Nuclear Astrophysics

A Trial to Measure $^{12}C + {}^{4}He \rightarrow {}^{16}O$ Reaction Rate of Astrophysical Interest in Kyushu University

S. Morinobu, K. Sagara, N. Ikeda, Y. Miwa and K. Tsuruta
Department of Physics, Faculty of Sciences, Kyushu University,
812-8581 Fukuoka, Japan

24/August/2000

Abstract

A trial to measure the $^{12}C + {}^{4}He \rightarrow {}^{16}O$ reaction rate at low energies down to $E_{c.m}$ = 700 keV has been initiated at the Kyushu University Tandem Accelerator Laboratory. A brief description is given of the project with some emphasis placed on the present status of the measurement with a new recoil separator constructed as a main device to detect ^{16}O ions.

1. $^{12}C(\alpha, \gamma)^{16}O$ reaction

The $3\alpha \rightarrow {}^{12}C$ and $^{12}C(\alpha, \gamma)^{16}O$ reactions are the main processes in the He-burning stage of a massive star. The reaction rates of these two processes determine the $^{12}C/^{16}O$ abundance ratio in the star, which has a critical importance in the subsequent stellar evolution as well as in the synthesis of heavier elements therein. Since the "triple-α" reaction rate has been estimated to the accuracy of ±15 %, experimental determination of the $^{12}C(\alpha, \gamma)^{16}O$ reaction rate with comparable accuracy is of great importance.

For the typical He-burning temperature of $\sim 2 \times 10^{8}$ K, Gamow peak locates at about $E_{c.m.}$ = 300 keV. At this low energy, the cross section of the $^{12}C(\alpha, \gamma)^{16}O$ reaction is greatly reduced by the presence of Coulomb barrier to less than 10^{-5} pb and the contributions of the subthreshold states at -45 keV (1^-) and -245 keV (2^+) in ^{16}O play important roles. At higher energies around 1 MeV, on the other hand, the cross section is dominated by the E1 radiative capture to the broad 1^- state at 2.42 MeV and by direct E2 radiative capture. As a result, the extrapolation of the experimental data down to 300 keV has been quite uncertain. Recently the E1 contribution of the subthreshold state have been estimated from the beta-delayed α spectrum of ^{16}N to the accuracy of ±26 % [1,2]. The total reaction rate, however, is still uncertain by a factor of 3 [3]. From this reason, the systematic direct measurement of the cross section with good accuracy is highly desired at energies as low as possible.

2. Kyushu plan of measurement

Most of the previous measurements on $^{12}C(\alpha, \gamma)^{16}O$ have been based on the detection of the gamma rays from the reaction. Rather poor efficiency of the gamma ray detector, however, has been a limiting factor in extending the measurement to low energy. In order to overcome the difficulty, our new trial at the Kyushu University Tandem Accelerator Facility aims at direct detection of ^{16}O, making use of the advantage of inverse kinematics.

When a ^{12}C beam is used to bombard a He target, product ^{16}O ions are emitted in a forward cone of a half angle of, for example, 1° at $E_{c.m}$ = 1 MeV. The rather small angular spread could be covered by an acceptance angle of a properly designed recoil separator, which can also serves to separate the ^{16}O ions from the high flux of the incident ^{12}C particles. The energy of ^{16}O is modulated by the recoil of the gamma ray emission in flight and hence the energy spectrum becomes a reflection of gamma ray angular distribution. This would allow the determination of relative yields of the E1 and E2 radiative capture processes.

The most important here is to efficiently separate ^{16}O ions from the incident ^{12}C beam. Our present goal is placed on measuring the reaction rate at energies down to $E_{c.m}$ = 0.7 MeV where the expected cross section is about 1 pb.

3. Instrumental developments

To make the above measurement of very small yield feasible, a ^{12}C beam of good emittance is desired at an intensity of up to 10 pμA on target. The He gas target with a thickness of about 20 μg/cm^2 should be of windowless type for not deteriorating the reaction information carried by the ^{16}O ions. The solid angle of the recoil separator is desired to be around 10 msr and a high beam rejection capability is required. To meet these requirements, instrumental developments were carried out both at accelerator and at measuring instruments.

(i) New acceleration mode

The Kyushu University tandem accelerator is optimized for operation with terminal voltages of as high as 10 MV. For a low voltage operation around 1 MV, the beam acceptance of the accelerator is about 10 times reduced, due to the ion optical mismatch between the injection beam line and the acceleration tube. The problem was solved by introducing a new acceleration method [4], in which the beam undergoes repetition of acceleration and deceleration forces. The method proved to be quite effective and the acceptance was found to be 13 times increased at low acceleration voltages of around 1 MV.

(ii) Gas charge stripper

For obtaining a high current beam of good emittance, the use of conventional C-foil charge stripper is not adequate, since the beam energy dissipation easily destroys the foil and since multiple scattering in the foil causes poor emittance and large

energy spread in the beam. A gas stripper with a large beam aperture and high gas confinement capability was specially developed [5]. With this charge stripper, the C^{1+} yield in 1 MV operation was 4 times increased and the beam emittance 2-5 times reduced relative to the case with a C-foil stripper. The reduced emittance was found to increase the transmission efficiency of the beam line by a factor of around 4.

(iii) Beam buncher

A TOF method is effective to reduce the back ground in the practical measurement and the beam pulsing technique is of considerable importance for this purpose. A two-stage beam bunching system (pre-buncher) was developed and installed in the injection beam line, to yield beam pulse width of 6 ns with a bunching efficiency of 60 % [6]. The beam chopper together with the post-buncher is currently being developed.

(iv) Overall gain in beam intensity

With these developments, the overall improvement factor for the beam intensity on target has reached 10^3 and the beam current of 10 pμA is now considered feasible within the coverage of conventional operation of the ion source.

(v) He gas target

A gas target of high gas confinement capability was developed, based on a similar concept to that of the above mentioned gas charge stripper [7]. The new gas target is 40 mm in total length and the beam aperture is 5 mm in diameter. With this compact configuration, the He thickness of 40 Torr cm or 10 $\mu g/cm^2$ was achieved for a gas consumption rate as low as a few l/hr. To further increase the target thickness, a trial to cool the He gas to liquid N_2 temperature is in progress.

(vi) Recoil separator

To efficiently separate ^{16}O ions from overwhelming flux of ^{12}C beam particles, a new recoil separator was constructed. The separator covers the whole solid angle of ^{16}O emission and the beam separation capability is now being investigated experimentally. Some details of the separator is given in the following section, together with the examples of the test measurements.

4. Test measurement with recoil separator

(i) Recoil separator

The recoil separator consists of an electrostatic deflector ED, two dipole magnets (D1, D2) and some magnetic quadrupoles and multiploes. The conceptual layout without auxiliary magnetic lenses is depicted in Fig.1. The separator has two focus points; velocity dispersive and mass non-dispersive first focus point F1 and velocity non-dispersive and mass dispersive second focus point F2. As seen in the figure, the ^{12}C beam is separated at F1, making use of the velocity difference of ^{12}C projectiles from the ^{16}O products. The ^{16}O ions are focused achromatically at F2 and other back ground particles passing F1 are deflected out by the dipole magnet D2.

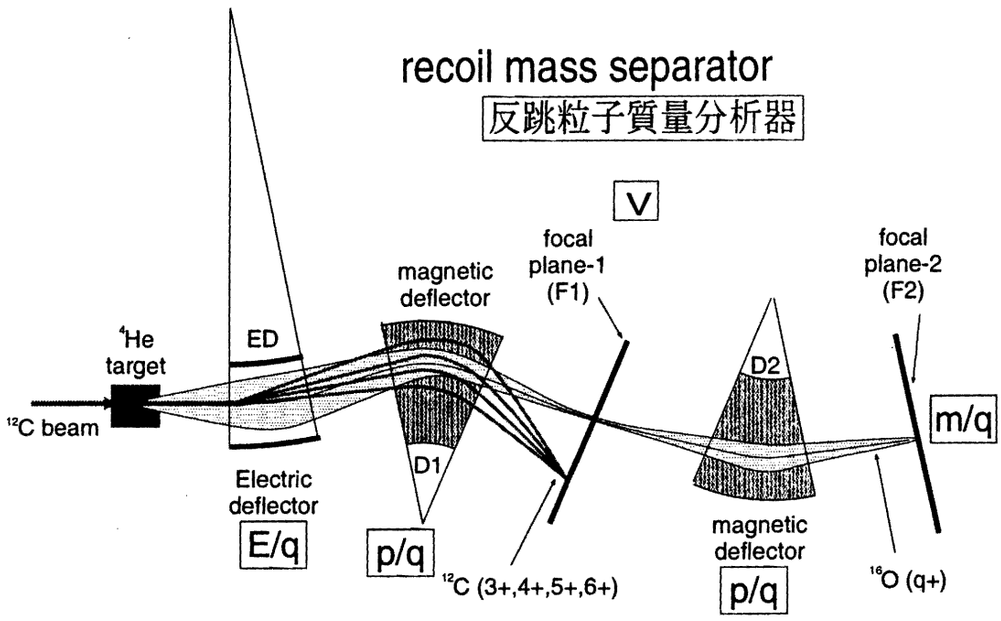

Fig.1 Conceptual layout of the recoil separator constructed for the measurement of $^{12}C(\alpha, \gamma)^{16}O$ reaction. The quadrupole and multipole lenses have been omitted.

The most important for the separator is to achieve a high beam rejection capability at the final focus point F2. Since the incident ^{12}C beam splits into several widely separated beams of different charges after passing through the electrostatic deflector ED, it is of especial importance to prevent beam scatterings on the vacuum walls from causing background at F2. For this reason, several baffles are placed on the vacuum walls with careful consideration on their locations and sizes, especially at the part between ED and D1.

(ii) Back ground measurement

Test measurement to examine the beam rejection capability was performed using a thin C foil as a target in place of He gas. In this case, the charge stripper at the terminal of the tandem accelerator was also a conventional C foil stripper. The beam emittance, therefore, was rather poor. When the ^{12}C beam was allowed to pass through the beam line, it was observed that trace amount of ^{16}O ions with an energy of 3/4 ^{12}C energy are sometimes mixed in the beam, depending on the condition of the charge stripper. Since the energy is just the expected energy for the ^{16}O product of the $^4He(^{12}C, ^{16}O)\gamma$ reaction, the admixed ^{16}O ions were used as a probe for the focusing properties of the recoil separator. A conventional position sensitive solid state detector (PSD) was placed at the F2 focus point in the examination.

Fig.2 shows the scatter plot of the detected events on particle position (vertical axis) vs. energy (horizontal axis) plane. The beam intensity was about 10 nA and the measurement was made without baffles to stop scattered particles on the vacuum

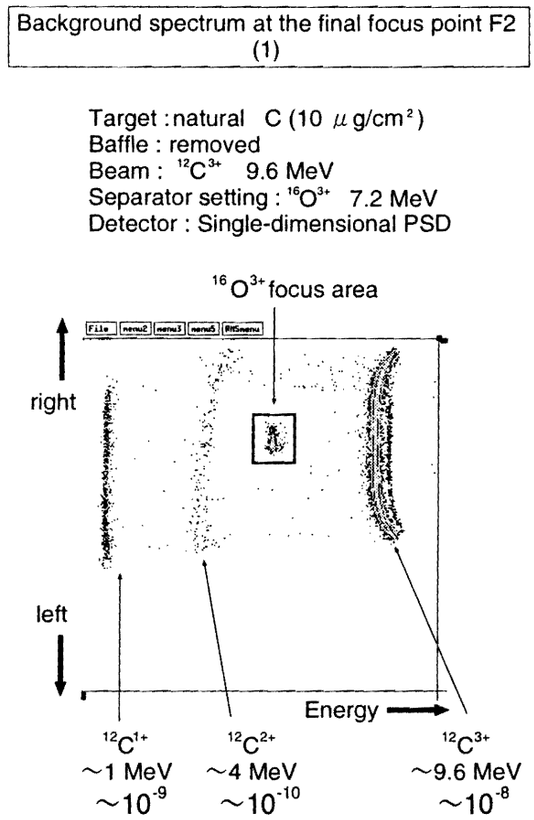

Fig.2 Back ground events observed at the F2 focus point for a target of 10 μg/cm^2 thick C foil. Baffles on the vacuum walls have been removed. The vertical axis is position of particle incidence on the detector and the abscissa is particle energy. The ^{16}O events are due to the impurity of the beam. The numbers at the bottom represent the ratios of event rates to the flux of beam particles on the target.

walls. The ^{16}O ions are seen to be successfully focused on the detector. There are three vertical loci in the figure. From the examination with different electric and magnetic field settings, it was concluded that the loci correspond, from left to right, ^{12}C particles with charges of 1+, 2+ and 3+, respectively.

Fig.3 is the similar plot observed in the measurement with the baffles installed on the vacuum walls. It is clear that the $^{12}C^{1+}$ events have completely disappeared. The $^{12}C^{2+}$ and $^{12}C^{3+}$ loci, on the other hand, still remain. By changing the strengths of the quadrupole lenses, the most intense $^{12}C^{3+}$ component was found to be able to be focused on the detector, showing that it is not due to the scattering of the beam on the walls of the separator. The ion optical consideration showed that the component is due to the charge changing reaction of the beam with the residual gas in the separator, especially in the region between ED and D1. The $^{12}C^{2+}$ locus was finally

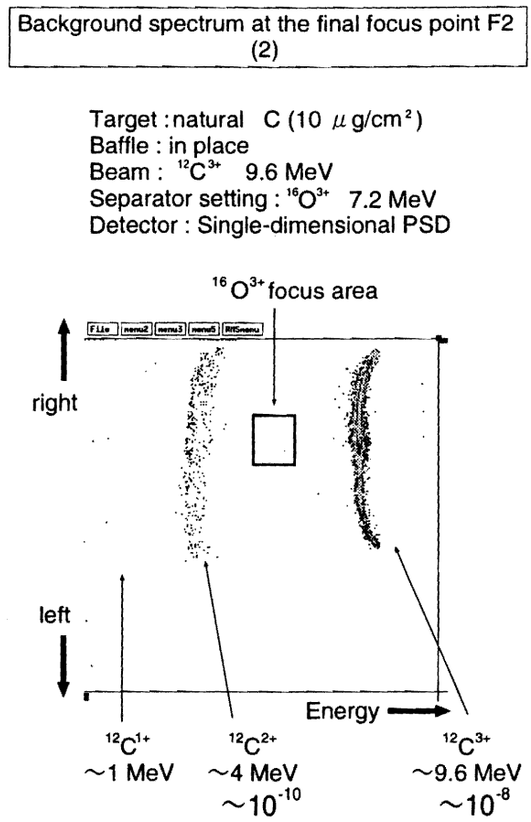

Fig.3 Back ground events observed at the F2 focus point, similar to Fig.2 except that baffles have been installed on the vacuum walls to stop scattered particle.

concluded to be due to the impurity of the beam, most probably caused by the beam scattering on the vacuum walls of the beam line.

(iii) Further reduction of the back ground

It is to be noted in both the figures that fortunately the background in the region of the ^{16}O events is not serious. In this sense, it may be concluded that the separator has an enough applicability to the measurement of the $^{4}He(^{12}C, ^{16}O)\gamma$ reaction. However, when the beam intensity is increased by three orders of magnitude in the practical measurement, the detector would seriously suffer from too high counting rates of the $^{12}C^{2+}$ and $^{12}C^{3+}$ events. To reduce the $^{12}C^{2+}$ component, the vacuum chamber in the beam-analyzing magnet is being remodeled to place the beam scattering points at larger distance from the central orbit. The beam baffles to stop the scattered beam are also to be installed in the beam line. The difficulty exists in reducing the $^{12}C^{3+}$ component which is caused by charge changing atomic collisions of the beam with the residual gas in the separator. The vacuum pressure in the separator is of the order of 10^{-7} Torr at present, and substantial improvement in the

reduction of the residual gas may be difficult. From this view point, another but small electric deflector is planned to be placed just in front of the detector, to vertically deflect ^{16}O products, preventing $^{12}C^{3+}$ ions from hitting the detector.

5. Summary and present status

A trial to measure the $^{12}C + {}^{4}He \rightarrow {}^{16}O$ reaction rate at low energies down to $E_{c.m}$ = 700 keV has been started at the Kyushu University Tandem Accelerator. It makes use of the advantage of inverse kinematics reaction to efficiently collect the reaction product of ^{16}O. The measurement has required many instrumental developments both in the tandem accelerator and in the measuring devices. The accelerator development has enabled the increase in the intensities of low energy beams by about three orders of magnitude with even better emittance than so far obtained.

The newly constructed recoil separator has shown a good capability of efficiently collecting ^{16}O ions separated from the high flux of beam particles. Some further efforts, however, are still required to reduce the back ground particles at the detector. The remodeling of the beam line and the installation of a new devices in the separator are currently in progress for this purpose. The He gas target has recently been installed in the separator and a trial to increase the target thickness is currently being continued by cooling the He gas to liquid N_2 temperature.

With all these developments made so far and being made at present, we are about to start the measurement of the $^{12}C(\alpha, \gamma)\,^{16}O$ reaction.

Reference

[1] L. Buchmann et al., Phys. Rev. Lett. 70, 726(1993)

[2] R. E. Azuma et al., Phys. Rev. C50, 1194(1994)

[3] L. Buchmann et al., Phys. Rev. C54, 393(1996)

[4] K. Sagara et al., Kyushu University Tandem Accelerator Laboratory Report 7, 146(2000)

[5] M. Nakamura et al., Kyushu University Tandem Accelerator Laboratory Report 7, 143(2000)

[6] Y. Tsubusaki et al., Kyushu University Tandem Accelerator Laboratory Report 7, 151(2000)

[7] K. Sagara et al., Nucl. Instr. and Meth. A 378, 392(1996)

Screening effects by bound electrons in nuclear reactions at extremely low energies

Noboru Takigawa, * and Sachie Kimura †
Department of Physics, Tohoku University, Sendai 980-8578, Japan

We discuss the screening effects by bound electrons in the target nucleus on nuclear reactions at extremely low energies in laboratories based on a semiclassical mean field theory for quantum tunneling. Taking D+^{3}He and ^{3}He$^+$+d reactions as examples, we show that the screening potential significantly varies under the tunneling barrier contrary to what is often assumed in literatures, and that the variation is especially drastic in the D+^{3}He reaction, where the bound electron initially occupies an excited state of the total system due to the large non-adiabatic transition to the lowest state stimulated by the enhancement of the tunneling probability. We suggest that the screening energy can exceed the simple minded adiabatic limit given by the difference of the binding energies of the electrons in the target and the united atom. Comments on the screening effects in the sun are also added.

I. INTRODUCTION

Nuclear reactions at extremely low energies are interesting subjects for their own sake and also to extract informations on nucleosynthesis in stars. The cross section for such reactions is usually discussed in terms of the astrophysical factor S. The discovery that the measured S factor at low energies is systematically larger than the extrapolated value from high energy data has stimulated many experimental as well as theoretical studies. Most of them are attributing this enhancement of the reaction cross section to the screening effect by the target electrons. One interesting observation is that the screening energy obtained by fitting the data exceeds the value in the adiabatic limit , which is supposed to give the upper bound. For example, they are 130 eV and 119 eV, respectively for ^{3}He(d,p)^{4}He reactions [1] and 323±51 eV and 240 eV for ^{3}He(^{3}He,2p)^{4}He reactions [2]. In this connection, however, we wish to stress that the adiabatic limit used in literatures are not the true adiabatic limit, which can never be exceeded [3], but the simple minded adiabatic limit, which is the difference of the binding energy of electrons in the target and in the united atom.

Though the huge screening energy reported in the first generation experiments using gas target has later been modified to a somewhat smaller value by correcting the estimate of the stopping power, the remaining screening energy is still larger than the simple minded adiabatic limit for all systems experimentally so far studied [4]. Among many theoretical attempts to understand this puzzling phenomenon, the series of works by Koonin, Langanke and their coworkers are the most advanced [5,1]. They determined the time evolution of the relative motion between the two reacting nuclei and the electronic cloud in a coupled way, and drew the following conclusions: (1) The resultant screening energy agrees with that estimated in the fast tunneling limit at high energies. (2) It agrees with the estimate of the simple minded adiabatic limit at low energies. (3) Non-adaiabatic effects are important for intermediate cases.

Refs. [5,1] treated only the classically allowed region and identified the screening energy with the work done by the interaction between the electrons and nuclei in approaching from infinity to the classical turning point. This is based on the assumption that the screening potential is constant under the tunneling barrier in common with all the phenomenological data analyses. However, this will be correct only when the tunneling region is much smaller than the spatial extension of the electrons in the ground state of the united atom. Also, as will be remarked later, Refs. [5,1] ignore the change of the intrinsic energy of the electrons, i.e. the expectation value of the unperturbed Hamiltonian of electrons, caused by the change of their wave function on the way of collision.

*E-mail address: takigawa@nucl.phys.tohoku.ac.jp
†E-mail address: sachie@nucl.phys.tohoku.ac.jp

In this work, we discuss the validity of the assumption of a constant shift of the fusion barrier. We also discuss the dependence on the initial state of the electrons. Our interest is to find out whether some extraordinary effect arises if the electrons initially occupy an excited state instead of the ground state in the sense of the united atom. To this end, we use a semiclassical mean field theory [6], which can be applied to describing the coupling between the relative motion of the colliding nuclei and the electrons in both classical and tunneling regions. Numerical calculations will be performed for the D+^{3}He and ^{3}He$^+$+d reactions. The former suits the study of the second question raised above, because the electron occupies the 2nd excited state in the sense of the united atom at the beginning of the reaction. The latter is the counter system, where the electron occupies the ground state of not only the target atom, but also of the united atom at the beginning of the reaction. These systems have been chosen to demonstrate the novel aspects of the screening phenomenon which we clarify in this work with a relatively light numerical load. The analyses of actual data will be reported in forthcoming papers.

II. THEORETICAL FRAMEWORK

A. Brief survey of basic formulae

Let us first survey some basic formulae. The S factor is defined by

$$\sigma(E) = S(E)E^{-1}exp(-2\pi\eta) \tag{1}$$

where the exponential factor is called the Gamow factor, and $\eta = Z_T Z_P e^2/\hbar v$ is the Sommerfeld parameter. We define the enhancement factor f as the ratio of the true cross section $\sigma(E)$ to the bare cross section $\sigma_0(E)$ in the absence of screening electrons

$$f = \frac{\sigma(E)}{\sigma_0(E)} \tag{2}$$

In almost all analyses, one assumes that the effects of screening can be represented by a constant lowering of the potential barrier. This shift is called the screening energy, which we denote by U_e. Further assuming that the major energy dependence originates from the Gamow factor in eq.(1), we obtain

$$\begin{aligned} f &= \frac{\sigma_0(E+U_e)}{\sigma_0(E)} \\ &\sim exp\{\pi\eta(E)\frac{U_e}{E}\} \end{aligned} \tag{3}$$

Eq.(3) is often used in data analyses. Contrary to this standard procedure, we do not presume that the effects of electrons can be expressed by a constant shift of the potential barrier. Instead, we calculate the fusion probability by the method to be described later. We then convert the enhancement of the reaction cross section to the language of the screening energy by

$$U_e \equiv \frac{E}{\pi\eta(E)}logf = \frac{E}{\pi\eta(E)}log(\frac{\sigma(E)}{\sigma_0(E)}) \tag{4}$$

In actual calculations, we approximate the ratio of the cross section by the ratio of the tunneling probability in the s-wave scattering with and without screening effects.

The following two analytic expressions of the screening energy often appear in literatures:

$$U_e^{(AD;0)} = \epsilon^T_{g.s.} - \epsilon^{UA}_{g.s.} \tag{5}$$

$$U_e^{(F;1s)} \sim 2Z_T Z_P \times 13.6eV \tag{6}$$

where $\epsilon^T_{g.s.}$ and $\epsilon^{UA}_{g.s.}$ are the binding energy of the electrons in the target and united atoms, respectively. The upper indices AD and F stand for the adiabatic and fast tunneling limits, respectively. As we remarked in the introduction, eq.(5) is not the true adiabatic limit, though it is the formula which one

often uses for that quantity. That is why we added (0) in the upper index. Also, eq.(5) presumes the case, where electrons occupy the ground state also in the sense of united atom at the beginning of the reaction. More generally, one should replace the r.h.s. of eq.(5) by the difference of the binding energies at $R \to \infty$ and $R \to 0$, R being the separation distance between the projectile and target, of the state with the same numbering level in the adiabatic basis. Eq.(6) is valid when the electrons initially occupy the 1s state of the target atom. That is the origin of the upper index 1s. The formula also requires that the tunneling region is much smaller than the Bohr radius of the target electrons.

B. Semiclassical mean field theory

We freeze the intrinsic degrees of freedom of the colliding nuclei. The problem then reduces to a three body problem for our examples, whose coordinates are taken to be the standard Jacobi coordinates (see Fig.1). It is straightforward to generalize to the case, where there are more than one screening electrons. The coordinate of the relative motion between the nuclei R is the macroscopic coordinate, which undergoes a quantum tunneling, while the degrees of freedom of electrons ξ represent the environmental degrees of freedom.

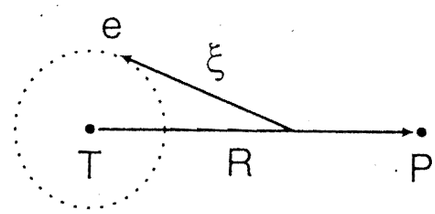

Figure 1: Jacobi coordinates

We describe the time evolution in the classical region by the following coupled equations,

$$i\hbar\frac{\partial\phi(\xi,t)}{\partial t} = [H_0(\xi) + V_c(R(t),\xi)]\,\phi(\xi,t), \tag{7}$$

$$M\frac{d^2}{dt^2}R(t) = -\frac{d}{dR}\left[V^{(0)}(R) + \Delta V(R)\right], \tag{8}$$

$$\Delta V(R) = <\phi(t)|\left[H_0(\xi) + V_c(R(t),\xi)\right]|\phi(t)>, \tag{9}$$

$$\frac{1}{2}M(\frac{dR(t)}{dt})^2 + V^{(0)}(R(t)) + \Delta V(R(t)) = E, \tag{10}$$

where $\phi(\xi,t)$ and $H_0(\xi)$ are the wave function and the unperturbed Hamiltonian of the electrons, $V_c(R,\xi)$ the interaction between the electrons and nuclei. In order to solve eq.(7), one needs to know $R(t)$, which is determined by the Newtonian eq.(8), where the interaction potential consists of the sum of the bare interaction potential between the colliding nuclei $V^{(0)}(R)$ and the screening potential by electrons $\Delta V(R)$, which is given by eq.(9). These equations are solved in a coupled way, and guarantees the energy conservation as given by eq.(10). They are identical with those in [5]. They can be derived from the original time dependent Schrödinger equation for the total system by a variational principle based on the assumption that the total wave function is given by the product of the wave functions for the relative motion and for the electronic degrees of freedom, and further treating the relative motion classically.

We start to solve these coupled equations with the scattering boundary condition until the relative motion encounters the potential barrier, i.e. until the speed of the relative motion becomes zero. We then proceed along the negative imaginary time axis by setting t=-iτ to describe the time evolution in the tunneling region. The equations corresponding to eqs.(7) through (10) in the tunneling region read

$$\hbar\frac{\partial\phi(\xi,\tau)}{\partial\tau} = -\left[H_0(\xi) + V_c(R(\tau),\xi)\right]\phi(\xi,\tau), \tag{11}$$

$$M\frac{d^2}{d\tau^2}R(\tau) = \frac{d}{dR}\left[V^{(0)}(R) + \Delta V(R)\right], \tag{12}$$

$$\Delta V(R(\tau))) = \frac{<\phi(\tau)|\left[H_0(\xi) + V_c(R(\tau),\xi)\right]|\phi(\tau)>}{<\phi(\tau)|\phi(\tau)>}, \tag{13}$$

$$-\frac{1}{2}M(\frac{dR(\tau)}{d\tau})^2 + V^{(0)}(R(\tau)) + \Delta V(R(\tau)) = E. \tag{14}$$

A remark would be worth being given for these equations. The theory to describe quantum tunneling of a system with many degrees of freedom, or of quantum tunneling of a macroscopic variable in the presence of environments, has not yet been established. The fully quantum mechanical mean field theory of real time suffers from the problem of a spurious correlation in describing tunneling phenomena, because the major component, i.e. the reflected component, will strongly influence the minor, i.e. the tunneling, component. On the other hand, the use of the imaginary time is a standard method to describe tunneling phenomena, and has been mathematically founded in [7] based on the path integral method for a one-dimensional problem. Though solid foundation is still missing for the quantum tunneling in the system with many degrees of freedom, this method is attractive, because one can hope that the imaginary time converts the tunneling component into the major component reducing the problem of the spurious correlation. In [3], one of the authors presented a practical method, named the dynamical norm method, where one first calculates the tunneling rate for the effective potential including the static potential renormalization in the adiabatic limit by the imaginary time method, and then takes the non-adiabatic effects into account through the reduction of the norm of the environmental space during the tunneling process. We show in [6] that the dynamical norm method is equivalent to eqs.(11) through (14).

III. NUMERICAL RESULTS FOR THE SCREENING POTENTIAL AND ENERGY

Once eqs.(11) through (14) have been solved until the end of the tunneling procedure, i.e. until the speed of the relative motion again gets zero, we calculate the tunneling probability by

$$P(E) = exp\Big(\frac{-4}{\hbar}\int_{\tau_a}^{\tau_b} d\tau[V^{(0)}(R(\tau)) - E]\Big)exp\Big(\frac{-4}{\hbar}\int_{\tau_a}^{\tau_b} d\tau\Delta V((R(\tau)))\Big) \tag{15}$$

where $\tau_a = 0$ and τ_b the tunneling time. The corresponding screening energy is then calculated by

$$U_e = \frac{E}{\pi\eta(E)}log\Big(\frac{P(E)}{P_0(E)}\Big) \tag{16}$$

where $P_0(E)$ is the tunneling probability in the absence of the screening electrons.

The screening energy thus defined agrees with the value of the screening potential at the outer classical turning point if the screening potential does not change in the tunneling region,

$$U_e^{CS} = -\Delta V(R(\tau_a)). \tag{17}$$

As already mentioned, on the other hand, [5,1] used a slightly different definition of the screening energy,

$$U_e^{CS(IP)} = -\int_{\infty}^{R(\tau_a)} dR\frac{\partial}{\partial R} < \phi(R(t))|V_c(R(t),\xi)|\phi(R(t)) > . \tag{18}$$

In eqs.(17) and (18) the upper indices CS and IP stand for the constant-shift and the work of the interaction-potential-only. The difference between U_e^{CS} and $U_e^{CS(IP)}$ is the work done by the unperturbed Hamiltonian of electrons in the approach phase from infinity to the external turning point.

Figs.2 and 3 show the screening potential $\Delta V(R)$ as a function of the separation distance R for D+^{3}He and ^{3}He$^+$+d reactions, respectively. The scale of R is the atomic unit along the bottom abscissa and Å along the top abscissa, while that of $\Delta V(R)$ is the atomic and eV units along the left and right axes, respectively. The incident energy is 0.025 keV in the center of mass system in both cases. The outer classical turning point is around 1 Å for the D+^{3}He reaction, while it is marked by the filled triangle for the ^{3}He$^+$+d reaction. We notice that the screening potential is not constant in the tunneling region in both systems. We also notice a drastic increase of the screening potential soon after the system enters into the tunneling region in the D+^{3}He reaction. The time evolution of the density profile of the electron shows that this drastic increase of the screening potential is caused by the non-adiabatic transition of the electron to the lowest state.

Figs.4 and 5 compare the screening energy calculated by the present method using eqs.(15) and (16) (the filled circles) and by eq.(17) of the constant shift approximation (the open squares). We notice that the former gives systematically larger screening energy than the latter.

Figs.2 through 5 suggest that one should properly treat the tunneling region in order to have a correct understanding of the screening effects and to extract the correct bare reaction rate.

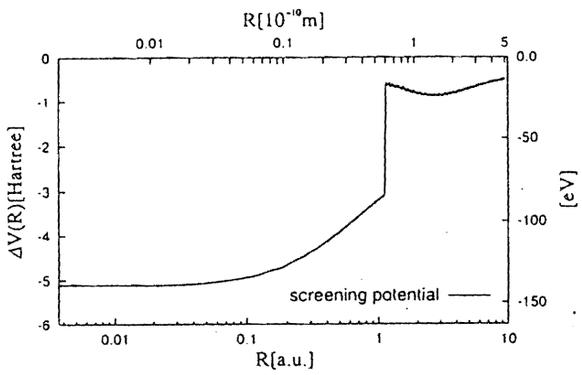

Fig.2 The screening potential as a function of the distance between the projectile and target nuclei for the D+^{3}He reaction.

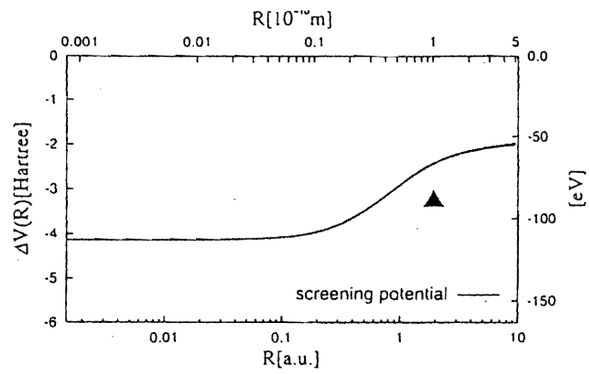

Fig.3 The same as Fig.2, but for the ^{3}He$^+$+d reaction.

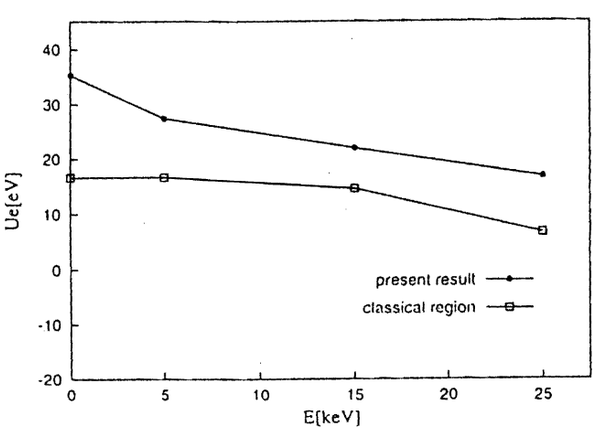

Fig.4 The screening energy as a function of the bombarding energy for the D+^{3}He reaction.

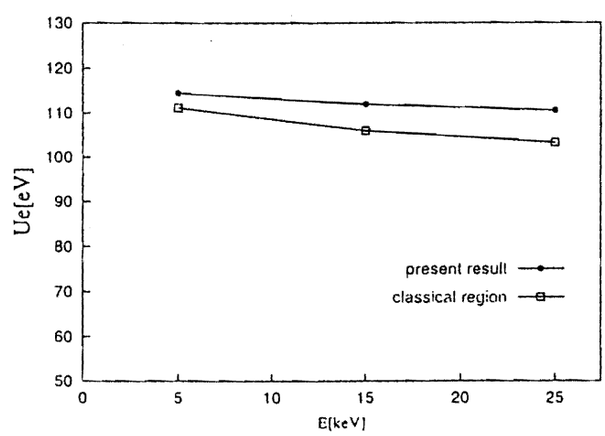

Fig.5 The same as Fig.4, but for the ^{3}He$^+$+d reaction.

IV. COMMENTS ON THE SCREENING EFFECTS IN THE SUN

Finally we wish to comment on the screening effects in the sun. The temperature in the solar interior where the ^{7}Be(p,γ)^{8}B reaction, the key reaction of the solar neutrino problem, is most active is about 15×10^6 K. The corresponding Gamow peak energy and the outer turning point for this reaction are 18 keV and 0.003 Å, respectively. One interesting question is whether the screening effects by bound electrons which we discussed in this contribution has any relevance to this reaction in the sun. In this connection, we wish to refer to ref. [8], where the authors argue that the screening by K shell electrons enhance the rate of this reaction in the sun as large as 10-20 %. It would be interesting to study the screening effects by bound electrons on this reaction in the light of the present study, i.e. to elucidate the role of the tunneling region and also to study the effects of non-adiabatic transition from excited states to lower states during the tunneling procedure. The latter is especially interesting, because many electrons will be occupying excited bound states following the Boltzmann distribution at this temperature.

A more standard screening in stars is the screening by free electrons and ions. In the case of weak screening, it leads to the following well known formula for the screened Coulomb potential,

$$V(R) \sim Z_a Z_b e^2 \frac{e^{-\kappa R}}{R} \sim Z_a Z_b e^2 \frac{1}{R} - Z_a Z_b e^2 \kappa + \cdots \tag{19}$$

where κ, the inverse of the Debye-Hückel radius, is given by

$$\kappa^2 \sim \frac{e^2}{kT} \sum Z^2 \bar{n} \cdots \tag{20}$$

Using the parameters relevant to the solar interior [8,9], the enhancement factor of the ^{7}Be(p,γ)^{8}B reaction by the screening effects of free electrons and ions are estimated to be of the order of 10-20 % similarly to that by bound electrons.

This is concerned with the electrostatic screening. Though the dynamical effect, which was advocated first in [10], has been claimed to be small [11], it would be quite interesting to reexamine it for the tunneling region. This is because, for example, the adiabaticity condition is quite different in classical and tunneling regions.

ACKNOWLEDGMENTS

We wish to thank Profs. D.M. Brink, J. Arafune, K. Sato, T. Itabashi and Dr. K. Hagino for useful discussions.

---

[1] K. Langanke et al., Phys. Letts. B369(1996) 211.
[2] M. Junker et al., Phys. Rev. C57(1998) 2700.
[3] N. Takigawa et al., Phys. Rev. C 51(1995) 187.
[4] C. Rolfs et al., Nucl. Inst. Methods, B99 (1995) 297.
[5] T.D. Shoppa et al., Phys. Rev. C48(1993) 837.
[6] N. Takigawa, S. Kimura, K. Hagino and D. Brink, to be published.
[7] D.M. Brink and U. Smilansky, Nucl. Phys. A405(1983) 301.
[8] V.B. Belyaev et al., Phys. Letts. A247(1998) 241.
[9] A.V. Gruzinov and J.N. Bahcall, Astrophys. J. 504(1998) 996.
[10] C. Carraro, A. Schäfer and S.E. Koonin, Astrophys. J. 331(1988) 565.
[11] E.G. Adelberger et al., Rev. Mod. Phys. 70(1998) 1265.

Nuclear Astrophysics with Laser-induced Inverse Compton γ Rays

(逆コンプトンγ線による天体核物理研究)

H. Utsunomiya

Department of Physics, Konan University, Okamoto 8-9-1, Higashinada, Kobe 658-8501, Japan

Abstract

The usage of laser-induced inverse Compton γ rays in the field of nuclear astrophysics is discussed. An application to the measurement of photoneutron cross sections on ^{9}Be is demonstrated in conjunction with the nucleosynthesis in the neutrino-driven wind of core-collapse supernovae. Further applications to the γ-process as the origin of the p-nuclei as well as some interesting cases are discussed.

1. LASER-INDUCED INVERSE COMPTON (LIC) γ rays

γ rays of 1 – 40 MeV have become available at the Electrotechnical Laboratory (ETL) in the form of a pencil-like beam with a flux of $\sim 10^4$ photons /(sec mm^2) and energy spread of a few % in FWHM below 9 MeV [1]. The quasi-monochromatic γ rays are produced by inverse Compton scattering of Nd:YLF laser photons incident on relativistic electrons in the accumulator ring TERAS. The γ-ray energy can be varied by changing the electron energy. The feature of this type of γ source is that 1) it is energy-variable compared with radioactive isotopes; 2) it provides better energy resolution compared with the Bremsstrahlung; and 3) it is free from the Bremsstrahlung component compared with the positron annihilation in flight.

2. MEASUREMENT OF ^{9}Be(γ,n)αα CROSS SECTIONS

The LIC γ rays were used to measure photoneutron cross sections of ^{9}Be(γ,n)αα in the excitation energy region from 1.78 to 6.11 MeV [2]. The inverse reaction, α(αn,γ)^{9}Be, occurs in the neutrino-driven wind of core-collapse supernovae as a first step of the reaction network [3]. Resonance parameters (E_R, B(E1), Γ_n) for the $1/2^+$ and $5/2^+$ states were deduced from the least-squares fit to the data, while Γ_γ for the $5/2^-$ state was deduced from the energy-integrated cross section. The reaction rate for α(αn,γ)^{9}Be was evaluated based on the resonant contribution to the reaction $\alpha + \alpha \Leftrightarrow {}^8$Be with $\Gamma_\alpha(^8\mathrm{Be}) = 6.8 \pm 1.7$ eV. This resonant condition is known to hold at $T > 2.8 \times 10^7$ K. The photoneutron cross sections were converted to radiative capture cross sections for $n + {}^8\mathrm{Be} \rightarrow {}^9\mathrm{Be} + \gamma$ by the detailed balance theorem.

The present reaction rate was compared with those in the CF88 [4] and NACRE [5] compilations. It was found that the rate of the NACRE compilation is rather consistent with the present rate, while

the CF88 rate needs to be modified considerably in both temperature dependence and absolute magnitude.

3. STUDY OF THE ORIGIN OF THE P-NUCLEI

The origin of approximately 30 neutron-deficient stable nuclei with low abundances of 0.01 – 1 % that cannot be produced by neutron capture is not known [6]. Photodisintegration of the s- and r-process nuclei and proton capture are possible reaction mechanisms. A possible site is the O/Ne rich-layer in type II supernovae [7]. (γ,n) reactions take place in a narrow energy window defined by the product of the Planck distribution for a thermal photon bath and the photoneutron cross section. The energy window for the (γ,n) reactions is in good contrast with the Gamow window for non-resonant charged-particle reactions [8]. It lies just above neutron thresholds with a typical width of $\sim$ 1 MeV. Thus, cross sections in the low-energy tail of the E1 giant resonance play an important role in producing the p-nuclei.

The activation technique with the Bremsstrahlung is being used at Technishe Universität Darmstadt for determining (γ,n) reaction rates for the p-nuclei [8]. The quasi-monochromatic LIC γ rays at ETL can be used to directly measure (γ,n) cross sections near the neutron thresholds. An example of such measurements is ^{139}La(γ,n)^{138}La(γ,n)^{137}La [7], where both the production cross section (^{139}La(γ,n)^{138}La) and the destruction cross section (^{138}La(γ,n)^{137}La) for the p-nucleus ^{138}La need to be measured. Another example is ^{181}Ta(γ,n)^{180}Ta, where the branchings of ^{181}Ta in the narrow energy window to the nature's rarest element ^{180}Ta(9^-) with a lifetime > 10^{15} y and the ground state of ^{180}Ta with a lifetime of 8.1 h need to be determined.

4. OTHER APPLICATIONS

Some of other applications are related to the big bang nucleosynthesis p(n,γ)D and the cosmochronometer ^{188}Os(γ,n)^{187}Os. In the latter, the determination of the branchings to the first excited state ^{187}Os(9.8 keV) [9,10] and the ground state will be a big challenge to nuclear experimentalists.

References

[1] H. Ohgaki *et al.*, IEEE Tran. Nucl. Sci. **38**, 386 (1991).
[2] H. Utsunomiya *et al.*, Phys. Rev. C, in press.
[3] S.E. Woosley and R.D. Hoffman, Astrophys. J. **395**, 202 (1992).
[4] G.R. Caughlan and W.A. Fowler, Atomic Data and Nuclear Data Tables **40**, 283 (1988).
[5] C. Angulo *et al.*, Nucl. Phys. **A656**, 3 (1999).
[6] D.L. Lambert, Astron. Astrophys. Rev. **3**, 201 (1992).
[7] V. Costa *et al.*, Astro. Astrophys. **358**, L67 (2000).
[8] P. Mohr *et al.*, Phys. Lett. B, in press.
[9] S.E. Woosley and W.A. Fowler, Astrophys. J. **233**, 411 (1979).
[10] R.R. Winters *et al.*, Phys. Rev. **C34**, 840 (1986).

Experiment

@ ETL: Electrotechnical Lab.

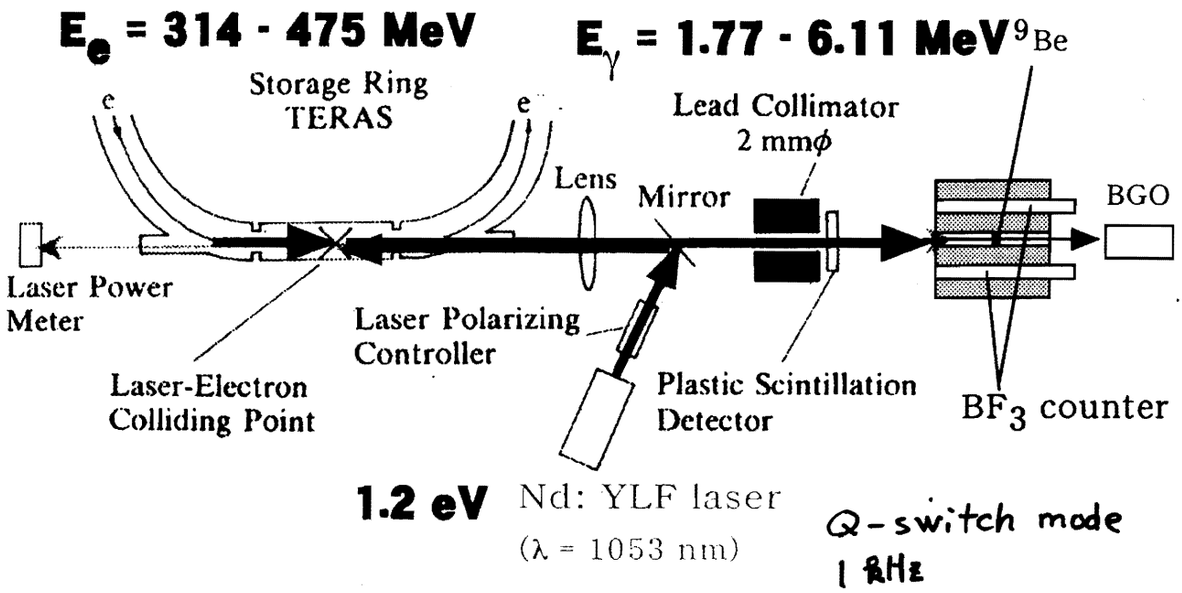

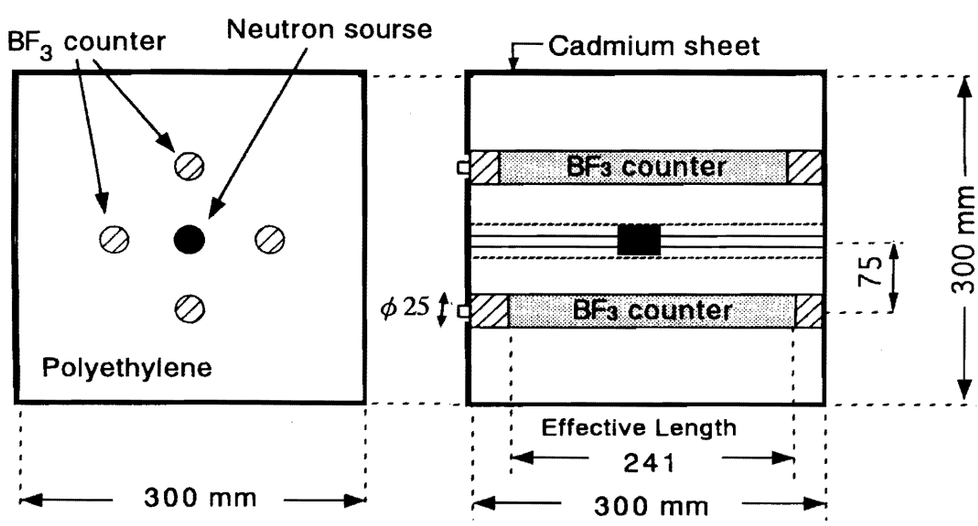

Neutrino-Driven Windとは？

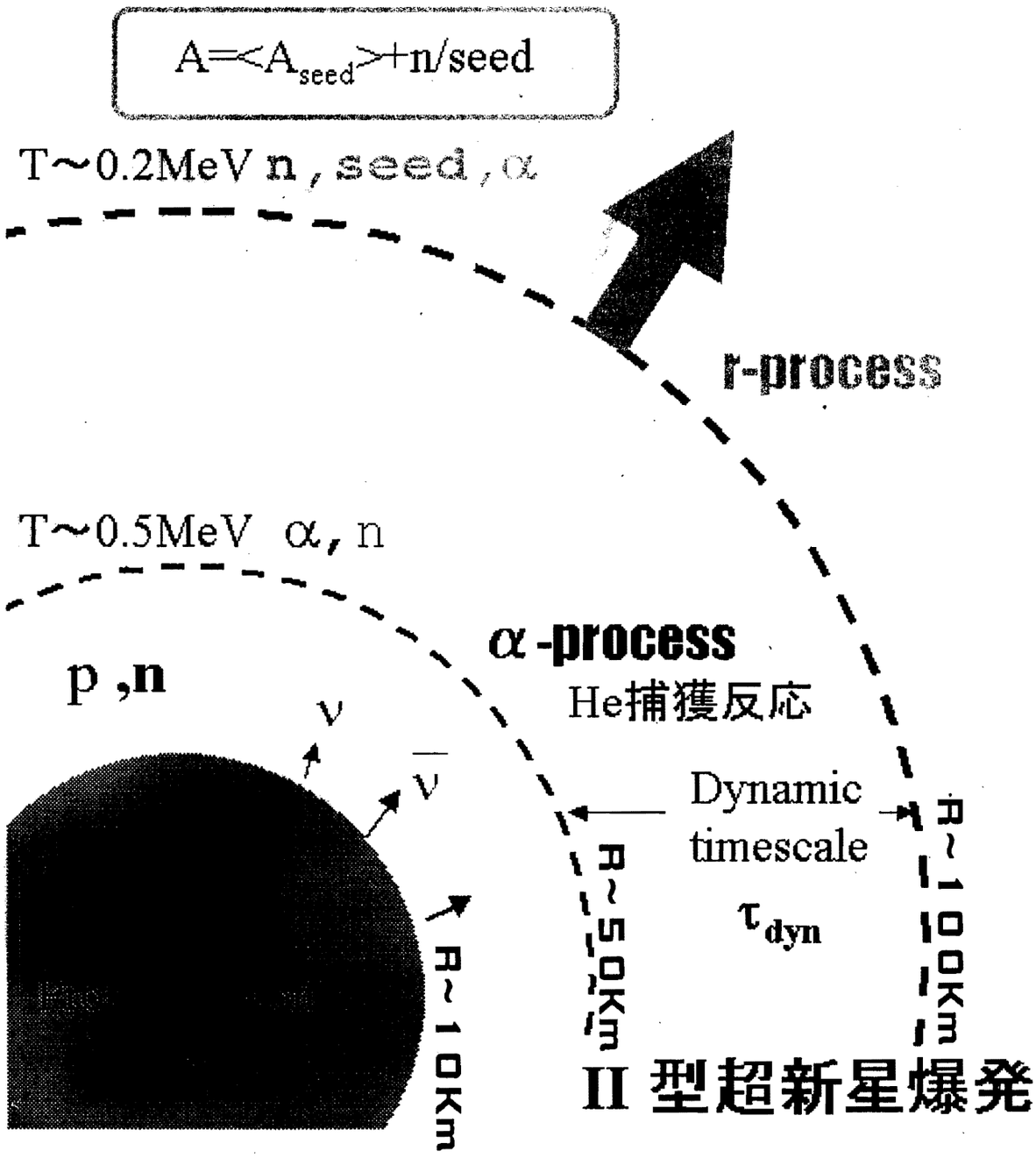

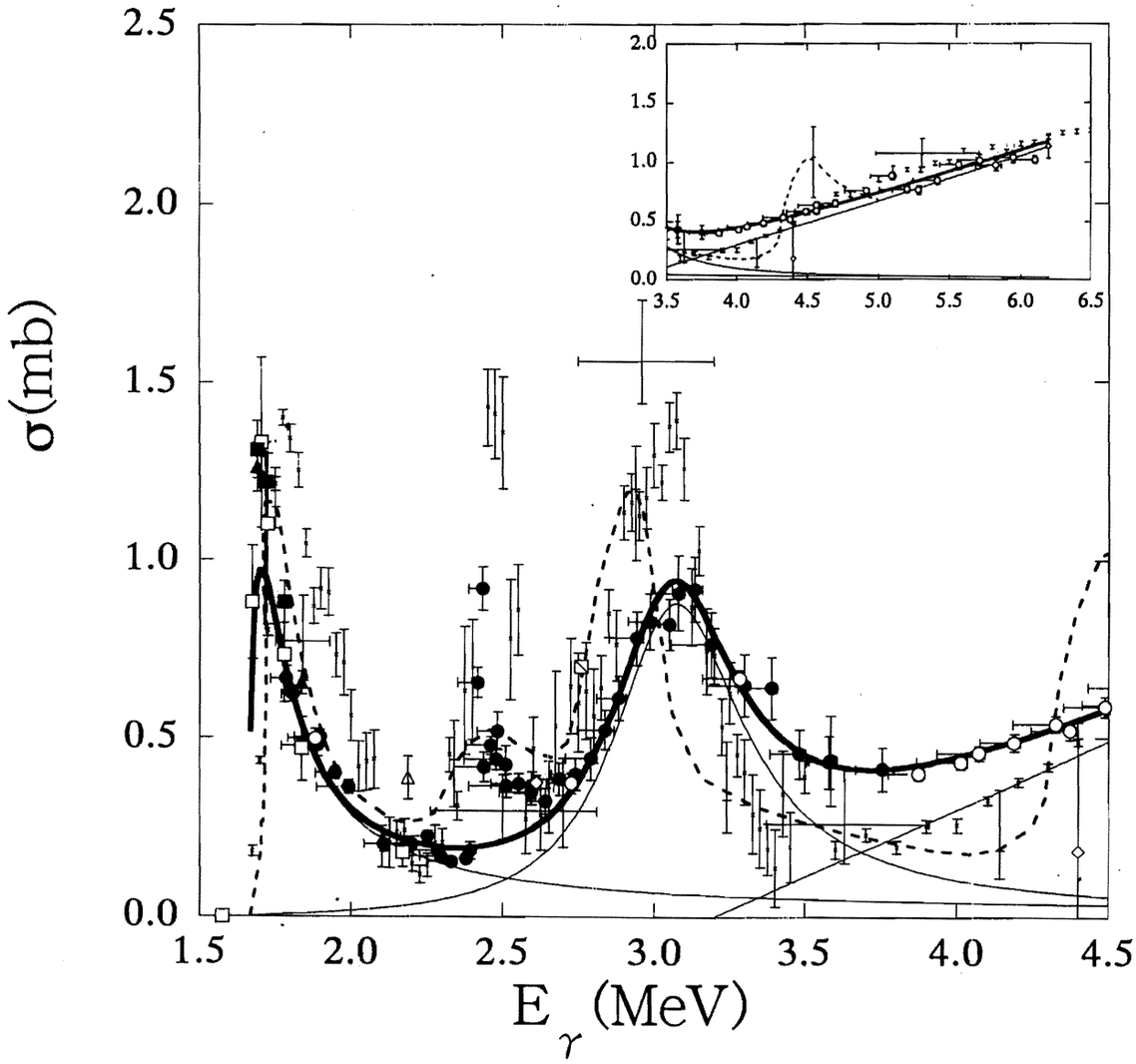
σ(mb)
2.5
2.0
1.5
1.0
0.5
0.0
1.5
2.0
2.5
3.0
3.5
4.0
4.5
E γ (MeV)
2.0
1.5
1.0
0.5
0.0
3.5
4.0
4.5
5.0
5.5
6.0
6.5

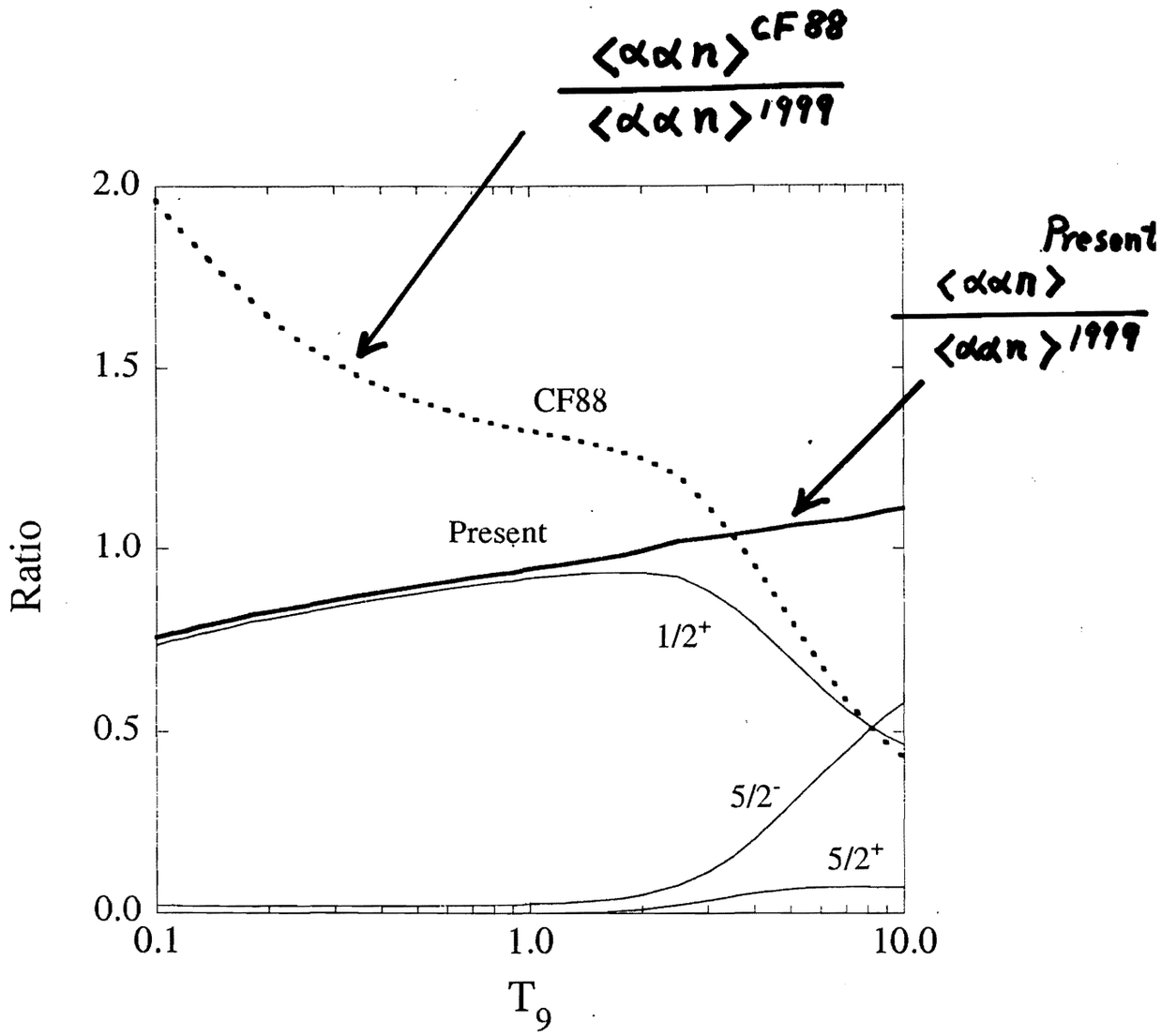
$\frac{\langle\alpha\alpha n\rangle^{CF88}}{\langle\alpha\alpha n\rangle^{1999}}$
Present
$\frac{\langle\alpha\alpha n\rangle}{\langle\alpha\alpha n\rangle^{1999}}$
2.0
1.5
1.0
0.5
0.0
Ratio
CF88
Present
1/2+
5/2-
5/2+
0.1
1.0
10.0
T9

(γ,n) Reactions and Nuclear Astrophysics

Thermal photon bath

Planck distribution

$$n_\gamma(E,T) = \left(\frac{1}{\pi}\right)^2 \left(\frac{1}{\hbar c}\right)^3 \frac{E^2}{\exp(E/kT) - 1}$$

Reaction Rate

$$\lambda(T) = \int_0^\infty c\, n_\gamma(E,T)\, \sigma_\gamma(E)\, dE$$

Superposition of Bremsstrahlung γ-rays with different end-point energies

Effective energies

another *Gamow* peak near the neutro nthreshold

P. Mohr NIC 2000

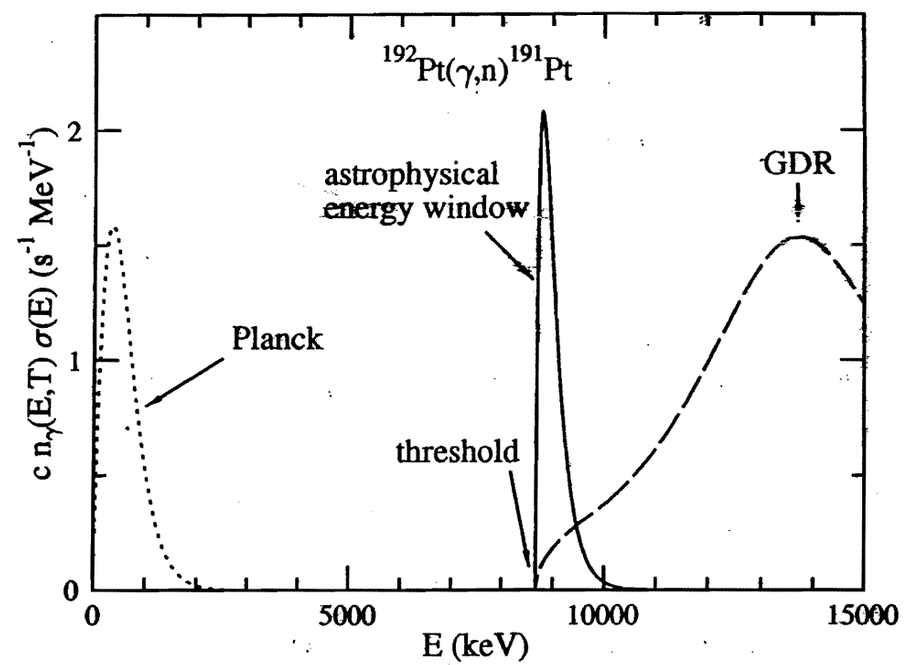

Study of p-nuclei Neutron-defficient, ~~0.1~~ 0.01 – 1% abundances,

e^+-capture, p-capture, (γ,n) (γ,p), (γ,α) starting from more neutron-rich s- and r-nuclei: SNII Origin?

Rayet NIC 2000

$^{139}La(\gamma,n)\boxed{^{138}La}(\gamma,n)\,^{137}La$

$^{116}Sn(\gamma,n)\,^{115}Sn(\gamma,n)\,^{114}Sn$

$Hg(\gamma,n)$

$Pb(\gamma,n)$

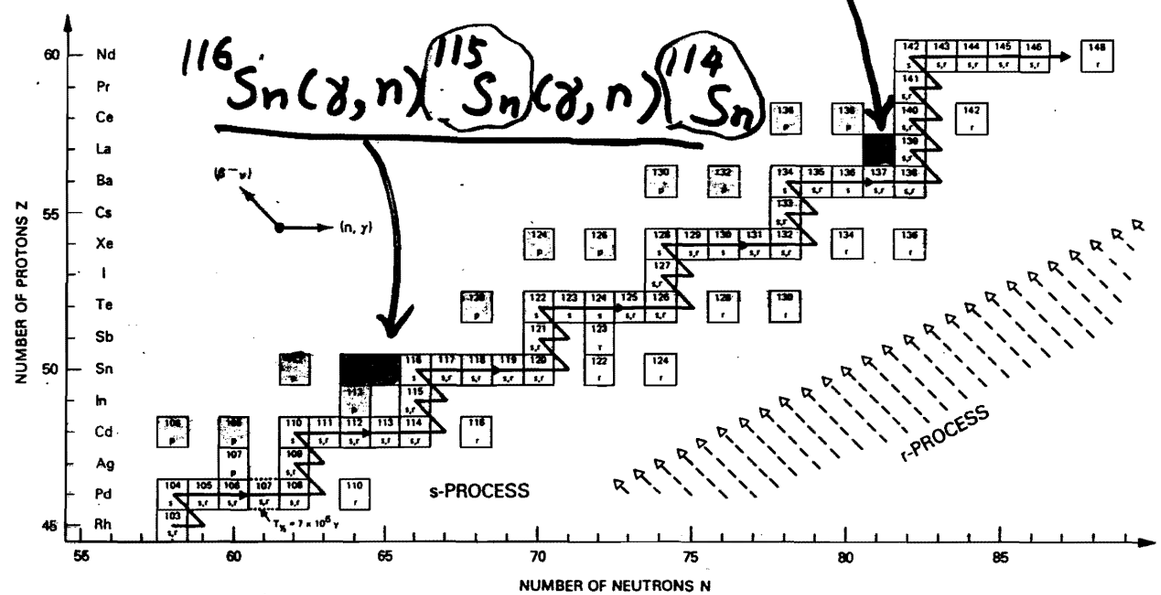

Origin of ^{180}Ta Nature's Rarest Isotope (0.012 %)

Exotic s-process von Neumann-Cosel NIC2000

(β-decay of an isomer in ^{180}Hf, β-decay of excited states in ^{179}Hf into ^{179}Ta followed by neutron capture)

γ-process: ^{181}Ta(γ,n)^{180}Ta$_{gs}$(1+), ^{180}Ta^{m}(9-), …

ν-process: ^{181}Ta(ν,ν'n) ^{180}Ta

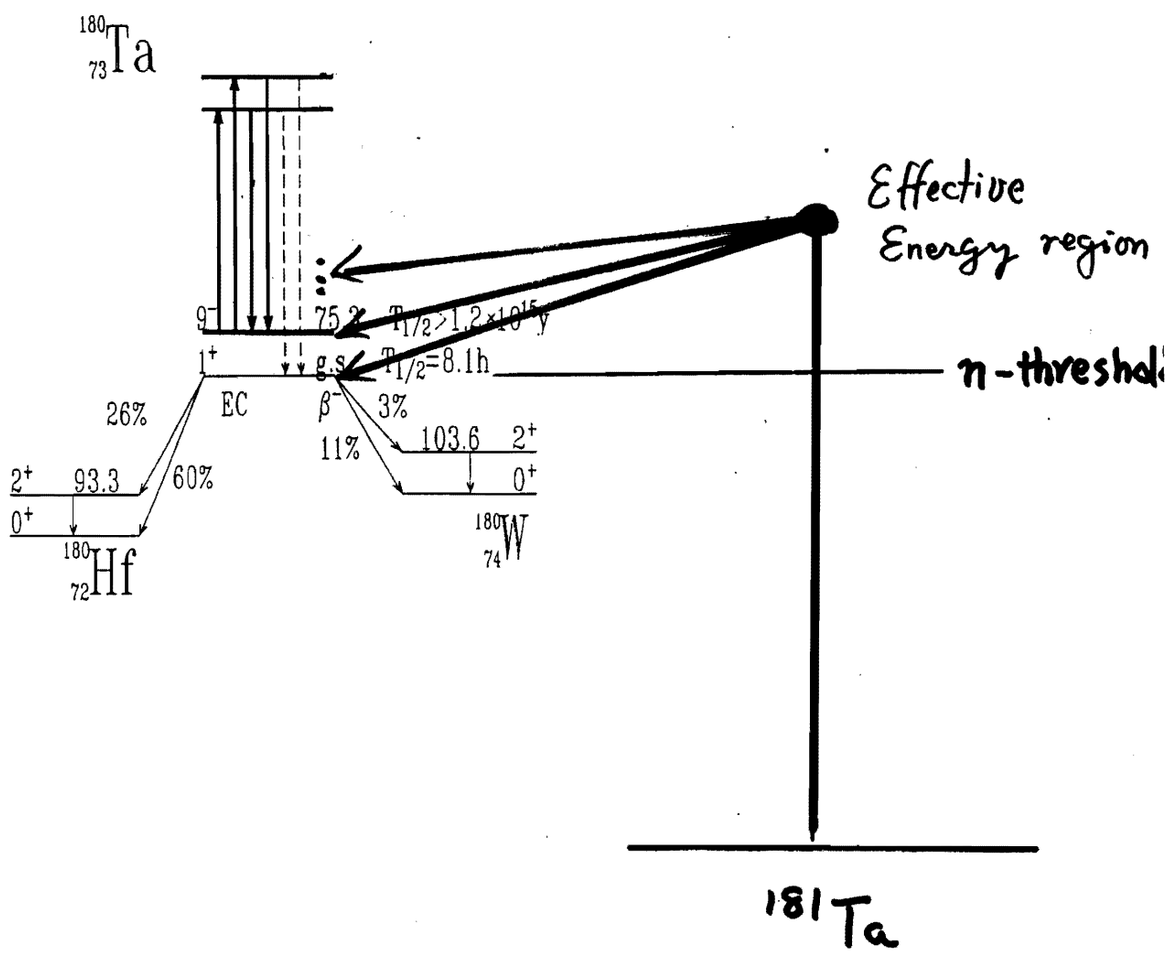

Mengoni 2000

Complication: ^{186,187}Os neutron capture

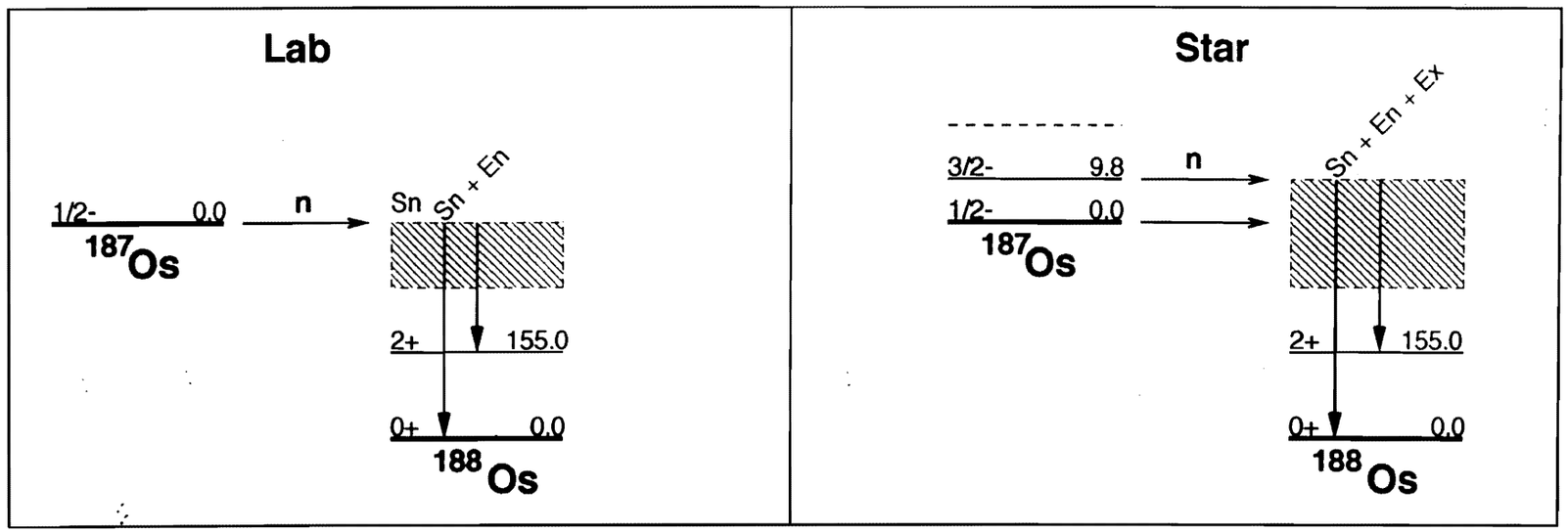

Supernova and r-process: challenges with unstable nuclei

K. Sumiyoshi
Numazu College of Technology (NCT)
Ooka 3600, Numazu, Shizuoka 410-8501, Japan
E-mail: sumi@la.numazu-ct.ac.jp

Abstract

We have studied the ν-driven winds from the nascent proto-neutron star. We have found in the general relativistic hydrodynamical simulations using the relativistic EOS table that the short expansion time scale is realized in the cases of massive and compact proto-neutron stars. Having the trajectories of ejecta, we have performed r-process calculations to find that a successful r-process up to A $\sim$ 195 occurs in the ν-driven winds with a short expansion time scale.

1 Introduction

Physics of supernovae and r-process nucleosynthesis are both fascinating problems where the interplay of nuclear physics and astrophysics takes the important keys. To attack these problems, one has to perform careful numerical simulations with the information of nuclear physics at extreme conditions, and then, one has to compare with observational signature of stellar evolution. Here I focus on our recent studies of the r-process in ν-driven winds in supernovae with two strong motivations from the recent progress in astronomy and nuclear physics.

The first motivation is what the recent observations of r-process elements in extremely metal-deficient stars[1, 2] have exhibited. Metal-deficient stars, whose metal abundance is 10^{-3} or less relative to the solar system abundance, are thought to have formed as first or second generation stars in the early stage of the evolution of the Galaxy. The abundance patterns have been found to match very well with a scaled solar system r-process abundance pattern. These observations strengthen our interests to study the

nucleosynthesis in ν-driven winds as a primary process. We would like to clarify whether the r-process occurs and how much amount of heavy elements are produced in ν-driven winds.

The second motivation is the recent advance in the physics of unstable nuclei which have been developed in radioactive nuclear beam facilities in the world[3, 4]. There are increasing experimental data of unstable nuclei in neutron-rich region, which can help to probe the neutron-rich matter in neutron stars and supernovae. Along this line of research, we have extensively studied the nuclear structure and nuclear matter in the relativistic many body framework[5, 6, 7, 8]. Recently, we have completed the relativistic EOS table in order to apply to supernova simulations from these theoretical studies[9, 10]. Reliability of the EOS table has been checked by comparing with the data of unstable nuclei, which ensures the validity of application to various simulations of supernova phenomena. In the light of this progress in physics of unstable nuclei, we perform the hydrodynamical simulations of ν-driven winds. I report in this article that a short expansion time scale is found in our hydrodynamical studies[11] to be a promising condition for successful r-process in ν-driven winds, as was previously proposed by Otsuki et al. in the semi-analytic studies of the winds[12].

2 R-process in ν-driven winds

2.1 Relativistic EOS table

The relativistic EOS table, which has been completed recently by the present author and his collaborators[9, 10], spans the wide range of density, composition and temperature relevant to supernova explosions. This EOS is based on the relativistic mean field theory, which is known to be a successful model for the studies of nuclear structure[5, 6, 7]. We have constructed the RMF theory based on the relativistic Brückner-Hartree-Fock theory[13]. The RMF theory has been carefully polished by incorporating the experimental data such as masses and radii[8, 14] in order to set up the theoretical parameters. There have been accumulated successful applications to a variety of studies in nuclear physics and astrophysics. The relationship between EOS and neutron-skin thickness has been discussed[15]. The relativistic EOS table has been applied to numerical simulations of core collapse[16] and neutrino emission from proto-neutron stars[17]. The EOS table is available for open use upon request to the author.

2.2 Condition of r-process in ν-driven winds

The ν-driven wind occurs in supernovae shortly after the core bounce. At this time, there is a hot neutron star containing neutrinos at the center. A part of neutrinos emitted as supernova neutrinos heats the surface material in the nascent neutron star. As a result, a small portion of material is ejected forming a ν-driven wind. During the expansion of ejected material, nucleosynthesis starts from neutrons and protons at high temperature above 1 MeV. At around 0.5 MeV, α-process goes on through three-body reactions to produce a small amount of seed elements. At around 0.2 MeV, r-process takes place if neutrons are still abundant enough.

Woosley et al. have indicated a profound implication that the r-process could occur if neutron-to-seed abundance ratio is high enough at the end of the α-process in the ν-driven winds with high entropy per baryon $\sim$400 k_B[18]. In their case the density is low, because $S \sim T^3/\rho$, so that the three-body reaction ($\alpha\alpha n \rightarrow {}^9$Be) creates not very large amount of seeds, leaving plenty of free neutrons. Consequently the neutron-to-seed abundance ratio becomes very high. However, in other studies, entropy has been found to be too low ($\sim$100 k_B)[19, 20]. In addition, ν-process is found to reduce neutron fraction significantly to unfavor the r-process[21].

It has recently been proposed in the semi-analytic studies of the ν-driven winds[12] that a high neutron-to-seed abundance ratio is realized in the winds of short expansion time. If the expansion time scale is short enough, there is little time for the three-body reaction to create many seed elements, leading to high neutron-to-seed abundance ratio. Moreover, one can avoid harmful ν-process due to short time period[12, 22]. Since these findings in the semi-analytic studies are quite favorable for the successful r-process, we tried to establish the validity by carrying out hydrodynamical simulations of the ν-driven winds[11].

2.3 Numerical simulations

Numerical simulations have been carried out by solving general relativistic hydrodynamics[23] with neutrino heating and cooling being taken into consideration. The relativistic EOS table has been adopted for these simulations. We follow the hydrodynamics of surface layers of a proto-neutron star. Having trajectories of density and temperature of ejected material, we calculate nucleosynthesis by solving r-process reaction network[24]. We have studied the dependence on the mass and radius of neutron star, and

neutrino spectrum and luminosity as a first step. We are currently linking with supernova simulations.

Figure 1 demonstrates mass trajectories as a function of time in the case of the neutron star of $2M_\odot$ and 10 km with a total ν-luminosity of 6×10^{52} [erg/s]. The material is heated up by neutrinos, and the surface layers are ejected successively. In this particular case, the expansion time scale is 5 msec and the entropy per baryon is 160 k_B. Picking up a trajectory from numerical simulations, we have calculated the r-process nucleosynthesis with an extended nuclear reaction network including very light neutron-rich nuclei[24]. Figure 2 shows the final abundance yields of r-process calculation. We can observe that the heavy elements up to third peak around A $\sim$ 195 are successfully reproduced. Relative height of second peak is also nicely reproduced in the present work. In the current study, we have seen that massive and compact neutron stars are preferable. We have also found that a new nuclear-reaction flow runs through the light neutron-rich nuclei near the drip line and changes dramatically the final abundances. This new nuclear-reaction flow can change the final heavy element abundances by orders of magnitudes[24].

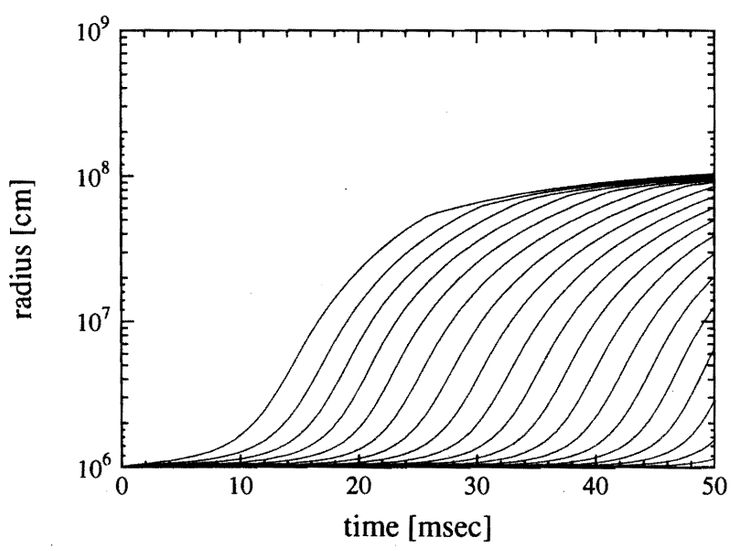

Figure 1: Calculated mass trajectories in neutrino-driven wind.

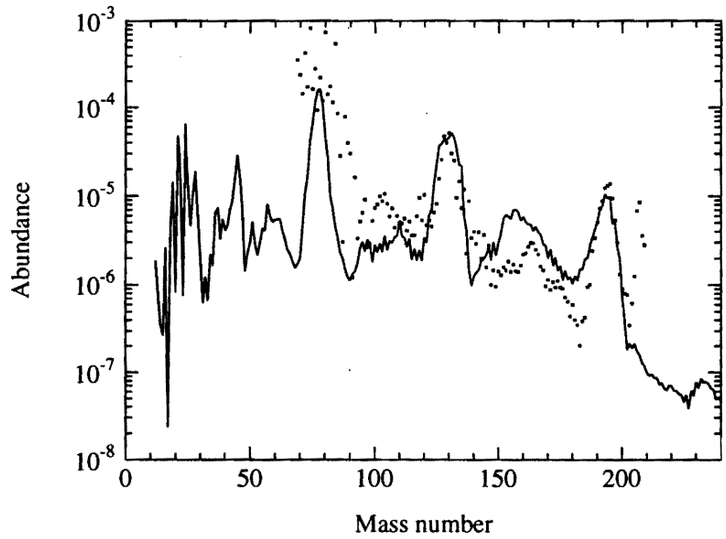

Figure 2: Calculated r-process abundance.

3 Summary

By performing hydrodynamical simulations with the relativistic EOS table, which has recently been completed, we have found that the r-process is possible in ν-driven winds with short expansion time scale. Further simulations of the ν-driven winds are now underway by taking care of the evolution of proto-neutron star and ν-spectrum in order to derive the total amount of r-process yields in supernovae from various progenitor masses.

Acknowledgments

The author is grateful to M. Terasawa, K. Otsuki, H. Shen, H. Suzuki, S. Yamada, G. Mathews, H. Toki, and T. Kajino for continuous, fruitful collaborations. The numerical simulations have been performed on the supercomputers at RIKEN and KEK, Japan.

References

[1] C. Sneden, A. McWilliam, G. W. Preston, J. J. Cowan, D. L. Burris and B. J. Armosky, *Astrophys. J.* **467**, 819 (1996).

[2] C. Sneden, J. J. Cowan, I. I. Ivans, G. M. Fuller, S. Burles, T. C. Beers and J. E. Lawler, submitted to *Astrophys. J.*, (2000); astro-ph/0003086.

[3] I. Tanihata *et al.*, *Phys. Rev. Lett.* **55**, 2676 (1985).

[4] I. Tanihata *et al.*, *Phys. Lett.* B **289**, 261 (1992).

[5] K. Sumiyoshi, D. Hirata, H. Toki and H. Sagawa, *Nucl. Phys.* A **552**, 437 (1993).

[6] Y. Sugahara and H. Toki, *Nucl. Phys.* A **579**, 557 (1994).

[7] K. Sumiyoshi, H. Kuwabara and H. Toki, *Nucl. Phys.* A **581**, 725 (1995).

[8] D. Hirata, K. Sumiyoshi, I. Tanihata, Y. Sugahara, T. Tachibana and H. Toki, *Nucl. Phys.* A **616**, 438c (1997).

[9] H. Shen, H. Toki, K. Oyamatsu and K. Sumiyoshi, *Nucl. Phys.* A **637**, 435 (1998).

[10] H. Shen, H. Toki, K. Oyamatsu and K. Sumiyoshi, *Prog. Theor. Phys.* **100**, 1013 (1998).

[11] K. Sumiyoshi, H. Suzuki, K. Otsuki, M. Terasawa and S. Yamada, *Pub. Astron. Soc. Japan* **52**, 601 (2000).

[12] K. Otsuki, H. Tagoshi, T. Kajino and S. Wanajo, *Astrophys. J.* **533**, 424 (2000).

[13] R. Brockmann and R. Machleidt, *Phys. Rev.* C **42**, 1965 (1990).

[14] T. Suzuki *et al.*, *Nucl. Phys.* A **658**, 313 (1999).

[15] K. Oyamatsu, I. Tanihata, Y. Sugahara, K. Sumiyoshi and H. Toki, *Nucl. Phys.* A **634**, 3 (1998).

[16] K. Sumiyoshi, H. Suzuki, S. Yamada and H. Toki, in preparation for submission to *Nucl. Phys.*, (2000).

[17] K. Sumiyoshi, H. Suzuki and H. Toki, *Astron. Astrophys.* **303**, 475 (1995).

[18] S. E. Woosley, J. R. Wilson, G. J. Mathews, R. D. Hoffman and B. S. Meyer, *Astrophys. J.* **433**, 229 (1994).

[19] J. Witti, H.-Th. Janka and K. Takahashi, *Astron. Astrophys.* **286**, 841 (1994).

[20] Y.-Z. Qian and S. E. Woosley, *Astrophys. J.* **471**, 331 (1996).

[21] B. S. Meyer, G. C. McLaughlin and G. M. Fuller, *Phys. Rev.* C **58**, 3696 (1998).

[22] M. Terasawa, K. Sumiyoshi, T. Kajino, K.-H. Langanke and G. J. Mathews, in preparation.

[23] S. Yamada, *Astrophys. J.* **475**, 720 (1997).

[24] M. Terasawa, K. Sumiyoshi, T. Kajino, I. Tanihata and G. J. Mathews, submitted to *Astrophys. J.*, (2000).

Abundance Anomaly in Globular Cluster Red Giants

M. Aikawa, M. Y. Fujimoto, K. Kato, Hokkaido Univ.

October 31, 2000

Abstract

The observations of the globular cluster red giants show the abundance anomalies which are different from those in other stars. One of the most different elements is ^{24}Mg, which is decreased in such stars although it is not broken in the ordinary steller evolution. The mechanism to destroy ^{24}Mg is discussed and the decreasing of ^{24}Mg is reproduced by using the Mixing-Induced Hydrogen Shell Flash Model.

The stars in which aluminum enhanced and ^{24}Mg decreased have been observed in some of globular cluster red giants [1]. The abundance profiles shown by Langer and Hoffman [2] indicate that ^{25}Mg and ^{26}Mg depleted and Al enhanced. Because the abundance of ^{24}Mg little changes, we can not understand the observed result in which ^{24}Mg depleted in some globular cluster red giants. In this report, we discuss the abundances under the conditions on the temperature higher than that in ordinary steller evolution. As one of mechanisms to make high temperature the Mixing-Induced Hydrogen Shell Flash Model [3] is proposed. In this model, the mixing of hydrogen into the He-core is occurd and it can provide us the high temperature enough to burn ^{24}Mg.

The abundance profiles are calculated by the reaction network consisting of the 61 isotopes of the 16 lightest species, and the reaction rates are taken from the compilation by Caughlan and Fowler [4] and some updated ones [5]. We assume the same initial abundances as Langer and Hoffman userd [2], and the abundances in the He-core are taken as the calculational result with the constant temperature and constant density at the time when hydrogen is depleted and the mixed ones are initial ones because we consider the mixing of a small amount of hydrogen shell into the hydrogen depleted He-core. If hydrogen mixes into the He-core, hydrogen burning makes a thermal runaway and the temperature at the burning shell becomes higher. The detail of this model is explained by Fujimoto et al [3]. The present calculation is performed under the assumptions that the core-mass is $0.3M_{\odot}$, $0.4M_{\odot}$ and $0.45M_{\odot}$ and the mixing depth is between 0.5 and 5 pressure scale hight(Hp). For example, Figure 1 shows the changes of temperature and density under $0.4M_{\odot}$ and 3 Hp. The abundance profiles in the burning shell is calculated by taking into account a rapid change of temperature and density due to the Mixing-Induced Hydrogen Shell Flash Model.

In Figure 2, we show the ratio of initial to final abundance of ^{24}Mg under the calculation of the Mixing-Induced Hydrogen Shell Flash Model. It is shown that ^{24}Mg decreases when the temperature increases rapidly. This model can show the decrease of ^{24}Mg. The details of mixing mechanism are under consideration.

Reference

[1] M. D. Shetrone, AJ, 112, 2639(1996)

[2] G.E. Langer and R.D. Hoffman, PASP, 107, 1177(1995)

[3] M. Y. Fujimoto et al., ApJ, 519, 733(1999)

[4] G.R. Caughlan and W.A. Fowler, At. Data Nucl. Data Tables, 40, 283(1988)

[5] M. F. El Eid and A. E. Chanpagne, ApJ, 451, 298(1995)

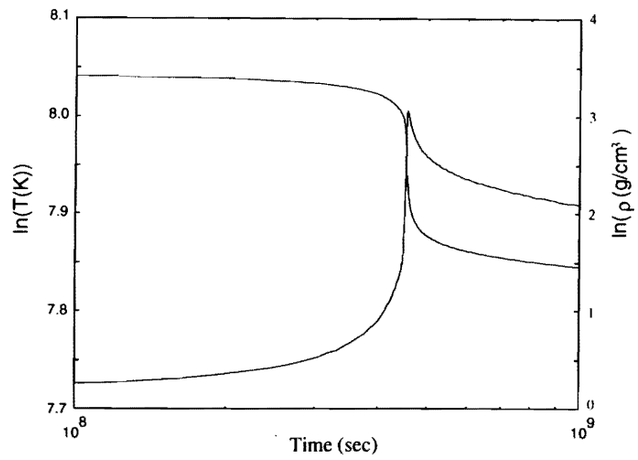

Figure 1: The changes of temperature and density under $0.4M_{\odot}$ and 3 Hp

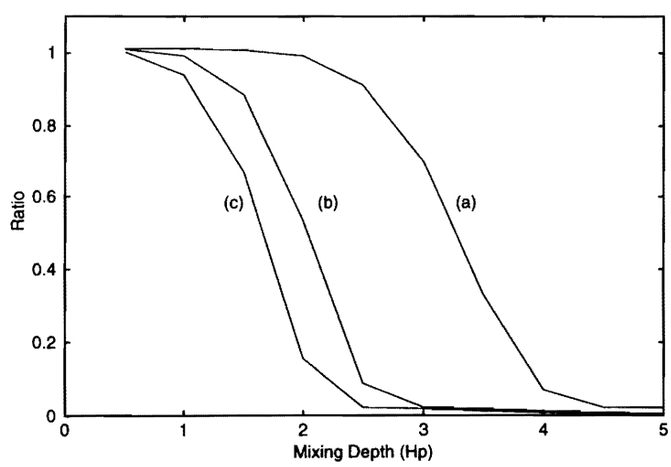

Figure 2: The ratio of initial to final abundance of ^{24}Mg under the calculation of the Mixing-Induced Hydrogen Shell Flash Model. The core-mass is (a) $0.3M_{\odot}$, (b) $0.4M_{\odot}$ and (c) $0.45M_{\odot}$ and the mixing depth is between 0.5 and 5 pressure scale hight(Hp).

Determination of Ω_b; Constraints from Big Bang Nucleosynthesis and CMB Anisotropy Measurements

M. Orito[a] , T. Kajino[a] * † , G. J. Mathews[b] , and R. N. Boyd[c]

[a]National Astronomical Observatory, 2-21-1, Osawa, Mitaka, Tokyo 181-8588, Japan

[b]Center for Astrophysics, and Department of Physics, University of Notre Dame, Notre Dame, IN 46556

[c]Department of Physics, Department of Astronomy, Ohio State University, Columbus, OH 43210

We reanalyze primordial nucleosynthesis in the presence of a net lepton asymmetry. We show that a previously unnoted region of the parameter space exists in which very large baryon densities $0.1 \leq \Omega_b \leq 1$ can be accommodated within the light-element constraints assuming that some destruction of primordial lithium has occurred. this parameter space consists of large ν_μ, ν_τ degeneracies together with a moderate ν_e degeneracy. Constraints on this parameter space from non-big-bang considerations, such as Cosmic Background Radiation measurements, are also discussed [1].

1. Introduction

The universe appears to be charge neutral to very high precision. Hence, any universal net lepton number beyond the net baryon number must reside entirely within the neutrino sector. Since the present relic neutrino number asymmetry is not directly observable there is no firm experimental basis for postulating that the lepton number for each species is zero. It is therefore possible for the individual lepton numbers L_l of the universe to be large compared to the baryon number of the universe, B, while the net total lepton number is small ($L \sim B$). It has been proposed recently [2] that models based upon the Affleck-Dine scenario of baryogenesis might generate naturally lepton number asymmetry which is seven to ten orders of magnitude larger than the baryon number asymmetry. Neutrinos with large lepton asymmetry and masses $\sim$ 0.07 eV might even explain the existence of cosmic rays with energies in excess of the Greisen-Zatsepin-Kuzmin cutoff [3]. It is, therefore, equally important for both particle physics and cosmology to carefully scrutinize the limits which cosmology places on the allowed range of both the lepton and baryon asymmetries.

The consequences of a large lepton asymmetry and associated neutrino degeneracy for

*Graduate University for Advanced Studies, Department of Astronomical Science, 2-21-1, Osawa, Mitaka, Tokyo 181-8588, Japan

†University of Tokyo, Department of Astronomy, 7-3-1 Hongo, Bunkyo-ku, Tokyo 113-0033, Japan

big bang nucleosynthesis (BBN) have been considered in many papers [4] (and references therein).

The present work differs from all of those listed above primarily in that we carefully examine models with large neutrino degeneracies. We show that there is a correction to the neutrino reaction rates which causes the neutrino decoupling temperature to be significantly higher than previous estimates. That fact causes new solutions for BBN in which significant baryon density is possible without violating the various cosmological constraints.

2. Neutrino Decoupling

Neutrinos and anti-neutrinos drop out of thermal equilibrium with the background thermal plasma when the weak reaction rate per particle, Γ, becomes slower than the expansion rate, H. Since the decoupling occurs quickly, it is a good approximation to estimate a characteristic decoupling temperature T_D, at which the slowest weak-equilibrating reaction per particle Γ becomes slower than the expansion rate.

Our decoupling temperers are significantly higher than those estimated in Kang & Steigman (1992) for reasons which we now explain.

First, the existence of a lepton asymmetry represented by a finite positive neutrino chemical potential will cause the number density of antineutrinos to be significantly less than that of neutrinos. Hence, the annihilation rate per neutrino $\Gamma_\nu = n_{\bar{\nu}}\langle\sigma_{\nu\bar{\nu}}\rangle$ can be significantly less than the reaction rate per antineutrino, electron or positron.

Another difference between our results and that of Kang & Steigman (1992) is twofold: The first is that we have included the finite temperature corrections to the mass of the electron and photon [5]. The second is that we have calculated the average neutrino annihilation rate in the cosmic comoving frame, in which the Møller velocity instead of the relative velocity is to be used for the integration of the collision term in the Boltzmann equations [6,7].

If the neutrinos decouple early, they are not heated as the number of particle degrees of freedom change. Hence, the ratio of the neutrino to photon temperatures, T_ν/T_γ, is reduced. The biggest drop in temperature for all three neutrino flavors occurs for $\xi_\nu \approx 10$. This corresponds to a decoupling temperature above the cosmic QCD phase transition. The low temperature is the result of the decrease in particle degrees of freedom during this phase transition. This discontinuity will have important consequences in the subsequent discussions.

3. Big Bang Nucleosynthesis

Non-zero lepton numbers primarily affect nucleosynthesis in two ways. First, degeneracy in any neutrino species leads to an increased universal expansion rate independently of the sign of ξ_{ν_e}. As a result, the weak interactions that maintain neutrons and protons in statistical equilibrium decouple earlier to predict increased ^{4}He production.

Secondly, The equilibrium n/p ratio is related to the electron neutrino degeneracy by n/p $= \exp\{-(\Delta M/T_{n\leftrightarrow p}) - \xi_{\nu_e}\}$, where ΔM is the neutron-proton mass difference and $T_{n\leftrightarrow p}$ is the freeze-out temperature for the weak reactions converting protons to neutrons and vice versa. This effect leads to either increased or decreased ^{4}He production,

depending upon the sign of L_e or ξ_{ν_e}.

There is also a third effect which we emphasize in this paper. As discussed in the previous section, T_ν/T_γ can be reduced if the neutrinos decouple at an earlier epoch. This lower temperature reduces the energy density of the highly degenerate neutrinos during the BBN era, and hence, slows down the expansion of the universe. This leads to decreased ^{4}He production.

The values for ξ_{ν_μ} and ξ_{ν_τ} primarily affect the expansion rate. This means that ξ_{ν_μ} and ξ_{ν_τ} are roughly interchangeable as far as their effects are nucleosynthesis concerned. Therefore, in what follows, we describe results for $|\xi_{\nu_\mu}| = |\xi_{\nu_\tau}| \equiv \xi_{\nu_{\mu,\tau}}$.

Figure 1 highlights the basic result of this study. For low $\Omega_b h_{50}^2$ models, only the usual low values for ξ_{ν_e} and $\xi_{\nu_{\mu,\tau}}$ are allowed. Between $\Omega_b h_{50}^2 \approx 0.188$ and 0.3, however, more than one allowed region emerges. For $\Omega_b h_{50}^2 \gtrsim 0.4$ only the large degeneracy solution is allowed. Neutrino degeneracy can even allow baryonic densities up to $\Omega_b h_{50}^2 = 1$. What is different here with previous studies is that the high $\Omega_b h_{50}^2$ models are made possible for smaller values of ξ_{ν_e} by careful accounting of the relic neutrino temperature. This suggests that baryons and degenerate neutrinos might provide a larger contribution to the universal closure density than has previously been assumed based upon light-element constraints from BBN.

The resultant elemental abundances as a function of $\Omega_b h_{50}^2$ allows us to consider whether there exists an abundance signature in other elements which might distinguish this new degenerate neutrino solution from standard BBN. For the most part the yields of the light and heavy species are similar to those of the standard non-degenerate big bang. However, the boron abundance exhibits an increase with baryon density due to alpha captures on ^{7}Li. Thus, in principle, an anomalously high boron abundance together with beryllium and ^{6}Li similar to that expected from standard BBN might be a signature of neutrino-degeneracy.

In this context a recent compilation of the nuclear reaction rates relevant to the production of ^{11}B ([Orito, Kajino, & Oberhummer 1998]) was useful because several important LiBeB(a,x) and (n,γ) reaction rates in the literature sometimes differ from one another by 2-3 orders of magnitude. The calculated abundances of heavier elements based upon these rates can also differ from one another by 1-2 orders of magnitude.

The uncetainty of the predicted abundances mainly come from the reaction rates. We need the more precise data to determined the reaction rates, especially for ^{3}He, B,^{11} C(α,γ).

4. Cosmic Microwave Background Constraint

Perhaps, the most stringent remaining constraint on neutrino degeneracy comes from its effect on the cosmic microwave background. Several recent works [8–10] have shown that neutrino degeneracy can dramatically alter the power spectrum of the CMB. The essence of the constraint is that degenerate neutrinos increase the energy density in radiation at the time of photon decoupling in addition to delaying the time of matter-radiation energy-density equality as discussed above. One effect of this is to increase the amplitude of the first acoustic peak in the CMB power spectrum at $l \approx 200$.

However, in the existing CMB constraint calculations (Kinney and Riotto 1999: Lesgourgues and Pastor 1999; Hannestad 2000) only small degeneracy parameters with the

standard relic neutrino temperatures were utilized in their derived constraint. Hence, the possible effects of a diminished relic neutrino temperature need to be reconsidered. To investigate this we have done calculations of the CMB power spectrum, based upon the CMBFAST code of Seljak & Zaldarriago (1996).

The solid line on Figure 2 shows a $\Omega_\Lambda = 0.4$ model for which $n = 0.78$. For this fit $\Delta\chi^2 = 27$ which makes this large degeneracy model marginally consistent with the data at a level of 5.2σ. The dotted line in Figure 2 shows the matter dominated $\Omega_\Lambda = 0$ best fit model with $n = 0.83$. For this fit $\Delta\chi^2 = 9$ which makes this large degeneracy model consistent with the data at the level of 3σ. The main differences in the fits between the

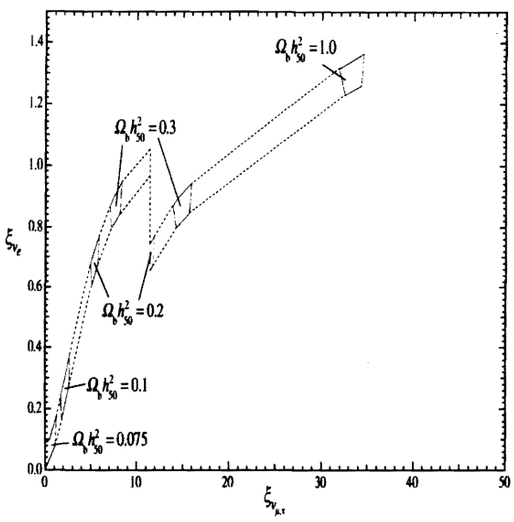

Figure 1. Allowed values of ξ_{ν_e} and $\xi_{\nu_{\mu,\tau}}$ for which the constraints from light element abundances are satisfied for values of $\Omega_b h_{50}^2 = 0.075$, 0.1, 0.2, 0.3 and 1.0 as indicated.

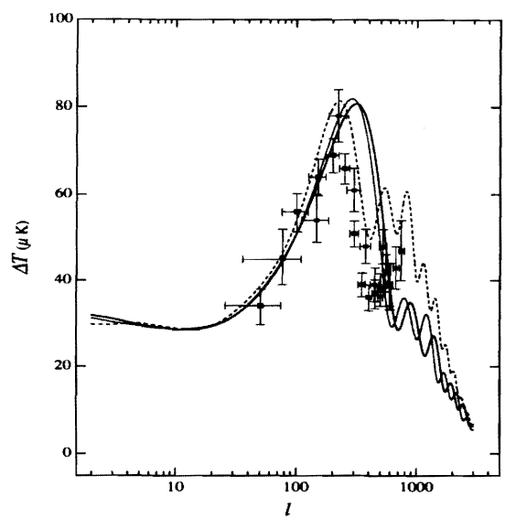

Figure 2. CMB power spectrum from the recent MAXIMA-1 [12] (circles) and BOOMERANG [11] (squares) binned data compared with calculated $\Omega = 1$ models.

large degeneracy models and our adopted benchmark model are that the first peak is shifted to slightly higher l values and the second peak is somewhat suppressed. It thus becomes important to quantify the amplitude of the second peak in order to constrain the large degeneracy models proposed herein.

Here one can clearly see that the suppression of the second acoustic peak in the observed power spectrum is consistent with our derived neutrino-degenerate models. In particular, the MAXIMA-1 results are in very good agreement with the predictions of the neutrino-degenerate cosmological models described herein.

It is clear, that these new data sets will substantially improve the goodness of fit for the neutrino-degenerate models [9]. Moreover, both data sets seem to require an increase

in the baryonic contribution to the closure density as allowed in our neutrino-degenerate models. In a subsequent paper we will examine the implications of those data in detail [13]

REFERENCES

1. M. Orito, T. Kajino, G. J. Mathews, and R. N. Boyd, astro-ph/0005446, submitted to ApJ (2000)
2. A. Casas, W. Y. Cheng, & G. Gelmini, Nucl. Phys. B., **538**, 297, (1999)
3. G. Gelmini & A. Kusenko Phys. Rev. Lett., **82**, 5202, (1999)
4. H. Kang & G. Steigman Nucl. Phys. B., **372**, 494, (1992)
5. N. Fornengo, C. W. Kim, & J. Song, Phys. Rev. D., **56**, 5123, (1997)
6. P. Gondolo, & G. Gelmini, Nucl. Phys. B., **360**, 145, (1991)
7. K. Enqvist, K, K. Kainulainen, & V. Semikoz, Nucl. Phys. B., **374**, 392, (1992)
8. W. K. Kinney & A. Riotto, Phys. Rev. Lett., **83**, 3366, (1999)
9. J. Lesgourgues & S. Pastor, Phys. Rev. D., **60**, 103521,, (1999)astro-ph/0004412
10. S. Hannestad, Phys. Rev. Lett., submitted, (2000), astro-ph/0005018
11. P. Bernardls, et al. (Boomerang Collaboration) Nature., **404**, 955, (2000)
12. S. Hanany, et al. (MAXIMA-1 Collaboration), ApJL submitted, astro-ph/0005123
13. G. J. Mathews, M. Orito, T. Kajino, in preparation (2000).
14. Orito, M., Kajino, T., & Oberhummer, H. 1998, in "Nuclei in the Cosmos V, Proc. 5th International Conference, Volos, Greece, July 6-12, (Editions Frontieres; France), N. Prantzos, ed. pp. 37-40

Allowed Light Elemental Abundances as Function of Ω_b

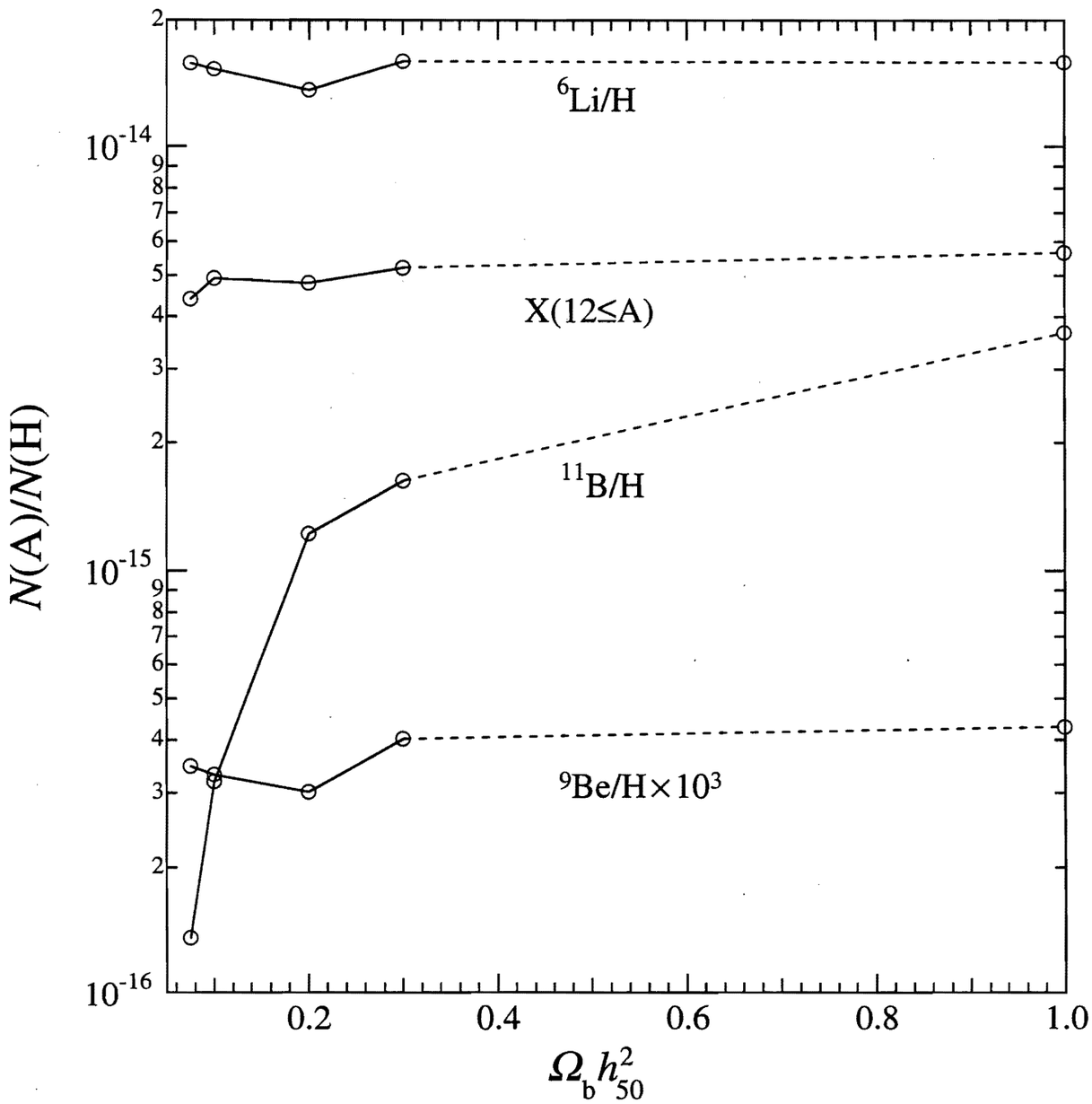

Present Status of Nuclear Data Evaluation Work at JAERI Nuclear Data Center

Tsuneo Nakagawa
Nuclear Data Center
Department of Nuclear Energy System
Japan Atomic Energy Research Institute

10/October/2000

Abstract

The Nuclear Data Center has been compiling Japanese Evaluated Nuclear Data Libraries, JENDL with the aid of Japanese Nuclear Data Committee. The most recent version of JENDL is JENDL-3.2 containing the neutron-induced reaction data for 340 nuclides. Maxwellian-averaged capture cross sections were calculated from JENDL-3.2 and compared with other recommendations.

1. Introduction

The Nuclear Data Center of Japan Atomic Energy Research Institute (JAERI) has been developing various nuclear data files with the aid of Japanese Nuclear Data Committee (JNDC). JNDC was established in JAERI and Atomic Energy Society of Japan in 1963. Work of nuclear data evaluation started in 1970. The first version of our own evaluated nuclear data library, JENDL-1 (Japanese Evaluated Nuclear Data Library-1) was released in 1977. After JENDL-1, we have made efforts to improve the nuclear data and released several versions of JENDL. The currently used version is JENDL-3.2.

This paper describes outline of JENDL-3.2 and Maxwellian-averaged capture cross sections calculated from JENDL-3.2.

2. Domestic and International Collaboration on Nuclear Data

JNDC has about 120 members from universities, institutes, private companies, etc. They belong to working groups to make evaluation of nuclear data, to test the evaluated data, and so on. Domestic collaboration on the nuclear data has been well organized under JNDC and the Nuclear Data Center.

International collaboration is also inevitable. We have the so-called four-center network on the nuclear data. Information on the nuclear data is gathered and distributed via the four-center network which consists of OECD NEA Data Bank, IAEA NDS, NNDC of the United States, NDC of Russia. Since Japan is a member country of OECD NEA Data Bank, Japanese users can obtain the information from the Data Bank..

The work concerning nuclear data in Japan is being performed under those collaborations.

3. JENDL

The first version of JENDL was released in1977. That contains the neutron induced reaction data for 72 nuclides which are important to fast breeder reactors. The second version, JENDL-2, was released in 1982 including the data for 84 nuclides, and revised in 1985 by including many fission product nuclides. Finally the data for 181 nuclides were given in JENDL-2. JENDL-3 was released in 1989, and updated in 1990 to JENDL-3.1. Furthermore it was improved to JENDL-3.2 [1] in 1994 which stores the data for 340 nuclides. The nuclides compiled in JENDL-3.2 are listed in Table 1.

The JENDL-3.2 contains various types of nuclear data; cross sections, resonance parameters,

angular and energy distributions of secondary neutrons, gamma-ray production cross sections, angular and energy distributions of gamma-rays. For heavy nuclides, data for fission are also given; neutrons per fission, fission product yields, etc. These data are given in the incident neutron energy range from 10^{-5} eV to 20 MeV.

Figure 1 shows an example of cross sections given in JENDL-3.2. In JENDL-3.2, the cross sections in the resonance region are represented with resonance parameters which were adjusted so as to reproduce well measured cross sections. Figure 2 is another example of the ^{148}Sm capture cross section. The most recent experimental data measured by Wisshak et al.[2] are in very good agreement with JENDL-3.2. Other evaluated data are also shown in this figure. ENDF/B-VI that is an evaluated data library of the United States is the same as JEF-2.2 of European countries in this case, and larger than JENDL-3.2. JENDL-3.1 is a previous version of JENDL. It is seen that JENDL-3.2 was improved to reproduce the more recent experimental data.

We are making also JENDL special purpose files which contain only the data needed to specific fields of data applications. JENDL Dosimetory File 99 contains the cross section and covariance data for 67 neutron-induced reactions which are used for neutron dosimetory. JENDL Fusion File was compiled to be used in fusion neutronics fileds. This file provides the reliable energy-angle distributions of emitted particles (double differential cross sections) for the nuclides important to fusion reactors. The version released in 1999 contains the data for 92 nuclides. The activation cross sections are complied in JENDL Activation Cross Section File 96. This file consists of 1246 reactions for 233 nuclides. JENDL FP Decay File 2000 has been released recently containing decay data for 1229 fission product nuclides.

Above-mentioned data of JENDL are available from the following URL; http://wwwndc.tokai.jaeri.go.jp. We are revising JENDL-3.2 by considering new experimental data and feedback from JENDL-3.2 users. The new version, JENDL-3.3, will be released in Spring 2001.

4. Maxwellian-averaged Capture Cross Sections

Since JENDL-3.2 provides the cross section data in the neutron energy range up to 20 MeV, one can calculate Maxwellian-averaged cross sections from JENDL-3.2, which can be applicable to the study of s-process in the nucleosynthesis;

$$\langle\sigma\rangle = \frac{\langle\sigma v\rangle}{v_T} = \frac{2}{\sqrt{\pi}}(kT)^{-2}\int_0^\infty \sigma(E)E\exp\left(-\frac{E}{kT}\right)dE .$$

The average cross section was calculated for 317 nuclides in the temperature range from 1 keV to 1 MeV. The results of the calculation has been published as Ref. [3].

The Maxwelllian-averaged cross sections at kT=30 keV are compared with those recommended by Beer et al.[4] in Fig.3. Nuclides in the both sets are almost the same below the mass number of 160. Between 160 and 210, the number of nuclides in JENDL-3.2 is less than Beer et al. because the nuclides in this region are not so important for reactor applications. On the contrary, many actinide nuclides are given in JENDL-3.2. Figure 4 shows the ratios of JENDL-3.2 and Beer et al. Most of nuclides are in the range of + 50 % and – 50 %.

However, large discrepancies are found to some nuclides. The largest discrepancy is the case of ^{16}O. Figure 5 shows the comparison of Maxwellian averaged capture cross section of ^{16}O. JENDL-3.2 agrees well with the experimental data of Igashira et al.[5] JENDL-3.2 is also in good agreement with the measured capture cross sections in the keV region [5,6] as shown in Fig.6. Therefore, the recommendations by Thielmann et al.[7], Bao et al.[8] and Beer et al. are too small and their temperature dependence might be incorrect.

Figure 7 is another example of the Maxwellian-averaged capture cross section of ^{12}C. In this case, the values at 30 keV of JENDL-3.2 and Beer et al. agree with measured data of Ohsaki et al.[9] However, the temperature dependence is different. JENDL-3.2 is more correct than Beer et al. also in this case because JENDL-3.2 is based on the measured cross sections in the keV region.

Figure 8 is the Maxwellian-average capture cross section of ^{209}Bi. JENDL-3.2 has the same shape of temperature dependence as the recent measurement of Mutti et al.[10]

References

1) Nakagawa T., Shibata K., Chiba S., Fukahori T., Nakajima Y., Kikuchi Y., Kawano T., Kanda Y., Ohsawa T., Matsunobu H., Kawai M., Zukeran A., Watanabe T., Igarasi S., Kosako K., and Asami T.: *J. Nucl. Sci. Technol.*, **32**, 1259 (1995).
2) Wisshak K., Guber K., Voss F., Käppeler F. and Reff G.: "Neutron capture in ^{148,150}Sm: A Sensitive Probe of the s-Process Neutron Density," *KfK* 5067 (1992).
3) Nakagawa T., Chiba S., Ohsaki T. and Igashira M.: "Maxwellian-Averaged Cross Sections Calculated from JENDL-3.2," *JAERI-Research* 2000-002 (2000).
4) Beer H., Voss F. and Winters R.R.: *Astrophys. J. Suppl.*, **80**, 403 (1992).
5) Igashira M., Nagai Y., Masuda K., Ohsaki T. and Kitazawa H.: *Astrophys. J.*, **441**, L89 (1995).
6) Igashira M., Kitazawa H. and Takaura K.: *Nucl. Phys.*, **A536**, 285 (1992).
7) Thielemann F.-K., Arnould M. and Truran J.W.: *Advances in Nuclear Astrophysics*, ed. Vangiona-Flam, Editions Frontière, 525 (1987). The tables of fitting functions are available at http://isotopes.lbl.gov/isotopes/astro/friedel.html (1999).
8) Bao Z.Y. and Käppeler F.: *At. Data Nucl. Data Tables*, **36**, 411 (1987).
9) Ohsaki T., Nagai Y., Igashira M., Shima T., Takeda K., Seino S. and Irie T.: *Astrophys. J.*, **422**, 912 (1994).
10) Mutti P., Corvi F., Athanassopulos K., Beer H. and Krupchitsky P.: *Proc. International Conf. Nuclear Data for Science and Technology*, Trieste, Italy, 19-24 May 1997, *Italian Phys. Soc. Conf. Proc.* Vol. **59**, Part II, p.1584 (1997).

Table 1 Nuclides whose data are given in JENDL-3.2

A mass number of 0 means a natural element, and that with 'm' a meta-stable state.

1-H - 1	1-H - 2	2-He- 3	2-He- 4	3-Li- 6
3-Li- 7	4-Be- 9	5-B - 10	5-B - 11	6-C – 12
7-N - 14	7-N - 15	8-O – 16	9-F - 19	11-Na- 23
12-Mg- 0	12-Mg- 24	12-Mg- 25	12-Mg- 26	13-Al- 27
14-Si- 0	14-Si- 28	14-Si- 29	14-Si- 30	15-P – 31
16-S - 0	16-S - 32	16-S - 33	16-S - 34	16-S – 36
17-Cl- 0	17-Cl- 35	17-Cl- 37	18-Ar- 40	19-K – 0
19-K - 39	19-K - 40	19-K - 41	20-Ca- 0	20-Ca- 40
20-Ca- 42	20-Ca- 43	20-Ca- 44	20-Ca- 46	20-Ca- 48
21-Sc- 45	22-Ti- 0	22-Ti- 46	22-Ti- 47	22-TI- 48
22-Ti- 49	22-Ti- 50	23-V - 51	24-Cr- 0	24-Cr- 50
24-Cr- 52	24-Cr- 53	24-Cr- 54	25-Mn- 55	26-Fe- 0
26-Fe- 54	26-Fe- 56	26-Fe- 57	26-Fe- 58	27-Co- 59
28-Ni- 0	28-Ni- 58	28-Ni- 60	28-Ni- 61	28-Ni- 62
28-Ni- 64	29-Cu- 0	29-Cu- 63	29-Cu- 65	31-Ga- 0
31-Ga- 69	31-Ga- 71	32-Ge- 0	32-Ge- 70	32-Ge- 72
32-Ge- 73	32-Ge- 74	32-Ge- 76	33-As- 75	34-Se- 74
34-Se- 76	34-Se- 77	34-Se- 78	34-Se- 79	34-Se- 80
34-Se- 82	35-Br- 79	35-Br- 81	36-Kr- 78	36-Kr- 80

Table 1 (continued)

36-Kr- 82	36-Kr- 83	36-Kr- 84	36-Kr- 85	36-Kr- 86
37-Rb- 85	37-Rb- 87	38-Sr- 86	38-Sr- 87	38-Sr- 88
38-Sr- 89	38-Sr- 90	39-Y - 89	39-Y - 91	40-Zr- 0
40-ZR- 90	40-Zr- 91	40-Zr- 92	40-Zr- 93	40-Zr- 94
40-Zr- 95	40-Zr- 96	41-Nb- 93	41-Nb- 94	41-Nb- 95
42-Mo- 0	42-Mo- 92	42-Mo- 94	42-Mo- 95	42-Mo- 96
42-Mo- 97	42-Mo- 98	42-Mo- 99	42-Mo-100	43-Tc- 99
44-Ru- 96	44-Ru- 98	44-Ru- 99	44-Ru-100	44-Ru-101
44-Ru-102	44-Ru-103	44-Ru-104	44-Ru-106	45-Rh-103
45-Rh-105	46-Pd-102	46-Pd-104	46-Pd-105	46-Pd-106
46-Pd-107	46-Pd-108	46-Pd-110	47-Ag- 0	47-Ag-107
47-Ag-109	47-Ag-110m	48-Cd- 0	48-Cd-106	48-Cd-108
48-Cd-110	48-Cd-111	48-Cd-112	48-Cd-113	48-Cd-114
48-Cd-116	49-In-113	49-In-115	50-Sn-112	50-Sn-114
50-Sn-115	50-Sn-116	50-Sn-117	50-Sn-118	50-Sn-119
50-Sn-120	50-Sn-122	50-Sn-123	50-Sn-124	50-Sn-126
51-Sb- 0	51-Sb-121	51-Sb-123	51-Sb-124	51-Sb-125
52-Te-120	52-Te-122	52-Te-123	52-Te-124	52-Te-125
52-Te-126	52-Te-127m	52-Te-128	52-Te-129m	52-Te-130
53-I -127	53-I -129	53-I -131	54-Xe-124	54-Xe-126
54-Xe-128	54-Xe-129	54-Xe-130	54-Xe-131	54-Xe-132
54-Xe-133	54-Xe-134	54-Xe-135	54-Xe-136	55-Cs-133
55-Cs-134	55-Cs-135	55-Cs-136	55-Cs-137	56-Ba-130
56-Ba-132	56-Ba-134	56-Ba-135	56-Ba-136	56-Ba-137
56-Ba-138	56-Ba-140	57-La-138	57-La-139	58-Ce-140
58-Ce-141	58-Ce-142	58-Ce-144	59-Pr-141	59-Pr-143
60-Nd-142	60-Nd-143	60-Nd-144	60-Nd-145	60-Nd-146
60-Nd-147	60-Nd-148	60-Nd-150	61-Pm-147	61-Pm-148
61-Pm-148m	61-Pm-149	62-Sm-144	62-Sm-147	62-Sm-148
62-Sm-149	62-Sm-150	62-Sm-151	62-Sm-152	62-Sm-153
62-Sm-154	63-Eu- 0	63-Eu-151	63-Eu-152	63-Eu-153
63-Eu-154	63-Eu-155	63-Eu-156	64-Gd-152	64-Gd-154
64-Gd-155	64-Gd-156	64-Gd-157	64-Gd-158	64-Gd-160
65-Tb-159	72-Hf- 0	72-Hf-174	72-Hf-176	72-Hf-177
72-Hf-178	72-Hf-179	72-Hf-180	73-Ta-181	74-W – 0
74-W -182	74-W -183	74-W -184	74-W -186	82-Pb- 0
82-Pb-204	82-Pb-206	82-Pb-207	82-Pb-208	83-Bi-209
88-Ra-223	88-Ra-224	88-Ra-225	88-Ra-226	89-Ac-225
89-Ac-226	89-Ac-227	90-Th-227	90-Th-228	90-Th-229
90-Th-230	90-Th-232	90-Th-233	90-Th-234	91-Pa-231
91-Pa-232	91-Pa-233	92-U -232	92-U -233	92-U -234
92-U -235	92-U -236	92-U -237	92-U -238	93-Np-236
93-Np-237	93-Np-238	93-Np-239	94-Pu-236	94-Pu-238
94-Pu-239	94-Pu-240	94-Pu-241	94-Pu-242	95-Am-241
95-Am-242	95-Am-242m	95-Am-243	95-Am-244	95-Am-244m
96-Cm-241	96-Cm-242	96-Cm-243	96-Cm-244	96-Cm-245
96-Cm-246	96-Cm-247	96-Cm-248	96-Cm-249	96-Cm-250
97-Bk-249	97-Bk-250	98-Cf-249	98-Cf-250	98-Cf-251
98-Cf-252	98-Cf-254	99-Es-254	99-Es-255	100-Fm-255

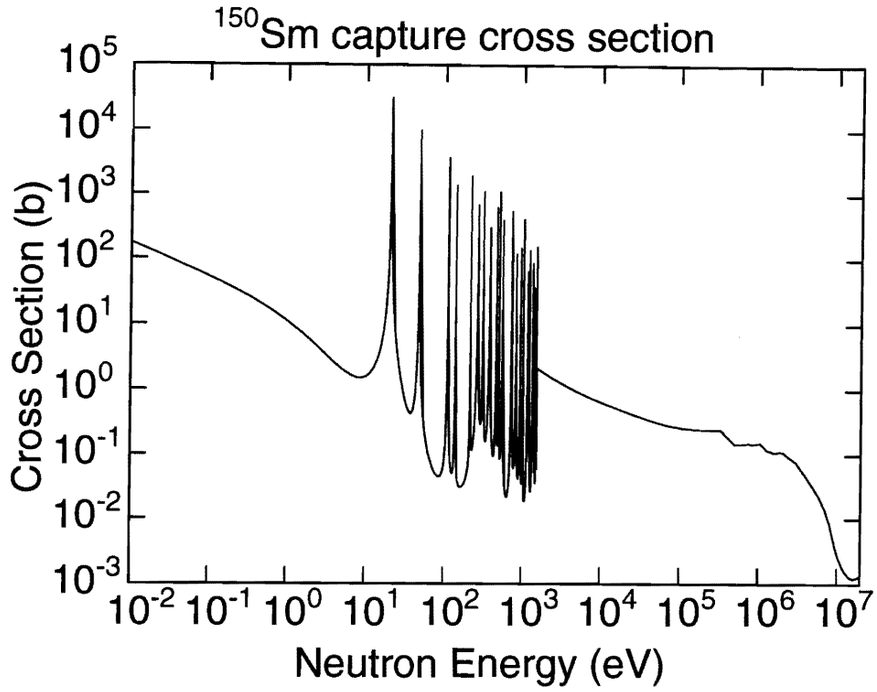

Fig. 1 Example of cross section data in JENDL-3.2

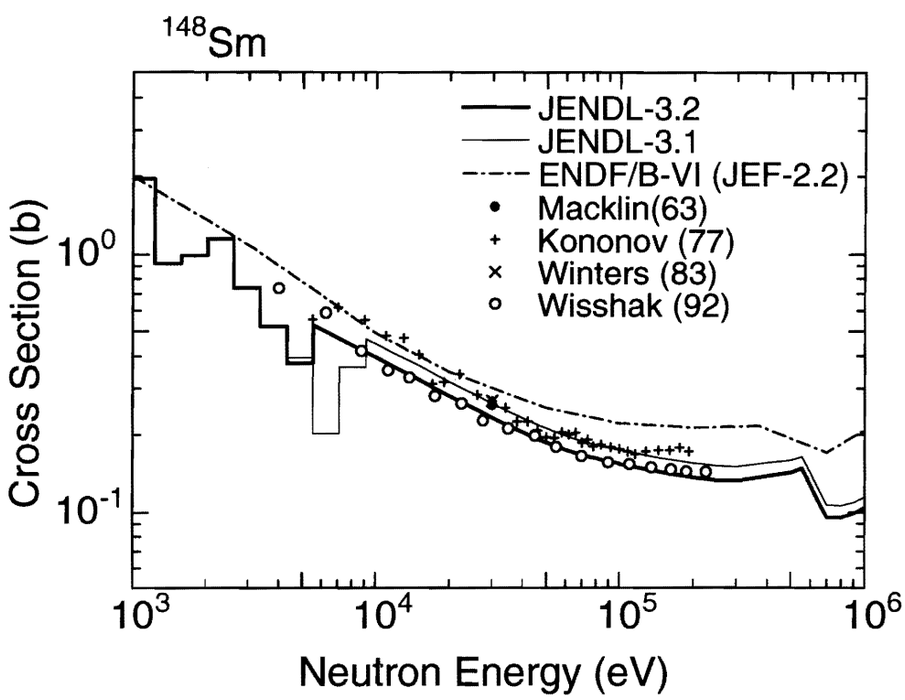

Fig. 2 ^{148}Sm capture cross section

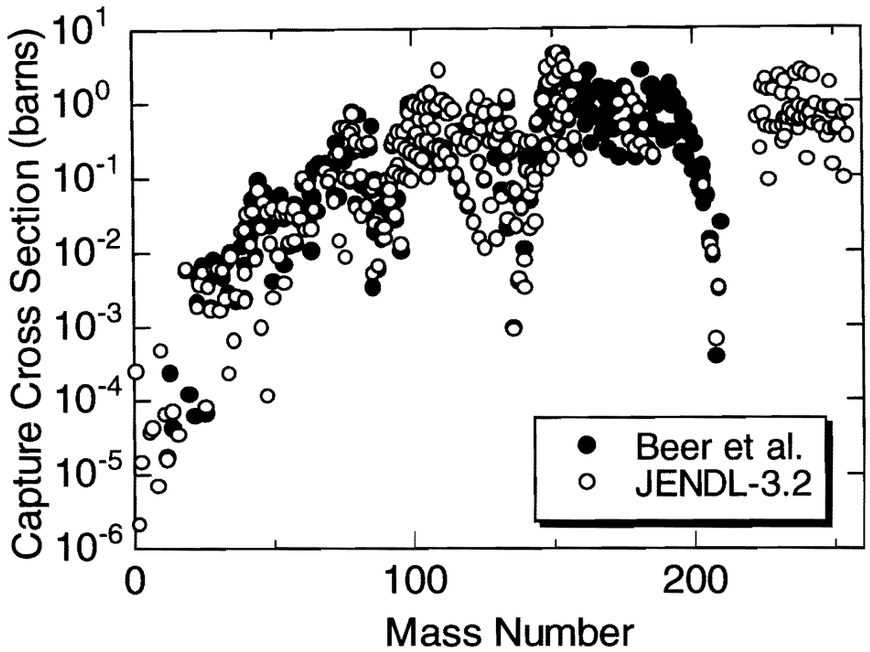

Fig. 3 Maxwellian-averaged capture cross section at kT=30 keV

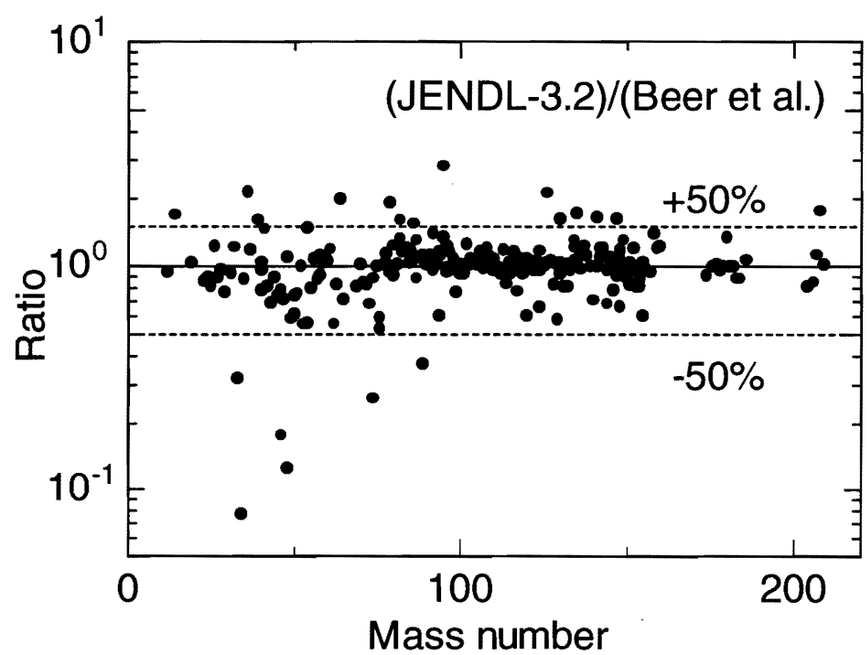

Fig. 4 Ratios of Maxwellian-averaged capture cross sections calculated from JENDL-3.2 and recommended by Beer et al.[Be92]

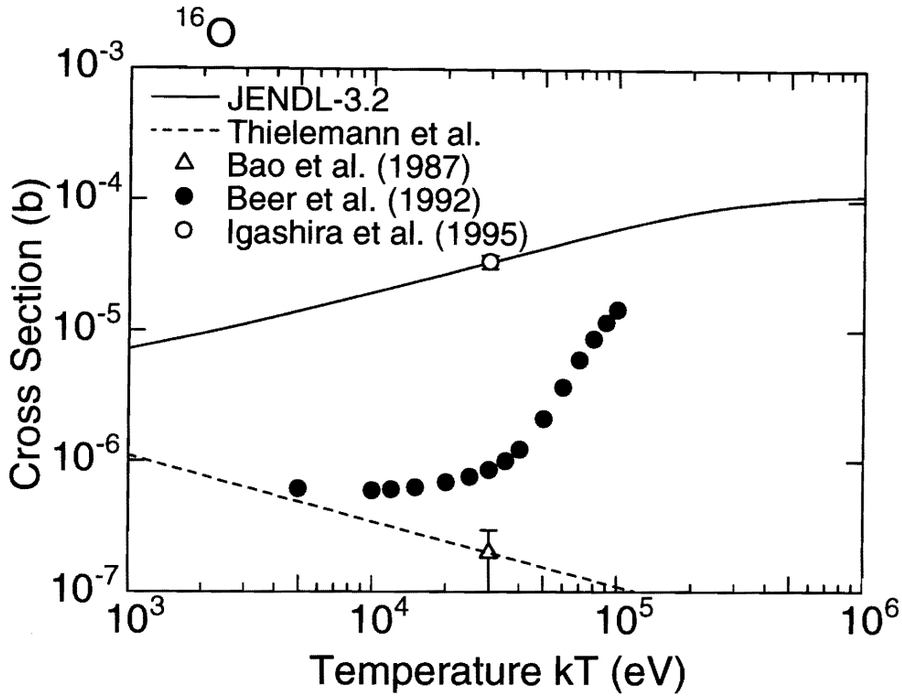

Fig. 5 Maxwellian-averaged capture cross section of ^{16}O

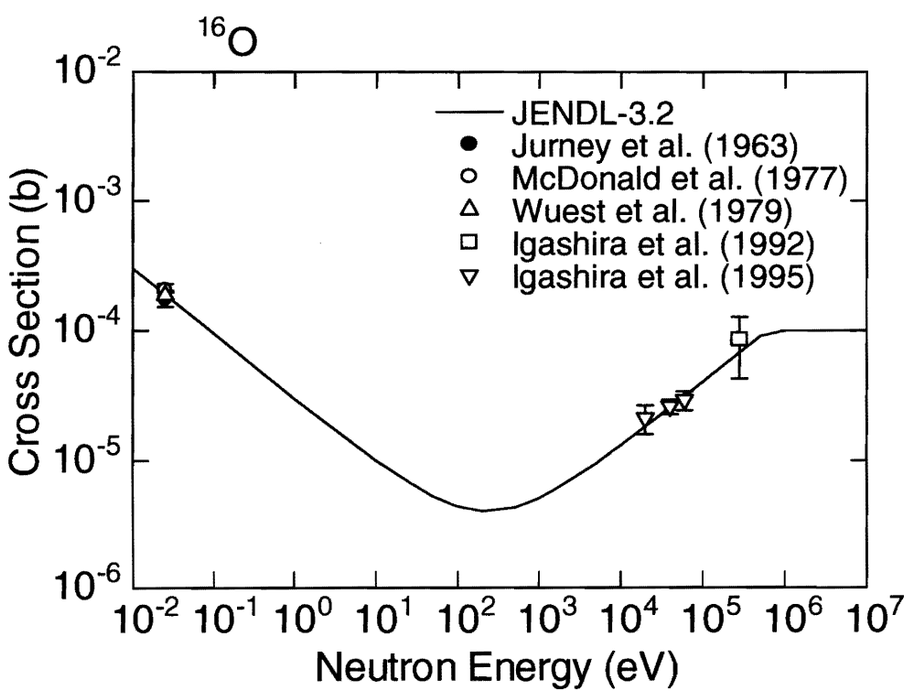

Fig. 6 ^{16}O capture cross section

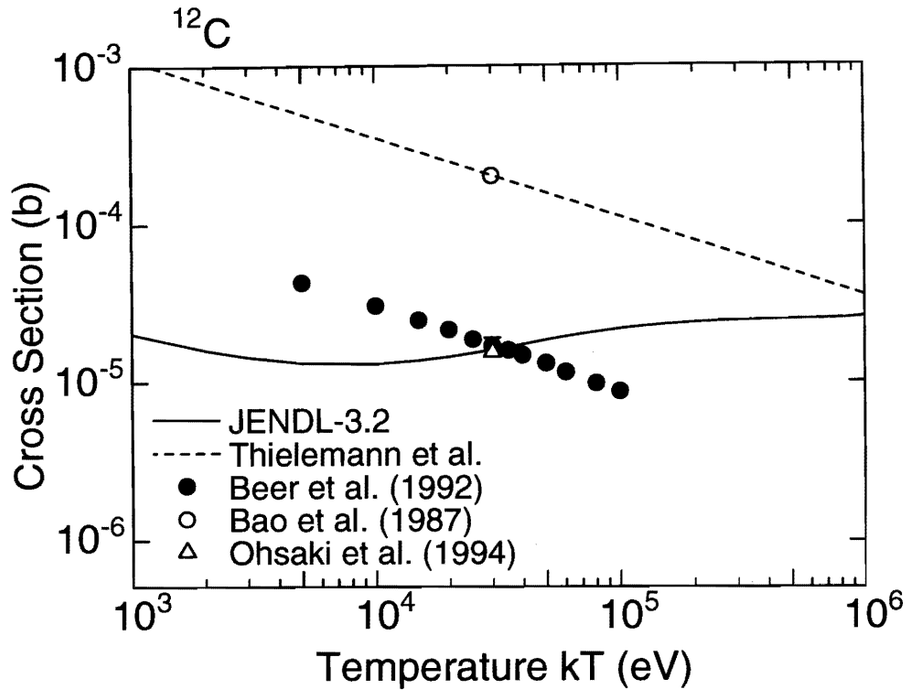

Fig. 7 Maxwellian-averaged capture cross section of ^{12}C

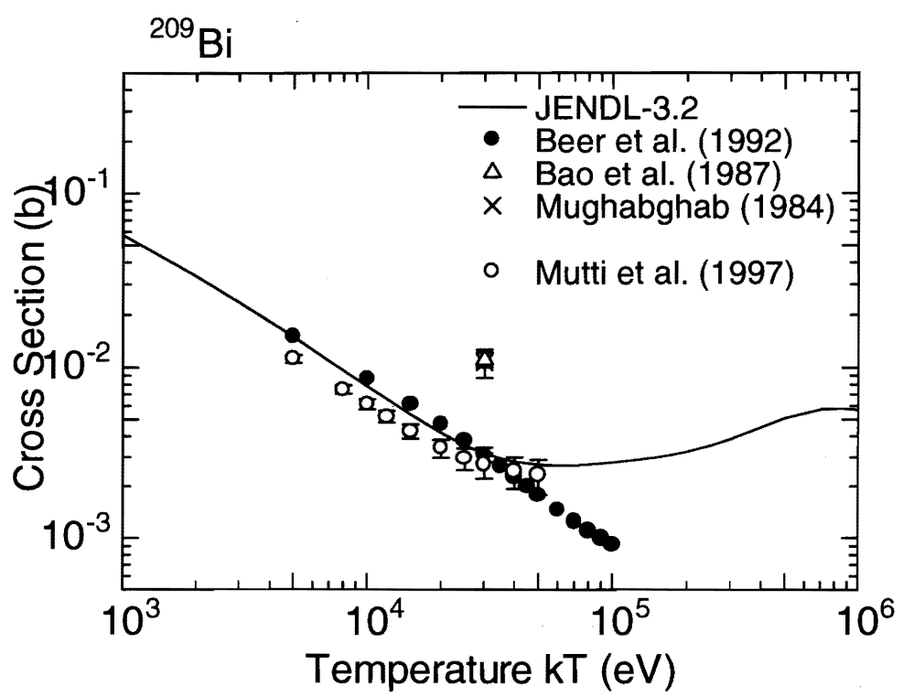

Fig.8 Maxwellian-averaged capture cross section of ^{209}Bi

Discovery of s-process Element-rich Extremely Metal-deficient Star and the Impact on Stellar Models

Nobuyuki Iwamoto

National Astronomical Observatory and Graduate University for Advanced Studies, Mitaka, Tokyo 181-8588, Japan

Abstract

Carbon star (C/O > 1 by number) LP 625-44 shows a high abundance of lead (Pb) and a peculiar distribution of s-process elements ([Pb/Ba]≈ -0.09 and [Sr/Ba]≈ -1.59). The abundance pattern can be reproduced with a narrow range of neutron exposure $\tau \sim 0.7\mathrm{mb}^{-1}$. This high neutron exposure may indicate that there exist alternative sites for s-process nucleosynthesis in metal-dificient star and/or defects in stellar modelling and input physics.

Recent observation of heavy elements, which were detected by using High Dispersion Spectrographs equipped with the world biggest telescopes KECK, SUBARU, and also the Hubble Space Telescope, has indicated that several extremely metal-deficient stars with [Fe/H] < -2.5 show remarkable enhancement of the r-process elements. Discovery of extremely metal-deficient AGB stars, which might exhibit enhancement of the s-process elements, also has long been wanted to study the stellar evolution of low and intermediate mass stars, especially nucleosynthesis of s-process elements observed in a large range of metallicity and material mixing such as third dredge-up and convective shell driven by thermal runaway of He shell burning.

Aoki et al. (2000) have discovered quite recently that the extremely metal-deficient ([Fe/H] $= -2.7$) carbon star LP625-44 contains very enhanced s-process elements. They also have succeeded in the first detection of lead (Pb) by using the ground-base Telescope AAT. Since LP 625-44 belongs to a binary system, whose evidence comes from radial velocity variations, most s-process elements found in this star are presumed to originate in ejecta from the counter AGB star under very active mass loss. The detected abundance pattern for the heavy elements from Ba to Pb was found to match very well with a scaled solar-system s-process abundance and Pb/Ba$\approx$1, while exhibiting about two orders of magnitude smaller Sr-Y-Zr abundances. This result is very different from a theoretical prediction, which results in Pb/Ba ≈ 100, derived from a stellar evolution model with low metallicity (Busso et al. 1999).

Motivated by this discovery of the LP625-44 star and disagreement between theory and observation, we have studied the s-process nucleosynthesis theoretically in canonical method by using large dimension network code (Iwamoto et al. 2000). We then found; (1) neutron exposure $\tau \sim 0.7\mathrm{mb}^{-1}$, which is one order of magnitude stronger than the standard model for the solar-system, can best fit the observed abundances in LP625-44, (2) Pb/Ba$\approx$1 and Sr-Y-Zr/Ba$\approx$1/10 are explained, (3)in the canonical method one cannot distinguish inter-pulse model in which the s-process nuclosynthesis occurs under radiative condition from thermal-pulse model in which the s-process nucleosynthesis occurs under convective condtion because the same neutron exposure reproduces the same abundance distribution of s-process elements. This neutron exposure we obtained is too high relative to the one in the evolution models with radiative ^{13}C burning. This may indicate that there exist alternative sites for the s-process nucleosynthesis in metal-dificient star (e.g. Fujimoto et al. 2000) and/or defects in stellar modelling and input physics.

References

W. Aoki, J. E. Norris, S.G. Ryan, T.C. Beers, & H. Ando, 2000, Astrophys. J., **536**, L97.
M. Busso, R. Gallino, & J. Wasserburg 1999, Annu. Rev. Astron. & Astrophys. **37**, 239.
N. Iwamoto, T. Kajino, G.J. Mathews, M.Y. Fujimoto, & W. Aoki, 2000, submitted to Astrophys. J.
M.Y. Fujimoto, Y. Ikeda, & I. Iben, Jr, 2000, Astrophys. J. **529**, L25.

Slow Neutron Capture Nucleosynthesis in AGB star

- Slow neutron capture process ....

  不安定核が中性子を捕獲するよりも早く
  β 崩壊を起こすような反応のこと

  $N_n = 10^7 \sim 10^{11}\ cm^{-3}$

- AGB星でのneutron source reactionは

  $^{22}Ne(\alpha,n)^{25}Mg$ と $^{13}C(\alpha,n)^{16}O$

  と考えられている。

^{22}Ne の起源

^{22}NeはH-burning CNO cycle の main product である ^{14}N の$^{14}N(\alpha,\gamma)^{18}F(\beta^+)^{18}O(\alpha,\gamma)^{22}Ne$ という一連の反応から合成される。しかしながら、^{14}N はsecondary elementであるので metallicity依存性がある。

^{13}C の起源

^{13}CはHe intershell への^{1}Hのmixing により$^{12}C(p,\gamma)^{13}N(\beta^+)^{13}C$ という反応を通じて合成されたと考えられている。核となる ^{12}C は He intershell での$^{4}He(2\alpha,\gamma)^{12}C$ の反応により合成されているので metallicity には依存しない。

Observational Results of Extremely Metal-Deficient star: LP 625-44
Aoki et al. (2000)

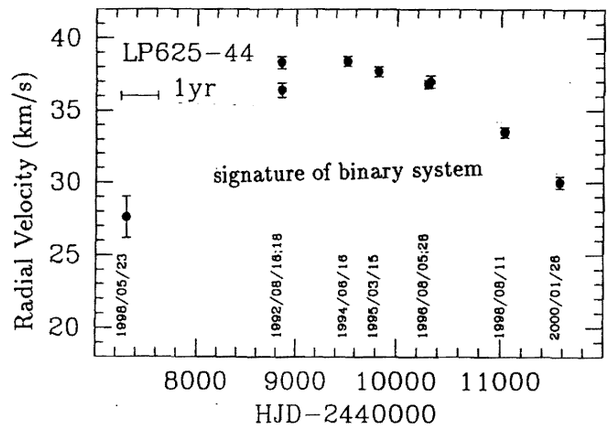

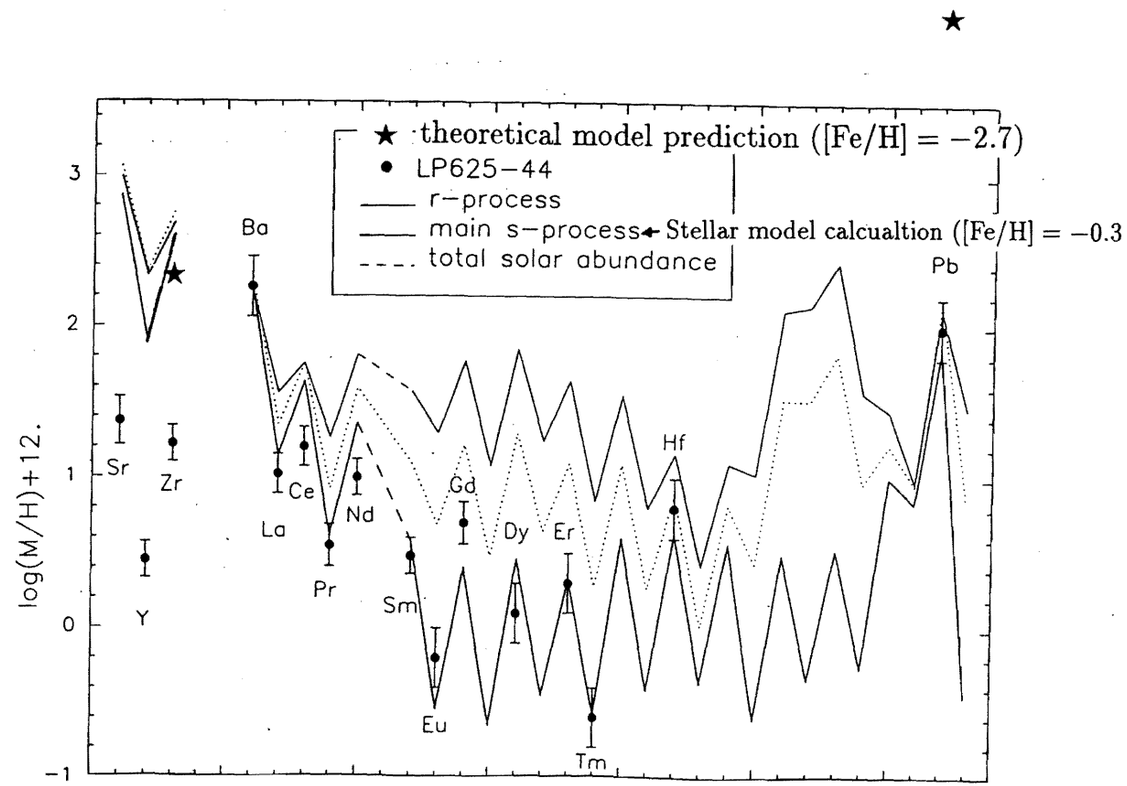

HEAVY ELEMENT ABUNDANCES FOR LP 625-44

Element	[X/Fe]	log ϵ_{el}	n	σ
Fe I ([Fe/H])	−2.71	4.78	34	0.13
Fe II ([Fe/H])	−2.70	4.79	3	0.18
Sr II	+1.15	1.37	3	0.16
Y II	+0.92	0.45	2	0.12
Zr II	+1.31	1.22	4	0.12
Ba II	+2.74	2.26	3	0.20
La II	+2.50	1.02	5	0.13
Ce II	+2.27	1.20	26	0.12
Pr II	+2.45	0.55	5	0.12
Nd II	+2.22	1.00	16	0.12
Sm II	+2.20	0.48	16	0.12
Eu II	+1.97	−0.2	2	0.20
Gd II	+2.31	0.70	6	0.13
Dy II	+1.98	0.1	4	0.2
Er II	+2.04	0.3	2	0.2
Tm II	+1.96	−0.6	1	0.2
Hf II	+2.76	0.8	2	0.2
Pb I	+2.65	2.0	1	0.2

Observational Results for LP 625-44

LP625-44は連星系《周期～12年》に属している

$T_{eff} = 5500$ K
Log g = 2.8
[Fe/H] = -2.7

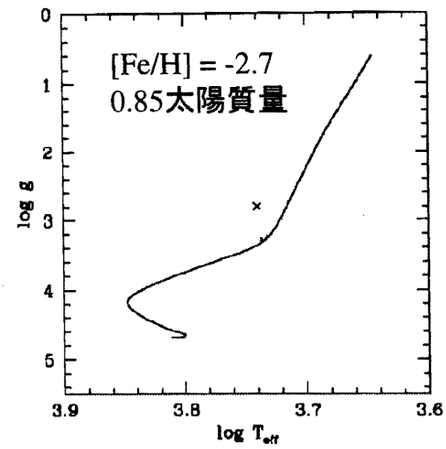

Unevolved objectであるにもかかわらず、観測されたようなheavy element-richであるのは

「companionであるAGB星からの質量降着によりLP625-44にs-process elementを多く含んだ物質が供給されたためである」と考えられる。

結果

LP625-44のheavy elementの分布からは理論的に予想されていたほどのPb abundanceの増加は見られなかった。

⬇

恒星進化モデル及びinput physicsの改良が要請される

改良すべき点

◆ 恒星進化モデル

- ^{13}C-pocket の広がりとその質量（現在の進化モデルではパラメータとして扱われている）
- Metal-rich star とは異なる合成メカニズム
- Third dredge-up の始まる時期とその大きさ
  s-process-rich star へ進化する速さを決める

◆ Nuclear reaction rate

現在考えられているs-processが起こる環境は
正しいか？

→ ^{13}C(α,n)^{16}O,^{22}Ne(α,n)^{25}Mg rateの信頼性

Single & multiple pulse model による
LP625-44 s-process abundance distribution の再現

★ Multiple pulse(r = 0.285) [#1] & r-process abundance

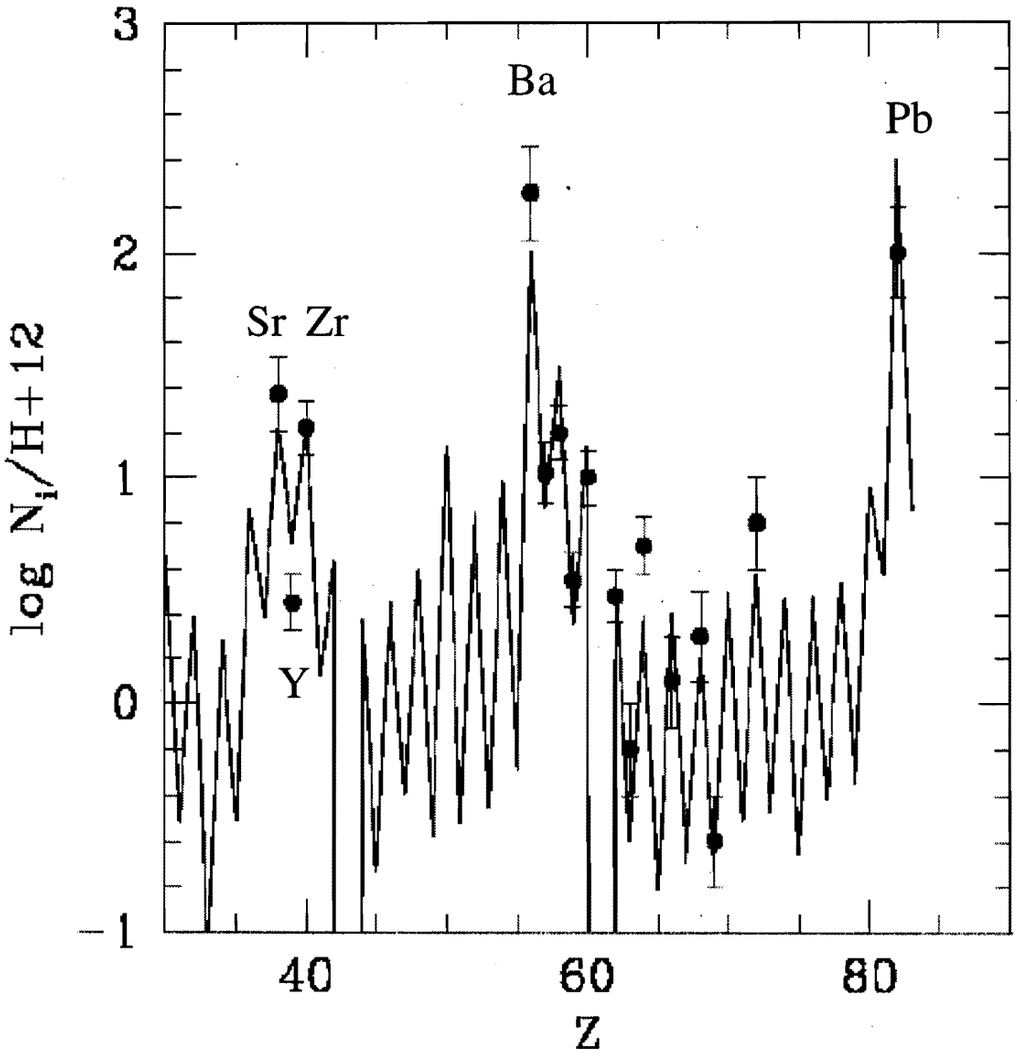

$N_n=6*10^7 cm^{-3}$ $\Delta t = 9*10^{10}$ sec
$\tau = 0.70$ mbarn^{-1}

[#1]次の n-exposure を受ける物質のうち r は以前の n-exposure を受けていたもの、残りの (1-r) はinitial seed abundance ということを表す。

まとめ

- Metal poor AGB 星 LP625-44 ([Fe/H]= -2.7) の観測により n-capture element-rich AGB 星で 初めてPb の検出に成功。

- Metal-rich AGB 星での観測を説明していた恒星進化モデルでは metal-poor AGB 星の s-process abundance distribution を説明できないことが明らかとなった。

- 恒星進化モデル及びnuclear reaction rate に更なる改良の必要性を指摘した。

- 恒星モデルに依らない s-process の計算によると n-exposure τ が ～0.7 mb^{-1} (N_n～$6*10^7 cm^{-3}$) を必要としていることが分かった。これは恒星モデルで予想されているものよりも 2 倍程度大きい値であった。
  したがって、恒星進化モデルを用いて得られた結果を再現するような環境が存在するかどうか調べる必要がある。

- Branching にあたる element (例えば、Kr,Zr,Ba,Nd,Gd など) を利用して、さらに AGB 星における s-process の物理環境に制限をつけるために (n, γ) 反応率を高精度で決定することが重要である。

A method to deduce a direct capture reaction rate from a corresponding transfer reaction

N. Imai[A], N. Aoi[A], S. Kubono[B], D. Beaumel[C], K. Abe[D], S. Kato[D], T. Kubo[E], K. Kumagai[F], M. Kurokawa[E], X. Liu[B], A. Mengoni[G], S. Michimasa[B], H. Ohnuma[H], H. Sakurai[A], P. Strasser[E], T. Teranishi[B], and M. Ishihara[E]

[A] *Department of Physics, University of Tokyo*
[B] *Center for Nuclear Study, University of Tokyo*
[C] *Institut de Physique Nucléaire*
[D] *Department of Physics, Yamagata University*
[E] *RIKEN*
[F] *Department of Physics, Tohoku University*
[G] *ENEA*
[H] *Chiba Institute of Technology*

Email: imai@nucl.phys.s.u-tokyo.ac.jp

Cross sections of direct radiative capture reactions are important to reveal the paths of the nucleosynthesis. It is difficult, however, to measure them directly because they become very small at astrophysical energies. Recently a peripheral proton transfer reaction has been proposed as an experimental tool to extract cross sections of a radiative proton capture reaction at astrophysical energies [1]. This method requires that both a radiative capture process and a corresponding transfer process should occur mainly outside the target nucleus. In such case, both cross sections depend mainly on the amplitude of tail of the overlap wave functiom between $^{A+1}$(Z+1) and ^{A}Z+p. The amplitude is called Asymptotic Normalization Coefficient (ANC). In the case of a radiative proton capture reaction, this method had been certified in ^{16}O$(p,\gamma)^{17}$F reaction [2]. In order to extend the validity of this method, we applied this method to a *neutron* radiative capture reaction, ^{12}C(n,γ)^{13}C$^{*}(1/2^{+})$. This reaction is one of the candidates which can be applied this method, because this neutron capture process was found to take place mainly outside the nucleus at astrophysical energies [3]. We have deduced the (n,γ) cross sections with the ANC values which were determined from the measurement of the corresponding neutron transfer reaction, ^{12}C(d,p)^{13}C$^{*}(1/2^{+})$.

We performed the experiment on the (d,p) reactions with a 11.8 MeV deuteron beam at SF-cyclotron facility of Center for Nuclear Study. To satisfy the peripherality of the transfer process, the differential cross sections were measured at angles down to a very forward angles of 2.0 degrees in laboratory frame. From the measured differential cross sections, the ANC value have been determined to be 3.65 $\pm$ 0.34 (statistical error) $\pm$ 0.35 (systematic error) fm^{-1}. We found that the (n,γ) cross sections deduced from the present ANC value are in good agreement with those determined in the direct measurement [4] within the errors.

References

[1] H.M. Xu *et al.*, Phys. Rev. Lett. **73**(1994)2027.
[2] C.A. Gagliardi *et al.*, Phys. Rev. C **59**(1999)1149.
[3] T. Otuka *et al.*, Phys. Rev. C **49**(1994)2289.
[4] T. Ohsaki *et al.*, Astrophys. J. **422**(1994)912.

How about in (n,γ) reaction ?

$$\sigma(^{12}C(n,\gamma)^{13}C^*(1/2^+)) \xleftarrow{\text{ANC}} \frac{d\sigma}{d\Omega}_{\theta\sim 0}(^{12}C(d,p)^{13}C^*(1/2^+))$$

Reason 1

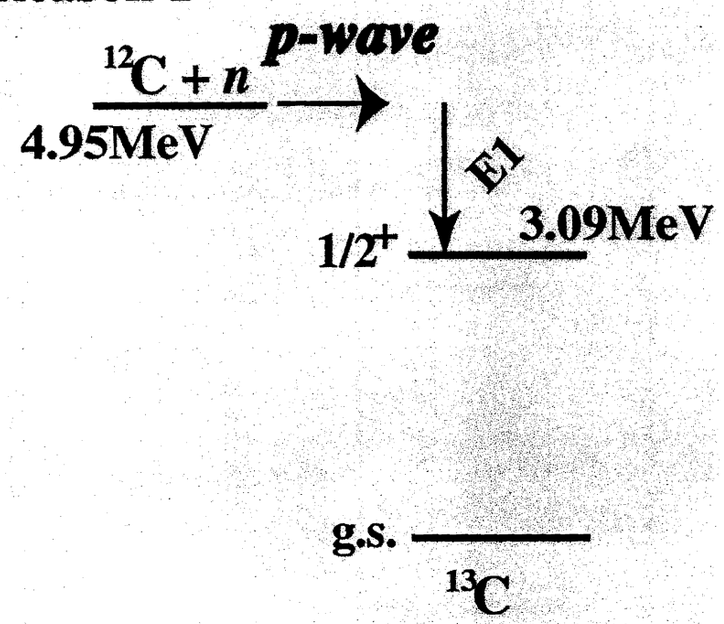

take place outside nuclei !!

Reason 2

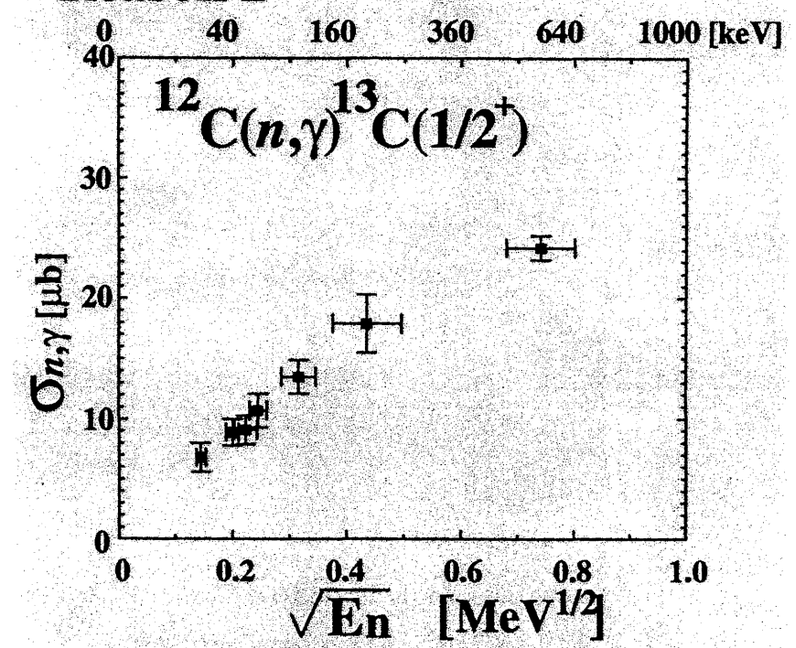

T. Ohsaki, et al., Astrophys. J.422(1994)912

σ (30 < En < 500 keV) is known !!

Experiment

Energy spectrum

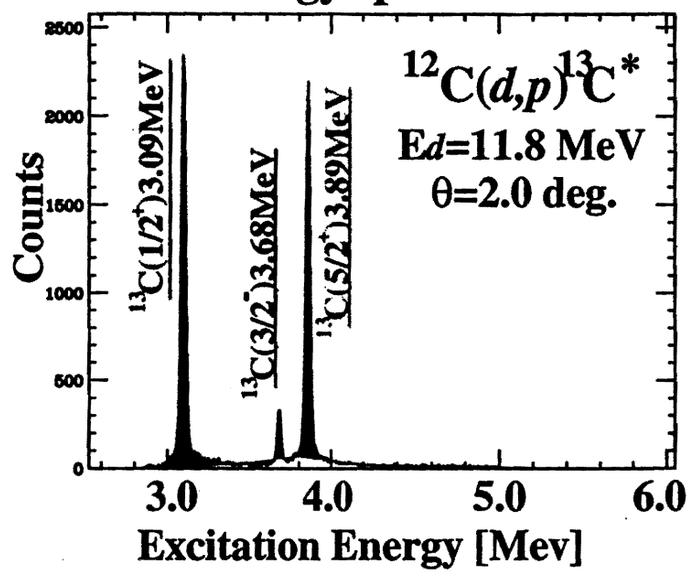

Angular distributions

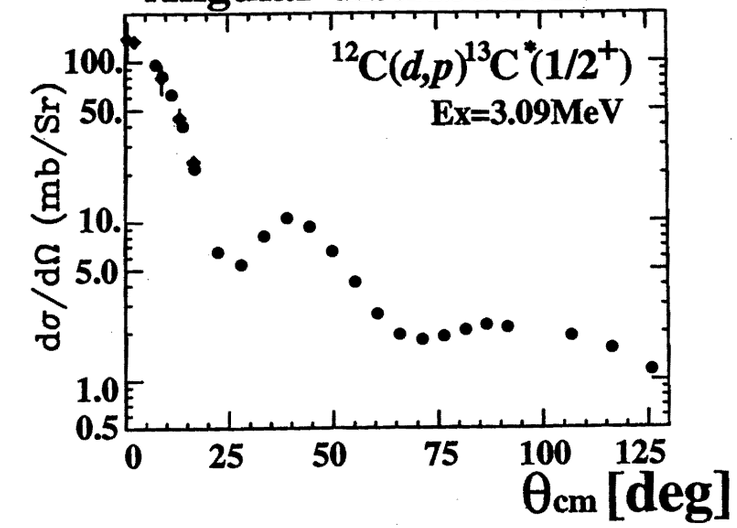

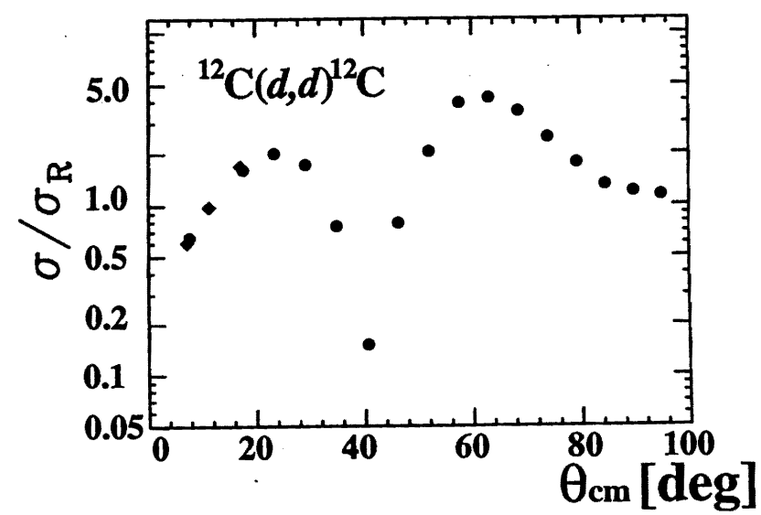

Discussion

Differential cross sections of $^{12}C(d,p)^{13}C(1/2^+)$

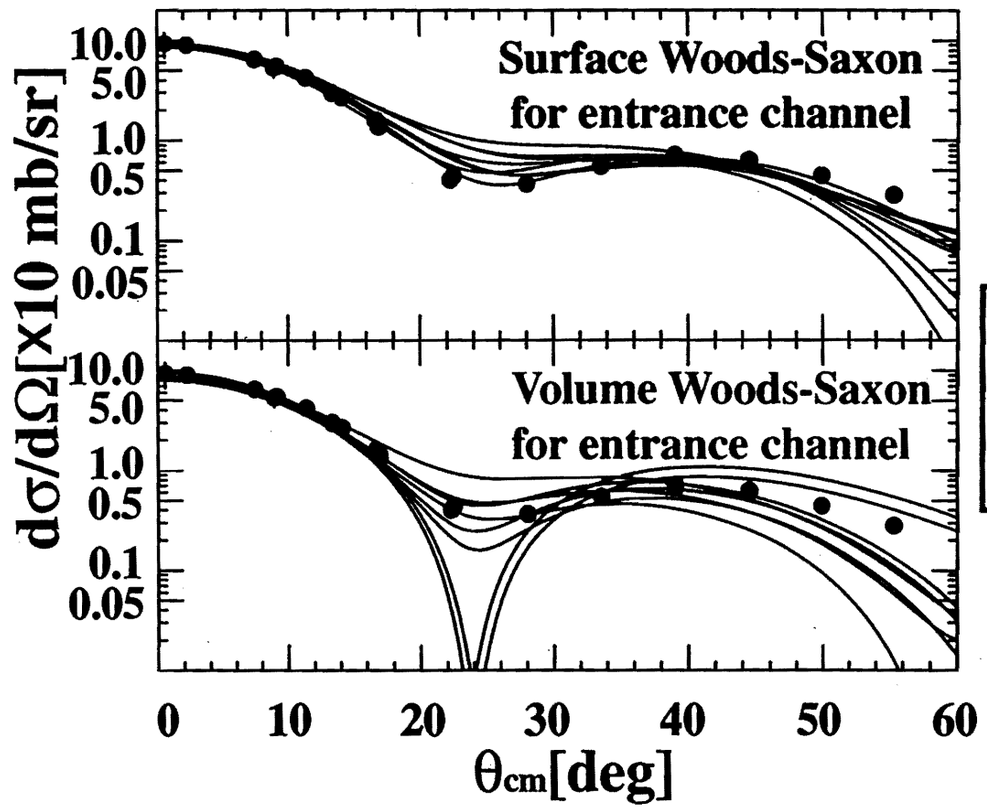

Spectroscopic factor : 1

Points : experimental data x 0.8

At forward angles, all calculated cross sections **reproduce** angular distribution of experimental data.

standard deviation/mean value at 2 deg. 3.6%(surface type)
6.4%(volume type)

Uncertainty from optical potential~ **6.4%**

2) Bound state potential dependence

Radius(r_0): 1.1~1.4fm

Diffuseness(a): 0.5~0.7fm

Depth: reproduce the B. E.

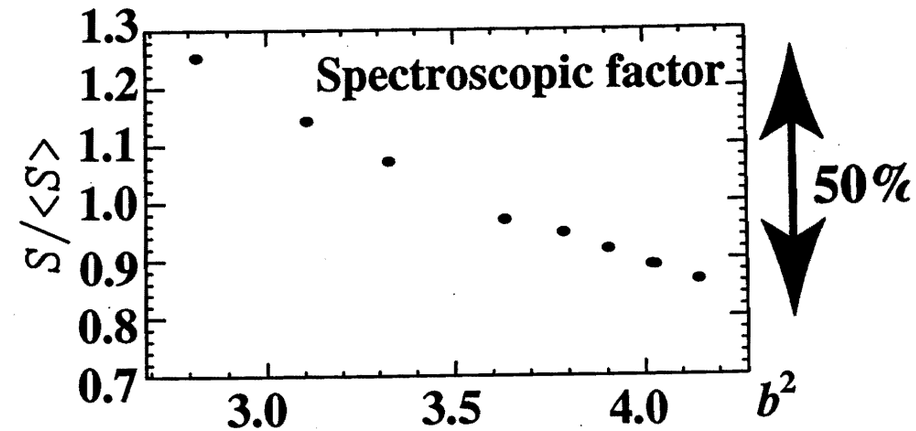

The spectroscopic factor changes largely

but...

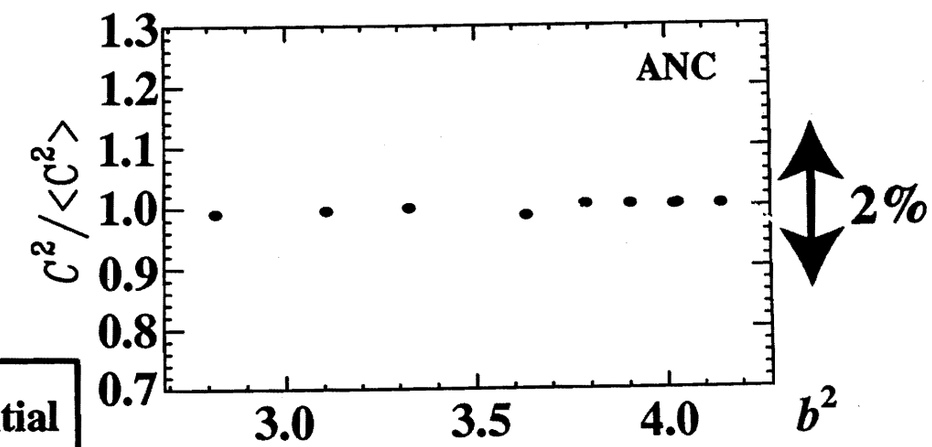

Uncertainty from bound state potential ~ 2%

Cross sections of $^{12}C(n,\gamma)^{13}C(1/2^+)$ Discussion

The value of $ANC^2 = 3.65 \pm 0.34 \pm 0.35\ fm^{-1}$
(statistic) (systematic)

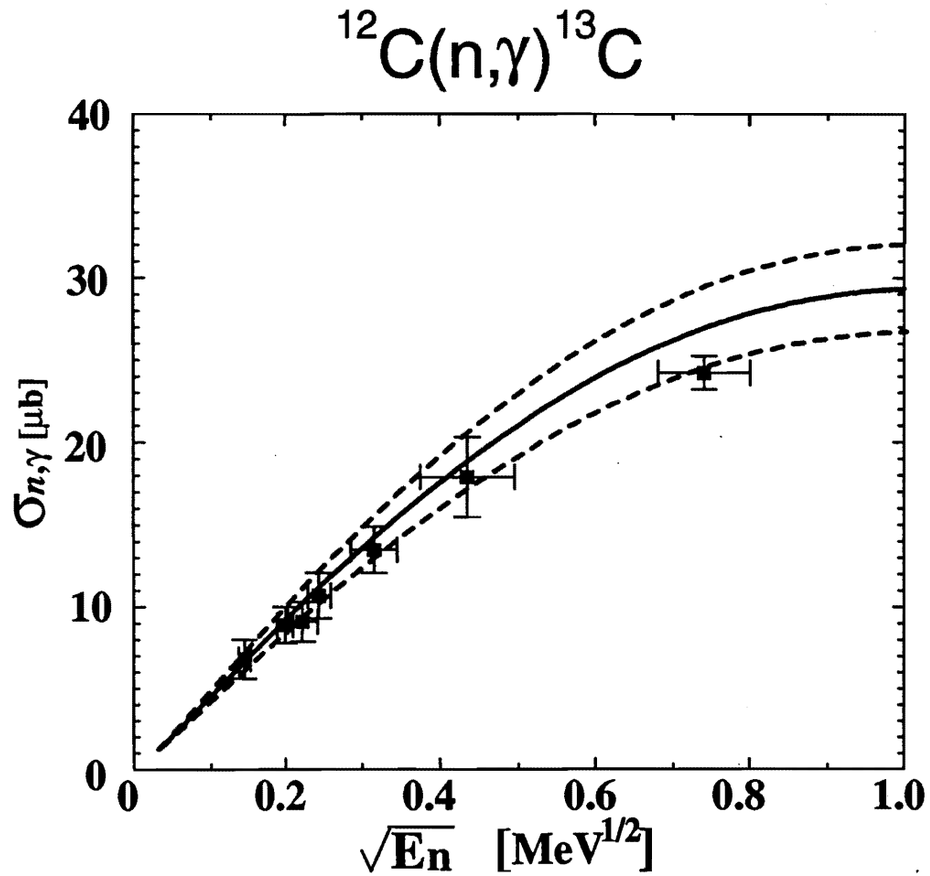

——— : calculated with mean value

----- : systematic error included

$\sigma(n,\gamma)$ is determined with the value of ANC

reproduce
very well !

Experimental methods for nuclear astrophysics research

Tohru Motobayashi, Rikkyo University

1 Astrophysical reactions involving unstable nuclei

Short-lived nuclei play essential roles in "explosive" stellar nuclear burning, where the temperature and density are so high that capture reactions on unstable nuclei can be faster than their weak decays. However, to study directly these capture reactions in laboratories is very difficult, because these nuclei can hardly be served as targets. One of the solution is to employ low-energy radioactive beams, and to perform experiments in inverse kinematics. The first measurement was for the ^{13}N(p,γ)^{14}O reaction, a key of the hot CNO cycle. In the experiment performed at Louvain la Neuve [1], a 0.6 A MeV ^{13}N beam bombarded a $(CH_2)_n$ target, and emitted γ ray was measured by Ge detectors. As indicated in Table 1, 85 γ ray events were measured in 30 hour with 3×10^8 s^{-1} intensity. It should be noted, however, that the observed yield is for the process through the strong 1^- resonance at 5.17 MeV excitation energy, and hence the cross section of around 100 μb is very large among the (p,γ) reactions of astrophysical interest. Therefore, other reactions with smaller cross sections are very hard to study directly, especially for radiative capture processes. The process with strong interaction, such as (p,α) and (p,n) reactions, may be studied due to their large cross sections. Such an example is the ^{8}Li(α,n)^{11}B reaction studied at RIKEN [2] and Notre Dame University [3].

Table 1: Comparison of the Coulomb dissociation (CD) and direct capture (DC) measurements for the ^{13}N(p,γ)^{14}O reaction.

	Coulomb dissociation[a]	direct capture[b]	ratio: CD/DC
Projectile	^{14}O	^{13}N	
Beam energy	87.5 AMeV	0.6 AMeV	
Beam intensity	3×10^4 s^{-1}	3×10^8 s^{-1}	10^{-4}
Target material	^{208}Pb	$(CH_2)_n$	
Target thickness	350 mg/cm^2	180 μg/cm^2	65
Cross-section	10 mb	100 μb	10^2
Efficiency	0.5	2×10^{-3}	350
Data taking	36 h	30h	1.2
Total counts	1.5×10^4	85	180

[a] ^{208}Pb(^{14}O,^{13}N p)^{208}Pb at RIKEN [4]
[b] ^{1}H(^{13}N,γ)^{14}O at Louvain la Neuve [1]

2 Coulomb dissociation

Various indirect methods have been proposed to study these hard-to-measure reactions of astrophysical interest. One of the promising method is the Coulomb dissociation. It has been applied to several (p,γ) reactions of astrophysical interest, such as the ^{14}O [4, 5] and ^{8}B [6, 7]

dissociation for studying the $^{13}N(p,\gamma)^{14}O$ reaction and the solar neutrino production reaction $^{7}Be(p,\gamma)^{8}B$, respectively. The Coulomb dissociation and its corresponding direct capture are related through the virtual photon intensity calculated by an appropriate model. An advantage of the method is expected large yield due to the large cross section and possibility to use thick targets. As demonstrated in Table 1, the experimental yield of the Coulomb dissociation is much larger, and hence it opens up a possibility to study weaker processes.

Further applications of the method have been made for some reactions in the hot pp mode burning: $^{8}B(p,\gamma)^{9}C$ [8], $^{11}B(p,\gamma)^{12}N$ [9, 10], and $^{12}N(p,\gamma)^{13}O$ [10]. High-precision tests of the Coulomb dissociation method is in progress for the $^{12}C(p,\gamma)^{13}N$ and $^{14}N(p,\gamma)^{14}O$ reactions at RIKEN [11].

The Coulomb dissociation method assumes a one-step electromagnetic excitation mechanism. Possible higher-order processes become important at low incident energies. For example, Nunes and Thompson [12] and Esbensen and Bertsch [13] calculated very large multi-step excitation components in the ^{8}B dissociation data taken at Notre Dame University with 3.2 *A*MeV beam energy [14]. Another disadvantage of low-energy experiments is their thinner targets that require higher beam intensities. Therefore, the Coulomb dissociation might not match to the CRIB facility as far as for extracting astrophysical capture cross sections.

3 "ANC" determination

Recently, the "ANC" method is proposed for extracting the cross section of the radiative capture through continuum states [15]. The Asymptotic Normalization Coefficient (ANC) is a normalization factor for the tail part of a single particle wave function. Since the low-energy radiative capture is only sensitive to the wave function at distances far from the nuclear radius, the ANC can be related to the capture cross section with a good accuracy. The ANC method employs a particle transfer reaction to determine the coefficient. The validity of the method was successfully tested for the reactions of $^{16}O(p,\gamma)^{17}F$ [16] and $^{12}C(n,\gamma)^{13}C$ [17] by the (^{3}He,d) reaction and (d,p) reactions, respectively, at 6-10 *A*MeV incident energies. Experiments with RI beams have already started by $^{2}H(^{7}Be,^{8}B)n$ at Beijing [18] and RIKEN [19], and (^{7}Be,^{8}B) on ^{10}B and ^{14}N at Texas A&M [20]. The method is being applied also to the $^{8}B(p,\gamma)^{9}C$ and $^{11}C(p,\gamma)^{12}N$ at RIKEN [19] and Texas A&M [21], respectively. The suitable incident energy is around 10 *A*MeV, and it matches the CRIB facility. The angle-integrated cross section is usually relatively large, *i.e.* in the order of 1 mb. Further studies may be necessary to verify the method in connection with well-discussed mechanism of (d,p) type reactions at low energies.

4 Resonance spectroscopy

4.1 REACTION RATES AND RESONANCE PARAMETERS

When the astrophysical reaction of interest is dominated by a process through a resonant state, its parameters are essential to determine the astrophysical reaction rate P_{12} defined as,

$$P_{12} = n_1 n_2 \langle \sigma v \rangle, \tag{1}$$

where $\langle \sigma v \rangle$ is the convolution of the Maxwell-Boltzmann distribution and energy-dependent cross section, and n_1 n_2 are the density of "1" and "2", the particles in the incident channel of the relevant reaction. For an isolated resonance with the resonance energy E_0, the total width

Γ_{tot}, and the partial width of the incident and final channels Γ_i and Γ_f, the cross section is written by the Breit-Wigner formula,

$$\sigma(E) = \pi\lambda^2\omega\frac{\Gamma_i\Gamma_f}{(E-E_0)^2+\Gamma_{tot}^2/4}, \tag{2}$$

where ω denotes the spin factor $[(2j_{f1}+1)(2j_{f2}+1)]/[(2j_{i1}+1)(2j_{i2}+1)]$. If the width is narrow compared with the energy dependence of the Boltzmann distribution and $\Gamma_f \ll \Gamma_i \approx \Gamma_{tot}$, the reaction rate is calculated approximately to be proportional to Γ_f. The latter condition is usually satisfied for (p,γ) reactions, and therefore the determination of the electromagnetic width Γ_γ is enough to evaluate the astrophysical reaction rate. The study of the ^{14}O Coulomb dissociation discussed in sect. 2 determines Γ_γ of the first 1^- state in ^{14}O, since the hot CNO cycle burning is dominated by this resonance. However, there exist many cases where the direct determination of Γ_f is difficult or even impossible. For these cases, the independent determination of both the total width Γ_{tot} and the branching ratio Γ_f/Γ_{tot} can deduce the width of interest as their product.

4.2 TOTAL WIDTH

A good method to determine the resonance width of unstable nuclei has been proposed recently. An example is for the p+^{13}N system studied at Louvain la Neuve [22]. A low-energy ^{13}N beam bombarded a polyethylene target, and the proton recoiled from the elastic scattering was detected. The incident energy and target thickness were adjusted so that the energies of ^{13}N before and after punching through the target were respectively above and below the resonance. Since the energy of the recoil proton was close to the energy when the elastic scattering took place in the target due to its small energy loss in the target, the measured proton energy-spectrum affected the excitation function of the elastic scattering. Therefore, by analyzing the shape of the spectrum, the resonance energy E_0 and the total width Γ_{tot} were extracted with good accuracies, almost independent of the energy spread of the incident beam. Therefore, this is an useful method for RI beam experiments not only for the determination of Γ_{tot} but for the precise measurement of E_0, which is quite important because of the high sensitivity of the reaction rate to the location of the resonance.

Due to the above advantages together with its expected large cross section, this method is suitable for studies using the CRIB system, as pointed out by Teranishi [23].

4.3 BRANCHING RATIO

The branching ratio can be extracted by measuring the production yield of the resonance of interest and the intensity of the decay. To determine the partial width of interest by coupling it with the total width, the branching ratio for the weaker decay should be measured.

Attempts to apply this method to the 1^- state in ^{14}O have been made in connection with the ^{13}N(p,γ)^{14}O reaction. The ^{12}C(^{3}He,n) [24] or ^{14}N(p,n) [25] reaction was used to populate the state of interest, and its γ decay was measured in coincidence with the outgoing particle. The coincidence probability can be related to the branching ratio. However, only results with large ambiguities could be obtained due to the small branching ratio of the order of 10^{-4} and the experimental background for the γ ray measurement.

Another example is for the ^{15}O(α,γ)^{19}Ne reaction, the most important reaction for the break-out from the hot CNO to rp process hydrogen-burning. The key state is located 504 keV above the α decay threshold in ^{19}Ne. In contrast to usual radiative capture processes, the α decay

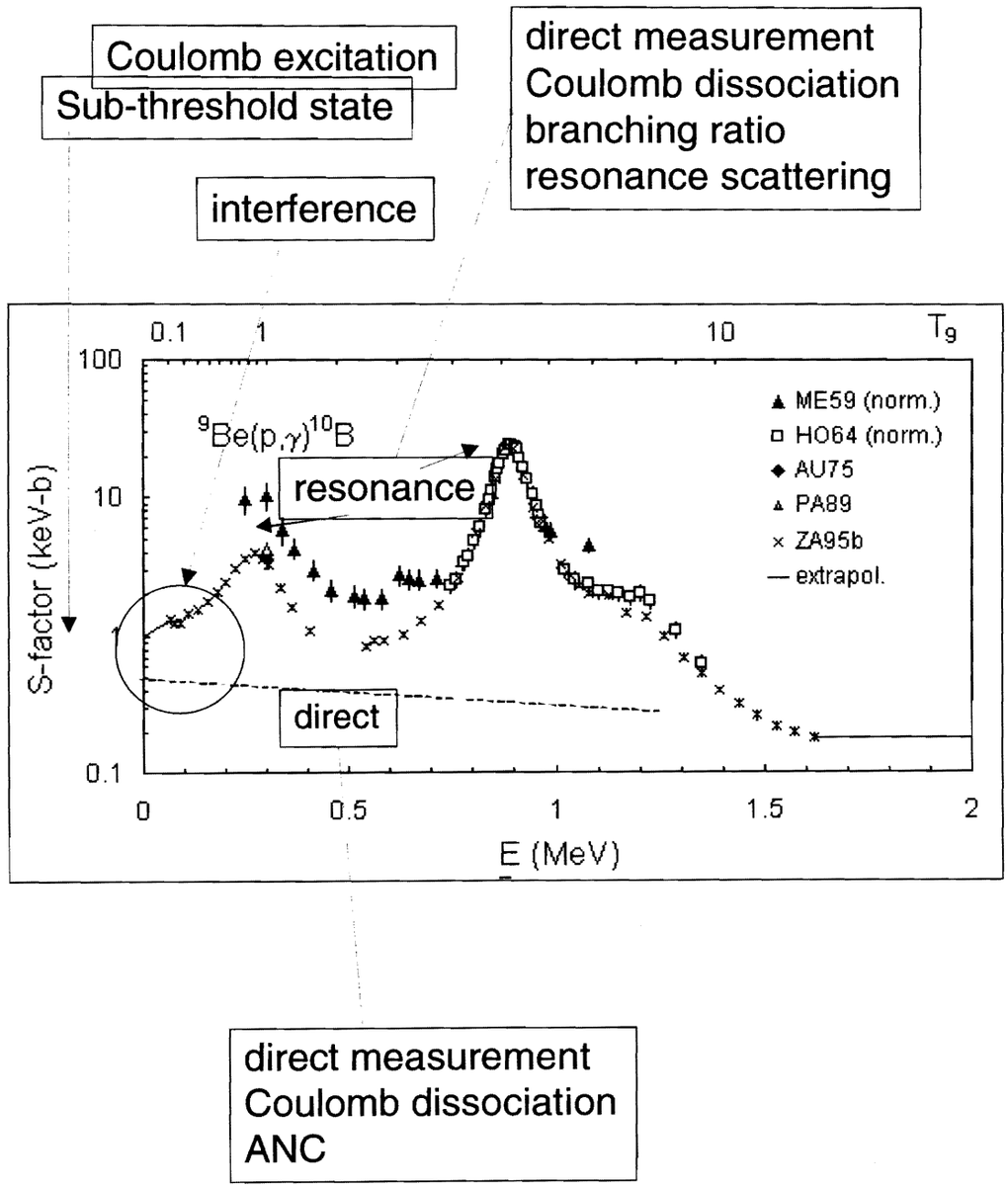

Figure 1: Low-energy behavior of a (p,γ) reaction of astrophysical interest. Various methods of studies are indicated.

width Γ_α is much smaller than the γ-width, due to the large Coulomb barrier effect and the nuclear structure of the state which has only a small overlap with the α+^{15}O configuration. Magnus *et al.* [26] used the ^{19}F(^{3}He,t) reaction to excite the $3/2^+$ state of interest, and its α decay was measured in coincidence with the outgoing triton to determine the branching ratio $\Gamma_\alpha/\Gamma_{\rm tot}$. However the α decay branch could be obtained only for higher states. This is due to the low decay energy that suffers the α particle measurement, together with the low branching ratio of the order of 10^{-4}. Another measurement at CNS SF cyclotron could not either extract a finite number for the α branching ratio of the $3/2^+$ state [27].

A possible idea to overcome the difficulty mentioned above might be to employ the inverse kinematics, where the resonance in ^{19}Ne is produced in the moving frame. The decaying α particle has a high velocity similar to that of the beam, and hence is detected without experimental problem. The experiment requires simultaneous detection of both decaying α and residual ^{15}O. This might be possible by the DUMAS system of CRIB by some sophistication for the detector system.

4.4 SUBTHRESHOLD STATES

The high-energy tail of a subthreshold state can affect the behavior of low-energy capture cross sections. The ^{12}C(α,γ)^{16}O reaction, which is discussed by Morinobu [28], is a well-known case. The astrophysical S factor is expected to rise toward zero energy, affected by the 1^- state located 45 keV below the threshold. The effect of the tail can be evaluated essentially from the γ width and the spectroscopic factor of the state [29].

We made an experiment to determine Γ_γ of the $3/2^+$ state in ^{15}O to study the influence of this subthreshold state to the low-energy cross sections of the CNO-cycle reaction ^{14}N(p,γ)^{15}O [30]. An RI beam of ^{15}O at 85 AMeV bombarded a thick (1.5 g/cm^2) lead target, and γ rays from the $3/2^+$ state, which was populated by the Coulomb excitation mechanism, were measured. In almost the same procedure as for the Coulomb dissociation, the γ width can be extracted from the measured Coulomb excitation cross section. The analysis is in progress. It should be noted that the spectroscopic factor of the state is known with a certain accuracy from proton-transfer reaction studies and also from the ^{14}N(p,γ)^{15}O*($3/2^+$) measurement [31].

Since the Coulomb excitation is applicable at lower incident energy, CRIB-based RI beams can be used for such studies, though the disadvantage of necessity to use thinner targets should be overcome.

5 Summary

Figure 1 shows an overview of the experimental methods to study various aspects of a reactions of astrophysical interest. These methods have their own advantages and limitations as discussed in this report. Among them, the ANC method, resonance scattering and determination of branching ratios might be well suited for studies with RI beams with 5-15 AMeV energies.

References

[1] P. Decrock *et al.*, Phys. Rev. Lett. 67 (1991) 808; Th. Delbar *et al.*, Phys. Rev. C 48 (1993) 3088.

[2] R.N. Boyd *et al.*, Phys. Rev. Lett. **68** (1992) 1283.

[3] X. Gu *et al.*. Phys. Lett. **343B** (1995) 31.

[4] T. Motobayashi *et al.*, Phys. Lett. **B264** (1991) 259.

[5] J. Kiener *et al.*, Nucl. Phys. A552 (1993) 66.

[6] T. Motobayashi *et al.*, Phys. Rev. Lett. 73 (1994) 2680; N. Iwasa *et al.*, J. Phys. Soc. Jpn. 65 (1996) 1256: T. Kikuchi *et al.*, Phys. Lett. B391 (1997) 261; T. Kikuchi *et al.*, Eur. Phys. J. A3 (1998) 209.

[7] N. Iwasa *et al.*, Phys. Rev. Lett. **83** (1999) 2910.

[8] T. Motobayashi *et al.*, RIKEN Acc. Progr. Rep. **33** (2000) 60.

[9] A. Lefebvre *et al.*, Nucl. Phys. **A592** (1995) 69.

[10] T. Minemura *et al.*, Proc. Symp. Origin of Matter and Evolution of the Galaxies (OMEG2000), Jan. 2000, Tokyo, to be published.

[11] M. Serata *et al.*, Proc. Symp. Origin of Matter and Evolution of the Galaxies (OMEG2000), Jan. 2000, Tokyo, to be published.

[12] F.M. Nunes and I.J. Thompson, Phys. Rev. **C 59** (1999) 2652.

[13] H. Esbensen and G.F. Bertsch, Phys. Rev. **C 59** (1999) 3240.

[14] J. Schwarzenberg *et al.*, Phys. Rev. **C53** (1996) R2598; V. Guimarães *et al.*, Phys. Rev. Lett. **84** (2000) 1862.

[15] G,N, Xu *et al.*, Phys. Rev. Lett **73** (1994) 2027; A.M. Mukhamedzhanov *et al.*, Phys. Rev. **C 56** (1995) 1302.

[16] C.A. Gagliardi *et al.*, Phys. Rev. C 59 (1999) 1149.

[17] N. Imai *et al.*, Proc. "Nuclei in the Cosmos" Conference, to be published.

[18] X. Bai *et al.*, Nucl. Phys. A588 (1995) 273c; W. Liu *et al.*, Nucl. Phys. A616 (1997) 131c.

[19] D. Beaumel *et al.*, private communication.

[20] A. Azhari *et al.*, Phys. Rev. Lett. 82 (1999) 3960; A. Azhari *et al.*, Phys. Rev. C60 (1999) 055803.

[21] C.A. Gagliardi, NS2000 Symposium, Aug. 2000, Michigan State University.

[22] Th. Delbar *et al.*, Nucl. Phys. **A542** (1992) 263.

[23] T. Teranishi, this symposium.

[24] P.B. Fernandez, E.G. Adelberger and A. Garcia, Phys. Rev. **C40** (1989) 1887.

[25] M.S. Smith *et al.* Phys. Rev. **C47** (1993) 2740.

[26] P.V. Magnus *et al.*, Nucl Phys. **A506** (1990) 332.

[27] M. Kurokawa *et al.*, Proc. Int. Symp. Origin of Matter and Evolution of Galaxies 97, Atami 1997, ed. S. Kubono, T. Kajino, K.I. Nomoto and I. Tanihata, (World Scientific, Singapore) p. 245.

[28] S. Morinobu, this symposium.

[29] C.E. Rolfs and W.S. Rodney, Cauldrons in the Cosmos, The University of Chicago Press, 1988.

[30] K. Yamada *et al.*, Proc. Symp. Origin of Matter and Evolution of the Galaxies (OMEG2000), Jan. 2000, Tokyo, to be published.

[31] U. Schröder *et al.*, Nucl. Phys. A467 (1987) 240.

【4】 Techniques for Production and Experiment of RIB

KEK-JAERI RNB facility

H. Miyatake, IPNS, KEK

24/Aug./00

Abstract

The RNB facility at KEK-Tanashi was closed in September 1999 and all of the instruments, which are ion-source systems, isotope separator on-line (ISOL), split-coaxial radio-frequency (SCRFQ), inter-digital H-type (IH) linac, and measuring devices, have been tentatively stored at KEK. For the swift resumption of the research activities relating to this facility, these instruments will be transferred to the Tandem facility of JAERI based on the recommendation of the third-party review committee for the Joint Project. We, KEK and JAERI people, thus will jointly construct a new RNB facility in coming three years.

This facility will consist of the 18MV Tandem accelerator, ISOL, charge-breeding electron cyclotron resonance ion-source (ECRIS), SCRFQ-linac, two IH-linacs (IH1 and IH2), three Bunchers and superconducting (SC) linac, in which Bunchers, IH2-linac and the charge-breeding ECRIS will be newly constructed and only the slight modification of rf-frequencies for the existing SCRFQ- and IH1-linacs is required to match the rf-frequency of the SC-linac.

Radioactive nuclei are produced by the nuclear fusion, transfer, and induced fission processes with using proton and heavy-ion beams from the Tandem accelerator. The mass-separated ions of exotic nuclei having with A/q¡7 can be accelerated by the linac complex up to 5 MeV/u to utilize for research fields in nuclear physics, nuclear chemistry, nuclear astrophysics, and material science. It is noted that the high quality RNB with its energy of 5 MeV/u, which is above the Coulomb barrier for the almost target species, will be available in 2005.

The intense stable-nuclear beams will be also available from the linac complex. These beams can be provided to the experimental halls in parallel with the Tandem beam with the help of the ECRIS for the SCRFQ-linac. Hence this facility will supply an additional machine time for the existing research activities.

短寿命核分離加速実験装置の原研東海移転案

IPNS, KEK　宮武宇也

- KEK-田無,短寿命核分離加速実験装置の説明
- 装置建設後の成果
- 原研東海移転案、目的と特徴

（• 統合案における短寿命核実験装置）

短寿命核分離加速実験装置

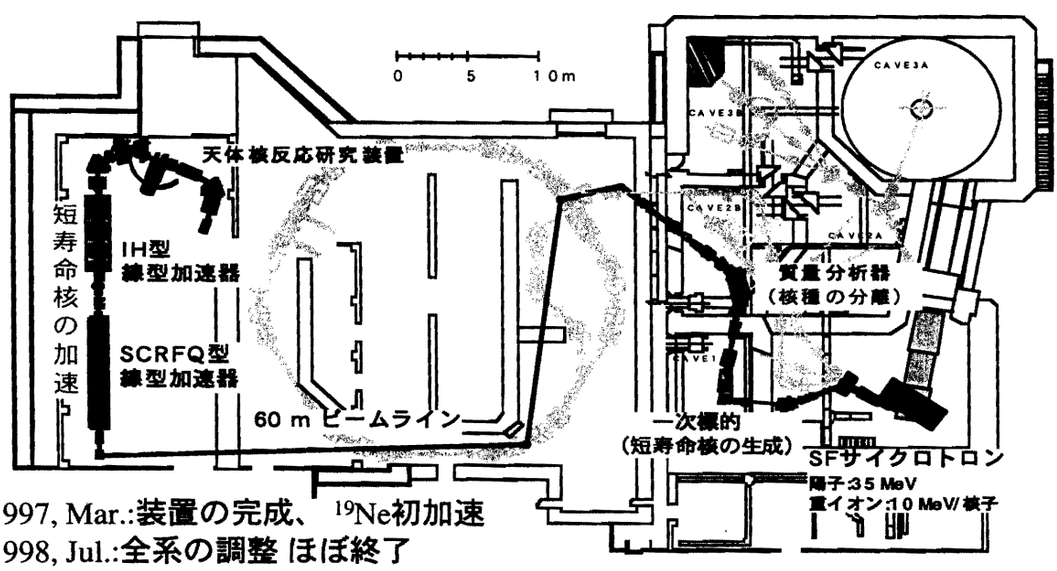

1997, Mar.:装置の完成、 ^{19}Ne初加速
1998, Jul.:全系の調整 ほぼ終了
1999, Sep.:実験中断（移転作業 のため）

Main Specifications of the Linac Complex

	SC-RFQ	IH1
Frequency(MHz)	25.5	51
Charge-to-MassRatio(q/A)	≥1/30	≥1/10
Input Energy(keV/u)	2	172
Output Energy(MeV/u)	0.134-0.172	.172-1.053
Normalized Emittance	0.6 πmm•mr	
Energy Spread(%)	1.03	≤2.80
Duty Factor(%)	100% for q/A≥1/16, 270x(q/A)^{2}x100% for q/A≥1/30	
Repetition Rate (Hz)	20-1000	
Transmission Efficiency(%)	~95	~95
Total Length(m)	8.6	5.6

全系の効率($^{19}Ne^{2+}$-beamによる)

	1997 Mar.	1998 Dec.	Louvain-la-Neuve	comment
Primary beam	30 MeV, 2 μA		30 MeV, 150 μA	Proton Beam
Production Yield(LiF)	0.32x10^{-3}		0.7x10^{-3}	C-powder, Cu-wall
Ionization Eff.(%)	~17	27(20)	10	for $^{19}Ne^{2+}$, 60%(tot.)
Extraction Eff.(%)	(~30)	30	25	
Bunching Eff.(%)	20	60	-	duty=30%@100Hz
Transp. Eff.(%)	3.0	72(54)	-	20->90%(ISOL)
				14->80%(BTL)
Acc. Eff.(%)	80	85	2	Beam Stabilization
HEBT Transp. Eff.(%)	80	90	-	Optics Change
Overall Eff.(%)	.02	2.5(1.4)	.05	
2ndary Beam(pps/μA)	4x10^5	5x10^7	2.2x10^6	

RNB-list**(1999 Sep.)

Elements(half-life)	Intensity@ISOL exit (pps/μA)	Target/Primary beam /Ion Source
$^{19}Ne^{2+}$(17.2 s)	$2x10^8$	LiF/proton 30 MeV/ECR
$^{18}Ne^{2+}$(1.67 s)	$1x10^6$	LiF/proton 40 MeV/ECR
$^{38}K^{1+}$(7.61 m)	$3x10^8$	$CaF_2/^3He$ 70 MeV/Surface(Re)
$^{37}K^{1+}$(1.23 s)	$1x10^7$	$CaF_2/^3He$ 70 MeV/Surface(Re)
$^{21}Na^{1+}$(22.5 s)	$2x10^6$	$CaF_2/^3He$ 70 MeV/Surface(Re*)
$^{20}Na^{1+}$(0.45 s)	$1x10^5$	$CaF_2/^3He$ 70 MeV/Surface(Re*)

*Na-beamについては、off-line実験の結果IonizerをRe-foilからIr-foilにすることで、強度が約2.5倍になるものと考えられる。
**^{8}Li-beamについては、ビーム開発途上で中断。

天体核実験(1998 Jul. to 1999 Sep.)

Thema	Reaction type	Required Intensity(pps)	status
HCNO,rp-proccess	$^{19}Ne(p, \gamma)^{20}Na$	$>1x10^8$	Beam intensity: OK ^{19}F contamination problem Detector Development
HCNO,rp-proccess	$^{18}Ne(p,p')$	$\sim10^{3-4}$	Beam intensity: OK Contamination: OK Detector problem
Primodial Nucleo-Synthesis	$^8Li(\alpha, n)^{11}B$	$\sim10^3$	Beam development Detector: OK

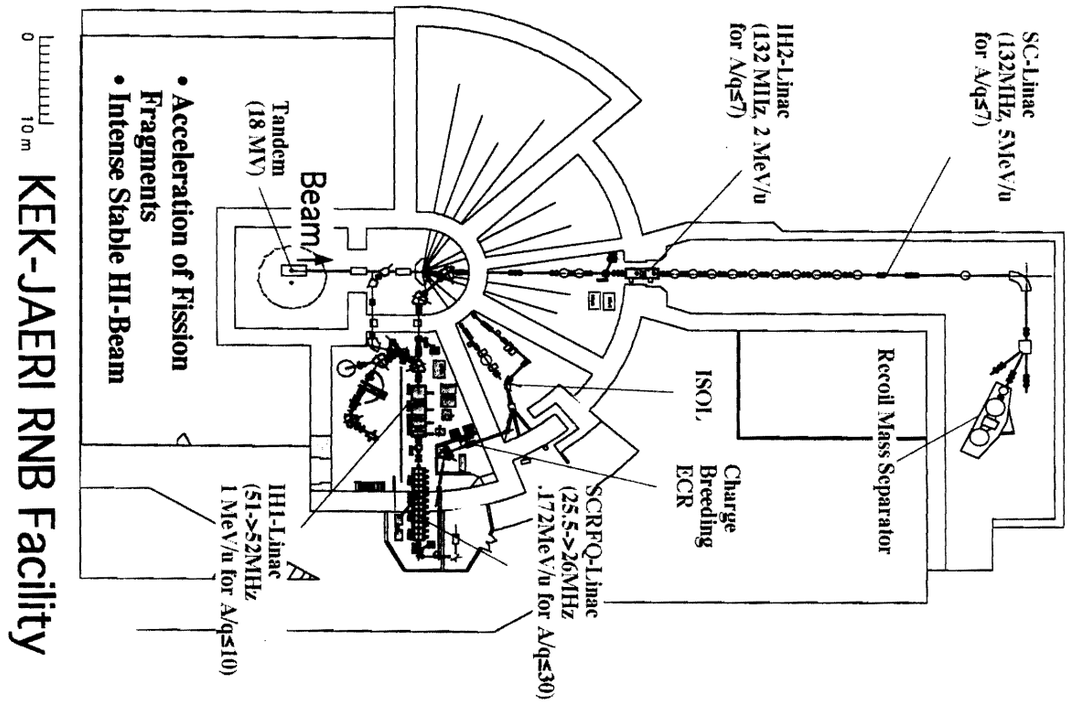

Some parameters of the proposed facility

Primary Beam	energy, intensity	36MeV proton, 3μA, HI (18MV)
Production Target		UC_2-target, etc.
ISOL	mass resolving power	2000
	injection energy to SCRFQ	2 keV/nucleon
SCRFQ	frequency, output energy	26 MHz*, 134-172 keV/u (A/q≤30)
IH1	frequency, output energy	52 MHz*, 0.17–1.05 MeVu (A/q≤10)
IH2	frequency, output energy	132 MHz, 1.05-2 MeV/u (A/q ≤ 7)
S.C. Linac	frequency, output energy	132 MHz, 5 MeV/u (A/q ≤ 7)

* The frequencies of SCRFQ and IH1 linacs are modefied to match one of SC linac from 25.5 MHz and 51 MHz, respectively.

研究テーマと特色（1）

1)天体核反応の研究(^{19}Ne, ^{20,21}Na, neutron-rich nuclei(N=50,82))

- 核反応率の直接測定
- 核子移行反応によるr-過程（早い中性子捕獲過程）核の質量測定
- 天体核燃焼の実験室での再現
- 高品質短寿命核ビームにより精密測定が可能

2）中性子過剰な中・重核領域での核構造、核反応機構 (^{78}Ni, ^{132}Sn, $^{134\text{-}145}$Cs, ..)

- クーロン励起による原子核の大変形領域解明
- レーザー分光、弾性散乱による同位体シフト、核半径測定
- 過剰中性子による融合反応の促進過程の解明
- 陽子誘起核分裂反応による中性子過剰核ビームの供給

研究テーマと特色（2）

3)物質科学などの研究(^{8}LI, ^{140}Cs, ^{91}Rb, ^{111}Ag, ^{153}Nd)

- 短寿命核打ち込みによる物質の内部場、結晶構造、熱拡散現象
- 高性能半導体素材、耐放射線素材などの新素材開発
- 高純度不純物元素の打ち込み（非破壊的）
- 高感度測定（放射線検出）

4)超ウラン及び超アクチノイド元素の核化学、核物理
(stable O, F, Ne, Kr, Xe-beam)

- 相対論的効果による化学的挙動異常の系統的研究
- 超重元素の原子核構造、生成過程の研究
- 大効率反跳核質量分析器の使用
- 高強度安定核ビームによる系統的研究の開始

陽子誘起反応によるRNB強度

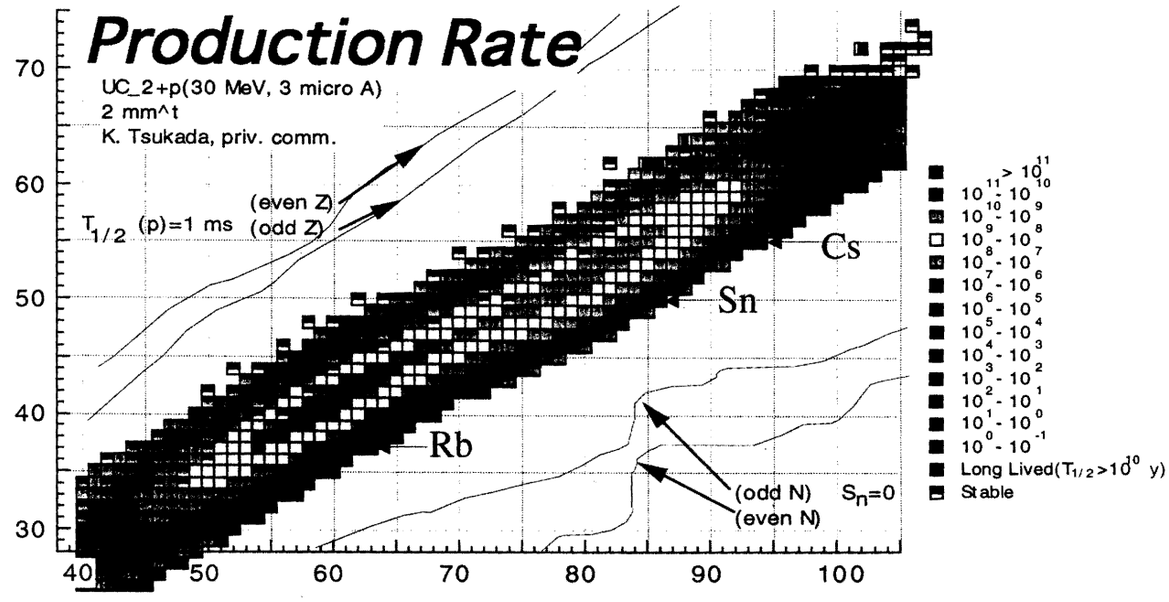

中性子過剰核による融合反応機構

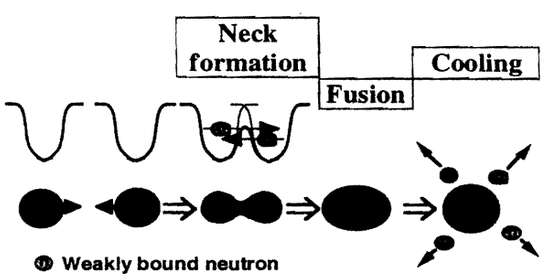

Candidate:

^{133}Cs(stable)--->^{145}Cs(0.6 s: 10^4pps)

10–50 cpd for $\sigma_{fus.}$=10 mb

$I_{RNB}=10^4$ pps

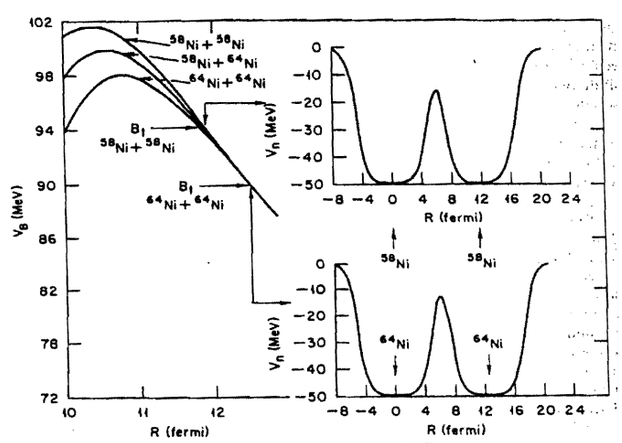

P.H.Stelson, Phys. Lett. B205('88)190

N. Takigawa et al., Nucl. Phys. A588('95)91c

R-process waiting nucleiの核分光

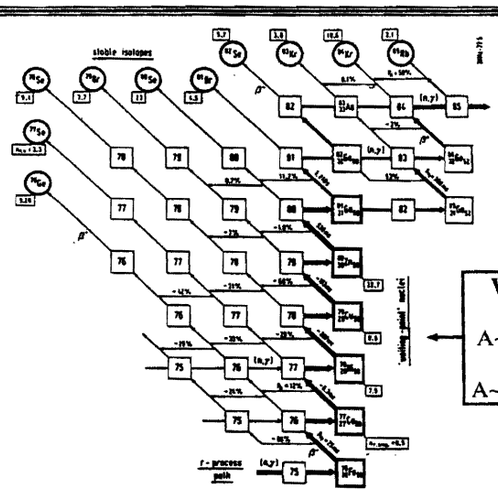

Fig. 3. Schematic view of the r-process path and the r-abundance features in the A = 80, N = 50 region. $T_{1/2}$ and P_n-values indicated in this figure are either experimental values [10,27] or RPA predictions. For details, see text.

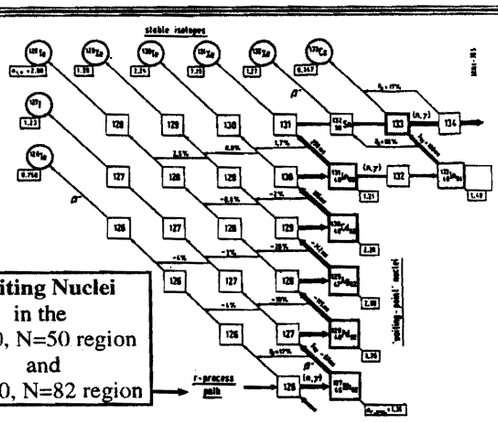

Fig. 2. Schematic view of the r-process path and the r-abundance features in the A = 130, N = 82 region. $T_{1/2}$ and P_n-values indicated in this figure are either experimental values or RPA predictions. For details, see text.

Waiting Nuclei
in the
A~80, N=50 region
and
A~130, N=82 region

- known elements (K. L. Kratz et al.)
- unknown elements ($T_{1/2}$, P_{dn})
- candidate for RNB (~10^{5-6} pps) in the S_n measurement

Example

$d(^{81}Ga, ^{80}Zn)^3He$	σ~1-100 mb, E(^{81}Ga)>4MeV/u
$d(^{81}Ga, ^{79}Zn)^4He$	N_b~10^{5-6}pps, 40-400 events/h

Charge Breeding ECR

Possible Time Sequence of the Charge Breeding

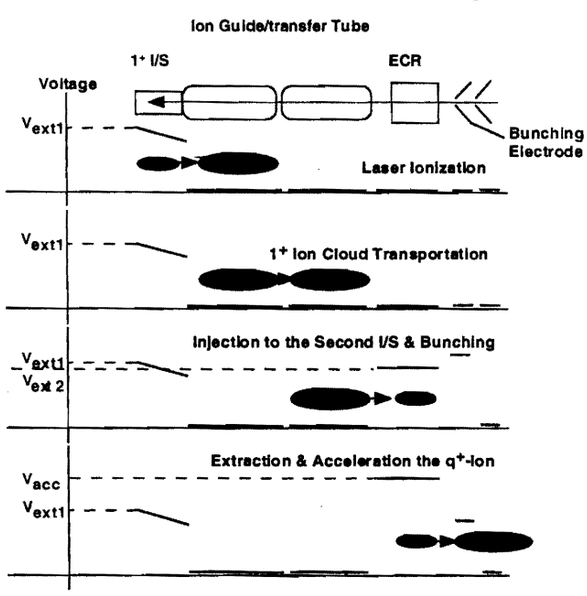

MINIMAFIOS (10 GHz) ECRISによる 1+ ->n+ breeding efficiency

Element	$1^+ \rightarrow n^+$	η	η_G
$_{84}Kr$	$Kr^{1+} \rightarrow Kr^{11+}$	11 %	40 %
$_{40}Ar$	$Ar^{1+} \rightarrow Ar^{8+}$	9 %	40 %
$_{85}Rb$	$Rb^{1+} \rightarrow Rb^{15+}$	5.5 %	35 %
$_{208}Pb$	$Pb^{1+} \rightarrow Pb^{22+}$	4.5 %	35 %
$_{64}Zn$	$Zn^{1+} \rightarrow Zn^{9+}$	3.5 %	23 %
$_{56}Cr$	$Cr^{1+} \rightarrow Cr^{11+}$	3.5 %	21 %
$_{32}S$	$S^{1+} \rightarrow S^{7+}$	2.5 %	11 %

Table 1: *$1^+ \rightarrow n^+$ breeding efficiencies for various elements.*

DC-breeding/Bunching Breeding
ECR confinement time: 520 ms for Rb^{15+}
Charge states equibration time: ~20 ms
N. Chauvin et al.,Proc. 14th ECRIS99('99)151.

Production of low energy radioactive nuclear beam and measurement of the (α, n) reaction for astrophysical interest at JAERI tandem facility

T.Hashimoto, Science University of Tokyo

24/Aug/00

Abstract

We plan the experiments to measure the (α, n) reactions using Radioactive Nuclear Beams(RNB) for astrophysical interest. RNB produced by transfer reactions should be separated with stable nuclear beam using JAERI Recoil Mass Separator(RMS). MSTPC and neutron counters are main components of measurement system. This experimental data set will use for estimation of element abundance in astrophysical neucleosynthesis.

So far,r-process seed nuclei are produced mainly by α-capture reaction near the β-stable line. The r-process starts from those seed nuclei. Therefore, only limited number of the light nuclei near the stability line ware selected. However, light neutron-rich nuclei are important in the r-process neucleosynthesis. But those cross section of light neutron-rich nuclei are not determined by direct measurements, because it is generally difficult to obtain sufficiently intense and low-energy RNB owing to their short lives. We are particularly interested in the (α, n) reactions involving neutron-rich unstable nuclei. At first, we plan the experiment to measure ^{8}Li$(\alpha, n)^{11}$B reaction at JAREI tandem facility.

The ^{8}Li beam produced by ^{9}Be(^{7}Li,^{8}Li) reaction. This beam with E/A=1$\sim$2MeV/u, dE/E$\sim$3% and I=7$\times$10^{4}pps estimated for E=17MeV and 300pnA ^{7}Li beam. The main component of contamination in the beam is ^{7}Li, which is separated using JRERI-RMS. In comparison the RNB beamline at University of Notre Dame, JAERI-RMS obtained a high purity RNB. Because, the Notre Dame beamline is only momentum selection , compared with JAERI-RMS is momentum and energy selection. Beam suppression factor of ^{7}Li beam at JAERI-RMS should be estimated 1.0×10^{-11} for experiment using ^{14}N. Therefore, ^{7}Li/^{8}Li ratio is 1%.

The ^{8}Li will be injected into the MSTPC (Multiple-sampling and tracking proportional chamber).The MSTPC will be filled with helium gas with a little admixture of methane gas for the reaction measurement. The filled gas works as a detector gas and serves a target, therefore the detection efficiency achieves almost 100%. The MSTPC can measure stopping power (dE/dx) along with a charged-particle trajectory and has an ability of a TPC (Time-projection chamber), then the event-selection ability is very high. In the JAERI experiment, the estimated ^{8}Li beam intensity is 1.4×10^{4} pps. Due to the space charge limit of the gas counter is difficult to perform over 10^{4} cps. In order to accept such a high intensity beam, the present MSTPC will be installed with a gating-grid system which works as a shutter to control drifting electrons in the field cage and charge multiplication by an anode wire.

Neutron counters is installed surrounding the MSTPC for an exclusive measurement in order to obtain precious reaction data such as the angular distribution and the individual cross sections of the individual final states. The solid angle covered by neutron counter is 31.4% of 4π and averaged intrinsic detection efficiency for a neutron energy region around 10MeV is about 31.8%, which was estimated by Monte-Carlo simulation. The yeild estimation of the reaction is 40events/bin/day.

原研タンデム施設における低エネルギー不安定核ビームの生成と天体核反応の測定

東京理科大学　橋本尚志

東京理科大　中井浩二
KEK　宮武宇也、福田共和、石山博恒、鄭淳讃、田中雅彦、
吉川宣治、川上広金、東条榮喜、渕好秀、小柳津充弘、
片山一朗、野村亨
原研　池添博、市川進一、杉山康治、西尾勝久、光岡真一、松田誠
CNS　久保野茂、溝井浩
理研　吉田敦、渡辺裕

Explosive Nucleosynthesis

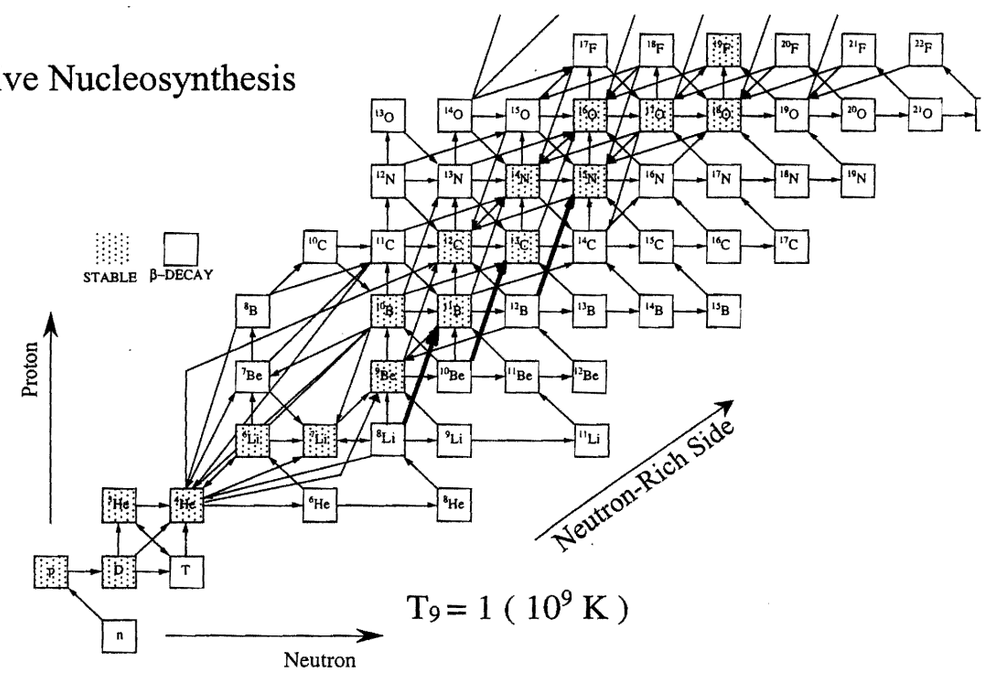

$T_9 = 1$ (10^9 K)

IM Big-Bang, Supernova Explosion, etc

(α,n) reaction

Direct-Exclusive Measurement of (α ,n) reaction

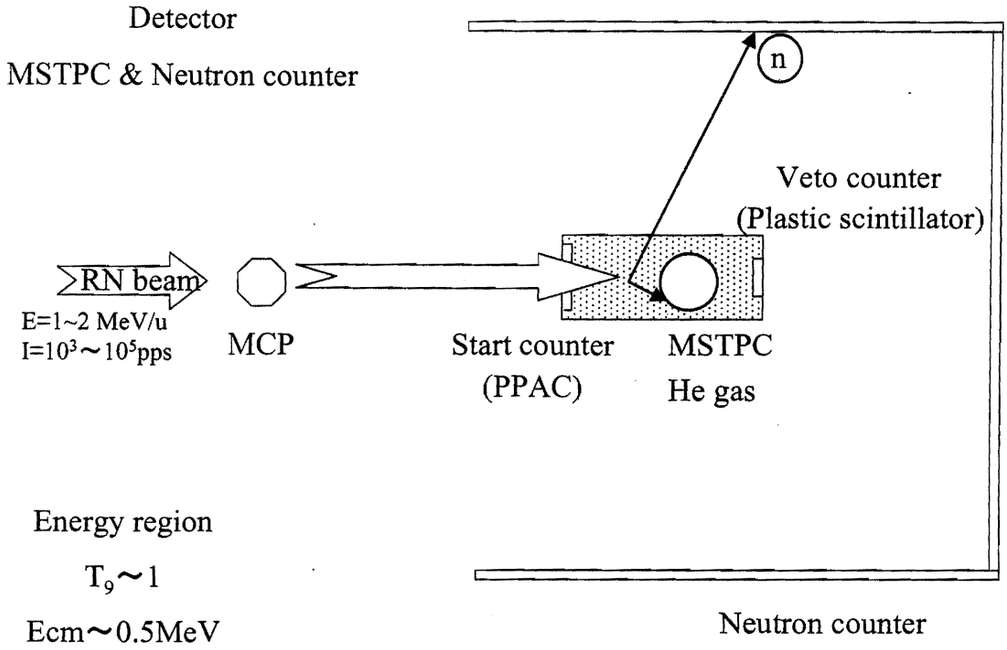

Multiple Sampling and Tracking Proportional Chamber
~MSTPC~

Y.Mizoi et al. NIM A432,112(1999)

MSTPC
- MUSIC : Multiple-Sampling Ionization Chamber
- TPC : Time-Projection Chamber

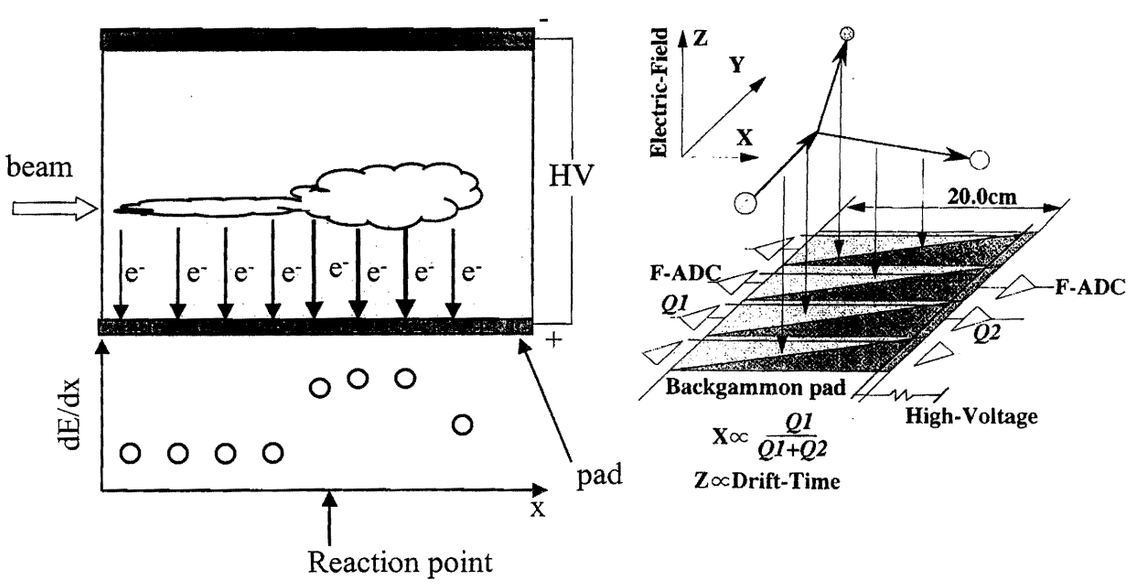

Gating grid

P.Nemethy et.al NIM212(1983)273-280

I > 10^4pps→空間電荷の飽和から測定困難

→reaction が起こったときのみガス増幅をかけるシステム

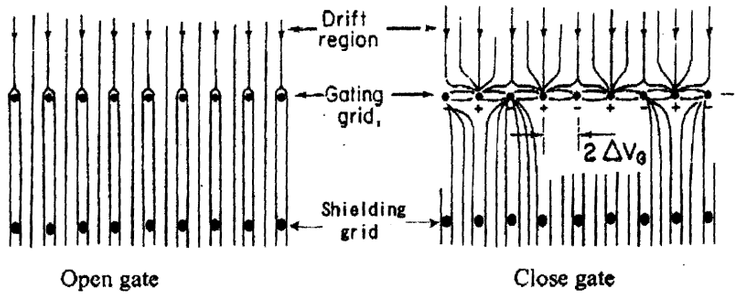

電場形状

Pulser output signal

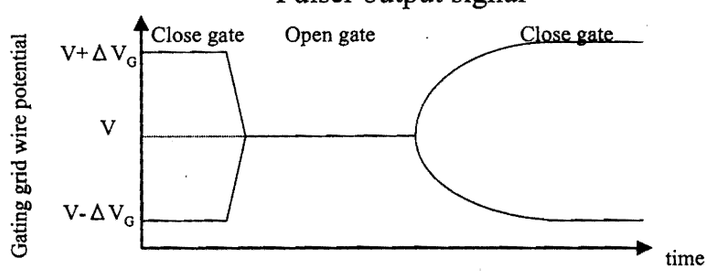

Neutron counter set up

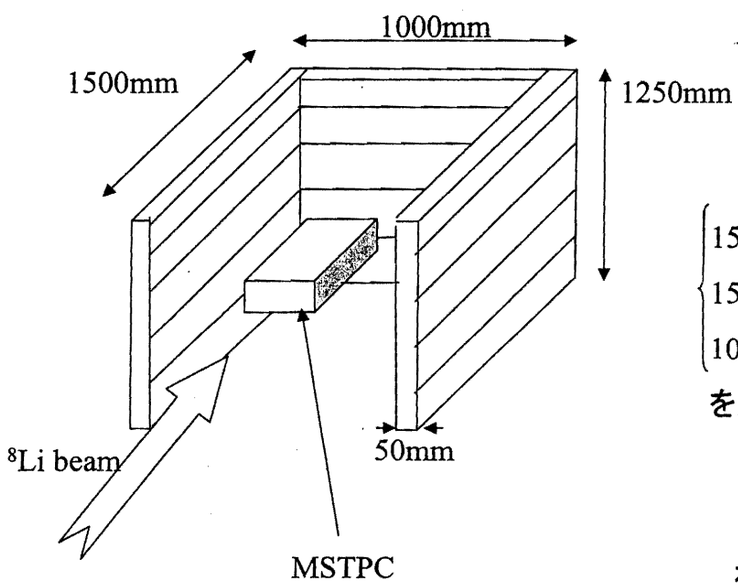

He+CH_4(5% or10%) gas

100～200torr

1500×150×50[mm] 7本×2
1500×50×50[mm] 4本×2
1000×150×50[mm] 6本

を用いてflight path 90cmを覆う

⇩

有効立体角:31.4% of 4π

Energy resolution:16%(FWHM)

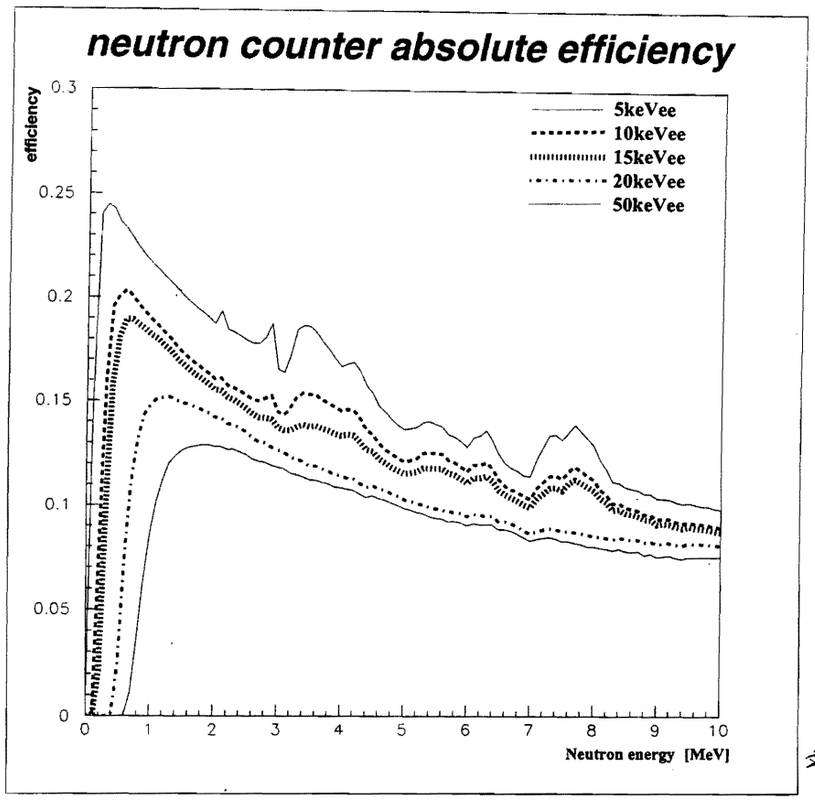

立体角を含む.

Low Energy RN beam production

JAERI Recoil Mass Separator

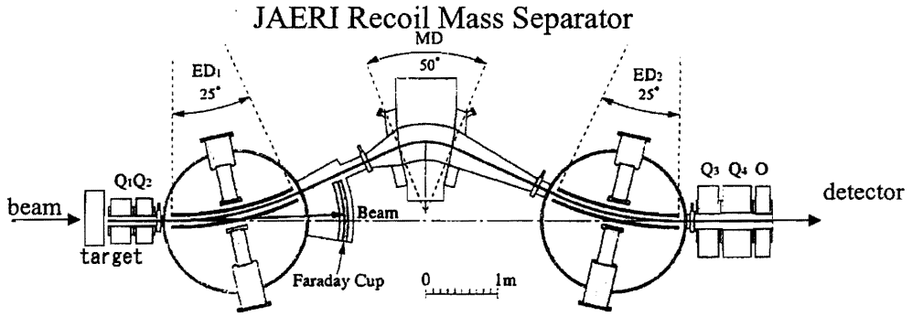

Required ^{8}Li beam

1.intensity ~10^4~10^5pps

2.Energy 1~2MeV/u

3.Energy resolution <3%(FWHM)

9Be(7Li,8Li) reaction

^{7}Li beam energy =17MeV

^{9}Be target t=12.7 μ m (2.3mg/cm^2)

^{8}Li expected yield = 7 × 10^4pps /300pnA ^{7}Li

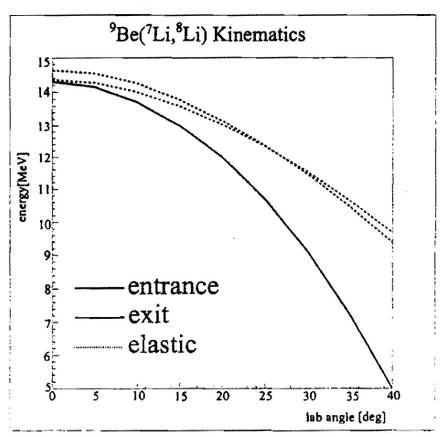

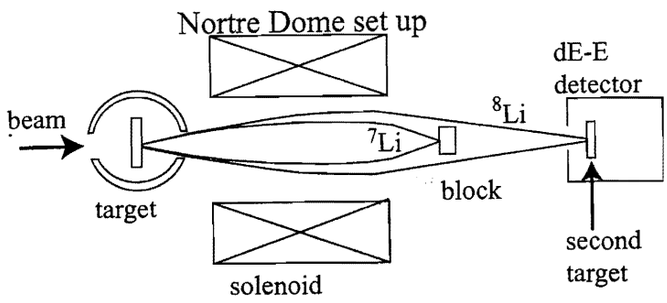

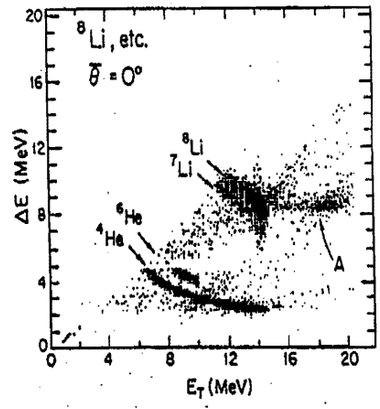

Set A/q=8/3 E=14MeV,

RMSの全てのED、MDでenergy acceptanceを±12%とする時

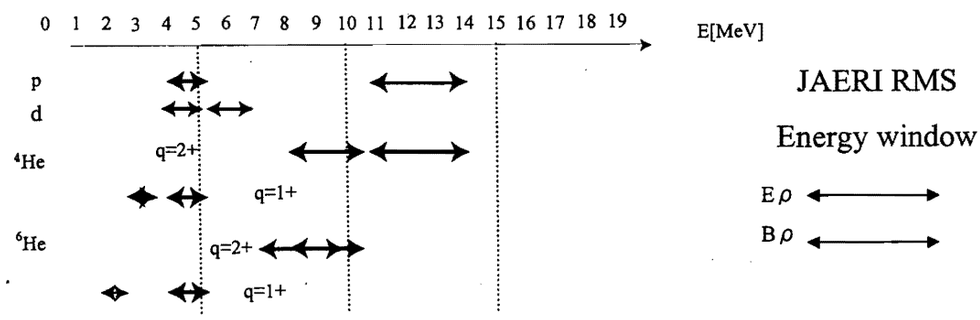

$^7Li^{3+}$、E=14MeV(exit of target)と同じ
A/q、E/Aを持つ$^{14}N^{6+}$、28MeVでsuppression factorのシミュレーション実験

良いシミュレーションか？

同立体角、同角度での^{7}Liと^{14}Nのラザフォード散乱の比較(target: Fe)

$\sigma(^{14}N)/\sigma(^7Li)=1.67$

^{14}Nのcharge state:1+~7+

^{7}Liのcharge state:1+~3+

上限は抑えられ、factor程度では正しいと予想される。

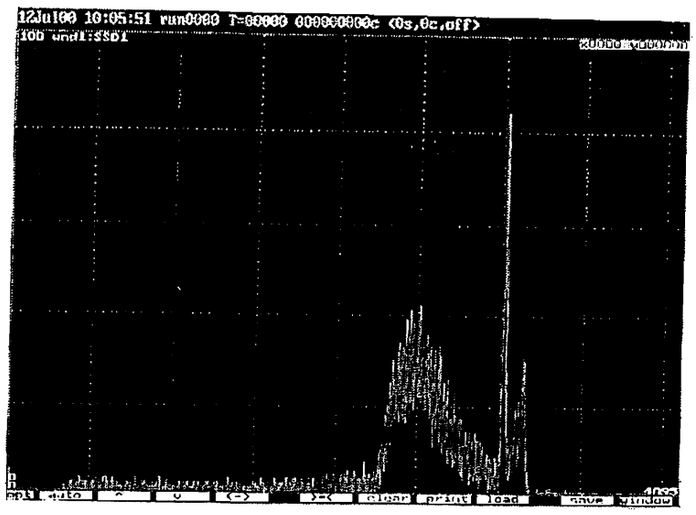

Energy spectrum

θ_{RMS}=0.0°

Target:blank

RMS optics 8/3+

E=28MeV

Beam suppression

4.0×10^{-9}

③ ② ①

①: beam halo (Energy : 28MeV)

②: 散乱の影響 ($^{14}N^{5+}$ Energy :23.1MeV)

③: 得に構造のないback ground。Charge changing collision 等

→ $^{7}Li^{3+}$beamはED2手前のcollimatorに垂直に衝突

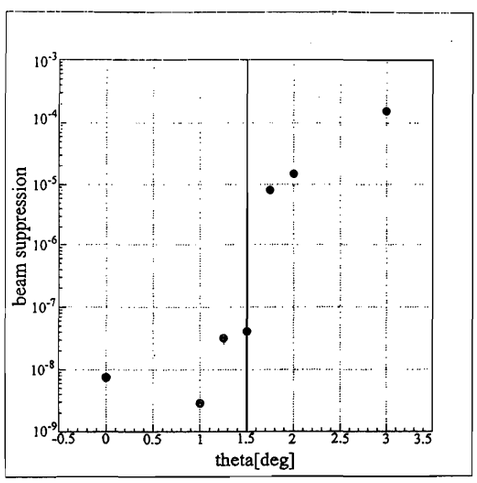

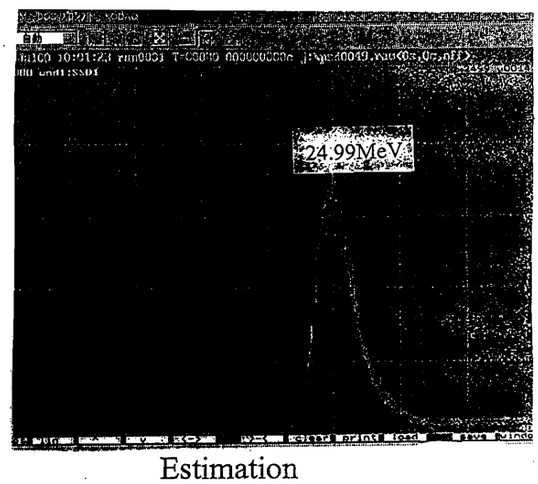

Estimation

Rutherford scatteringを仮定

Effective thickness 8.1 μm(^{14}N ½ range)

beamの1/10が衝突

EDのenergy window 考慮

EDギャップ内に入ったものは全て通過

⇩

Beam suppression =1.9×10^{-5}

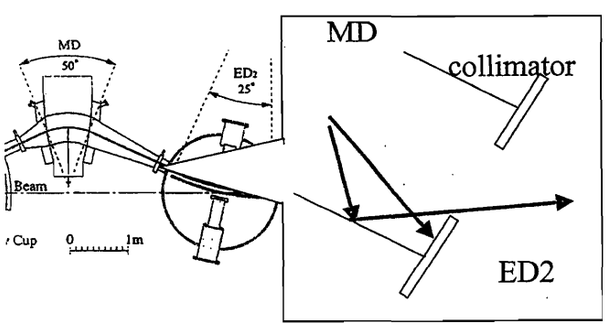

^{7}Li beamに対する推定suppression factor

θ_{RMS}	slit	^{8}Li yield [pps]	Beam suppression	^{7}Li yield [pps]
0°	XR=1.0° XL=-7.5° Y=±1.9°	3.3×10^{4}	4.5×10^{-8}	8.4×10^{4}
4°	XR=1.0° XL=-2.0° Y=±3.0°	1.4×10^{4}	1.0×10^{-11}	1.0×10^{2}

いずれも300pnA ^{7}Liでの計算

Summary

Neutron counter

有効立体角31.4%

Energy resolution 16%(n_3,n_4まで分離可能)

Absolute efficiency >10%

MSTPC

Gating gridの導入で>10^4ppsのbeamに対応可能

Pure beam

Beam suppression < 10^{-11}

Beam intensity

~10^4pps/300pnA ^{7}Li

Yield estimation

cross section ～100mb

⇩

40events/bin/day

Design conception and ion-optical properties of DUMAS

T. Noro, RCNP Osaka

Sep. 30, 2000

The dual magnetic spectrograph DUMAS, the former name of CLIB, was constructed at RCNP as a spin transfer spectrograph which is dedicated to double scattering experiments. Before the construction of DUMAS, major activities on polarization physics with the AVF-cyclotron facilities at RCNP had been made by using high-purity Ge-detectors. DUMAS was designed so as to extend such activities to spin-transfer measurements with similar level of data quality as those by using the Ge-detectors.

The design goal was set to be moderate energy resolution of 10^{-3}, wide momentum range of $\pm 10\%$ and large acceptance angle of 10 mr. In addition to those, an achromatic focus point with spot size of 1 cm was required for placing the second target of a polarimeter system.

Those requirements are mostly achieved in actual design in limited meaning. Namely, each requirement is mostly achieved only when other requirements are limited. The specifications quoted in some reports[1),2)] are values when all the requirements are satisfied at the same time and significantly lower than the requirement values. Therefore, for specific purposes, DUMAS may be used with better specifications than quoted there.

In order to realize to join two spectrograph in tandem for preparing two focus, a dispersive focal line and an achromatic focus point, ion-optics of DUMAS is rather complicated especially in higher order aberration. In the talk, this ion-optics as well as achieved specifications were presented.

Some of specifications are summarized in the following.

- Acceptance: maximum 9.9 mr for narrow ρ region
  $\geq$9.0 mr for $(83cm \leq \rho \leq 97cm)$
- Momentum resolution: 6×10^{-4} for $(90cm \leq \rho \leq 97cm)$
  $\leq 2 \times 10^{-3}$ for $(84cm \leq \rho \leq 102cm)$
- Maximum vertical target-size: 1 mm for $(81cm \leq \rho \leq 103cm)$
  4 mm for $(\rho \leq 95cm)$
- Maximum deviation of flight path: 2 cm (calculated value)

1)T. Noro *et al.* RCNP Annual Report 1983 p.173.

2)T. Noro *et al.* Proc. 6th Int. Sympo. on Pol. Phenom. in Nucl. Phys. (1985, Osaka) p.470.

○当時の状況

・AVF サイクロトロンによる偏極ビームの加速
（世界有数の強度・偏極度）

・「偏極グループ」は主として HP-Ge を利用
エネルギー分解能　160～180 keV (@65MeV)
反応は、(p,p_0), (p,p'), (d,d_0), (d,d'), (p,d), (p,t), $(p,{}^3He)$

・Si-Ge (+Q 磁石) を用いた偏極移行測定の試み

・世界では、LAMPF, SIN で焦点面ポラリメータが稼働

↓

2 回散乱(偏極移行)測定を 1 回散乱並の精度で !!!

(HP-Ge 測定)

・分解能　ΔP/P～1/1000 (130keV/65MeV)

・広運動量領域

・大立体角 × 高効率の 2 回散乱測定(DAQ の負担を軽く)

↓

運動量タギング付き 3 重収束型スペクトログラフ

原案：２台の双極磁石の対称的連結

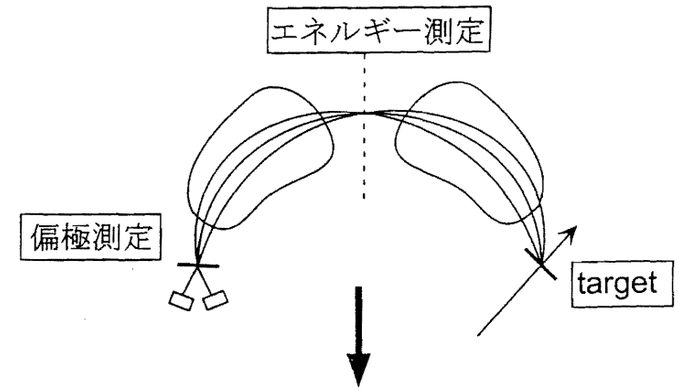

●大立体角化・高分解能化 --> Ｑ１、Ｑ３磁石の追加
●広運動量領域化 --> Ｑ２磁石の追加
●第１焦点での検出器使用 --> 若干の非対称性化

現実案：Q-D-Q-D-Qスペクトログラフ

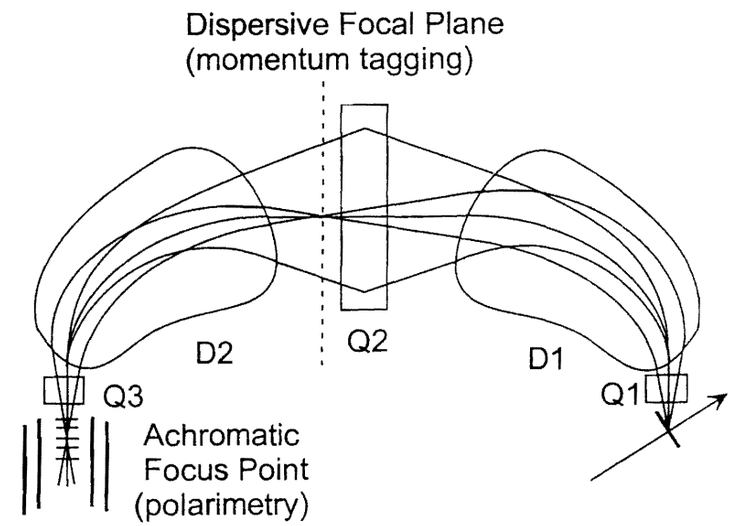

しかし...

ACHIEVED OR CONFIRMED PROPERTIES OF DUMAS

Maximum energy	$E_{max} = 110\ Z^2/A$ MeV $E_p \lesssim 110$ MeV, $E_d \lesssim 56$ MeV
Orbit radius	ρ = 84-98 cm
Spectrum range	±7.7% in momentum (±15% in energy)
Maximum solid angle	$\Delta\Omega_{max}$ >5.6 msr full open : ~10 msr (75 mr horizontal × 75 mr vertical)
Deflection angle	185°
Length of central orbit (ρ=90cm)	ℓ = 7.80 m
Maximum deviation of the path length for particles with central momentum	$\Delta\ell/\ell$ = 0.12% (計算値) ≲ 2cm (~0.2 msec for E_p · 60 MeV)
1st focal plane	Target size for full momentum range : 1% ≲ 1mm.
Size	40 cm horizontal × 8 cm vertical
Energy dispersion	$\Delta x \cdot E/\Delta E$ = 700 mm (ρ = 98 cm) 1015 mm (ρ = 84 cm)
Tilted angle	0° (normal to the central orbit)
Energy resolution	$\Delta E/E$ = 1/850* (monochromatic beam transport) 1/350 (achromatic beam transport)
2nd focal point	
Energy dispersion	0 (less than 10 mm)
spot size (FWHM)	7 mm horizontal × 5 mm vertical

* solid angle : 24 mr horizontal × 54 mr vertical
= 1.3 msr

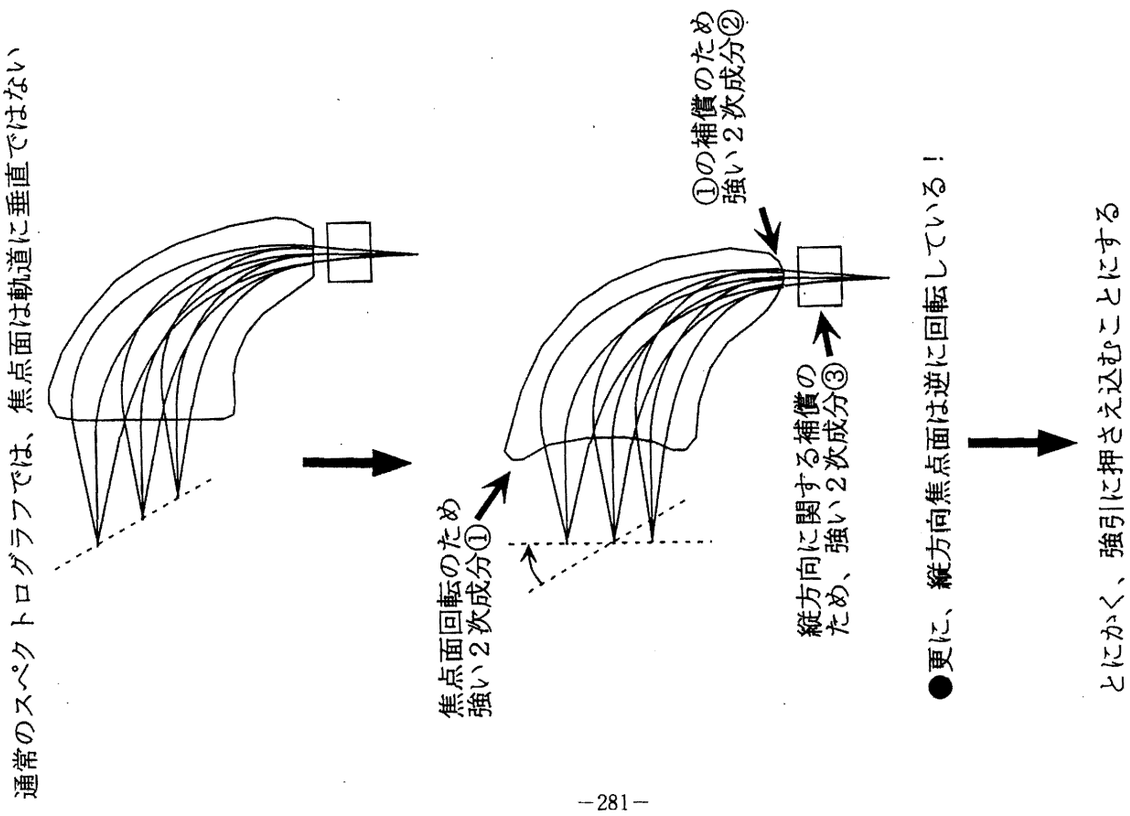

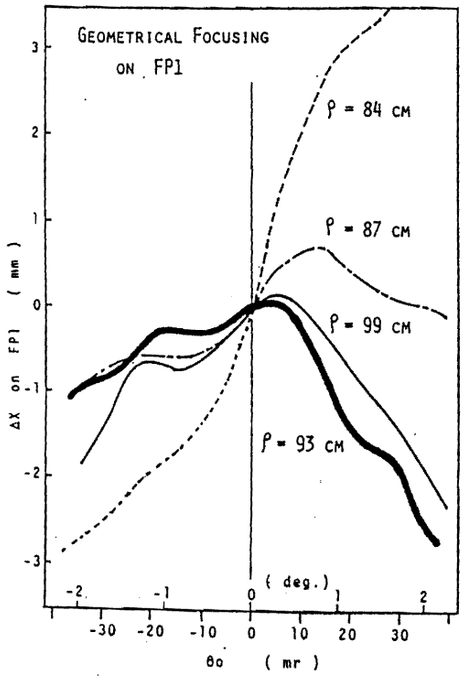

Fig.3. DUMAS への入射方向（θ_0）による粒子の第一焦点通過位置の変化（Δx）測定には ^{197}Au で弾性散乱した陽子（Ep＝65MeV）を用いている為，所謂運動学的効果は無視出来る。

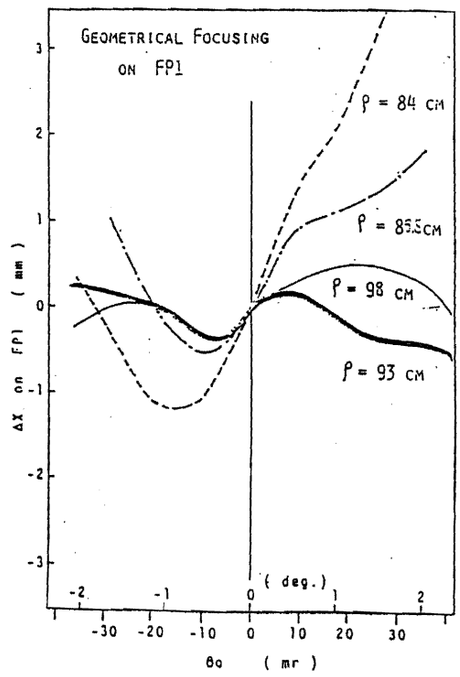

Fig.7 M1磁石で補正を行った時の第一焦点での収束性

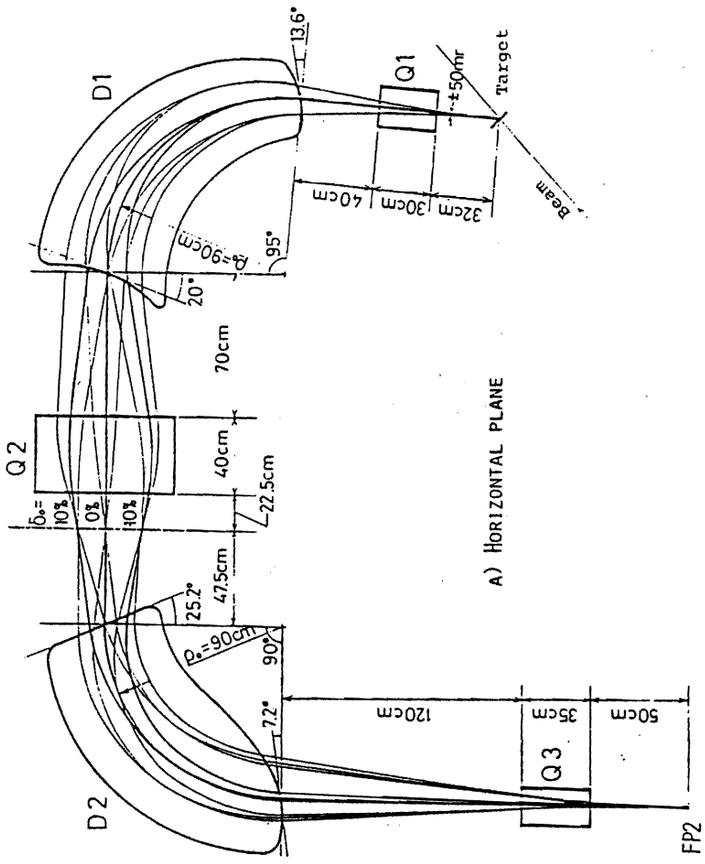

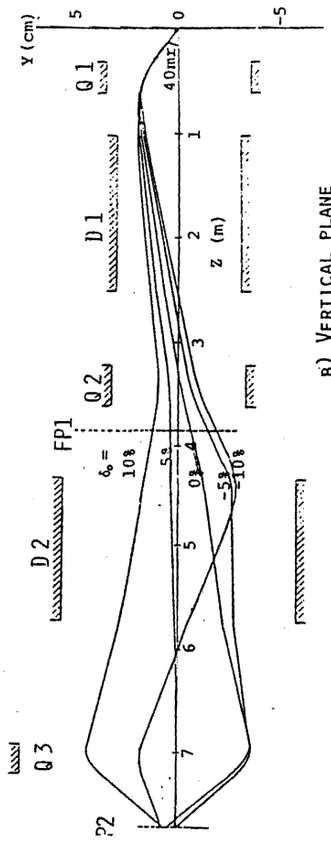

OPTICAL GEOMETRY AND CALCULATED TRAJECTORIES.

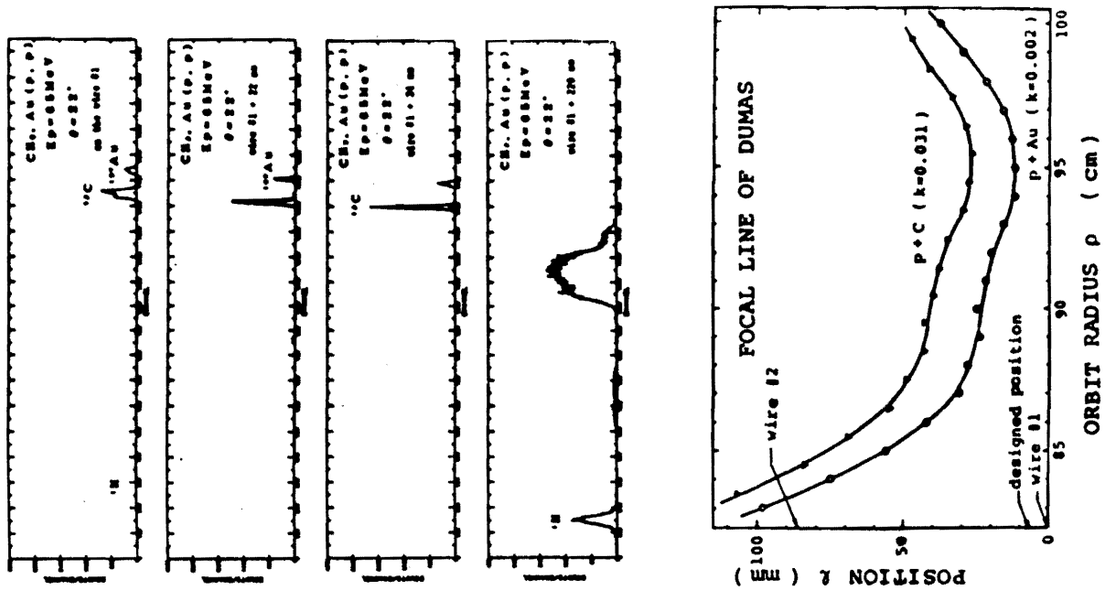
FOCAL LINE OF DUMAS
wire #2
p + C (k=0.031)
designed position
wire #1
p + Au (k=0.002)
POSITION y (mm)
ORBIT RADIUS ρ (cm)

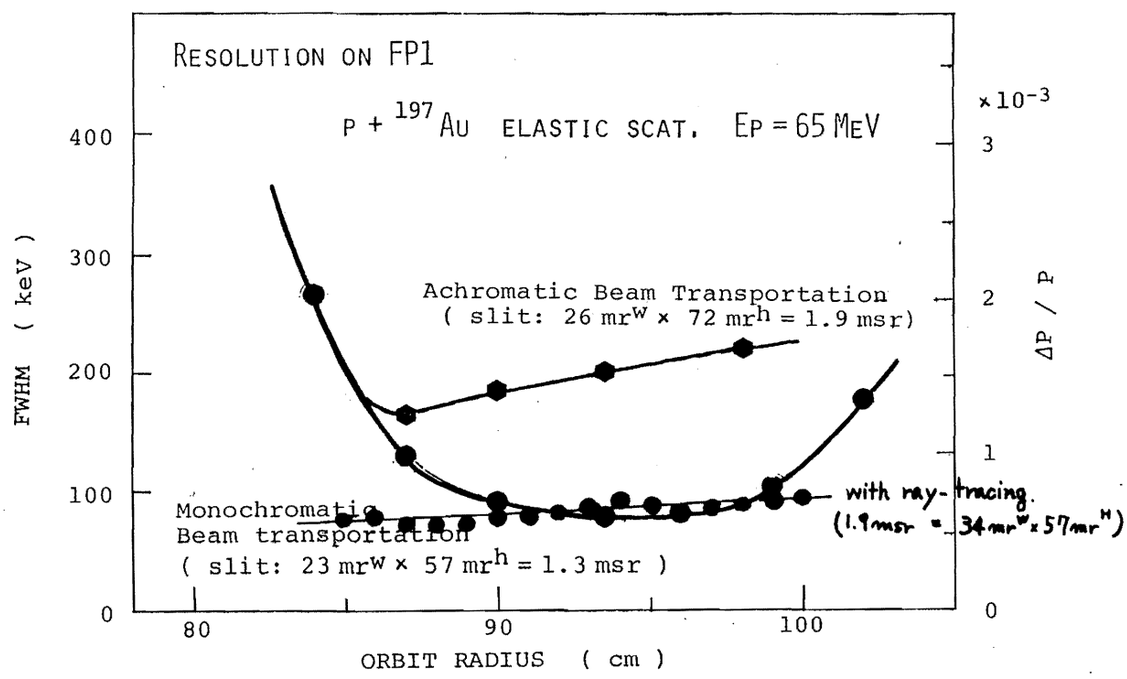
RESOLUTION ON FP1
p + 197Au ELASTIC SCAT. Ep = 65 MeV
Achromatic Beam Transportation
(slit: 26 mrW × 72 mrh = 1.9 msr)
with ray-tracing
(1.9msr = 34mrW × 57mrH)
Monochromatic
Beam transportation
(slit: 23 mrW × 57 mrh = 1.3 msr)
FWHM (keV)
ΔP / P
×10-3
ORBIT RADIUS (cm)

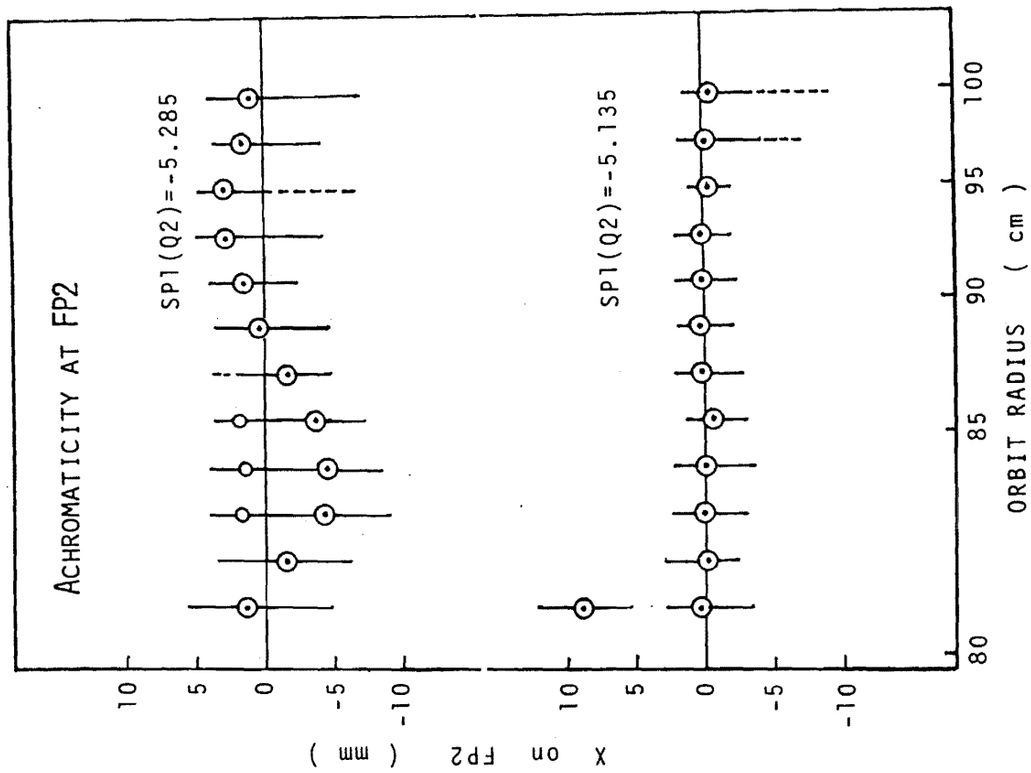

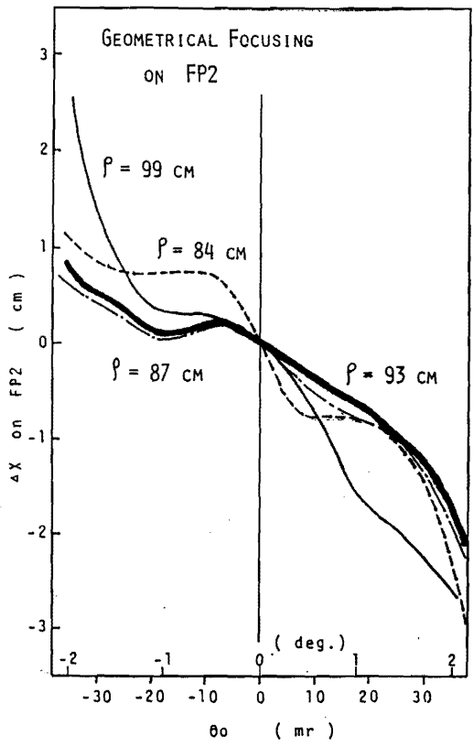

Fig.5. 第二焦点に於ける空間集束性
測定方法等についてはFig.3と同様であるが，縦軸の単位が異なっている。

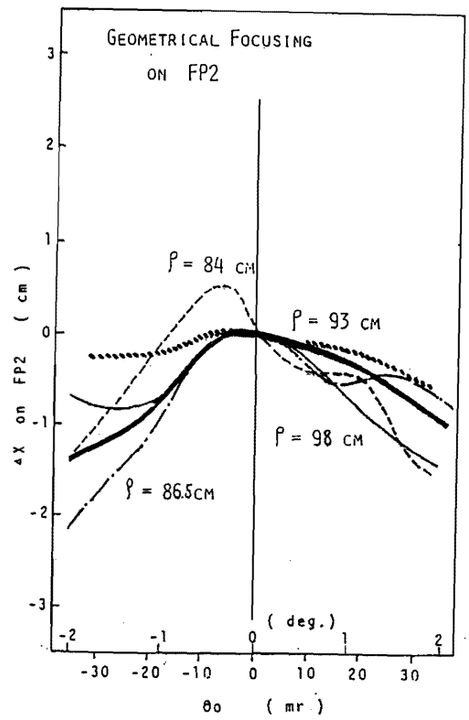

Fig.9. M3磁石で補正を行った時の第二焦点での空間集束性，M1が励磁されている為，新たに二次収差が生じている。M1をOFFにすれば，例えば太実線（ρ＝93cm）は太点線の様になり集束性は更に良くなる。

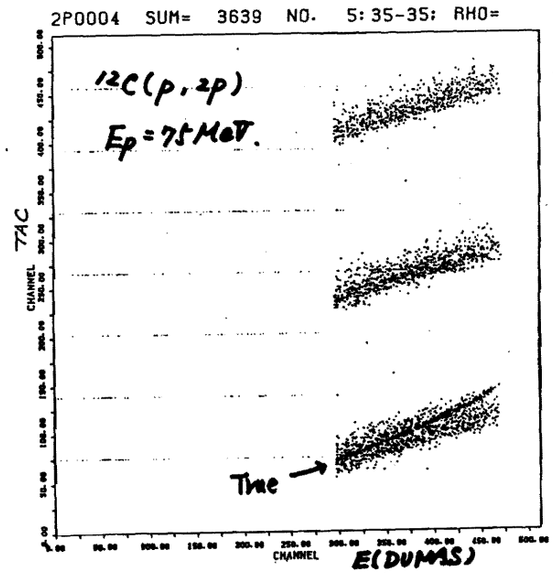

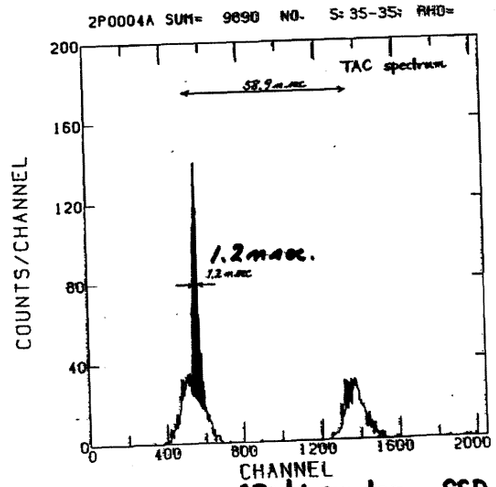

TAC { Right counter. SSD
Left counter. DUMAS FP2. plastic

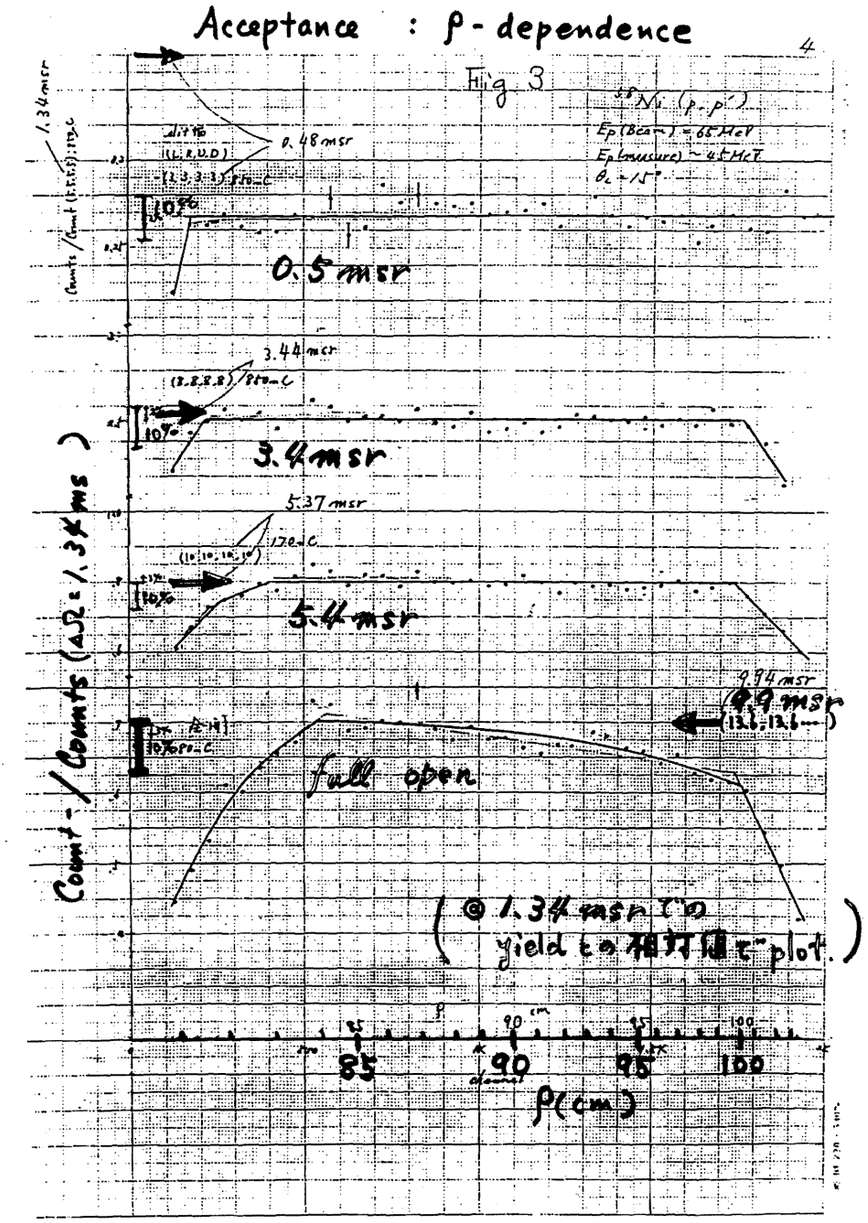

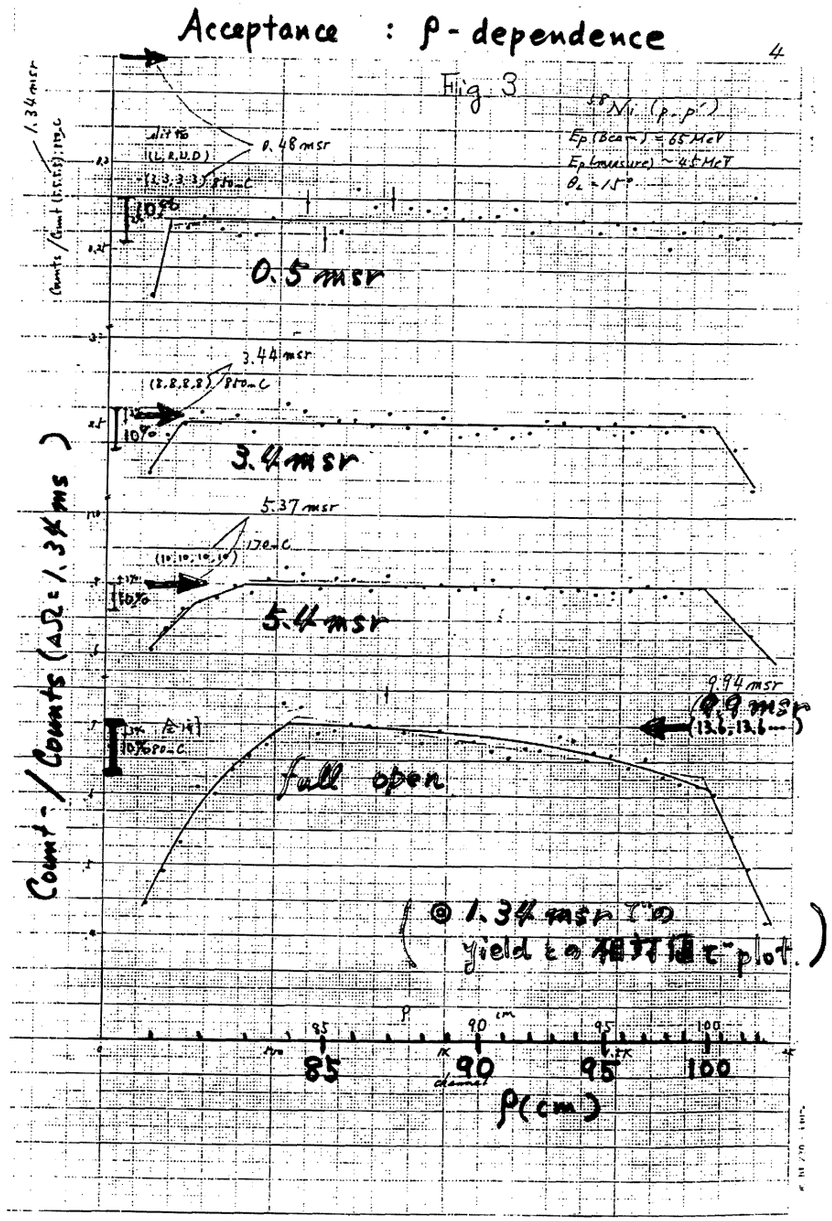

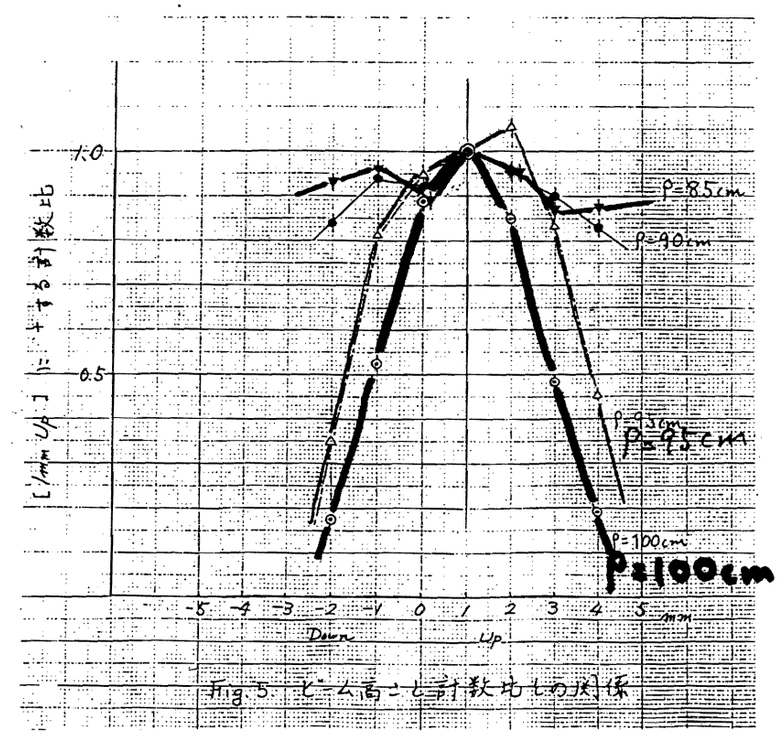

Fig. 5 ビーム面ごとの計数比の関係

The Fragment Separator at RCNP

T. Shimoda, Dept. Phys., Osaka Univ.

25/Nov/00

Abstract

The basic idea of fragment separators for use with high energy heavy-ion beams is discussed. We developed a method to treat the effect of the energy degrader as one of the ion-optical elements. This allows flexible design of the system which copes with a wide variety of beam requirements. Specifically at the RCNP fragment separator, a homogenously thick degrader is used and achromatic focus is achieved by the optics of the magnetic system. The practical performance is discussed.

Similarly to the projectile fragment separators in the world, the separator at RCNP is a two-stage magnetic analyzer and uses particle energy-loss in a solid material placed at the midpoint to achieve isotopic separation for the projectile fragments. However, it specifically employs a homogeneously thick energy degrader to allow a simple operation in the practical use. By explicitly treating the ion-optical transfer matrix of the degrader, the RCNP separator was designed so as to possess such high ion-optical flexibility that allows the use of degraders of widely ranged thickness and control of the image size as well as image location for the fragments [1].

For commissioning the separator, a detailed experimental analysis of the optics was carried out to realize the design performance. The focusing properties were studied without using an actual degrader, in order to avoid the possible ambiguities to be caused by energy-loss straggling and multiple scattering of the particles. Following the optical analysis, a prescription was established to correctly determine the strengths of the focusing devices according to the transfer matrix element $(\delta|\delta)_d$ of the degrader. This procedure further provided a means to relate the practical field strengths to the optics calculation.

The practical performance of the separator was just as designed [2]: It was confirmed that the achromatic focus was satisfactorily achieved with reasonably small aberrations. The observed image widths were explained by the third order optics calculation together with the effects due to energy-loss straggling and multiple scattering of the fragments in the degrader. The isotopic resolving power was measured for various combinations of the fragment energies and the degrader thicknesses. It was experimentally confirmed that the resolving power is principally governed by $(\delta|\delta)_d$, irrespective of the fragment energy and the physical thickness of the degrader.

The effects of energy-loss straggling and multiple scattering were present as expected in the image profiles of the fragments and in the transmission efficiency of the separator. It was shown that for the RCNP separator tuning to keep the image magnification fixed, the image broadening due to straggling was nearly constant against the change of the degrader thickness. The transmission efficiency of the system was found to decrease with increasing degrader thickness. The efficiency variation was interpreted in terms of the effect of multiple scattering to cause a growth in the transverse plane beam envelope in the second dipole magnet.

The RCNP separator has so far been used in the experiments to implant radioactive nuclei into superfluid helium and to measure energy and angular distributions and polarizations of the fragments. All these have been greatly benefited by the easy tuning method as established above. For example, the implantation of radioactive nuclei has required examination of isotopic resolution for different degraders as well as changes of the image location keeping small image size, and in the measurements of energy spectra, there has been a need for very frequent changes of the field settings of the system corresponding to different $(\delta|\delta)_d$ values. The requirements have been met, without any additional examination, by using the results of the above optical study together with, when necessary, the optics calculation.

Reference

[1] T. Shimoda, H. Miyatake and S. Morinobu, Nucl. Instrum. Meth. B70, 320 (1992).
[2] S. Mitsuoka *et al.*, Nucl. Instrum. Meth. A372, 489 (1996).

ＲＣＮＰ二次ビームコース

下田　正（阪大）、光岡真一（原研）、宮武宇也（ＫＥＫ）、森信俊平（九大）、
溝井　浩（ＣＮＳ）、村上哲也（京大）、高橋憲明（阪大）

ＲＣＮＰリングサイクロトロン：Ｋ＝４００

→　≦１００　MeV／ｕ　の軽い重イオンビームによる不安定核ビーム生成

●入射核破砕反応（前方集中、厚い標的）

●エネルギーディグレーダーを用いた粒子弁別・二次ビーム生成

ＲＩＰＳ、ＬＩＳＥ、ＦＲＳ、Ａ１２００、・・・・

特徴

エネルギーディグレーダーの効果をイオン光学計算に取り込む

↓

汎用性の高いシステム

様々な形のディグレーダーの使用：くさび形、平板
像幅の制御
収束位置の制御
高次収差の制御：小さなビームサイズ
エネルギー幅の制御

Transfer Matrix of an Ion-Optical System

Coordinate Vector: $(x, \theta, \delta, m, z)$
(y, ϕ)

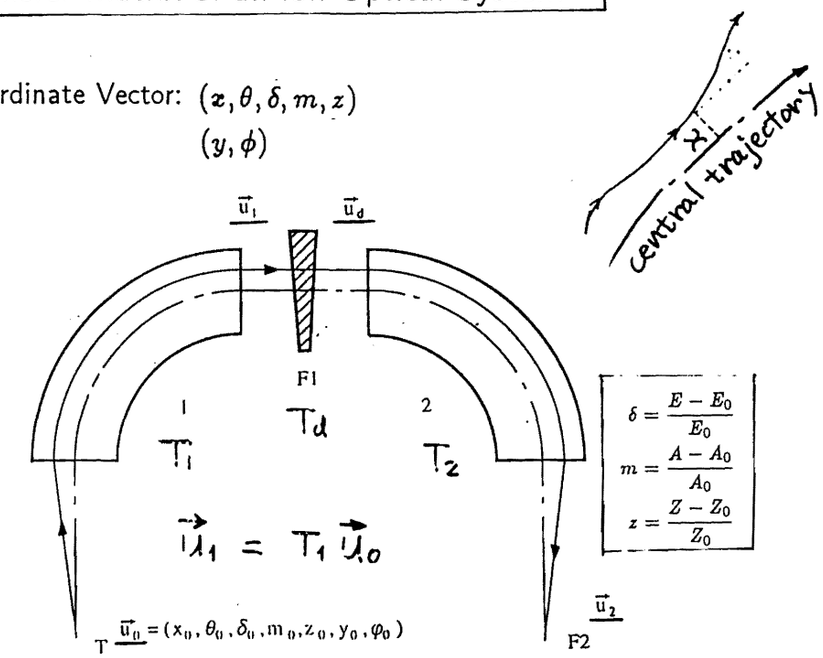

$$\delta = \frac{E - E_0}{E_0}$$
$$m = \frac{A - A_0}{A_0}$$
$$z = \frac{Z - Z_0}{Z_0}$$

Vectors at EXIT are expressed in terms of vectors at ENTRANCE;

$$\xi_{i1} = \sum_j (\xi_i|\xi_j)_1 \xi_{j0} + \sum_j \sum_k (\xi_i|\xi_j\xi_k)_1 \xi_{j0}\xi_{k0} + \cdots,$$

$\xi_i = x, \theta, \delta, m, z$　　0 for entrance, 1 for exit

$(\xi_i|\xi_j)_1$: Transfer Matrix Elements (1st order)
$(\xi_i|\xi_j\xi_k)_1$:　(2nd order)

Transfer Matix for the Dipole Magnet System

$$\begin{pmatrix} (x|x) & (x|\theta) & (x|\delta) & (x|m) & (x|z) \\ (\theta|x) & (\theta|\theta) & (\theta|\delta) & (\theta|m) & (\theta|z) \\ 0 & 0 & 1 & 0 & 0 \\ 0 & 0 & 0 & 1 & 0 \\ 0 & 0 & 0 & 0 & 1 \end{pmatrix} \begin{pmatrix} x \\ \theta \\ \delta \\ m \\ z \end{pmatrix}$$

no change in energy, mass, atomic number

angular focusing in each dipole system : $(x|\theta) = 0$

$(x|x) = M$: magnification

$(x|\delta) = D$: energy dispersion

$(x|m) = D$

$(x|z) = -2D$

$(\theta|\theta) = 1/M$

$$x_1 = (x|x)x_0 + (x|\theta)\theta_0 + (x|\delta)\delta_0 + (x|m)m_0 + (x|z)z_0$$

Transfer Matrix for the Degrader

degrader changes only energy of ions

$$\begin{pmatrix} 1 & 0 & 0 & 0 & 0 \\ 0 & 1 & 0 & 0 & 0 \\ (\delta|x)_d & (\delta|\theta)_d & (\delta|\delta)_d & (\delta|m)_d & (\delta|z)_d \\ 0 & 0 & 0 & 1 & 0 \\ 0 & 0 & 0 & 0 & 1 \end{pmatrix} \begin{pmatrix} x \\ \theta \\ \delta \\ m \\ z \end{pmatrix}$$

Degrader Matrix Elements

$$\underbrace{\frac{E_d(\xi_i, \xi_j, \cdots) - E_d(0,0,\cdots)}{E_d(0,0,\cdots)}}_{\delta_d} = \sum_i (\delta|\xi_i)_d \xi_i + \sum_{i \geq j} (\delta|\xi_i\xi_j)_d \xi_i\xi_j + \cdots ,$$

$$(\delta|\xi_i)_d = \left(\frac{1}{E_d} \cdot \frac{\partial E_d}{\partial \xi_i}\right)_{\xi_1,\cdots,\xi_7=0} \qquad \xi_1 = x,\ \xi_2 = \theta \cdots\cdots,\ \xi_7 = \phi$$

E_d : energy at the exit of the degrader

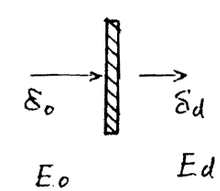

E_d is expressed using the range of ions in the degrader

empirical range formula (by Dufour et al.)

NIM A248 ('86) 267

$$R' = k\, A^{1-\gamma} E^{\gamma}/Z^2 + \underbrace{C\, A}_{\text{small}} \quad (mg/cm^2),$$

$$k = k_1 + k_2\, Z.$$

$\gamma \sim 1.75$ 40Ar

$k \sim 3.02$ 40 MeV/A

$$E_d = E_0(1 - d/R)^{1/\gamma},$$

E_d : energy at the exit of the degrader

E_0 : energy at the entrance of the degrader

d : degrader thickness

EXAMPLE

$$(\delta|x)_d = \frac{-1}{\gamma R(1 - d_0/R)} \left(\frac{\partial d}{\partial x}\right)_{x=0},$$

$$(\delta|\delta)_d = \frac{1}{1 - d_0/R}.$$

d_0 : degrader thickness for $x = 0$

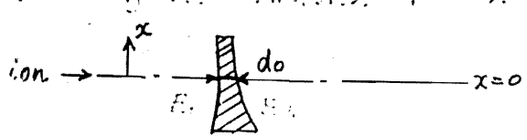

I. Double Achromatic Condition

first order

angular focus $(x|\theta) = 0,$

energy focus $(x|\delta) = 0.$

beams as much as we can.

Transfer Matrix of the Total System

T = T2•Td•T1

$$(x|x)_2(x|\theta)_1 + (x|\theta)_2(\theta|\theta)_1 + (x|\delta)_2\{(\delta|x)_d(x|\theta)_1 + (\delta|\theta)_d(\theta|\theta)_1\} = 0,$$

$$(x|x)_2(x|\delta)_1 + (x|\theta)_2(\theta|\delta)_1 + (x|\delta)_2\{(\delta|x)_d(x|\delta)_1 + (\delta|\theta)_d(\theta|\delta)_1 + (\delta|\delta)_d\} = 0.$$

- Approximation: $(\delta|\theta)_d \sim 0$ $\left(\frac{(\delta|\theta)_d}{(\delta|\delta)_d} \sim 10^{-3}\right)$
- $(x|\theta)_2 = 0$: eliminate effects of multiple scattering in the degrader

$(x\|\theta)_1 = (x\|\theta)_2 = 0,$	angular focus
$D_1 M_2 + D_2\{D_1(\delta\|x)_d + (\delta\|\delta)_d\} = 0.$	energy focus

1. Achromatic Degrader

achromatic condition in the absence of the degrader

$$D_1 M_2 + D_2 = 0.$$

Butler et al.
NIM A274(1989)27

condition for the degrader shape

"achromatic degrader"

$$D_1(\delta|x)_d + (\delta|\delta)_d = 1.$$

$$\left(\frac{\partial d}{\partial x}\right)_{x=0} = \gamma \frac{d_0}{D_1}$$

empirical range formula

$$d(x) = d_0(1 + x\gamma/D_1)$$

Wedge Shape !

simple tuning

$$M_x = M_1 M_2 \frac{1}{1 - d_0/R},$$

image enlarges

$$D_m = D_1 M_2 \frac{2\gamma - 1}{\gamma} \frac{d_0/R}{1 - d_0/R},$$

higher order effects

$$D_z = -2 D_1 M_2 \frac{\gamma - 1}{\gamma} \frac{d_0/R}{1 - d_0/R}.$$

ディグレーダーがない状態でアクロマティックフォーカスを実現しておく

↓

くさび形ディグレーダーの挿入

↓

エネルギー損失分、下流系の全ての電磁石強度を下げる

↓

アクロマティックフォーカスとなっている

2. Uniform Degrader

$$\frac{\partial d}{\partial x} = 0$$

achromatic condition

$$D_1 M_2 + D_2(\delta|\delta)_d = 0, \qquad \text{since } (\delta|x)_d = 0.$$

$$M_x = M_1 M_2,$$

$$D_m = D_1 M_2 \frac{2\gamma - 1}{\gamma} d_0/R,$$

$$D_z = -2 D_1 M_2 \frac{\gamma - 1}{\gamma} d_0/R.$$

Less Higher Order Aberrations due to Degrader

TUNING : Numerical Calculation taking into account Degrader Matrix EXPLICITLY

$$R_A = \frac{D_1}{M_1 x_0} \cdot \frac{2\gamma - 1}{\gamma} \cdot d_0/R,$$

$$R_Z = \frac{D_1}{M_1 x_0} \cdot \frac{2(\gamma - 1)}{\gamma} \cdot d_0/R.$$

分析したい粒子の運動量の変化、ディグレーダー厚さの変化、に応じて

$$D_1 M_2 + D_2(\delta|\delta)_d = 0$$

を満たすように、系を調整する。

下流の双極電磁石系の分散D_2は可変でなければならない。

二つの双極電磁石系の間に４極電磁石が必要

ディグレーダー直下流に置くなら、上流系は調整不要

平板ディグレーダーの特徴

●高次収差に対して有利（ディグレーダー由来の高次収差が少ない）

→ ビームの大きさ（断面のサイズ）を小さくするのに有利

●分析したい粒子の運動量の変化（ディグレーダーの厚さの変化に等価）に対してビームの大きさが不変

●ディグレーダー中でのエネルギー・ストラグリングに由来するビームの大きさの増大が比較的小さい

●ディグレーダー出口でのビームのエネルギーの広がりは増大する（同じ厚さのくさび型ディグレーダーに比べて）

S. Mitsuoka et al. / Nucl. Instr. and Meth. in Phys. Res. A 372 (1996) 489–500 491

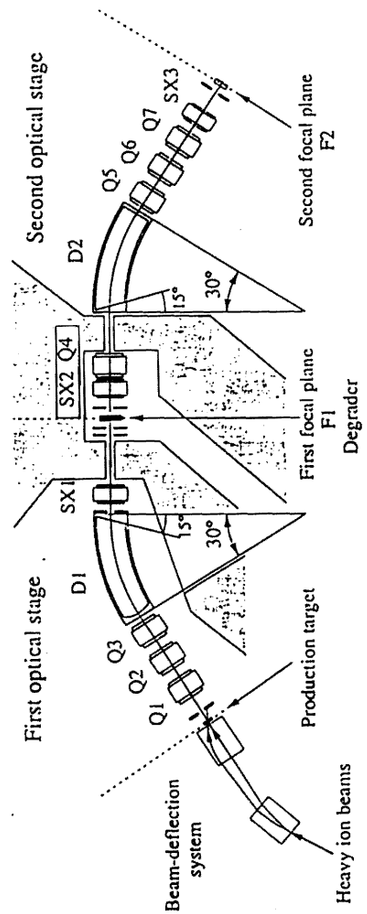

Fig. 1. Schematic layout of the projectile fragment separator SBL at RCNP. Magnetic dipoles, quadrupoles and sextupoles are denoted, respectively, by D, Q and SX with numbers showing the orders of the respective arrangements. The area of the final focal plane is shielded by concrete walls (shaded part) from the radiations from the target, the slits and the energy degrader.

Fragment Separator at RCNP, Osaka

多数のQ電磁石をどうやって計算値にのせるか?

計算値

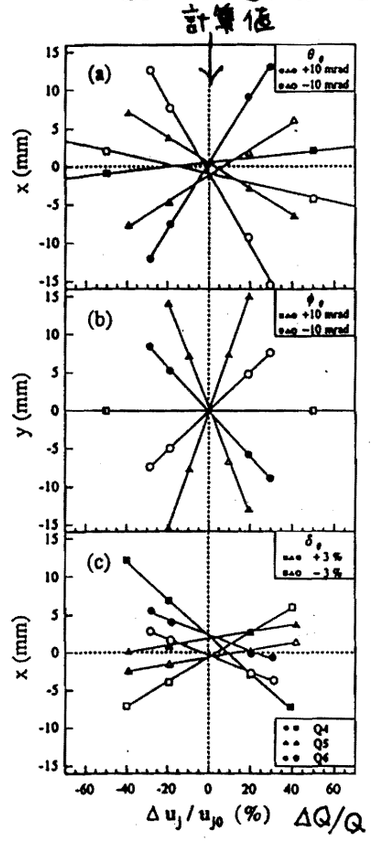

Fig. 3. Examples of the x- and y-coordinates of the rays, measured at the F2 focal position as a function of the strengths of the quadrupoles as denoted in (c). The initial coordinates of the rays are presented in the boxes.

最適化法

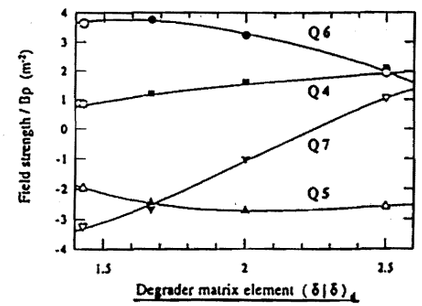

Fig. 6. Experimental values of the optimum quadrupole strengths as a function of $(\delta|\delta)_d$. The methods to obtain the data shown by open symbols and closed symbols are different (see text). The solid lines are the results of the optics calculations.

$(\delta|\delta)_d$ の関数として
Qの値を求めておく,

粒子の A, Z, E
degraderの厚さ

$(\delta|\delta)_d$による像の変化

粒子の分解能はDegraderが厚いほど大きくなる

くさび型Degraderでは

Degraderが厚い → X像が大きくなる

1. $(\delta|\delta)_d$が大きくなる

$$M = M_1 M_2 (\delta|\delta)_d$$

2. energy straggling が大きくなる ($D_2 \delta_{str}$)

$$D_2 = -D_1 M_2$$

平板型Degraderでは

Degraderが厚い　　像巾は一定

1. 倍率は$(\delta|\delta)_d$によらない

$$M = M_1 M_2$$

2. D2は小さくなる

$$D_2 = -D_1 M_2 / (\delta|\delta)_d$$

例えば、$(\delta|\delta)_d$ 1.6 → 2.5

平板型Degrader
像巾は20%増加

くさび型Degrader
像巾は70-90%増加

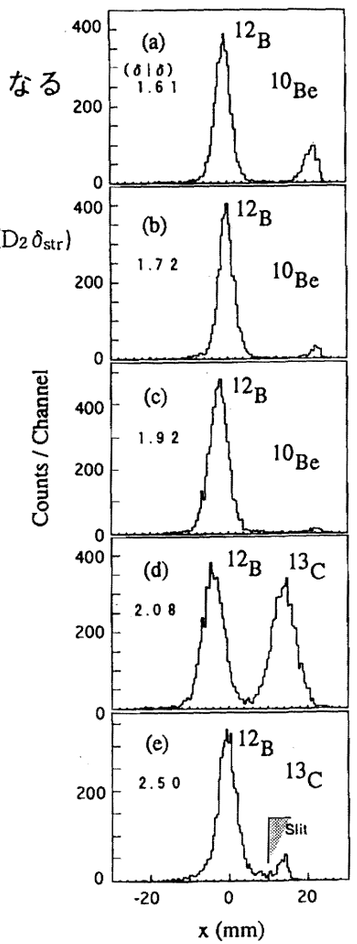

教訓

ディグレーダー中での多重散乱による角度の広がりによる輸送効率の劣化

↓

下流系の双極電磁石のポール間隔は、出来るだけ広げておきたい

低エネルギーでの問題

ターゲット／ディグレーダー出口での平衡電荷分布の広がりによる粒子分離の劣化：重い粒子は難しい？

RCNP 二次ビームコースでの実験

核偏極生成機構： S. Mitsuoka et al.

14N + 9Be → 12B

大きな核偏極

直接反応の寄与

超流動ヘリウム中での不純物イオンの振舞い

: S. Shimizu et al.

snowball 中での核偏極の保持

snowball 生成率

snowball の移動度

39.3 MeV/u $^{14}N + {}^{9}Be \longrightarrow {}^{12}B$

Large negative polarization up to $\simeq -35\%$ was observed at $\theta_L \geq 3°$.

CHARACTERISTIC FEATURES which can not be explained by the projectile fragmentation mechanism;

- The peak momenta in the yield distribution are rather higher at forward angles ($\theta_L \leq 6°$) than the prediction by projectile fragmentation model.
- The peak momentum strongly depends on θ_L.
- Large polarization at the momentum of yield peak: high figure of merit.

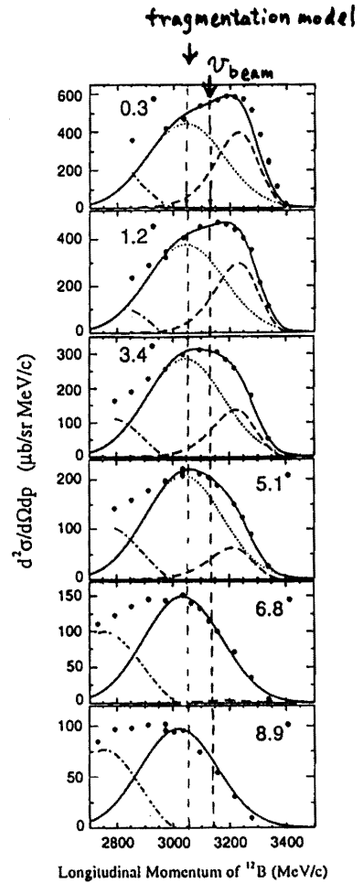

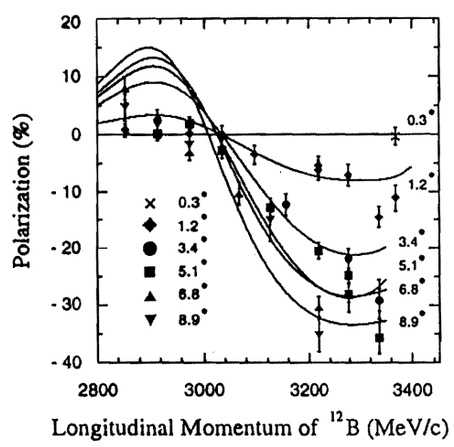

RCNP E119

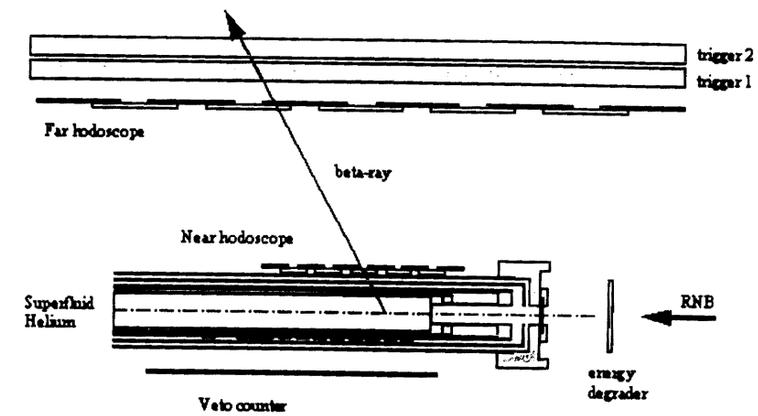

sensitive to individual impurities

sensitive both to snowballs and neutrals

space-time correlation

(position sensitive $\sigma \sim 7$ mm)

【5】 Applications of RIB

Measurement of β-unstable ^{12}B mobility in superfluid helium

Suguru Shimizu
Department of Physics, Graduate School of Science, Osaka University

Abstract

We report on the first observation of an impurity motion in superfluid helium by using a high energy β-unstable ^{12}B beam. A mobility of $^{12}B^+$ was successfully obtained as a function of a helium temperature from a time-space correlation spectrum which was yielded by detecting the emitted β-ray and decay time. This method is much more sensitive to the ion motion than those based on current measurement so far. It was found that the mobility of $^{12}B^+$ was remarkably lower than that of other ion spices.

It has known so far that a positive ion in liquid helium attracts the neighboring neutral atoms sufficiently to generate a high-density cluster around ion (snowball). One important consequence of this picture is that the ion drags a large number of surrounding helium atoms and therefore has a very large effective mass [1]. An experimental evidence of the snowball was first presented by the mobility measurement of He^+ ion [2]. Later experiments have disclosed the snowball radius and the effective mass to be $\sim 6\AA$ and $\sim$45 helium atomic mass, respectively. However, recent measurement revealed that the mobilities of alkaline ions and alkaline earth ions are lower and higher than that of He ion, respectively, contrary to the model prediction. It is needless to say that further experiments with wide variety of ion species are necessary to investigate the detail structure of the helium cluster.

Motivated by this physics issue, we have developed a new experimental technique to study the behavior of impurities by using radioactive nuclear beam (RNB). The RNB was implanted into superfluid helium and the individual motion of the beam ions was recognized by measuring the emitted β-ray track and decay time with a position sensitive detector. Here we present the first experiment using the RNB, in which the mobility of radioactive ^{12}B (τ=30 ms) ion was successfully observed as a function of a helium temperature.

The experiment was performed at the Research Center for Nuclear Physics (RCNP), Osaka University. Fig.1 shows a schematic cross sectional side view of an experimental apparatus. The implanted ^{12}B came to rest by losing its kinetic energy. During the stopping process, two categories of ^{12}B were simultaneously generated. One was a singly charged ion with a large number of the helium cluster and the other was a neutralized atom. The ions could be extracted with an associated mobility by a static electric field applied along the beam direction, while the neutralized atom remained at rest. The motion of the implanted ^{12}B was successfully observed in the time-space correlation spectrum, as shown in Fig.2. The measurement was carried out in the temperature range of 1.1−1.5 K at the s.v.p. Since the lifetime of ^{12}B was comparable with an ion transit time, a part of $^{12}B^+$ decayed during the transportation, and thus, a trajectory of the ions became a diagonal locus, as seen in Fig.2. A slope of the diagonal locus corresponded to

the inverse velocity of ions, and the mobility was thus derived from the ratio of the ion velocity and the applied electric field.

Fig.3 shows the observed ^{12}B mobility (closed circle) distribution as a function of inverse of the helium temperature. The mobility of alkaline (K, Rb, Cs) and alkaline earth (Ca, Sr, Ba) ions obtained in the previous experiment are also shown in the figure as open symbols. The figure shows obvious discrepancy between the $^{12}B^+$ mobility and others. Along the simple kinetic theory of an ion-roton scattering interaction, the mobility (μ) is written in terms of the effective mass of the helium cluster (M) and an average ion-roton cross section (σ_{ir}) as,

$$\mu = (\sigma_{ir} M)^{-1} \exp(\Delta/kT),$$

where Δ and T are the roton energy gap and helium temperature, respectively. In this description, the mobility is inversely proportional to $\sigma_{ir}M$ which should be relevant to the structure of the helium cluster, while $\exp(\Delta/kT)$ corresponds to the temperature dependence of the roton density in th fluid.

Fitting the ^{12}B mobility distribution with a function of $\alpha \cdot \exp(\Delta/kT)$, α and Δ/k were obtained to be $(5.4 \pm 0.7) \times 10^{-4}$ cm^2/Vs and (9.1 ± 0.3) °K, respectively. It should be noted that Δ/k was yielded from the roton density measurement using different methods, i.e., neutron scattering ($\Delta/k = 8.65$°K), oscillating disk techniques (10.6°K), and combination of second sound and thermal data (8–9.6°K). It is also obtained from the He^+ mobility, which yielded $\Delta/k = 8.8$°K. Since Δ/k obtained from the ^{12}B mobility is consistent with other measurements, it could be concluded that $^{12}B^+$ moving in superfluid helium suffers collisions with the rotons. On the other hand, α of ^{12}B was approximately 40, 30, and 20 % smaller than that of alkaline earth, helium, and alkaline ions, respectively. These features indicate that the helium cluster around $^{12}B^+$ have a distinct structure.

The classical model suggested that the snowball radius and the helium density in the vicinity of the ion are a function of only the ion charge state. Therefore, the ion mobility should be independent of the nature of the core ion. The mobility discrepancy between alkaline and alkaline earth ions were explained by taking into account their electron configurations [3]. Since the alkaline ion's outermost electrons fill a shell completely, its structure must differ only slightly from the classical model. On the other hand, the new principal factor relevant to the alkaline earth ion is the presence of a remaining valence electron outside the filled shell, and are considered to form the helium cluster of a light effective mass and small radius. In the case of ^{12}B, there are two valence electrons outside the filled shell and ^{12}B should have higher mobility than alkaline earth ion. Therefore, the mobility of ^{12}B is not successful in explaining in the framework of the electron configuration, and we have to introduce a new idea in order to reproduce such a remarkably small value.

Reference

[1] K. R. Atkins, Phys. Rev. **116**, 1339 (1959).
[2] F. Reif and L. Meyer, Phys. Rev. **119**, 1164 (1960).
[3] M. W. Cole and R. A. Bachman, Phys. Rev. **B15**, 1388 (1977).

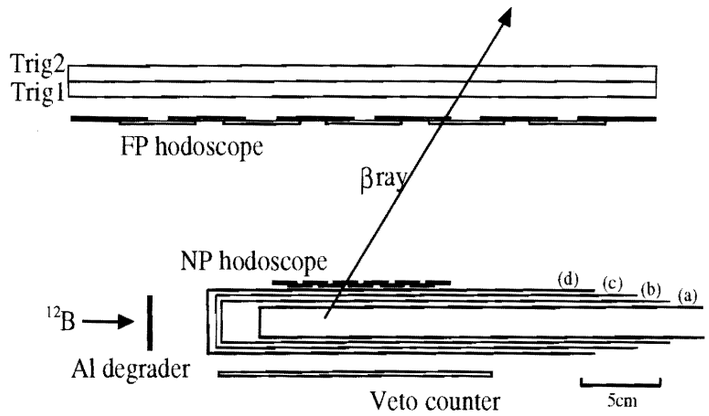

Figure 1: Schematic cross sectional side view of the helium chamber and the β-ray tracking detector. Two sheets of position sensitive hodoscope were installed on the top of the chamber. The cryostat was comprised of the helium chamber (a), 4.2°K radiation shield (b), 77°K radiation shield (c), and vacuum jacket (d). They had a cylindrical structure around the beam axis.

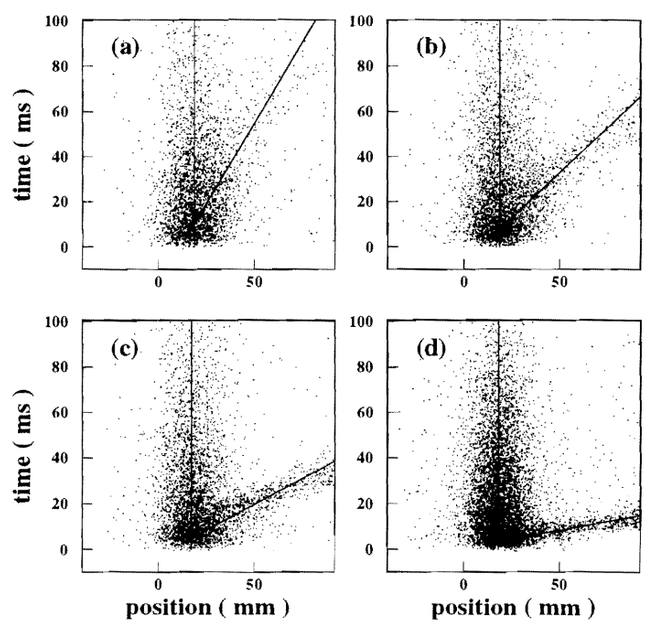

Figure 2: Time-space correlation spectra of ^{12}B. The entrance window of the chamber is placed at 0 mm. Solid lines show the actual trajectories of the ion and neutralized atom. The helium temperature was 1.50 (a), 1.39 (b), 1.27 (c), and 1.10 (d)°K.

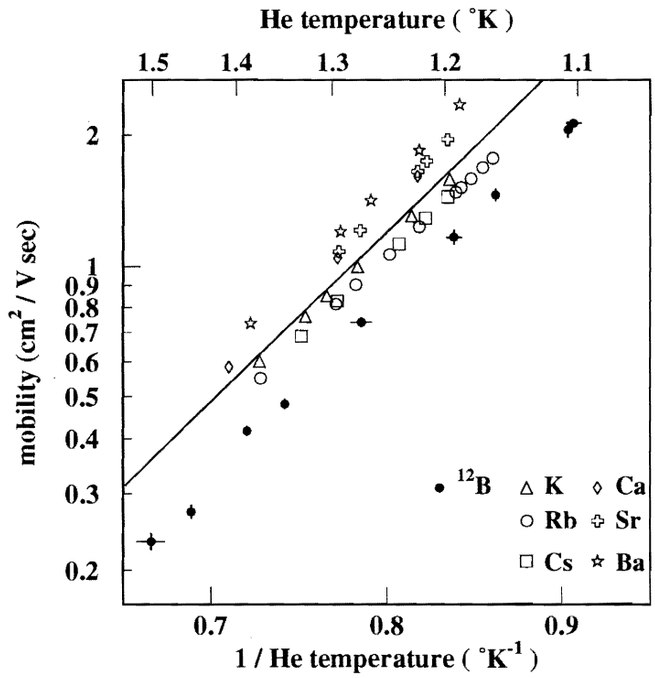

Figure 3: Closed circles denote the mobilities of $^{12}B^{+}$. The statistical error of the mobility and the fluctuation of a temperature are also shown. The mobilities of alkaline (K^{+}, Rb^{+}, Cs^{+}) and alkaline earth (Ca^{+}, Sr^{+}, Ba^{+}) ions are also shown as open symbols.

A research project on chemical properties of the heavy actinide and trans-actinide elements

A. Yokoyama and A. Shinohara, Osaka University

25/Aug/00

Abstract

We plan several experiments to determine the chemical properties of heavy elements covering the heavy actinide and trans-actinide regions. New techniques and apparatuses for investigation on the atoms of very short life and extremely low concentration including a case of one atom at a time are discussed. The collaboration of Japan's nuclear chemists, as a part of the project, succeeded in the production of the Rutherfordium and Dubnium atoms by using the JAERI tandem Van de Graaff accelerator.

Recently the success of synthesis of the 118 element was reported. The result does not seems to be confirmed up to the present. It is no doubt, however, that the nuclear chart of our interest is still being spread out to the heavy nuclides of trans-actinides. In that connection, the research on chemical properties of such elements is now very active and chemists try to spread out the periodic table of chemical elements.

In Japan, a research group including most of nuclear chemists started collaboration for investigation of the chemical properties on the heavy actinide and trans-actinide elements. In order to enable the research work, apparatuses designed for rapid chemical separation and detection systems for a very small number of atoms are needed. At the same time, a systematic study on one atom chemistry is inevitable, because it is known in some cases that chemical properties depend on the amounts of chemicals at very low concentration.

At Osaka University, we are in developing a gas-jet transport system and a chemical apparatus for rapid separation of aqueous solution using ion exchange chromatograph. Up to now, tracer solutions with radioisotopes of Hf and Zr are used to test the columns filled with ion exchange resin in Osaka University Radioisotope Research Center. The radioactive tracers are produced in Kyoto University Research Reactor Institute and Research Center for Nuclear Physics, Osaka University.

At Japan Atomic Energy Research Institute, the first priority of the research target is the chemistry of Rf at this moment. Synthesis of Rf(Z=104) and Db(Z=105) is accomplished by using the JAERI tandem Van de Graaff accelerator. A gas-jet coupled automated liquid chromatography apparatus was developed in order to perform rapid, repetitive and high performance liquid chromatography separations on the second scale in time. It is equipped with two magazines, each of which contains twenty micro-columns (1.6mm i.d. , 8 mm long). A series of chromatographic pumps, valves, mechanical sliders, and micro-columns are all controlled by a personal computer. The system is similar to that called ARCA developed at GSI in Germany [1]. The apparatus of JAERI is being subjected to the various tests using radioactive atoms of Hf and Zr produced in the tandem accelerator. The obtained data will be also utilized in the analysis of chemical properties of the Rf element because those elements are homologues to Rf.

Furthermore, new projects are planned in connection to the renewal of the Tohoku University Cyclotron and RIKEN Liniac accelerator. Especially, RIKEN is expected to be the future center of production of heavy actinides and trans-actinides enjoying the excellent beam of enormous intensity and various ions including very heavy ions. It is also expected to have facilities which allow us to use heavy targets such as U, Th and even heavier unstable isotopes and to handle as many nuclides as possible including alpha emitters.

Reference

[1] M. Schädel et al., Radiochim. Acta. **48**, 171(1989)

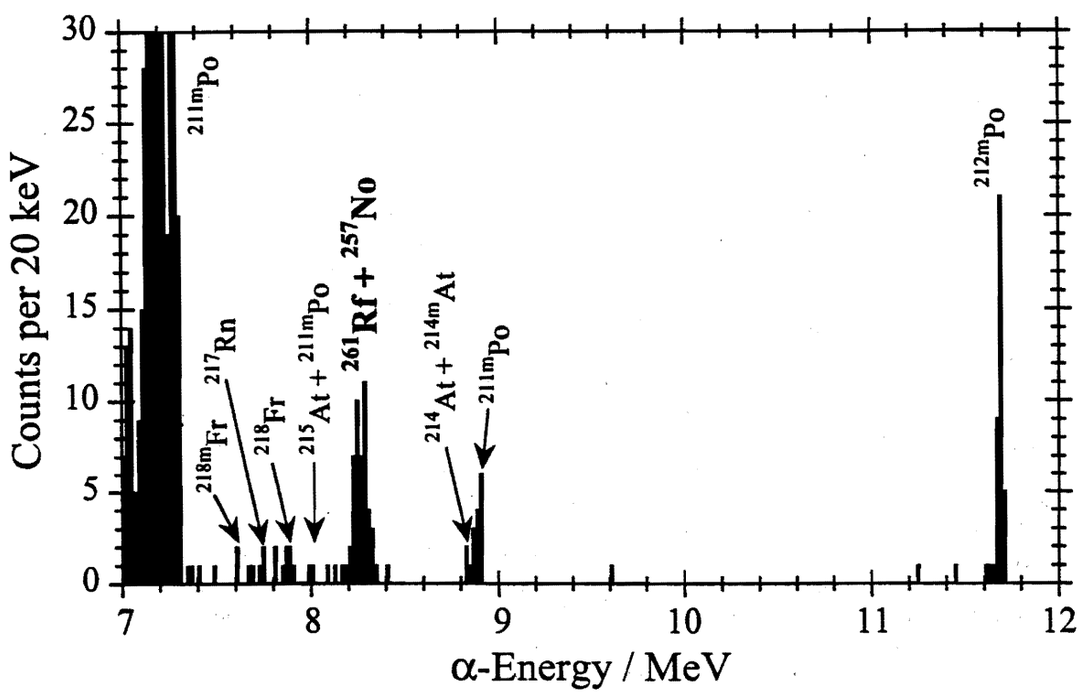

Fig. 1. Sum of α-particle spectra measured in the six top detectors.

「重元素の核化学」研究プロジェクト（阪大 Ver.）

研究拠点・テーマの流れ（案）　　'00.7.31.　篠原

阪大院理（RI 実、RIC）
＜装置開発・テスト、単一原子化学の基礎＞
・ガスジェット搬送システムの開発、テスト
・溶液系迅速化学分離装置（イオン交換法）
　の開発、基礎実験(トレーサー、252Cf)
・将来（原子ビーム反応法、イオントラップ
　　－レーザー分光）

阪大核物理センター(RCNP)
・I-コース利用　トレーサー製造
＜単一原子の化学の展開＞
・AVF-Ｉコースの改装（RI 製造用照射装置＋
　ニューマ、ガスジェット搬送装置）
・オンライン単一原子化学実験(RI 実)
　（イオン交換、ガスクロマト、、、検出系）

京大原子炉実験所（ISOL、加速器?）
・KUR-マルチトレーサー、トレーサー製造、α放射体利用
将来計画？：加速器利用同位体製造
・RI ターゲット利用、重核ターゲット
・ｐ、ｎビームのみ？大電流

原研東海（GradeUp-タンデム、2-3y 後）
＜TRA の化学の展開＞　(永目 Gr.)
・原研 Ver.OKAMA＋ARCA＋ROMA(Rf,Bh,Sg,,)
　旧核研不安定核ビーム施設の移設→×10
・OKAMA＋阪大 Ver.Chem.＋ROMA（？）

東北大 New サイクロ（すぐに！）
・オンライン単一原子化学実験の展開
・Recoil Separater とのリンクなど
　TRU ターゲットの使用？
＜重元素の化学＞
・重アクチニド、TRA の製造、化学

理研 RIBF(GradeUp-LINIAC、CRIB)
超大強度ビーム、TRU ターゲットの使用？
＜重核合成 NewRI、重元素の化学＞
・GARIS＋ガスジェットシステムの設置
・Cold fusion, Transfer → 重アクチニド New RI
　　気相化学の展開(工藤 Gr.)、

「重元素化学の基礎研究」

阪大院理　篠原　厚

重アクチニドー超アクチニド元素（原子）の化学を開拓する
そのために、迅速化学操作装置と検出系の開発、及び「単一原子の化学」の化学的基盤づくりを行う。基礎実験と「単一原子の化学」の系統的研究は阪大院理－KUR 及び RCNP 加速器利用により行い、重元素製造－化学実験は原研及び理研で行う。

理研に重元素製造の拠点として、自由度のある照射設備を期待している。（ビームの種類、ビーム量、重ターゲット使用、RI 実験室の設備、簡便な照射ポート）

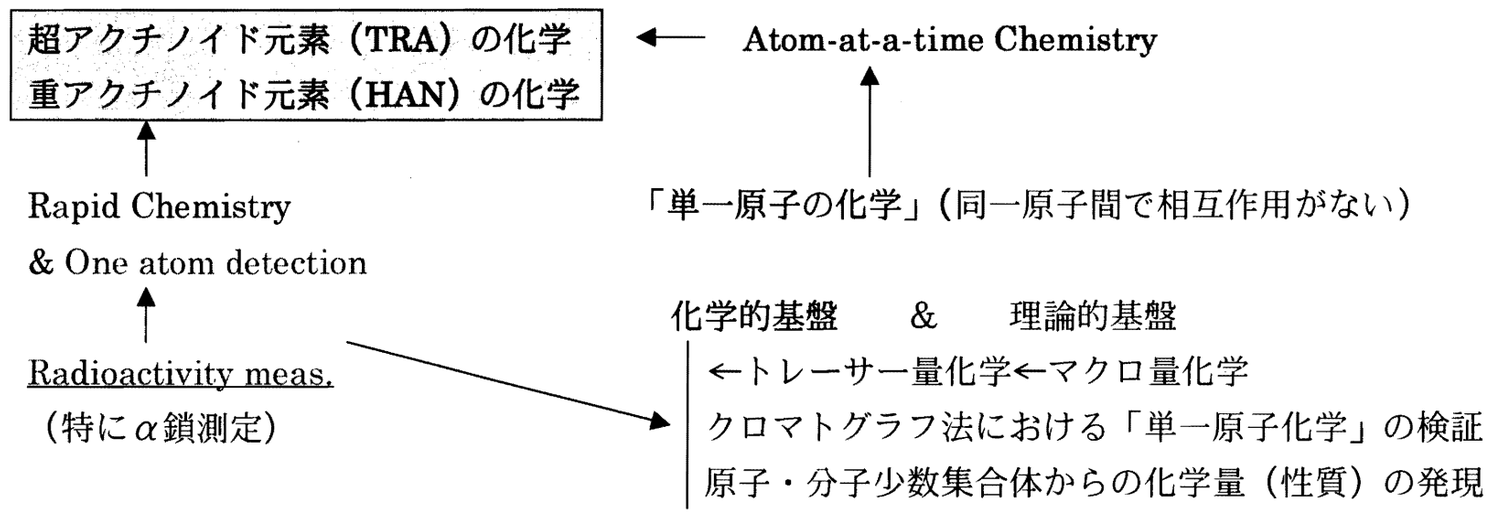

■ 重元素化学のための基礎実験

同族元素の「単一原子化学」の展開

重アクチノイド（Md,No,Lr）　ランタノイドとの比較、相互分離（イオン交換分離）

超アクチノイド（Rf,Db,Sg,,,,）　同族元素比較（イオン交換、溶媒抽出）　→原研にて進行中

新しい系で基礎データ蓄積　阪大 Ver.化学

超重元素(Z=114,116,118,,,)　長寿命 SHE を期待して　→同族元素比較

イオン交換、ガスクロマトグラフィー、

マクロ量トレーサー実験　→　トレーサー実験　→　オンラインテスト実験（252Cf）

（実験室）　（実験室）　↓

オンライン実験（加速器－ガスジェット－化学装置）

RCNP　I-コース改装（計画を検討中）

CYRC　1コース（ガスジェット設置済み）

理研 RIBF(GradeUp-LINIAC、CRIB)

↓

系統的・継続的実験可能な設備を構築

単一原子・分子 ⟶ 化学的性質の発現へ

クロマトグラフ法：　分配係数　化学平衡　－　確率分布　［理論的サポート、条件あり］

（マクロ量　－　単一原子）

・マクロ量－トレーサー量－単一原子

・化学系依存性、平行の早さ　　要検証

・トレーサー量、単一原子固有の特性？　→　検出に放射能を利用

マクロ量？化学的性質　（ex.　電気化学、金属形成、、、）

↓　↳ 少数多体系化学へ、クラスター？

電子のポテンシャル－化学ポテンシャル→　どの程度の原子数で性質が発現されるか？

⟶ 検出に放射能を利用

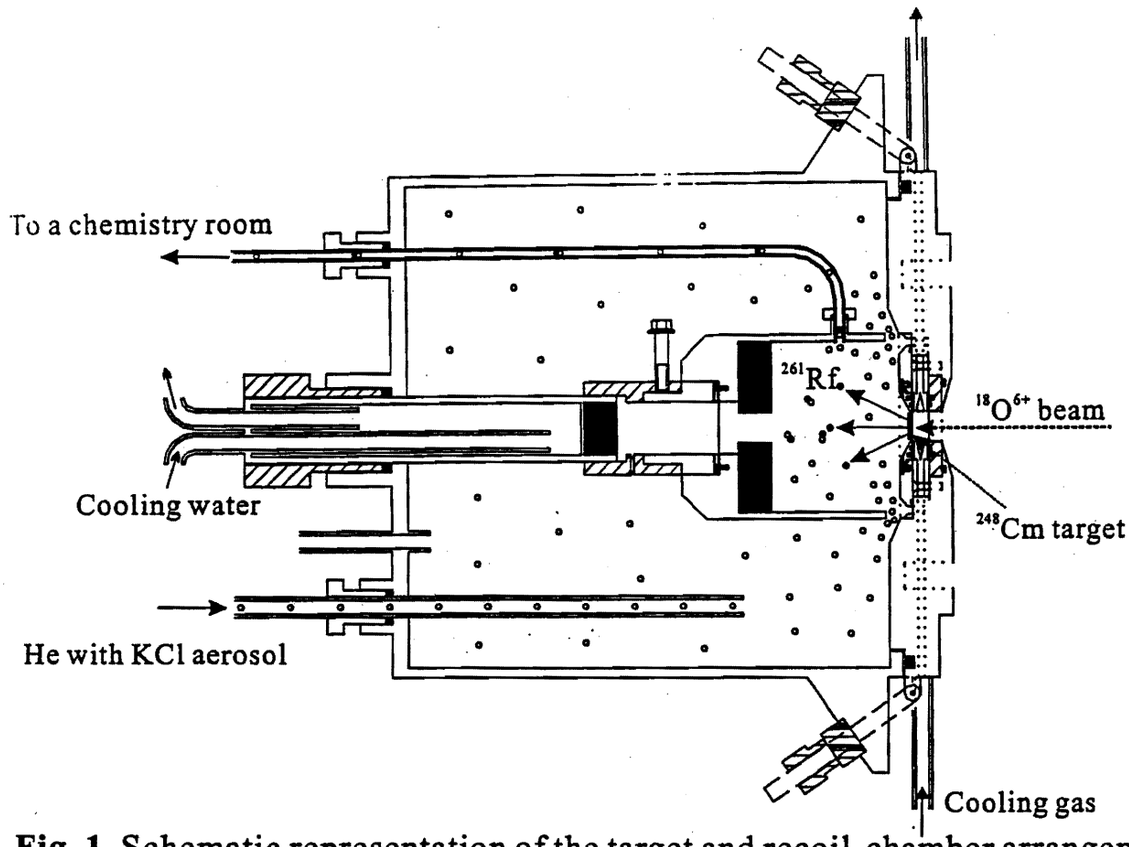

Fig. 1. Schematic representation of the target and recoil-chamber arrangement in transactinide chemistry experiments.

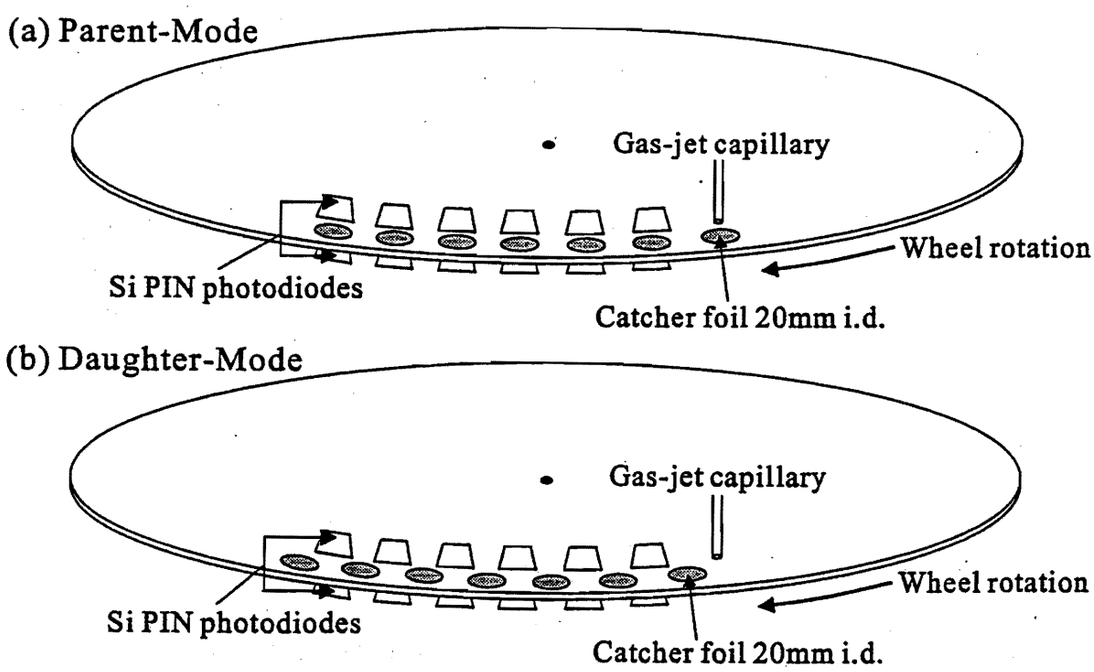

Fig. 2. Schematic of the detection system showing the parent-daughter stepping mode.

原研実験の写真—①

ARCA（degasser 部）

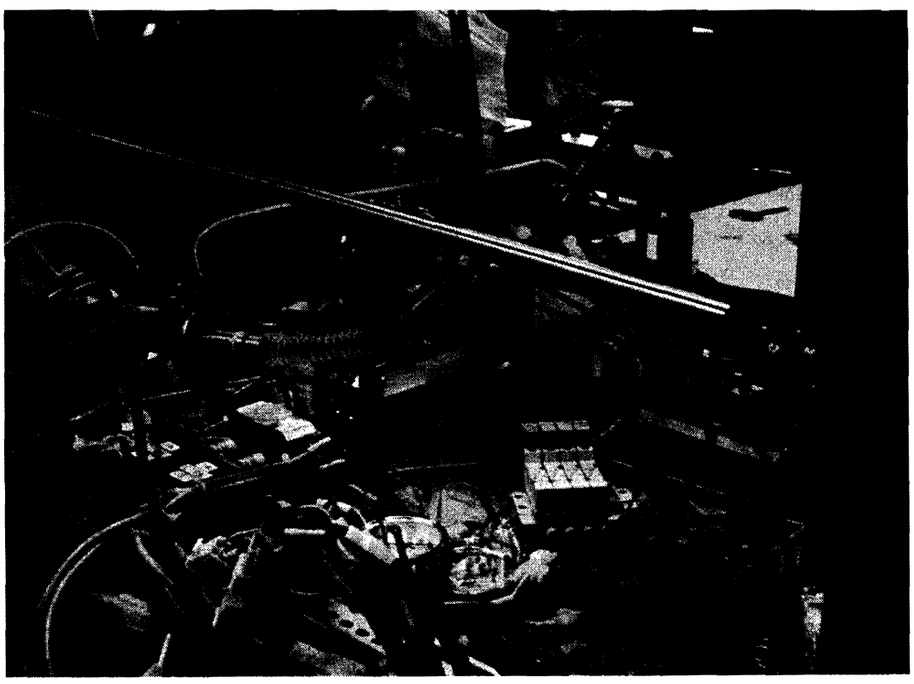

ARCA（後方コントロール部）

原研実験の写真—②

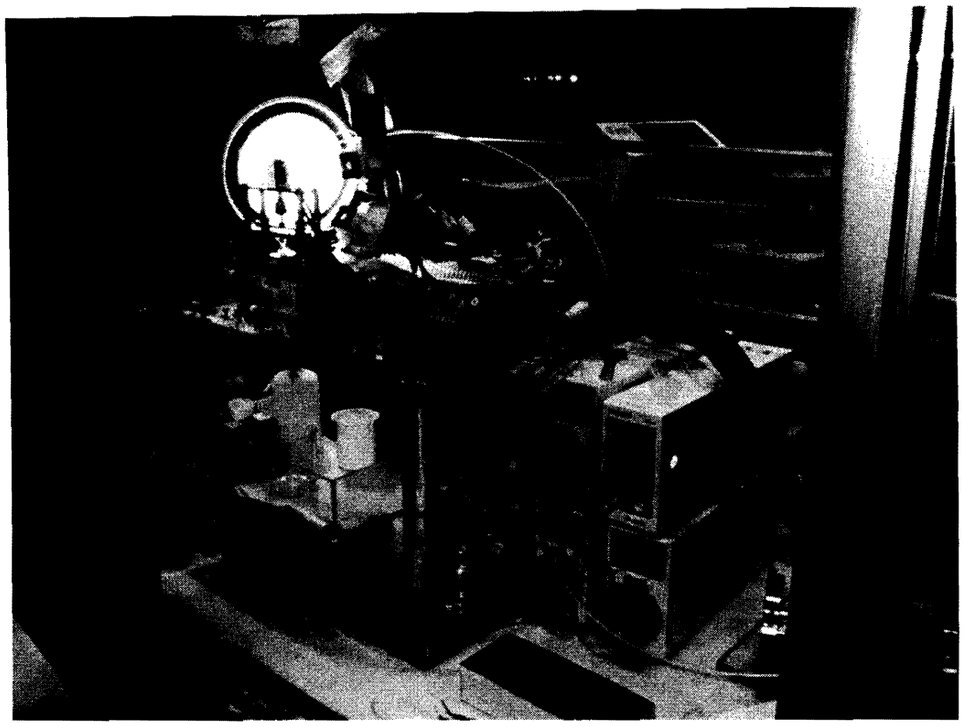

ARCA（全体）

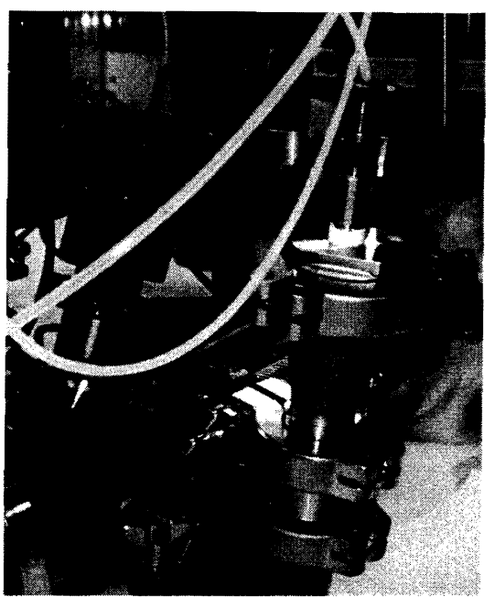

OKAMA 捕集装置

化学分離装置の制御システム

(Labo View)

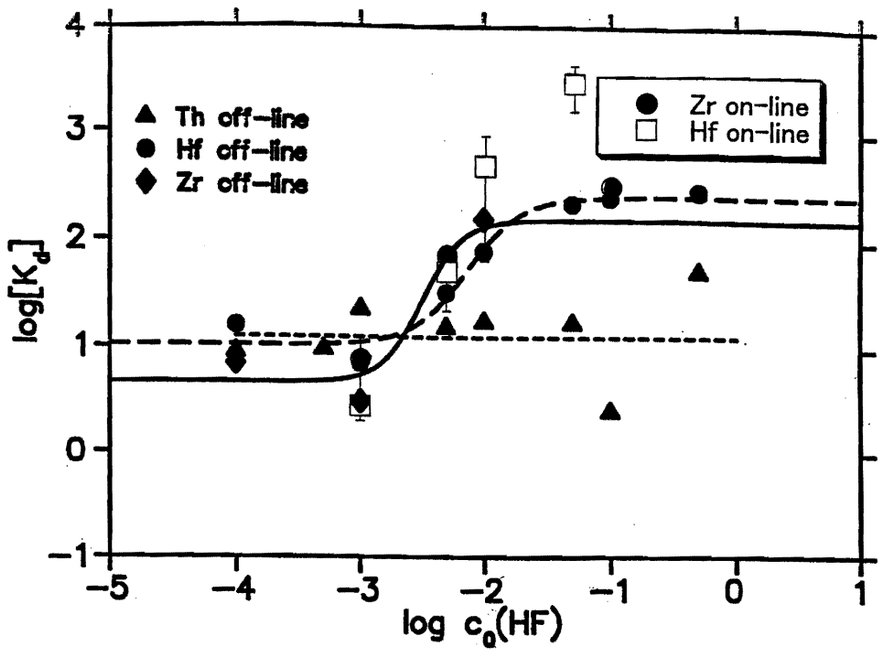

Figure 7: Sorption of Zr, Hf and Th (in batch experiments) on the AIX resin (Riedel-de Haën) in 0.1 M HNO_3 at various HF concentrations. The lines are fitted to the data points.

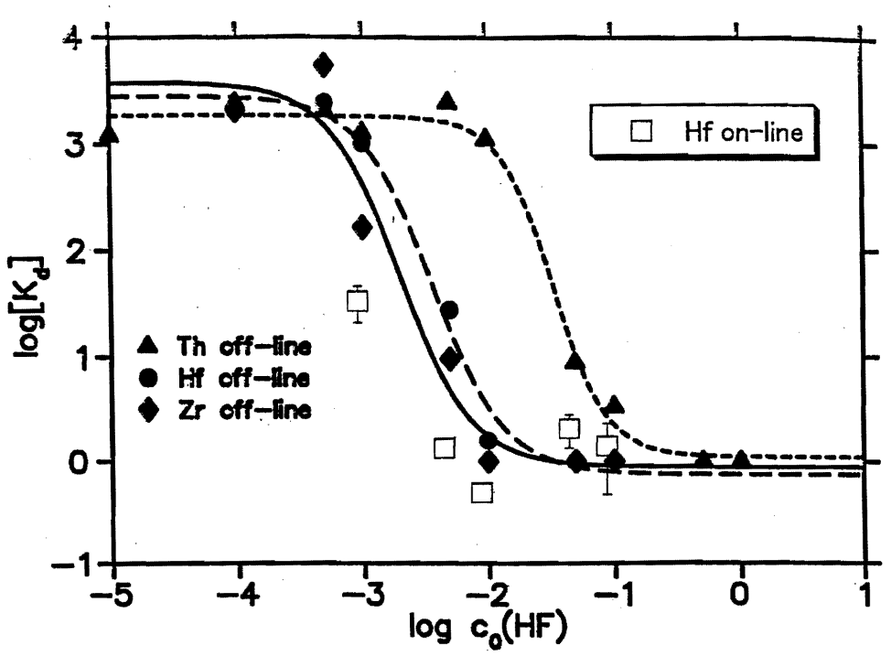

Figure 8: Sorption of Zr, Hf and Th (in batch experiments) on the CIX resin (Aminex A6) in 0.1 M HNO_3 at various HF concentrations. The lines are fitted to the data points.

■ 阪大 Gr.の現状

(2000.7.30.メモ)

平成１２年度　研究進捗状況

１）ガスジェット搬送装置の作成　→　テスト中
（受容部分の安定性、後段化学への影響？）←→　生成物搬送法の検討（他の方法も？）

２）迅速化学分離装置の試作（イオン交換分離装置）　→　テスト中
（駆動準備・テスト、実験系の選択のための基礎テスト、自動化の準備）

３）バッチ処理によるイオン交換装置のトレーサー実験開始
（KUR-マルチトレーサー、RCNP-RI 製造、による）

４）He ジェットーイオン交換系のオンラインテスト（^{252}Cf による FF 利用）→　準備中

５）具体的研究計画の立案　←「重元素の化学勉強会」開催（阪大-KUR）

年次計画	研究室　＋　RI 実験室	原研
１１	・ガスジェット搬送システムの設計、作成開始	・原研-ARCA 試作
１２	・迅速連続イオン交換分離装置(RCA1)の試作とテスト ・RCA1 トレーサー実験、化学実験系の検討	・トレーサー実験 ・Rf 製造テスト
１３	・ガスジェット-RCA1 オンラインテスト(252-Cf) ・RCA1→ARCA1（自動化） ・SISAC or マルチカラムシステム？の開発・テスト	・Rf 製造-化学実験 -化学実験（原研 Ver.） ・阪大 Ver.化学実験 ＜重元素の化学＞
１４	・トレーサーーオンライン化学実験準備 RCNP and/or CYRC にて開始 ＜Atom-at-a-time chemistry の基礎実験＞ ↓　化学の多様化（ガスクロ、溶媒抽出、電気化学？、、、）	
？	・KUR-加速器ーオンライン化学 ↓	

Spectroscopy of Highly Charged Ions using Tokyo-EBIT

Shunsuke Ohtani

The University of Electro-Communications, Chofu, 182-8585 Tokyo, JAPAN

A number of different experiments are progressing in parallel for the study of the physics of highly charged ions using the Tokyo-EBIT. In those studies, this paper gives the general feature of the apparatus and the brief survey of spectroscopy works.

Introduction

The electron beam ion trap(EBIT) was developed at Lawrence Livermore National Laboratory to study highly charged ions(HCIs)[1], which was based on the earlier electron beam ion source(EBIS) concepts[2] but with a shorter ion-trap length to limit plasma-like instabilities and hence to increase the residence time of trapped ions. The long residence time is essentially important for producing the higher charge-state ions and observing them in the spectroscopic study.

Several EBITs have been constructed throughout the world. Most of EBITs have similar operation parameters with an electron beam energy of up to 25keV. For highly stripped ions of heavy atoms (high-Z elements),the ionization cross sections by electron impact increase gradually with the electron energy. Therefore a high energy electron beam is favorable for producing high-Z ions with very high-charge states. In Liveremore, a high-energy EBIT is in operation presently to perform the spectroscopic studies for systematic investigation of the relativistic and QED effects in simple atomic systems. A new high-energy EBIT is under development in Freiburg to perform the atomic collision experiments with extracted HCIs as well as the spectroscopy.[3]

A few years ago, we have also constructed a newly designed, high-energy EBIT in Tokyo to develop a new research field in atomic physics with HCIs[4]. In the first stage of the operation, our experimental activity has been concentrated mainly on the spectroscopy of HCIs in the trap. Recently, we have started to use the extracted ions from the trap and to investigate the HCI-interaction with matters.

Tokyo EBIT

In general, the EBIT device consists of three parts; an electron gun, a trap region with three drift tubes and an electron collector. The electron beam emitted from the gun is accelerated upwards by the potential difference between the gun and the drift tubes, whilst being compressed to a radius of about 30μm by a 4.5T magnetic field generated by a superconducting Helmholtz coils. After passing through the drift rubes, the electrons are decelerated and collected by the electron collector. Both the electron gun and the collector are designed to be floated to max.-300kV.

Neutrals or ions are injected into the trap through a gas valve or from a pulsed ion source of vacuum-spark-type. Through interaction with the high current-density electron beam, they are ionized successively in the trap region. Ions produced are trapped radially by the space charge potential(~10V)of the electron beam,and axially by voltages(~100V)applied to the drift tubes. The electron beam also serves to excite the trapped ions. Radiation from the excited ions can be observed through radial ports on the center drift tube in the horizontal plane.

The EBIT has several advantages for spectroscopic studies. The ions are nearly at rest, so Doppler shift corrections are not required. The EBIT forms a line light source, that is, the source size is approximately defined by the electron beam radius, so this source can be used directly for dispersive spectroscopy without the need for an entrance slit. The EBIT source is a low-density, low-collisional, weak-field non-neutral plasma, so the absorption of emission lines is negligible and the population of matastable states is also negligible. In addition, because the charge-state distribution in the trap is simple, and subsequently the spectral structure observed is also simple compared with other plasma sources, the identification of the transition and the measurement of the wavelength can be easily performed.

Figure 1 shows an X-ray spectrum measured with a Ge solid state detector. The electron beam parameter in this observation is 75 keV, 150mA. Krypton gas is introduced into the trap. In the X-ray energy region below the electron beam energy Ee, series of K-X-ray lines from highly charged ions of Kr, Ba and W are observed. The Ba and W atoms are evaporated from the cathode, subsequently ionized and trapped. The bremsstrahlung radiation continues up to the beam energy Ee. Radiative recombination(RR) lines of highly charged ions are also observed in the higher X-ray energy region. RR lines appears at energies above the Ee, as clearly seen in the expanded X-ray spectrum of the lower figure, since the energy of an RR line is the sum of the Ee and the ionization energy of the captured electron. The lines observed here are RR to the n=1, 2 and 3 levels of Kr, Ba and W ions, converging to the Ee. RR lines to n=1 level split into two peaks for Ba and Kr ions. The peak at the higher energy side is due to RR into bare ions, and that at the lower side is due to RR into H-like ions. This spectrum shows the production of bare Ba ions(Ba^{56+}) in the trap. For Ba, the peak for RR into bare ions is smaller than that for RR into H-like ions, while for Kr the situation is reversed. This imply that the bare Kr^{36+} ions are more abundant than the H-like ions in the trap at this EBIT operation.

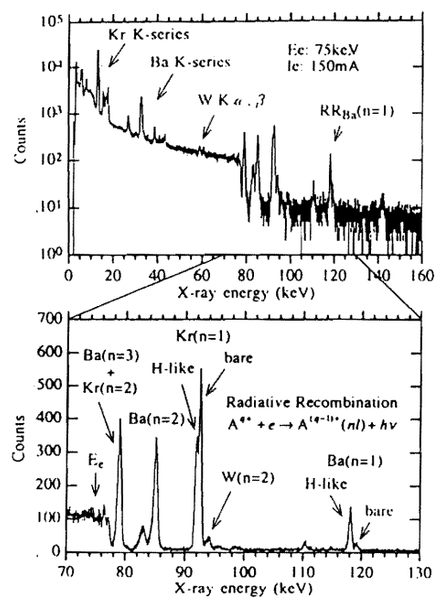

Fig 1

Experimental and Theoretical Results

1. X-ray spectroscopy

In the course of the spectroscopic studies in Tokyo, various kinds of X-ray spectroscopy have been performed, such as the precise measurements of the wavelengths for X-ray transitions, the observation of dielectronic recombination(DR) processes, and the measurements of collision strengths and polarizations as a function of the beam energy in electron-HCI interactions.

In this report, we just show recent systematic measurements of the wavelengths for X-ray transitions in Ne-like, high-Z ions[5]. Because of high abundance in a hot plasma due to its closed shell structure, the investigation of X-ray transitions in the Ne-like sequence is important for applications such as plasma diagnostics and X-ray lasers. From the view point of atomic physics, the systematic study for Ne-like ions is also important to understand the relativistic atomic structure since there is strong configuration mixing of the wave functions of the excited states in high-Z region.

In the present observation, the spectrometer used consists of a flat LiF(200) crystal with a high-pressure, position-sensitive proportional counter. Figure 2 shows X-ray spectra for the transitions from the n=3 excited states to the ground state($2p^6$) in Ne-like ions ofBa(Z=56), Cs(55), Xe(54), I(53), Te(52), Sb(51) and Sn(50) as a function of the scaled transition energy: E(transition energy) /Eav(configuration averaged energy). In this figure, 3D, 3F and 3E denote some electronic configurations in the n=3 excited states, which are $(2p^{-1}_{3/2}3d_{5/2})_{J=1}$, $(2p^{-1}_{1/2}3s)_{J=1}$ and $(2p^{-1}_{3/2}3d_{3/2})_{J=1}$, respectively. As seen in Fig.2, the order of excited levels changes between 3D and 3F, and also between 3F and 3E. For example, the 3D and 3F lines become closer, change positions at Z=54(Xe^{54+}) and then become far again as Z increases. This means that in this Z region the energy levels of these states become degenerate, so that the wave functions of these states might mix strongly.

The experimental wavelengths are compared to the theoretical values calculated with the multi-configuration Dirac-Fock(MCDF)method. The experimental and the theoretical results of the transition energies for 3D, 3F and 3E lines are plotted in Fig.3. Two types of calculations have been performed ,1) with configuration mixing of the wavefunctions and 2) without mixing, respectively. The calculated values with configuration mixing reproduce the experimental results quite well. As is shown in Fig.3, both of experimental and theoretical investigations clearly indicate that the two levels get close each other around Z=55 for 3D and 3F, Z=51 for 3F and 3E, but avoid to degenerate. This suggests that they are coupled through strong mixing of two electronic configurations.

Fig 2

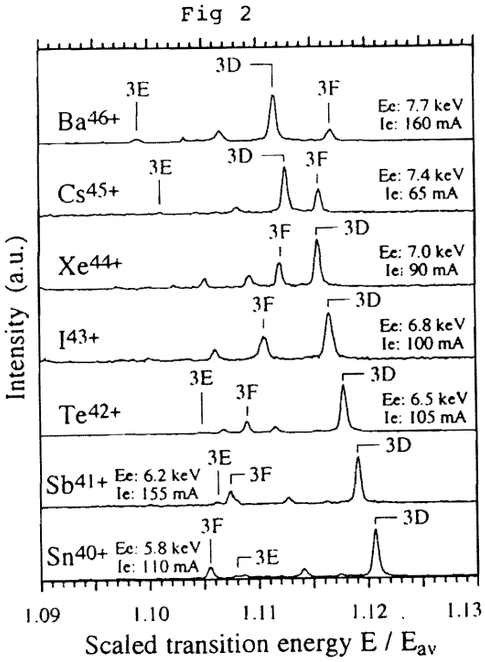

Fig 3

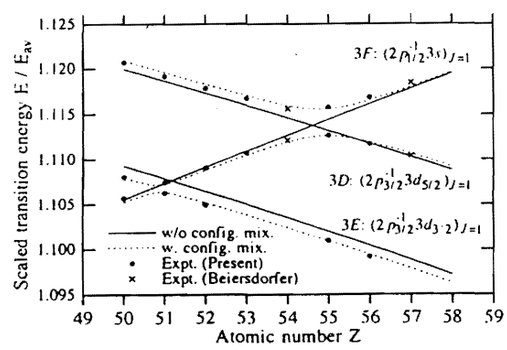

2. Visible spectroscopy

Forbidden transitions with long wavelengths sometimes play important roles in diagnostics of hot plasmas. In the visible region, the ion temperature and the local magnetic field could be easily determined through the measurements of Doppler and polarization profiles of emission lines from HCIs in a plasma.

At lower interaction energies of electrons with the trapped HCIs, we have systematically observed visible spectra due to fine structure M1 transitions, $(3D^4)^5D_2$-$^5D_3$, in the ground term of Ti-like ions for several elements with Z=51-78[6]. The present observation has been made by using the 32-cm monochromator of Czerny-Turner type with a liquid nitrogen cooled CCD detector. The spectra obtained are shown in Fig.4. In this figure, the target elements of

Ti-like ions observed are given together with the atomic number Z, the electron beam parameter and the data acquisition time. From Sb(Z=51) toPt(78), all of the M1 transitions, $^5D_2$-$^5D_3$, in the Ti-like ions exhibit anomalous wavelength independence of Z, lying in the visible or near UV region, which is qualitatively in agreement with the prediction by Feldman *et al.*[7].

This anomalous stability in the wavelength variation with Z has been discussed based on our theoretical calculation with the MCDF method. From consideration of mixin coefficients in the coupling scheme with respect to Z, the levels which are well described by the LS coupling scheme in low Z become characterized by the JJ coupling scheme in high Z. The transition from LS to JJ coupling takes place in the narrow intermediate region between Z=40 and 60. According to the calculation of the $^5D_2$-$^5D_3$ transition energies, a plateau, that is , the anomalous wavelength-stability with Z, is formed accidentally due to the transition from LS to JJ coupling.

The present calculations for the transition energies are in excellent agreement with all the existing measurements reducing the discrepancy to less than 1%(Fig.5). This suggests that the present calculation may well fill the void of unmeasured elements from Sn(Z=50) to U(92).

Fig 4

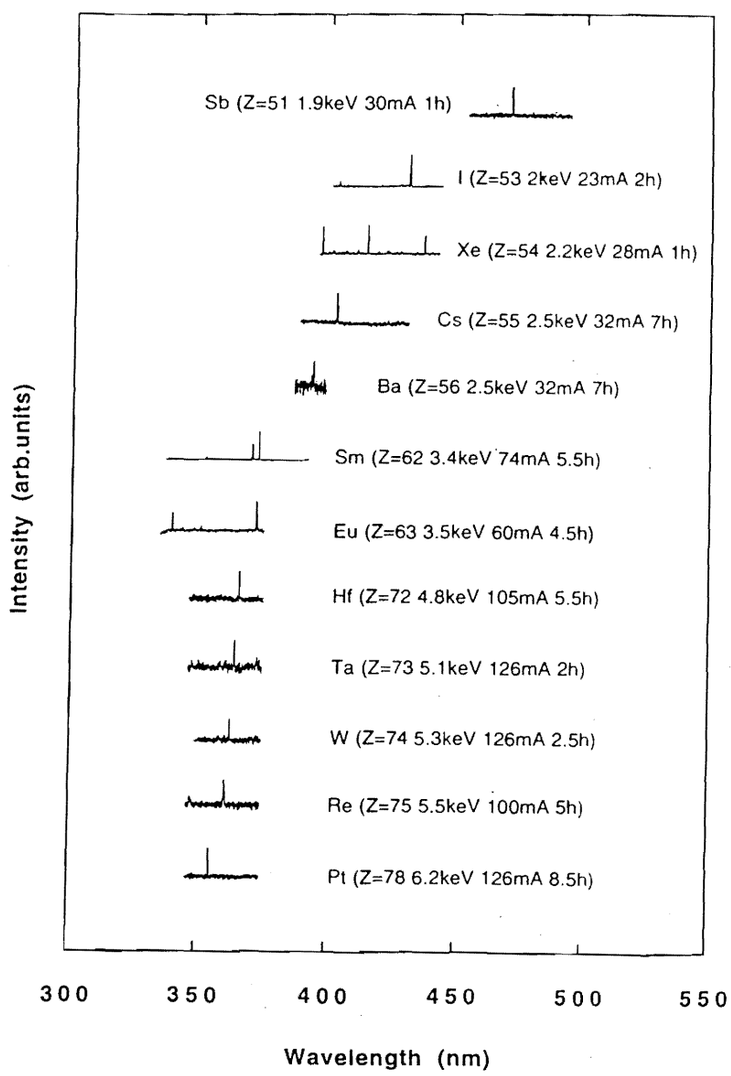

Fig 5

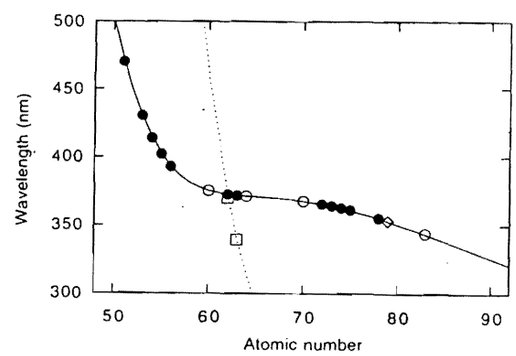

Acknowledgments

The research activity described above is being performed under auspices of the International Co-Operative Research Project(ICORP) of the Japan Science and Technology Corporation(JST). The collaborative study is in progress with Prof. J. D. Silver of the University of Oxford on the HCI business and also with Dr. H. A. Klein of the National Physical Laboratory on the ion trap physics.

Finally, are listed below the names of JST colleagues and also of collaborators from other institutions.

D. Kato, T. Kinugawa, H. Kuramoto, N. Nakamura, H. Shimizu, X-M. Tong, C. Yamada and H. Watanabe

E. J. Sokell (Univ. College Dublin), F. J. Currell (Queens Univ. Belfast), T. Hirayama (Gakushuin Univ.), K. Motohashi (Tokyo Univ. Agric. Technol.), K. Okazaki (RIKEN), M. Sakurai (Kobe Univ.), S. Tsurubuchi (Tokyo Univ. Agric. Technol.), I. Yamada and T. Watanabe (Int. Christian Univ.)

A number of graduate students have been participating in this research project. The author is grateful to all of the above colleagues for their collaborations

Reference

1). Levine, M. A.; Marrs, R. E.; Henderson, J. R.; Knapp, D. A.; Schneider, M. B., Physica Scripta **1998** T 22, 157.

2). Donets, E. D.; Orsyannikov, V. P., Sov.Phys.JETP **1981** 53, 466.

3). Crespo López-Urrutia J. R.; Bapat B.; Dorn, A.; Moshammer, R.; Ullrich, J., Abstract of ICPEAC, Sendai, **1999** 742.

4). Watanabe, H.; Asada, J.; Currell, F. J.; Fukami, T.; Hirayama, T.; Motohashi, K.; Nakamura, N.; Nojikawa, E.; Ohtani, S.; Okazaki, K.; Sakurai, M.; Shimizu, H.; Tada, N.; Tsurubuchi, S., J. Phys. Soc. Jpn. **1997** 66, 3795.

5). Nakamura, N.; Kato, D.; Ohtani, S., Phys.Rev. **2000** A61 052510.

6). Watanabe, H.; Crosby, D.; Currell, F. J.; Fukami, T.; Kato, D.; Ohtani, S.; Silver, J. D.; Yamada, C., Phys. Rev. A, to be published.

7). Feldman, U.; Indelicato, P., Sugar, J., J. Opt. Soc. Am. **1991** B8, 3

fitted to delayed neutron summation calculation with preliminary ENDF/B-VI fission yields and decay data

Motivation

strange behavior of ENDF/B-VI Delayed Neutron Data

More than 10% difference from conventional calculation!

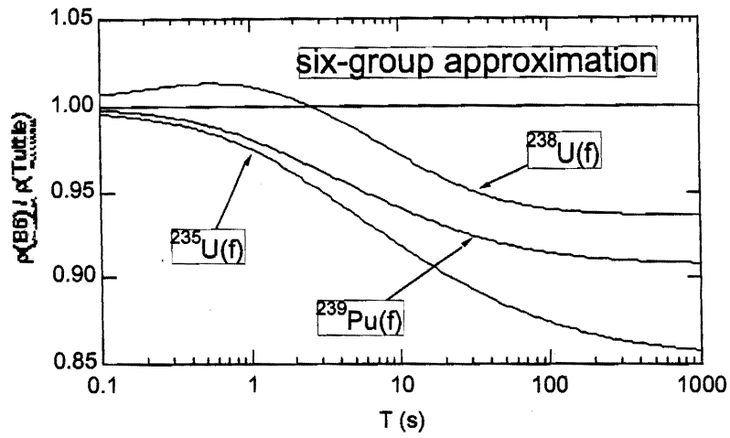

Reactivity in dollar vs reactor period calculated with ENDF/B-VI Delayed neutron data

Purpose

Identify sources of strange behavior of reactor kinetics calculated with ENDF/B-VI Delayed Netron data

ν_d and six-group parameters (time dependence)

Strategy

Calculate reactor kinteic directly* from Fission-Product (FP) yields and their decay data in ENDF/B-VI

* NOTE : This is the work that, for the first time, calculates reactor kinetics directly from real FP yields and decay data.

Identify erroneous FP data to result in a strange behavior in reactor kinetics

Reactor kinetics in a generalized form

Master Equation for power p(t)

$$\frac{dp}{dt} = \frac{\rho - \beta}{\Lambda} p(t) + \int_{-\infty}^{t} du \frac{p(u)}{\Lambda} \frac{n_d(t-u)}{\bar{\nu}}$$

reactivity : $\rho = (k-1)/k$

neutron multuplication : k= (neutron production)/(neutron loss)

mean neutron generation time : $\Lambda = 1/k$

neutron lifetime : $l = 10^{-2}$ (s) (thermal) , $l = 10^{-5}$ (s) (fast)

$$p(t) \to const \times \exp(-st) \; as \; t \to \infty$$

T=1/s : reactor period

Reactivity vs reactor period (T=1/s)

$$\rho = s \frac{\int_0^{\infty} dt \exp(-st)\, m_d(t)}{\bar{\nu}} \quad \text{with} \quad m_d(t) = \int_{-\infty}^{0} du\, n_d(t-u)$$

Physical interpretaion of $m_d(t)$

the delayed neutron activity after infinite irradiation

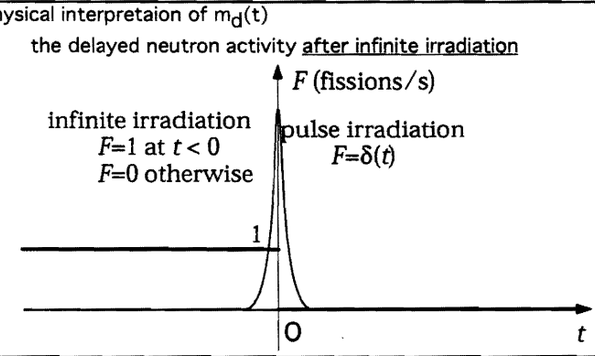

Asymptotic formula for a large period T

$$\rho = (N/\bar{\nu})\, s \quad \text{with} \quad N = \int_0^{\infty} dt\, m_d(t)$$

Physical interpretation of N

the total number of delayed neutrons emitted after the infinite irradiation

Delayed Neutron (DN) data in ENDF/B-VI

total delayed neutrons after a pulse fission : $\bar{\nu}_d$

its time dependence : $n_d(t) = \bar{\nu}_d \sum_{j=1}^{6} \alpha_j \lambda_j \exp(-\lambda_j t)$

ENDF/B-VI gives the empirical parameters, α's and λ's.

They were fitted to $n_d(t)$ obtained from the summation calculation with preliminary ENDF/B-VI fission yield and decay data file.

Summation calculation of DN data

$$\bar{\nu}_d = \sum_i Y_i P_{ni}$$

$$n_d(t) = \sum_i Y_i P_{ni} \lambda_i \exp(-\lambda_i t) + (decay\ chain)$$

Input data

decay constant : λ
delayed neutron emission probability : Pn
cumulative fission yield : Y

Result 1 : Similar underestimate of reactivity

Reactivity vs reactor period calculated directly from FP fission yields and decay data

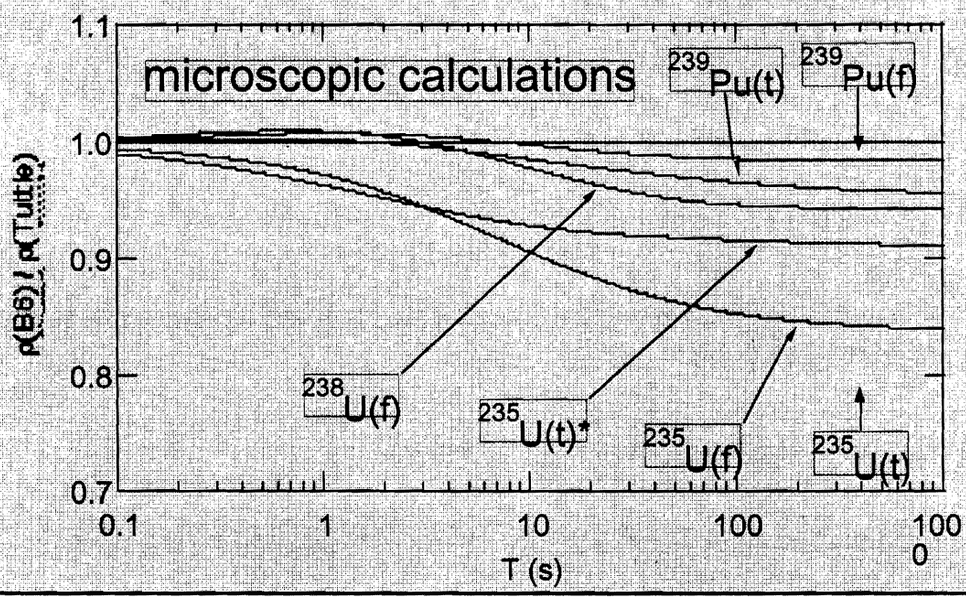

Result 2: ^{137}I, ^{88}Br and ^{87}Br are important

^{137}I is the most important, not ^{87}Br.
^{137}I and ^{88}Br covers more than 50%.
^{136}Te gives appreciable contributions.

Delayed neutrons emission after infinite irradiations (inf.) and after a pusle fission (pulse)

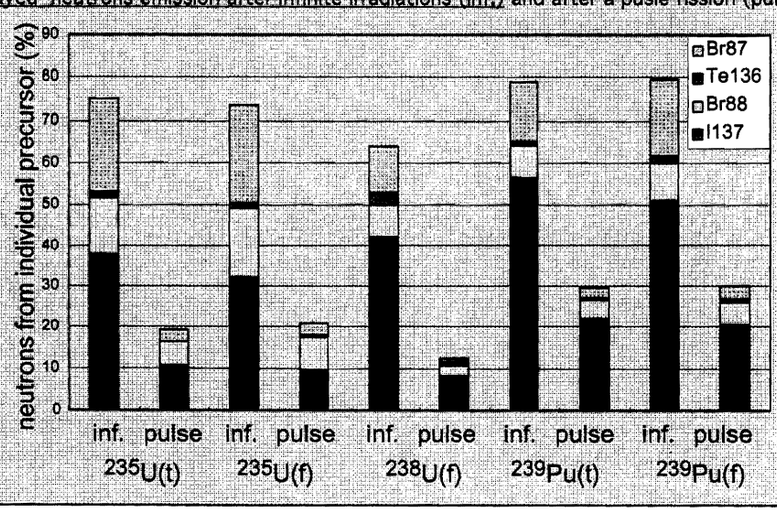

Result 3 : $^{137}I_{(24.5s)}$, $^{88}Br_{(16.5s)}$ and $^{136}Te_{(17.5s)}$ questionable from time dependence $m_d(t)$

The $m_d(t)$ difference can be fitted with ^{137}I, ^{88}Br and ^{136}Te.

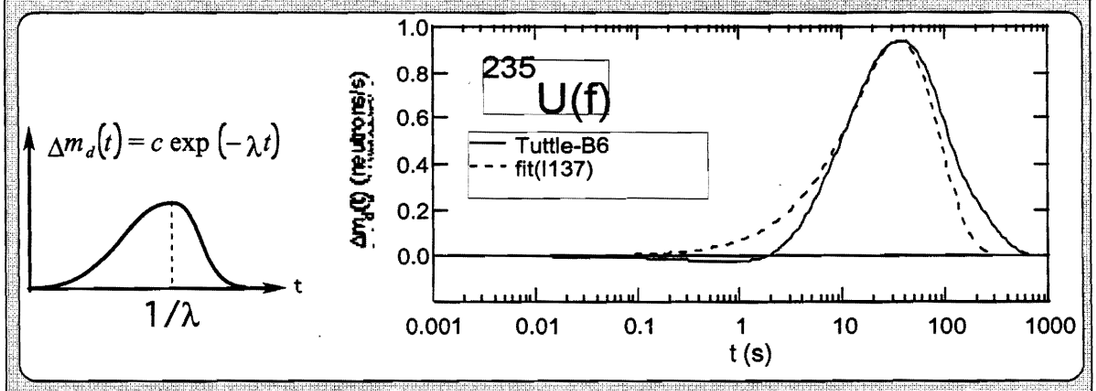

lifetime $1/\lambda \sim 30$ s → precursor half life $\ln 2/\lambda \sim 20$ s

Conclusions

1. We calculate the reactor kinetics directly from FP fission yields and decay data for the first time.
2. The obtained inhour equations show the underestimate of reactivity at long periods.
They are similar to the ones from the DN data in ENDF/B-VI.
3. ^{137}I is the most important for the long period behavior.
^{137}I, ^{88}Br and ^{87}Br covers 60-80% of the reactivity.
4. The major sources of the underestimate are ^{137}I and ^{88}Br.
^{136}Te could also be a source.
5. Refinement of their Pn and fission yields might bring the summation calculation of reactivity to a practical level.

Decay data of ^{137}I, ^{88}Br and ^{136}Te

Half lives : GOOD! (1% or smaller)
Pn values : **large** (6% even for the most important ^{137}I)

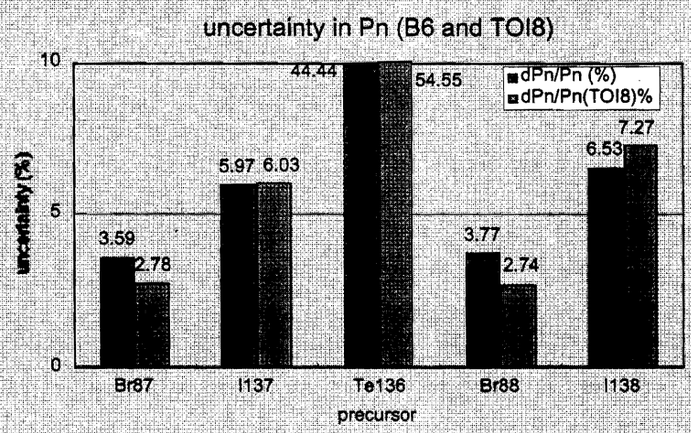

Fission yields of ^{137}I, ^{88}Br and ^{136}Te

Too large uncertainties!
Systematic study is needed for fission yield evaluation

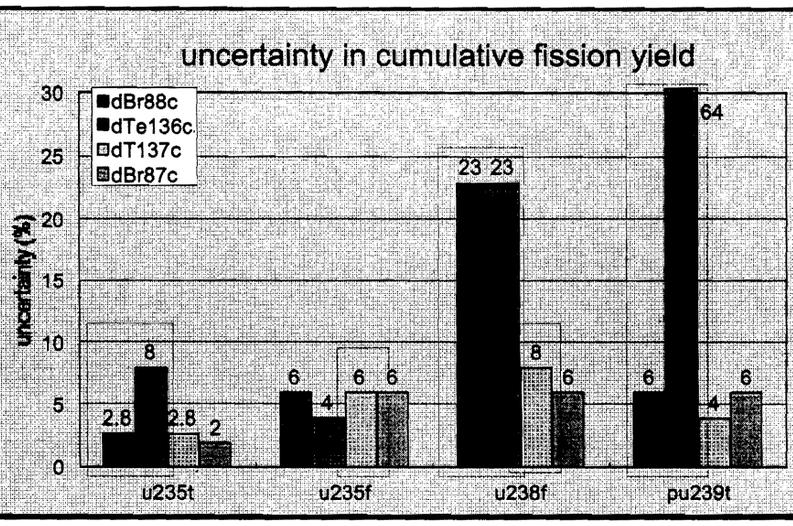

Required precision for $n_d(t)$ = 5%

Simple consideration

$(dPn/Pn)^2 + (dY/Y)^2 = (5\%)^2$ (because T is OK)

Pn : 3%, Y : 4%

Recommendation :

Solve Pn uncertainties first!

Systematic refinement of Pn and fission yield data will enable us to calculate reactivity precisely from FP data

1. Improve Pn precision
   (better than 3% to be free from the Pn uncertainties)
   2% for the most important ^{137}I, ^{88}Br and ^{87}Br
   5% for ^{136}Te

2. Then, improve their fission yields

参加者リスト

郷農 靖之(九大理)、
宇都宮 弘章(甲南大理)、
滝川 昇(東北大学理)、
篠塚 勉(東北大サイクロ)、
谷畑 勇夫(理研RIビーム)、
久保野 茂(東大CNS)、
牟田 淳(筑波大)、
寺西 高(東大CNS)、
柳澤 善行(理研ビーム物理)、
溝井 浩(東大CNS)、
折戸 学(国立天文台)、
道正 新一郎(東大CNS)、
明 孝之(北大理)、
延与 佳子(KEK素核研)、
中川 庸雄(原研)、
高階 正彰(大阪市大理)、
軽部 直人(筑波大学理)、
清水 俊(阪大理)、
住吉 光介(沼津工専)、
石山 博恒(KEK素核研)、
藤本 林太郎(東大理)、
久保 敏幸(理研加速器基盤)、
堀内 昶(京大理)、
小林 義男(理研応用原子核)、
Zhogzhou Ren(阪大RCNP)、
藤森 秀彦(千葉大)、
青井 考(東大理)、
森田 浩介(理研加速器基盤)、
武内 聡(立教大理)、
飯田 圭(東大理)、
酒井 英行(東大CNS)、
森本 幸司(理研RIビーム)、
米田 健一郎(理研応用原子核)、
藤 暢輔(原研)、
吉見 彰洋(理研応用原子核)、
井手口 英治(理研RIビーム)、
鈴木 英之(東京理科大)、
杉本 崇(東工大理)、
福田 直樹(理研放射線)
小浦 寛之(早稲田大理工)、
太田 雅久(甲南大理)、
福田 光順(阪大理)、
本林　透(立教大理)、
大塚 孝治(東大理)、
下田 正(阪大理)、
上野 秀樹(理研応用原子核)、
望月 優子(理研RIビーム)、
野谷 将広(東大核CNS)、
合川 正幸(北大理)、
佐藤 勝彦(東大理)、
宮武 宇也(KEK素核研)、
佐川 弘幸(会津大総合数理)、
堀口 隆良(広島国際大保健)、
木村 幸恵(東北大理)、
橋本 尚志(東京理科大)、
福地 知則(九州大理)、
佐藤 和則(阪大産業科学)、
親松 和浩(愛知淑徳大)、
升井 洋志(北大工知識メディア)、
野呂 哲夫(阪大RCNP)、
横山 明彦(阪大理)、
阿部 恭久(京大基研)、
渡辺 寛(理研応用原子核)、
吉田 智(法政大第一教養)、
大津 秀暁(東北大理)、
池田 清美(理研RIビーム)、
橘 孝博(早稲田大学)、
間所 秀樹(理研RIビーム)、
石田 佳久(理研RIビーム)、
鹿取 謙二(理研RIビーム)、
五味 朋子(立教大理)、
吉田 敦(理研RIビーム)、
中村 隆司(東工大基礎物理)、
Liu Xin(東大CNS)、
米田　晃(理研加速器基盤)、
櫻井 博儀(東大理)、
鷹野 正利(早稲田大理工)、
森信 俊平(九大理)、
森川 恒安(九大理)、
旭 耕一郎(東工大理)、
梶野 敏貴(国立天文台)、
和田 道治(理研原子物理)、
吉田 豊(静岡理工)、
鈴木 俊夫(日大文理)、
小川 博嗣(東工大理工)、
伊藤 誠(北大理)、
寺澤 真理子(東大天文)、
岸田 隆(理研放射線)、
今井 伸明(東大理)、
中田 仁(千葉大理)、
青山 茂義(北見工大)、
山崎 明義(東北大サイクロ)、
宇都野 譲(原研)、
中山 信太郎(徳島大総合科学)、
川端 正徳(阪大理)、
岩本 信之(国立天文台)、
渡辺 裕(理研放射線)、
下浦 享(東大CNS)、
大谷 俊介(電通大)、
加藤 静吾(山形大理)、
板垣 直之(東大理)、
今川 博人(筑波大理)、
佐藤 真樹(千葉大理)、
小沢 顕(理研RIビーム)、
須田 利美(理研RIビーム)、
小濱 洋央(理研RIビーム)、
山口 貴之(理研RIビーム)、
上 浩二(東大CNS)、
山路 修平(理研加速器基盤)、
大島 真澄(原研)、
菅原 昌彦(千葉工大)、
岩佐 直仁(東北大理)、
鄭 淳讃(KEK素核研)、
関口 仁子(東大理)、
八尋 正信(琉球大理)、